Algorithmes de contrôle sans modèle pour les micro drones de type tail-sitter

Jacson Miguel Olszanecki Barth

THÈSE

En vue de l'obtention du

DOCTORAT DE L'UNIVERSITÉ DE TOULOUSE

Délivré par :

Institut Supérieur de l'Aéronautique et de l'Espace

Présentée et soutenue par :
Jacson Miguel OLSZANECKI BARTH
le jeudi 28 mai 2020

Titre :

Algorithmes de contrôle sans modèle pour les micro drones de type tail-sitter

Model-Free Control Algorithms for Tail-Sitter Micro Air Vehicles

---

École doctorale et discipline ou spécialité :
ED AA : Automatique et Dynamique des fluides

Unité de recherche :
Équipe d'accueil ISAE-ONERA EDyF et ENAC UAV LAB

Directeur(s) de Thèse :

M. Jean-Marc MOSCHETTA (directeur de thèse)
M. Jean-Philippe CONDOMINES (co-directeur de thèse)

Jury :
Mme Caroline BERARD Professeur ISAE-SUPAERO - Présidente
M. Laurent BURLION Professeur Assistant Rutgers Université Etats-Unis - Rapporteur
M. Jean-Philippe CONDOMINES Professeur Assistant ENAC - Co-directeur de thèse
M. Eric FERON Professeur Georgia Institute of Technology Etats-Unis
M. Pascal MORIN Professeur Sorbonne Université
M. Jean-Marc MOSCHETTA Professeur ISAE-SUPAERO - Directeur de thèse
M. Hugues MOUNIER Professeur CentraleSupélec - Rapporteur

A minha mãe (*In memoriam*)
fonte inegostável de alegria,
sabedoria, positivismo,
fé e amor ...

Model-Free Control Algorithms for Tail-Sitter Micro Air Vehicles

by

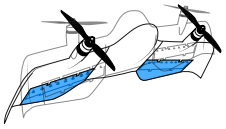

Jacson Miguel Olszanecki Barths

Submitted on April 17, 2020
in partial fulfillment of the requirements for the
Degree of Doctor of Philosophy in Aeronautics and Astronautics

Abstract

Micro Air Vehicle (MAV)s with transitioning flight capabilities, or simply Hybrid Micro Air Vehicle (HMAV)s combine the beneficial features of fixed-wing configurations in terms of endurance, with vertical take-off and landing capabilities of rotorcraft to perform five different flight phases during typical missions : vertical takeoff, transitioning flight, forward flight, hovering, and vertical landing. This promising MAV class has a wider flight envelope than conventional MAVs, which implies new challenges for both control community and aerodynamic designers. One of the major challenges of HMAVs is the fast variation of aerodynamic forces and moments during the transition flight phase, which is difficult to model and control accurately. In this thesis, we focus on the development of control laws for a specific class of HMAVs, namely tail-sitters.

In order to stabilize the HMAV and overcome its modeling problem, we propose a flight control architecture that estimates in realtime its fast nonlinear dynamics with an intelligent feedback controller. The proposed flight controller is designed to stabilize the HMAV attitude, velocity and position during all flight phases. By using Model-Free Control (MFC) algorithms, the proposed flight control architecture bypasses the need for a precise HMAV model that is costly and time consuming to obtain. A comprehensive set of flight simulations covering the entire flight envelope of the HMAV is presented, with the respective analysis for each of the flight phases.

Furthermore, the control performance and the limitations of the MFC architecture are discussed in order to introduce further applications in real flight experiments. Flight tests clarify and validate the proposed control methodology in a practical context, thus solving the principal issue of HMAVs; that is, the formulation of accurate HMAV dynamic equations to design control laws. In addition, from simple mathematical algorithms, MFC is easily implemented on a microprocessor without the need for high computational costs, such as time processing and memory resources. The results obtained provide a straightforward way in which to validate the methodological principles presented in this thesis, to certify the designed MFC parameters and to establish a conclusion regarding MFC advantages and disadvantages in theoretical and practical contexts related to aerospace systems.

Algorithmes de contrôle sans modèle pour les micro drones de type tail-sitter

par

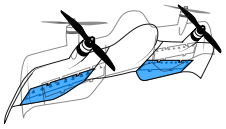

Jacson Miguel Olszanecki Barth

Thèse soumise le
17 avril 2020 en vue de l'obtention du titre de
docteur en philosophie en aéronautique et astronautique

Résumé

Les micro drones à capacités de vol de transition, ou simplement HMAVs (de l'anglais Hybrid Micro Air Vehicles), regroupent les principales caractéristiques aérodynamiques des configurations à voilure fixe, en termes d'endurance, avec les capacités de décollage et d'atterrissage vertical des voilures tournantes afin d'effectuer cinq phases de vol au cours de ses missions, telles que le décollage vertical, le vol de transition, le vol en croisière, le vol stationnaire et l'atterrissage vertical. Cette nouvelle classe de micro drones a un domaine de vol plus large que les micro drones conventionnels, ce qui implique de nouveaux défis pour les automaticiens et les concepteurs aérodynamiques. L'un des principaux défis des HMAVs est la variation rapide des forces et des moments aérodynamiques pendant la phase de vol de transition, qui est difficile à modéliser et à contrôle avec précision. Dans cette thèse, nous nous concentrons sur le développement de lois de pilotage pour une classe spécifique des HMAVs, à savoir les tail-sitters.

Afin de stabiliser la dynamique des tail-sitters et de surmonter leur problème de modélisation, nous proposons une architecture de contrôle de vol qui estime en temps réel leurs dynamiques grâce à un contrôleur à rétroaction intelligent. Le contrôleur de vol proposé est conçu pour stabiliser l'attitude du tail-sitter ainsi que sa vitesse, et sa position pendant toutes ses phases de vol. En utilisant des algorithmes de la commande sans modèle, l'architecture de contrôle de vol proposée contourne le besoin d'un modèle dynamique précis dont l'obtention est coûteuse et longue. Une série complète de simulations de vol couvrant l'ensemble du domaine de vol des tail-sitters est présentée et, pour chaque phase de vol, son analyse respective.

Avant d'introduire des expériences de vol réel, nous évaluons les performances et les limites de l'architecture de commande sans modèle en simulation. Les essais en vol permettent de clarifier et de valider notre méthodologie de contrôle dans un contexte pratique, résolvant ainsi le principal problème des tail-sitters, à savoir la formulation d'équations dynamiques précises pour concevoir les lois de commande. En outre, à partir d'algorithmes mathématiques simples, la commande sans modèle est facilement implémentée sur microprocesseurs sans nécessiter de coûts de calcul élevés, tels que la fréquence de traitement et les ressources de mémoire. Les résultats obtenus fournissent un moyen simple de valider les principes méthodologiques présentés dans cette thèse, de certifier les paramètres obtenus lors de la conception de la commande sans modèle et d'établir une conclusion concernant ses avantages et ses inconvénients dans des contextes théoriques et pratiques liés aux systèmes aérospatiaux.

Algoritmos de controle sem modelo para micro drones de tipo tail-sitter

por

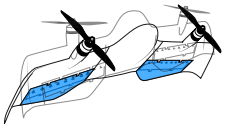

Jacson Miguel Olszanecki Barth

Tese submetida em
17 de abril de 2020 a fim de obter o
título de doutor em Aeronáutica e Astronáutica

Resumo

Micro drones com capacidades de voo de transição, ou simplesmente HMAVs (do inglês Hybrid Micro Air Vehicles) combinam as características benéficas das configurações de asa fixa em termos de resistência aerodinâmica, com as capacidades de decolagem e de aterrissagem vertical das aeronaves de asa rotativa para realizar cinco fases de voo diferentes durante missões típicas, tais como decolagem vertical, voo de transição, voo de cruzeiro, voo estacionário e aterrissagem vertical. Esta classe promissora de micro drones tem um envelope de voo mais amplo do que os micro drones convencionais, o que implica novos desafios tanto para os engenheiros de controle e automação quanto para os engenheiros aerodinâmicos. Um dos principais desafios dos HMAVs é a variação rápida das suas forças e dos seus momentos aerodinâmicos durante a fase de voo de transição, que são difíceis de modelar e de controlar com precisão. Nesta tese, nós focamos no desenvolvimento de leis de controle para uma classe específica de HMAVs, ou seja, os tail-sitters.

A fim de estabilizar o tail-sitter e superar seu problema de modelização, propomos uma arquitetura de controle de voo que estima em tempo real suas dinâmicas não lineares através de um controlador "inteligente". O controlador de voo proposto foi concebido para estabilizar a orientação do tail-sitter, bem como a sua velocidade e sua posição durante todas suas fases de voo. Usando algoritmos de controle sem modelo, a arquitetura de controle de voo proposta contorna a necessidade de um modelo dynamique preciso de tail-sitter, que é caro e demorado para ser obtido. Um conjunto abrangente de simulações de voo cobrindo todo o envelope de voo dos tail-sitters é apresentado e para cada fase de voo sua respectiva análise.

Além disso, a performance e as limitações da arquitetura de controle sem modelo são discutidas a fim de introduzir sua aplicação em experimentos de voo reais. Os testes de voo esclarecem e validam a metodologia de controle proposta num contexto prático, resolvendo assim uma das principais questões dos tail-sitters que é a formulação de suas equações dinâmicas precisas para projetar leis de controle. Além disso, a partir de algoritmos matemáticos simples, o controle sem modelo é facilmente implementado em microprocessadores sem a necessidade de altos custos computacionais, tais como frequência de processamento e recursos de memória. Os resultados obtidos proporcionam uma forma simples de validar os princípios metodológicos apresentados nesta tese, certificar os parâmetros obtidos na concepção do controle sem modelo e tirar uma conclusão sobre suas vantagens e desvantagens em contextos teóricos e práticos relacionados aos sistemas aeroespaciais.

Preface

Acknowledgments

I would first like to thank my two thesis supervisors, Jean-Marc and Jean-Philippe, for giving me the opportunity to work in the fascinating field of autonomous flight systems. Thank you Jean-Marc for your advice over the past three and a half years. Despite your personal obligations and your overbooked schedule, you provided me guidance and feedback throughout this project. Jean-Philippe, I admire the quality of your work, your organized approach to solve problems and your scientific background in the field of filtering and control. I am forever grateful for sharing part of it with me. I would like to thank you for all the support you gave me when I had my doubts, for sharing your experience and your motivation, which certainly motivated me to conclude this thesis.

I wish to thank the members of my dissertation committee: Caroline BERARD, Laurent BURLION, Hugues MOUNIER, Pascal MORIN, and Eric FERON for generously offering their time, support, guidance and good will throughout the preparation and review of this document. Then, a particular thanks is addressed to Michel Fliess and Cédric Join for sharing with me their experience in the field of Model-Free Control. Thank you Cédric for initiating me to this innovative control approach and your availability to answer my questions either remotely or presentially during my stay at the CRAN-CNRS Nancy. I would also like to thank you for accepting me into your lab and for lending me your office and some vital coffee capsules. A great thank you also goes to all the administrative staff of ENAC, especially Mathy Gonon, Patrick Senac and Hélène Weiss.

My thoughts naturally go to the ENAC UAV Lab members, from Yannick for its full support during these three and half years. Murat for all exchanges on aerodynamics and especially for the time dedicated as security pilot during flight tests in different flight conditions. Thank you also Murat for your solidarity during the AIAA SciTech Forum, you answered present whenever I asked for help. Xavier, I would like to thank you for your teamwork and your assiduous availability to carry out flight tests. Thank you Gautier for your precious knowledge on flight dynamics and your exceptional debugging skills on the Paparazzi system, which you make available to the team. Thank you Jim for the exchanges about your experience on flight dynamics and control. I also wish to thank all my colleagues from ENAC who took part in one way or another in this work: Alex, Elgiz, Fabien B., Fabien G., Guido, Michel, Titouan, and Thierry. Thank you Nicolas and Yuchen for all running moments that allowed me to decompress in times of stress. Nicolas, I admire your ability to listen, your humanism and your point of view, which differs from that of most people I know. So, thank you for our heartfelt conversations.

I will never thank enough all my family. Thank you Mon (*In Memoriam*) for all the great times I spent with you, I know you would have been so proud of me. Thank you Dad for always

supporting me in my decisions, even my most difficult ones. You are my real teachers and the reason I am who I am today. Thank you also to my brother Jan, my sister Janice, my brother in law Joel and my cousin/brother Yan. You have always inspired me so much and even without knowing it, you contributed to the achievement of this thesis.

My last words are addressed to my wife Lucie and our children Miguel and Joaquim. Thank you Lucie for your love and constant support, for all the late nights and early mornings, and for keeping me sane over the past few months, especially during my doubting moments. Thank you for being my secretary, proofreader, editor and personal advisor. But most of all, thank you for being yourself with your charm, your patience (yes, even if it seems strange, you have shown undeniable patience with me during these three and a half years) and your love that make me a fortunate man. Thank you Miguel and Joaquim, because without knowing you have been an inexhaustible source of inspiration during this period. I am proud to have you as children.

Finally, and most importantly, it is with respect for each person's convictions and without wishing to offend anyone that I thank God and the communities of the Neocatechumenal Way for supporting me in everything and for giving me the strength to live day by day with the conviction that everything comes from him.

Scientific & Industrial Contributions

This thesis contributed to the development of processes in both scientific and industrial domains. The main results obtained during this research projet were submitted, accepted, presented on international conferences, and also published on prestigious international journal (cf. appendix A). A distinguished and innovative contribution of this thesis led to the application of a national patent. According to the European Patent Convention (EPC) analysis, this patent has been validated and applied in France, and its license scope is being studied for applications in other countries.

International Journal

1. [cf. page 198] Barth, J. M. O., Condomines, J.-P., Bronz, M., Moschetta, J.-M., Join, C., and Fliess, M., "Model-free control algorithms for micro air vehicles with transitioning flight capabilities," *International Journal of Micro Air Vehicles (IJMAV)*, 12:1-22, April 2020. doi: https://doi.org/10.1177/1756829320914264.

International Conferences

1. [cf. page 221] Barth, J. M. O., Condomines, J.-P., Bronz, M., Hattenberger, G., Moschetta, J.-M., Join, C., and Fliess, M., "Towards a Unified Model-Free Control Architecture for Tail Sitter Micro Air Vehicles: Flight Simulation Analysis and Experimental Flights," *AIAA SciTech Forum: Guidance, Navigation, and Control*, Orlando, Florida, USA, pp. 1-22, January 2020. doi: https://doi.org/10.2514/6.2020-2075.

2. Bronz, M., Tal, E., Barth, J. M. O., Favalli, F., Karaman, S., "Mission-Oriented Additive Manufacturing of Modular Mini-UAVs," *AIAA SciTech Forum*, Orlando, Florida, USA, pp. 1-11, January 2020. doi: https://doi.org/10.2514/6.2020-0064.

3. [cf. page 244] Barth, J. M. O., Condomines, J.-P., Moschetta, J.-M., Cabarbaye, A., Join, C., and Fliess, M., "Full Model-Free Control Architecture for Hybrid UAVs," *American Control Conference (ACC)*, Philadelphia, PA, USA, pp. 71-78, August 2019. doi: https://doi.org/10.23919/ACC.2019.8814993.

4. Cabarbaye, A., Verdu, T., Barth, J. M. O., and Hattenberger, G., "Accurate control law for low-cost uav," *10th International Micro Air Vehicles Conference and Flight Competition*, Melbourne, Australia, pp. 150-159, November 2018.

5. [cf. page 253] Barth, J. M. O., Condomines, J.-P., Moschetta, J.-M., Join, C., and Fliess, M., "Model-Free Control Approach for Fixed-Wing UAVs with Uncertain Parameters Analysis," *23rd International Conference on Methods and Models in Automation and Robotics (MMAR)*, Miedzyzdroje, Poland, pp. 527-532, August 2018. doi: https://doi.org/10.1109/MMAR.2018.8486083.

6. [cf. page 260] Barth, J. M. O., Condomines, J.-P., Bronz, M., Lustosa, L. R., Moschetta, J.-M., Join, C., and Fliess, M., "Fixed-wing UAV with transitioning flight capabilities : Model-Based or Model-Free Control approach? A preliminary study," *International Conference on Unmanned Aircraft Systems (ICUAS)*, Dallas, TX, USA, pp. 1157-1164, June 2018. doi: https://doi.org/10.1109/ICUAS.2018.8453404.

7. Lustosa, L. R., Barth, J. M. O., Condomines, J.-P., Defaÿ, F., and Moschetta, J.-M., "Team MAVion entry in the IMAV'17 outdoor challenge–A tail-sitting trajectory-tracking Micro UAV," *9th International Micro Air Vehicles Conference and Flight Competition*, Toulouse, France, pp. 156-161, September 2017.

Patent

1. V/Ref: 18-1976. N/Ref: 071776 FR YTA-LRE.

Contents

List of Figures

List of Tables

List of Acronyms

UAV Unmanned Aerial Vehicle

DoF Degrees of Freedom

MAV Micro Air Vehicle

VTOL Vertical Take-Off and Landing

HMAV Hybrid Micro Air Vehicle

GNC Guidance, Navigation, and Control

MFC Model-Free Control

MRAC Model Reference Adaptive Control

LQR Linear Quadratic Regulator

INDI Incremental Nonlinear Dynamic Invertion

INS Inertial Navigation System

IMU Inertial Measurement Unit

AHRS Attitude and Heading Reference System

CFD Computational Fluid Dynamics

P Proportional

PD Proportional Derivative

PID Proportional Integral Derivative

LMS Least Mean Square

NLMS Normalized Least Mean Square

RLMS Recursive Least Mean Square

EKF Extended Kalman Filter

MMAC Multiple-Model Adaptive Control

LHS Left-Hand Side

SISO Single-Input Single-Output

MIMO Multiple-Input Multiple-Output

FFT Fast Fourier Transform

GPS Global Positioning System

RC Radio Control

RPM Revolutions Per Minute

DCM Direction Cosine Matrix

NASA National Aeronautics and Space Administration

DAA Detect And Avoid

MPC Model Predictive Control

SLMPC Successive Linearization Based Model Predictive Control

Nomenclature

Model-Free Control

$\hat{F} \in \mathbb{R}$ Estimator

$\lambda \in \mathbb{R}$ Non-physical constant parameter

$K_d \in \mathbb{R}$ Derivative gain

$K_p \in \mathbb{R}$ Proportional gain

Physics Parameters

$b \in \mathbb{R}$ Reference wingspan

$c \in \mathbb{R}$ Reference chord

$C_{d0} \in \mathbb{R}$ Minimal drag coefficient

$C_l \in \mathbb{R}^{1\times 3}$ Aerodynamic rolling moment coefficient

$C_m \in \mathbb{R}^{1\times 3}$ Aerodynamic pitching moment coefficient

$C_n \in \mathbb{R}^{1\times 3}$ Aerodynamic yawing moment coefficient

$C_{y0} \in \mathbb{R}$ Minimal side force coefficient

$J \in \mathbb{R}^{3\times 3}$ HMAV inertia matrix

$J_p \in \mathbb{R}$ Propeller inertia

$k_f \in \mathbb{R}$ Propeller force coefficient

$k_m \in \mathbb{R}$ Propeller moment coefficient

$S \in \mathbb{R}$ Reference wing surface

Physics Variables

$\boldsymbol{\omega_\infty} \in \mathbb{R}^3$ Freestream angular velocity

$\boldsymbol{\omega} \in \mathbb{R}^3$ Angular velocity

$\boldsymbol{v_\infty} \in \mathbb{R}^3$ Freestream velocity

$\delta_l \in \mathbb{R}$ Left flap deflection

$\delta_r \in \mathbb{R}$ Right flap deflection

$\mathcal{B}$ Body coordinate frame

$\mathcal{I}$ Inertial coordinate frame

$\omega_l \in \mathbb{R}$ Left propeller angular velocity

$\omega_r \in \mathbb{R}$ Right propeller angular velocity

$\phi \in \mathbb{R}$ Roll angle

$\psi \in \mathbb{R}$ Yaw angle

$\rho \in \mathbb{R}$ Freestream air density

$\theta \in \mathbb{R}$ Pitch angle

$M \in \mathbb{R}$ Mach number

$R_e \in \mathbb{R}$ Reynolds number

$v_{xb} \in \mathbb{R}$ Longitudinal velocity in the body coordinate frame

$v_{xi} \in \mathbb{R}$ Longitudinal velocity in the inertial coordinate frame

$v_{yb} \in \mathbb{R}$ Lateral velocity in the body coordinate frame

$v_{yi} \in \mathbb{R}$ Lateral velocity in the inertial coordinate frame

$v_{zb} \in \mathbb{R}$ Vertical velocity in the body coordinate frame

$v_{zi} \in \mathbb{R}$ Vertical velocity in the inertial coordinate frame

$x \in \mathbb{R}$ Longitudinal position in the inertial coordinate frame

$y \in \mathbb{R}$ Lateral position in the inertial coordinate frame

$z \in \mathbb{R}$ Vertical/altitude position in the inertial coordinate frame

Part I

Background

Chapter 1

Introduction

"*Start by doing what's necessary; then do what's possible; and suddenly you are doing the impossible.*"
— Francis of Assisi

The objective of this PhD thesis is to design control algorithms for HMAVs. Using only a limited prior knowledge of the system, we estimate their nonlinear dynamics and develop a control architecture to stabilize the entire HMAV flight envelope. This chapter introduces different configurations of HMAVs with their advantages and disadvantages, and focuses on the problem of modeling for control design of tail-sitter MAVs. The main guidelines of the thesis are also presented.

Contents

1.1 Autonomous Flight Systems

In the past decade, the field of UAVs has exploded. Tremendous progress has been made in the design of autonomous flight systems, which can carry out repetitive, complex, or dangerous missions more safely and more effectively than remotely controlled aircraft. UAVs have been proving their prowess in a wide range of civilian applications, whereas they were previously designed for surveillance and destruction purposes in the military sector. The possibility of using autonomous flight systems in the civil sector started with the rising accessibility proposed by the commercial industry through low-cost solutions for aerial imagery applications. Focus by aerial imagery applications has motivated the development of several projects including humanitarian aid, disaster relief, search and rescue, security operations, surveillance, precision agriculture, and civil infrastructure inspections.

In addition, this enabling technology offers the possibility to create even more improvements in the civil airspace, including delivery services for stores and urban air taxis for commuters. Therefore, UAVs are expected to be increasingly integrated in the field of civil aviation. Faced with this reality and in order to ensure their traffic across urban areas, the European Commission has adopted some rules on UAV operations through the development of an institutional, regulatory and architectural framework for the provision of airspace services, which aims to manage complex UAV operations with a high degree of automation and connectivity. The main contribution is the definition of concepts, services and potential applications to facilitate the insertion of UAVs into the civil airspace, particularly for air transports. Finally, a systematic review of existing aviation rules is underway in order to identify the necessary changes to prepare safe and secure insertion of UAV services into the airspace. This enabling framework, namely U-space, combines a set of new services and specific procedures that rely on a high level of automation and connectivity (see Figure 1.1). These services can be gradually introduced into any kind of routine mission by respecting four phases according to the desired objectives and available technologies. The first U-space (U1) has been designed for foundation services that

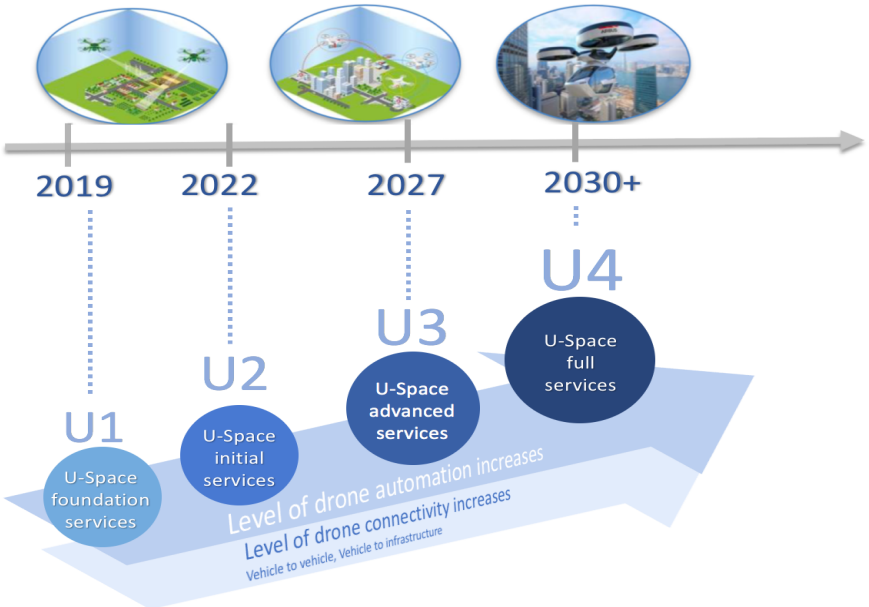

Figure 1.1: U-space framework.

Figure 1.2: Airbus A^3 Vahana Prototype Aircraft.

provide simple functions, such as the registration and identification of the UAV in a database system or geofence tools to locate a UAV in a geographical area. The second U-space (U2) offers services to support the management of UAV operations and may include flight planning, flight approval, tracking, airspace dynamic information, and procedural interfaces with air traffic control. More advanced services can be found in the third U-space (U3), with more complex operations in dense areas. For example, assistance for conflict detection with intelligent Detect And Avoid (DAA) functionalities and more reliable means of communication would lead to a significant increase in operations in different environments. The last U-space (U4) contains full services. In particular, services that offer integrated interfaces with manned aviation relying a high level of automation and connectivity for both the UAV and the entire U-space system. This framework aims to provide flexibility and open access to the airspace while ensuring safe and secure UAV operations for those on the ground or in the air. By enforcing airspace control

Figure 1.3: DHL transitioning air vehicle for delivery purposes.

through the registration and identification of UAVs, regulatory authorities will be able to safeguard privacy and minimize environmental impacts. The expected benefits of a safer airspace could encourage the development of new business models, stimulating new jobs and a more autonomous urban air mobility. These potential future services aim to address the major urban planning challenges foreseen over the next ten years by providing concrete solutions to air traffic management with more technical control research. Furthermore, the common denominator of U-spaces indicates the indispensable need for developing intelligent control systems in order to stabilize the aircraft dynamics and assist the guidance systems that accomplish the missions. This has been seen not only in the development of urban air taxi prototypes (see Figure 1.2), but also in the case of UAV configurations for delivery purposes (see Figure 1.3). The fulfillment of delivery flight missions in urban areas requires a high level of autonomy in terms of energy—in order to perform long endurance flights—combined with Vertical Take-Off and Landing (VTOL) capabilities, which are not naturally compatible.

For long endurance flight missions, the use of fixed-wing configurations is more appropriate due to their optimized aerodynamic surfaces that, in contact with a mass of air in movement, generate lift force and relieve the energy consumption of the propulsion system. Depending on their size and payload, fixed-wings can remain in flight beyond one hour. The constraint of this technology is related to take-off and landing flight phases that require a specific runway length. In terms of flight maneuverability, rotorcraft configurations are suitable because of their versatility to perform vertical take-off and landing, as well as stationary flights. However, rotorcraft configurations present a disadvantage related to their energy consumption, which results in a reduced flight time, generally ranging between 15 and 30 minutes.

Therefore, the drawbacks of rotorcraft MAVs (e.g., helicopters, quad-rotors and multi-rotors) in terms of endurance and range, with the lack of capability to take-off and landing from small areas of fixed-wing MAVs, have also encouraged the development of a new configuration, namely HMAV (see Figure 1.4). HMAV configurations are able to perform complex flight missions with VTOL capabilities combined with fast and enduring forward flights to reach distant areas. HMAVs will be one of the key players of urban air transport operations. Although the combination of two different MAV configurations in a single one provides a wider application field, the control system needs to consider the particularities of each one in order to properly carry out the designed flight mission. According to their wide flight envelope, HMAVs can be applied in a large variety of scenarios and missions. On the other hand, this complex system introduces challenges that remain to be solved, particularly in the design process of autopilot systems.

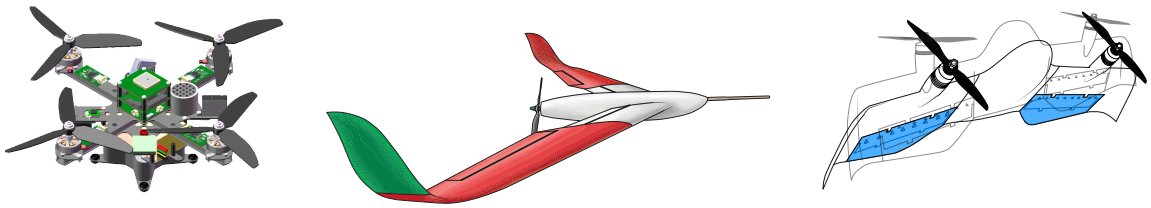

Figure 1.4: Main MAV configurations : Rotorcraft, fixed-wing and HMAV.

1.2 Hybrid Micro Air Vehicles

HMAVs remains an interesting and active research domain after decades of studies in the subject. The wide variety of complex missions involving HMAVs, combined with advances in the fields of materials and computer science, have contributed to the design of advanced MAV technological solutions with either innovative aerodynamic designs or useful mechanical structures.

1.2.1 Flight Envelope

HMAVs combine the beneficial features of fixed-wing configurations, in terms of long range and long endurance, with VTOL capabilities of rotorcrafts to perform different flight phases during typical missions, such as vertical takeoff, transitioning flight, forward flight, stationary flight, and vertical landing. A classic illustration of this wide flight envelope is shown in the Figure 1.5. This promising MAV class has a wider flight envelope than conventional ones, which implies a new challenge for both control community and aerodynamic designers.

Indeed, the increasing level of complexity across these different flight phases necessitates the development of new technological solutions. The design of efficient control techniques in order to stabilize the HMAV attitude seems to be of major concern due to of the complexity of dealing with their nonlinear dynamics, particularly during transitioning flights. This particular flight domain presents unsteady aerodynamic effects that are challenging to manage. Therefore, the use of accurate control algorithms are essential so as to improve both the safety of operations and the HMAV stability, even in windy flying conditions. From an aerodynamic and structural point of view, different HMAV concepts have been designed. In addition, new mechanical solutions have been developed in order to facilitate the control design process for transitioning flights. In the following, an overview of the main HMAV configurations is presented in order to show the particularity of each one and its transition mechanisms.

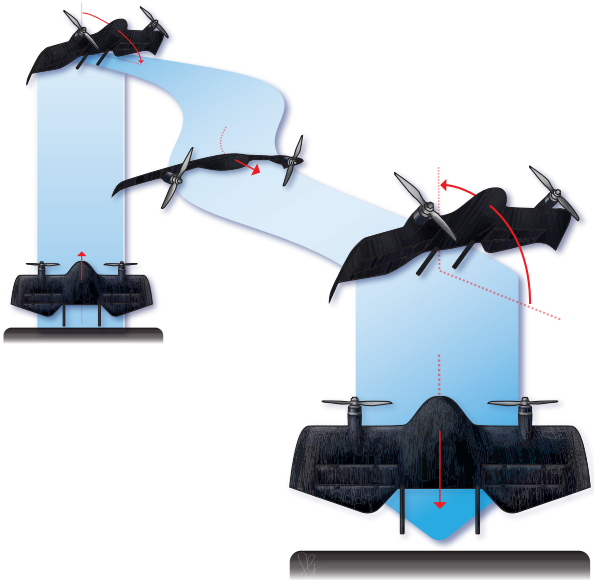

Figure 1.5: Typical flight phases of HMAVs.

1.2.2 Airframe Configurations

Airframe design remains a crucial factor in performing smooth and stable transitioning flights. In addition, the choice of the best HMAV configuration varies according to the requirements of the mission. Because of the large number of missions, the aerodynamic community has developed different HMAV configurations, which can be classified into main four types : quadplanes, tilt-wings, tilt-rotors and tail-sitters.

(a) Jouav CW-10

(b) DHL Parcelcopter

(c) KARI TR-60

(d) WingtraOne

Figure 1.6: Examples of hybrid UAV configurations.

▶ Quadplanes

Quadplanes are designed with two propulsion systems, which simplifies the control strategy to stabilize its entire flight envelope (see Figure 1.6a). The first propulsion system, composed of four rotors and four propellers is mounted upwards and controls—for most of the flight—the vertical motions of the aircraft. These actuators are mainly requested during take-off, landing and stationary flights. The second propulsion system is composed of an additional rotor-propeller in order to reach forward speeds.

Transitioning mechanisms are not required for quadplane configurations, which provide an enhanced degree of reliability for the system. Therefore, the quadplane layout presented in Figure 1.7 is relatively simple, with a reduced risk of mechanical failure (Wang, 2017). On the other hand, during forward flights with relatively high speeds, the vertical motion controlled by the aerodynamic lift force generated by the wings and the first propulsion system are disabled,

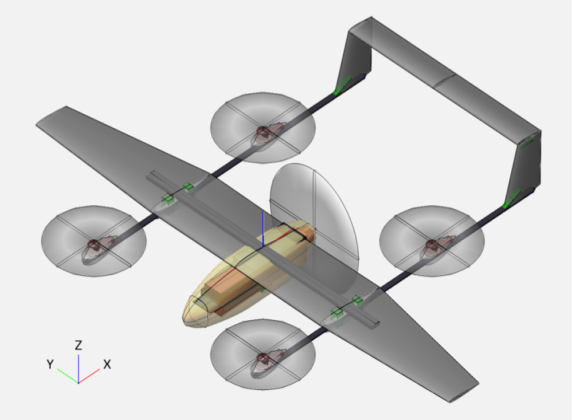


Figure 1.7: Quadplane structure proposed by (Wang, 2017).

which could create undesirable aerodynamic effects. Indeed, the fixed mounting of the propellers in a perpendicular orientation with respect to the forward flight direction, produce aerodynamic drag force who opposes the motion direction. This undesirable force results in an additional burden for the second propulsion system, and thus extra energy consumption.

For the most part, quadplane MAV configurations are stabilized by switching control methods (Gu u. a., 2017)(Flores u. a., 2017)(Hadi u. a., 2016). The switching criterion is based on the current flight speed of the quadplane MAV. Thus, at low flight speeds, the autopilot activates the stabilization algorithms for the hover flight domain, which essentially involves the stabilization of an quadcopter airframe. Then, at relatively high flight speeds, the stabilization algorithms is switched to the control of a fixed-wing configuration. The switching between flight modes is often considered as a critical and challenging point in the control of quadplanes (Hadi u. a., 2016).

▶ Tilt-Wings

The particularity of the tilt-wing's configuration is related to transitioning flights, wherein the wings need to be tilted together with the rotors (see Figure 1.6b). As such, an additional and powerful actuator is required in order to overcome the wing's torque in order to position it to the desired orientation. The input to control this additional actuator requires consideration during the design of the autopilot system. During take-off, landing and stationary flights, the wings must be positioned upwards in order to produce a thrust force that is opposed to the HMAV weight vector, which provides flight level control (see Figure 1.8). In these flight domains, with

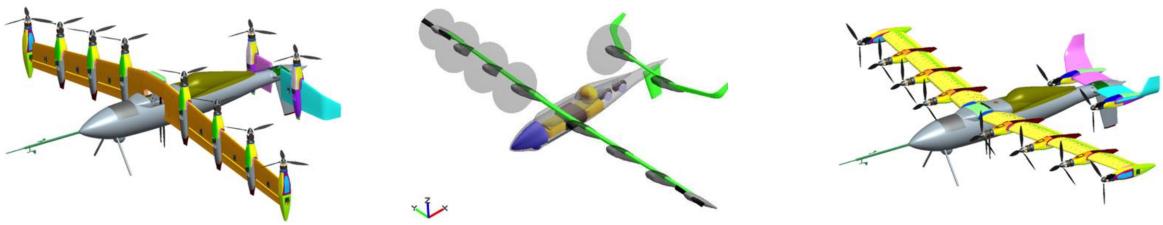

Figure 1.8: GL-10 tilt-wing CAD models showing different flight phases: hover, transition and forward flight (Rothhaar u. a., 2014).

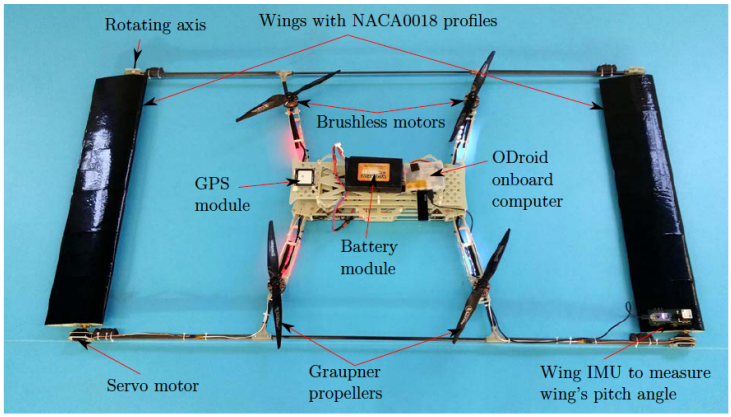

Figure 1.9: Tilt-wing MAV airframe proposed by (Phung, 2015).

the wings are oriented upwards, the aircraft will be more vulnerable to crosswinds and the autopilot system must use extra effort to deal with these disturbances. A new tilt-wing MAV design has been proposed by (Phung, 2015). Inspired by classical quadrotor MAVs, the authors have included two wings in the airframe, which can be rotated separately from the propulsion system, see Figure 1.9. The modeling approach developed for such an HMAV configuration as well as the evaluation of its energy consumption can be found in (Phung und Morin, 2014a). In addition, a control methodology for this particular tilt-wing MAV has been proposed by (Phung und Morin, 2014b) evaluating the flight control performance without airspeed measurements. In the literature, there are several tilt wing configurations and different control approaches designed to stabilize their flight dynamics (Rohr u. a., 2019)(Binz u. a., 2019)(Yildiz u. a., 2017)(Tran u. a., 2017).

▶ Tilt-Rotors

Similar to tilt-wing configurations, tilt-rotors require the implementation of an additional actuator in order to perform transitioning flights. The rotors are mounted on tilting shafts, and the transition from hover to forward flight—and from forward flight to hover—is gradually performed according to the rotor inclination (see Figure 1.6c and Figure 1.10). From a mechanical point of view, this configuration presents an advantage over tilt-wings. In the case of tilt-rotors,

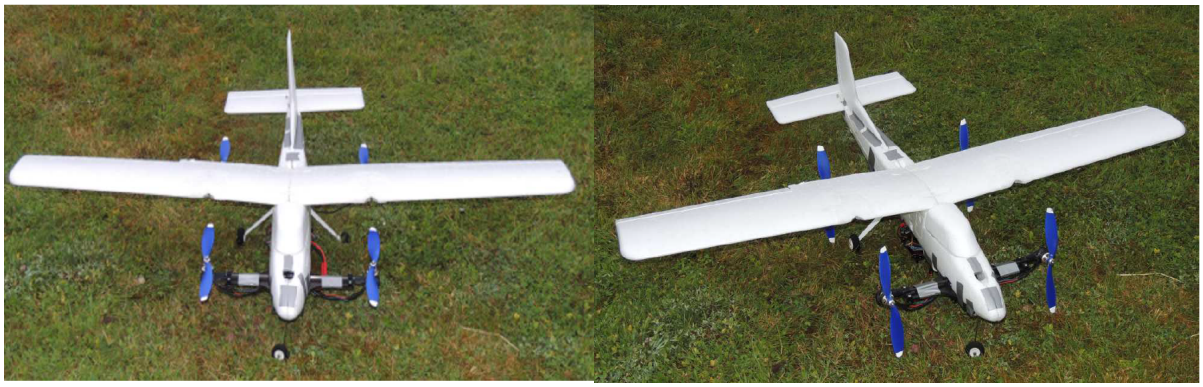

Figure 1.10: Quadplane tilt-rotor configuration showing different flight phases: hover and forward flight (Flores u. a., 2014).

Figure 1.11: Tilt-Rotor airframes.

the angle between the wing and the propeller slipstream can be adjusted by controlling the tilting shaft system. This angle plays an important role in the control of aerodynamic forces and moments: controlling it leads to better management, not only of aerodynamic flight performance during transitioning flights, but also of the stability of the system for the entire flight envelope. Figure 1.11 shows additional tilt-rotor airframes. The control literature review of tilt-rotors (Zhong u. a., 2017) presents a critical point: "*A reasonable flight dynamics model is the basis of control methods. Hence, it is necessary to focus on accurate tilt-rotors UAV modeling, model simplification and compromise between model accuracy and complexity. Simultaneously, system identification combined with the active modeling technique would result in a more accurate dynamics model, and combining the model error correction technique with traditional control design would improve the controller adaptability in the transition mode*". However, modeling of dynamics remains a challenging, time-consuming and costly process not only for tilt-rotors, but also for all HMAV configurations (Bronz u. a., 2017) (Verling u. a., 2016). Therefore, the implementation of model-based controllers and their performance will be directly affected by the quality of the dynamic model.

▶ Tail-Sitters

In contrast to the previous HMAV configurations, the tail-sitter takes off and lands vertically on its tail. During the transition from hovering to forward flight, the entire structure is inclined from the vertical to the horizontal position. Depending on the tail-sitter configuration, transitioning flights can be performed by either the generation of the aerodynamic moment created by the flaps or by the torque created by the propulsion system. Figure 1.12 shows three tail-sitter configurations. The first two perform the transition by creating an aerodynamic moment through

Figure 1.12: Tail-Sitter MAV airframes.

flap deflections, and the third most by the torque created by the propulsion system. During forward flight, in horizontal position, the tail-sitter flies like a conventional aircraft. By using classical aerodynamic techniques, designers can optimize the tail-sitter wing profile to make it more enduring in order to reduce energy consumption. Through this aerodynamic optimization process, tail-sitters can perform flight missions beyond one hour.

The disadvantage related to this HMAV configuration concerns the hovering flight domain. In this flight phase, tail-sitters are more vulnerable to crosswinds due to the vertical position of the wings. However, the disturbances caused by the wind can be tackled by using an efficient autopilot system. In addition, conventional missions involving tail-sitters are characterized by 90% in forward flight and only the rest for take-off, landing and stationary flights. Particular attention by the control community is focused on stabilizing the attitude of tail-sitters during its entire flight envelope. Their flight domain presents singularity problems while representing the tail-sitter UAV attitude in terms of Euler angles (Zeng und Guo, 2018). To overcome this problem, a mathematical attitude representation is generally adopted with quaternions (Liu u. a., 2018).

1.3 Tail-Sitter Micro Air Vehicles

The current section aims to introduce the main properties of tail-sitter MAVs and the challenges around their particular flight envelope. A brief description of relevant mechanical properties and aerodynamic phenomena are presented to show the complexity involved in obtaining a model that describes, with accuracy, the dynamics of tail-sitter MAVs. An overview of flight mechanics is presented, highlighting the challenges that rely on the control of underactuated systems and nonlinear dynamics with high coupled interactions.

1.3.1 Mechanical Properties

From a mechanical point of view, tail-sitter MAVs are characterized as underactuated systems with highly coupled dynamics. These mechanical characteristics make the process of modeling and identification a difficult task. This can be explained by the fact that, for this type of system, a given control-input acts simultaneously on different dynamics. Thus, identifying the influence of a given control-input on particular dynamics remains an important process that requires further focus.

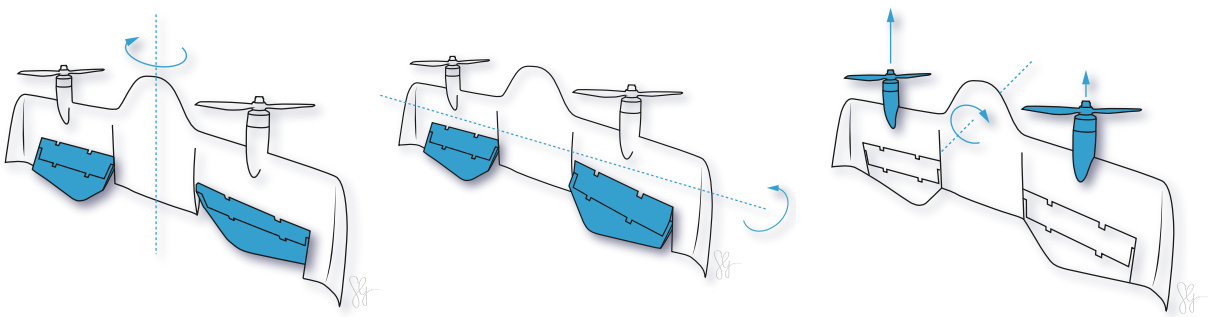

Figure 1.13: Tail-Sitter actuator effects on the attitude dynamics. From left to right : roll (ϕ), pitch (θ) and yaw (ψ) angle.

The clear definition of underactuated systems is when the system has a lower number of actuators than Degrees of Freedom (DoF). The concept of DoF is related to the number of independent parameters or coordinates that define their current state. For instance, to define the position a single particule in a plane, two coordinates are needed, which results in two DoF. To define the same particule in space, three DoF are required. In order to understand the mathematical conditions which led to the underactuated systems, consider the following definition :

Definition 1. *Underactuated systems*

Consider the following equation that describes the dynamic acceleration ($\ddot{\boldsymbol{q}}$) of a generalized coordinate :

$$\ddot{\boldsymbol{q}} = f_1(\boldsymbol{q}, \dot{\boldsymbol{q}}, t) + f_2(\boldsymbol{q}, \dot{\boldsymbol{q}}, t)\boldsymbol{u} \tag{1.1}$$

where $\boldsymbol{q} \in \mathbb{R}^n$ is the state vector, $\boldsymbol{u} \in \mathbb{R}^m$ is the vector of control-inputs and t is time. When the rank of f_2 is smaller than the dimension of the vector $\boldsymbol{q}$, the system is said to be underactuated :

$$Rank[f_2(\boldsymbol{q}, \dot{\boldsymbol{q}}, t)] < dim[\boldsymbol{q}] \tag{1.2}$$

In the case of rigid body systems, the concept of DoF is simplified and it directly concerns the translation and rotation capabilities of the system. In order to represent the current tail-sitter MAV state in space, which can be defined as a rigid body system, three translational and three rotational movements are required, resulting in six DoF. The propulsion system of tail-sitter MAVs usually have two propeller-rotors and two aerodynamic control surfaces or flaps, resulting four actuators. Therefore, tail-sitters can be classified as underactuated systems with less actuators than DoF. Although naturally underactuated and extremely unstable, tail-sitters are still a controllable system.

On the other hand, their actuators cannot accelerate the state of the system in arbitrary directions. As a consequence, this HMAV configuration cannot be commanded and oriented to follow arbitrary trajectories. Figure 1.13 illustrates the effects of actuators on the attitude dynamics of tail-sitter MAVs. The roll angle (ϕ) can be controlled by asymmetric flap deflections, the pitch angle (θ) by symmetric flap deflections and the rotation around the yaw axis (ψ) is controlled from a differential thrust setup, which creates a temporary, non-zero torque around its axis. The differential thrust setup creates a difference between the left and right propeller rotations, and so modifies the aerodynamic behavior around the flaps.

This can be explained by the slipstream effect caused by the propeller movement. This aerodynamic effect is located in a region behind the propeller where the flaps are situated. When the airflow behavior is laminar, the pressure behind the propeller is higher than the surrounding air, which increases the flap effectiveness according to the propeller rotation. When the differential thrust is activated, the slipstream in one side of the wing is different to the slipstream in the other one. This implies a different control effectiveness with an impact on the pitch and roll dynamics controlled by these flaps. Thus, an aerodynamic coupling is generated by the propeller-wing interaction. In addition, a mechanical coupling is also observed on the roll and pitch dynamics, as they are controlled by the same aerodynamic control surfaces.

1.3.2 Aerodynamic Phenomena

Based on flight mechanics, and assuming calm flight conditions without wind, tail-sitter MAVs that are in forward flight domain at equilibrium trajectories compensate for its weight by the lift force. While the drag force is compensated for by the horizontal component of the thrust. This equilibrium relationship is more complex when we evaluate the entire flight equilibrium points of tail-sitter MAVs. Indeed, in hovering flight mode, both weight and drag force are equilibrated by the vertical component of the thrust vector and the lift force by the horizontal component of thrust. During transitioning flights from hovering to forward flight and vice-versa, the equilibrated flight transition is ensured by the correct mixing of aerodynamic and propulsion forces.

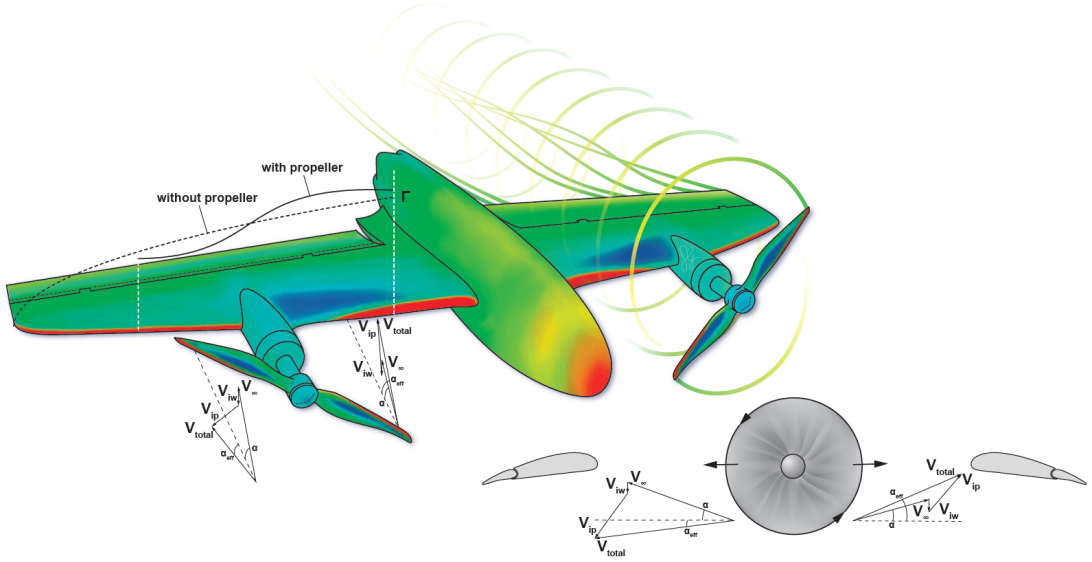

Figure 1.14: Propeller-Wing interaction.

The aerodynamic interactions between propeller and wing surface are known to be mutual. Induced velocity downstream in the propeller slipstream brings variation to the local angle of attack and dynamic pressure variations at immersed wing sections, hence a different lift distribution exists (see Figure 1.14). Wing induced velocity in return changes propeller inflow condition, and thus additional force and moment is created in the rotor disk. Analysis and design of closely coupled propeller-wing interaction should take these effects into consideration to ensure desirable flight characteristics and/or benefits from the combinations.

For these reasons, different research works can be found in the literature on the propeller-wing interaction (Leng u. a., 2019a) (Leng u. a., 2019b). The identification of these aerodynamic effects requires, for each flight operating point, the information of the surrounding air, the values of the control-inputs plus the measures of aerodynamic forces and moments acting on the system. The most accurate and reliable way of identifying aerodynamic phenomena is likely through wind tunnel campaigns, which are costly and time-consuming.

1.4 Thesis Context

In the field of autonomous flight systems, several flight missions require the use of MAVs that can fly for long periods of time. Simultaneously, these missions impose some constraining of flight trajectories that call for agile MAV configurations. The natural way to obtain power efficiency and maneuverability in one aircraft platform is by combining the features of rotorcraft with those of fixed-wings. This is the reason why new conception methods, which tie HMAV structural dynamics and the design of autopilot systems together, have emerged. Figure 1.15 illustrates an example of a flight mission involving tail-sitter MAVs from a vertical take-off, followed by the transition from hovering to forward flight; then, forward flight followed by the transition back to hovering and vertical landing. Therefore, the entire flight envelope of tail-sitter MAVs can be summarized into the following flight phases :

1. Vertical take-off
2. Hover-to-forward transition
3. Forward flight
4. Forward-to-hover transition
5. Vertical landing

Rotorcraft dynamics can be seen in flight domains related to vertical take-off and vertical landing, which are illustrated, respectively, by (1) and (5). Clearly, the dynamic behavior of fixed-wings can be observed during forward flight, which is illustrated by (3). Therefore, flight domains represented by (2) and (4) highlight the interactions between the dynamics of rotorcraft and fixed-wings during transitioning flights. The dynamics of rotorcraft and fixed-wings are known and well modeled in their respective flight domains. However, transitioning flights introduce particular dynamics with fast nonlinear behaviors that are challenging to accurately model and control.

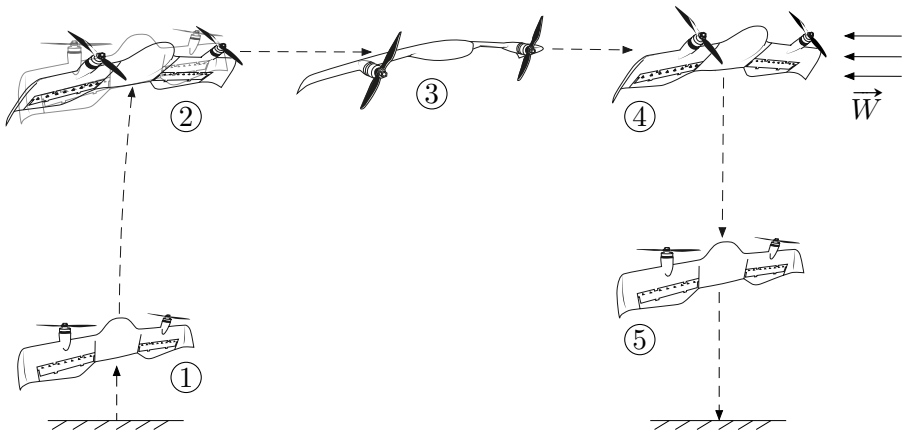

Figure 1.15: Typical flight domains of tail-sitter MAVs. The vector $\vec{W}$ represents wind disturbances.

The design of autopilot systems for tail-sitter MAVs remains a challenging task. Model-based controllers call for increased understanding of their complex dynamics. However, unsteady nonlinear aerodynamic effects present in transitioning flights are still difficult to characterize in terms of the mathematical equations for control design purposes. In view of these observations, we believe that there is a strong potential benefit in providing control techniques for tail-sitter MAVs with real-time dynamic estimation. The present thesis takes a step in this direction by proposing a unified control strategy able to stabilize the entire flight envelope.

1.5 Thesis Overview

The objective of this research project is to deliver an autopilot system for tail-sitter MAVs in which the design of the control law uses little prior knowledge of the system dynamics. Therefore, the thesis approach allows us to reduce both the costs of the wind tunnel campaigns during the identification of aerodynamic phenomena, and the time to obtain dynamic models. More precisely, model-free control architecture will be designed and evaluated to stabilize all flight phases of tail-sitter MAVs. This study involves not only simulation flights but also flight tests to demonstrate the practical benefits of such a control approach.

The thesis continues with the evaluation of the proposed control law comparing its performance with different control strategies, such as LQR and INDI. The present chapter recalls the context of this thesis and introduces the different configurations of HMAVs. The problem of modeling for designing control laws for tail-sitter MAVs was briefly summarized. Finally, the main objective of this thesis was presented.

Chapter 2 provides the literature review of current research topics on the modeling and control of tail-sitter MAVs. Their flight dynamics, aerodynamic phenomena and propulsion systems are presented in detail. In addition, a simplified tail-sitter MAV model is provided. We conclude this chapter by relating the modeling issues for designing model-based controllers and the interest of model-free control approaches.

Chapter 3 presents the Model-Free Control algorithms as well as some previous work on on-line dynamic estimation for control purposes. Additionally, we present three illustrative experiments in order to show both the principles and the potential properties of such a controller.

Chapter 4 introduces the proposed MFC architecture for tail-sitter MAVs. Simulation flight results are evaluated as well as the properties of each control block in the MFC architecture. A comparative analysis is performed in simulation in order to highlight advantages and disadvantages of model-based and model-free control approaches. For this comparative study, the LQR was designed according to the tail-sitter MAV model described in Chapter 2.

Chapter 5 validates the MFC algorithms in real-world flight conditions. The attitude stabilization provided by MFC algorithms are presented during both indoor and outdoor flight conditions. In addition, additional indoor flight tests were conducted in order to compare the performance of the INDI controller with that of the MFC approach.

Chapter 6 concludes this thesis dissertation and introduces directions for future work.

Chapter 2

Literature Review

"*The more I learn, the more I realize how much I don't know.*"
— Albert Einstein

This chapter summarizes the state-of-the-art regarding methodological approaches for the modelling and control of the different HMAV flight phases. The entire flight envelope of HMAVs currently has highly unsteady and nonlinear effects, which are challenging to model and control. The vast majority of studies dealing with the dynamics modeling of HMAVs is presented. In addition, the development of control architectures and the design of control laws are discussed for the whole flight domain of HMAVs regarding theoretical and practical contribution for their flight performances, with a particular focus on tail-sitter MAVs.

Contents

2.1 Modeling Literature Review

The formulation of mathematical equations to describe the dynamics of HMAVs has been a major focus in recent decades because of their particular flight envelope, which offers advanced flight capabilities with an attractive trade-off between power efficiency and maneuverability. These advanced flight capabilities introduce nonlinear dynamics and aerodynamic interactions that are challenging to model. On the one hand, rotorcraft and fixed-wing configurations fly at small angles of incidence, which results in small variations of aerodynamic coefficients. On the other hand, the aerodynamic coefficients of HMAVs are subject to significant variations due to the wide range of angle of incidence in transitioning flights.

2.1.1 Tail-sitter MAV dynamics and motion

Tail-sitter MAV dynamics are described by a set of differential equations that characterize the current state of the system in terms of position, orientation, but also linear and angular velocities. These variables are defined with respect to some coordinate frames.

▶ Coordinate frames and rotations

Any description of the tail-sitter MAV motion must always be made in relation to some coordinate frame. Figure 2.1 represents two coordinate frames; that is, the inertial coordinate frame, represented by $\mathcal{I} = \{\boldsymbol{x_i}, \boldsymbol{y_i}, \boldsymbol{z_i}\}$, and the body coordinate frame $\mathcal{B} = \{\boldsymbol{x_b}, \boldsymbol{y_b}, \boldsymbol{z_b}\}$, which is fixed to the MAV body.

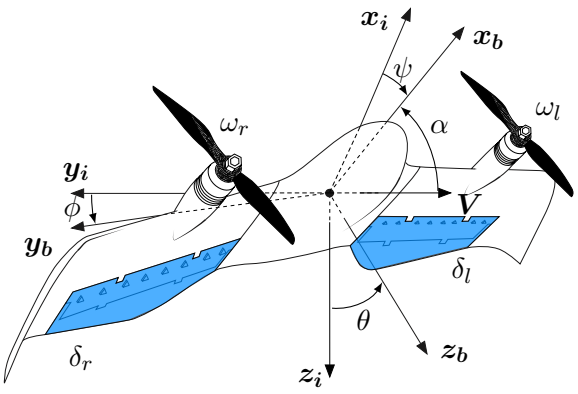

Figure 2.1: Illustration of the coordinate frames, angles and control-inputs used.

The orientation of the MAV with respect to the inertial coordinate frame is represented by Euler Angles, which are defined by ϕ the roll angle, θ the pitch angle and ψ the yaw angle. This set of angles is used to move any vector from one coordinate frame to another using a specific sequence of rotations with the following matrices :

$$\mathrm{Rot}_1(\phi) = \begin{bmatrix} 1 & 0 & 0 \\ 0 & \cos\phi & \sin\phi \\ 0 & -\sin\phi & \cos\phi \end{bmatrix} \tag{2.1}$$

$$\mathrm{Rot}_2(\theta) = \begin{bmatrix} \cos\theta & 0 & -\sin\theta \\ 0 & 1 & 0 \\ \sin\theta & 0 & \cos\theta \end{bmatrix} \tag{2.2}$$

$$\mathrm{Rot}_3(\psi) = \begin{bmatrix} \cos\psi & \sin\psi & 0 \\ -\sin\psi & \cos\psi & 0 \\ 0 & 0 & 1 \end{bmatrix} \tag{2.3}$$

For instance, the sequence of rotations Yaw-Pitch-Roll (2.7), allows us to move a vector $\boldsymbol{n} \in \mathbb{R}^3$ from the inertial coordinate frame to the body coordinate frame. This sequence of rotations is represented by the Direction Cosine Matrix (DCM). In this case, $\mathrm{DCM}_{\mathcal{B}\leftarrow\mathcal{I}}$

$$\boldsymbol{n}_{\mathcal{B}} = \mathrm{Rot}_1(\phi)\mathrm{Rot}_2(\theta)\mathrm{Rot}_3(\psi)\,\boldsymbol{n}_{\mathcal{I}} \tag{2.4}$$

$$\boldsymbol{n}_{\mathcal{B}} = \mathrm{DCM}_{\mathcal{B}\leftarrow\mathcal{I}}\,\boldsymbol{n}_{\mathcal{I}} \tag{2.5}$$

The rotation matrices (2.1), (2.2) and (2.3) are orthogonal matrices. Therefore, their inverse is equal to their transpose matrix :

$$\mathrm{Rot}(x)^{-1} = \mathrm{Rot}(-x) = \mathrm{Rot}(x)^T \tag{2.6}$$

In addition, to move a vector from the body coordinate frame to the inertial coordinate frame, the inverse of the sequence of rotations Yaw-Pitch-Roll can be used, which yields

$$\boldsymbol{n}_{\mathcal{I}} = (\mathrm{Rot}_1(\phi)\mathrm{Rot}_2(\theta)\mathrm{Rot}_3(\psi))^{-1}\,\boldsymbol{n}_{\mathcal{B}} \tag{2.7}$$

$$= \mathrm{Rot}_3(\psi)^{-1}\mathrm{Rot}_2(\theta)^{-1}\mathrm{Rot}_1(\phi)^{-1}\,\boldsymbol{n}_{\mathcal{B}} \tag{2.8}$$

$$= \mathrm{Rot}_3(-\psi)\mathrm{Rot}_2(-\theta)\mathrm{Rot}_1(-\phi)\,\boldsymbol{n}_{\mathcal{B}} \tag{2.9}$$

$$= \mathrm{DCM}_{\mathcal{I}\leftarrow\mathcal{B}}\,\boldsymbol{n}_{\mathcal{B}} \tag{2.10}$$

Thus, abbreviating cosine and sine to c and s, we have,

$$\mathrm{DCM}_{\mathcal{I}\leftarrow\mathcal{B}} = \begin{bmatrix} c\theta c\psi & s\phi s\theta c\psi - c\phi s\psi & s\phi s\psi + c\phi s\theta c\psi \\ c\theta s\psi & c\phi c\psi + s\phi s\theta s\psi & c\phi s\theta s\psi - s\phi c\psi \\ -s\theta & s\phi c\theta & c\phi c\theta \end{bmatrix} \tag{2.11}$$

The DCM represented in (2.11) has some singularities for the precise values of Euler Angles, which are known by gimbal lock problem. In order to avoid attitude singularities in the representation of high maneuverability flights, the quaternion formulation is often used. Quaternions provide a convenient mathematical notation for representing orientations and rotations in three dimensions. Compared to Euler angles they are simpler to compose and avoid the problem of gimbal lock. This mathematical notation is represented by the variable $\boldsymbol{q}$, which contains scalar and complex terms :

$$\boldsymbol{q} = q_0 + q_1\boldsymbol{i} + q_2\boldsymbol{j} + q_3\boldsymbol{k} \tag{2.12}$$

where $\boldsymbol{i}$, $\boldsymbol{j}$, $\boldsymbol{k}$ are unit vectors representing the three Cartesian axes. The quaternion scalar term is denoted by q_0, while q_1, q_2 and q_3 are its complex components. By using the quaternion formulation and the DCM in (2.13), an arbitrary vector can be moved from the inertial coordinate frame to the body coordinate frame without singularity problems.

$$\mathrm{DCM}_{\mathcal{B}\leftarrow\mathcal{I}} = \begin{bmatrix} (q_0^2 + q_1^2 - q_2^2 - q_3^2) & 2(q_1q_2 + q_0q_3) & 2(q_1q_3 - q_0q_2) \\ 2(q_1q_2 - q_0q_3) & (q_0^2 - q_1^2 + q_2^2 - q_3^2) & 2(q_2q_3 + q_0q_1) \\ 2(q_1q_3 + q_0q_2) & 2(q_2q_3 - q_0q_1) & (q_0^2 - q_1^2 - q_2^2 + q_3^2) \end{bmatrix} \tag{2.13}$$

The quaternion formulation allows us to compute the transpose of (2.13) in order to obtain the coordinate transformation of a vector in the body coordinate frame to the inertial coordinate frame, which yields

$$\mathrm{DCM}_{\mathcal{I}\leftarrow\mathcal{B}} = \begin{bmatrix} (q_0^2 + q_1^2 - q_2^2 - q_3^2) & 2(q_1q_2 - q_0q_3) & 2(q_1q_3 + q_0q_2) \\ 2(q_1q_2 + q_0q_3) & (q_0^2 - q_1^2 + q_2^2 - q_3^2) & 2(q_2q_3 - q_0q_1) \\ 2(q_1q_3 - q_0q_2) & 2(q_2q_3 + q_0q_1) & (q_0^2 - q_1^2 - q_2^2 + q_3^2) \end{bmatrix} \tag{2.14}$$

▶ Equations of Motion

An arbitrary rigid body and its motion can be modeled through two main concepts : dynamics and kinematics. Dynamics is more general, since forces and moments are taken into account to derive differential equations in order to describe the motion of the physical system. Kinematics concerns only variables that are derived from time and from the linear or angular position of the system; for example, state output variables, such as linear displacement, attitude angles, velocities and accelerations. Therefore, assuming the propulsion system and the aerodynamic models are known, we can formulate the state outputs of the tail-sitter MAV as a function of its control-inputs. The tail-sitter MAV states can be controlled via four control-inputs, such as left and right flaps plus left and right rotor-propeller rotations, represented by δ_l, δ_r, ω_l and δ_r, respectively.

Differential equations of motion, or simply equations of motion, are used to formulate the dynamics of the tail-sitter MAV. The MAV motion can be classified into translational and rotational motion, or any combinations of these. Usually, equations of motion are based on some physical law, for example, Newton's laws or Euler-Lagrange equations. In the field of HMAVs, only (Escareno u. a., 2006a) (Escareno u. a., 2006b) (Sanchez u. a., 2008) adopted the Euler-Lagrange equations, which employ the energy conservation theory, to derive equations of motion. Newton's laws are the most used formulation in the field of HMAVs, since its simplicity is to represent the total force $\boldsymbol{F} \in \mathbb{R}^3$ and the total moment $\boldsymbol{M} \in \mathbb{R}^3$ that act in the system.

Therefore, the total force can be expressed as a function of the MAV linear acceleration $\boldsymbol{a} \in \mathbb{R}^3$ and the MAV mass m. The total moment can be represented as a function of the MAV inertia J and the angular rotation vector of the MAV about its center of mass denoted by $\boldsymbol{\omega_I} = [p\ q\ r]^T$. This vector represents the angular rotation of each axis of the MAV, where p is the rotation about the x_b-axis, q is the rotation about the y_b-axis and r is the rotation about the z_b-axis. The following Newton's laws are valid and applied on the inertial coordinate frame.

$$\boldsymbol{F} = \sum_i \boldsymbol{F}_i \Leftrightarrow m \frac{d}{dt}\boldsymbol{v} \Leftrightarrow m\,\boldsymbol{a} \tag{2.15}$$

$$\boldsymbol{M} = \sum_i \boldsymbol{M}_i \Leftrightarrow \frac{d}{dt}H \Leftrightarrow J\,\boldsymbol{\omega_I} \tag{2.16}$$

Where $\boldsymbol{v}$ represents the MAV velocity defined in the inertial coordinate frame and $H = J\,\boldsymbol{\omega_I}$ denotes the MAV angular momentum. The moment of inertia matrix is defined by

$$J = \begin{bmatrix} J_{xx} & -J_{xy} & -J_{xz} \\ -J_{yx} & J_{yy} & -J_{yz} \\ -J_{zx} & -J_{zy} & J_{zz} \end{bmatrix} \tag{2.17}$$

and its inertial terms $J_{(..)}$ are fixed in the body coordinate frame. Newton's laws are only applied on the inertial coordinate frame. Thus, if the body coordinate frame is rotating with rotation vector $\boldsymbol{\omega_b}$, then for any vector denoted by $\boldsymbol{n}$, its derivative $\frac{d}{dt}\boldsymbol{n}$ in the inertial frame is :

$$\left.\frac{d\,\boldsymbol{n}}{dt}\right|_I = \left.\frac{d\,\boldsymbol{n}}{dt}\right|_B + \boldsymbol{\omega_b} \times \boldsymbol{n} \tag{2.18}$$

Based on the previous equation, Newton's laws can be rewritten as

$$\boldsymbol{F} = m\ \left.\frac{d\,\boldsymbol{v}}{dt}\right|_B + m\,\boldsymbol{\omega_b} \times \boldsymbol{v} \tag{2.19}$$

$$\boldsymbol{M} = \left.\frac{d\,H}{dt}\right|_B + \boldsymbol{\omega_b} \times H \tag{2.20}$$

Therefore, we obtain

$$\begin{bmatrix} F_x \\ F_y \\ F_z \end{bmatrix} = m \begin{bmatrix} \dot{v}_{xb} + q\,v_{zb} - r\,v_{yb} \\ \dot{v}_{yb} + r\,v_{xb} - p\,v_{zb} \\ \dot{v}_{zb} + p\,v_{yb} - q\,v_{xb} \end{bmatrix} \tag{2.21}$$

and

$$\begin{aligned}
\begin{bmatrix} M_x \\ M_y \\ M_z \end{bmatrix} &= \begin{bmatrix} J_{xx} & -J_{xy} & -J_{xz} \\ -J_{yx} & J_{yy} & -J_{yz} \\ -J_{zx} & -J_{zy} & J_{zz} \end{bmatrix} \begin{bmatrix} \dot{p} \\ \dot{q} \\ \dot{r} \end{bmatrix} + \boldsymbol{\omega_b} \times \begin{bmatrix} J_{xx} & -J_{xy} & -J_{xz} \\ -J_{yx} & J_{yy} & -J_{yz} \\ -J_{zx} & -J_{zy} & J_{zz} \end{bmatrix} \begin{bmatrix} p \\ q \\ r \end{bmatrix} \\
&= \begin{bmatrix} J_{xx}\dot{p} & -J_{xy}\dot{q} & -J_{xz}\dot{r} \\ -J_{yx}\dot{p} & J_{yy}\dot{q} & -J_{yz}\dot{r} \\ -J_{zx}\dot{p} & -J_{zy}\dot{q} & J_{zz}\dot{r} \end{bmatrix} + \boldsymbol{\omega_b} \times \begin{bmatrix} J_{xx}p & -J_{xy}q & -J_{xz}r \\ -J_{yx}p & J_{yy}q & -J_{yz}r \\ -J_{zx}p & -J_{zy}q & J_{zz}r \end{bmatrix} \\
&= \begin{bmatrix} J_{xx}\dot{p} - J_{xy}\dot{q} - J_{xz}\dot{r} + q(-pJ_{xz} - qJ_{yz} + rJ_{zz}) - r(-pJ_{xy} + qJ_{yy} - rJ_{yz}) \\ -J_{xy}\dot{p} + J_{yy}\dot{q} - J_{yz}\dot{r} - p(-pJ_{xz} - qJ_{yz} + rJ_{zz}) + r(pJ_{xz} - qJ_{xy} - rJ_{xz}) \\ -J_{xz}\dot{p} - J_{yz}\dot{q} + J_{zz}\dot{r} + p(-pJ_{xy} + qJ_{yy} - rJ_{yz}) - q(pJ_{xz} - qJ_{xy} - rJ_{xz}) \end{bmatrix}
\end{aligned}$$

For symmetrical MAVs about the x_b-z_b plane, we have $J_{xy} = J_{yz} = 0$.

$$\begin{bmatrix} F_x \\ F_y \\ F_z \end{bmatrix} = m \begin{bmatrix} \dot{v}_{xb} + q\,v_{zb} - r\,v_{yb} \\ \dot{v}_{yb} + r\,v_{xb} - p\,v_{zb} \\ \dot{v}_{zb} + p\,v_{yb} - q\,v_{xb} \end{bmatrix} \tag{2.22}$$

And,

$$\begin{bmatrix} M_x \\ M_y \\ M_z \end{bmatrix} = \begin{bmatrix} J_{xx}\dot{p} - J_{xz}\dot{r} - qpJ_{xz} + qrJ_{zz} - rqJ_{yy} \\ J_{yy}\dot{q} + J_{xz}p^2 - prJ_{zz} + rpJ_{xx} - J_{xz}r^2 \\ -J_{xz}\dot{p} + J_{zz}\dot{r} + J_{yy}pq - J_{xx}qp + J_{xz}qr \end{bmatrix} \tag{2.23}$$

We can notice in (2.22) that translational variables (v_{xb}, v_{yb}, v_{zb}) depend on rotational terms (p, q, r), but according to (2.23) rotational dynamics are not a function of effects due to translational movements. On the other hand, total moments (M_x, M_y, M_z) depend on both the current orientation and the velocity of the MAV. For this reason, the MAV moments depend on rotational and translational variables.

▶ Forces and Moments

Once the equations of motion have been formulated, the different forces and moments need to be characterized in order to properly represent the MAV dynamics. In aerospace systems, these forces and moments can be classified into three main sources, such as forces and moments generated by the propulsion system ($\boldsymbol{F_p}$, $\boldsymbol{M_p}$), by the gravitational effect ($\boldsymbol{F_g}$, $\boldsymbol{M_g}$) and by aerodynamics ($\boldsymbol{F_a}$, $\boldsymbol{M_a}$). In the following, forces (2.24) and moments (2.25) will be modeled and represented in the body coordinate frame.

$$\boldsymbol{F_b} = \sum_i \boldsymbol{F}_i \Leftrightarrow \boldsymbol{F_{pb}} + \boldsymbol{F_{gb}} + \boldsymbol{F_{ab}} \tag{2.24}$$

$$\boldsymbol{M_b} = \sum_i \boldsymbol{M}_i \Leftrightarrow \boldsymbol{M_{pb}} + \boldsymbol{M_{gb}} + \boldsymbol{M_{ab}} \tag{2.25}$$

With regard to the modelling of the propulsion system, three coupled actuator components are involved; that is, propeller, rotor and aerodynamic control surfaces or plaps. Generally speaking, the thrust T_i, created by the rotor-propeller rotation ω_i, varies as flight speed changes. In general flight domains, for the ith rotor-propeller, the thrust can be modeled as (Powers u. a., 2013) :

$$T_i = \frac{\rho\, a\, n_b\, c_b\, \omega_i^2\, R^3}{2}\left(\frac{\theta_r}{3} + \frac{(v_{xb}^2 + v_{yb}^2)\,\theta_r}{2\,\omega_i^2\, R^2} + \frac{v_{zb} + \nu_i}{2\,\omega_i\, R}\right) \tag{2.26}$$

where a is the lift curve slope of the blade profile, n_b refers to the number of blades, c_b is the blade chord, R indicates the rotor radius, θ_r is the rotor pitch angle and ν_i is the velocity induced to pass through the propeller disk. The thrust model in (2.26) can be derived from additional aerodynamic force on the thrust direction and is mainly caused by a so called thrust variance effect (Huang u. a., 2009). However, in practical designs of model-based control laws, the propulsion system is simplified assuming constant air density and neglecting the interactions between the propeller and the flaps. In addition, the MAV velocity is often neglected as well to describe the thrust force (Kai u. a., 2017) :

$$T_i = k_f\, \omega_i^2 \tag{2.27}$$

where k_f is a positive constant coefficient, which can be experimentally determined using averaged thrust to rotor-propeller rotations. The thrust force T_i generated by the propulsion system acts in a specific axis of the system according to its location and orientation. Assuming the body coordinate frame illustrated above, the propulsion system force acts in the x_b-axis of the tail-sitter MAV, and it is given by

$$\boldsymbol{F_{pb}} = \begin{bmatrix} \sum_i T_i \\ 0 \\ 0 \end{bmatrix} \tag{2.28}$$

The moment created by the propulsion system M_{pb} can be modeled according to the thrust created by the ith rotor-propeller and its distance $\boldsymbol{d_i}$ with respect to the tail-sitter MAV center of mass.

$$\boldsymbol{M_{pb}} = \sum_i T_i \times \boldsymbol{d_i} \tag{2.29}$$

Gravitational force is proportionally modeled to the mass acting on the tail-sitter MAV center of mass in the z_i direction. In the body coordinate frame it is

$$\boldsymbol{F_{gb}} = m\, \mathrm{DCM}_{\mathcal{B}\leftarrow\mathcal{I}} \begin{bmatrix} 0 \\ 0 \\ g \end{bmatrix} \Leftrightarrow\; m\, g \begin{bmatrix} 2(q_1 q_3 - q_0 q_2) \\ 2(q_2 q_3 + q_0 q_1) \\ q_0^2 - q_1^2 - q_2^2 + q_3^2) \end{bmatrix} \tag{2.30}$$

where g is the acceleration due to gravity. Because the gravitational force acts on the system center of mass, it does not generate a moment $\boldsymbol{M_{gb}} = 0$. Finally, aerodynamic forces $\boldsymbol{F_{ab}} \in \mathbb{R}^3$ and moments $\boldsymbol{M_{ab}} \in \mathbb{R}^3$ can be defined in the body coordinate frame by

$$\boldsymbol{F_{ab}} = \frac{1}{2}\,\rho\, S\, V^2 \begin{bmatrix} C_X \\ C_Y \\ C_Z \end{bmatrix} \tag{2.31}$$

$$\boldsymbol{M_{ab}} = \frac{1}{2}\,\rho\, S\, V^2 \begin{bmatrix} c\, C_l \\ b\, C_m \\ c\, C_n \end{bmatrix} \tag{2.32}$$

where $\rho \in \mathbb{R}$ is the air density, $S \in \mathbb{R}$ represents the reference surface, V is the airspeed, $c \in \mathbb{R}$ denotes the wing chord and $b \in \mathbb{R}$ is the wingspan. Aerodynamic coefficients related to forces (C_X, C_Y, C_Z) and moments $(C_l, C_m, C_n,)$ can be identified from wind tunnel campaigns as function of the system control-inputs and the surrounding air flow. In the case of the control of classical MAVs, such as rotorcraft and fixed-wings, these aerodynamic coefficients are characterized on specific flight operating domains. Therefore, aerodynamic coefficients of rotorcraft MAVs are identified in hovering flight domains and in forward flight domain for fixed-wing MAV configurations. However, tail-sitter MAVs introduces new challenges with a time-consuming process for identifying aerodynamic coefficients within their entire flight envelope.

The particularity of tail-sitter MAV modeling is related to the interactions between the propulsion system and aerodynamic effects. The block diagram illustrated in Figure 2.2 highlights the interaction between them, an additional complexity can be noted in the modelling of aerodynamic forces and moments, which are functions of the propulsion system, and vice versa. Finally, these interactions also affect the identification of aerodynamic phenomena.

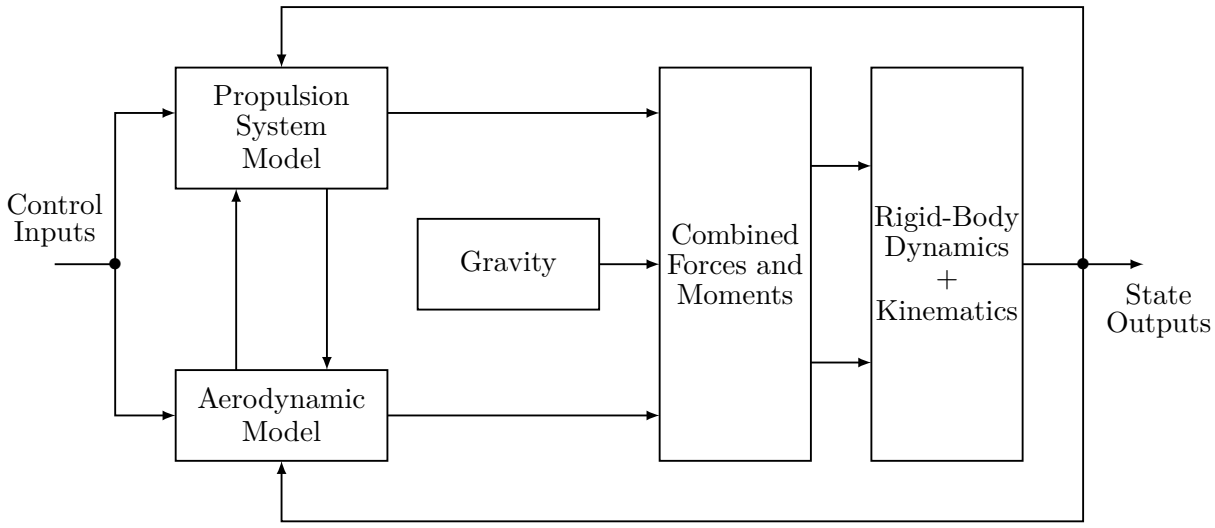

Figure 2.2: Overall tail-sitter MAV flight dynamics modeling.

2.1.2 Aerodynamic identification

Differential equations of motion introduced in the previous section will be used in order to describe the dynamics of tail-sitter MAVs as functions of their control-inputs. The accuracy of these equations and their reliability to represent the real dynamics of tail-sitter MAVs depend on the coefficients used in these equations. For this reason, these coefficients must be carefully identified. The critical point of their identification, which has been highlighted by various works in the literature, concerns the challenging and time-consuming approach of identifying aerodynamic coefficients.

Indeed, the wide flight envelope of tail-sitter MAVs, and their unusual flying conditions at high angles of attack, have introduced some challenges for the aerodynamic community. The most sensitive issues are related to the challenges of low Reynolds number flow, propeller-wing interactions and the fast variation of aerodynamic forces and moments during transitioning flight phases. Low-Reynolds number flows associated with MAVs tend to be less efficient than those of

larger ones. Furthermore, in the critical regime where MAVs fly, it is difficult to predict whether the boundary layer is going to be laminar or turbulent (Moschetta, 2014), which increases the level of complexity in identifying aerodynamic coefficients. One method to identify aerodynamic coefficients is related to numerical analysis, such as Computational Fluid Dynamics (CFD). However, the literature review in the field of tail-sitter MAVs presents few existing works based on this approach (Ang u. a., 2014) (Carrión u. a., 2017). In view of analyzing different flight regimes, CFD has its strengths and weaknesses, as remarked by (Frink u. a., 2017) : *"After eight years of focused collaboration among a diverse international body of computational and experimental aerodynamicists and flight simulation experts, the resounding conclusion was that, although current CFD methodology could readily predict the S&C (stability and control) behavior of an aircraft flying in linear regions of a flight envelope, it is still extremely difficult to adequately capture the static and dynamic S&C characteristics associated with highly nonlinear flows."*

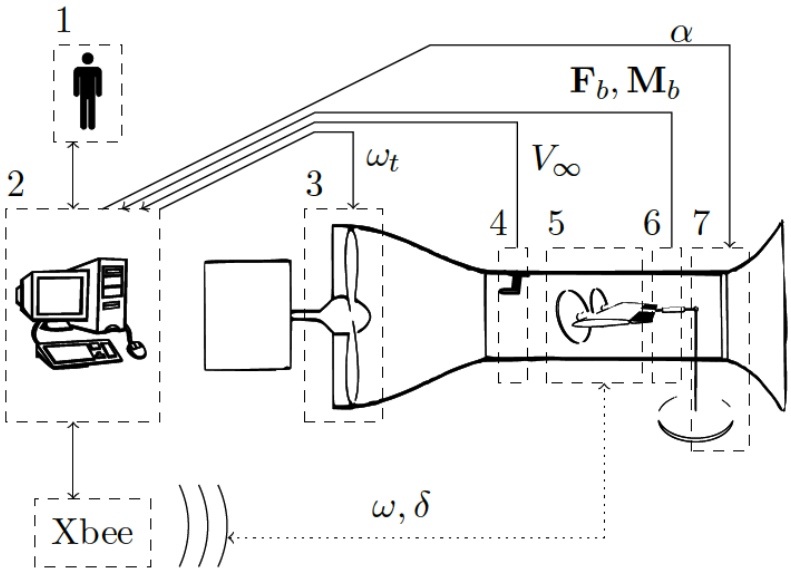

Figure 2.3: Low wind tunnel campaign from (Lustosa, 2017, p. 45).

Probably the most accurate and reliable way of identifying aerodynamic coefficients is through wind tunnel campaigns. However, this experimental approache requires, for each flight operating point, the information of the surrounding air, the values of the control-inputs plus the measures of aerodynamic forces and moments ($\boldsymbol{F_b}$, $\boldsymbol{M_b}$) acting in the body system (see Figure 2.3). In such a setup, different components are required, among which we can mention :

1. The user in order to manage the experiment, the different calibrations and the acquired data;

2. A computer system to synchronize the different measurements, record data and send commands to the wind tunnel or to the MAV. For instance, send changes to the wind tunnel propeller rotation (ω_t) or send new values to the MAV actuators (ω, δ);

3. Low speed wind tunnel in order to match the MAV flight speeds, with sufficiently stable air flows. Low speed is referred to the air flow lower than 100 m/s, for which the incompressible flow condition is satisfied;

4. Pitot tube device in order to measure the flow speed (V_∞) in the test section of the wind tunnel;

5. MAV model adapted to the wind tunnel campaign with an external or its own power supply;

6. Six component wind tunnel balance in order to measure, three forces (lift, side, and drag) and three moments (roll, pitch and yaw), to completely describe the conditions on the MAV model. Wind tunnel balances, comprised by several hardware and software components, directly provide the pursued measurements, with high accuracy and reliability;

7. A mechanism for fixing the MAV model through different orientations. This mechanism defines the angles of the MAV nose with respect to the air flow (α, β);

A comprehensive analysis of a quadrotor tail-sitter MAV dynamics was presented by (Lyu u. a., 2018b) based on this wind tunnel campaign setup. In order to understand the behavior of aerodynamic forces and moments within the entire flight envelope, the authors proposed to study different flight operating points, for which a variety of angles of attack and wind speeds were defined. Figure 2.4 shows the wind tunnel campaign with the sensors and the rotation mechanism used to place the tail-sitter MAV in different orientations. The aerodynamic coefficients shown in Figure 2.5 have been identified for different wind speed values, varying from 2.9 m/s to 18.9 m/s. The full range of angles of attack has been evaluated.

The authors interpolated the variations of lift and drag coefficients as a function of the angle of attack without the contribution of the propulsion system. Therefore, the effect of propeller-wing interaction in the aerodynamic coefficients has been neglected. A similar approach is employed in (VanderMey, 2011) (Lustosa u. a., 2014), who neglect the aerodynamics forces and moments created from the interaction of the propeller slipstream with the wing. Indeed, from the point of view of HMAV modeling for control design, the propeller-wing interaction is

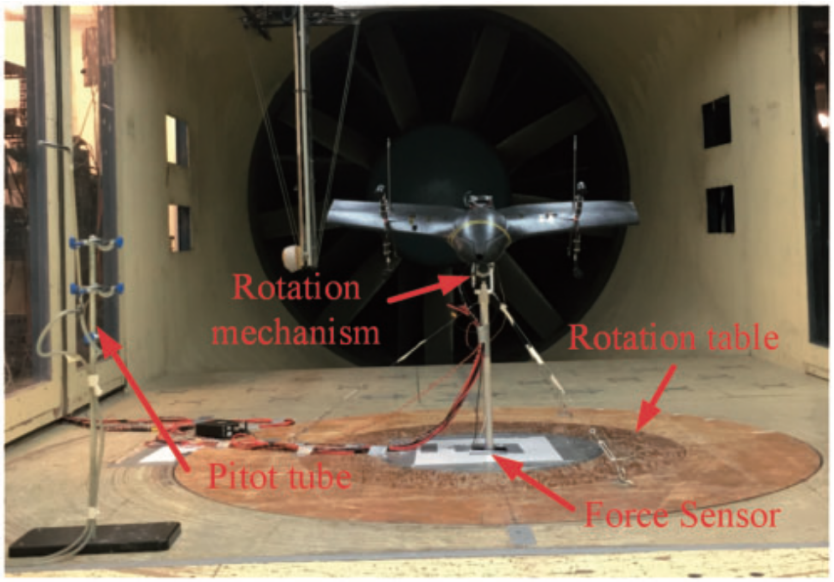

Figure 2.4: Full-scale quadrotor tail-sitter MAV without propellers in wind tunnel test from (Lyu u. a., 2018b, p. 310).

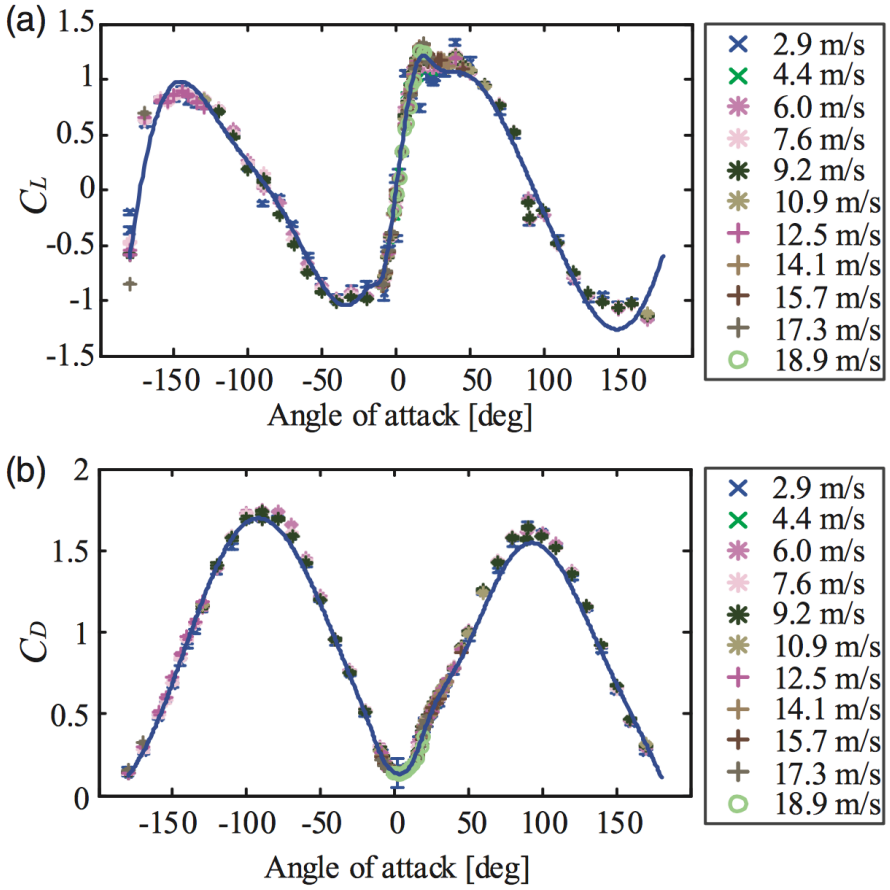

Figure 2.5: Identified lift and drag coefficients from (Lyu u. a., 2018b, p. 311).

often neglected or simplified. However, the authors in (Stone, 2004) modeled a tail-sitter MAV using a standard 6-DoF nonlinear model considering this aerodynamic interaction. The authors mentioned a particular complexity for modelling aerodynamic nonlinearities due to the change in the forces generated by the propeller in comparison to those due to the freestream dynamic pressure. This change occurs as the MAV goes from low speed hovering flight (propeller and propeller slipstream forces dominate) to high speed forward flight (freestream dynamic pressure dominate). Aerodynamic effects on tail-sitter MAVs are directly associated with the surrounding airflow, which is affected by the flow induced by the propellers as well as by the perturbation of this flow due to both the tail-sitter MAV motion and gust disturbances.

In order to determine the propeller slipstream velocity and its effects in the wing, (Escareno u. a., 2007) proposed a model based on actuator disc theory (Chattot, 2014), with the following assumptions; that is, the propeller normal force was neglected, the slipstream angle of attack is assumed to be small, the aerodynamic surface of tail-sitter MAV are fully submerged in the propeller slipstream, the drag force is assumed small compared to thrust and lift forces in hovering flight, in addition, the drag force is supposed to be small compared to lift force during forward flight. During transitioning flight phases, the slipstream angle of attack and the drag force should be modeled more accurately in order to predict their realistic effect in the tail-sitter MAV dynamics. As the authors have argued, it is important to consider these forces properly because they are fundamentally affected by the vehicle's motion and thus modify its dynamics.

There is a relatively small body of literature that is concerned with analytical modelling of the global tail-sitter MAV dynamics. (Lyu u. a., 2017a) fits wind tunnel data to a given aerodynamic coefficient formula in function of the angle of attack to obtain analytical models. Particular attention should be paid to the pitch moment aerodynamic coefficient (C_m) in Figure 2.6, which is challenging to identify from its data. The author in (Pucci, 2013) employs a different approach with a family of algebraic functions to approximate experimental aerodynamic characteristics into analytical equations. The experimental data used by the author are available in (Davis u. a., 2004) and correspond to a flat wing of airfoil NACA 0021 with Mach and Reynolds numbers equal to (M, Re) $\approx$ (0.3, 160.10^3). Figure 2.7 shows the obtained analytical equations as a function of the angle of attack. These equations were used, along with the equations of motion, to develop a generic flight simulator in order to represent the dynamics of a transitioning aerial vehicle.

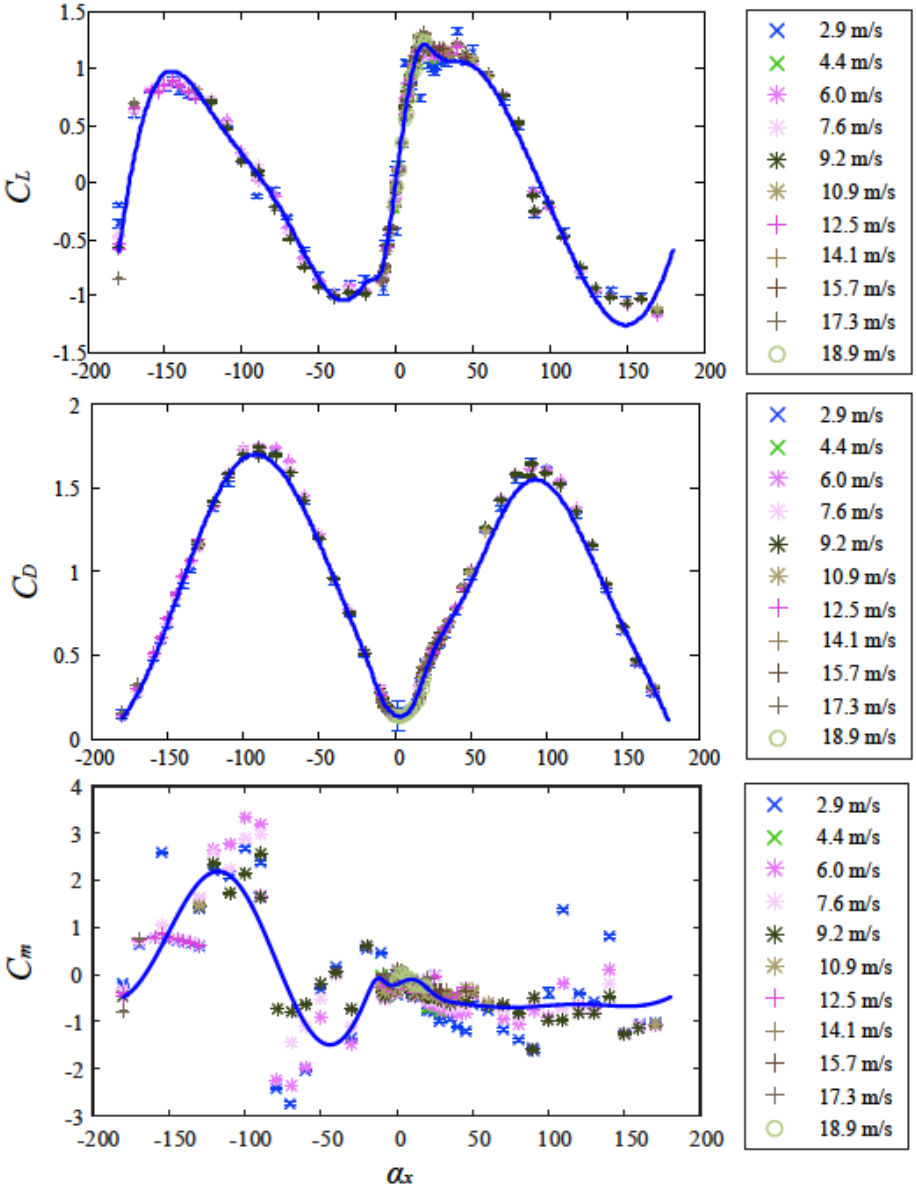

Figure 2.6: Aerodynamic coefficients from (Lyu u. a., 2017a, p. 3928).

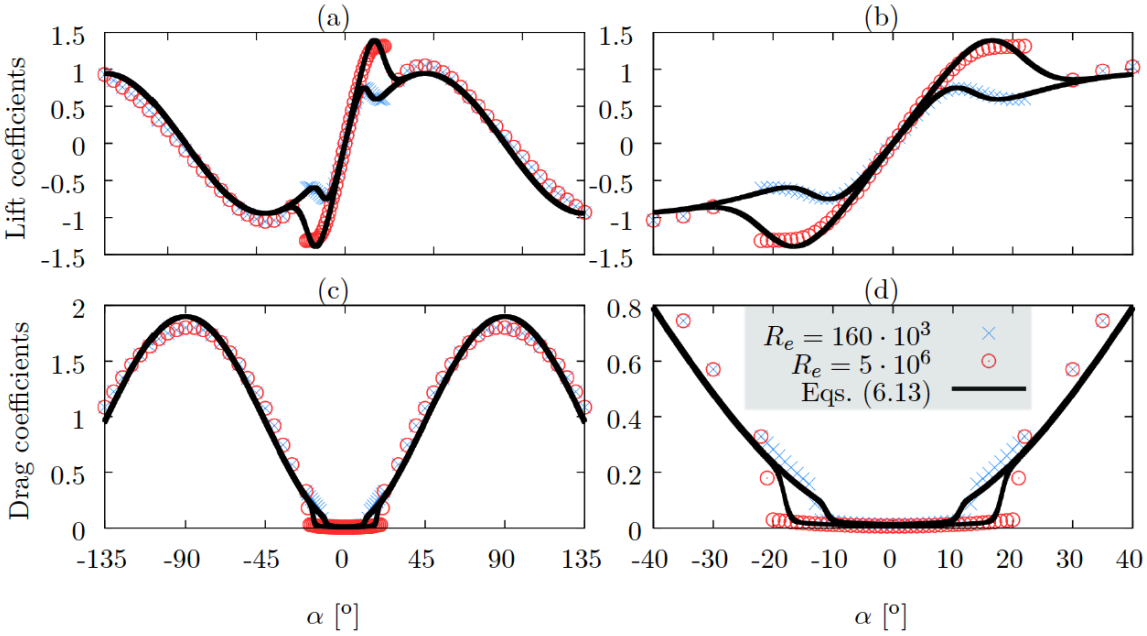

Figure 2.7: Aerodynamic coefficients from (Pucci, 2013, p. 62).

In the field of PIV measurements, (Kubo und Suzuki, 2012) proposed the analysis of the airflow around the flaps of a tail-sitter MAV prototype at high angles of attack. In this analysis, the problem of control effectiveness has been illustrated at 60° of angle of attack, which shows the limits of such a system. At 60° of angle of attack, the flaps produced insufficient pitch moment to ensure a stable transitioning flight. The authors invoked two options to improve the aerodynamic pitch moment, such as the use of a variable pitch propeller or an additional cyclic pitch control mechanism, which would likely complicate the identification and the control of the system.

To conclude this brief literature review on identication of tail-sitter MAVs, we present a more complete work on the modeling of aerodynamic effects taking into account the propeller-wing interaction (Lustosa, 2017). From wind tunnel campaign, the author analyzed the different forces and moments of the system, for different values of angles of attack, sideslip angles, wind speeds, rotor-propeller rotations and flap deflections. In addition, an analytical model has been developed describing, as accurately as possible, the tail-sitter MAV dynamics according to the wind tunnel data. This model will be detailed in the following section, with minor modifications, and will be used in this work for flight simulation purposes.

2.1.3 Revisited $\Phi-$theory

An analytic continuous singularity-free formulation of aerodynamic forces and moments acting in a wing over a complete 360° angle of attack, called $\Phi-$theory is presented (Lustosa u. a., 2019). The wing with a surface S, is immersed in an incompressible and inviscid airflow with air density ρ. The freestream velocity is composed by the linear term $\boldsymbol{v}_\infty \in \mathbb{R}^3$ and the angular component defined by $\boldsymbol{\omega}_\infty \in \mathbb{R}^3$ which, in the absence of wind, is equal to the tail-sitter MAV angular velocity $\boldsymbol{\omega}_b \in \mathbb{R}^3$. This formulation of aerodynamic forces and moments is defined in

the body coordinate frame and given by :

$$\begin{pmatrix} \boldsymbol{F_{a_b}} \\ \boldsymbol{M_{a_b}} \end{pmatrix} = -\frac{1}{2}\rho S\eta C\Phi(\boldsymbol{\eta_b})C\boldsymbol{\eta_b} \tag{2.33}$$

where

$$\eta = \sqrt{v_\infty^2 + \mu\, c^2\omega_\infty^2}, \text{ with } \mu \in \mathbb{R} > 0 \tag{2.34}$$

and

$$\boldsymbol{\eta_b} = \begin{pmatrix} \boldsymbol{v}_\infty \\ \boldsymbol{\omega}_\infty \end{pmatrix} \tag{2.35}$$

The vector $\boldsymbol{\eta_b}$ describes the linear and angular freestream velocities defined in the body coordinate frame. The matrix C denotes the reference wing parameters in an extended representation,

$$C = \begin{pmatrix} I_{3\times3} & 0_{3\times3} \\ 0_{3\times3} & \begin{bmatrix} \mathrm{b} & 0 & 0 \\ 0 & \mathrm{c} & 0 \\ 0 & 0 & \mathrm{b} \end{bmatrix} \end{pmatrix} \tag{2.36}$$

where b and c are, respectively, the wingspan and the mean chord. The matrix $\Phi \in \mathbb{R}^{6\times6}$, which is subdivided into four matrices $\Phi^{(\cdot)} \in \mathbb{R}^{3\times3}$, represents the interactions between aerodynamic forces and moments with linear and angular freestream velocities :

$$\Phi = \begin{pmatrix} \Phi^{(fv)} & \Phi^{(fw)} \\ \Phi^{(mv)} & \Phi^{(mw)} \end{pmatrix} \tag{2.37}$$

The Φ parameters are deduced from thin airfoil theory (we refer the interested reader to (Lustosa, 2017, p. 30) for further information). Nonetheless, we mention that,

$$\Phi_0^{(fv)} = \begin{pmatrix} C_{d0} & 0 & 0 \\ 0 & C_{y0} & 0 \\ 0 & 0 & 2\pi + C_{d0} \end{pmatrix} \tag{2.38}$$

$$\Phi^{(f\omega)} = \begin{pmatrix} 0 & 0 & 0 \\ 0 & 0 & b^{-1}\Delta r C_{y0} \\ 0 & -c^{-1}\Delta r(2\pi + C_{d0}) & 0 \end{pmatrix} \tag{2.39}$$

$$\Phi_0^{(mv)} = \begin{pmatrix} 0 & 0 & 0 \\ 0 & 0 & -c^{-1}\Delta r(2\pi + C_{d0}) \\ 0 & b^{-1}\Delta r C_{y0} & 0 \end{pmatrix} \tag{2.40}$$

$$\Phi^{(m\omega)} = \frac{1}{2}\begin{pmatrix} C_{l_p} & C_{l_q} & C_{l_r} \\ C_{m_p} & C_{m_q} & C_{m_r} \\ C_{n_p} & C_{n_q} & C_{n_r} \end{pmatrix} \tag{2.41}$$

with C_{d0} the minimal drag coefficient and C_{y0} the minimal side force coefficient. The parameter Δr represents the distance between the center of gravity location and the aerodynamic center (neutral point). According to the defined coordinate system, negative values of Δr imply a positive static margin of the tail-sitter MAV. The aerodynamic coefficients C_l, C_m and C_n denote the aerodynamic moment created from the angular rate of the tail-sitter MAV (p, q, r). The lift curve slope corresponding to 2π, in (2.38), (2.39) and (2.40), was deduced from the thin airfoil theory, which is valid for a two-dimensional stream around a thin airfoil that can

be envisioned as tending to an airfoil of zero thickness and infinite wingspan. In this work, we evaluate the lift curve slope in a three-dimensional stream considering the wing aspect ratio (AR) according to Diederich's formula, which yields :

$$\Phi_0^{(fv)}(:,3) = \begin{pmatrix} 0 \\ 0 \\ \frac{\pi AR}{1+\sqrt{1+(\frac{AR}{2})^2}} + C_{d0} \end{pmatrix} \tag{2.42}$$

$$\Phi^{(f\omega)}(:,2) = \begin{pmatrix} 0 \\ 0 \\ -c^{-1}\Delta r\Big(\frac{\pi AR}{1+\sqrt{1+(\frac{AR}{2})^2}} + C_{d0}\Big) \end{pmatrix} \tag{2.43}$$

$$\Phi_0^{(mv)}(:,3) = \begin{pmatrix} 0 \\ -c^{-1}\Delta r\Big(\frac{\pi AR}{1+\sqrt{1+(\frac{AR}{2})^2}} + C_{d0}\Big) \\ 0 \end{pmatrix} \tag{2.44}$$

where

$$AR = \frac{b^2}{S} \tag{2.45}$$

Finally, the flap deflections are modeled as varying cambered airfoils and the aerodynamic forces and moments created from the flap deflections are approximated by the following equations :

$$\Phi^{(fv)}(\delta_i) = \Phi_0^{(fv)}(I - [\boldsymbol{\xi_f}]_\times \, \delta_i) \tag{2.46}$$

$$\Phi^{(mv)}(\delta_i) = \Phi_0^{(mv)}(I - [\boldsymbol{\xi_m}]_\times \, \delta_i) \tag{2.47}$$

the flap effectiveness is represented by two skew-symmetric matrices, $[\boldsymbol{\xi_f}]_\times$ for the force effectiveness and $[\boldsymbol{\xi_m}]_\times$ for the moment effectiveness.

$$[\boldsymbol{\xi_f}]_\times = \begin{bmatrix} 0 & -\xi_f & \xi_f \\ \xi_f & 0 & -\xi_f \\ -\xi_f & \xi_f & 0 \end{bmatrix}$$

$$[\boldsymbol{\xi_m}]_\times = \begin{bmatrix} 0 & -\xi_m & \xi_m \\ \xi_m & 0 & -\xi_m \\ -\xi_m & \xi_m & 0 \end{bmatrix}$$

▶ Φ-Theory Propeller-Wing Interaction

The fundamental principle to model the propeller-wing interaction is that the freestream velocity field $\boldsymbol{v_\infty}$ is disturbed by the induced propeller slipstream velocity $\boldsymbol{v_i}$, such that the intensity $|\boldsymbol{v_\infty}|$ is increased while the induced angle of attack $|\alpha_i|$ and the induced sideslip angle $|\beta_i|$ are decreased. The propeller slipstream velocity induced by the thrust force can be modeled via the momentum theory or disk actuator theory, assuming small freestream velocity. We denote the propeller disk area by S_p, the increased slipstream velocity created by the propeller disk rotation contracts the airflow, which results in a smaller area than the propeller itself, in compliance with Bernoulli's Theorem. The point of airflow constriction is known as the *Vena Contracta*. According to momentum conservation arguments developed in their integral form (Anderson, 2010), the author in (Lustosa, 2017, p. 32) neglects the body forces, assumes incompressible and

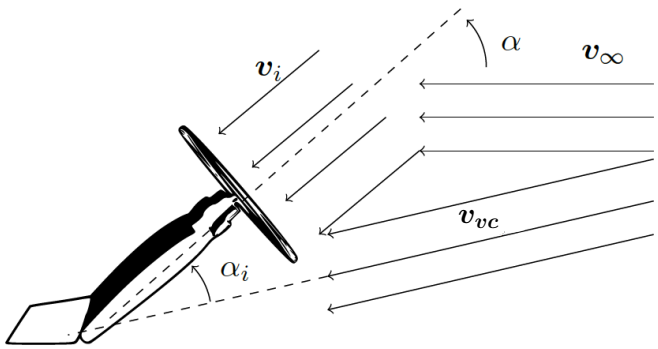

Figure 2.8: Illustration of freestream velocity field $\boldsymbol{v_\infty}$, induced propeller slipstream velocity $\boldsymbol{v_i}$ and resulting slipstream velocity $\boldsymbol{v_{vc}}$.

steady flows in order to define the resulting slipstream velocity $\boldsymbol{v_{vc}}$ in the *Vena Contracta* (see Figure 2.8), which yields

$$v_{vc}\boldsymbol{v_{vc}} = v_\infty \boldsymbol{v_\infty} + \frac{\boldsymbol{T_k}}{\rho S_p} \tag{2.48}$$

For the computation of static aerodynamic forces and moments created from propeller-wing interactions, Φ-Theory requires only the information of velocity airflows, which are described in (2.48). For instance, assuming zero angular rates ($\boldsymbol{\omega_b}$), static aerodynamic forces can be modeled as

$$\boldsymbol{F_b} = -\frac{1}{2}\rho S v_{vc}\boldsymbol{\Phi}^{(fv)}\boldsymbol{v_{vc}} \Leftrightarrow \underbrace{-\frac{1}{2}\rho S v_\infty \boldsymbol{\Phi}^{(fv)}\boldsymbol{v_\infty}}_{\boldsymbol{F_b^{(\infty)}}} \underbrace{-\frac{S}{2S_p}\boldsymbol{\Phi}^{(fv)}\boldsymbol{T_k}}_{\boldsymbol{F_b^{(p)}}} \tag{2.49}$$

Under the presented assumptions, the above equation (2.49) characterizes the force experienced by the wing with a superposition of an aerodynamic force $\boldsymbol{F_b^{(\infty)}}$ due to the freestream $\boldsymbol{v_\infty}$, plus an additional force term $\boldsymbol{F_b^{(p)}}$ representing the contribution due to the force intensity $\boldsymbol{T_k}$ created by the rotor-propeller rotations of the propulsion system.

▶ Equations of Motion

In order to model the dynamics of the tail-sitter MAV, we consider the system as a rigid body system with a continuous distribution of mass (m). Therefore, the tail-sitter MAV was divided into four rigid bodies; that is, two rotor-propellers and one fuselage composed of two wings. The system is controlled via four control-inputs, $\boldsymbol{u} = (\omega_l, \omega_r, \delta_l, \delta_r)$, respectively, the left and right rotor-propeller rotations plus the left and right flap deflections, which are illustrated in Figure 2.1. The state output of the system is represented by ten states, $\boldsymbol{x} = (\boldsymbol{v_b}, \boldsymbol{\omega_b}, \boldsymbol{q})$, where $\boldsymbol{v_b} \in \mathbb{R}^3$ is the vehicle's linear velocity, $\boldsymbol{\omega_b} \in \mathbb{R}^3$ is the vehicle's angular velocity equal to $[p\ q\ r]^T$ both expressed in the body coordinate frame, and $\boldsymbol{q} \in \mathbb{R}^4$ denotes the quaternion. We define two segments in order to compute the wing-propeller interactions on the system. Each segment is composed of one wing and by one rotor-propeller component. The sum of aerodynamic forces and moments acting on the wing (j) with the thrust force $\boldsymbol{T}_k$ generated by the rotor-propeller rotation ω_k, are given in (2.50) and (2.51), respectively.

$$\boldsymbol{F_b} = \sum_{j,k=1}^{2} (\boldsymbol{F_{a_{b_j}}} + \boldsymbol{T}_k) \tag{2.50}$$

$$\boldsymbol{M_b} = \sum_{j,k=1}^{2} (\boldsymbol{M_{a_{b_j}}} + \boldsymbol{\tau_{b_k}} + \boldsymbol{p_p} \times \boldsymbol{T}_k + \boldsymbol{p_a} \times \boldsymbol{F_{a_{b_j}}}) \tag{2.51}$$

The vector $\boldsymbol{p_p} = [p_{p_x}\ p_{p_y}\ p_{p_z}]^T$ denotes the distance between the propeller and the tail-sitter MAV center of mass. Both propellers are positioned symmetrically with respect to the tail-sitter MAV center of mass. The distance between the aerodynamic center location and the center of mass is represented by the vector $\boldsymbol{p_a} = [p_{a_x}\ p_{a_y}\ p_{a_z}]^T$. The thrust force and the internal torque ($\boldsymbol{\tau_{b_k}}$) of the rotor-propeller, which is a function of the tail-sitter MAV angular rate, are defined by :

$$\boldsymbol{T}_k = \begin{bmatrix} k_f\, \omega_k^2 \\ 0 \\ 0 \end{bmatrix} \tag{2.52}$$

and

$$\boldsymbol{\tau_{b_k}} = \boldsymbol{N_{b_k}} - J_p\,(p + \omega_j) \begin{bmatrix} 0 \\ r \\ -q \end{bmatrix} \tag{2.53}$$

where

$$\boldsymbol{N_{b_k}} = \begin{bmatrix} -\text{sign}(\omega_k)\, k_m\, \omega_k^2 \\ 0 \\ 0 \end{bmatrix} \tag{2.54}$$

with k_f and k_m positive coefficients of the rotor-propeller force and moment, respectively. The rotor-propeller moment is defined by $\boldsymbol{N_{b_k}}$. Equation (2.53) describes the gyroscopic interaction between the rotor-propeller and the tail-sitter MAV, where J_p denotes the rotor-propeller inertia. Finally, the equations of motion of the tail-sitter MAV are given by :

$$\begin{cases} m\,\dot{\boldsymbol{v}} & = \text{DCM}_{\mathcal{I} \leftarrow \mathcal{B}} \boldsymbol{F_b}(\boldsymbol{x}, \boldsymbol{u}, \boldsymbol{W}) + m\boldsymbol{g} \\ J\,\dot{\boldsymbol{\omega}}_{\boldsymbol{b}} & = \boldsymbol{M_b}(\boldsymbol{x}, \boldsymbol{u}, \boldsymbol{W}) - [\boldsymbol{\omega_b}]_\times J \boldsymbol{\omega_b} \\ \dot{\boldsymbol{q}} & = \frac{1}{2} \boldsymbol{q} \otimes \boldsymbol{\omega_b} \\ \dot{\boldsymbol{p}} & = \boldsymbol{v} \end{cases} \tag{2.55}$$

The gravitational acceleration vector is equal to $\boldsymbol{g} = g\boldsymbol{z_i}$ and $\boldsymbol{W} \in \mathbb{R}^3$ represents the wind disturbance vector. We assume that the inertia matrix of the tail-sitter MAV is diagonal and equal to

$$J = \begin{bmatrix} J_{xx} & 0 & 0 \\ 0 & J_{yy} & 0 \\ 0 & 0 & J_{zz} \end{bmatrix} \tag{2.56}$$

This assumption considers a symmetric relation about the x_b-z_b plane of the tail-sitter MAV and a second symmetric relation about its x_b-y_b plane, which is valid for MAVs without a vertical stabilizer. Thus, $J_{xy} = J_{yx} = J_{yz} = J_{zy} = J_{xz} = J_{zx} \approx 0$. The vector $\boldsymbol{p} = [x\ y\ z]^T$ represents the position of the tail-sitter MAV in the inertial coordinate frame. The highly maneuverable nature of the system calls for a global numerically stable formulation of attitude and justifies the use of quaternions. In the previous equation, the symbol $\otimes$ corresponds to the quaternion product.

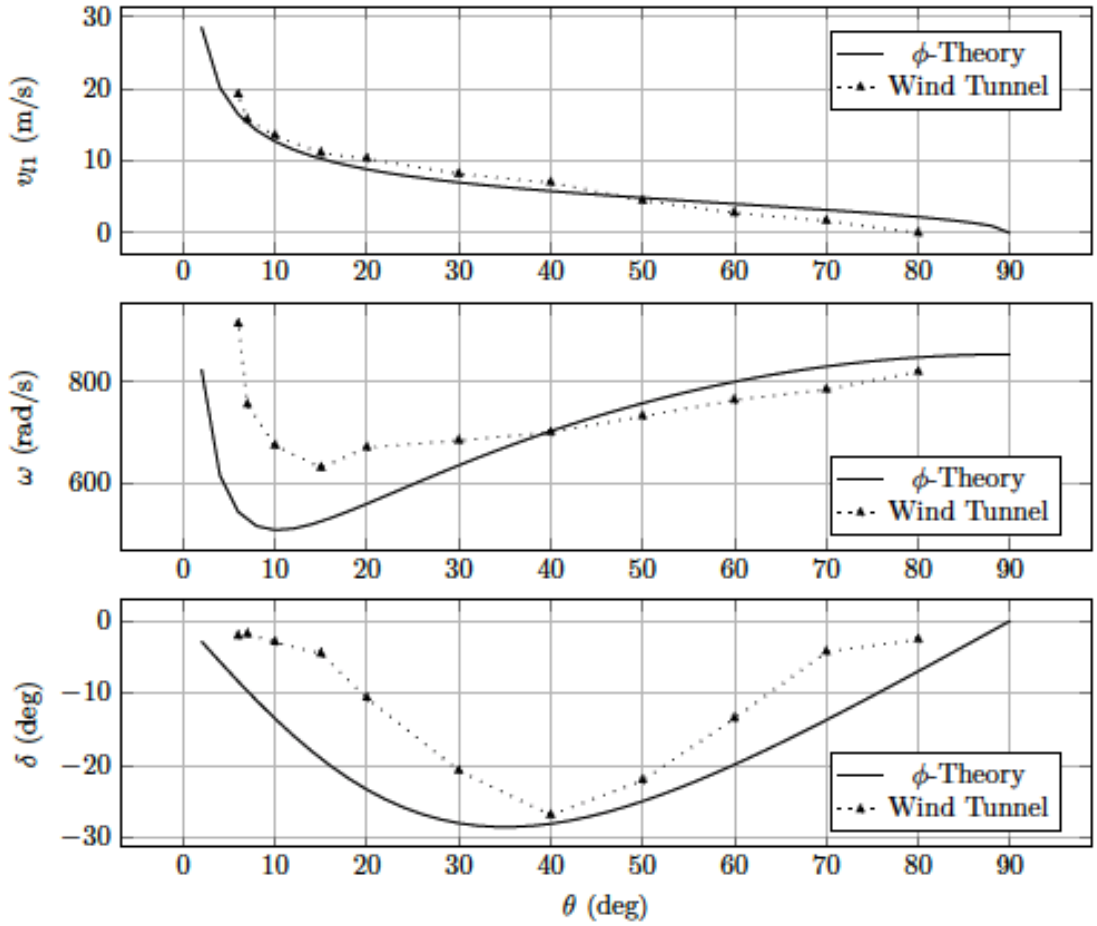

Figure 2.9: Φ-theory results compared to wind tunnel measurements (Lustosa, 2017, p. 46).

2.1.4 Summary

Obtaining a complete and realistic representation of tail-sitter MAV dynamics for flight simulations is challenging, as evidenced by different works in the literature, and is the result of an extremely time-consuming process. First, aerodynamic forces and moments experienced by the tail-sitter MAV change continuously during its entire flight envelope. The dynamic pressure increases according to the fluid's motion: for this reason, aerodynamic coefficients should be identified for each flight operating point, from hovering to forward flight. In the same way, the effectiveness of aerodynamic control surfaces is modified according to the current flight domain and the flap effectiveness increases as function of dynamic pressure.

Second, wind tunnel campaigns are expensive and were used to analyze, in the field of tail-sitter MAVs, only steady aerodynamic phenomena. Unsteady aerodynamics and their effects on tail-sitter MAV dynamics are little researched. Third, the nonlinear coupled dynamics of tail-sitter MAVs linked with propeller-wing interactions remain a challenge for the aerospace community. Furthermore, different works in the literature have defined assumptions in order to derive mathematical models, which are not totally consistent with the dynamics encountered in actual flight conditions. Through the Φ-Theory, aerodynamic forces and moments were represented by analytical models with a continuous singularity-free formulation. The modeled output dynamics presented some divergences when compared with the measurements obtained

during wind tunnel campaigns. Figure 2.9 highlights these divergences with a particular focus on actuators dynamics. The assumption used to derive such a model could be at the origin of these discrepancies.

To conclude, modeling approaches for control design should be defined as a delicate task. In this sense, model-based controllers designed from simplified dynamic models with poorly identified parameters will affect the global stability of the system and their control performance could be inadequate during flight tests. For instance, autopilot systems designed from inaccurate tail-sitter MAV models could lead to oscillatory dynamics or even more dangerous phenomena, such as unstable flights.

2.2 Control Literature Review

The control domain of HMAVs has been and continues to be a very active research domain due to their wide flight envelope, which enables the operation of complex flight missions. On the one hand, the combination of power efficiency with maneuverable flight capabilities in a single MAV configuration allowed us to cross the flight limits of rotorcraft and fixed-wing MAVs. On the other hand, the design of control algorithms to stabilize the different flight domains of HMAVs, poses interesting challenges for the control community. In fact, the open problems concerning HMAV modeling have introduced some obstacles to both the design and the performances of model-based controllers.

As seen in the previous section, the dynamics of HMAVs and their nonlinearities are challenging to model, in particular, with regard to aerodynamic phenomena. These challenges have motivated the development of new control strategies and new control architectures, which will be presented in this literature review. Therefore, a large scope of control methodologies applied to HMAVs, plus the advantages and disadvantages of each of them, will be discussed, with a particular focus on control techniques designed for tail-sitter MAV configurations.

2.2.1 Flight control architecture

From a control point of view, in order to carry out tail-sitter MAV flight missions more or less autonomously, three main points need to be addressed; that is, the stabilization of the tail-sitter MAV attitude with regard to the control of its orientation, the velocity control and the tracking of trajectories or control of positions. Through the block diagram shown in the Figure 2.10, we present the hierarchical control architecture generally used in the aerospace field and also for tail-sitter MAVs. This cascading approach is a method of control combining different control loops, with the output of one controller adjusting the setpoint of the next controller.

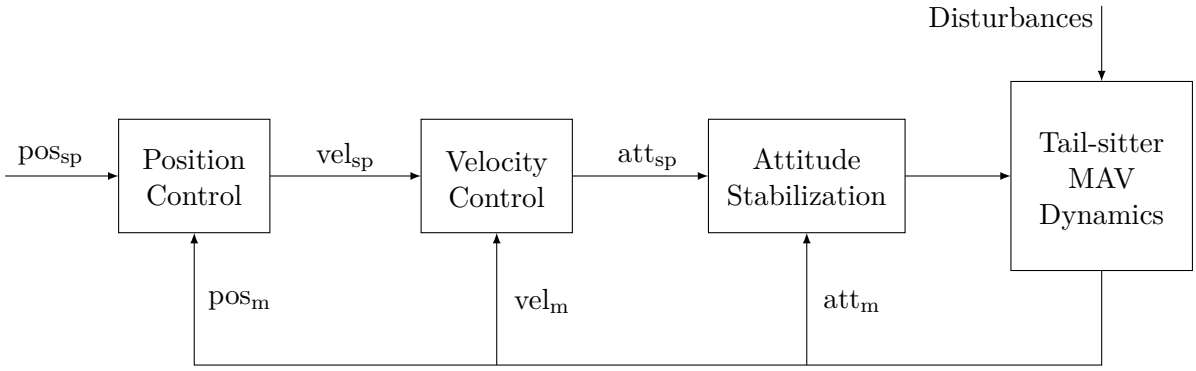

Figure 2.10: Hierarchical control architecture for tail-sitter MAVs.

Therefore, the position control block sends desired velocities (vel_{sp}) for the velocity control block that computes the necessary thrust value as well as the setpoints (att_{sp}) for attitude stabilization control loop. Different works in the literature have adopted this conceptual control architecture in order to provide autonomous flights. Therefore, a variety of control laws have been designed to address the problem of each control block. For instance, the challenges of position and velocity control are related to their robustness against external disturbances such

as wind gusts. Common requirements for the attitude control of tail-sitter MAVs is the capability to stabilize their nonlinear dynamics over their different flight phases. In addition, the control algorithm must be able to adapt its commands to variations in system dynamics, which are known to be different according to the tail-sitter MAV flight domain.

2.2.2 Control approaches for tail-sitter MAVs

The control approaches listed in Figure 2.11 have been applied on tail-sitter MAVs. Essentially, these controllers can be classified according to their linear or nonlinear aspects. Furthermore, based on adaptive or predictive capabilities and with respect to their design methodology, they can be separated into model-based or model-free control methodologies. The performance of model-based control algorithms is related to the accuracy of dynamic models. In Section 2.1, the different challenges and issues concerning the modeling of tail-sitter MAVs were presented. Therefore, the first question that appears is : If the performance of a given controller depends on the modeling accuracy, and the modeling of tail-sitter MAVs remains a time-consuming and complex task (in which aerodynamic assumptions are used to describe an approximate representation of the tail-sitter dynamics that is hardly coherent with its actual flight dynamics), why design model-based controllers for tail-sitter MAVs?

The first answer can be related to the fact that model-based controllers have been studied and discussed by a great number of authors in the literature. A wide range of model-based control design methodologies have been proposed, applied and validated on different systems with efficient control performances for well-modeled systems. In addition, the closed-loop stability of model-based controllers can be easily analyzed, even more so in the case of linear controllers

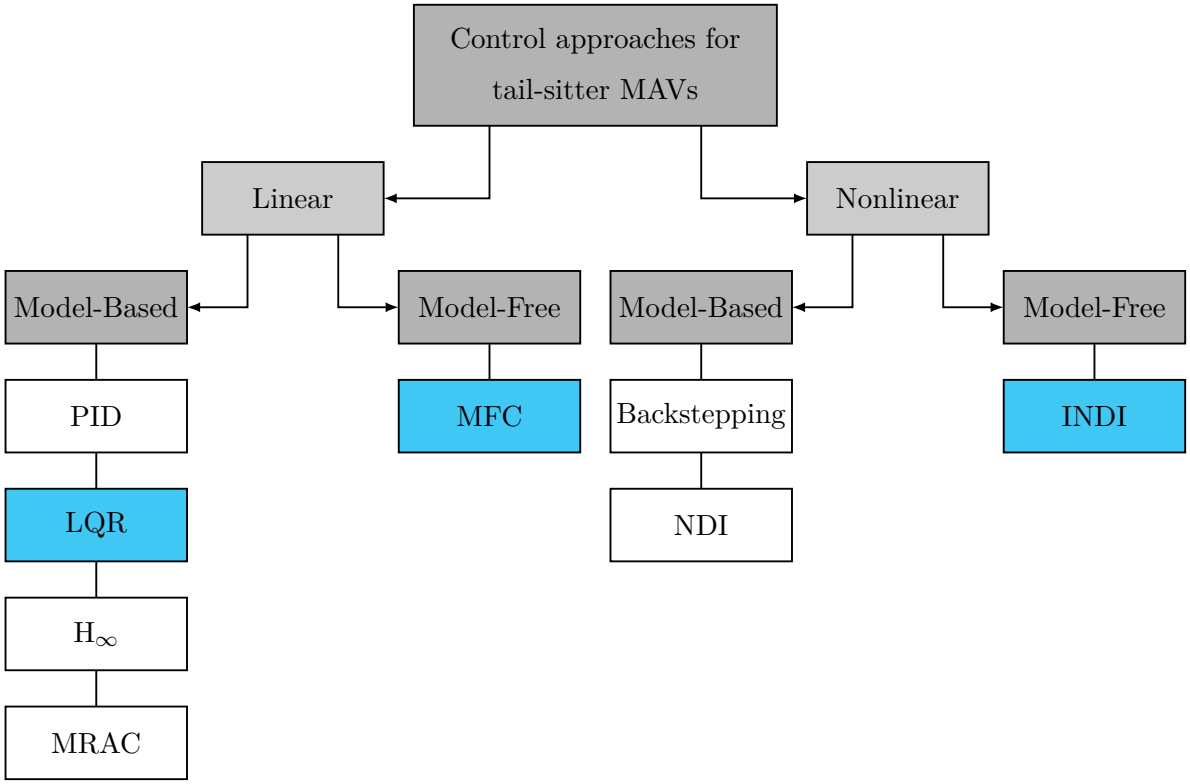

Figure 2.11: Control approaches designed for tail-sitter MAVs.

which have appropriated tools to evaluate the poles of the system. These analytical tools have certainly motivated the use of such a control approach. However, the design of linear controllers requires the choice of equilibrium operating points on which the nonlinear dynamics will be linearized. This linearization is usually represented by a steady-state condition, as steady wings-level flight, steady turning flight, steady pull up and steady roll. All of these steady-state effects are characterized by zero MAVs linear and angular accelerations. This simplification facilitates the design process of linear model-based controllers, but neglects the nonlinear dynamics when determining the control parameters. In the case of tail-sitter MAVs, for instance, the propeller-wing interaction and others' coupled nonlinear dynamics would be neglected because they cannot be properly described by linearized equations.

Alternatively, nonlinear controllers have been designed. These controllers have multiple isolated equilibrium points and cover the dynamics of a wider flight domain when compared to linear control laws. The last category of controllers presented in this literature review is for model-free control approaches. Their particularity can be explained by the fact that they can be designed with little prior knowledge of the system. For this purpose, estimation algorithms or measurement techniques are used in the control-loop to obtain information about the controlled dynamics.

▶ PID controllers

Classical linear control algorithms have been designed to tail-sitter MAVs using PID gains (Bilodeau und Wong, 2010) (Hochstenbach u. a., 2015) (Verling u. a., 2016) (Fuhrer u. a., 2019) (Liu u. a., 2019) (Ramirez und Nahon, 2020). Although simple to tune without the knowledge of the controlled system (Oosedo u. a., 2013), PID gains can be designed according to a common control system design technique called Root Locus, in which the closed-loop system poles and zeros are analyzed as a function of the controller gains. The Root Locus technique consists of plotting the closed-loop pole trajectories in the complex plane as the controller gain varies. Therefore, the controller gain can be defined in order to meet performance requirements, such as response time, overshoot, etc. Since the closed-loop poles depend on the model of the system, if the model is poorly defined, the controller gain will be too. In addition, PID controllers are known for their lack of robustness against wind disturbances and internal parameter-varying.

A hierarchical control approach was developed by (Lyu u. a., 2017b) to control the position and the attitude of a tail-sitter MAV with PID gains. Figure 2.12 presents the block diagram of such a control architecture. Its Altitude Holding Control block is designed with a PID controller combined with a model-based feedforward term in order to maintain desired altitudes. The Tail-Sitter Attitude Controller is subdivided in two control-loops; that is, the inner loop controlling

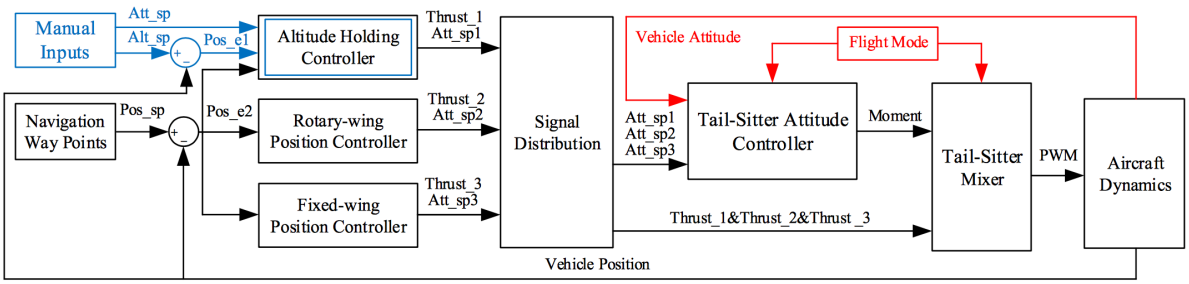

Figure 2.12: Hierarchical control architecture proposed by (Lyu u. a., 2017b).

the angular rates, also with a PID controller, plus the outer loop, with a simple proportional gain to ensure attitude stabilization. This hierarchical control architecture was validated in experimental flights using a switching strategy to permute the PID gains according to the current flight phase. The switching strategy is represented by the red block in the figure. Furthermore, one position control strategy was used during hovering flights (Rotary-wing Position Controller) and another (Fixed-wing Position Controller) during forward flights. Setpoint values can be sent manually to the tail-sitter (blue block) via an RC transmitter or autonomously via the Navigation Way Points block.

► **LQR approach**

A second reason for applying model-based controllers on tail-sitter MAVs can be justified by means of optimal control theory. For instance, the LQR, that can be optimized according to the controlled system model (Stone u. a., 2008) (Forshaw und Lappas, 2011) (Lustosa u. a., 2015). The authors in (Lustosa u. a., 2015) have designed and applied LQR gains on a tail-sitter MAV previously modeled via the $\Phi-$theory presented in Section 2.1.3. However, the performance of model-based controllers differs primarily in the fidelity with which the system is modeled and the accuracy of the identified model parameters. Hence, model-based control techniques seem to be neither optimal for tail-sitter MAVs nor easily transposable for a new tail-sitter MAV configuration, because it would require a new expensive and time-consuming identification.

The LQR is a linear control approach that, for applications on nonlinear systems, calls for linearized models. Therefore, the entire nonlinear flight dynamics of tail-sitter MAVs are represented by a set of linear models and, for each linear model, one LQR is designed. A common approach to manage these LQRs within the entire flight envelope of tail-sitter MAVs is the gain scheduling. The authors in (Lustosa, 2017) proposed the gain scheduling approach illustrated by the block diagram in Figure 2.13.

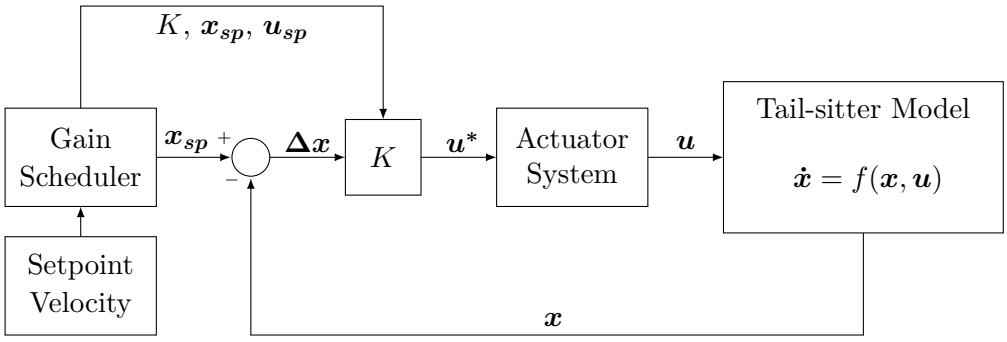

Figure 2.13: Scheduled-LQR block diagram proposed by (Lustosa, 2017, p. 80).

This LQR control architecture optimizes the closed-loop gain K in order to meet both the velocity and the attitude control requirements defined by the user. Through flight simulations and experimental flights, the author emphasizes and proves that a single matrix of LQR gains is not sufficient to stabilize the tail-sitter MAV in its entire flight envelope, which justifies the use of gain scheduling methods. Figure 2.14 shows the flight test results obtained with such a controller. The critical region illustrated by the author in the shaded area corresponds to the transitioning flight domain ($\theta \approx 45°$). In this critical region, LQR gains ensure system stability, but is difficult to conclude on LQR performance because the setpoints are not presented.

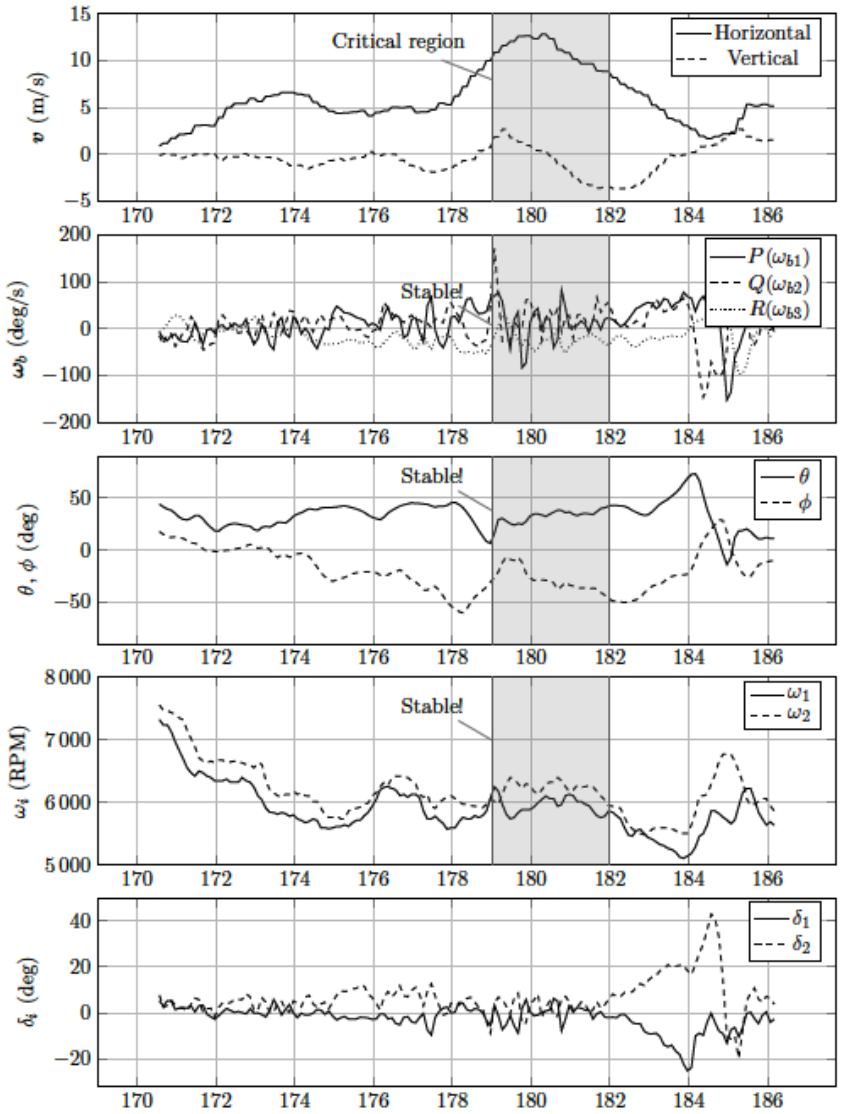

Figure 2.14: Experimental fight results from (Lustosa, 2017, p. 107).

▶ H_∞ control synthesis

The robustness properties of the H_∞ controller have been widely evaluated in a range of systems with respect to model uncertainties. The principle of such a controller is to guarantee the existence of a closed-loop gain that makes the H_∞ norm smaller than a prescribed value, the system model must be both controllable and observable (Kalman, 2010). Based on H_∞ control synthesis combined with a gain scheduling approach, the authors in (Mix u. a., 2004) (Dickeson u. a., 2005) (Dickeson u. a., 2006) (Dickeson u. a., 2007) proposed the stabilization of an HMAV over its entire flight envelope. The controller has been designed around two distinct equilibrium operating points; that is, one around the hovering flight domain and another one around the forward flight domain. The stabilization during the transitioning flight is ensured by the gain scheduling technique, which employs the appropriate gain according to the current flight phase. The performance of such a controller has been analyzed in both frequency and time domains during simulation flights. However, the control parameters have been defined according to

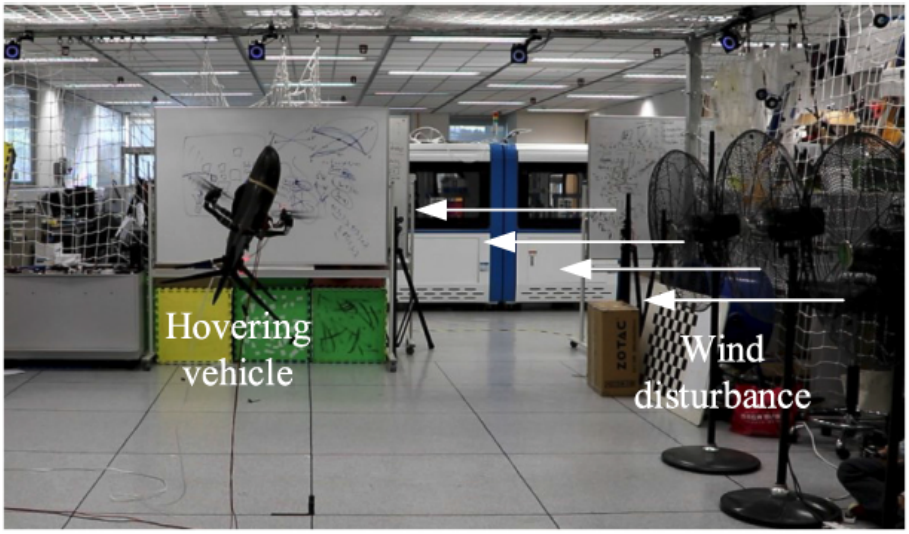

Figure 2.15: The indoor flight experiment proposed by (Lyu u. a., 2018a).

linearized and simplified models. Thus, despite its robust properties, the control performance may be different in flight tests. The authors in (Lyu u. a., 2018a) analyzed the disturbance rejection properties of the H_∞ controller during the tracking of trajectories in the hovering flight domain (see Figure 2.15). To the best of our knowledge, this control approach remains to be evaluated on experimental transitioning flights with tail-sitter MAVs.

▶ Nonlinear controllers

Theoretical research in nonlinear feedback controllers has developed closed-loop system for MAVs (Pucci u. a., 2013) proposing an extended control solution to a larger set of generic aerodynamic models with their nonlinearities (Pucci u. a., 2015). Additionally, a variety of nonlinear control techniques based on Lyapunov's stability concepts have been designed for HMAVs (Flores u. a., 2018a) (Wang u. a., 2018). In (Flores u. a., 2018b), the authors proposed a control approach in order to stabilize the tail-sitter MAV and its nonlinear dynamics during transitioning flights. The controller has been designed based on saturation functions that were tuned according to Lyapunov functions, which ensures the closed-loop system asymptotic stability.

In (Kuang u. a., 2017), the dynamics of a tail-sitter MAV have been stabilized during hovering and forward flight phases. The difference between hovering and forward flight dynamics has been highlighted with respect to the aerodynamic changing as a function of airspeed and angle of attack. In order to control these distinct flight phases and their respective dynamics, the authors proposed a switch control strategy with an ad hoc hysteresis methodology in order to prevent oscillations at the switching point, which is situated between the hovering and the forward flight domains. Despite the demonstration of stabilized nonlinear dynamics during flight tests, the proposed nonlinear controller could be sensitive to windy flight conditions, in particular, during the tracking of trajectories when the tail-sitter MAV needs to maintain its position in spite of the presence of winds. In such a case, the tail-sitter may need to maintain its flight between hovering and forward flight close to the switching point, which may result in oscillating dynamics or even to unstable flights due to discontinuities and unsmooth transitioning flights generated by the switching strategy. Backstepping techniques which are nonlinear control approaches based on the augmented Lyapunov function candidate have also been applied on tail-sitter MAVs (Argyle,

2016). This control strategy has a recursive structure in which the controlled system is built from subsystems. The control designer can start the design process at a known-stable subsystem and "back out" new controllers that progressively stabilize the others' subsystems into the entire system. For this reason, this control process is known as backstepping. We can mention, among others, the following nonlinear controllers applied on tail-sitter MAVs (Miyazaki und Tsubakino, 2017) (Wang u. a., 2017).

▶ Gain scheduling methodologies

Gain scheduling methods can be designed to stabilize tail-sitter MAVs employing different control algorithms, such as linear (Kita u. a., 2012) and nonlinear control approaches (Silva u. a., 2018). Therefore, gain scheduling techniques allow an easy understanding and simple implementation of control gains in order to cover the entire flight envelope of HMAVs. However, the principal disadvantage of this control method, found in the literature (Saeed u. a., 2018), is the expensive computational cost for operations in real-time. A unified flight controller able to fly at different flight conditions was proposed by (Hartmann u. a., 2017). According to static wind tunnel campaigns, model-based gain-scheduled controllers were designed and implemented for an extensive set of trim points covering the entire HMAV flight envelope. The transitioning flight is performed by changing the trim states via a lookup table approach.

Similar to previous work, an attitude controller based on optimal control algorithms was proposed by (Ritz und D'Andrea, 2017). Different optimal control solutions for a set of attitude errors were precomputed and stored in a lookup table. According to the current flight conditions and for each autopilot system update, the desired control parameters are obtained by reading the predefined values from the table. Experimental flights have demonstrated the capability of such a controller to recover and stabilize the HMAV from a wide range of attitude errors. The authors in (Ritz und D'Andrea, 2017) proposed a global controller for tracking nominal trajectories with a tail-sitter MAV. The control approach is based on cascaded architecture in which the outer control-loop – in charge of position and velocity control – computes the desired attitude for the inner control-loop. It uses an onboard algorithm to estimate the unknown aerodynamic coefficients in flight according to simplified aerodynamic equations. Despite the demonstration of stable flights, significant attitude errors can be observed which can also degrade the accuracy of the trajectory tracking. These errors can be justified by the use of inaccurate models in the control-loop, in particular, the simplified aerodynamic equations as the authors point out.

▶ Predictive controllers

There is a relatively small body of literature that is concerned on designing predictive controllers for tail-sitter MAVs. Even so, we can mention the following works (Boyang u. a., 2018a) (Boyang u. a., 2018b) (Zhou u. a., 2019). The authors in (Boyang u. a., 2018a) (Boyang u. a., 2018b) proposed an approach based on Model Predictive Control (MPC) algorithms to address both the tracking of positions and the attitude stabilisation of a tail-sitter MAV in its hovering flight domain. Still in hovering flight phase, (Zhou u. a., 2019) developed a Successive Linearization Based Model Predictive Control (SLMPC) emphasizing its capability to reject wind disturbances during experimental flights. The reason for this lack of MPC designs on tail-sitter MAVs can be explained by the fact that, MPCs are based on optimization algorithm that require accurate dynamic model and high computational costs. In addition, the uncertainties in the dynamic model make the problem very difficult to solve.

▶ Adaptive control approaches

Other control techniques with adaptive terms have been created to address the stabilization problem of time-varying systems. Adaptive controllers can be classified into three categories : direct, indirect and hybrid adaptive methods, which depend on how the parameters of the controller are adjusted. Direct methods compare the output of the controlled system to that of a reference model creating an error signal. According to the error evolution, the relevant parameters of the controller are adapted in order to lead this error to zero. In contrast, the foundation behind indirect adaptive control methods is parameter estimation, which is a branch of system identification. The control-loop is updated and changed according to the estimated parameters of the system that are used to determine the required controller gain. Hybrid methods rely on both the estimation of parameters and the direct adjustments of the controller gain.

In the field of adaptive control theory, Model Reference Adaptive Control (MRAC) is the most classic and widely used algorithm (Shekhar und Sharma, 2018). The MRAC is composed of three items : reference model, controller and an adjustment mechanism to adapt the parameters of the controller, in order to match the output of the controlled system y_m with the output of the reference model y_{sp} (see Figure 2.16). The adjustment mechanism can be developed from MIT rule (Jain und Nigam, 2013), Lyapunov theory (Ge u. a., 1999) (Chakrabarty und Bhattachary, 2016) and other mathematical approaches, such as covariance adjustment functions, etc. The adjustment mechanism technique proposed by (Chakrabarty und Bhattachary, 2016), based on Lyapunov functions, aims to track the output of the system and its states with the reference model. For this purpose, all of the states are assumed to be available for measurement, which is not always the case in practical control applications.

According to the MIT rule (Shekhar und Sharma, 2018), the adjustment mechanism aims to minimize the error between the output of the controlled system and the output of the reference model via a cost function that updates the controller gain (K). These parameters are changed in the direction of the negative gradient of the cost function. We note that the reference model plays an important role in the control performances provided by this adaptive controller because the MIT rule tries to match the output of the controlled systems with the output of the reference model. If this model is poorly modeled, the control performance will therefore be directly poor. In addition, the MIT rule is very sensitive to changes in the amplitude of the reference input. The indirect adaptive controller divides the controller's gain adaptation process into two steps.

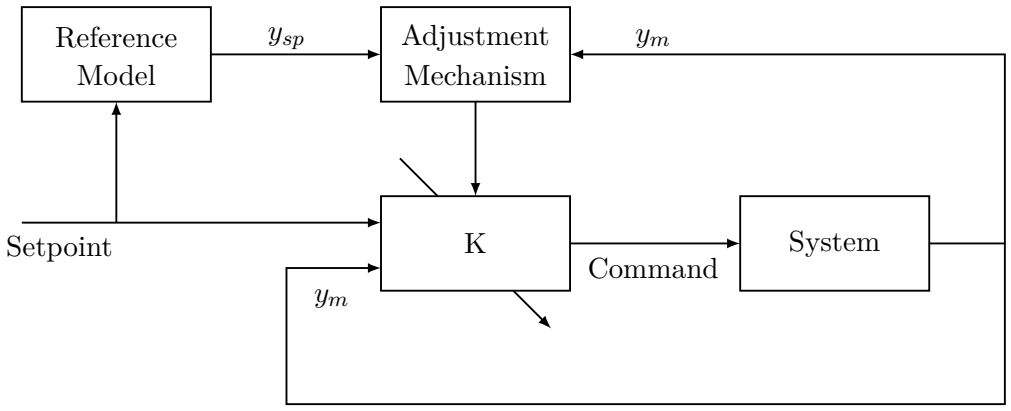

Figure 2.16: Direct adaptive control block diagram.

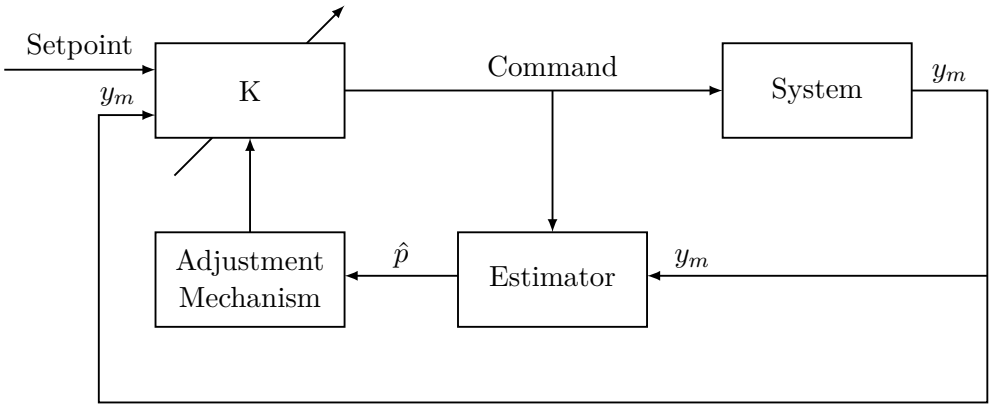

Figure 2.17: Indirect adaptive control block diagram.

Differently from the direct adaptive controller that continuously updates the controller's gain, the indirect form estimates the parameters of the system in order to synthesize an adapted controller's gain to the current situation. The closed-loop performance depends directly on the adaptation frequency that must follow the evolution of the system dynamics. In the same way, the control frequency must be compatible and synchronized with the updating of the estimated parameters. For real-time parameters estimation, the most commonly used methods are the derivatives of Least Mean Square (LMS), such as Normalized Least Mean Square (NLMS), Recursive Least Mean Square (RLMS), and Extended Kalman Filter (EKF). These methods allow the identification of linear models that are represented by a vector of parameters, which is defined by $\hat{p}$ in Figure 2.17. The EKF provides the parameter identification of nonlinear systems by using successive linearization around the operating point in which the parameter will be identified.

Regarding the adaptation algorithms that update the controller's gain according to the estimated vector of parameters $\hat{p}$, we could consider more complex methods if these methods are fast enough for real-time applications. Adaptive control techniques which account for time-varying HMAV parameters were developed by (Knoebel und McLain, 2008) (Jung und Shim, 2011). In addition, the control algorithm can continuously adapt to the evolution of the MAV dynamics when the transitioning flight is performed. The authors in (Zhang u. a., 2018) proposed a

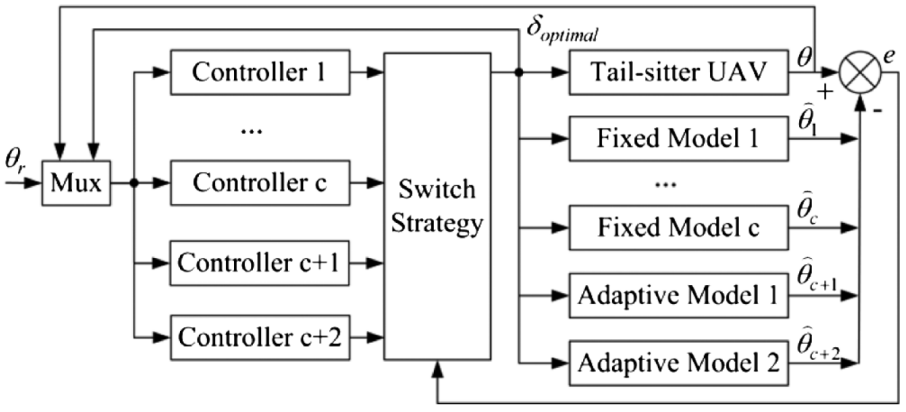

Figure 2.18: Architecture of the MMAC flight controller proposed by (Zhang u. a., 2018).

Multiple-Model Adaptive Control (MMAC) composed of multiple-model set with subcontrollers and switching index. The principle shown in Figure 2.18 is based on multiple linear submodels to represent the tail-sitter MAV dynamics within its entire flight envelope. Linearized models are hiding the nonlinear dynamics of a such system. Different adaptive control architectures for tail-sitter MAVs can be found in (Jung und Shim, 2011) (Jin u. a., 2015) (Zhong u. a., 2019). However, poor control performances with adaptive control methods can still exist with regard to inaccurate models or unmodeled dynamics due to simplified equations used in the adaptation criterion of the controller's gain.

▶ INDI and MFC

Finally, to conclude the literature review, we present two control techniques that will be examined in more detail in this thesis and compared with each other through flight tests; that is, the INDI and MFC. The INDI controller, which is a sensor-based approach, is less-model dependent and has been experimentally tested via flight tests with tail-sitter MAVs providing excellent performance against wind disturbances. However, this controller requires the identification of the actuator system in order to design its control parameters, such as the actuator control effectiveness. Given that the effectiveness of the aerodynamic control surfaces are not constant during the entire flight envelope of tail-sitter MAVs, for example, hovering or forward flight, a gain scheduling method was implemented to fit these effectiveness values under the respective flight domain (Smeur u. a., 2019).

Alternatively, the MFC methodology proposed by (Fliess und Join, 2013) requires little prior knowledge of the controlled system to design the controller. The block diagram presented in Figure 2.19 illustrates the principle of such a controller. We emphasize that the estimator block does not modify the feedback control gains, in contrast to the direct and indirect adaptive control methods presented above. The MFC adaptive process is performed by the estimator block in which the computed estimation $\hat{F}_y$ is directly affected in the closed-loop command u. Based on such an estimator, it is possible to implement a robust and adaptive controller that ensures the stability of time-varying systems by estimating in real-time their dynamics from periodic measurements of y_m and u.

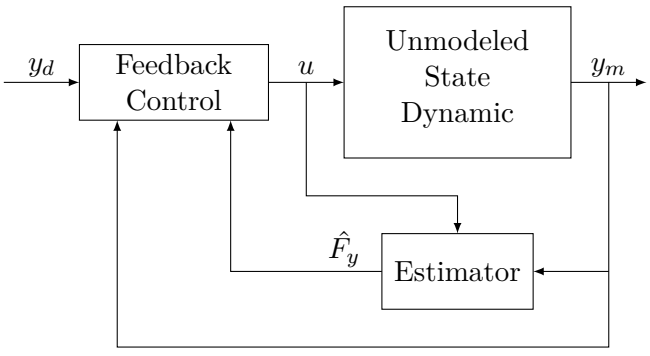

Figure 2.19: Overall Model-Free Control schema.

A number of works in literature have addressed their challenges with the MFC approach (Join u. a., 2017) (Rodriguez-Fortun u. a., 2013) (Bara u. a., 2018). Obviously, the common denominator between these works is related to the complexity on modeling the system dynamics. The work proposed by (Menhour u. a., 2018) has focused on the control of longitudinal and lateral

vehicle motion, which the definition of mathematical models to describe its motion remains a complex task due to uncertainties and disturbances, such as friction and nonlinear tyre-road interactions. Although not applied in the aerospace field, the encouraging results obtained by the authors have demonstrated the benefits of MFC in practice. A more in-depth presentation of the MFC technique will be given in the next chapter. First results of the MFC approach in the field of tail-sitter MAVs and the main contributions of this thesis can be found in (Barth u. a., 2020b) (Barth u. a., 2020a) (Barth u. a., 2019) (Barth u. a., 2018b) and (Barth u. a., 2018a). These articles can also be found respectively in the pages 198, 221, 244, 253 and 260 on this manuscript.

2.3 Summary of Chapter 2

This chapter provides a brief summary of the literature relating to both modeling and control of tail-sitter MAVs. The aerodynamic challenges involved in the different flight domains of tail-sitter MAVs, such as Low-Reynolds number flows, propeller-wing interaction and the costly identification of aerodynamic coefficients through wind tunnel campaigns have been summarized. These challenges have been emphasized by different works of literature and the difficulty of developing a reliable dynamic model of tail-sitter MAVs remains an open problem.

The difficulty of accurately modeling the dynamics of tail-sitter MAVs, in particular the unsteady dynamics in transitioning flights characterized by fast changing of aerodynamic forces and moments, calls for the development of innovative control strategies which aim to reduce the dependencies of a model during the controller design. Thus, the control literature review indicates that the implementation of a control law for tail-sitter MAVs in which the controller is not based on prior dynamic models remains to be explored.

In order to reduce inaccuracies due to poor modeling processes in the control performance and motivated by adaptive control properties found in the control literature review, MFC algorithms will be designed in this thesis. The principle is to estimate online the dynamics of the controlled system only from measurements of its outputs and from the last values of its control-inputs. The output of the estimation process will be directly used in the closed-loop command to stabilize the system. Even if theoretically performant and elegant, a flight control algorithm has practical use only if validated in experimental flights. With regard to this point, the control literature review is not yet exhaustive.

Nevertheless, the control laws previously introduced by (Lustosa, 2017) and (Smeur u. a., 2019) will be analyzed in the following chapters via flight simulations and flight tests. By explaining the similarities and differences between these control approaches against the proposed MFC methodology, we can increase our understanding of both controllers. This thesis continues with the evaluation of these different control methodologies which are linear model-based and nonlinear, less-model dependent, in order to conclude about flight performance and implementation requirements. In addition, these distinguished control strategies will be compared with the MFC control approach for tail-sitter MAVs in order to indicate the practical interest of each controller.

Part II

Study

Chapter 3

Model-Free Control

"*All models are approximations. Essentially, all models are wrong, but some are useful. However, the approximate nature of the model must always be borne in mind.*"
— George Box

This chapter aims to describe the MFC principle, which is designed to control for unknown dynamics. Through particular numerical differentiation algorithms, unknown dynamics are estimated and stabilized by the MFC closed-loop system. All features of the MFC are presented, from its closed-loop structure to the methodology used to design its parameters. Finally, illustrative examples are presented in order to evaluate the main features of the MFC and compare its performance with that of the PID controller.

Contents

3.1 Preliminary Concepts

This section introduces some previous work based on estimation of derivative signals from the numerical approximations of derivatives to explain the MFC algorithms according to (Fliess und Join, 2013). We consider the fact that conventional estimation techniques are generally impossible to apply on systems with strong non-linearities. The definition of observability given in (Diop und Fliess, 1991b) confirms this assumption. This definition states that

" [...] a nonlinear input-output system is observable if, and only if, any variable of this system, including its state variables, is written as a differential function of its input and output, i.e., a function of these variables and their derivatives up to some finite order [...] "

Through differential algebra operations, the authors in (Diop und Fliess, 1991a) have demonstrated that observability is a linear concept, in the sense that a nonlinear system is observable if, and only if, its linearized tangent or variational linearized system is such. In addition, the authors have highlighted the notion of identifiability that is strongly linked to observability. According to (Fliess und Sira-Ramirez, 2003) (Fliess u. a., 2007), an unknown dynamic quantity can be estimated/determined if, and only if, it is expressible as a differential function of its control-input and its output variable.

This natural concept asserts that nonlinear estimation is essentially a question of numerical differentiation. The proposed derivative estimation method used in this work is based on the possibility of representing the signal during a short time interval using a polynomial representation (Mboup u. a., 2009). The estimated signal can be approximated by a polynomial representation that is clearly related to the Weierstrass approximation theorem, which states that every continuous function defined on a closed interval can be uniformly approximated as closely as desired by a polynomial function. In order to introduce the estimation approach used in this work, let's consider an illustrative example with the estimation of first-order dynamics :

$$y(t) = a_0 + a_1\, t \tag{3.1}$$

The derivative term in (3.1) that we aim to estimate can be highlighted by differentiating one the previous equation with respect to time :

$$\frac{d}{dt}\, y(t) = \frac{d}{dt}\, a_0 + \frac{d}{dt}\, a_1\, t \tag{3.2}$$

with a_0 a constant term, we obtain

$$\dot{y}(t) = a_1 \tag{3.3}$$

Therefore, the derivative term that we must estimate is a_1. For this purpose, we apply the *Laplace Transform* in (3.1) and we get

$$Y(s) = \frac{a_0}{s} + \frac{a_1}{s^2} \tag{3.4}$$

with s the Laplace variable in the frequential domain. We multiply by s all terms of the previous equation

$$s\, Y(s) = a_0 + \frac{a_1}{s} \tag{3.5}$$

and by differentiating (3.5) with respect to s, we obtain

$$Y(s) \; + \; s\, \frac{d}{ds}\, Y(s) = -\frac{a_1}{s^2} \tag{3.6}$$

Now, we multiply both sides of (3.6) by a power of s sufficiently negative. In this case, s^{-2} is enough in order to obtain at least one integrator ($\frac{1}{s}$) for each term in the following equation :

$$\frac{Y(s)}{s^2} + \frac{1}{s}\frac{d}{ds}Y(s) = -\frac{a_1}{s^4} \tag{3.7}$$

From this previous equation, we can deduce the expression of a_1, in the time domain, using the following correspondences between the frequency and time domains, where

$$\begin{aligned} s^{-1} &\longrightarrow \int_0^t \\ s^{-n} &\longrightarrow \int^{(n)} \text{, multiple integrals} \\ \frac{d}{ds} &\longrightarrow -t \\ \frac{d^n}{ds^n} &\longrightarrow (-1)^n t^n \end{aligned}$$

Thus,

$$a_1 = -\frac{6}{T^3}\left(\int^{(2)} y(t)\,dt - \int t\,y(t)\,dt \right) \tag{3.8}$$

The integral terms in (3.8) provide excellent robustness to noise (Fliess, 2006). In addition, the low-pass feature of the integrals ensures the attenuation of high frequency phenomena created by the noise in the measured signal $y(t)$. In order to reduce the multiple integrals into a simple one, and facilitate the implementation of such an estimation algorithm in microprocessor boards, we apply the Cauchy's theorem in (3.8),

$$\int_0^T \int_0^{t_1} \cdots \int_0^{t_{\gamma-1}} u(t_\gamma)\,dt_\gamma \cdots dt_1 = \int_0^T \frac{(T-t)^{\gamma-1}}{(\gamma-1)!}\,u(t)\,dt, \quad \text{with } \gamma > 1 \tag{3.9}$$

and we get

$$\dot{y}(t) = a_1 = -\frac{6}{T^3}\int_{t-T}^{t} (T-2t)\,y(t)\,dt \tag{3.10}$$

This function provides a local estimation of the derived signal $\dot{y}(t)$ valid during the integration interval defined by T. The estimation algorithm presented here is used in many engineering fields : signal processing, digital image processing, estimation, control, fault-diagnosis systems and its performances are widely recognized and appreciated. In the next section, we illustrate the application of such an algorithm in the case of control of systems, in particular for systems that are difficult to model in which the use of estimator in order to determine their dynamics seems to be appropriated.

3.2 MFC Principle

The estimation of derivative signals, which was introduced in the previous section, is involved in the MFC algorithmic approach. From this particular estimation technique, an unknown dynamic may be determined in a quantified way and this information may be used to determine the closed-loop command. Therefore, the proposed controller is able to stabilize unknown dynamics by using conventional control gains. This control approach will be detailed in the following lines.

Let's consider an unknown finite dimensional system with a single control-input (u) and a single output (y) described by the following input/output relation in a differential equation formulation :

$$\mathbb{E}(y, \dot{y}, \ldots, y^{(a)}, u, \dot{u}, \ldots, u^{(b)}) = 0 \tag{3.11}$$

where $\mathbb{E}$ is a polynomial function with real unknown coefficients. We can also describe

$$y^v = \mathbb{E}(t, y, \dot{y}, \ldots, y^{(v-1)}, y^{(v+1)}, \ldots, y^{(a)}, u, \dot{u}, \ldots, u^{(b)}) \tag{3.12}$$

with $0 < v \leq a$ and $\frac{\delta \mathbb{E}}{\delta y^v} \neq 0$. The idea behind Fliess und Join (2013), is to approximate this unknown dynamic (3.12) by a purely numerical equation, namely *Ultra-Local Model* :

$$y^{(v)}(t) = F(t) + \lambda \cdot u(t) \tag{3.13}$$

In (3.13), v is the order derivative of $y(t)$, $\lambda \in \mathbb{R}$ is a non-physical constant parameter used to obtain the same order of magnitude between the three terms in (3.13). Moreover, the exploitation of this numerical model requires the knowledge of $F(t)$. This quantity represents the real dynamics of the system as well as the different disturbances which could damage the the control performance. Thus, an accurate estimation of $F(t)$, defined as $\hat{F}(t)$, is crucial and plays an important role in the MFC closed-loop.

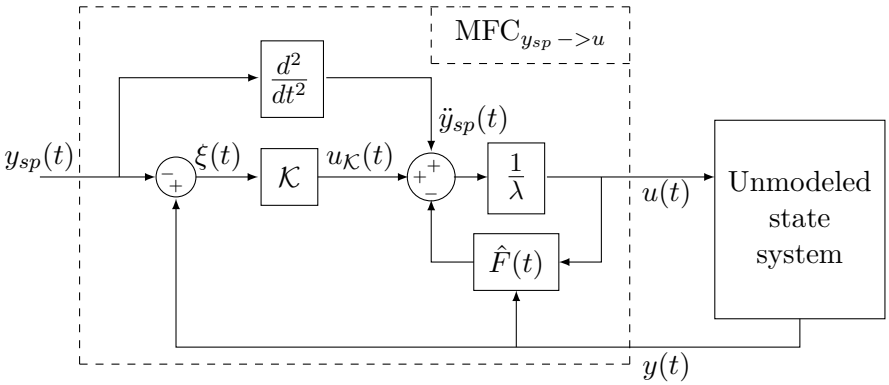

Figure 3.1: Model-free control schema for a second-order system.

Based on such an estimator, it is possible to design a robust controller that estimates the system dynamics online via a piecewise constant function $\hat{F}(t)$, periodically updated from measures of $y(t)$ and for the last values of $u(t)$. The detailed form of the MFC schema presented in Figure 3.1 defines the closed-loop command such as :

$$u(t) = \underbrace{-\frac{\hat{F}(t)}{\lambda}}_{\text{Estimation}} + \underbrace{\frac{\ddot{y}_{sp}(t) + u_{\mathcal{K}}(t)}{\lambda}}_{\text{Closed-loop tracking}} \tag{3.14}$$

where the quantity $\xi(t) = y(t) - y_{sp}(t)$ is the tracking error and $u_{\mathcal{K}}(t)$ is the closed-loop command of a feedback controller $\mathcal{K}(\xi(t))$, usually defined as a Proportional (P), Proportional Derivative (PD) or even as PID gains. In this work, we define the closed-loop feedback controller as a proportional K_p and derivative gain K_d. We recognize in (3.14) the typical mathematical expression of a nominal control in the flatness-based in which the nonlinear terms $\hat{F}(t)$ are

added with a closed-loop tracking of setpoint trajectory $y_{sp}(t)$. The error dynamics can be deduced from the combination of (3.13) with (3.14), for $v = 2$:

$$\ddot{\xi}(t) = \ddot{y}(t) - \ddot{y}_{sp}(t) = \overbrace{F(t) - \hat{F}(t)}^{\xi_F \approx 0} + K_p\,\xi(t) + K_d\,\dot{\xi}(t) \tag{3.15}$$

$$\ddot{\xi}(t) - K_d\,\dot{\xi}(t) - K_p\,\xi(t) = 0 \tag{3.16}$$

Note that, if the error between the estimator and the true dynamics (ξ_F) is approximately zero, a simple PD controller will be enough to ensure the error convergence to zero, because integration terms are implicitly involved in the MFC algorithm. In addition, we notice from (3.14) that closed-loop tracking is decoupled from the estimation algorithm. In this way, we can separately design the tracking control performance of the disturbance rejection properties.

3.2.1 Estimation algorithm

In order to obtain information of unknown dynamics, we describe the estimation equations used in the MFC estimator $\hat{F}(t)$ based on the approach presented in Section 3.1 for the estimation of derived signals. For this purpose, we present the mathematical equations to estimate both first and second-order dynamics. Finally, we propose an algorithm to obtain the MFC estimator for dynamics of arbitrary order (v).

- According to (3.13), for first-order dynamics ($v = 1$), we obtain :

  $$\dot{y}(t) = F(t) + \lambda \cdot u(t) \tag{3.17}$$

  The first step is to apply the *Laplace Transform* in (3.17), considering $F(t)$ as a constant piece-wise function, yields :

  $$sY(s) - y(0) = \frac{F}{s} + \lambda\,U(s) \tag{3.18}$$

  Where $Y(s)$ and $U(s)$ correspond respectively to the *Laplace transforms* of $y(t)$ and $u(t)$. By differentiating one the previous equation we are able to remove the initial condition :

  $$Y(s) + s\frac{dY(s)}{ds} = -\frac{F}{s^2} + \lambda\,\frac{dU(s)}{ds} \tag{3.19}$$

  However, s is the operation corresponding to differentiation in the time domain and it is noise-sensitive, which could amplify the noise measurement of $y(t)$ in the output of $\hat{F}(t)$. Therefore, in order to reduce both noise and numerical computation errors on the output estimation, we add two integrators ($\frac{1}{s^2}$) that have robust properties with respect to noise. Thus, multiplying both sides of (3.19) by s^{-2}, we obtain :

  $$\frac{Y(s)}{s^2} + \frac{dY(s)}{s\,ds} = -\frac{F}{s^4} + \frac{\lambda}{s^2}\frac{dU(s)}{ds} \tag{3.20}$$

  Finally, the expression of $\hat{F}(t)$ for the first-order dynamics can be determined in the time domain by using *Inverse Laplace transforms* with *Cauchy's theorem* to reduce multiple integrals into a simple one :

  $$\hat{F}(t) = \frac{-6}{T^3}\int_{t-T}^{t}\Big[(T - 2\sigma)y_(\sigma) - \lambda\sigma(T - \sigma)u(\sigma)\Big]d\sigma \tag{3.21}$$

Equation (3.21) estimates the dynamics of a first-order system from measurements of a corrupted signal $y(t)$. The result is a constant parameter $\hat{F}(t)$ which is valid during the interval $[t-T,t]$. Different practical works in literature proved that the use of a first-order *Ultra-Local Model* ($v=1$) is enough to stabilize unknown dynamics. However, if the unknown dynamics present second-order behavior with small friction coefficients, the use of a first-order *Ultra-Local Model* would be insufficient to stabilize poorly damped dynamics (Fliess und Join, 2013). In this context, we propose to develop MFC algorithms based on second-order *Ultra-Local Model* ($v=2$).

- Then, for the second-order dynamics, we have :

$$\ddot{y}(t) = F(t) + \lambda \cdot u(t) \tag{3.22}$$

The methodology for obtaining the MFC estimator remains the same as for a first-order dynamics. For that, the first step is to apply *Laplace Transforms* in (3.22) :

$$s^2Y(s) - sy(0) - \dot{y}(0) = \frac{F}{s} + \lambda U(s) \tag{3.23}$$

Where $Y(s)$ and $U(s)$ correspond to the *Laplace transforms* of $y(t)$ and $u(t)$ respectively. By twice differentiating the previous equation with respect to s, we can remove the initial conditions $y(0)$ and $\dot{y}(0)$:

$$2Y(s) + 4s\frac{dY(s)}{ds} + s^2\frac{d^2Y(s)}{ds^2} = \frac{2F}{s^3} + \lambda\frac{d^2U(s)}{ds^2} \tag{3.24}$$

In this case, in order to reduce both noise and numerical computation errors caused by the term s^2 in the numerator of the previous equation, we must multiply both sides of (3.24) by s^{-3}. This mathematical operation adds at least one integrator ($\frac{1}{s}$) to the equation, which guarantees robust properties with respect to noise :

$$\frac{2Y(s)}{s^3} + \frac{4}{s^2}\frac{dY(s)}{ds} + \frac{1}{s}\frac{d^2Y(s)}{ds^2} = \frac{2F}{s^6} + \frac{\lambda}{s^3}\frac{d^2U(s)}{ds^2} \tag{3.25}$$

Finally, the estimates of second-order dynamics can be obtained by applying *Inverse Laplace transforms* with *Cauchy's theorem* in (3.25) in order to reduce multiple integrals into a simple one :

$$\hat{F}(t) = \frac{5!}{2T^5}\int_{t-T}^{t}\left[\Big[(T-\sigma)^2 - 4\sigma(T-\sigma) + \sigma^2\Big]y(\sigma) - \Big[\frac{\lambda}{2}\sigma^2(T-\sigma)^2u(\sigma)\Big]\right]d\sigma \tag{3.26}$$

From measurements of both the corrupted signal $y(t)$ and the control-input $u(t)$ obtained from the last T seconds, the unknown dynamics of $y(t)$ and the disturbances acting in the system, are estimated by $\hat{F}(t)$, which is updated for each interval of integration $[t-T,t]$. This interval corresponds to the window width of a receding horizon strategy which results in a trade-off. The idea is to choose a window width small enough so as to calculate the estimation within an acceptable short delay but large enough to preserve the low-pass filter properties of the integrator in order to attenuate the noise in the measurements of $y(t)$.

- Generally, unknown dynamics with arbitrary order can be estimated using the methodology described in the algorithm (1).

Algorithm 1 Computing the estimator $\hat{F}$

1: **procedure**
2: $v \leftarrow$ Define the order of the dynamics to be estimated
3: **step 1:** Write the *Ultra-Local Model*
4: **step 2:** Calculate the *Laplace transforms* of step 1
5: **step 3:** Derive step 2, v times with respect to s
6: **step 4:** Multiply step 3 by $s^{-(v+1)}$
7: **step 5:** Calculate the *Inverse Laplace transforms* of step 4 with Cauchy's theorem
8: **end procedure**;

3.2.2 Computation of setpoint trajectories

Setpoint trajectories are filtered according to the features of a second-order dynamics.

$$\frac{Y_{sp}(s)}{Y_f} = \frac{1}{(T's+1)^2} \quad \Longleftrightarrow \quad \frac{1}{(T'^2s^2+2T's+1)} \tag{3.27}$$

$$Y_f = (T'^2s^2+2T's+1)\,Y_{sp} \quad \Longleftrightarrow \quad T'^2s^2\,Y_{sp}+2\,T's\,Y_{sp}+Y_{sp} \tag{3.28}$$

Its discrete form can be obtained with the following formulas

$$s\,Y_{sp} = \frac{y_{sp}(kT_s)-y_{sp}(kT_s-T_s)}{T_s} \tag{3.29}$$

$$s^2\,Y_{sp} = \frac{y_{sp}(kT_s)-2y_{sp}(kT_s-T_s)+y_{sp}(kT_s-2T_s)}{T_s^2} \tag{3.30}$$

With $T' = w_f\,T_s$, we obtain

$$Y_f = (w_f^2+2\,w_f+1)\,y_{sp}(kT_s)-(2\,w_f+2\,w_f^2)\,y_{sp}(kT_s-T_s)+w_f^2\,y_{sp}(kT_s-2T_s) \tag{3.31}$$

And

$$y_{sp}(kT_s) = \frac{Y_f+(2w_f+2w_f^2)\,y_{sp}(kT_s-T_s)-w_f^2\,y_{sp}(kT_s-2T_s)}{w_f^2+2w_f+1} \tag{3.32}$$

These setpoint trajectories can be tuned by using the parameter w_f, which defines how fast the trajectory reaches the final setpoint value, and they are computed from (3.32). For illustrative purposes, we present three different setpoint trajectories in Figure 3.2. The filter parameter corresponding to the trajectory 2 (——) was imposed superior to the trajectory 1 (.....) and inferior to the trajectory 3 (- - -), in accordance with the following relation ($w_1 < w_2 < w_3$) for equal sampling times T_s. Figure 3.3 illustrates the contribution of the setpoint trajectory double-derivative on the control-input $u(t)$. The double-derivative term introduces a direct action in the system from changes in the setpoint trajectory, which results in more reactive control-loop.

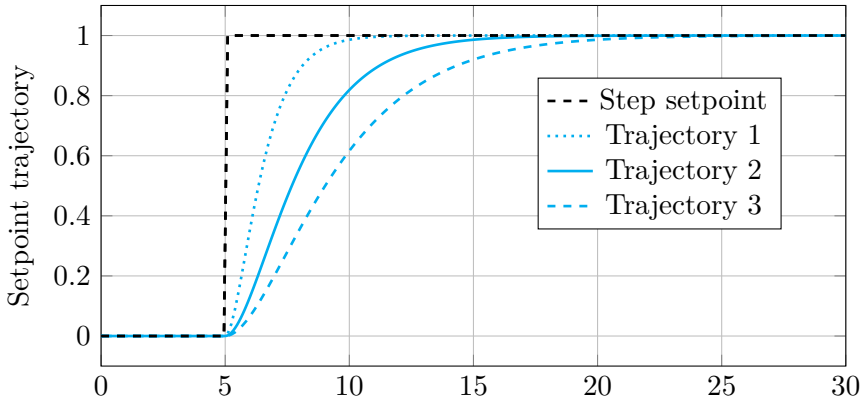

Figure 3.2: Filtered setpoint trajectories.

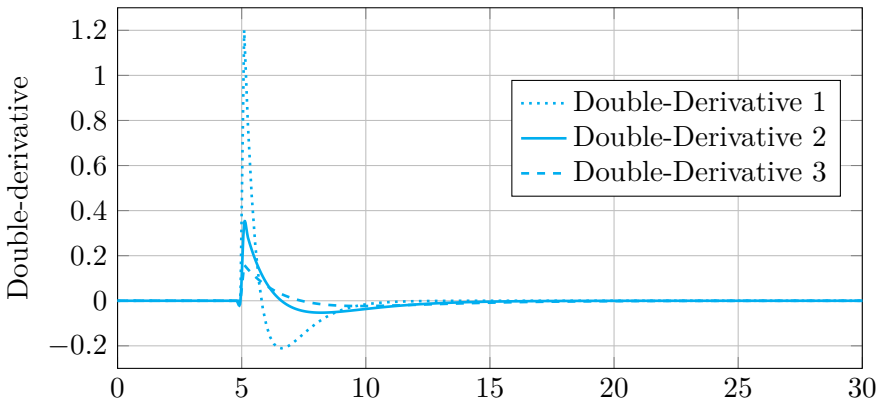

Figure 3.3: Double-derivative of setpoint trajectories.

3.2.3 Discretized equations

Expressing (3.22) in discrete-time domain, yields :

$$\frac{y(kT_s) - 2y(kT_s - T_s) + y(kT_s - 2T_s)}{T_s^2} = F(kT_s) + \lambda u(kT_s) \tag{3.33}$$

where the Left-Hand Side (LHS) of (3.33), represents the discrete second-order derivative of $y(t)$. The discretized plant model $F(kT_s)$ represents not only the dynamics of $y[kT_s]$ but also the different disturbances which could damage the output-system. $u(kT_s)$ is the input-control signal, λ a constant parameter that allows us to set the same magnitude between the LHS of (3.33), $F(kT_s)$ and $\lambda u(kT_s)$. The parameter k is the index of the current sample time T_s. The dynamics of a Single-Input Single-Output (SISO) system is approximated by the *Ultra-Local Model*, that is valid during $[kT_s - T\,T_s, kT_s]$. The discretized closed-loop command is achieved by using a proportional and derivative gain, yielding the control-input $u(kT_s)$ in (3.34).

$$u(kT_s) = \underbrace{-\frac{\hat{F}(kT_s)}{\lambda}}_{\text{Nonlinear Cancellation}} + \underbrace{\frac{y_d^{(2)}(kT_s) + K_p\,\xi(kT_s) + K_d\,\dot{\xi}(kT_s)}{\lambda}}_{\text{Closed loop tracking}} \tag{3.34}$$

where $y_d^{(2)}(kT_s)$ denotes the 2-th order derivative of $y_d(t)$ in the discrete-time domain. The tracking error $\xi(kT_s)$ and the derivative of the tracking error $\dot{\xi}(kT_s)$, are defined respectively as

$$\xi(kT_s) = y(kT_s) - y_d(kT_s) \tag{3.35}$$

$$\dot{\xi}(kT_s) = \dot{y}(kT_s) - \dot{y}_d(kT_s) \tag{3.36}$$

Remark : The derivative of the tracking error can be measured directly in the system or computed with finite difference formulas such as backward finite difference. In this case, the derivative of the tracking error is :

$$\dot{\xi}(kT_s) = \frac{\xi(kT_s) - \xi(kT_s - T_s)}{T_s} \tag{3.37}$$

Substituting the control-input $u(kT_s)$ from (3.34) in (3.33), we obtain the following expression :

$$\begin{aligned}\underbrace{y(kT_s) - 2\,y(kT_s - T_s) + y(kT_s - 2T_s)}_{\text{Numerical second-order derivative of } y(t)} &= \overbrace{F(kT_s) - \hat{F}(kT_s)}^{\xi_F \approx 0} \\ &+ \underbrace{y_d(kT_s) - 2\,y_d(kT_s - T_s) + y_d(kT_s - 2T_s)}_{\text{Numerical second-order derivative of } y_d(t)} \\ &+ K_p\,\xi(kT_s) + K_d\,\dot{\xi}(kT_s)\end{aligned}$$

If $\xi_F \approx 0$, then the effect of disturbances is negligible on the error dynamics, which yields :

$$\begin{aligned}\ddot{\xi}(kT_s) = &\frac{y(kT_s) - 2y(kT_s - T_s) + y(kT_s - 2T_s)}{T_s^2} \\ &- \frac{y_d(kT_s) + 2y_d(kT_s - T_s) - y_d(kT_s - 2T_s)}{T_s^2}\end{aligned}$$

So, (3.38) shows that

$$\ddot{\xi}(kT_s) = K_p\,\xi(kT_s) + K_d\,\dot{\xi}(kT_s) \tag{3.38}$$

The system can be guaranteed to be stable if K_p and K_d are negative and the control law (3.34) can be shown to be stable resulting in $\xi(kT_s) \to 0$ as $kT_s \to \infty$.

3.2.4 Control design methodology

The MFC closed-loop allows the design of both tracking and regulation performance with distinguished parameters that can be tuned with little prior knowledge of the system. The following points describe the control design methodology used in this work to tune the MFC parameters :

1. The proportional-derivative gains (K_p and K_d) have been easily tuned according to classical root locus method. In practice, the MFC estimator provides an accurate estimation of the system ($\xi_F \approx 0$). Thus, the error dynamics of the closed-loop system can be approximated by a double integrator (3.16), which can be tuned by the pole location approach. From this perspective, we define double real closed-loop poles at $-s_d$, which results in the following characteristic polynomial :

$$(s + s_d)^2 = s^2 + 2\, s_d\, s + {s_d}^2 \tag{3.39}$$

   The feedback controller with these proportional-derivative gains can be identified by neglecting the initial conditions in the Laplace transform of (3.16) :

$$\frac{U_{\mathcal{K}}(s)}{\xi_y(s)} = s^2 - K_d\, s - K_p \tag{3.40}$$

   Therefore, we obtain from (3.39) and (3.40) :

$$K_p = -{s_d}^2 \quad \text{with} \quad s_d > 0 \tag{3.41}$$

$$K_d = -2 s_d \quad \text{with} \quad s_d > 0 \tag{3.42}$$

2. The integration window (T) could be defined with prior informations about the noise present in the measured signal $y(t)$. The choice of the integration window implies some expertise according to a trade-off between fast estimations and effective noise attenuations. For instance, due to the integrator in (3.26) with low-pass filter features, a large integration window provides an effective noise attenuation, but slow estimations with a direct impact on the control-loop responsiveness. On the other hand, small integration windows result in fast estimations with the constraint of estimating noises. In this context, oscillations could be observed in the closed-loop system with high frequency controls, known as *chattering*. In this work, we use an invariant observer (Martin und Salaun, 2010) in order to smooth the measured signals, allowing the set of small integration windows to estimate the fast dynamics of the system while suppressing the oscillations generated by the noises in the closed-loop system.

3. Finally, the constant coefficient λ is used to scale the amplitude between the command $u(t)$ and the dynamics of $\ddot{y}(t)$. This parameter can be represented as the control effectiveness of the nominal system. Nonetheless, if this parameter is poorly defined or if the actual control effectiveness of the system changes within a bounded domain, the estimator $\hat{F}(t)$ is able to compensate this bounded discrepancy ensuring closed-loop stability. A nominal setting of λ can be achieved by calculating the ratio between the command saturation and the maximum allowable value of $\ddot{y}(t)$.

From a practical point of view, the proposed MFC design allows a time-saving approach to stabilize complex dynamic systems. The fact that the closed-loop system can be approximated by the dynamics of a double integrator simplifies the design process of the controller parameters.

3.2.5 Control-loop algorithm

The algorithm 2 describes the main steps of the MFC closed-loop :

Algorithm 2 Model-free Control algorithm

procedure INITIALIZATION
    Define sampling time $\rightarrow T_s$
    Design MFC parameters $\rightarrow \lambda, T, K_p$ and K_d
end procedure;
procedure MFC COMMAND
Control loop:
    Define the desired trajectory $\rightarrow y_d[kT_s]$
    Read output measurement $\rightarrow y[kT_s]$
    Read control value from the last sampling period $\rightarrow u[kT_s - T_s]$
    Calculate the estimate of $F \rightarrow \hat{F}[kT_s]$
    Determine the error $\rightarrow \xi[kT_s]$
    Calculate closed-loop tracking $\rightarrow \mathcal{K}(\xi(t))$
    Compute new command from equation (3.34) $\rightarrow u[kT_s]$
goto *Control loop*
end procedure;

3.3 Illustrative Examples

Three experiments were conducted in order to evaluate the MFC algorithms and compare their performance with that of a PID controller. The PID controller was designed using the pole placement method proposed by (Wang u. a., 2009), which follows an identification process. For these experiments, we use the *Quanser Aero* which is an experimental platform designed for aerospace applications. Its reconfigurable structure allows the development of advanced control researches either for 1 DOF system or 2 DOF system, which corresponds to the axial dynamics of a quadrotor and the helicopter dynamics on two axes, respectively. In addition, some components of the *Quanser Aero* can be modified; for example, the propulsion system by changing its

Figure 3.4: Quanser Aero platform in half-quadrotor configuration.

propellers. Therefore, the adaptive properties of both controllers can be evaluated by varying the nominal configuration of the system.

3.3.1 Control Design

▶ Model-Based Controller

We propose to design the PID controller using model-based techniques, in particular the pole placement approach proposed by (Wang u. a., 2009). This control design methodology requires the identification of the system in order to describe the system dynamics via a transfer function denoted by $TF(s)$, where $N(s)$ and $D(s)$ are the transfer function numerator and denominator, respectively, which are represented by polynomials.

$$TF(s) = \frac{N(s)}{D(s)} \tag{3.43}$$

The transfer function is assumed to be proper and the numerator and denominator are coprime polynomials. The transfer function of the PID controller is denoted by :

$$C(s) = K_p + K_d\, s + \frac{K_i}{s} \tag{3.44}$$

The closed-loop system is illustrated in Figure 3.5, whose characteristic equation is equivalent to :

$$1 + C(s)\, TF(s) = 0 \Leftrightarrow C(s) = \frac{-1}{TF(s)} \tag{3.45}$$

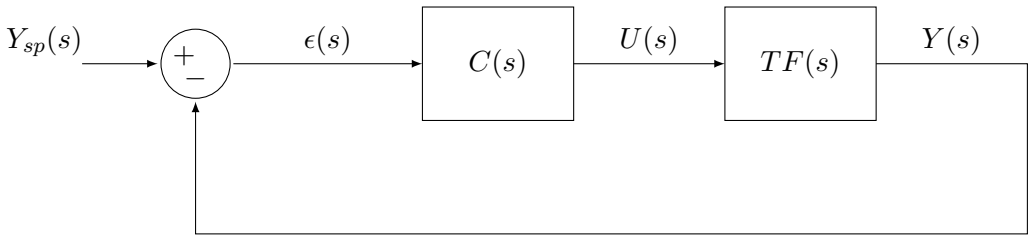

Figure 3.5: Unity Feedback Control-Loop

We can express the denominator $D_{cl}(s)$ of the closed-loop transfer function

$$H(s) = \frac{Y(s)}{Y_{sp}(s)} \tag{3.46}$$

as function of both numerator and denominator polynomials of the system with the parameters of the PID controller. For the unity feedback control-loop configuration illustrated earlier, we get

$$D_{cl}(s) = s\, D(s) + N(s)(K_d\, s^2 + K_p\, s + K_i) \tag{3.47}$$

Through the PID controller gains, we intend to impose the poles of $D_{cl}(s)$ in order to set the requirements of the closed-loop performance. For this purpose, we define a pair of conjugate poles $\{p_{sp}, \overline{p}_{sp}\}$:

$$\begin{cases} p_{sp} = a + j\, b \\ \overline{p}_{sp} = a - j\, b \end{cases} \Leftrightarrow \begin{cases} a = Re\,(p_{sp}) \\ b = Im\,(p_{sp}) \end{cases} \tag{3.48}$$

The proposed control design requires that the ratio between a and the real part of all poles of the system exceeds r, which is usually greater than 3. This constraint imposes the location of all other poles of the system on the left-hand side of the line $s = r\,a$. The objective of the guaranteed placement of the dominant poles is to find the PID gains in order to obtain all the closed-loop poles in this required region with the exception of the dominant poles $\{p_{sp}, \overline{p}_{sp}\}$. By replacing s by $p_{sp} = a + j\,b$ in (3.45) yields :

$$K_p + K_d(a + j\,b) + \frac{K_i}{a + j\,b} = \frac{-1}{TF(a + j\,b)} \tag{3.49}$$

This equation can be decomposed into two sub-equations; one from the real part and the other from the imaginary part. Solving the two equations for K_i and K_d as function of K_p yields :

$$\begin{cases} K_i = -(a^2 + b^2)\Big(\frac{K_p}{2\,a} + X_1\Big) \\ K_d = -\frac{K_p}{2\,a} + X_2 \end{cases} \tag{3.50}$$

with

$$\begin{cases} X_1 = \frac{1}{2\,b} Im\Big(\frac{-1}{F(a+j\,b)}\Big) - \frac{1}{2\,a} Re\Big(\frac{-1}{F(a+j\,b)}\Big) \\ X_2 = \frac{1}{2\,b} Im\Big(\frac{-1}{F(a+j\,b)}\Big) + \frac{1}{2\,a} Re\Big(\frac{-1}{F(a+j\,b)}\Big) \end{cases} \tag{3.51}$$

The previous equation simplifies the PID design to a one-parameter problem in terms of K_p. Therefore, the gain K_p can be determined for its positive values from the root locus method. According to the plot of the closed-loop characteristic equation roots, we are able to determine the range of K_p, such that the roots are in the required complex region. By substituting (3.50) in (3.45), we obtain :

$$1 + X_2 \frac{N(s)}{D(s)}\, s - (a^2 + b^2)\, \frac{X_1}{s} \frac{N(s)}{D(s)} - K_p\, \frac{s^2 - 2as + (a^2 + b^2)}{2as}\, \frac{N(s)}{D(s)} = 0 \tag{3.52}$$

By dividing both sides of the previous equation by the terms without K_p, and after some mathematical operations, we get

$$1 + K_p\, L(s) = 0 \tag{3.53}$$

with

$$L(s) = \frac{-N(s)\left(s^2 - 2as + (a^2 + b^2)\right)}{2aD(s)\, s + N(s)\left(2aX_2 s^2 - 2a(a^2 + b^2)X_1\right)} \tag{3.54}$$

The previous transfer function $L(s)$ is proper since the degree of its numerator and denominator is equal to the degree of the numerator and denominator of the closed-loop transfer function $H(s)$, respectively.

The following steps summarize the proposed design of the PID controller :

- Identify the polynomials that represent the numerator $N(s)$ and the denominator $D(s)$ of the controlled system;
- Define the dominant poles $\{p_{sp}, \overline{p}_{sp}\}$ according to the desired closed-loop performance;
- Plot the $L(s)$ transfer function according to (3.54) for positive values of K_p. The location of the poles $\{p_{sp}, \overline{p}_{sp}\}$ will not be affected by the values of K_p. Note that negative values of K_p can be achieved by plotting the root locus of $-L(s)$;

- From the root locus of $L(s)$ choose the value of K_p which guarantee that $\{p_{sp}, \overline{p}_{sp}\}$ are the dominant poles of the closed-loop system;
- Once K_p is defined, compute the gains K_d and K_i according to (3.50);

▶ PID design for the *Quanser Aero*

The proposed design process of the PID controller requires the identification of controlled dynamics. For this purpose, we have identified the system by using the Ho-Kalman method (Miller und de Callafon, 2012). Based on such an identification process, we have obtained the following transfert function :

$$\frac{Y(s)}{U(s)} = \frac{N(s)}{D(s)} \Leftrightarrow \frac{\theta(s)}{V(s)} = \frac{-0.02747\, s^2 + 0.6224\, s}{47.46\, s^4 + 62.93\, s^3 + 46.86\, s^2 + 25.93\, s + 0.1115} \tag{3.55}$$

with $\theta(s)$ the controlled output of the system and $V(s)$ the voltage signal used as control-input. The desired control performance for the closed-loop system was defined according to both response time $t_{5\%}$ and damping coefficient ζ as function of the overshooting percentage

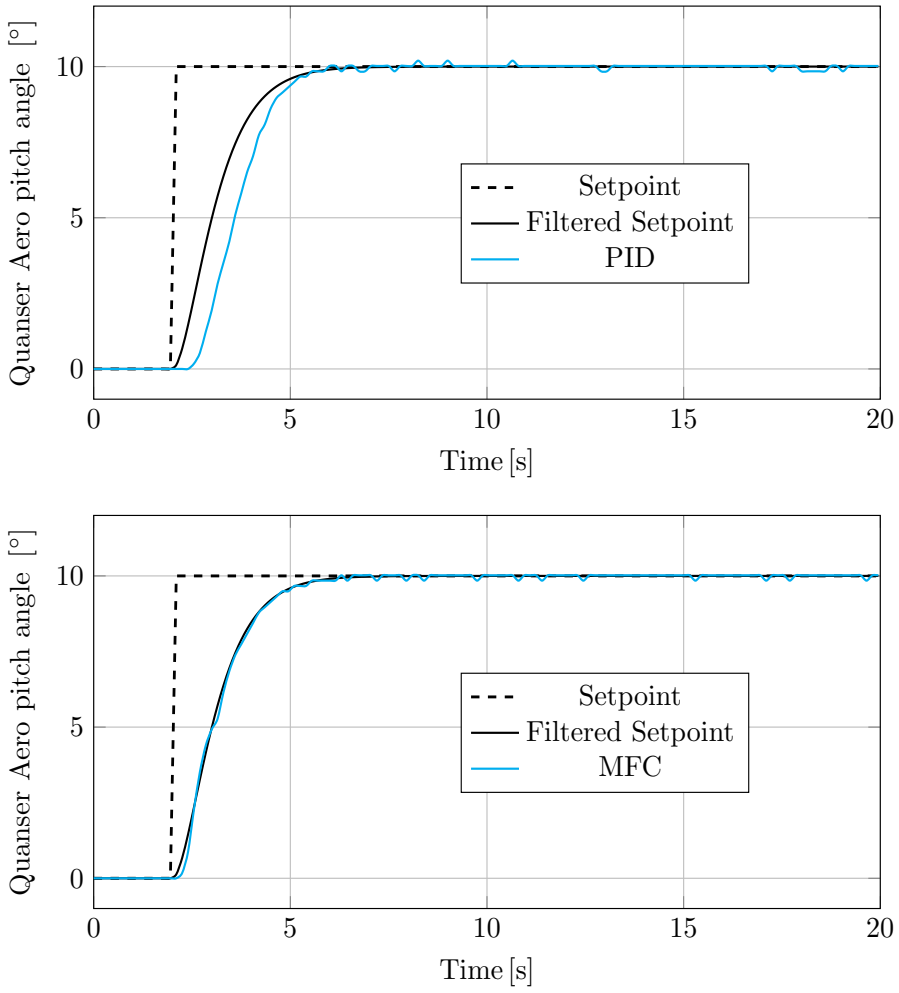

Figure 3.6: PID and MFC closed-loop validation.

$O_{\%}$. Therefore, the real part a and the imaginary part b of the dominant closed-loop poles can be described according to :

$$\begin{cases} a = -\zeta\,\omega_0 \approx -\frac{4}{t_{5\%}} \\ \zeta = \frac{-ln(O_{\%})}{\sqrt{\pi^2+ln^2(O_{\%})}} \\ \omega_0 \approx \frac{4}{\zeta\,t_{5\%}} \\ b = \omega_0\sqrt{1-\zeta^2} \end{cases} \tag{3.56}$$

We imposed a response time equal to 4 seconds and an overshoot equal to 0; that is, a damping coefficient equal to 1. These requirements result in a dominant pole at $-1 \pm j\,0$. By applying the root locus approach (3.54), we choose K_p equals to 4.5 in order to ensure the dominant poles on the other poles of the closed loop system. From (3.50) we get so $K_d = 6.4568$ and $K_i = 2.7615$.

► **MFC design for the *Quanser Aero***

The MFC parameters were designed according to Section 3.2.4. With the same closed-loop poles designed for the PID controller, we get the proportional and derivative gains of the MFC equals to -1 and -2, respectively. The integration window was defined equal to 20 in order to ensure fast estimations and effective noise attenuations. Finally, we set $\lambda = 0.125$. Figure 3.6 shows the performances achieved by both controllers. The setpoint signal imposed on the PID closed-loop system was filtered with a second-order filter in order to reduce the amplitude of the commands when the setpoint signal changes. The MFC structure also uses this filtering principle. Both controllers ensured the performance requirements; that is, 4 seconds for the response time without overshoot. However, MFC provided better trajectory tracking performance during the transient response compared to that of the PID technique. In the steady phase, both controllers cancel the static error. The particularities of both controllers have been analyzed and compared during three experiments that will be presented in the following. In the first one, we control the nominal system and check the tracking of different trajectories. Then, the adaptative properties of each controller was analyzed by changing the nominal propulsion system according to Figure 3.8. Finally, in the third experiment, the disturbance rejection was evaluated.

3.3.2 Nominal system

The closed loop system has been evaluated according to different setpoint shapes, such as step signals, sine-waves and triangular trajectories, which are still filtered. We observe the achieved trajectory tracking performance of each controller, for the nominal system, in Figure 3.7. The PID controller (—-) presents small delays over the setpoint trajectories (- - -) with overshoots, mainly for triangular setpoint trajectories. This differs from the MFC controller (—-), which presents an effective tracking performance for all trajectory shapes.

The double-derivative term illustrated in the MFC structure, as a function of the setpoint signal, introduces a direct action in the system providing more reactive responses (see Figure 3.1). This term added in the closed-loop command assists the tracking of complex setpoints, such as triangular trajectories. The command calculated by the PID approach is based on the closed-loop error without the term calculated directly from the setpoint signal, which may justify delays in the pitch dynamics controlled by the PID.

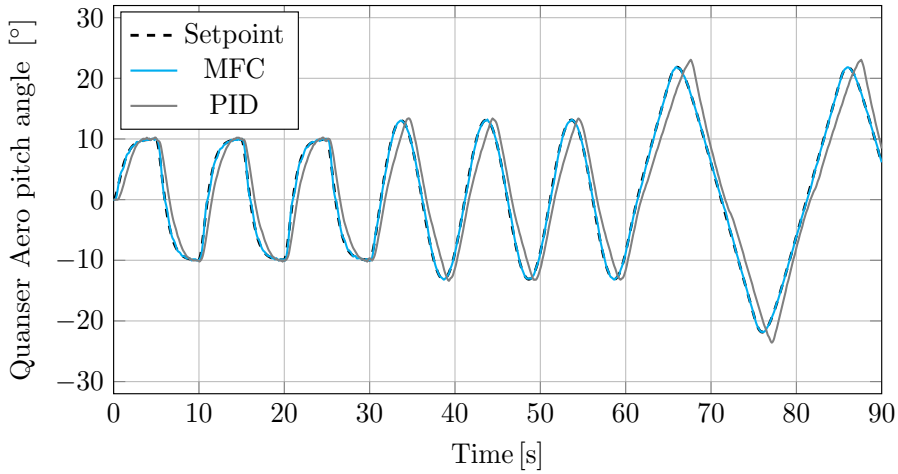

Figure 3.7: Comparison between MFC and PID controllers for the nominal *Quanser Aero*.

3.3.3 Parameter-varying analysis

In the second experiment, we have modified the propulsion system of the *Quanser Aero* by imposing a new propeller configuration, which directly affects the control effectiveness of the system. The new propeller is composed by ten blades according to Figure 3.8. Given this change in the nominal system, we evaluate the control performance of each controller in terms of adaptive properties.

Propeller 1

Mass	4,2 g
Diameter	0.128 m
Pitch propeller	0.117 m

Propeller 2

Mass	20,3 g
Diameter	0.1367 m
Pitch propeller	n/a

Figure 3.8: Propellers general specifications.

The control of the pitch dynamics provided by the PID approach — compared to that of its previous results in the nominal system (propeller 1) — has deteriorated and the pitch angle presents larger overshoots. On the other hand, the modified propulsion system configuration (propeller 2), and thus the changes in the control effectiveness, did not directly affect the closed-

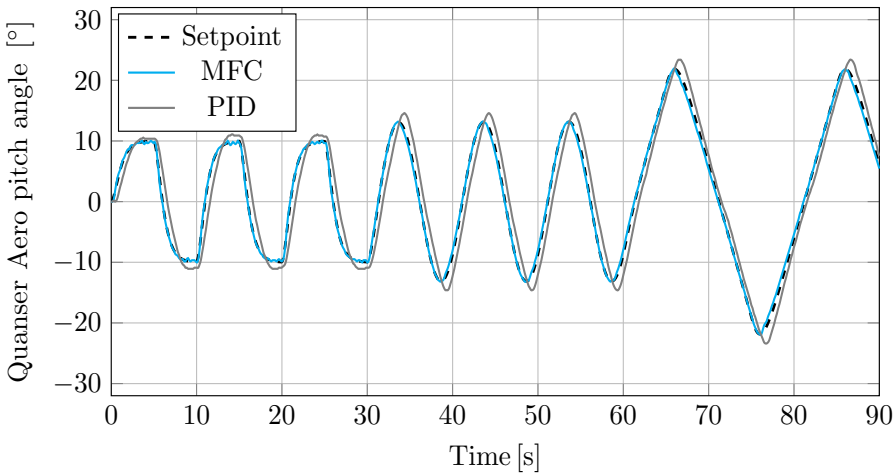

Figure 3.9: Comparison between MFC and PID for parameter-varying analysis.

loop performance provided by the MFC algorithms. Therefore, we note the MFC self-adaptation with respect to system variations in this illustrative example. Through the estimator in the MFC closed-loop $\hat{F}$ that, from information about the previous control-input $u(kT_s - T_s)$ and from measurements of the output signal $y(kT_s)$, adapts the current control-input $u(kT_s)$ in order to tackle this undesirable modification in the system that could damage the tracking performance. Figure 3.10 shows the estimator $\hat{F}(t)$ behavior during the control of both nominal and parameter-varying cases. We observe that the second propeller introduces vibrations into the system, which are measured in the output signal and then estimated by $\hat{F}$. Despite the poor aerodynamics of propeller 2, the MFC closed-loop ensures correct tracking of the setpoint trajectory (see Figure 3.9).

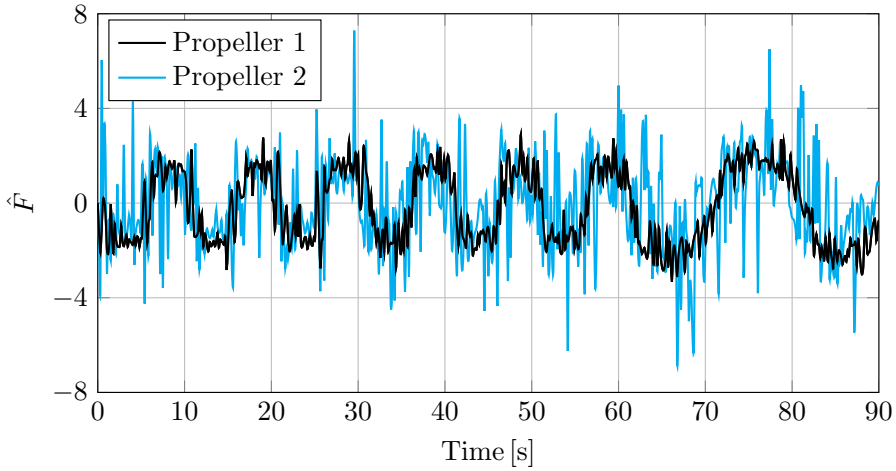

Figure 3.10: Estimator $\hat{F}$ for both nominal and parameter-varying cases.

3.3.4 Disturbance rejection

The third experiment illustrates the disturbance-rejection properties of both controllers. For this purpose, we introduce a magnetic mass of 24.4 grams to 23 centimeters of the center of

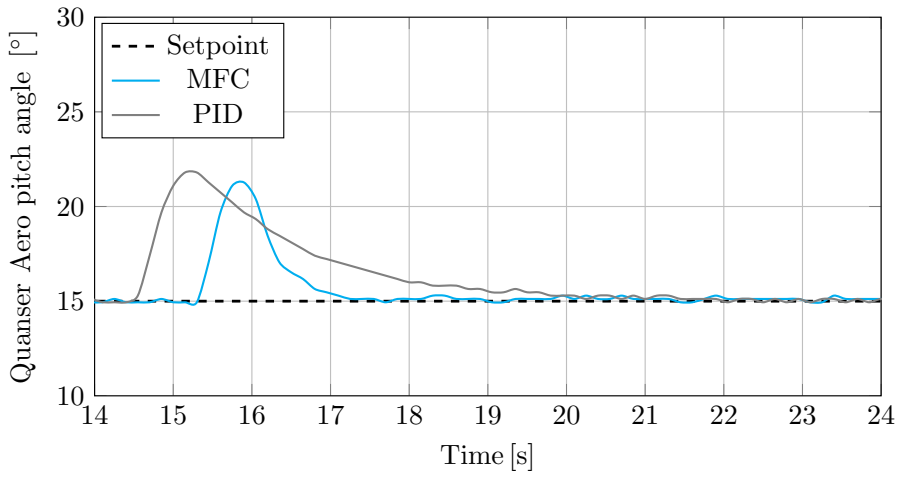

Figure 3.11: Disturbance rejection response time.

rotation resulting in a torque in the pitch axis. This mass was chosen to generate an acceptable torque disturbance such that the motors can compensate for it. For comparison reasons, we tried to place the mass at the same time in the system (around 15 seconds) in order to adequately compare the response time and the disturbance rejection properties of both controllers in the same time window (see Figure 3.11). The system was not disturbed in exactly the same way and the initial disturbance was likely different for the two controllers. Indeed, when we introduce this mass into the system, its magnetic properties produce an attractive force causing a non-zero contact speed and a combination of a step and a delta pulse disturbance. However, we consider that the effective disturbance is the same for both experiments because the weight has exactly the same mass. We observe that the disturbance rejection performed by the PID controller takes 6 seconds until the pitch angle is again reached at 15 degrees, which is approximately 3 times more than the results obtained with the MFC technique. The PID controller rejects this disturbance very slowly because it takes time for its integrator to accumulate errors. We mention here that the integral gain of the PID controller could be larger in order to improve its

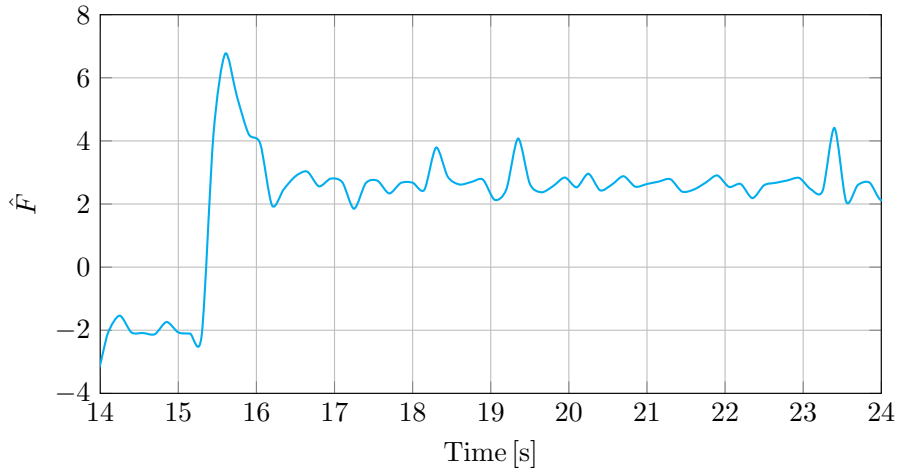

Figure 3.12: Estimator $\hat{F}(t)$ during the disturbance-rejection analysis.

disturbance rejection, but this will deteriorate the performance of the previous experiment with the nominal system. Through the estimator $\hat{F}$, Figure 3.12 shows the adaptation term of the MFC closed-loop when the disturbance was introduced into the system.

3.4 Summary of Chapter 3

In practical control applications, defining a representative and accurate mathematical model to describe the dynamics of the controlled system remains a challenge and a time-consuming process. The dynamic models are often different from the behaviour of the real system. In addition, poor dynamic models could impact the performance of model-based controllers in real-world applications.

That being said, this chapter has described the MFC approach based on particular techniques for estimating unknown dynamics. Through robust properties of integral functions, the proposed estimation algorithm is able to determine unknown dynamics while attenuating the noise from measured signals. Therefore, numerical differentiation techniques and algebraic operations have been presented to derive such an estimator, which was used in the MFC closed-loop in order to adapt the command as a function of changes in the dynamics of the controlled system.

All features of the MFC have been presented, from its closed-loop structure to the methodology used to design its parameters. After the description of the MFC design, we have illustrated preliminary experiments in order to evaluate its features and compare its performance with that of the PID controller. The disturbance rejection properties of both controllers were analyzed, as well as their performance with respect to system parameter-varying. For both experiments, the MFC approach has demonstrated better tracking of trajectories plus better disturbance rejection properties compared to that of the PID controller.

In addition, the PID has been designed from an identification process in order to determine the dynamics of the system. In this case, the pitch dynamics of the *Quanser Aero* system. For a different system, a new identification process will be necessary in order to design appropriated gains for the PID controller. On the other hand, the MFC can be designed with little prior knowledge of the system and its command can be adapted via its estimator, which allows the stabilization of a variety of similar systems with a single controller design. Furthermore, the proposed MFC design allows a time-saving approach to stabilize complex dynamic systems.

Chapter 4

Model-Free Control Assessment Through Flight Simulations

"*Learning is creation, not consumption. Knowledge is not something a learner absorbs, but something a learner creates.*"
— George Couros

This chapter introduces the MFC architecture and provides a comprehensive set of flight simulations covering the entire flight envelope of tail-sitter MAVs. We present an overview of each flight phase capability with its challenges and constraints with respect to both control and flight dynamics. The closed-loop performance is also evaluated in order to define worst-case stability with respect to unmodeled dynamics and parametric-varying, but also against external disturbances. In addition, a preliminary analysis comparing the MFC performance with that of the LQR is also presented with a special focus on the transitioning flight domain. This comparative analysis highlights the advantages and disadvantages of each controller regarding both the control performance and the implementation process of autopilot systems for tail-sitter MAVs.

Contents

4.1 Tail-Sitter Flight Simulator

A comprehensive set of flight simulations, discretized at 500 Hz, were performed from MATLAB/Simulink using the tail-sitter MAV model described in Chapter 2. Our flight simulator (cf. Figure 4.1) describes the dynamics of the DarkO tail-sitter MAV, with its parameters presented in Table 4.1. The outputs of the DarkO are corrupted by Gaussian white noise, for which the standard deviations can be found in (Chahl u. a., 2007). An invariant observer (Martin und Salaun, 2010) is used providing a smoother signal measurement of the DarkO states, however, this operation adds delays in the closed-loop and have been taken into account during the design of the controller.

In order to evaluate our control algorithm, we have introduced external disturbances, such as a crosswind, during these flights. The results provide a straightforward way in which to validate the methodological principles presented in this work, as well as to certify the designed MFC parameters, and establish a conclusion regarding MFC in both theoretical and practical contexts. Flight simulation results are presented in a series of case studies in order to separately analyze each flight domain and the capabilities of the tail-sitter MAV in hovering, transitioning and forward flights.

Table 4.1: DarkO tail-sitter MAV parameters.

Parameters	Values			SI Units
Mass (m)	0.492			[Kg]
Mean Chord (c)	0.135			[m]
Wingspan (b)	0.55			[m]
Wing Area (S)	0.0743			[m^2]
J_{xx}	0.00493			[Kg m^2]
J_{yy}	0.00532			[Kg m^2]
J_{zz}	0.00862			[Kg m^2]
J_p	5.1116e-06			[Kg m^2]
k_f	5.13e-6			[Kg m]
k_m	2.64e-7			[Kg m^2]
C_{d0}	0.133			No units
C_{y0}	0.145			No units
C_l	[0.47;	0.00;	0.00]	No units
C_m	[0.00;	0.54;	0.00]	No units
C_n	[0.00;	0.00;	0.52]	No units

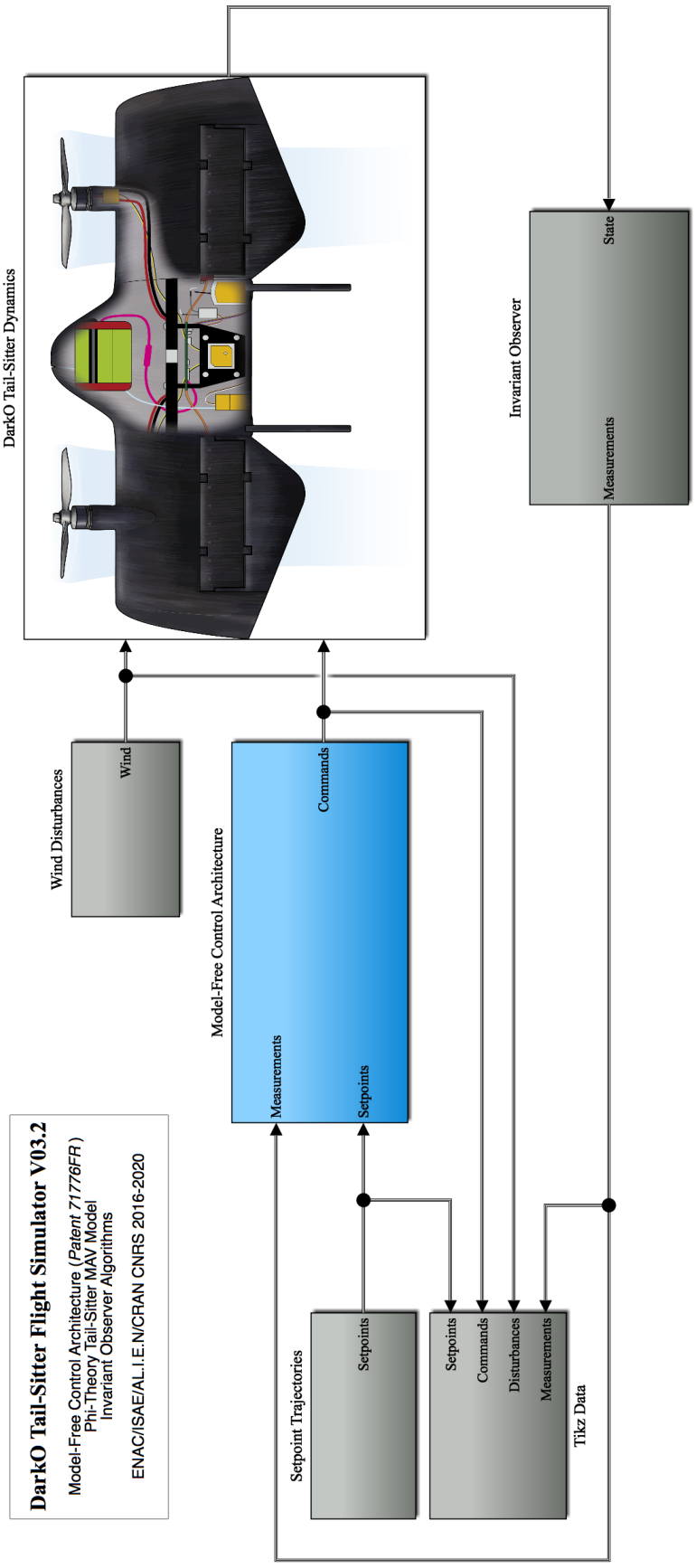

Figure 4.1: Matlab/Simulink - DarkO Tail-Sitter MAV Flight Simulator.

4.2 MFC Architecture for Tail-Sitter MAVs

The "Model-Free Control Architecture" block in Figure 4.1 will be detailed in this section. The MFC algorithms can be implemented on Multiple-Input Multiple-Output (MIMO) systems by assuming an approximate decoupling between their dynamics. This major assumption has been verified by different practical experiments (Lafont u. a., 2015), but never for tail-sitter MAVs. Despite this decoupling assumption, the MFC algorithms can compensate the effect of an arbitrary state of the system on the one being controlled by measuring its output with the MFC estimator. In order to develop the correct interactions between the blocks in the proposed control architecture, we use a prior knowledge of sign-convention between control-inputs and tail-sitter MAV states based on flight mechanics equations.

4.2.1 Principle

Figure 4.2 shows the main ideas of our control architecture. The block *Trajectory generator* is composed of a state flow algorithm that constantly defines the desired positions (x_{sp}, y_{sp}, z_{sp}) in the inertial coordinate system. These references are taken into account by the *Position control* block and are compared with the respective measures (x_m, y_m, z_m) creating three errors that are minimized by the MFC algorithms in the *Position control* block. These three MFC algorithms in charge of the position tracking also compute the desired velocity in their respective axes. These references values which are defined in the inertial coordinate frame are transformed to the body coordinate frame as well as the velocities measurements.

Thus, the velocity control MFC$_{v_{xb}}$ computes the required thrust T_d to reach this desired velocity along $\overrightarrow{\boldsymbol{x_b}}$, the block MFC$_{v_{zb}}$ assures the velocity control along $\overrightarrow{\boldsymbol{z_b}}$ and determines the necessary pitch angle θ_{sp} to reach this desired velocity $v_{zb_{sp}}$. Both blocks control their respective velocities and inform the desired thrust and pitch angle for the entire flight envelope; that is, hover, transition and forward flight. However, the velocity control along $\overrightarrow{\boldsymbol{y_b}}$ is designed depending on the current HMAV flight phase. Therefore, in hover flight, the block MFC$_{v_{yb}}$ set the desired yaw angle ψ_{sp} and the block MFC$_{\psi}$ actuates in the system by a differential-thrust command creating a moment around $\overrightarrow{\boldsymbol{z_b}}$ in order to reach the desired velocity along $\overrightarrow{\boldsymbol{y_b}}$.

In forward flight, this lateral velocity is reached from roll rotations around $\overrightarrow{\boldsymbol{x_b}}$. These rotations orient the lift force and the HMAV can perform left-right turns with, respectively, negative and positive roll angles ϕ. The propeller speeds (ω_l, ω_r) are defined by the sum of nominal propeller rotation ω_n with a differential propeller speed Δ_ω which is in charge of the yaw control. The negative sign of ω_n for the left-propeller ω_l is due to the counter-rotation sense. The flap-deflections (δ_l, δ_r), which are in convention negative for pitch-up, are composed by the sum of symmetrical flap deflection δ_n with anti-symmetrical flap deflections Δ_δ that are the control-input for the pitch angle θ and for the roll angle ϕ, respectively.

4.2.2 Design of control blocks

Generally, the control requirements are defined for particular operating conditions and time periods. However, the control design process used in this work aims to respect the control requirements for the entire flight envelope of the tail-sitter MAV. According to the MFC design methodology described in Section 3.2.4, the designed MFC parameters presented in Table 4.2,

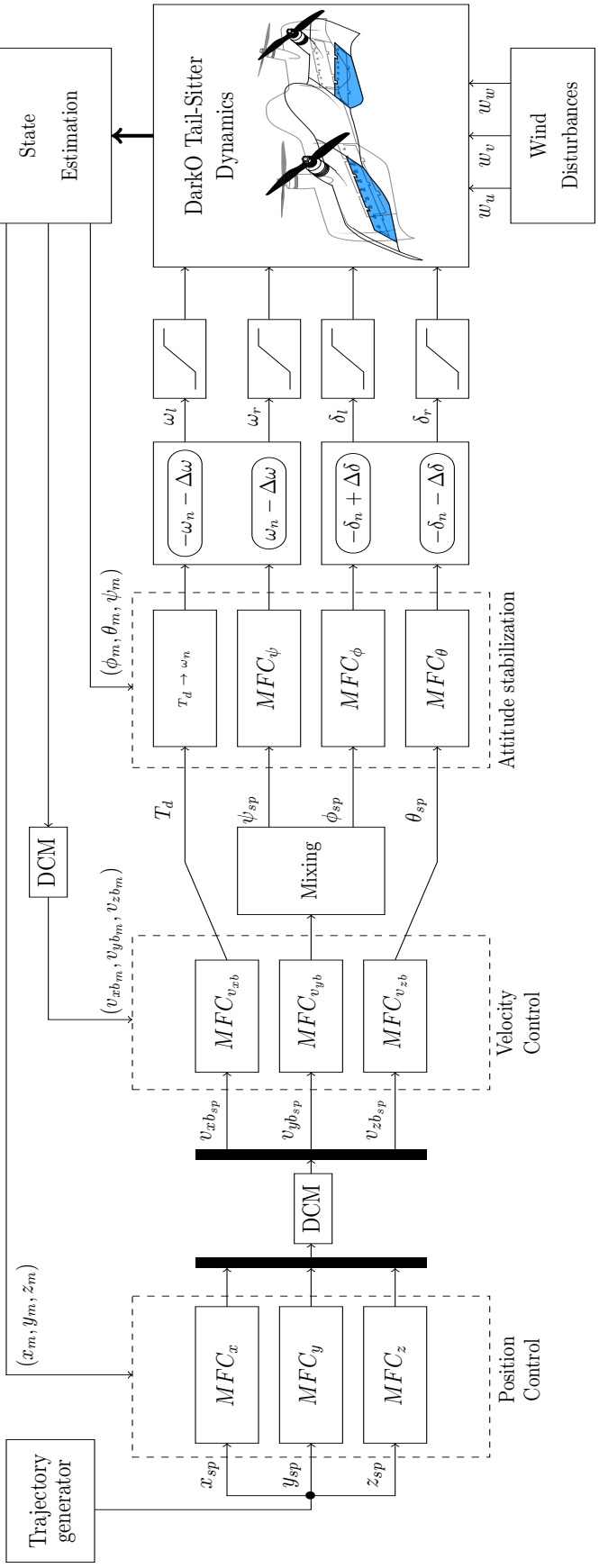

Figure 4.2: Cascaded MFC architecture designed for tail-sitter MAVs. Position control blocks send desired velocities for the velocity control blocks that compute the necessary thrust value as well as the references for attitude stabilization control-loop. Based on these desired values, propeller speeds (ω_l, ω_r) and flap deflections (δ_l, δ_r) are defined.

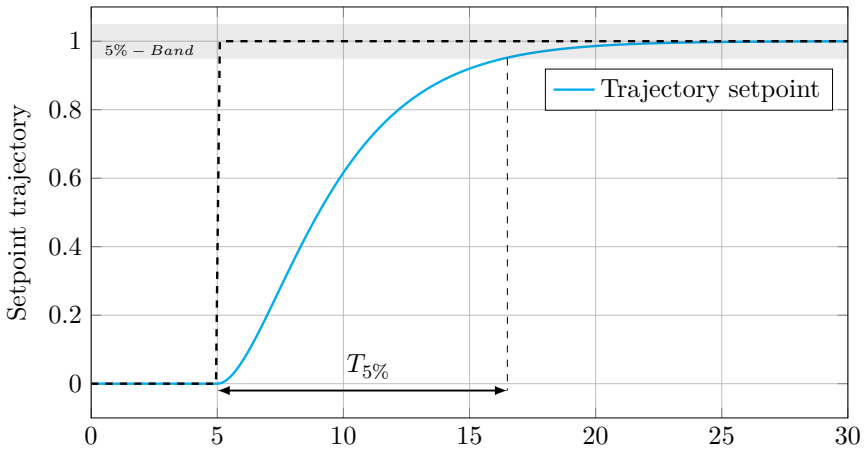

Figure 4.3: Classical control requirements.

i.e. λ_i, T_i, Kp_i and Kd_i, were tuned for the entire flight envelope and are the same for all flight simulations. The main objective is to obtain fast response times ($T_{5\%}$) with minimum overshoot according to the setpoint trajectory illustrated in Figure 4.3. The desired response time is ensured by the gains Kp_i and Kd_i. Tail-sitter MAVs are known to be a time-varying system, their internal dynamics vary according to their flight domain. Nevertheless, their internal dynamics are also affected by external disturbances, which can be estimated by the MFC estimator, and then controlled by the MFC closed-loop. Therefore, disturbance rejection properties and the adaptation of the closed-loop to variations of internal parameters were designed via the parameter T. Given that sensor delays and noises are usually a limiting factor which degrade the control performance, the parameter T was also designed according to the trade-off between fast estimations and effective noise attenuation.

Table 4.2: MFC parameters used in the simulations.

States	T_i	λ_i	Kp_i	Kd_i
x	5	25	-0.1225	-0.7
y	10	25	-0.04	-0.4
z	5	20	-0.25	-1
v_{xb}	2	10	-16	-8
v_{yb}	2	70	-7.84	-5.6
v_{zb}	5	2350	-4.6225	-4.3
ϕ	5	300	-4	-4
θ	5	450	-16	-8
ψ	3	1.15	-0.16	-0.8

4.3 Flight Simulations

4.3.1 Hovering Flight

In hovering flight, we analyze the velocity and attitude control capability to recover the MAV from different unstable initial conditions. We present an average frequency content of yaw and pitch angle signals using the Fast Fourier Transform (FFT) algorithm over the entire time that the signals were acquired. In addition, we present two position tracking missions in hovering flight and we verify the interaction between the position, velocity and attitude control blocks.

► Initial condition analysis

The initial conditions for pitch angle and forward speed during the hovering flight (θ_{ic} and $V_{x_{ic}}$), follow a normal distribution law according to (4.1) and (4.2).

$$\theta_{ic} \sim \mathcal{N}\left(\frac{\pi}{2}, \left(\frac{\pi}{6}\right)^2\right). \tag{4.1}$$

$$V_{x_{ic}} \sim \mathcal{N}\left(0, \left(\frac{5}{3}\right)^2\right). \tag{4.2}$$

The stability boundary presented in Figure 4.4 was empirically defined by evaluating all recovery trajectories from initial conditions to the desired setpoint. The desired setpoint corresponds to a stationary flight in the vertical position, with 0 m/s for the forward speed and 90 ° for the pitch angle. Basically, three classes of trajectories were distinguished during these simulations. The first combines trajectories with initial pitching angles larger than 90 ° with positive initial conditions for forward speeds. Likewise, trajectories with initial pitching angles smaller than 90 ° and negative initial conditions for forward speeds are also included in this class.

The peculiarity of these trajectories is that both converge directly to the desired equilibrium setpoint with small oscillations in the response time. This can be explained by the fact that, for initial pitching angles larger than 90 °, the thrust vector is already well-oriented and it can be increased in order to decelerate the initial positive forward speeds. This thrust vector is increased from increments of the propeller rotations, which improves the flap effectiveness by creating a powerful pitch moment that can easily orientate the attitude of the tail-sitter MAV in the right direction, towards the attitude setpoint.

The same reasoning can be used for initial pitching angles smaller than 90 ° with negative forward speeds. In this initial flight condition and orientation, the controller generates the thrust vector in order to increase the forward speed resulting in an effective pitch moment which also steers the tail-sitter MAV towards the setpoint. The second class of trajectories is composed by all initial pitching angles smaller than 90 ° with positive initial forward speeds and by all initial pitching angles larger than 90 ° with negative initial forward speeds.

These trajectories diverge at the beginning of the simulation. The thrust vector, in these flight orientations, is unable to generate an opposing force to decelerate the initial forward speed to zero. The only force opposing the movement is the drag force. By increasing the pitch angle, in this case the angle of attack, the tail-sitter MAV generates more drag and can reach the forward speed setpoint. For extreme cases, within the stability boundary, we can observe flap saturations which justify the shape of the concerned trajectories with overshots or undershots.

Figure 4.4: Initial pitch angle and forward speed condition analysis during hovering flight phase without wind disturbances. Forward speed setpoint equals to 0 m/s, and the MFC architecture computes the pitch angle setpoint equals to 90° in order to reach the stationary flight.

By analyzing the altitude results, we note that the position control is not activated. However, we can observe that the altitude is stabilized at given values according to the velocity control block which cancels the vertical velocity component. The MFC can theoretically ensure a stable flight for all initial points inside the boundary, with more or less oscillations, according to the initial conditions. The third class of trajectories in this simulation is represented by the two particular initial points outside the stability boundary corresponding to unstable flights where the controller cannot stabilize the tail-sitter MAV.

▶ FFT analysis

This analysis focuses on the MFC tuning problem. Usually, the flight controller parameters are adjusted according to a setpoint trajectory and with trim points in a respective flight condition. However, tail-sitter MAV covers different flight domains which would imply a variety of setpoints trajectories with different frequencies. Thus, we analyze the entire bandwidth of frequencies corresponding to the yaw and the pitch angle during the hovering flight. We also compare its setpoint trajectory spectrum with its measured spectrum in order to determine if the MFC is over-tuned or under-tuned.

We excite the attitude dynamics adequately in order to capture the important frequencies by varying the velocity setpoint along the $y_b - axis$ and the velocity setpoint along the $z_b - axis$. According to Figure 4.2, the block MFC_{v_y} generates, in hovering flight, the setpoint to the yaw angle ψ_{sp} and the block MFC_{v_z} the setpoint to the pitch angle θ_{sp}. Figure 4.5 shows the comparison between the desired yaw angle and its respective measured signal in both time and frequency domains. High precision tracking for frequencies up to 4 rad/s is observed, which means that the controller is able to track, with high precision, yaw setpoint variations up to 285 °/s.

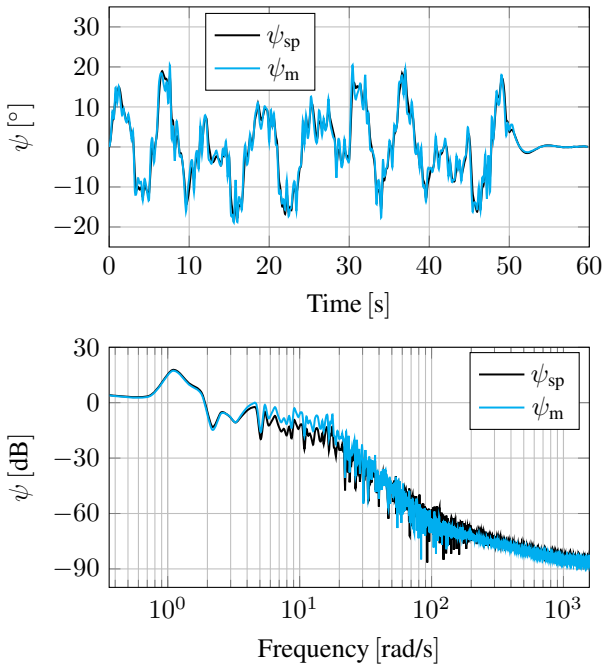

Figure 4.5: Frequential analysis of yaw angle in hover flight.

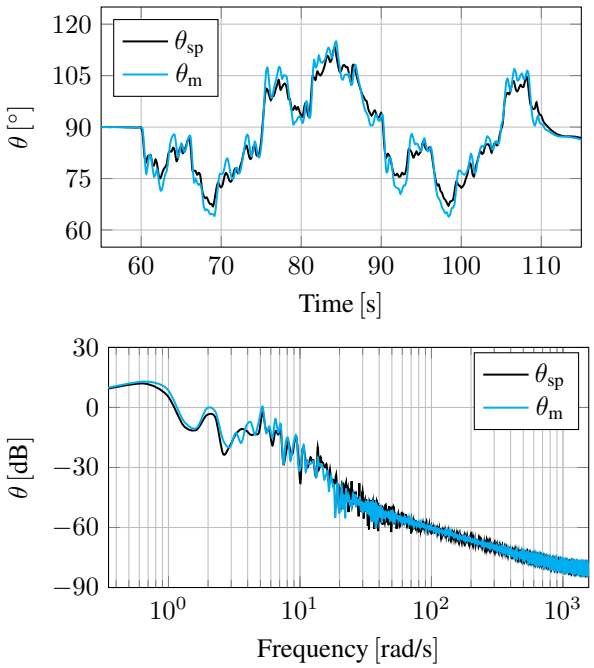

Figure 4.6: Frequential analysis of pitch angle in hover flight.

Furthermore, the tuned yaw control parameters present a reasonable trade-off to track low and high frequencies that compose its bandwidth. The results of the pitch angle presented in Figure 4.6 shows an effective tracking over its entire frequency spectrum. In addition, for high frequencies, the controller filters the references providing a smooth pitch output, but with an offset between the signals creating a small error.

▶ Hovering flight missions

The main objective of the first flight simulation in hovering mode, shown in Figure 4.7 is the study of wind influence in the position tracking, for the following desired positions :

$$
\begin{aligned}
x_{sp} &= 0, \forall\, t \\
y_{sp} &= 0, \forall\, t \\
z_{sp} &= \begin{cases} 10, & t \in]0; 155]s \\ 0, & t > 155s \end{cases}
\end{aligned}
$$

During this flight mode (**#Flight 1**), the tail-sitter MAV is more susceptible to aerodynamic disturbances. We can explain this by the fact that, in the vertical position, the wind gust along the $x_i - axis$ (respectively, along the $z_b - axis$), is in contact with the total reference wing area generating a considerable drag force. In addition, the tail-sitter MAV is not able to compensate this force in the vertical position. That is why the transition is performed and the drag force created by the wind can be compensated for by the thrust in order to ensure the position tracking. The thrust used to reject this perturbation can be seen in Figure 4.7d. The wind from the East with a magnitude of 5 m/s (see Figure 4.7f) also produces a side force in the $y_b - axis$. This force is compensated for by orienting the lift force with a symmetrical rotation around the $x_b - axis$ corresponding to the negative roll angle shown in Figure 4.7c.

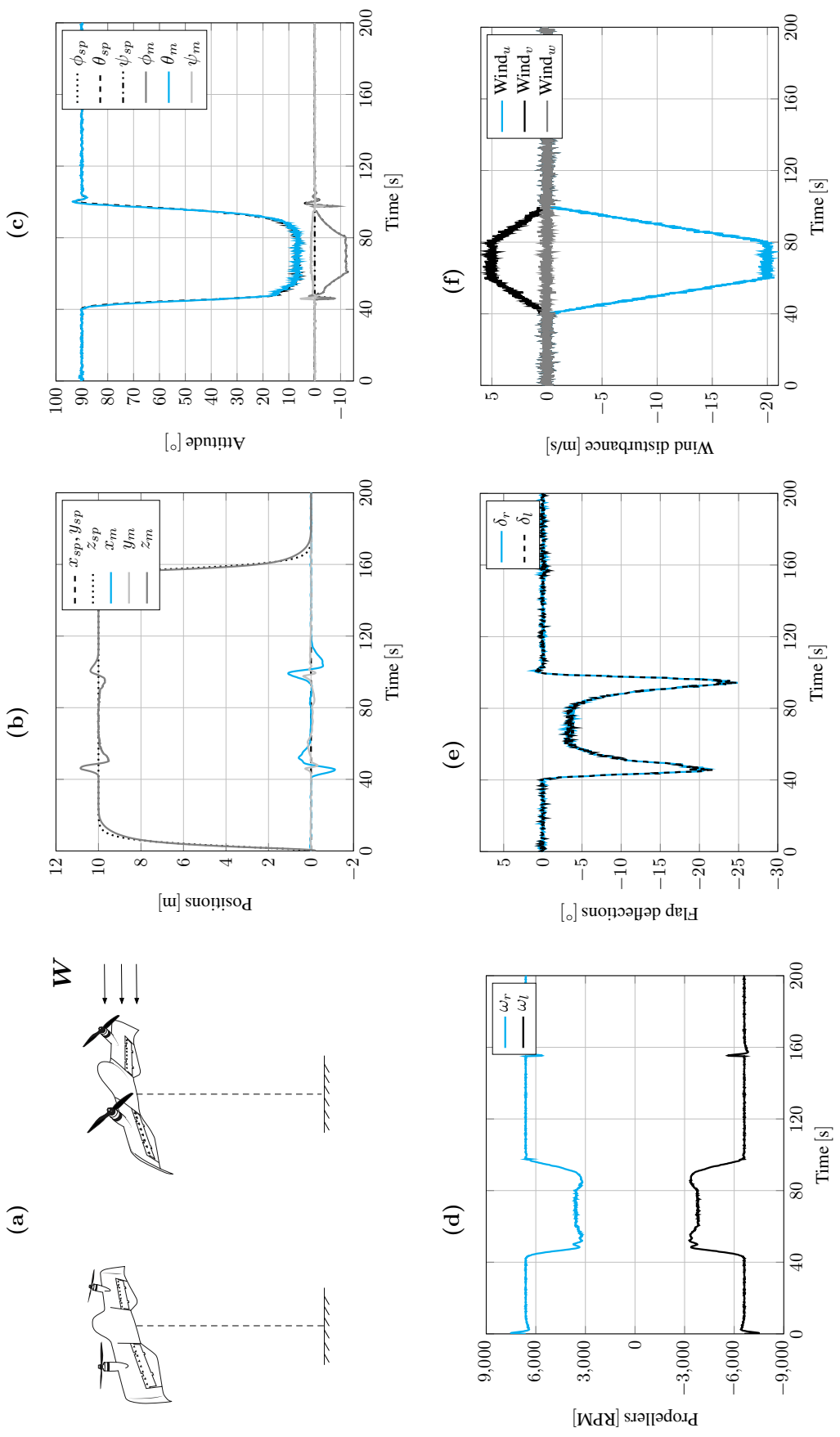

Figure 4.7: (#**Flight 1**) - Vertical take-off and transition flight to assure position tracking during high crosswind. On the top, from left to right: simulation illustration, positions in the inertial coordinate frame and attitude. On the bottom: propeller speeds ($\omega_l < 0$ and $\omega_r > 0$) due to counter-rotation sense, flap deflections (δ_l and δ_r) convention negative for pitch-up, and wind disturbance.

In the second flight simulation, we impose a circular setpoint path (**#Flight 2**) in order to validate the interaction between all control blocks in the proposed control architecture. The following equations define the desired trajectories (x_{sp}, y_{sp}, z_{sp}),

$$x_{sp} = \begin{cases} 0, & t < 30s \\ x_c + r\,cos\Big(\frac{2\pi}{40}t\Big), & t \in [30;130]s \\ 1, & t > 130s \end{cases}$$

$$y_{sp} = \begin{cases} 0, & t < 30s \\ y_c + r\,sin\Big(\frac{2\pi}{40}t\Big), & t \in [30;130]s \\ 5, & t > 130s \end{cases}$$

$$z_{sp} = \begin{cases} 10, & t \in [0;155]s \\ 0, & t > 155s \end{cases}$$

where x_c and y_c correspond to the center of the circle and r is its radius. This maneuver requires the tail-sitter MAV to fly along a circular trajectory while constantly pointing its nose towards a precise fixed point. Accurate position, velocity and especially yaw angle control are needed to accurately follow the desired flight plan. Figure 4.8 shows the simulation results, which validated the interaction between all the control blocks in the hovering flight phase.

Conclusion (Hovering flight phase)**.** *In hovering flight simulations, the proposed MFC architecture shown the capability to recover the tail-sitter MAV from a large range of initial conditions for both pitch angle and forward speed, thereby validating the interactions between attitude and velocity control blocks. The disturbances that damage the controlled output signal are estimated and annulled by the controller providing robust disturbance rejections in order to track a desired position. For strong wind disturbances, the tail-sitter MAV performs a smooth transition ensuring position tracking. Indeed, the FFT analysis validated the designed MFC parameters for the entire attitude frequency spectrum.*

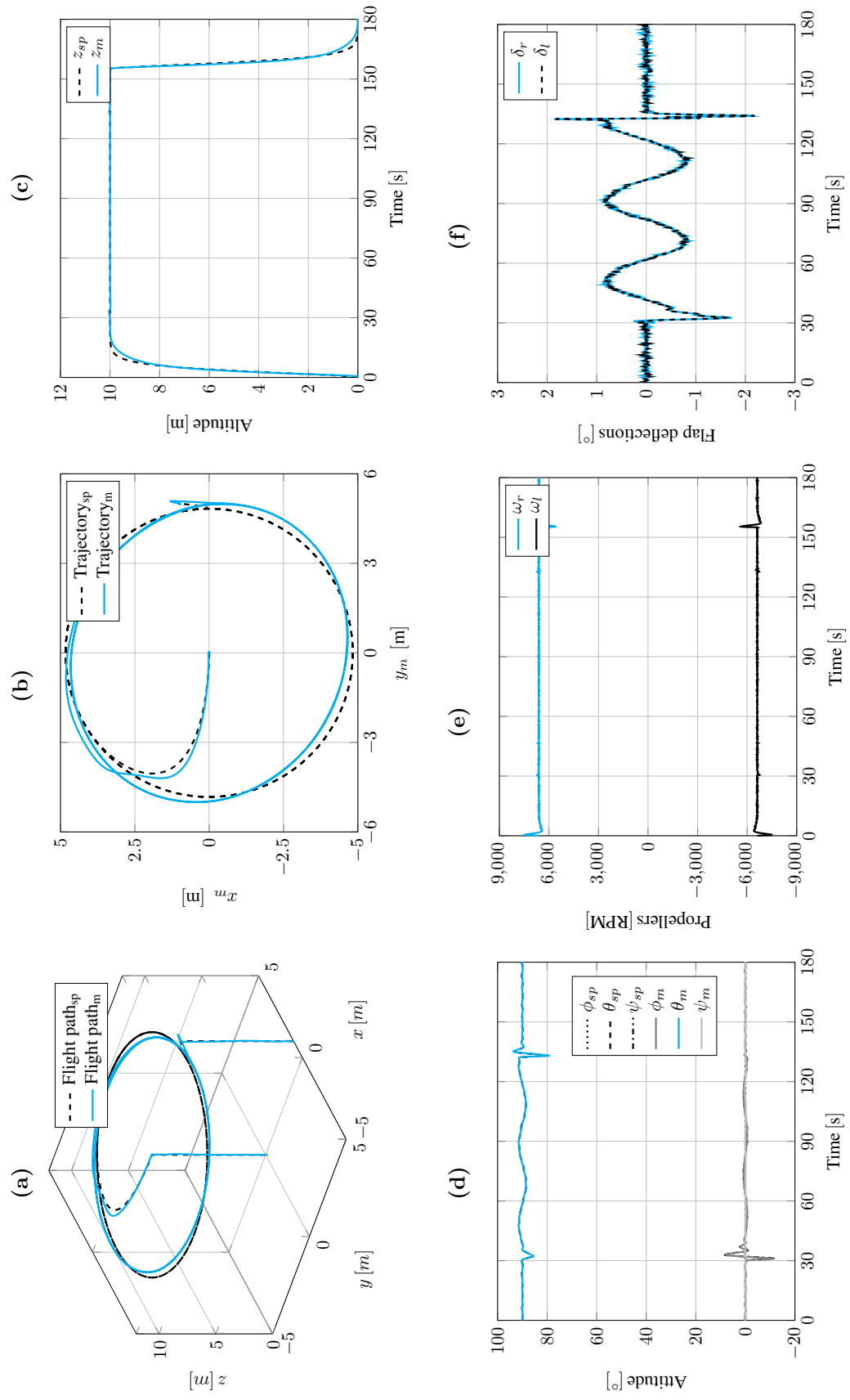

Figure 4.8: (**#Flight 2**) - Circular position tracking in hover flight mode. On the top, from left to right: the 3D flight path, North and East positions and altitude. On the bottom: attitude, propeller speeds and flap deflections.

4.3.2 Transitioning Flight

The transitioning flight simulations were examined into two parts. In the first one, similar to the hovering flight, we analyze the velocity and attitude controller's ability to recover the MAV from different unstable initial conditions to the desired stable setpoint. The second case study presents variations of nominal tail-sitter MAV parameters in flight at different pitch angles in order to evaluate the MFC adaptive properties during the forward-to-hover transition.

► Initial condition analysis

In this case study, we define a forward speed setpoint that equals 5 m/s and the MFC cascaded architecture computes a pitch angle setpoint of around 45 °. The desired forward speed setpoint was chosen in order to prove, by flight simulations without predefined gains or gain scheduling methods, that the proposed control architecture is able to stabilize the tail-sitter MAV in a critical flight domain, corresponding to the stall region where the tail-sitter MAV flies at low forward speed and a high angle of attack. The initial conditions during the transitioning flight analysis (θ_{ic} and $V_{x_{ic}}$), are defined from a normal distribution law given by the following equations (4.3) and (4.4).

$$\theta_{ic} \sim \mathcal{N}\left(\frac{\pi}{4},\, 30^2\right). \tag{4.3}$$

$$V_{x_{ic}} \sim \mathcal{N}\left(5,\, 2^2\right). \tag{4.4}$$

The empirically defined stability boundary for initial conditions in transitioning flight, is presented in Figure 4.9. The three classes of trajectories discussed in the hovering flight analysis can be also observed in this case study. These trajectories have a slower convergence time with respect to the trajectories in the hovering flight domain. Flap saturation affects the response time, but the main reason for the slower convergence time in the transitioning flight domain is the difficulty to decelerate the tail-sitter MAV, which depends only on the drag force.

Given that, the thrust controls the velocity along $\vec{z_i}$. For these initial condition analyzes, the tail-sitter MAV was not controlled in position allowing a supplementary degree of freedom to recover the stable attitude setpoint. During the transitional regime, which corresponds to the trajectory from the initial conditions to the setpoints, the tail-sitter MAV loses altitude for two reasons : first the initial condition for both pitch angle and forward speed precludes the production of lift force; and second, the thrust orientation is not adequate to compensate for the weight of the tail-sitter MAV. Thus, fast attitude stabilization is crucial to steer the thrust and bring the tail-sitter MAV back to safe flight conditions.

► Parameter-varying analysis

In this analysis, we evaluate the altitude tracking and the attitude stabilization : more precisely, the pitch angle stabilization, by imposing variations of mass and inertia at different points in the pitch angle trajectory during the forward-to-hover transition. For each point in which the variations occur, we compute the standard deviation between the altitude setpoint and its measurement. Figure 4.10 shows a typical pitch angle response time for the forward-to-hover transition with nominal tail-sitter MAV parameters. The altitude behavior and its standard deviation values computed for different mass and inertia values are also presented. We impose a

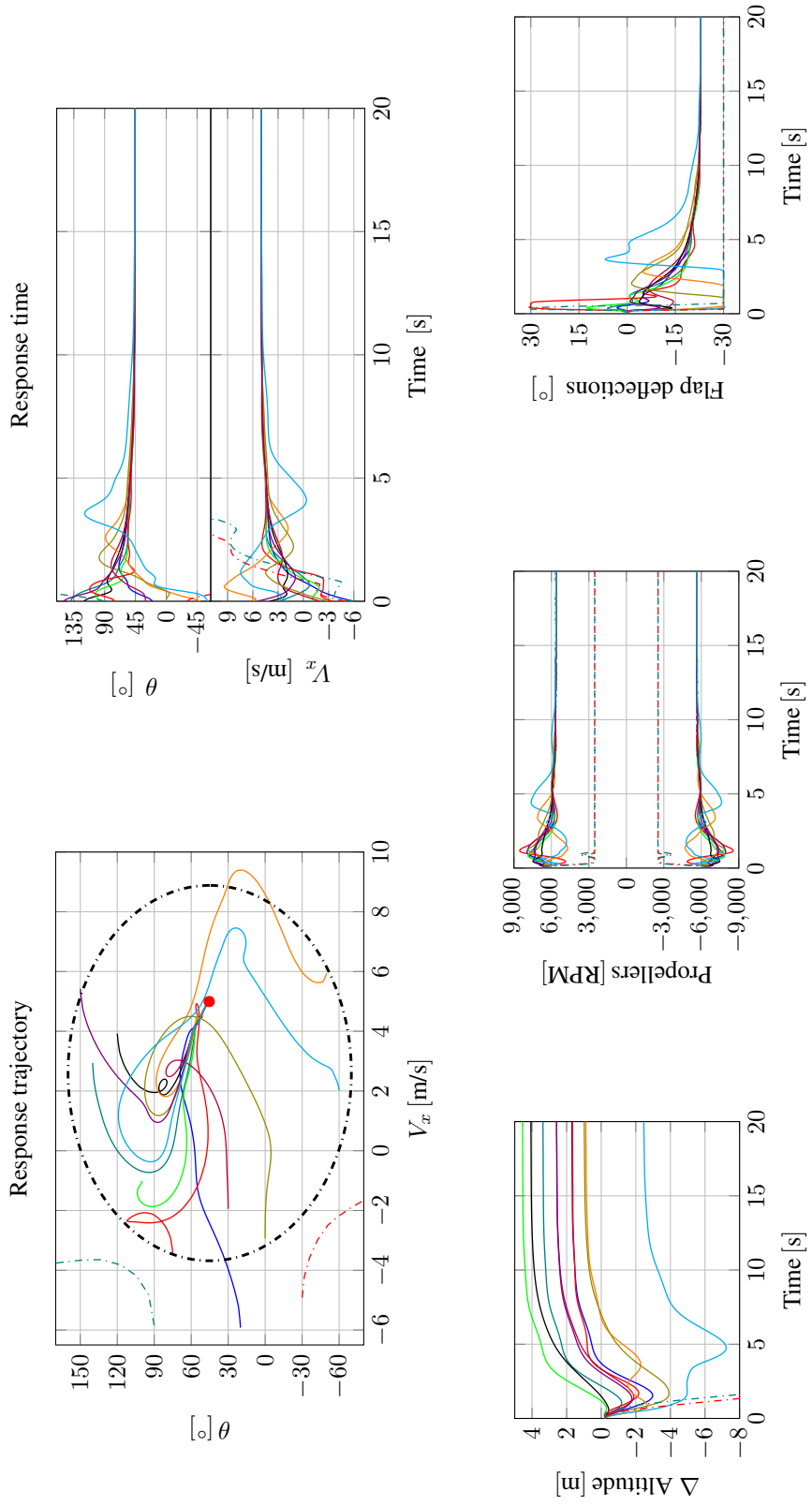

Figure 4.9: Initial pitch angle and forward speed condition analysis during the transitioning flight phase without wind disturbances. Forward speed setpoint equals to 5 m/s, the MFC architecture computes the pitch angle setpoint approximately equals to 45°.

maximum mass and inertia variations of around 45 % of the nominal tail-sitter MAV parameters. This study concludes that the tail-sitter MAV is less robust to variations of mass and inertia when it occurs between 20 ° and 40 ° of pitch angle. However, the impact of mass and inertia variations on altitude tracking remains trivial with a maximum standard deviation equal to 0.3 meters. The proposed control approach is able to stabilize the forward-to-hover transition without any knowledge about the tail-sitter MAV parameters. By using the estimator ($\hat{F}$) in the closed-loop, any impact on the tail-sitter MAV dynamics caused by parametric variations are estimated and immediately compensated for in order to reach the altitude setpoint trajectory previously imposed.

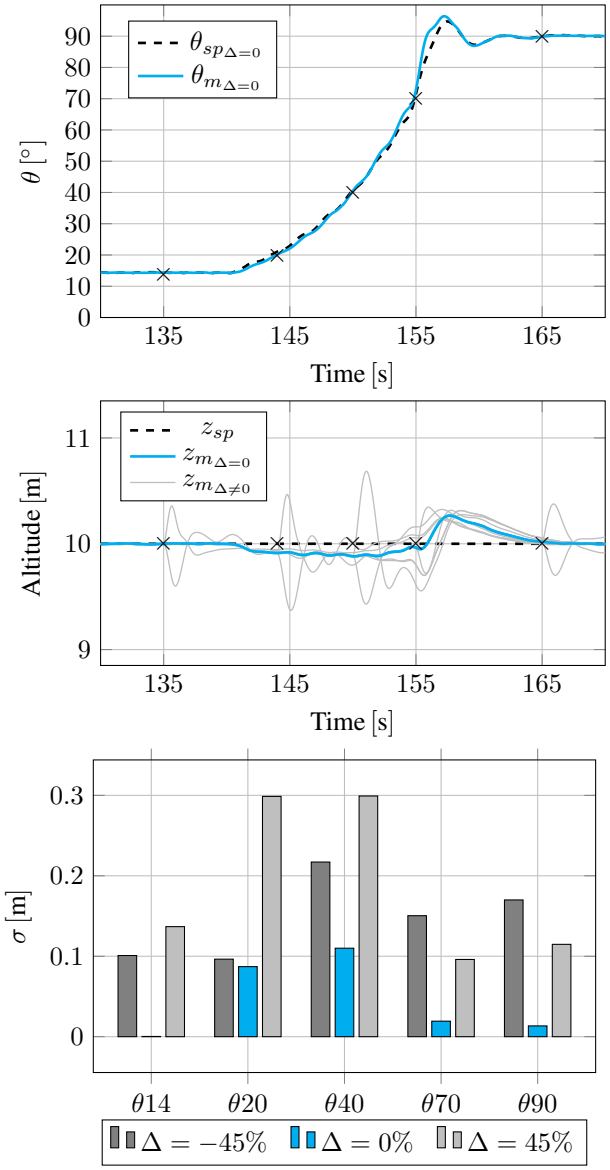

Figure 4.10: Parameter-varying analysis for different points in the forward-to-hover transition. The black crosses in altitude and pitch angle trajectories indicate the points in which the parameters were changed. Δ represents the variation of nominal mass and inertia by percentage. The standard deviation between the altitude setpoint and its measurements is denoted by σ.

Conclusion (Transitioning flight phase)**.** *The fast changing of aerodynamic forces and moments present in this critical flight domain have been countered by the proposed control architecture. The tail-sitter MAV was stabilized in a critical attitude setpoint from different initial conditions. Further, the parameter-varying analysis highlighted the promising adaptive properties of the proposed control technique.*

4.3.3 Forward Flight

The last studied flight phase corresponds to the forward flight. Given that, the MFC parameters are tuned for the entire flight envelope without any type of gain scheduled and the tail-sitter MAV dynamics change between the flight phases, we compute the FFT to the roll and the pitch angles in order to compare the frequential control performance with the previous results in hovering flight. In addition to this analysis, we present a full flight simulation exploring all tail-sitter MAV flight phases, with a major focus on forward flight, in which the tail-sitter MAV performs a position tracking.

▶ FFT analysis

In forward flight, the roll setpoint ϕ_{sp} is generated from the velocity control block along the $y_b - axis$. This velocity is excited in order to create different setpoint values and frequencies to the roll angle. The roll tracking results in both time and frequency domains are presented in Figure 4.11. The proposed controller provides a high quality tracking up to 3 rad/s which is equivalent to 170 °/s. An offset between the roll setpoint trajectory and the roll measurement is perceived at high frequencies. However, in this frequency range, the signals are almost negligible, given their respective attenuation in decibels (dB). Pitch angle results are presented in Figure 4.12. We

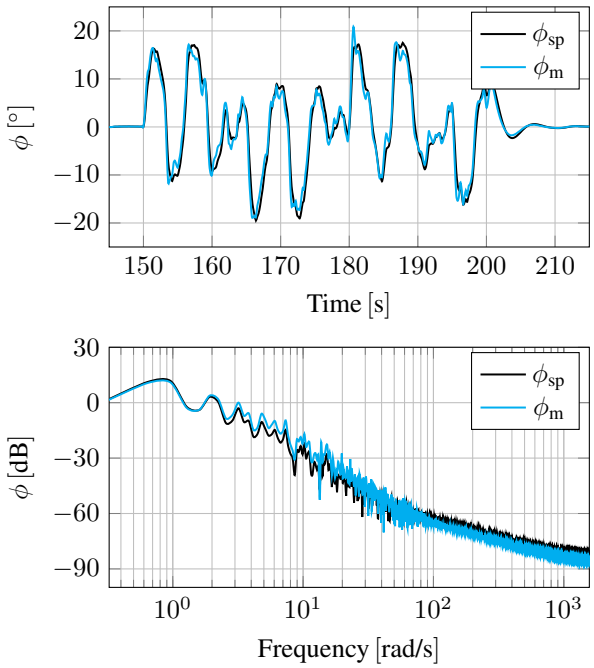

Figure 4.11: Frequential analysis of roll angle in forward flight.

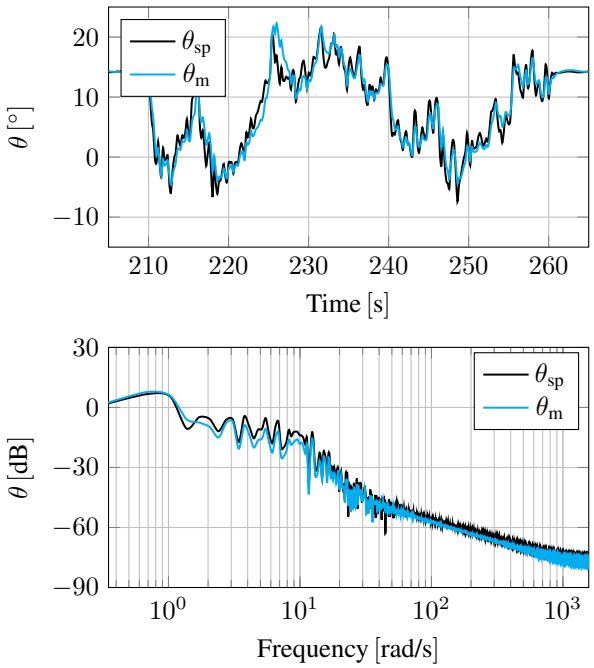

Figure 4.12: Frequential analysis of pitch angle in forward flight.

quantify a maximum pitch tracking error of 1.58 ° for pitch angle setpoints varying between 1 and 10 rad/s, equivalent to 57 and 573 °/s. Overall, the FFT analysis has revealed, the promising performance of MFC for attitude tracking in both hovering and forward flight. Further, this analysis shows that the MFC parameters were well adjusted considering the trade-off between the quality of attitude stabilization with delays and noises in the control-loop.

▶ Forward flight mission

A complete flight mission (**#Flight 3**) is presented in Figure 4.13. Here, we evaluate all tail-sitter MAV flight capabilities through a vertical take-off from zero to 10 meters of altitude, followed by the hover-to-forward transition with a position tracking in the $xy - plane$ and an altitude change in forward flight. Then, the forward-to-hover transition is performed with a position tracking in hovering flight. The flight simulation ends with a vertical landing. The complete 3D flight path is presented in Figure 4.13a.

The controller assures the position tracking during the entire mission. As we can see in Figure 4.13b, the altitude presents small oscillations at 45 and 165 seconds of simulation which is acceptable for this MAV class. These oscillations are due to the fast variations of aerodynamic forces and moments that occur during the transition flight phases where the pitch angle changes resulting in significant variations in the angle of attack (see Figure 4.13d).

In the same figure, between 45 and 90 seconds of simulation, we can see the roll angle behavior in charge of reach the desired east position in forward flight. Similarly, between 180 and 215 seconds of simulation, the yaw behavior in charge of reach the east position in hovering flight. Figure 4.13c presents the velocities in the body coordinate system and the actuator dynamics, which are, the propeller rotations and the flap deflections, as shown in Figure 4.13e and Figure 4.13f, respectively.

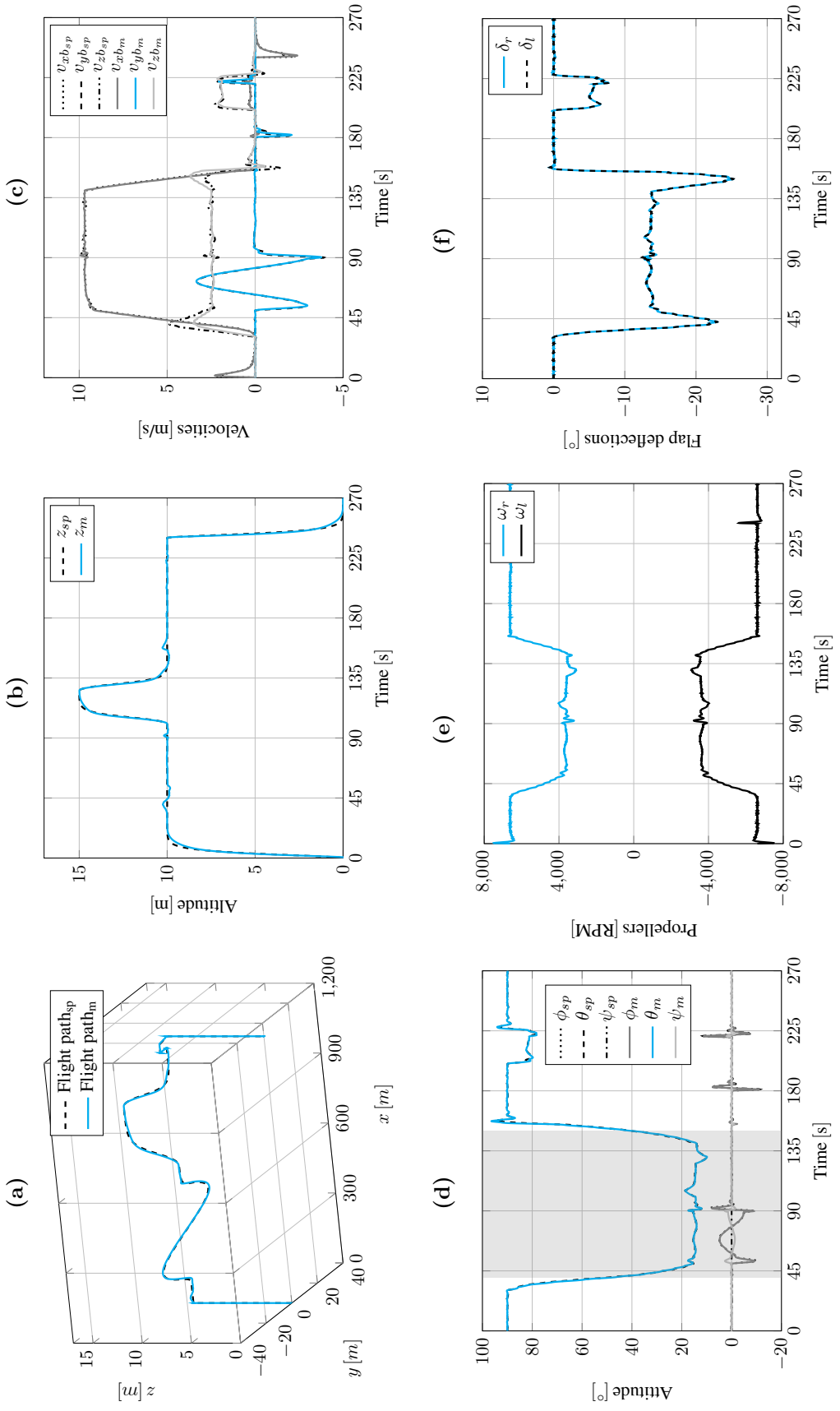

Figure 4.13: (**#Flight 3**) - Entire flight envelope simulation in relatively calm flight conditions. On the top, from left to right: the 3D flight path, altitude and velocities in the body coordinate system. On the bottom: attitude, propeller speeds and flap deflections.

Conclusion (Forward flight)**.** *We confirm in this subsection that, the proposed MFC architecture also ensures the position tracking, velocity control and attitude stabilization in forward flight. With the FFT analysis, we show the attitude control performance for a large range of frequencies. Furthermore, we validate the interactions between each control block for a wide range of the tail-sitter MAV attitude orientation within its flight envelope.*

4.3.4 Parameter-varying analysis by Monte Carlo method

Through the designed MFC parameters for a tail-sitter MAV model, this section addresses the usefulness, reliability and adaptiveness properties of the proposed control architecture. While the previous simulation flights emphasize MFC adaptiveness features in relation to external disturbances, this section demonstrates the MFC properties in relation to internal parameter-varying. Furthermore, this analysis aims to quantify the maximum allowable variations of the DarkO's parameters, for which the proposed MFC architecture, with the same designed MFC parameters, ensures flight stability.

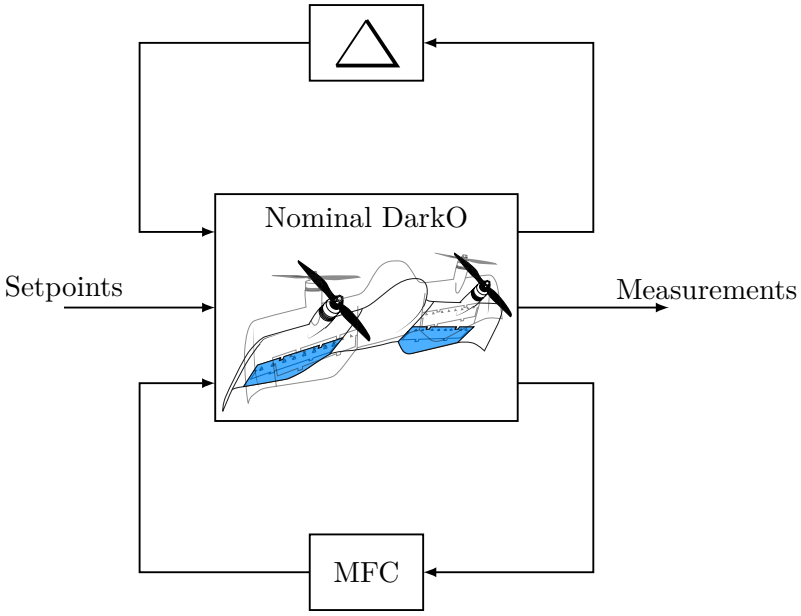

Figure 4.14: Parameter-varying analysis with MFC algorithms.

In order to reduce the computational effort that increases exponentially with the number of variable terms and due to the difficulty in understanding the results when varying more than three or four parameters in combination, we have opted to implement a Monte Carlo method in which the mass, inertia and geometric coefficients are properly modified. According to the aerodynamic formulation described in Chapter 2, aerodynamic coefficients depend on geometric parameters, such as wingspan and chord length. Thereby, variations in aerodynamic coefficients and their influence on the stability of the closed-loop system have also been taken into account. Quantifying the set of parameters for which the DarkO remains stable determines a tail-sitter MAV class that can be stabilized by the proposed architecture with the same designed MFC parameters.

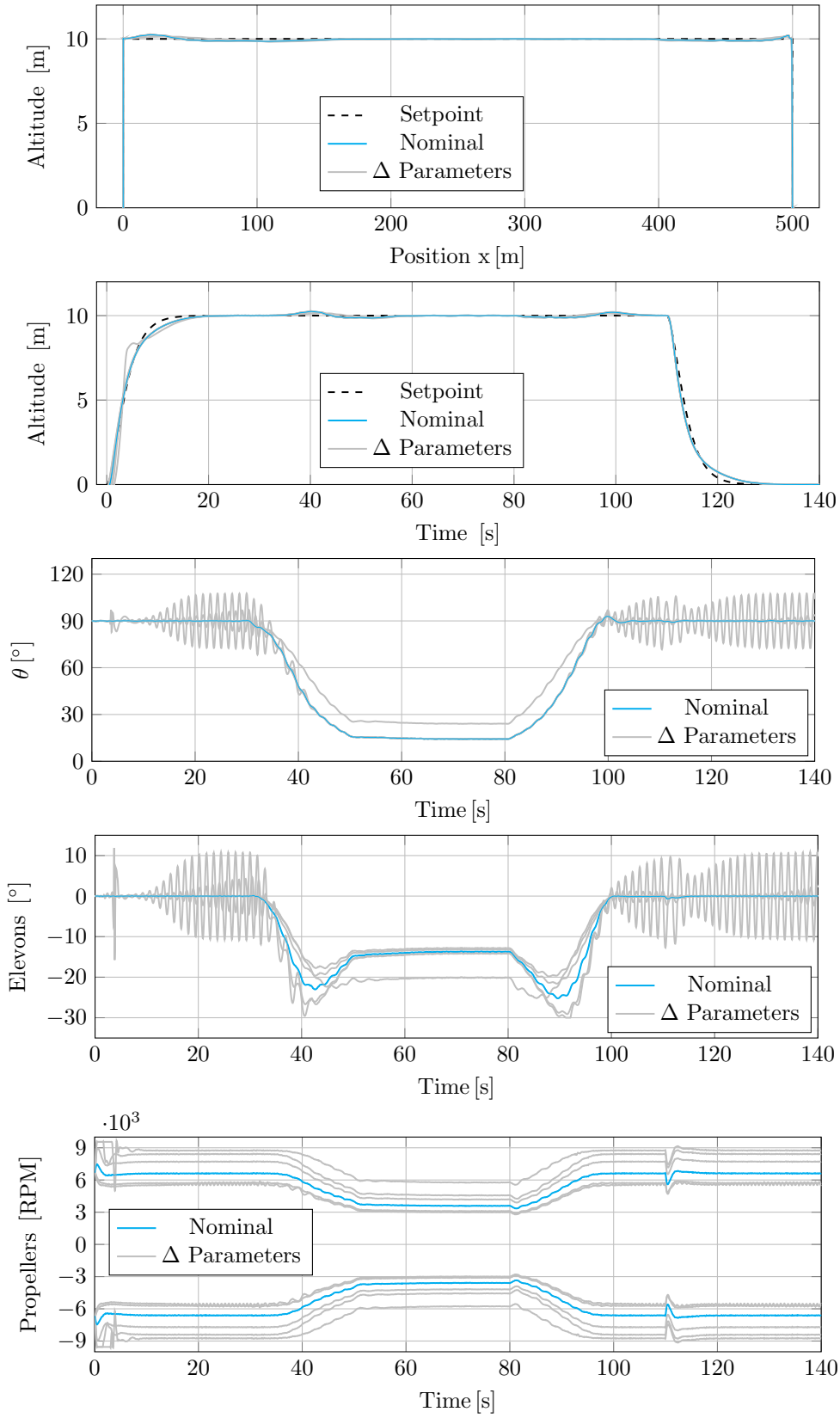

Figure 4.15: Parameter-varying analysis.

In Figure 4.14, we introduce the classical uncertain schema with the uncertainty block (Δ) in the control-loop system. This block represents all DarkO's parameters that will be evaluated, in which their variations are represented as a percentage of the DarkO's nominal parameters :

$$\Delta = \begin{cases} \text{mass} & \in [-50\%; +100\%] \\ \text{inertia} & \in [-50\%; +100\%] \\ \text{wingspan} & \in [-50\%; +100\%] \\ \text{chord} & \in [-50\%; +100\%] \end{cases}$$

In order to evaluate the effect of parameter variations on the dynamics of the system, several flight simulations have been performed. Figure 4.16 shows the proposed flight path in which the longitudinal dynamics of the DarkO have been analyzed. At the beginning of each flight simulation, the DarkO's parameters have been modified and identical setpoint trajectories have been imposed on the system.

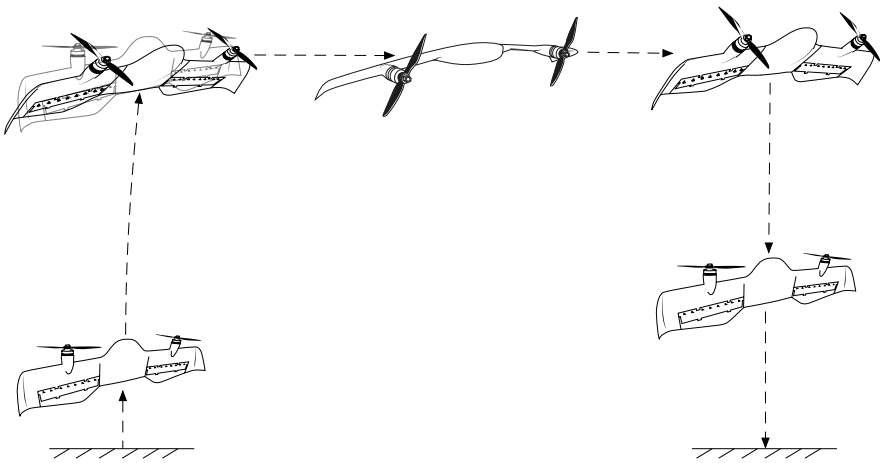

Figure 4.16: Flight path evaluated during the parameter-varying analysis.

For visibility reasons, Figure 4.15 presents the most significant flight simulations. The variation of internal parameters draw attention to the following points:

- (i) Negative parameter variations, less than $-25\,\%$ of the nominal parameters, lead to unstable pitch dynamics in the closed-loop system. This can be explained by the reduction of inertia values in this axis which introduces oscillatory dynamics characterized by low damping coefficients. In this case, the designed MFC parameters cannot precisely control these high oscillating dynamics.

- (ii) Positive parameter variations, such as increased mass, have led to the saturation of the propeller's rotations at the beginning of the simulations. The adaptiveness properties of the MFC are effective when system actuators are not saturated. Therefore, unstable dynamics result from the physical constraints of the system that prevents the controller from being able correctly adjust its commands.

- (iii) Altitude behavior was little affected by variations in parameters.

It can be concluded from this analysis that, MFC algorithms and its adaptiveness features were able to stabilize the DarkO's dynamics for variations between $-25\,\%$ and $+75\,\%$ of its nominal parameters.

4.4 Model-Based and Model-Free Control Comparison

This section compares the performance of the model-based control approach with that of the MFC technique. The LQR was chosen as model-based approach due to its optimal features, which are presented in the following. MFC and LQR were designed for the tail-sitter MAV called *MAVion* (see Figure 4.17). Simulation flights were performed in order to evaluate both controllers during hovering, transitioning and forward flight domains.

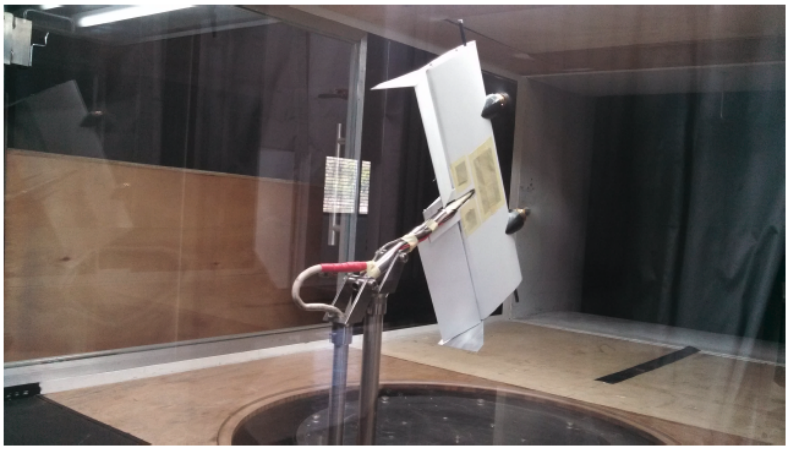

Figure 4.17: MAVion tail-sitter MAV.

4.4.1 Linear Quadratic Regulator

▶ LQR Overview

LQR is a type of optimal control synthesis which provides stability for a system according to performance criteria. Basically, it involves the stabilization of the system by placing the closed-loop poles at desirable locations. This may be achieved by designing the control-output vector $\boldsymbol{u} \in R^m$ to minimize a quadratic cost of the type

$$J = \frac{1}{2}\int_0^\infty (\boldsymbol{x}^T Q \boldsymbol{x} + \boldsymbol{u}^T R \boldsymbol{u})\, dt, \tag{4.5}$$

where $\boldsymbol{x} \in R^n$ represents the state vector of the system, and Q, and R are the weighting matrices that should be symmetric positive-semidefinite. In contrast with most of the controller presented earlier in the literature review, this method uses a state-space representation, also known as the time-domain approach. This state-space representation provides a compact way by which to analyze and synthesize controllers for systems with multiple inputs and outputs. If the dynamics of the system are time-invariant, finite-dimensional and can be linearized, then the differential equations may be written in matrix form, given by the following:

$$\begin{aligned} \dot{\boldsymbol{x}} &= A\boldsymbol{x} + B\boldsymbol{u} \\ \boldsymbol{y} &= C\boldsymbol{x} + D\boldsymbol{u} \end{aligned} \tag{4.6}$$

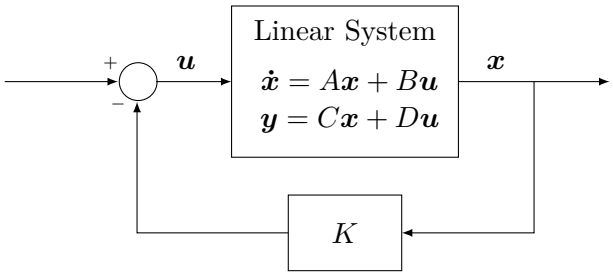

Figure 4.18: LQR design with full state feedback.

The closed-loop system provided by the LQR is achieved by the feedback matrix of gains K according to Figure 4.18. In the case of full state feedback, the control-output becomes $\boldsymbol{u} = -K\boldsymbol{x}$, which results in the following closed-loop system :

$$\dot{\boldsymbol{x}} = (A - BK)\boldsymbol{x} \equiv A_c\,\boldsymbol{x} \tag{4.7}$$

The LQR control solution $\boldsymbol{u}^*$ that minimizes the cost function in (4.5) for the system described by (4.6), can be obtained from (Stevens u. a., 2015, p. 470-474), resulting in

$$\boldsymbol{u}^* = -R^{-1}B^T P\,\boldsymbol{x} \tag{4.8}$$

where

$$K = R^{-1}B^T P \tag{4.9}$$

represents the Kalman Gain, plus P, the unique solution of the Algebraic Riccati Equation (4.10). This solution exists if the peer (A,B) is stabilizable and the peer $(A,\sqrt{Q})$ is detectable.

$$PA + A^T P - PBR^{-1}B^T P + Q = 0 \tag{4.10}$$

The performance of a such controller is directly impacted by the magnitudes of the weighting matrices R and Q, which implies a trade-off. For instance, a larger control-weighting matrix R reduces the energetic consumption of the system making it necessary for $\boldsymbol{u}^*$ to be smaller. On the other hand, to make $\boldsymbol{x}$ go to its reference more quickly with time, Q may be defined as larger. In addition, the position of the closed-loop poles — represented by the eigenvalues of the matrix A_c in (4.7) — depends on the choices of these weighting matrices. They may be chosen to provide good time responses while minimizing the generalized minimum-energy problem, as defined in (4.5).

▶ LQR design to a tail-sitter MAV

This controller can be exploited in many different ways. The approach proposed by (Lustosa, 2017, p. 79) to stabilize a tail-sitter MAV relies on the following procedure. Consider the mathematical formulation (4.11) that describes the non-linear dynamics of the system

$$\dot{\boldsymbol{x}} = f(\boldsymbol{x}, \boldsymbol{u}) \tag{4.11}$$

with the selected state vector and control-inputs

$$\begin{aligned} \boldsymbol{x} &= (\boldsymbol{v_b}\ \ \boldsymbol{\omega_b}\ \ \boldsymbol{q}) \\ \boldsymbol{u} &= (\omega_l\ \ \omega_r\ \ \delta_l\ \ \delta_r) \end{aligned} \tag{4.12}$$

Algorithm 3 Compute LQR gains for different operating points

procedure SCHEDULED LQR
  Operating points: $\boldsymbol{x} \in \boldsymbol{X_0}$ and $\boldsymbol{u} \in \boldsymbol{U_0}$
  Define weighting matrices: Q and R
  for each $\boldsymbol{x_i} \in \boldsymbol{X_0}$ and $\boldsymbol{u_i} \in \boldsymbol{U_0}$ **do**
    compute Jacobians $A_i = \frac{\delta f}{\delta x}$ and $B_i = \frac{\delta f}{\delta u}$
    solve $P_i A_i + A_i^T P_i - P_i B_i R^{-1} B_i^T P_i + Q = 0$
    compute $K_i = R^{-1} B_i^T P_i$
  Return K_i

where $\boldsymbol{v_b} \in \mathbb{R}^3$ is the vehicle's linear velocity, $\boldsymbol{\omega_b} \in \mathbb{R}^3$ is the vehicle's angular velocity equals to $[p\ q\ r]^T$ which are both expressed in the body coordinate frame and $\boldsymbol{q} \in \mathbb{R}^4$ is the quaternion formulation. The system is controlled via four control-inputs; respectively, the left and right propeller rotation speeds and the left and right flap deflections.

The non-minimal representation of quaternions introduces a lack of controllability for the system. This issue has been resolved by a change of coordinates in (Lustosa, 2017, p. 71) allowing the time-invariant LQR design. For this purpose, local linear models were computed for different operating points in order to cover the entire non-linear flight envelope of a tail-sitter. The linearization process and the LQR design for each operating point is described in the algorithm (3). Figure 4.19 introduces the proposed block diagram which schedules the LQR gains for different operating points within the flight envelope of the *MAVion*.

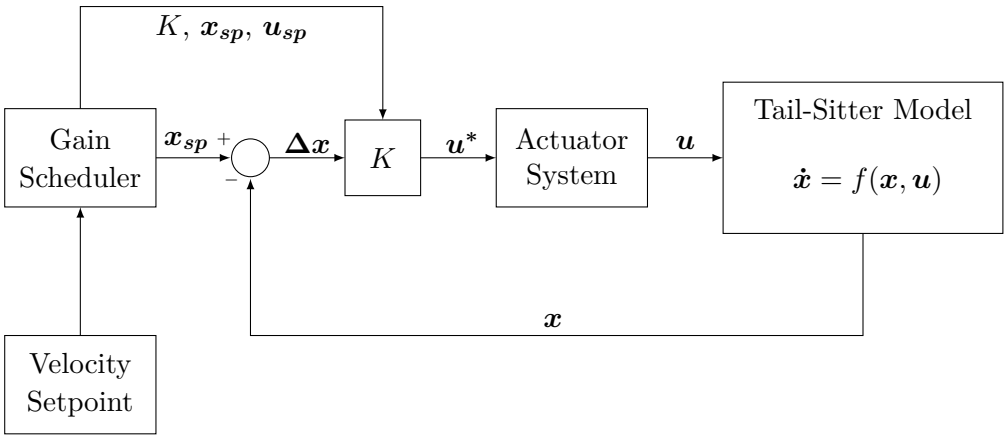

Figure 4.19: Scheduled-LQR block diagram proposed by (Lustosa, 2017, p. 80).

4.4.2 MFC and LQR comparative flight simulation results

The following flight simulation illustrates the control performance provided by the scheduled-LQR and by the MFC during transitioning flight. Both control strategies have been designed to stabilize the MAVion, the parameters of which are presented in Table 4.3. The dynamics of the tail-sitter MAV were discretized at 500 Hz, and the simulation includes additional sensor noises, state estimation errors and wind disturbances of 4 m/s (w_u, w_w), as we can see in Figure 4.20e. Wind disturbances are imposed along x and z axes in order to disturb the pitch dynamics, in particular during the transitioning flight phase. The actuators of the MAVion were saturated :

Table 4.3: MAVion tail-sitter MAV parameters.

Parameters	Values			SI Units
Mass (m)	0.45			[Kg]
Mean Chord (c)	0.21			[m]
Wingspan (b)	0.42			[m]
Wing Area (S)	0.0882			[m^2]
J_{xx}	0.0036			[Kg m^2]
J_{yy}	0.0036			[Kg m^2]
J_{zz}	0.0072			[Kg m^2]
J_p	3.46e-06			[Kg m^2]
k_f	4.48e-6			[Kg m]
k_m	2.4e-7			[Kg m^2]
C_{d0}	0.1			No units
C_{y0}	0.1			No units
C_l	[0.50;	0.00;	0.00]	No units
C_m	[0.00;	0.50;	0.00]	No units
C_n	[0.00;	0.00;	0.50]	No units

propeller speed at 9600 Revolutions Per Minute (RPM) and flap deflections at 30°. These saturations have not been reached, as we can see in Figures 4.20c and 4.20d.Figure 4.20 shows the transitioning flight simulation from hovering to forward flight. The transition was triggered by means of a forward speed setpoint, which is zero in hovering flight mode.

The tail-sitter MAV naturally performs the transition according to increments in the forward speed setpoint (see Figure 4.20a). Both controllers operate under this principle, but with small differences. The scheduled LQR uses a lookup table algorithm with predefined gains. Through this gain scheduling approach, pitch angle setpoints are selected in order to respect the trim point conditions which were defined from wind-tunnel campaigns. On the other hand, pitch angle setpoints are computed in the MFC architecture from its velocity control block, as presented in Figure 4.2. The MFC attitude setpoint is updated as a function of the current states of the system. In order to stabilize the MAV, this control strategy continuously defines the attitude setpoint, taking into account both external disturbances and changes in system dynamics. This cascaded control structure provides robust properties to the system against crosswind disturbances. In hovering flight domain, the attitude of the MAVion is more susceptible to crosswind disturbances (w_u), which explains the oscillating pitch behavior in Figure 4.20b. Despite these oscillations, both controllers ensured the stability of the system for pitch angle variation from hovering ($\theta = 90°$) to forward flight ($\theta \approx 10°$).

In order to stabilize the entire flight envelope of the MAVion and its non-linear dynamics with parametric-variations, the control strategy based on the LQR synthesis has employed 12 gain matrices covering the different operating points within the transitioning flight. On the other hand, the MFC algorithms have been designed only once and its adaptiveness features tackle the entire flight envelope and the different non-linearities present in the dynamics of the system. In forward flight domain, the pitch angle controlled by LQR approach presents a static error which could be solved by designing a new LQR synthesis with integral action terms. However, the integral action terms will result in a more complex LQR closed-loop system with new terms to design. In addition, the gain scheduling strategy will need to consider these new gains in

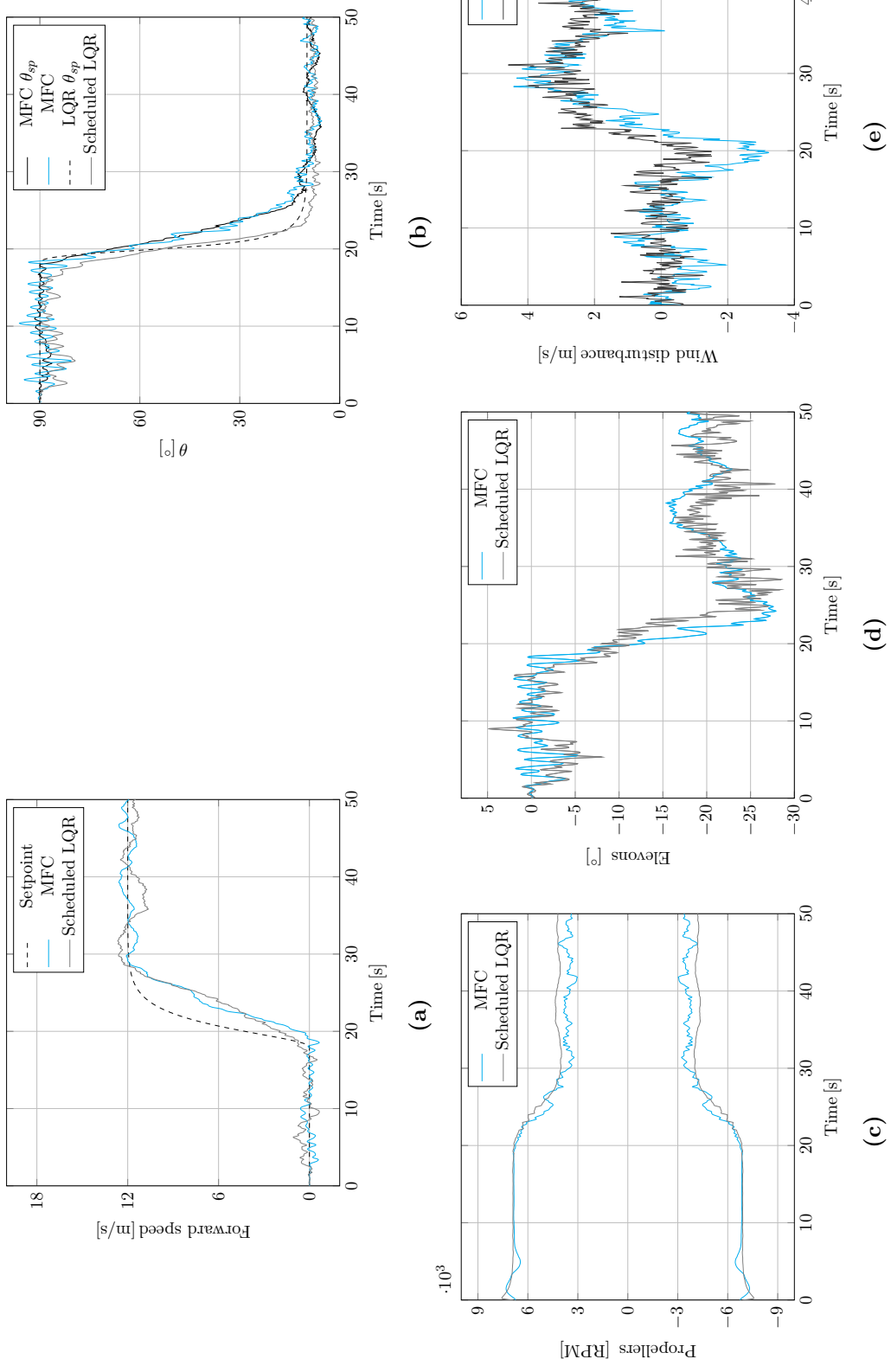

Figure 4.20: Transition flight simulation. On the top, from left to right: Flight path, forward-speed and pitch angle. On the bottom: propeller speeds ($\omega_l < 0$ and $\omega_r > 0$) due to counter-rotation sense, elevon deflections (δ_l and δ_r) convention negative for pitch-up, and wind disturbance along x and z axes.

the feedback control-loop. This comparative flight simulation draws attention to the fact that model-based control approaches require the use of scheduling methods in order to tackle the entire flight envelope of tail-sitter MAVs. The variation of aerodynamic coefficients over their different flight domains and their nonlinear dynamics are reasons for the implementation of a such methodology. In this case, the LQR gains were designed for each linearized operating point and the gain scheduling approach is used to manage them according to the correct flight domain of the tail-sitter MAV. On the other hand, the MFC illustrates the simplicity of its control algorithms with encouraging stability performance and effective disturbance rejection properties. In addition, the MFC parameters can be designed with little prior knowledge of the system. The following chapter address the analysis of the MFC approach in real-world flight conditions.

4.5 Summary of Chapter 4

This chapter illustrated a comprehensive set of flight simulations covering the entire flight envelope of tail-sitter MAVs. The proposed MFC architecture and its different control blocks have been presented. We have used a prior knowledge of sign-convention between commands and states of tail-sitter MAVs based on simple flight mechanics in order to determine the correct interactions between each block in the proposed control architecture. The particular challenge of each flight domain was controlled via the MFC architecture which is composed of position, velocity and attitude stabilization control blocks. We have investigated the correct interaction of each control block in the MFC architecture for different case studies through flight simulations.

In the hovering flight phase, the proposed MFC architecture has shown the capability to recover the tail-sitter MAV from a large range of initial conditions for both pitch angle and forward speed initial conditions. The disturbances that damage the controlled output signal were estimated and annulled by the controller providing robust disturbance rejections in order to track a desired position. For strong wind disturbances, the tail-sitter MAV performs a smooth transition ensuring position tracking. The FFT analysis has validated the designed MFC parameters for the entire attitude frequency spectrum in the hovering flight phase. In addition, a classical flight mission with the tracking of circular trajectories has been illustrated. For this flight simulation, the interaction between each control block has been validated via cascaded control strategy.

The transitioning flight domain has been also evaluated through flight simulations. First, the tail-sitter MAV was stabilized in a critical attitude setpoint from different initial conditions. In this flight simulation, the actuator saturations have been analyzed. Further, the parameter-varying analysis has highlighted the promising adaptive properties of the proposed MFC technique. A complete flight simulation has illustrated the control of the entire flight envelope of tail-sitter MAVs with a vertical take-off followed by the transition to forward flight. The proposed controller has also shown the feasibility of tracking trajectories in the forward flight domain, performing the transition back to the hovering flight and vertical landing. The FFT analysis has validated the designed MFC parameters for the aerodynamics conditions in the forward flight phase as well.

A Monte Carlo analysis has been conducted in order to quantify the maximum allowable variations of the tail-sitter MAV parameters for which the proposed MFC architecture, with the same designed MFC parameters, ensures flight stability. It can be concluded from this analysis that MFC algorithms and its adaptiveness features are able to stabilize the dynamics of the tail-sitter MAV for the important variations of its internal parameters. These variations are between $-25\,\%$ and $+75\,\%$ of the nominal parameters of the tail-sitter MAV. Finally, the last flight simulation compared the performance of the MFC with that of a model-based controller; for instance, the LQR approach during a transitioning flight. It can be concluded that the simplicity of the MFC algorithms and its properties, such as robust disturbance rejection, adaptiveness features and the fact that MFC requires little prior knowledge of the controlled system result in considerable time saving during both the control design and the implementation process with simple but effective control algorithms.

Chapter 5

Model-Free Control Validation Through Flight Tests

"*In theory, there is no difference between theory and practice. But, in practice, there is.*"
— Jan L. A. van de Snepscheut

This chapter discusses the MFC performance in real-world flight conditions, recalling and comparing its performance to that of simulation flight results presented in the previous chapter. Different experimental flights that cover all flight phases of tail-sitter MAVs to both indoor and outdoor environments are presented. Additional flight tests were conducted in order to evaluate the attitude tracking performance provided by MFC algorithms, and compare with that of the INDI controller.

Contents

5.1 Flight Test Setup

In real-world flight tests, we continue to use the DarkO MAV, which is a tail-sitter configuration. The objective is to validate the control performance delivered by MFC algorithms in simulation flights, for the first time, in flight tests. In this context, the Paparazzi open-source autopilot system (Hattenberger u. a., 2014) was used as the software and hardware platform for both the design and development of the MFC algorithms.

5.1.1 DarkO Tail-Sitter MAV

An overview of the DarkO with its propulsion system components and its main physical specifications is presented in Figure 5.1. The design of this tail-sitter configuration has been mainly oriented for forward flight with the capability of taking off and landing vertically. Therefore, its propulsion system has not been particularly defined for hovering for a long duration. The flap effectiveness has been optimized in order to provide a higher degree of authority for the pitch moment during transitioning flight phases. This improved pitching moment is obtained, in particular, by a mechanical system that allows a special flap deflection, as illustrated in Figure 5.2. A particular feature that is required by the tail-sitter configuration is to generate an

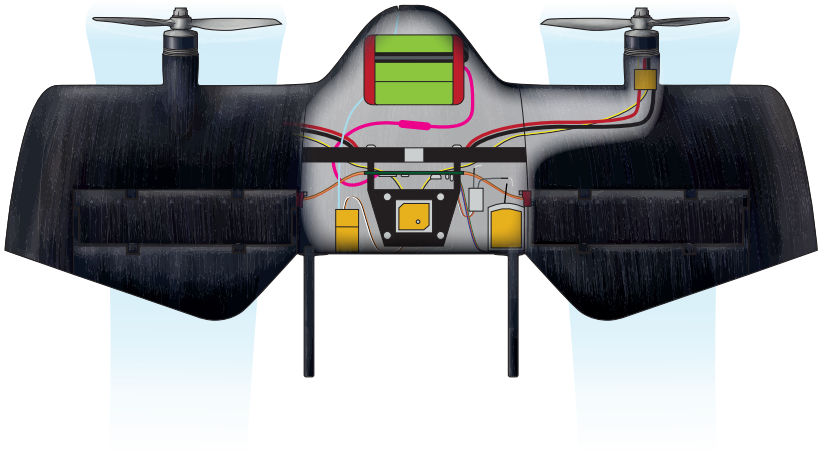

Mass	0.492 Kg
Wingspan	0.55 m
Mean Chord	0.13 m
Propellers	2-blades Bullnose 5x4.5
Motors	T-Motor Brushless F30 2800KV
Servos	MKS DS65K 0.2s/60° (4.8V)
Battery	3 cells 12.6V 3500 mAh

Figure 5.1: DarkO tail-sitter MAV specifications.

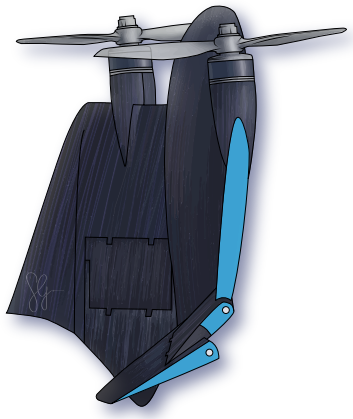

Figure 5.2: DarkO double-flap mechanism.

excessive amount of pitching moment in order to transition mainly from the forward flight phase to the hovering flight phase. Therefore, DarkO frame's control surfaces have been designed as a double-flap, which has a passive mechanical constant ratio. Traditionally, multi-section flaps have been designed for lift enhancement. However, in our case, the design objective is to generate as much positive pitching moment as possible without having a massive flow separation on the botton surface of the airfoil, as this could generate undesirable drag forces. The advantage of using double-flap (δ_{II}) control surface with respect to using a single-flap (δ_I) control surface is shown in Figure 5.4.

Variation of the sectional lift C_l, drag C_d, and moment coefficients C_m at different flap deflection angles have been compared for the two different flap configurations. The analysis has been done using the open-source program XFOIL (Drela, 1989), which allows an approximate analysis of aerodynamic phenomena. The Reynolds number used during the analysis corresponds to the slipstream velocity seen by the blown portion of the wing and is approximately $150k$. The motor mounts of DarkO have an incidence angle of -6 degrees with respect to the DarkO's wings. Therefore, the airfoil has been set to an angle of attack of $+6$ degrees and the flap angle has been varied to between -2 to -14 degrees (with the negative flap angle being upward). Particular attention should be given to the pitching moment C_m on the graph : it is clearly visible that the

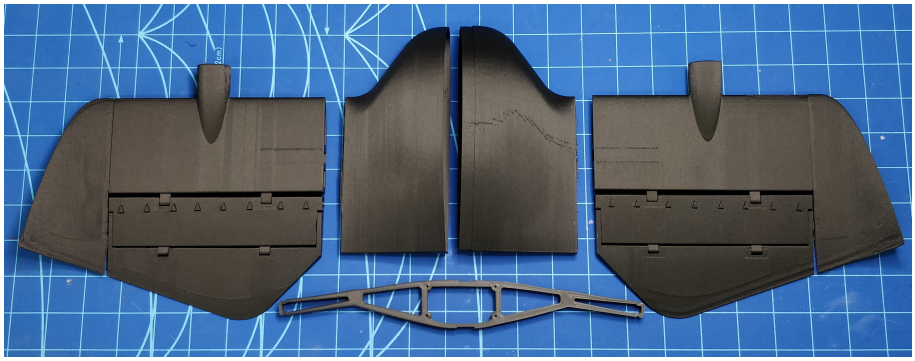

Figure 5.3: Printed parts of DarkO out of Onyx material.

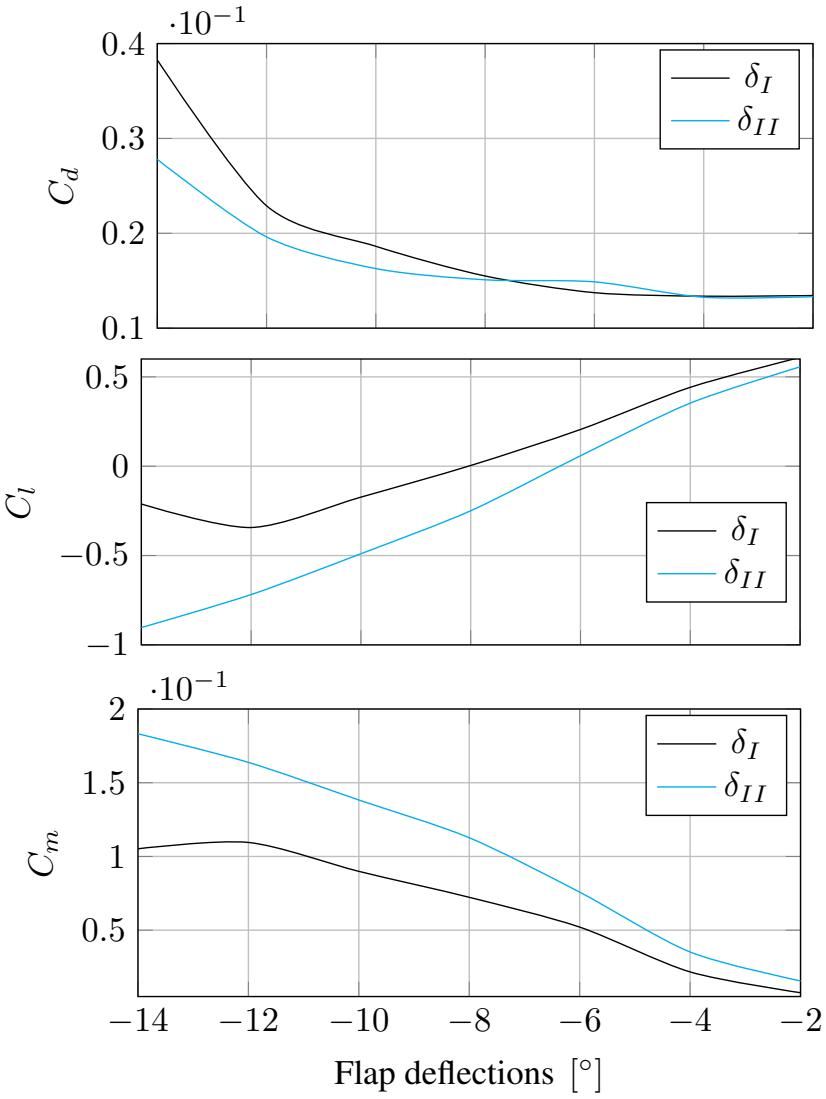

Figure 5.4: Variation of the sectional lift C_l, drag C_d, and moment coefficients C_m with respect to flap angles for different flap configurations: double-flap (δ_{II}) control surface and a single-flap (δ_I) control surface.

double-flap (δ_{II}) control surface can generate almost two times the pitching moment generated by the single-flap (δ_I) control surface. As a side effect, the double-flap control surface also works efficiently for lift generation, however as we are trying to increase the pitching moment (in a positive direction), the lift generation happens in a negative direction. As the vehicle requires the excessive amount of pitching moment only during the transition phase, the duration of this maneuver is very short, therefore lift reduction caused while increasing the pitching moment is not considered to be an issue.

The DarkO's frame was completely manufactured using a 3-D printing method with Onyx material. Figure 5.3 shows the printed pieces that are assembled in order to build the whole frame. The shell structure for the wing and the fuselage halves are manufactured as $0.7mm$ thick skins, and the spar is manufactured with the addition of unidirectional concentric carbon fibers embedded into the Onyx material. This method ensures a sufficiently rigid airframe to support

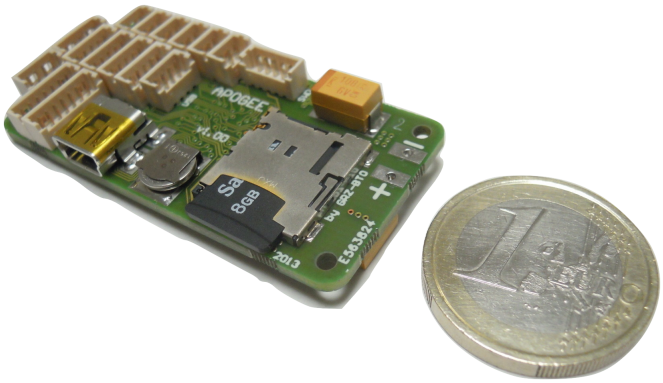

STM32F405RGT6 Cortex M4 168MHz processor
9(6) DOF integrated IMU MPU-9150(6050)
1 x Barometer/altimeter MPL3115A2
1 x MicroSD card slot
4 bit SDIO interface (high speed data logging)
6 x Servo PWM outputs
3 x UART, 2 x I2C bus, 1 x SPI bus
10.4 grams
53 mm x 25 mm

Figure 5.5: Overview of *Apogee v1.00* autopilot from *Paparazzi Autopilot system.*

aerodynamic forces, yet it remains flexible enough to absorb harsh impacts during landing and flight tests. During the flight tests, we equipped the DarkO with the Apogee V1.00 autopilot board, which is compatible with the Paparazzi open-source autopilot system, in order to process estimation and control algorithms. The Apogee V1.00 is equipped with 3-axis accelerometers, 3-axis rate-gyros, one barometer, and one magnetometer that is used especially for navigation purposes. The main features of each sensor device were obtained from manufacturer's datasheet, and are presented in Table 5.1.

Table 5.1: Apogee V1.00 and GPS sensors

	Device	Noise	Bias
Accelerometer	MPU-9150	400 $(\mu g/\sqrt{Hz})$	150 (mg)
Rate-Gyro	MPU-9150	0.005 $(^\circ/s/\sqrt{Hz})$	20 $(^\circ/s)$
Magnetometer	MPU-9150	N/A	N/A
GPS position	NEO-6M	$\sigma = 2.5$ (m)	0 (m)
GPS velocity	NEO-6M	$\sigma = 0.1$ (m/s)	0 (m/s)

► **Actuators**

The DarkO's propulsion system and its servo motors which control the flap deflections, are presented in Figure 5.6. The propulsion system combines two T-Motor Brushless F30 with two Bullnose 2-blade propellers. Each T-Motor provides a 2,800 KV rating, which refers to the constant velocity of the motor. The KV value represents the number of RPM that a motor turns when one volt is applied with no load attached to the motor. The nominal DarkO's propeller is characterized by a 5-inch tip diameter and by a 4.5-inch advance pitch, which represents the theoretical axial displacement in one turn. The MKS DS65K servo motor provides an operating speed of 0.2s/60° with a power supply of 4.8 volts.

Figure 5.6: DarkO actuators. From left to right, brushless motors, 2-blade propellers and an MKS DS65K servo motor.

5.1.2 Paparazzi UAV Open-Source Autopilot System

Paparazzi UAV is an open-source hardware and software project designed for the development of autopilot systems and ground station for a variety of UAV configurations, such as fixed-wings, rotorcraft and hybrid aircraft. Given its open-source functionality, the Paparazzi UAV project is constantly improved by a community of researchers in both industrial and academic fields. Each developer can make their contributions available, as well as their own methodological and technological progress. Therefore, the published contributions can be reused by several users around the world.

In addition to Paparazzi UAV project, there are other alternatives to develop autopilot systems, such as, OpenPilot, Pixhawk, ArduPilot:Copter, MikroKopter, KKMultiCopter, MultiWii, and Aeroquad, etc. We chose the Paparazzi UAV project because of its modular architecture that facilitates the design, implementation and validation of new algorithms in real flight tests. Furthermore, its stable communication between the UAV system and the ground station reduces the time required for testing code.

According to Figure 5.7, the Paparazzi architecture has distinctive processes that can be divided into different modules. From a control point of view, its modular architecture can mainly be described by three groups :

⇒ *Data acquisition* is composed of sensors, for instance, accelerometers, gyroscopes, Global Positioning System (GPS), pitot tubes, magnetometers, barometers, and cameras, etc. This group of devices, represented by green blocks in the figure, detects events or changes in the environment around the UAV, and sends this information to the microprocessor.

⇒ *State estimation system* provides smoother information about the states of the system, such as, orientation, acceleration, velocity, and position. Inertial systems are divided into three categories: Inertial Measurement Unit (IMU), Attitude and Heading Reference System (AHRS) and Inertial Navigation System (INS). By definition, an IMU consists mainly of three accelerometers and three gyrometers to measure the UAV acceleration and its rotational speed. The integration of these six measurements determines the linear velocity, position and orientation of the UAV. The process of sensor fusion is performed by the AHRS combined with the INS.

⇒ *GN&C system* is composed of Guidance, Navigation, and Control (GNC) algorithms, represented in the figure by three blue blocks, which allow the aircraft to perform autonomous flights, accomplishing the flight plan that was defined by the user in the ground station.

This structure was designed at the start of the Paparazzi project, and defines the control-loop process in a conventional way by inserting the stabilization control block between the guidance control block and the servos/actuators purple block. For autonomous flight missions, the attitude setpoints are defined by the guidance block, which computes the desired UAV orientation in view of reach of the desired trajectories of the flight plan.

The majority of attitude stabilization control techniques implemented on the Paparazzi UAV system use classical control theory, according to PID controllers or model-based principles. The disadvantage of PID controllers is that they rely primarily on their insufficient disturbance rejection properties. To the best knowledge of the authors, only the INDI controller has been implemented in the Paparazzi UAV system for hybrid UAVs, providing effective robustness properties during real flight tests. Its advantages and disadvantages will be described and compared to the MFC approach, with respect to the DarkO's attitude stabilization.

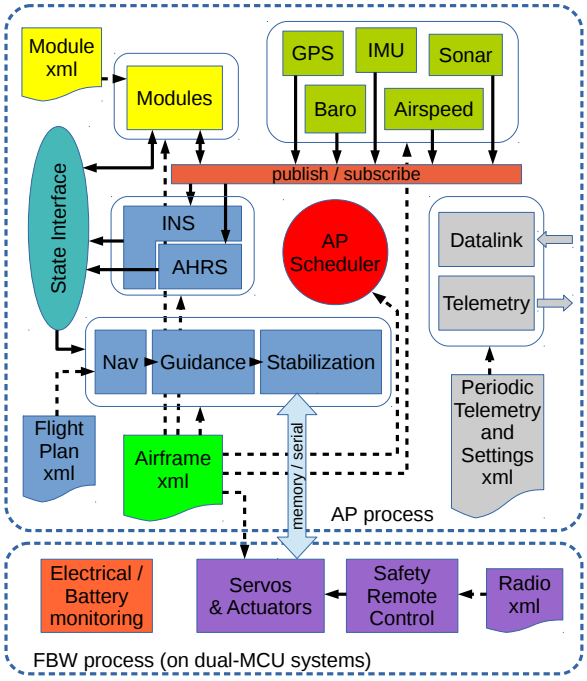

Figure 5.7: Paparazzi architecture system.

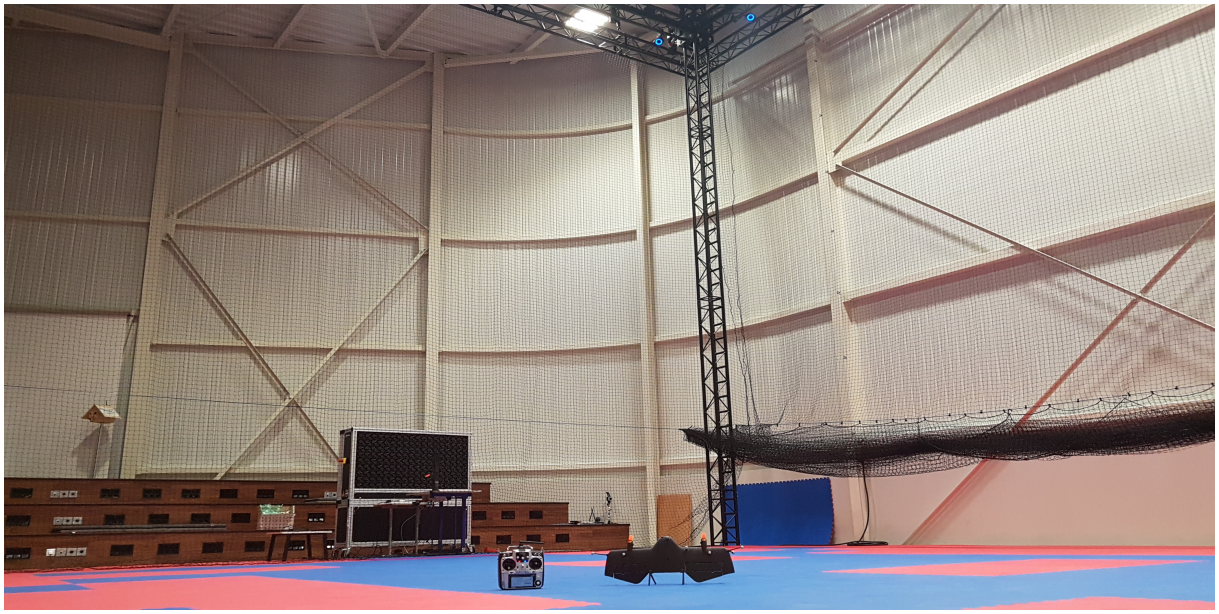

Figure 5.8: Dark0 MAV at rest in the *ENAC flying arena* showing two of sixteen *Optitrack* cameras in the top and the *WindShape* wind generator in the background.

5.2 MFC Flight Tests

Preliminary flight tests were conducted to evaluate the MFC performance in real-world flight conditions. The following results were obtained during indoor and outdoor flights by evaluating the designed MFC parameters for attitude stabilization purposes. The MFC algorithms that have been introduced in previous chapters were directly implemented on the autopilot system and the MFC parameters are the same as those used in simulation.

First, indoor flight tests in calm flight conditions are presented in order to verify both the smooth-functioning of MFC algorithms and the DarkO's flight stability with the MFC parameters used in flight simulations. Then, MFC disturbance rejection results are evaluated from a peculiar transitioning flight with significant winds, which have been generated by an open wind tunnel machine. Finally, outdoor flight tests are presented to show the MFC properties through smooth transitioning flights.

5.2.1 Indoor Flights

Indoor flights were conducted in the *ENAC flying arena* which has a flight volume of 10x10x10 meters (see Figure 5.8). The entire flight domain is covered by the *Optitrack* system that informs the MAV attitude orientation and position. In the following flight tests, we analyze only the attitude control loop using *Optitrack* cameras for heading measurements that were updated at 5 Hz. The entire MAV attitude is computed on-board at 500 Hz by an INS algorithm that combines both accelerometer and gyroscope signals. The attitude setpoints are set externally by the security pilot from an Radio Control (RC) transmitter. For reasons of space limitation, the DarkO's attitude was mainly evaluated in the hovering flight domain. In forward flight, the DarkO moves with relatively fast speeds which makes it difficult to operate in restricted areas. Despite these space constraints, the security pilot has imposed fast transitioning flights in order to evaluate the MFC performance in relation to important variations of pitch angle (see

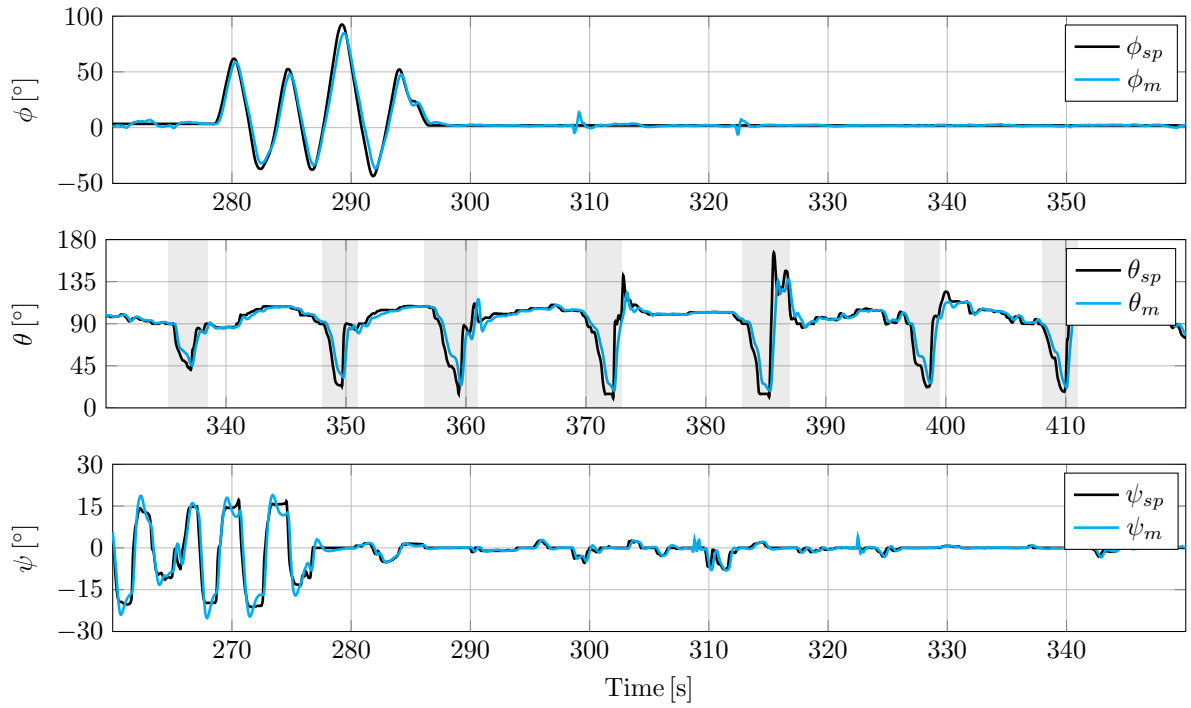

Figure 5.9: Attitude stabilization during indoor flights with fast transitioning flights.

Figure 5.9). The first indoor flight test shows the MFC capability to stabilize the system with large pitch angle variations. Pitch angle setpoint trajectory does not remain below 20 degrees for a long period in the forward flight domain, due to space limitations in the *ENAC flying arena*. The first test concludes that the designed MFC approach is able to stabilize the DarkO through hovering and transitioning flight domains in indoor flight conditions. Furthermore, fast transitioning flights induce significant variations of aerodynamic forces and moments that are properly estimated and stabilized by the MFC adaptive properties. This is a particularly powerful feature of this control approach that adapts its command to track desired dynamics, even if the controlled system presents variations in its internal parameters. In the case of tail-sitter MAVs, the variations of the aerodynamic coefficients are a function of the angle of attack.

Figure 5.10 illustrates the DarkO during a particular transitioning flight faced to the *Wind-Shape* open wind tunnel. The attitude behavior of the DarkO during this second indoor flight test is presented in Figure 5.11. The DarkO starts the experiment in hovering flight mode facing the *WindShape* open wind tunnel. The pitch angle setpoint was imposed by the security pilot in order to perform the transition from hovering to forward flight, following increased wind speeds from zero to $9\,m/s$, which were generated by the *WindShape*. The use of *WindShape* enables the analysis of a continuous transitioning flight in a restricted flight area.

The wind speeds generated by the *WindShape* create a disturbed flight environment around the DarkO which directly affects its attitude dynamics. The shaded area highlights the flight domain where the pitch angle decreases when approaching the forward flight, as well as the flight domain where the wind has been increased. Despite these wind disturbances, DarkO remained stable. Therefore, the MFC responsiveness has been highlighted through its effective

Figure 5.10: DarkO facing the WindShape open wind tunnel.

disturbance rejection properties. Roll oscillations can be observed at 100 seconds of flight with a maximum amplitude of 8°. This roll behavior occurs in the windy flight domain. The DarkO performance, in particular its roll dynamics, could be optimized by reducing the integration window of the MFC estimator which will provide more responsiveness to the system. However, the trade-off between fast estimations — fast MFC closed-loop responsiveness — and effective

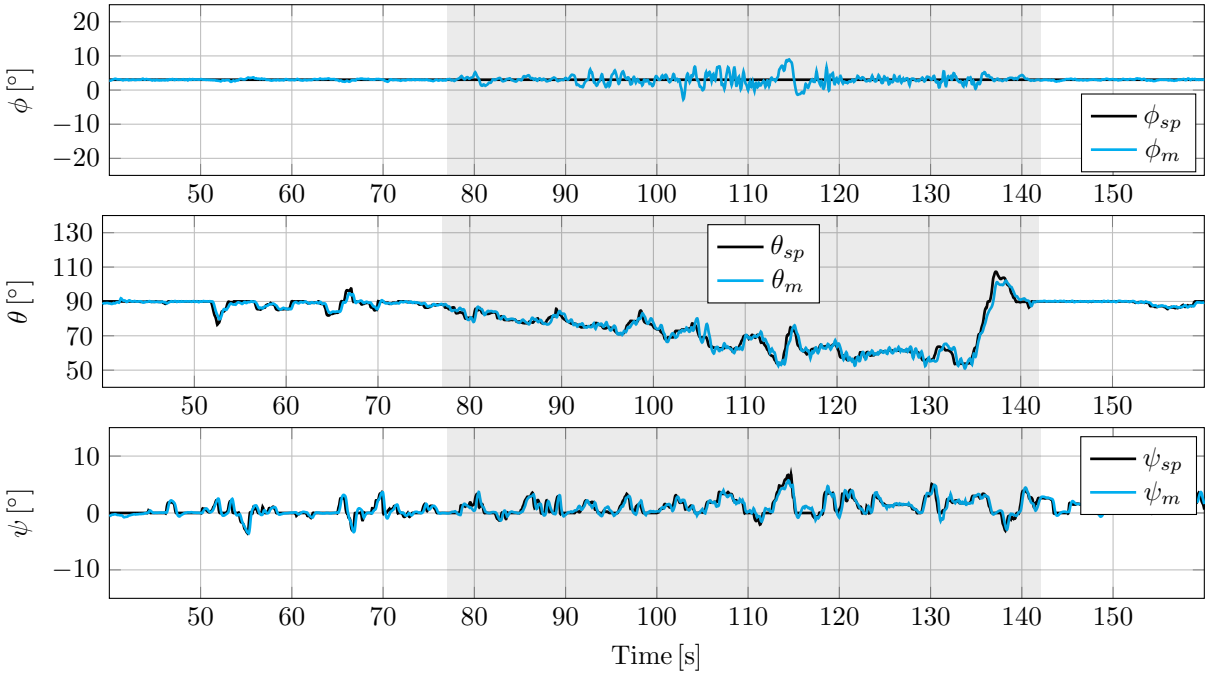

Figure 5.11: Indoor transitioning flight test facing the WindShape.

noise attenuation seems appropriate in calm flight conditions without wind, as observed in the previous indoor flight test. For this reason, the MFC performance and its disturbance rejection properties will be evaluated in outdoor flight conditions with the same designed MFC parameters that were used in the indoor flight tests.

5.2.2 Outdoor Flights

Outdoor flight tests have been performed at the Club Eole flight test facility presented in Figure 5.12. The flight test facility allows us to evaluate all tail-sitter flight phases without space limitations. The DarkO was equipped with a magnetometer device to measure its current heading in relation tothe magnetic poles of the earth. Similar to the indoor flight tests, the entire MAV attitude is computed on-board at 500 Hz by an INS algorithm that combines both accelerometer and gyroscope signals. Finally, attitude setpoints are set externally by the security pilot from an RC transmitter.

Figure 5.13 shows the DarkO's attitude behavior during the outdoor flight test. The objective of this flight test was to evaluate the MFC attitude control-loop performance in outdoor flight conditions, in particular the transitioning flight phase, and compare its results with those obtained in windy indoor flight conditions. For this outdoor flight test, the tail-sitter MAV has covered hovering, transitioning and forward flight domains. The DarkO started its initial flight test in the hovering flight phase and, according to pitch angle setpoints, different transitioning flights were performed. The detailed stabilization of the pitch angle is shown in Figure 5.14, from both hover-to-forward and forward-to-hover transitioning flights.

The MFC provided smooth, continuous and stabilized transitioning flights. The roll oscillations highlighted in the windy indoor flight test were not observed in the outdoor flight test, even though exactly the same MFC parameters were used. The entire flight envelope of the DarkO has been stabilized with a constant linear control effectiveness parameter λ in the MFC architecture. This parameter is not estimated during the flight. However, the estimator $\hat{F}$ adapts the

Figure 5.12: Club Eole (GPS 43°27'45"N, 001°16'25"E) outdoor flight test area.

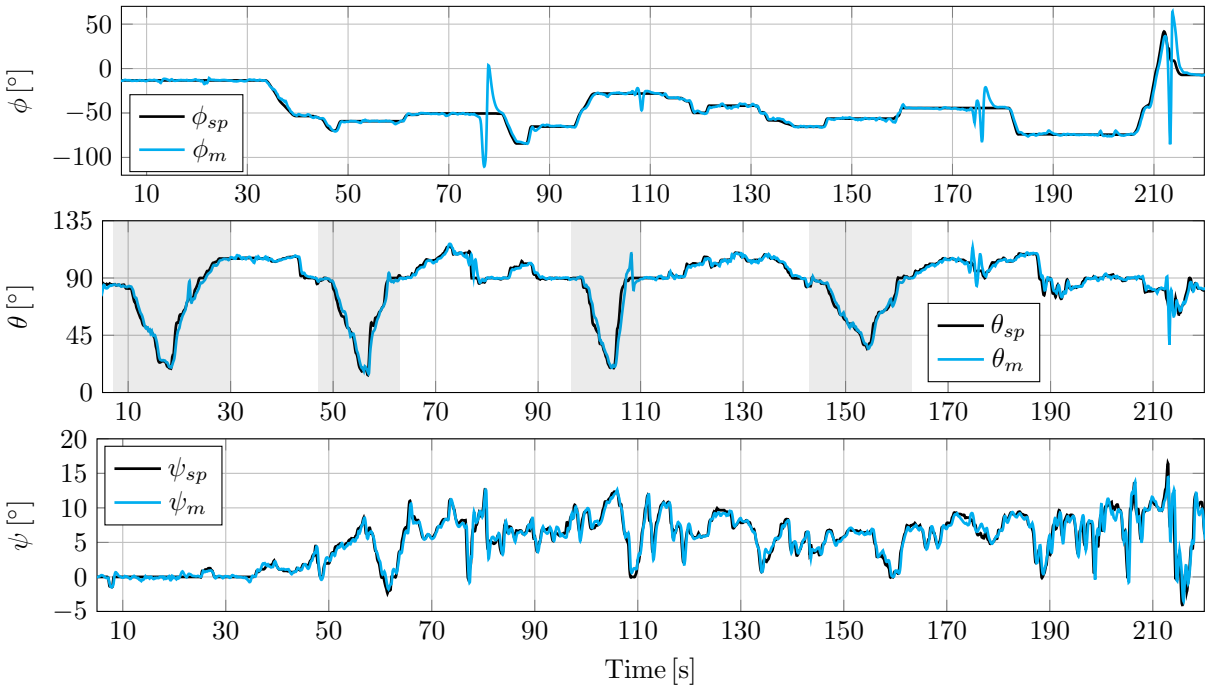

Figure 5.13: Attitude stabilization during outdoor flight test.

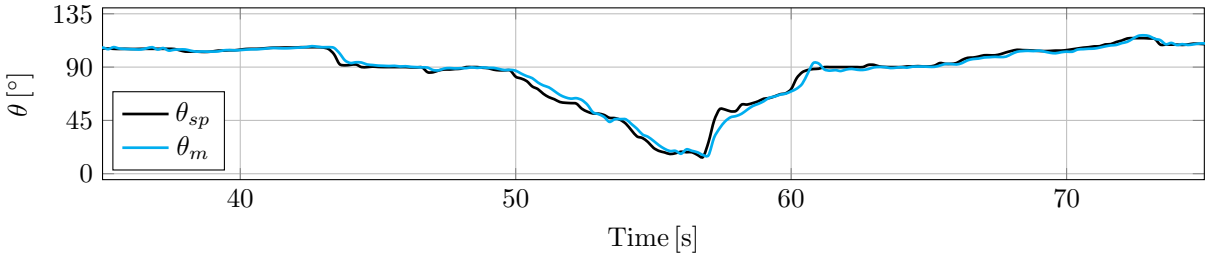

Figure 5.14: Pitch angle result for $t \in [35; 75]$ seconds during outdoor flight test.

MFC closed-loop command according to the current control effectiveness of the system, which is known to be different in hovering and forward flight. Therefore, the entire flight envelope of a tail-sitter MAV can be stabilized with only one set of MFC parameters.

5.3 MFC and INDI Comparative Flight Tests

This section presents additional real-world flight tests in order to compare the MFC attitude stabilization performance to that of the INDI controller in indoor flight conditions. MFC and INDI have similar features and both controllers require little prior knowledge of the controlled system. In this perspective, we explain in more detail the INDI principle that was first introduced by National Aeronautics and Space Administration (NASA) (Bacon und Ostroff, 2000) (Ostroff und Bacon, 2002), then designed for the control of different MAV configurations (Smeur u. a., 2016a) (Sman u. a., 2017), and finally refined by researchers until its application on HMAVs (Bronz u. a., 2017) (Smeur u. a., 2019). The main reason for the increased application of INDI for a variety of aircraft configurations can be explained by its good sta-

bility and robustness properties against external disturbances (Smeur u. a., 2016b), moderate computation costs and low requirements on modeling fidelity (Binz u. a., 2019).

5.3.1 INDI controller

Since it was reported by NASA, INDI has been attracting considerable interest in the field of MAVs. Often mentioned in the literature as simplified (Smith, 1998) or enhanced NDI (Ostroff und Bacon, 2002), the incremental form of NDI is more robust and less-model dependent. Its robustness properties, in particular against wind disturbances, show a higher performance compared to a conventional PID controller, for instance, during a position tracking flight experiment with a quadrotor (Smeur u. a., 2016b) with obvious advantages over the PID controller.

▶ INDI principles

An overview of the INDI controller applied to a tail-sitter MAV is now presented according to (Smeur u. a., 2018) and (Smeur u. a., 2019). For this explanation, we consider the control of angular accelerations ($\dot{\Omega}$). The angular rate vector of the MAV is defined by $\boldsymbol{\Omega}$ which is controlled by both angular rates of the propellers ($\boldsymbol{\omega}$) and flap deflections ($\boldsymbol{\delta}$). The entire actuator vector is denoted by $\boldsymbol{u} = [\delta_l \ \delta_r \ \omega_l \ \omega_r]$. Equation 5.1 gives the mathematical expression of the angular acceleration and the thrust, as function of the states and actuators of the following system :

$$\begin{bmatrix} \dot{\boldsymbol{\Omega}} \\ T \end{bmatrix} = \boldsymbol{F}(\boldsymbol{\Omega}, \boldsymbol{v}) + \boldsymbol{G}(\boldsymbol{\omega}, \dot{\boldsymbol{\omega}}, \boldsymbol{\delta}, \dot{\boldsymbol{\delta}}) \tag{5.1}$$

The angular rates and the velocity of the tail-sitter MAV generate moments that are described by the function $\boldsymbol{F}(\boldsymbol{\Omega}, \boldsymbol{v})$. Here, $\boldsymbol{F}(\boldsymbol{\Omega}, \boldsymbol{v})$ is a four-by-one matrix and its fourth row is zero due the fact that the thrust force only depends on the rotational rates of the motors. The function $\boldsymbol{G}(\boldsymbol{\omega}, \dot{\boldsymbol{\omega}}, \boldsymbol{\delta}, \dot{\boldsymbol{\delta}})$ expresses the effect of the actuators and the derivative of the actuators on the angular acceleration and thrust. If we apply a first order Taylor expansion in (5.1, we obtain) :

$$\begin{bmatrix} \dot{\boldsymbol{\Omega}} \\ T \end{bmatrix} = \boldsymbol{F}(\boldsymbol{\Omega}_0, \boldsymbol{v}_0) + \boldsymbol{G}(\boldsymbol{\omega}_0, \dot{\boldsymbol{\omega}}_0, \boldsymbol{\delta}_0, \dot{\boldsymbol{\delta}}_0) \tag{5.2}$$

$$+ \frac{\partial}{\partial \boldsymbol{\Omega}} (\boldsymbol{F}(\boldsymbol{\Omega}, \boldsymbol{v}_0))|_{\boldsymbol{\Omega}=\boldsymbol{\Omega}_0} (\boldsymbol{\Omega} - \boldsymbol{\Omega}_0) \tag{5.3}$$

$$+ \frac{\partial}{\partial \boldsymbol{v}} (\boldsymbol{F}(\boldsymbol{\Omega}_0, \boldsymbol{v}))|_{v=v_0} (\boldsymbol{v} - \boldsymbol{v}_0) \tag{5.4}$$

$$+ \frac{\partial}{\partial \boldsymbol{\omega}} (\boldsymbol{G}(\boldsymbol{\omega}, \dot{\boldsymbol{\omega}}_0, \boldsymbol{\delta}_0, \dot{\boldsymbol{\delta}}_0))|_{\omega=\omega_0} (\boldsymbol{\omega} - \boldsymbol{\omega}_0) \tag{5.5}$$

$$+ \frac{\partial}{\partial \dot{\boldsymbol{\omega}}} (\boldsymbol{G}(\boldsymbol{\omega}_0, \dot{\boldsymbol{\omega}}, \boldsymbol{\delta}_0, \dot{\boldsymbol{\delta}}_0))|_{\dot{\omega}=\dot{\omega}_0} (\dot{\boldsymbol{\omega}} - \dot{\boldsymbol{\omega}}_0) \tag{5.6}$$

$$+ \frac{\partial}{\partial \boldsymbol{\delta}} (\boldsymbol{G}(\boldsymbol{\omega}_0, \dot{\boldsymbol{\omega}}_0, \boldsymbol{\delta}, \dot{\boldsymbol{\delta}}_0))|_{\delta=\delta_0} (\boldsymbol{\delta} - \boldsymbol{\delta}_0) \tag{5.7}$$

$$+ \frac{\partial}{\partial \dot{\boldsymbol{\delta}}} (\boldsymbol{G}(\boldsymbol{\omega}_0, \dot{\boldsymbol{\omega}}_0, \boldsymbol{\delta}_0, \dot{\boldsymbol{\delta}}))|_{\dot{\delta}=\dot{\delta}_0} (\dot{\boldsymbol{\delta}} - \dot{\boldsymbol{\delta}}_0) \tag{5.8}$$

The subscript 0 in the previous equations describes the past value of the system states. Therefore, we can conclude from (5.2), that its two terms represent the previous value of the angular acceleration and thrust :

$$\boldsymbol{F}(\boldsymbol{\Omega}_0, \boldsymbol{v}_0) + \boldsymbol{G}(\boldsymbol{\omega}_0, \dot{\boldsymbol{\omega}}_0, \boldsymbol{\delta}_0, \dot{\boldsymbol{\delta}}_0) = \begin{bmatrix} \dot{\boldsymbol{\Omega}}_0 \\ T_0 \end{bmatrix} \tag{5.9}$$

The moments provided by changes in the function $\boldsymbol{F}(\boldsymbol{\Omega}, \boldsymbol{v})$ are assumed to be small compared to the moments created from the actuators in $\boldsymbol{G}(\boldsymbol{\omega}, \dot{\boldsymbol{\omega}}, \boldsymbol{\delta}, \dot{\boldsymbol{\delta}})$. In addition, around the operating point, the partial derivatives of $\boldsymbol{G}(\boldsymbol{\omega}, \dot{\boldsymbol{\omega}}, \boldsymbol{\delta}, \dot{\boldsymbol{\delta}})$ are assumed to be constant. Finally, partial derivatives can be approximated by the static matrix $\boldsymbol{G}_e$ which defines the control effectiveness matrix of the system. In our case, this matrix represents the effectiveness of each actuator on each controlled axis and thrust, which results in a four-by-four matrix. An increment in actuators results in an increment in angular accelerations and thrust, depending on the control effectiveness matrix $\boldsymbol{G}_e$:

$$\begin{bmatrix} \dot{\boldsymbol{\Omega}} \\ T \end{bmatrix} = \begin{bmatrix} \dot{\boldsymbol{\Omega}}_0 \\ T_0 \end{bmatrix} + \boldsymbol{G}_e(\boldsymbol{u} - \boldsymbol{u}_0) \tag{5.10}$$

The INDI attitude stabilization method considers that all of the moments acting in the system produce angular accelerations that can be determined by deriving the angular rates from gyroscopic devices. These angular accelerations are obtained by using the finite difference method, which introduces signals that are often very noisy due to the propeller rotation which causes vibrations in the airframe. Therefore, a second-order Butterworth filter (Bacon u. a., 2001) will be used to deal with the noise.

$$H(s) = \frac{\omega_n^2}{s^2 + 2\xi\omega_n s + \omega_n^2} \tag{5.11}$$

This mathematical operation introduces delays in the system and, in order to keep all signals synchronized, we apply the same filter on all terms in (5.10). All filtered signals will be described in the following with the subscript f. The INDI control law can be obtained by calculating the inverse of $\boldsymbol{G}_e$ and by finding the inverse function of (5.10). We introduce a new vector $\boldsymbol{\nu}$ that represents the INDI controlled variables, such as three angular accelerations and the desired thrust (T_d). The INDI closed-loop command is then :

$$\boldsymbol{u}_c = \boldsymbol{u}_f + \boldsymbol{G}_e^{+}\left(\boldsymbol{\nu} - \begin{bmatrix} \dot{\boldsymbol{\Omega}}_f \\ T_f \end{bmatrix}\right) \tag{5.12}$$

where

$$\boldsymbol{\nu} = \begin{bmatrix} K_\Omega(\boldsymbol{\Omega}_{ref} - \boldsymbol{\Omega}) \\ T_d \end{bmatrix} \tag{5.13}$$

Notice that, the angular rates can be controlled with a simple proportional feedback gain K_Ω. In addition, the desired angular rates are defined by the attitude stabilization control-loop with a second proportional gain K_η, depending of the vector part of the quaternion error $\boldsymbol{q}_{error}$:

$$\boldsymbol{\Omega}_{ref} = K_\eta \begin{bmatrix} q_{error_1} & q_{error_2} & q_{error_3} \end{bmatrix}^T \tag{5.14}$$

this error represents the difference between the quaternion setpoint $\boldsymbol{q}_{sp}$ and the measured quaternion $\boldsymbol{q}_m$:

$$\boldsymbol{q}_{error} = \boldsymbol{q}_{sp} \otimes \boldsymbol{q}_m^* \tag{5.15}$$

The operator $\otimes$ is the Kronecker product and $\boldsymbol{q}_m^*$ is the conjugate of the measured quaternion. According to (Smeur u. a., 2018), K_Ω and K_η can be designed based on the transfer function of the system actuators.

▶ INDI control structure

The inner-loop of the INDI attitude stabilization is presented in Figure 5.15, and the INDI outer-loop in Figure 5.16.

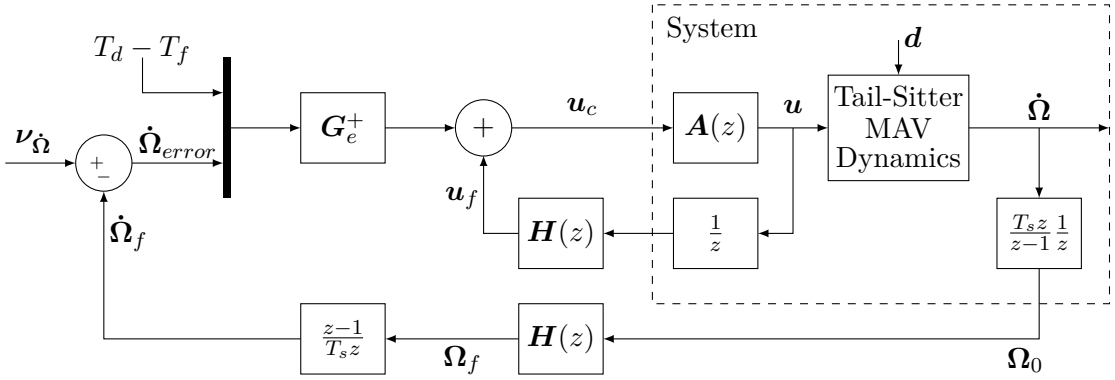

Figure 5.15: INDI inner-loop overview. The diagonal matrix $\boldsymbol{A}(z)$ represents the transfert function of each actuator, and the diagonal matrix $\boldsymbol{H}(z)$ represents the second-order filter.

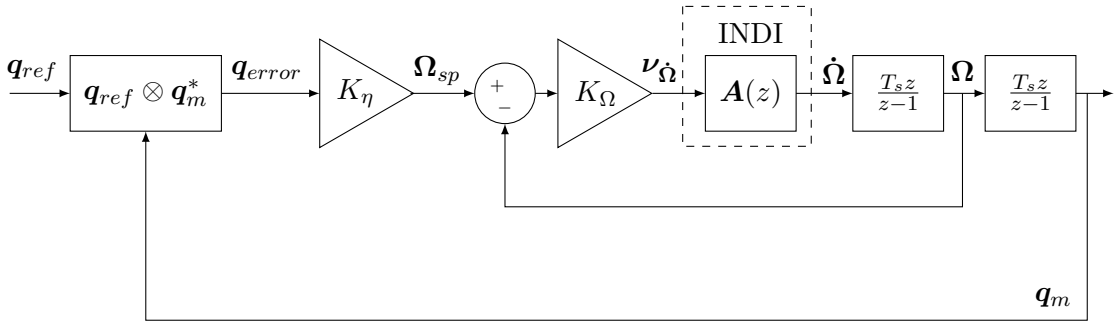

Figure 5.16: INDI outer-loop overview.

▶ Transfer function of system actuators

The INDI controller neglects the dynamic model of the system, because these dynamics are directly controlled from measurements of the angular acceleration. However, the INDI input-output principle requires knowing the current actuator state at each sampling time. Thus, the dynamics of each actuator are approximated by the following transfer function in the discrete time domain:

$$A(z) = \frac{a}{z - (1 - a)} \tag{5.16}$$

The actuator dynamics of the DarkO tail-sitter MAV have been characterized at 500 Hz. For the servo motors, we obtained $a = 0.04$ with a rate limit of 120 °/s. The brushless motors' dynamics were defined by $a = 0.025$ without a rate limit. According to (5.16) the actual actuator state $\boldsymbol{u}$, can be modeled as function of the control-input $\boldsymbol{u}_c$. An interesting analysis was proposed by (Binz u. a., 2019) in order to investigate the INDI closed-loop performance according to the identification of actuator parameters. By studying the effects of modeling uncertainty on the poles of the INDI closed-loop system, the authors confirmed the effective stability properties

of such a controller. However, special consideration needs to be made to the nonlinear rate-limit element of servo models in order to investigate how and if these nonlinearities should be considered in the INDI design process.

▶ Control effectiveness matrix

The control effectiveness of tail-sitter MAVs depends on the current flight phase, in particular, the control effectiveness of aerodynamic surfaces as functions of the dynamic pressure $q = 0.5\,\rho\,V^2$, where ρ is the air density and V is the airspeed. Therefore, the implementation of the INDI controller for the entire flight envelope of tail-sitter MAVs requires the use of a gain scheduling method to fit the control effectiveness matrix according to the current flight domain.

The control effectiveness matrix G_e mainly changes with airspeed, given that air density is almost constant during the flight. Thus, the first solution was to schedule the $\boldsymbol{G}_e$ matrix as a function of the airspeed. However, the large variation in the angle of attack precludes the measure of airspeed. In order to correctly measure this variable, the Pitot tube needs to be aligned with the airflow, which is not the case in the hovering flight domain where the angle of attack is important. In addition, the Pitot tube is able to measure airspeeds beyond a threshold for which airspeed measurements below this threshold are not reliable. For these reasons, a second variable was used to schedule the control effectiveness matrix during flights at low airspeed.

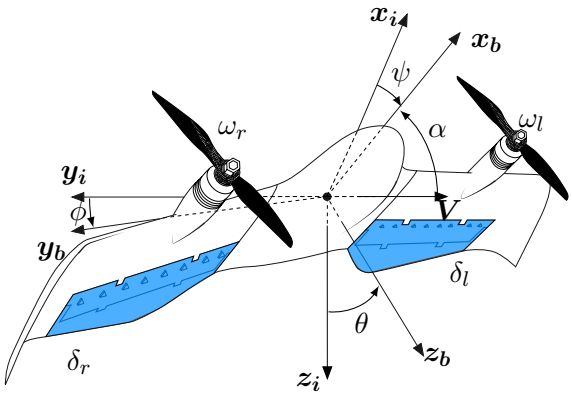

Figure 5.17: Illustration of the coordinate frames, angles and actuators used.

Finally, the gain scheduling approach proposed by (Smeur u. a., 2019) defines the control effectiveness terms in $\boldsymbol{G}_e$ as function of actuator state, airspeed (when it can be measured) and pitch angle, which is an easy and robust variable to measure. According to Figure 5.17, the control effectiveness of the flap deflections on roll dynamics are denoted by $G_{11}(\theta, V)$ and $G_{12}(\theta, V)$, respectively describing the left and right flap deflection control effectiveness. Then, the functions $G_{21}(\theta, V)$ and $G_{22}(\theta, V)$ model the effectiveness of the left and right flap deflections around the pitch axis, which is also modeled by the functions $G_{23}(\boldsymbol{u}_f)$ and $G_{24}(\boldsymbol{u}_f)$, depending on the left and right motor-propeller combinations. The effectiveness terms of the pair motor-propeller around the yaw axis are parametrized by $G_{33}(\boldsymbol{u}_f)$ and $G_{34}(\boldsymbol{u}_f)$. The last row in the $\boldsymbol{G}_e$ matrix represents the effectiveness of the left and right motor-propeller on the vectored thrust force.

$$\boldsymbol{G}_e = \begin{bmatrix} G_{11}(\theta, V) & G_{12}(\theta, V) & 0 & 0 \\ G_{21}(\theta, V) & G_{22}(\theta, V) & G_{23}(\boldsymbol{u}_f) & G_{24}(\boldsymbol{u}_f) \\ 0 & 0 & G_{33}(\boldsymbol{u}_f) & G_{34}(\boldsymbol{u}_f) \\ 0 & 0 & -0.0011 & -0.0011 \end{bmatrix} \tag{5.17}$$

The parameters of these functions were defined from flight data analysis for which the pitch angle and the airspeed are relatively constant. Different segments of the flight data were analyzed in order to calculate the control effectiveness of each axis of the tail-sitter MAV. The flap effectiveness was defined with a linear least squares method to fit the changes in angular acceleration, with changes in actuator commands.

5.3.2 Flight test results

In this section, two flight tests in an indoor environment comparing MFC to INDI controller are presented. In the first case, both controllers stabilize the DarkO in its nominal configuration; that is, wings and control surfaces are attached correctly. In the second case, the wingtips and half of the control surface are removed, and additionally, the propulsion system has been modified by using a different set of propellers (see Figure 5.18). The nominal components of the DarkO were changed to evaluate the adaptive properties of both controllers.

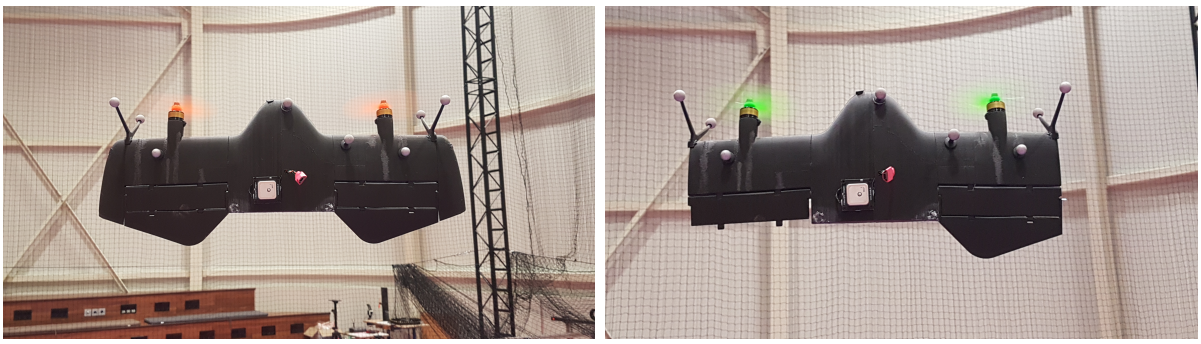

Figure 5.18: Tail-sitter MAV configurations used during MFC-INDI comparative flight tests. On the left side, DarkO with nominal wings, control surfaces and two-blade propellers. On the right side, DarkO has been modified by removing its wingtips, half of its control surface and three-blade propellers were used.

The methodology used during the flight tests to define the DarkO's attitude setpoints are based on four steps. First, with an RC transmitter, the security pilot imposes slow yaw setpoints generating lateral motions in the system. Second, slow pitch setpoints generate forward and backward movements according to positive and negative pitch setpoints, respectively. Third, slow roll setpoints define the DarkO's heading orientation. Finally, the security pilot imposes fast yaw and pitch setpoints to evaluate the response of the system for high frequency attitude setpoints.

The attitude stabilization results performed by MFC and INDI with the nominal DarkO, are presented in Figure 5.19 and Figure 5.20, respectively. Figure 5.21 and Figure 5.22 show the MFC and INDI attitude stabilization performances for the modified DarkO configuration. It is difficult to graphically compare each controller in the time domain because of their different setpoint trajectories. For this reason, we investigated their control performance in the frequency domain by calculating the FFT of the pitch angle, which is the dynamic most affected by a loss of control

surface effectiveness. We observe a better tracking performance with a larger frequency spectrum for the MFC (20 rad/s) when compared to that of the INDI (7 rad/s) for the nominal flight test. Both controllers stabilized the modified DarkO, showing their adaptive control properties. The present study concludes that MFC and INDI provide satisfactory performance for hovering and transitioning flight domains in indoor flight conditions. These results suggested a more in-depth analysis in order to evaluate the performance of both controllers for the entire flight envelope of the DarkO, in particular during forward flights in an outdoor environment.

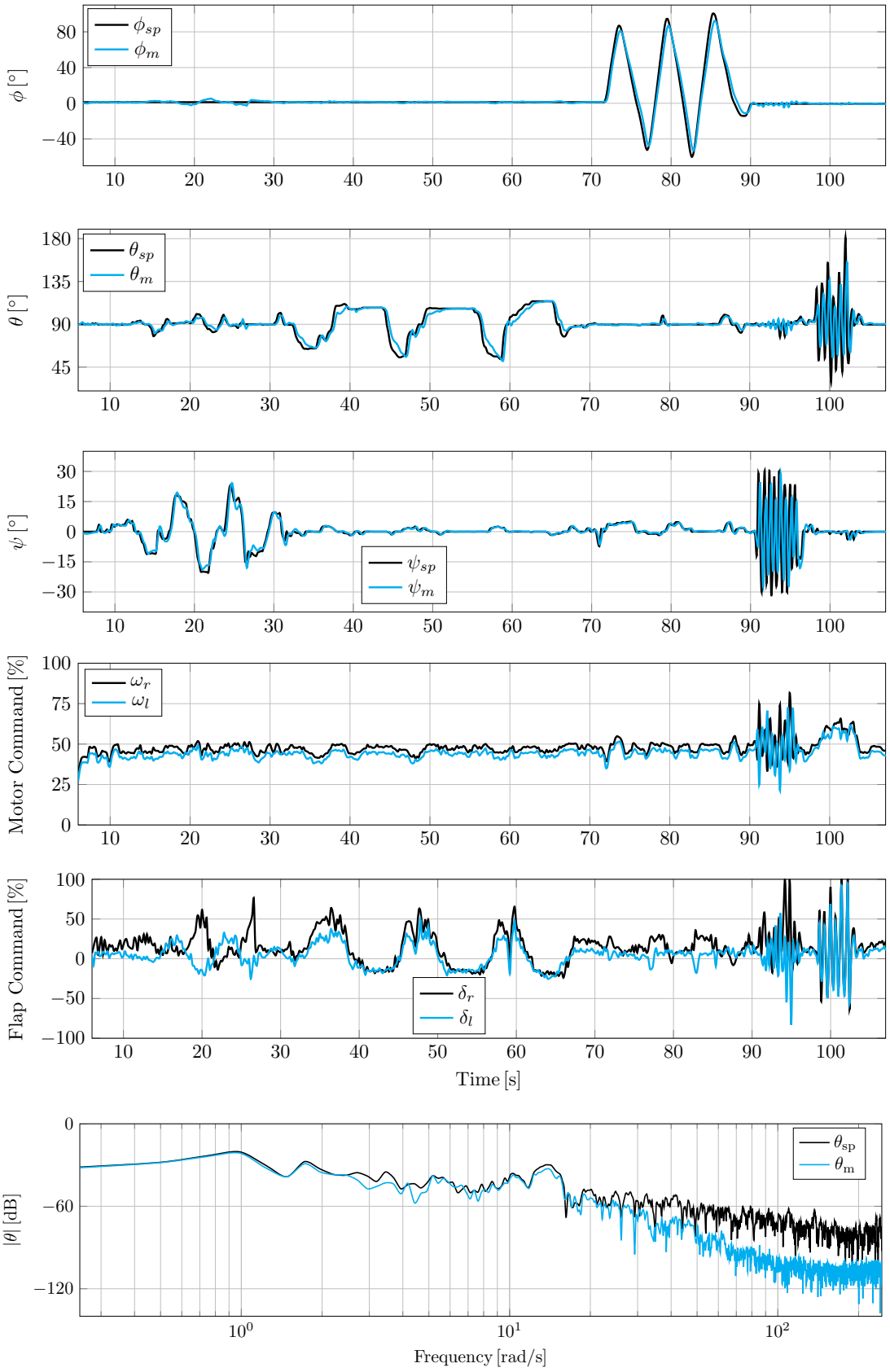

Figure 5.19: MFC attitude stabilization - nominal DarkO.

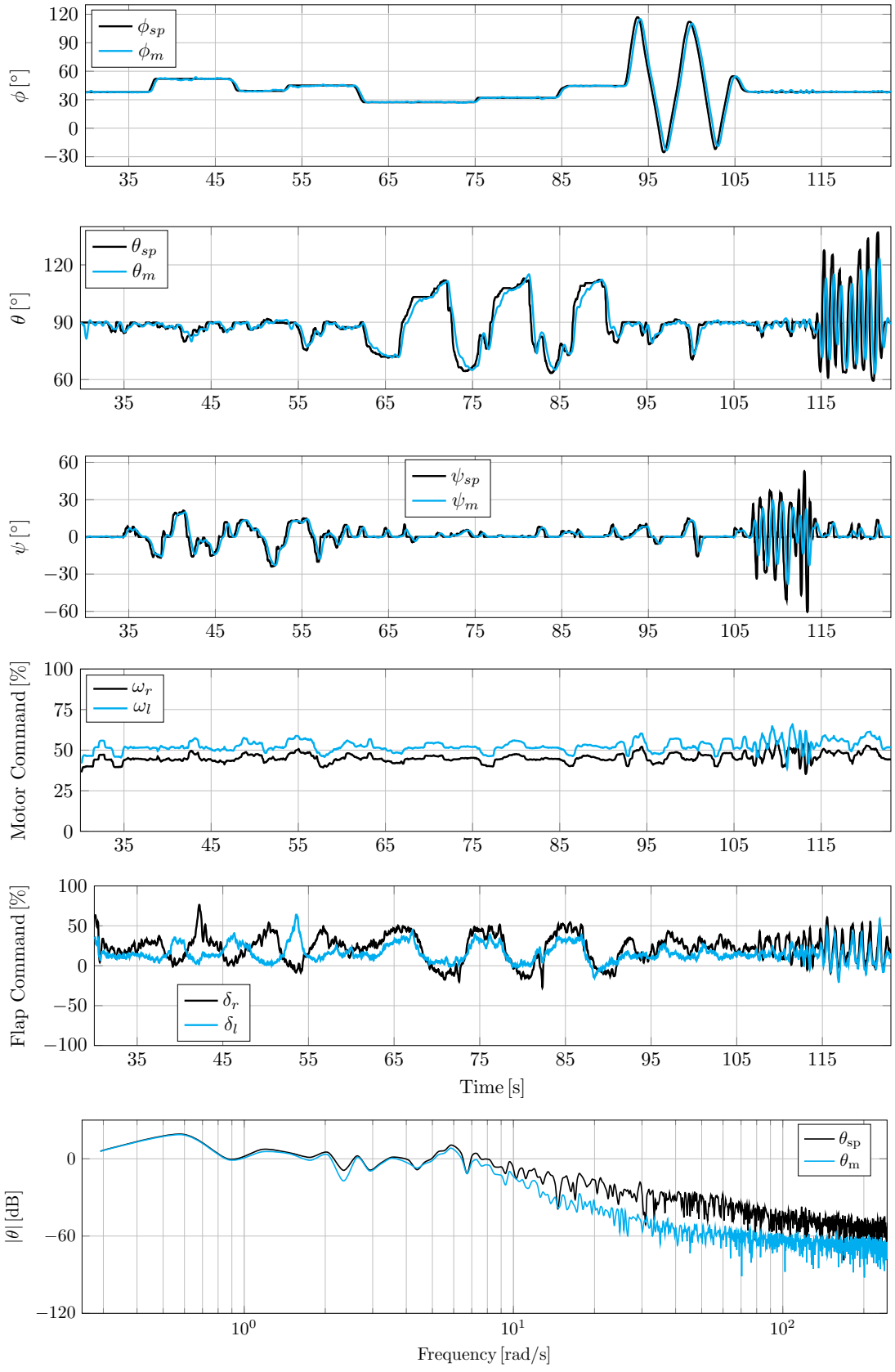

Figure 5.20: INDI attitude stabilization - nominal DarkO.

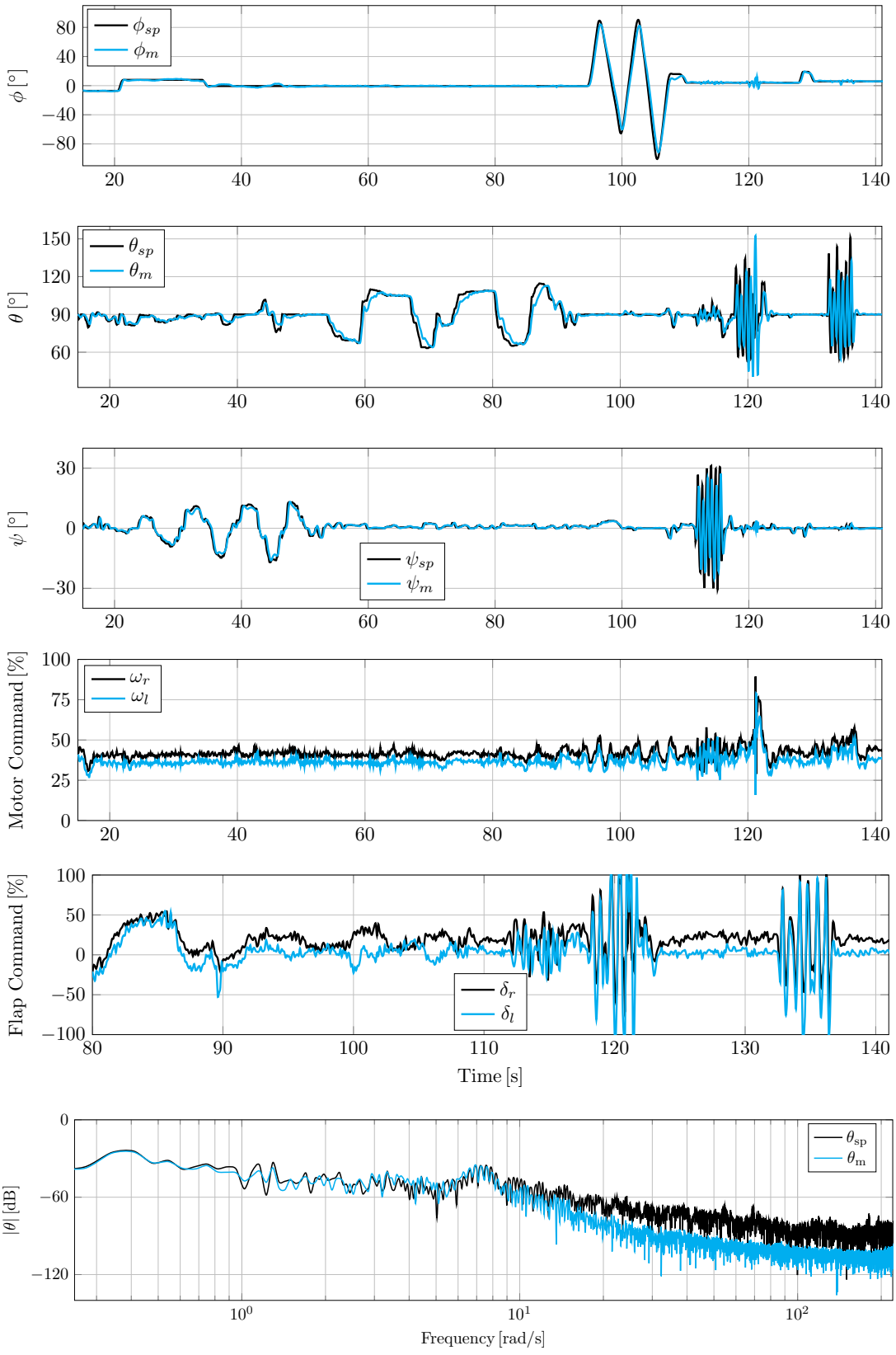

Figure 5.21: MFC attitude stabilization - modified DarkO.

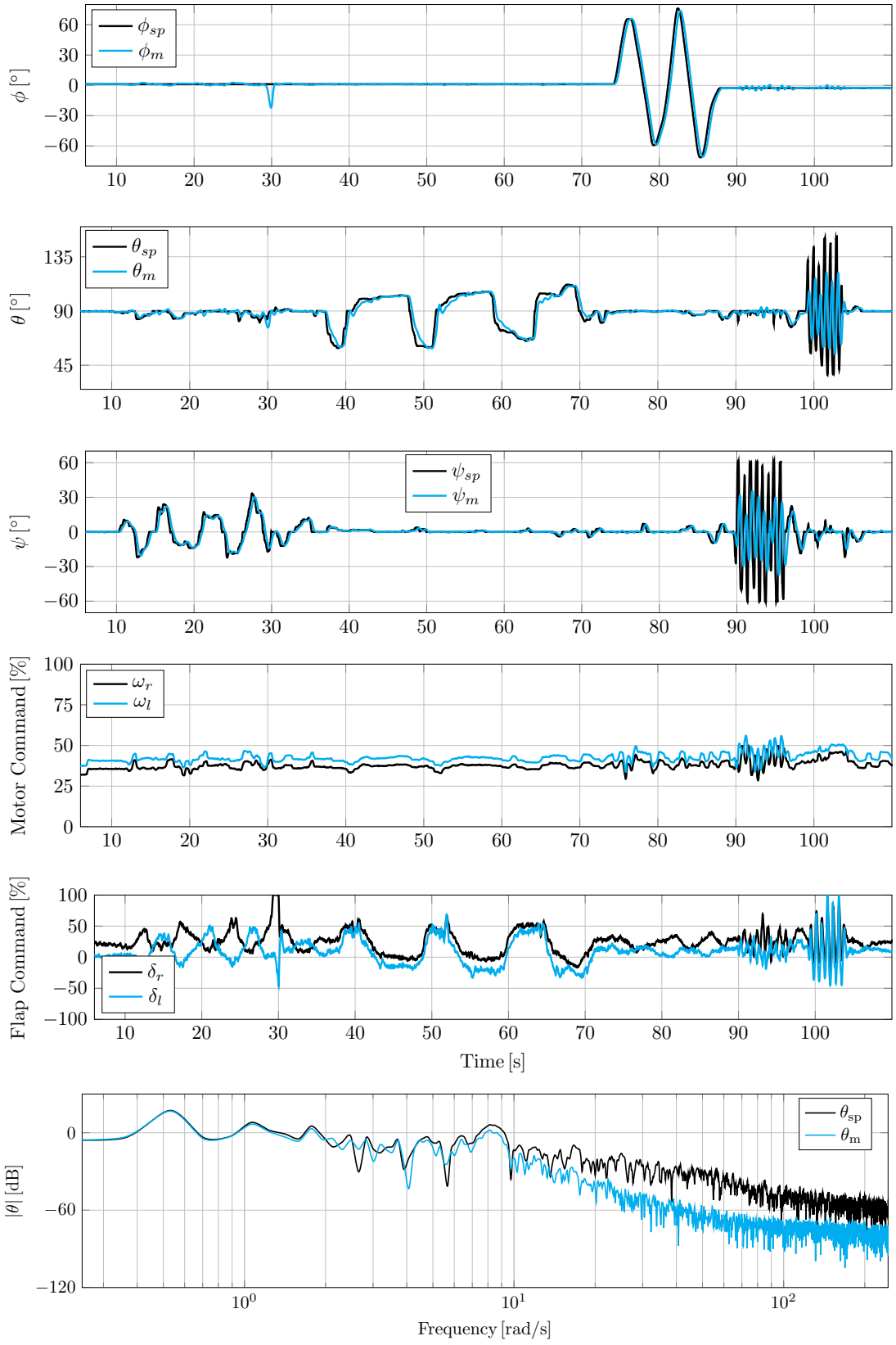

Figure 5.22: INDI attitude stabilization - modified DarkO.

5.4 Summary of Chapter 5

The presented experimental study shows the validity of developing an autopilot system, for the attitude stabilization of tail-sitter MAVs with MFC algorithms. The proposed control strategy provides effective stability performances, and can be designed with little knowledge of the controlled system.

Different flight tests covering hovering, transitioning and forward flight domains are demonstrated. These flight tests were conducted in both indoor and outdoor environments in order to evaluate the MFC performance in real-world flight conditions. During indoor flights, hovering and particular transitioning flight tests were conducted in disturbed flight conditions. Outdoor flight tests demonstrated a smooth and continuous stabilized transitioning flight. It can be concluded from flight tests that wind disturbances can be successfully estimated and then rejected by the MFC closed-loop system. In addition, the fast variations of aerodynamic forces and moments can also be estimated and then stabilized, ensuring stable flight over the entire flight domain of tail-sitter MAVs.

The INDI controller principle has been described and designed to stabilize the tail-sitter MAV attitude. Additional flight tests have been performed to compare the INDI attitude stabilization performance with that of the MFC algorithms. The effective known stability properties of INDI have been validated. In addition, the MFC provides similar flight results highlighting its fast adaptive properties which do not require a priori identification of the control effectiveness of the system. Of particular interest is the easy implementation of MFC algorithms for several potential applications with little knowledge of the controlled system.

This chapter serves to validate the practical application of MFC algorithms on parameter-varying systems. Given its fast adaptation property, MFC has demonstrated the capability to stabilize the tail-sitter MAV over its entire flight envelope. Therefore, MFC allows a considerable time reduction during the design of control laws for systems with poor modeling.

Part III

Conclusion

Chapter 6

Conclusion & Future Work

"*Discovery is new beginning. It is the origin of new rules that supplement, or even supplant, the old. Genius is creative. It is genius precisely because it disregards established routines, because it originates the novelties that will be the routines of the future. Were there rules for discovery, then discoveries would be mere conclusions.*"
— Bernard Lonergan

This chapter offers a general overview of the main contributions of this thesis, although throughout this manuscript, the majority of the results have been discussed and evaluated. Beyond the contributions of this thesis, which has addressed the design of control algorithms for tail-sitter MAVs, we present the scientific and technical limitations of such a control approach that could not be solved during this study. Finally, directions for future work are presented on the design of autopilot systems for autonomous flight missions with tail-sitter MAVs.

Contents

6.1 Final Discussion

In this thesis, the highly nonlinear and unstable dynamics of tail-sitter MAVs have been studied numerically and experimentally. The first objective is to estimate and control the fast variation of aerodynamic forces and moments related to transitioning flight phases of tail-sitter MAVs. The second is to stabilize the dynamic variations present in their wide flight envelope. The intention is to design an effective autopilot system that requires little prior knowledge of the controlled dynamics in order to perform autonomous flight missions.

The first contribution of this thesis is related to Chapter 2, in which we discuss not only the modeling literature review of tail-sitter MAVs and the challenges involving the identification of their aerodynamic effects, but also the current problem for designing control laws on this uncertain and time-varying system. By means of the control literature review, we present the advantages and disadvantages of model-based controllers. For instance, the properties of optimal control laws, which can be designed from dynamic models, have been highlighted. Although the theory of optimal control provides a margin of stability even if the dynamic model has inaccuracies, the performance provided by model-based controllers during flight tests with tail-sitter MAVs may differ from those defined in its control design process. This can be explained by the fact that, the dynamic models of tail-sitter MAVs are challenging to characterize and their aerodynamic coefficients are costly and time-consuming to identify. Thus, their dynamic models are often simplified for control design purposes and, in most cases, the simplified dynamics do not describe their real dynamics.

In addition, the control literature review highlights that the implementation of controllers that are not based on prior dynamic models remains to be explored in the field of tail-sitter MAVs (see §2.2). Nevertheless, it is true that the main contribution of this thesis is the implementation of a control law for tail-sitter MAVs, the control design of which requires little prior knowledge of the system dynamics and no knowledge of its parameters. The MFC algorithms proposed by (Fliess und Join, 2013) has been designed in order to address this challenge. Based on such control algorithms, we have developed a full control architecture for the tracking of trajectories, velocity control and attitude stabilization. The proposed MFC architecture has been analyzed through flight simulations in order to validate the interactions between its control blocks for different flight domains covering the entire flight envelope of tail-sitter MAVs (see Chapter 4). Then, through flight tests, we have evaluated the MFC attitude stabilization blocks during both indoor and outdoor flights (see Chapter 5).

Flight simulation results have shown a high performance for the tracking of trajectories, velocity control and attitude stabilization without gain scheduling methods, which is the most commonly used control technique in this context. Thus, variations in the dynamics of the tail-sitter MAV have been estimated and controlled only by the adaptive properties of the MFC algorithms. In order to assess these properties in more detail, an analysis of parameter-varying has been conducted using the Monte Carlo approach (see §4.3.4). MFC algorithms have demonstrated an ability to stabilize the system for important variations of its internal parameters. These variations are between 25% and +75% of the nominal system parameters. For the purpose of comparing model-based and model-free control techniques, a scheduled-LQR has been designed and compared with our control approach (see §4.4). For equal scenarios, both controllers ensured the stability of the tail-sitter MAV in the transitioning flight phase with simulated wind disturbances. The performance of the controllers was roughly similar, but the

advantage of the MFC approach has been highlighted during its control design. Indeed, the MFC parameters have been designed only once for the entire flight envelope of the tail-sitter MAV, while the LQR gains have been synthesized repeatedly to cover eleven linearized sub-models in the transitioning flight domain. Even if theoretically performant and elegant, flight control algorithms have practical use only if validated by experimental flights. This point has been analyzed during flight tests, in which the MFC algorithms have been designed to stabilize the tail-sitter MAV attitude during indoor and outdoor flight conditions. The attitude stabilization performance obtained with MFC algorithms during flight simulations have been validated this time by real flight experiments. Additional indoor flight tests have been conducted in order to compare the MFC performance with that of the INDI controller (see §5.3).

During the flight test, the MFC approach has shown a better control performance over the INDI. Moreover, the INDI controller requires the identification of actuator control effectiveness for hovering and forward flight phases. The control effectiveness of the actuators are then managed by a gain scheduling approach in order to fit their values to the entire flight domain, which implies the design and implementation of additional algorithms on microprocessors. On the other hand, the MFC approach adapts their closed-loop through its estimator, which is designed for the entire flight envelope. The MFC algorithms can be easily implemented without the use of gain scheduling methods. Thus, it can be concluded that MFC algorithms have been designed for the first time in the field of tail-sitter MAVs, providing similar control performances when compared to that of both the model-based (LQR) and the less-model dependent nonlinear approach (INDI). However, the MFC design reduces time and costs by bypassing the need to identify dynamic models, and its recursive equations can be easily implemented on microprocessors.

In the field of tail-sitter MAV modeling for control design, questions on parameter identification may lose their importance if the need for an accurate mathematical model diminishes. This point presents the novelties that can be improved in order to become *routines of the future*. For instance, the efforts to study robustness issues, with respect to "poor" modeling and/or to disturbances, may be viewed as obsolete and therefore less important (Fliess und Join, 2013).

6.2 Study Limitations

Despite the fact that the proposed control architecture has shown effective performances during both flight simulations and flight tests, it has some limitations. More precisely, the design of the MFC parameters. In another perspective from that used for designing classical model-based controllers, the MFC design is not established on the basis of dynamic models. In order to obtain information on controlled dynamics, the MFC closed-loop uses an estimator based on numerical differentiation algorithms. The input of the estimator is the system command and the measurement of the controlled signal, which is corrupted by noise. The noise could directly affect the performance of the controller, especially at high frequencies. It can be noticed that, beyond the required knowledge of flight dynamics and control theory, the design of the MFC algorithms for tail-sitter MAVs requires some technical expertise in signal processing in order to synthesize the parameters of the MFC estimator. Thus, not only do control requirements need to be addressed, but also filtering and estimation requirements for control purposes.

6.3 Future Work

Given the fact that developing autonomous flight systems address different engineering areas, this research project offers several possibilities for improvements in the field of control, estimation and signal processing, among others. However, we focus the priority list for future work involving the control of tail-sitter MAVs in view of achieving autonomous flight systems as follows :

First, the MFC and INDI approaches should be compared through flight simulations in order to consolidate the advantages and disadvantages of each one for equal scenarios in a controlled environment. We notice that the use of angular acceleration measurements in the attitude stabilization closed-loop improves the responsiveness of the command. It is true that the MFC attitude stabilization based on angle measurements has demonstrated a similar performance when compared with the INDI one, which is established on the basis of angular acceleration measurements. For these reasons, the implementation of MFC algorithms for stabilizing the tail-sitter MAV attitude, based on measurements of angular accelerations, would be of great relevance to both control and aerospace communities. In addition, more aggressive flight trajectories call for an attitude representation with quaternions in order to avoid singularities, however, their disadvantage is that they do not have an intuitive representation.

Second, it would be interesting to conduct an in-depth evaluation of the adaptive properties of the MFC approach through more flight tests. We have presented a numerical analysis highlighting these potential properties of the MFC by the Monte Carlo method. In this analysis, the proposed control strategy has ensured the stability of the tail-sitter MAV for variations between 25% and +75% of its nominal parameters. Further, the validation of these preliminary results through flight tests would certainly be an important contribution for the control community. Therefore, an interesting work would be the stability analysis of a fleet of tail-sitter MAVs of different sizes, geometries and aerodynamic patterns, using the same designed MFC parameters. For example, a first approach could be realized with the modular tail-sitter MAV configurations presented in Figure 6.1, in which their structures can be easily modified.

Future work may be conducted towards the development of guidance algorithms for tail-sitter MAVs. In order to properly manage their flight trajectories and maximize their contributions in autonomous flight missions, the control of positions and velocities is essential. About that, this work has presented flight simulations in which MFC algorithms demonstrated robust disturbance rejection properties for the tracking of positions. However, it would also be interesting to validate these MFC properties in real flight conditions. Despite the known principle behind the proposed control architecture, the cascaded MFC algorithms require further investigation. Indeed, the

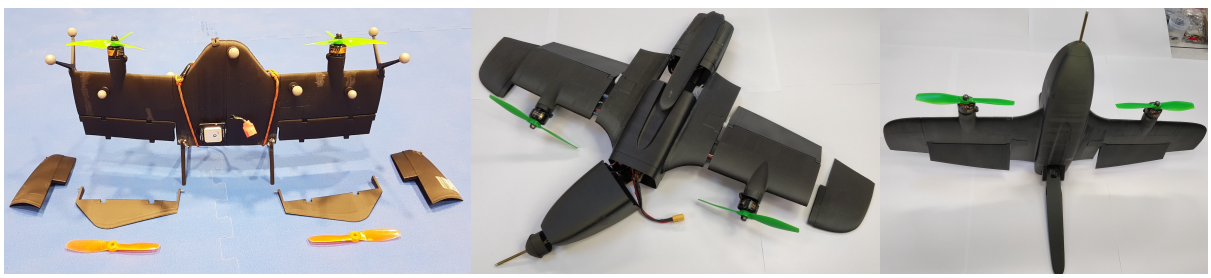

Figure 6.1: Modular tail-sitter MAVs designed at ENAC UAV Lab (Bronz u. a., 2020).

interaction between the position and velocity control blocks remains to be analyzed in real flight environments.

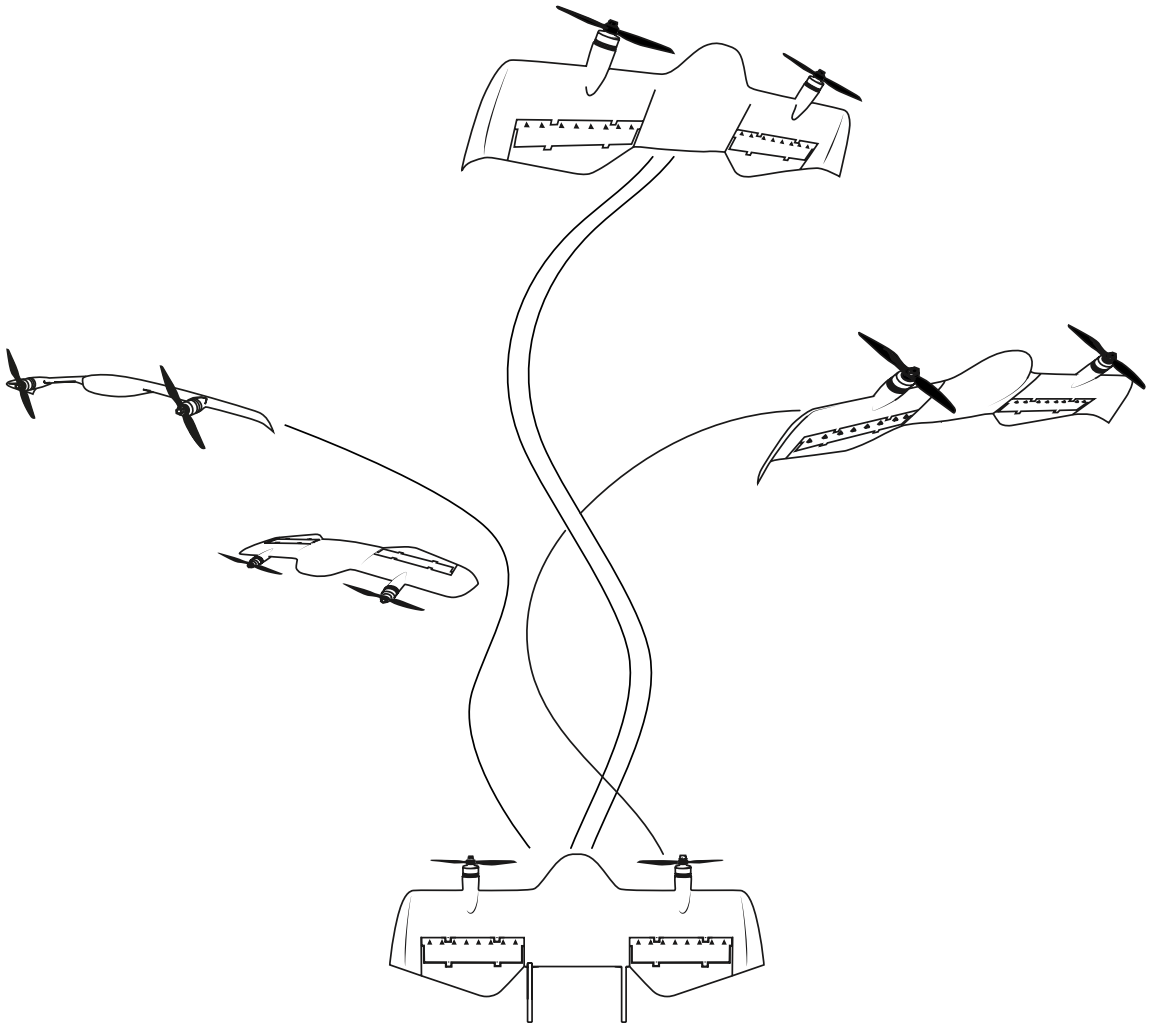

Bibliography

[Anderson 2010] Anderson, J. D.: *Fundamentals of aerodynamics*. McGraw-Hill, 2010

[Ang u. a. 2014] Ang, K. Z. Y. ; Cui, J. ; Pang, T. ; Li, K. ; Wang, K. ; Ke, Y. ; Chen, B. M.: Development of an Unmanned Tail-sitter with Reconfigurable Wings: U–Lion. In: *International Conference on Control & Automation (ICCA)*. Taichung, Taiwan, June 2014, S. 750–755

[Argyle 2016] Argyle, M. E.: *Modeling and Control of a Tailsitter with a Ducted Fan*, Brigham Young University - Provo, Ph.D. Thesis, June 2016

[Bacon u. a. 2001] Bacon, B. J. ; Ostroff, A. J. ; Joshi, S. M.: Reconfigurable NDI Controller Using Inertial Sensor Failure Detection & Isolation. In: *IEEE Transactions On Aerospace And Electronic Systems* 37 (2001), October, Nr. 4, S. 1373–1383

[Bacon und Ostroff 2000] Bacon, Barton J. ; Ostroff, Aaron J.: Reconfigurable Flight Control using Nonlinear Dynamic Inversion with a Special Accelerometer Implementation. In: *AIAA Guidance, Navigation, and Control Conference and Exhibit*. Denver, CO, USA, August 2000, S. 1–15

[Bara u. a. 2018] Bara, O. ; Fliess, M. ; Join, C. ; Daye, J. ; Djouadi, S. M.: Toward a model-free feedback control synthesis for treating acute inflammation. In: *Journal of Theoretical Biology, Elsevier* 448 (2018), July, Nr. 1, S. 26–37

[Barth u. a. 2020a] Barth, J. M. O. ; Condomines, J.-P. ; Bronz, M. ; Hattenberger, G. ; Moschetta, J.-M. ; Join, C. ; Fliess, M.: Towards a Unified Model-Free Control Architecture for Tail Sitter Micro Air Vehicles: Flight Simulation Analysis and Experimental Flights. In: *AIAA SciTech Forum: Guidance, Navigation, and Control*. Orlando, Florida, USA, January 2020, S. 1–22

[Barth u. a. 2018a] Barth, J. M. O. ; Condomines, J.-P. ; Bronz, M. ; Lustosa, L. R. ; Moschetta, J.-M. ; Join, C. ; Fliess, M.: Fixed-wing UAV with transitioning flight capabilities : Model-Based or Model-Free Control approach? A preliminary study. In: *International Conference on Unmanned Aircraft Systems (ICUAS)*. Dallas, TX, USA, June 2018, S. 1157–1164

[Barth u. a. 2020b] Barth, J. M. O. ; Condomines, J.-P. ; Bronz, M. ; Moschetta, J.-M. ; Join, C. ; Fliess, M.: Model-free control algorithms for micro air vehicles with transitioning flight capabilities. In: *International Journal of Micro Air Vehicles* (2020)

[Barth u. a. 2019] Barth, J. M. O. ; Condomines, J.-P. ; Moschetta, J.-M. ; Cabarbaye, A. ; Join, C. ; Fliess, M.: Full Model-Free Control Architecture for Hybrid UAVs. In: *American Control Conference (ACC)*. Philadelphia, PA, USA, August 2019, S. 71–78

[Barth u. a. 2018b] Barth, J. M. O. ; Condomines, J.-P. ; Moschetta, J.-M. ; Join, C. ; Fliess, M.: Model-Free Control Approach for Fixed-Wing UAVs with Uncertain Parameters Analysis. In: *International Conference on Methods and Models in Automation and Robotics (MMAR)*. Miedzyzdroje, Poland, August 2018, S. 527–532

[Bilodeau und Wong 2010] Bilodeau, P.-R. ; Wong, F.: Modeling and control of a hovering mini tail-sitter. In: *International Journal of Micro Air Vehicles* 2 (2010), November, Nr. 1, S. 211–220

[Binz u. a. 2019] Binz, F. ; Islam, T. ; Moormann, D.: Attitude control of tiltwing aircraft using a wing-fixed coordinate system and incremental nonlinear dynamic inversion. In: *International Journal of Micro Air Vehicles* 11 (2019), April, Nr. 1, S. 1–12

[Boyang u. a. 2018a] Boyang, L. ; Weifeng, Z. ; Jingxuan, S. ; Chih-Yung, W.: Model Predictive Control for Path Tracking of a VTOL Tail-sitter UAV in an HIL Simulation Environment. In: *AIAA SciTech Forum*. Kissimmee, FL, USA, January 2018, S. 1–14

[Boyang u. a. 2018b] Boyang, L. ; Weifeng, Z. ; Jingxuan, S. ; Chih-Yung, W. ; Chih-Keng, C.: Development of Model Predictive Controller for a Tail-Sitter VTOL UAV in Hover Flight. In: *Sensors* 18 (2018), August, Nr. 9, S. 1–21

[Bronz u. a. 2017] Bronz, M. ; Smeur, E. J. J. ; Marina, H. G. de ; Hattenberger, G.: Development of A Fixed-Wing mini UAV with Transitioning Flight Capability. In: *AIAA Aviation Forum - AIAA Applied Aerodynamics Conference*. Denver, CO, USA, June 2017, S. 1–14

[Bronz u. a. 2020] Bronz, M. ; Tal, E. ; Barth, J. M. O. ; Favalli, F. ; Karaman, S.: Mission-Oriented Additive Manufacturing of Modular Mini-UAVs. In: *AIAA SciTech Forum*. Orlando, FL, USA, January 2020, S. 1–11

[Carrión u. a. 2017] Carrión, M. ; Biava, M. ; Barakos, G. N. ; Stewart, D.: Study of Hybrid Air Vehicle Stability Using Computational Fluid Dynamics. In: *Journal of Aircraft* 54 (2017), July, Nr. 4, S. 1328–1339

[Chahl u. a. 2007] Chahl, J. S. ; Jain, L. C. ; Mizutani, A. ; Sato-Ilic, M.: *Innovations in Intelligent Machines-1*. Springer-Verlag, 2007. – 181 S

[Chakrabarty und Bhattachary 2016] Chakrabarty, A. K. ; Bhattachary, S.: Lyapunov Based Two-stage Robust Model Reference Adaptive Controller for Linear Plants with Time Varying Bounded Uncertainties. In: *IFAC-PapersOnLine* 49 (2016), February, Nr. 1, S. 213–218

[Chattot 2014] Chattot, J.-J.: Actuator Disk Theory—Steady and Unsteady Models. In: *Journal of Solar Energy Engineering* 136 (2014), March, Nr. 3, S. 1–10

[Davis u. a. 2004] Davis, K. ; Kirke, B. ; Lazauskas, L.: Material related to the aerodynamics of airfoils and lifting surfaces. http://www.cyberiad.net/foildata.htm, 2004

[Dickeson u. a. 2006] Dickeson, Jeffrey J. ; Cifdaloz, Oguzhan ; Miles, David ; Koziol, Paul M. ; Wells, Valana L. ; Rodriguez, Armando A.: Robust H_∞ Gain-Scheduled Conversion for a Tilt-Wing Rotorcraft. In: *Conference on Decision and Control (CDC)*. San Diego, CA, USA, December 2006, S. 5882–5887

[Dickeson u. a. 2007] Dickeson, Jeffrey J. ; Miles, David ; Cifdaloz, Oguzhan ; Wells, Valana L. ; Rodriguez, Armando A.: Robust LPV H_∞ Gain-Scheduled Hover-to-Cruise Conversion for a Tilt-Wing Rotorcraft in the Presence of CG Variations. In: *Conference on Decision and Control (CDC)*. New Orleans, LA, USA, December 2007, S. 2773–2778

[Dickeson u. a. 2005] Dickeson, Jeffrey J. ; Mix, David R. ; Kownig, John S. ; Linda, Karen M. ; Cifdaloz, Oguzhan ; Wells, Valana L. ; Rodriguez, Armando A.: H_∞ Hover-to-Cruise Conversion for a Tilt-Wing Rotorcraft. In: *Conference on Decision and Control (CDC)*. Seville, Spain, December 2005, S. 6486–6491

[Diop und Fliess 1991a] Diop, S. ; Fliess, M.: Nonlinear observability, identifiability, and persistent trajectories. In: *IEEE Conference on Decision and Control (CDC)*. Brighton, England, December 1991, S. 714–719

[Diop und Fliess 1991b] Diop, S. ; Fliess, M.: On nonlinear observability. In: *European Control Conference (ECC)*, 1991, S. 152–157

[Drela 1989] Drela, M.: XFOIL: An Analysis and Design System for Low Reynolds Number Airfoils. In: *Mueller T.J. (eds) Low Reynolds Number Aerodynamics. Lecture Notes in Engineering* 54 (1989), June

[Escareno u. a. 2006a] Escareno, J. ; Salazar-Cruz, S. ; Lozano, R.: Attitude stabilization of a convertible mini birotor. In: *International Conference on Control Applications*. Munich, Germany, October 2006, S. 2202–2206

[Escareno u. a. 2006b] Escareno, J. ; Salazar-Cruz, S. ; Lozano, R.: Modelling and Control of a Convertible VTOL Aircraft. In: *Conference on Decision and Control (CDC)*. San Diego, CA, USA, December 2006, S. 69–74

[Escareno u. a. 2007] Escareno, J. ; Stone, R. H. ; Sanchez, A. ; Lozano, R.: Modeling and control strategy for the transition of a convertible tail-sitter UAV. In: *European Control Conference (ECC)*. Kos, Greece, July 2007, S. 3385–3390

[Fliess und Join 2013] Fliess, M. ; Join, C.: Model-free control. In: *International Journal of Control, Taylor & Francis* 86 (2013), July, Nr. 12, S. 2228–2252

[Fliess u. a. 2007] Fliess, M. ; Join, C. ; Sira-Ramirez, H.: Non-linear estimation is easy. In: *International Journal of Modelling, Identification and Control* (2007)

[Fliess und Sira-Ramirez 2003] Fliess, M. ; Sira-Ramirez, H.: An algebraic frame-work for linear identification. In: *ESAIM Control, Optimisation and Calculus of Variations* 9 (2003), S. 151–168

[Fliess 2006] Fliess, Michel: Analyse non standard du bruit. Comptes rendus de l'Académie des sciences. Série I, Mathématique. In: *Elsevier*, May 2006, S. 797–802

[Flores u. a. 2018a] Flores, A. ; Oca, A. M. de ; Flores, G.: A simple controller for the transition maneuver of a tail-sitter drone. In: *Conference on Decision and Control (CDC)*. Miami Beach, FL, USA, December 2018, S. 4277–4281

[Flores u. a. 2018b] Flores, Alejandro ; Oca, A. M. de ; Flores, Gerardo: A simple controller for the transition maneuver of a tail-sitter drone. In: *Conference on Decision and Control (CDC)*. Miami Beach, FL, USA, December 2018, S. 4277–4281

[Flores u. a. 2017] Flores, G. ; Carrillo, L. R. G. ; Sanahuja, G. ; Lozano, R.: PID Switching Control for a Highway Estimation and Tracking Applied on a Convertible Mini-UAV. In: *Conference on Decision and Control (CDC)*. Maui, Hawaii, USA, December 2017, S. 3110–3115

[Flores u. a. 2014] Flores, G. ; Lugo, I. ; Lozano, R.: 6-DOF Hovering Controller Design of the Quad Tiltrotor Aircraft: Simulations and Experiments. In: *Conference on Decision and Control (CDC)*. Los Angeles, CA, USA, December 2014, S. 6123–6128

[Forshaw und Lappas 2011] Forshaw, J. L. ; Lappas, V. J.: High-Fidelity Modeling and Control of a Twin Helicopter Rotor Tailsitter. In: *AIAA Guidance, Navigation, and Control Conference*. Portland, Oregon, August 2011, S. 1–15

[Frink u. a. 2017] Frink, N. T. ; Murphy, P. C. ; Atkins, H. L. ; Viken, S. A. ; Petrilli, J. L. ; Gopalarathnam, A. ; Paul, R. C.: Computational Aerodynamic Modeling Tools for Aircraft Loss of Control. In: *AIAA Journal of Guidance, Control, and Dynamics* 40 (2017), April, Nr. 4, S. 789–803

[Fuhrer u. a. 2019] Fuhrer, S. ; Verling, S. ; Stastny, T. ; Siegwart, R.: Fault-tolerant Flight Control of a VTOL Tailsitter UAV. In: *International Conference on Robotics and Automation (ICRA)*. Montreal, Canada, May 2019, S. 4134–4140

[Ge u. a. 1999] Ge, S. S. ; Hang, C. C. ; Zhang, T.: A direct adaptive controller for dynamic systems witha class of nonlinear parameterizations. In: *Automatica* 35 (1999), April, Nr. 4, S. 741–747

[Gu u. a. 2017] Gu, H. ; Lyu, X. ; Li, Z. ; Shen, S. ; Zhang, F.: Development and Experimental Verification of a Hybrid Vertical Take-Off and Landing (VTOL) Unmanned Aerial Vehicle(UAV). In: *International Conference on Unmanned Aircraft Systems (ICUAS)*. Miami, FL, USA, June 2017, S. 160–169

[Hadi u. a. 2016] Hadi, G. S. ; Putra, H. M. ; Dewi, P. T. ; Budiyarto, A. ; Budiyono, A.: Switching Control Approach for Stable Transition State Process on Hybrid Vertical Take-off and Landing UAV. In: *Journal of Unmanned System Technology* 4 (2016), August, Nr. 2, S. 51–56

[Hartmann u. a. 2017] Hartmann, Philipp ; Meyer, Carsten ; Moormann, Dieter: Unified Velocity Control and Flight State Transition of Unmanned Tilt-Wing Aircraft. In: *Journal of Guidance, Control, and Dynamics* 40 (2017), June, Nr. 6, S. 1348–1359

[Hattenberger u. a. 2014] Hattenberger, G. ; Bronz, M. ; Gorraz, M.: Using the Paparazzi UAV System for Scientific Research. In: *International Micro Air Vehicle Conference and Competition (IMAV)*. Delft, Netherlands, August 2014, S. 247–252

[Hochstenbach u. a. 2015] Hochstenbach, M. ; Notteboom, C. ; Theys, B. ; Schutter, J. D.: Design and Control of an Unmanned Aerial Vehicle for Autonomous Parcel Delivery with Transition from Vertical Take-off to Forward Flight - VertiKUL, a Quadcopter Tailsitter. In: *International Journal of Micro Air Vehicles* 7 (2015), December, Nr. 4, S. 395–405

[Huang u. a. 2009] Huang, H. ; Homann, G. M. ; Waslander, S. L. ; Tomlin, C. J.: Aerodynamics and control of autonomous quadrotor helicopters in aggressive maneuvering. In: *International Conference on Robotics and Automation (ICRA)*. Kobe, Japan, May 2009, S. 3277–3282

[Jain und Nigam 2013] Jain, P. ; Nigam, M. J.: Design of a Model Reference Adaptive Controller Using Modified MIT Rule for a Second Order System. In: *Advance in Electronic and Electric Engineering* 3 (2013), Nr. 4, S. 477–484

[Jin u. a. 2015] Jin, W. ; Bifeng, S. ; Liguang, W. ; Wei, T.: L_1 Adaptive Dynamic Inversion Controller for an X-wing Tail-sitter MAV in Hover Flight. In: *Procedia Engineering* 99 (2015), February, S. 969–974

[Join u. a. 2017] Join, C. ; Bernier, J. ; Mottelet, S. ; Fliess, M. ; Rechdaoui-Guérin, S. ; Azimi, S. ; Rocher, V.: A simple and efficient feedback control strategy for wastewater denitrification. In: *20th World IFAC Congress* 50 (2017), July, Nr. 1, S. 7657–7662

[Jung und Shim 2011] Jung, Y. ; Shim, D. H.: Development and Application of Controller for Transition Flight of Tail-Sitter UAV. In: *Journal of Intelligent & Robotic Systems* 65 (2011), August, S. 137–152

[Kai u. a. 2017] Kai, J.-M. ; Allibert, G. ; Hua, M.-D. ; Hamel, T.: Nonlinear feedback control of Quadrotors exploiting First-Order Drag Effects. In: *IFAC-Papers OnLine* 50 (2017), July, Nr. 1, S. 8189–8195

[Kalman 2010] Kalman, R.: *Lectures on Controllability and Observability. In: Evangelisti E. (eds) Controllability and Observability. C.I.M.E. Summer Schools*. Bd. 46. Springer, Berlin, Heidelberg, 2010

[Kita u. a. 2012] Kita, K. ; Konno, A. ; Uchiyama, M.: Transition between Level Flight and Hovering of a Tail-Sitter Vertical Takeoff and Landing Aerial Robot. In: *Advanced Robotics* 24 (2012), April, Nr. 5-6, S. 763–781

[Knoebel und McLain 2008] Knoebel, N. B. ; McLain, T. W.: Adaptive quaternion control of a miniature tailsitter uav. In: *American Control Conference (ACC)*. Seattle, WA, USA, June 2008, S. 2340–2345

[Kuang u. a. 2017] Kuang, Minchi ; Zhu, Jihong ; Wang, Wufan ; Tang, Yunfei: Flight Controller Design and Demonstratin of a Thrust-Vectored Tailsitter. In: *Conference on Robotics and Automation (ICRA)*. Singapore, June 2017, S. 5169–5174

[Kubo und Suzuki 2012] Kubo, Daisuke ; Suzuki, Shinji: High angle of attack flight control of a tail-sitter unmanned aircraft. In: *International Congress of the aeronautical sciences (ICAS)*, 2012, S. 1–7

[Lafont u. a. 2015] Lafont, F. ; Balmat, J.-F. ; Pessel, N. ; Fliess, M.: A model-free control strategy for an experimental greenhouse with an application to fault accommodation. In: *Computers and Electronics in Agriculture, Elsevier,* 110 (2015), January, Nr. 1, S. 139–149

[Leng u. a. 2019a] Leng, Y. ; Bronz, M. ; Jardin, T. ; Moschetta, J.-M.: Comparisons of Different Propeller Wake Models for a Propeller-Wing Combination. In: *8th European Conference for Aeronautics and Space Sciences*. Madrid, Spain, July 2019, S. 1–15

[Leng u. a. 2019b] Leng, Y. ; Bronz, M. ; Jardin, T. ; Moschetta, J.-M.: Slipstream Deformation of a Propeller-Wing Combination Applied for Convertible UAVs in Hover Condition. In: *International Micro Air Vehicle Competition and Conference (IMAV)*. Madrid, Spain, September 2019, S. 95–102

[Liu u. a. 2019] Liu, D. ; Liu, H. ; Lewis, F. L.: Robust trajectory tracking control for unmanned tail-sitters in aggressive flight mode transitions. In: *International Journal of Robust and Nonlinear Control* 29 (2019), August, Nr. 12, S. 4270–4284

[Liu u. a. 2018] Liu, D. ; Liu, H. ; Li, Z. ; Hou, X. ; Wang, Q.: Robust attitude control for tail-sitter unmanned aerial vehicles in flight mode transitions. In: *International Journal of Robust and Nonlinear Control* 29 (2018), December, Nr. 4, S. 1–18

[Lustosa u. a. 2015] Lustosa, L. R. ; Defay, F. ; Moschetta, J.-M.: Longitudinal study of a tilt-body vehicle: modeling, control and stability analysis. In: *International Conference on Unmanned Aircraft Systems (ICUAS)*. Denver, Colorado, USA, June 2015, S. 816–824

[Lustosa u. a. 2019] Lustosa, L. R. ; Defaÿ, F. ; Moschetta, J.-M.: Global Singularity-Free Aerodynamic Model for Algorithmic Flight Control of Tail Sitters. In: *AIAA Journal of Guidance, Control, and Dynamics* 42 (2019), February, Nr. 2, S. 303–316

[Lustosa u. a. 2014] Lustosa, Leandro R. ; Defaÿ, François ; Moschetta, Jean-Marc: Development of the flight model of a tilt-body MAV. In: *International Micro Air Vehicle Conference and Competition (IMAV)*. Delft, Netherlands, August 2014, S. 1–6

[Lustosa 2017] Lustosa, Leandro R.: *The Φ-theory approach to flight control design of hybrid vehicles*, Institut Supérieur de l'Aéronautique et de l'Espace, Ph.D. Thesis, November 2017

[Lyu u. a. 2017a] Lyu, X. ; Gu, H. ; Wang, Y. ; Li, Z. ; Shen, S. ; Zhang, F.: Design and implementation of a quadrotor tail-sitter VTOL UAV. In: *International Conference on Robotics and Automation (ICRA)*. Marina Bay Sands, Singapore, May 2017, S. 3924–3930

[Lyu u. a. 2018a] Lyu, X. ; Zhou, J. ; Gu, H. ; Li, Z. ; Shen, S. ; Zhang, F.: Disturbance Observer Based Hovering Control of Quadrotor Tail-Sitter VTOL UAVs Using H_∞ Synthesis. In: *IEEE Robotics and Automation Letters* 3 (2018), October, Nr. 4, S. 2910–2917

[Lyu u. a. 2017b] Lyu, Ximin ; Gu, Haowei ; Zhou, Jinni ; Li, Zexiang ; Shen, Shaojie ; Zhang, Fu: A Hierarchical Control Approach For A Quadrotor Tail-Sitter VTOL UAV and Experimental Verification*. In: *Conference on Intelligent Robots and Systems (IROS)*. Vancouver, BC, Canada, September 2017, S. 5135–5141

[Lyu u. a. 2018b] Lyu, Ximin ; Gu, Haowei ; Zhou, Jinni ; Li, Zexiang ; Shen, Shaojie ; Zhang, Fu: Simulation and flight experiments of a quadrotor tail-sitter vertical take-off and landing unmanned aerial vehicle with wide flight envelope. In: *International Journal of Micro Air Vehicles* 10 (2018), December, Nr. 4, S. 303–317

[Martin und Salaun 2010] Martin, P. ; Salaun, E.: Design and implementation of a low-cost observer-based attitude and heading reference system. In: *Control Engineering Practice* 18 (2010), July, Nr. 7, S. 712–722

[Mboup u. a. 2009] Mboup, M. ; Join, C. ; Fliess, M.: Numerical differentiation with annihilators in noisy environment. In: *Numerical Algorithms, Springer Verlag* 50 (2009), Nr. 4, S. 439–467

[Menhour u. a. 2018] Menhour, L. ; Novel, B. d'Andréa ; Fliess, M. ; Gruyer, D. ; Mounier, H.: An efficient model-free setting for longitudinal and lateral vehicle control. Validation through the interconnected pro-SiVIC/RTMaps prototyping platform. In: *IEEE Transactions on Intelligent Transportation Systems* 19 (2018), February, Nr. 2, S. 461–475

[Miller und de Callafon 2012] Miller, D. N. ; Callafon, R. A. de: Identification of Linear Time-Invariant Systems via Constrained Step-Based Realization. In: *IFAC Symposium on System Identification*. Brussels, Belgium, July 2012, S. 1155–1160

[Mix u. a. 2004] Mix, David R. ; Koenig, John S. ; Linda, Karen M. ; Cifdaloz, Oguzhan ; Wells, Valana L. ; Rodriguez, Armando A.: Towards Gain-Scheduled H_∞ Control Design for a Tilt-Wing Aircraft. In: *Conference on Decision and Control (CDC)*. Atlantis, Paradise Island, Bahamas, December 2004, S. 1222–1227

[Miyazaki und Tsubakino 2017] Miyazaki, K. ; Tsubakino, D.: Nonlinear Hovering Control laws for Small Vectored-Thrust Tail-Sitter UAVs. In: *Conference on Control Technology and Applications (CCTA)*. Kohala Coast, Hawaii, USA, August 2017, S. 2102–2107

[Moschetta 2014] Moschetta, Jean-Marc: The aerodynamics of micro air vehicles: technical challenges and scientific issues. In: *International Journal of Engineering Systems Modelling and Simulation* 6 (2014), July, Nr. 3/4, S. 134–148

[Oosedo u. a. 2013] Oosedo, A. ; Abiko, S. ; Konno, A. ; Koizumi, T. ; Furui, T. ; Uchiyama, M.: Development of a Quad Rotor Tail-Sitter VTOL UAV without Control Surfaces and Experimental Verification. In: *International Conference on Robotics and Automation (ICRA)*. Karlsruhe, Germany, May 2013, S. 317–322

[Ostroff und Bacon 2002] Ostroff, Aaron J. ; Bacon, Barton J.: Enhanced NDI Strategies for Reconfigurable Flight Control. In: *American Control Conference (ACC)*. Anchorage, AK, May 2002, S. 3631–3636

[Phung und Morin 2014a] Phung, D.-K. ; Morin, P.: An Approach for Modeling, Design, and Energy Evaluation of Small Convertible Aerial Vehicles. In: *AIAA Modeling and Simulation Technologies Conference*. Atlanta, GA, USA, June 2014, S. 1–28

[Phung und Morin 2014b] Phung, D.-K. ; Morin, P.: Control of a new convertible UAV with a minimal sensor suite. In: *Conference on Decision and Control (CDC)*. Los Angeles, CA, USA, December 2014, S. 229–235

[Phung 2015] Phung, Duc K.: *Conception, modeling, and control of a convertible mini-drone.*, Automatic. Université Pierre et Marie Curie - Paris VI, Ph.D. Thesis, 2015

[Powers u. a. 2013] Powers, C. ; Mellinger, D. ; Kushleyev, A. ; Kothmann, B. ; Kumar, V.: *Infuence of aerodynamics and proximity effects in quadrotor flight, In Experimental robotics*. Springer, 2013. – 289–302 S

[Pucci 2013] Pucci, D.: *Towards an unified approach for the control of aerial vehicles*, Université de Nice-Sophia Antipolis, Sapienza Universita di Roma, Ph.D. Thesis, September 2013

[Pucci u. a. 2013] Pucci, D. ; Hamel, T. ; Morin, P. ; Samson, C.: Nonlinear Control of Aerial Vehicles Subjected to Aerodynamic Forces. In: *Conference on Decision and Control (CDC)*. Florence, Italy, December 2013, S. 4839–4846

[Pucci u. a. 2015] Pucci, D. ; Hamel, T. ; Morin, P. ; Samson, C.: Nonlinear feedback control of axisymmetric aerial vehicles. In: *Automatica* 53 (2015), March, S. 72–78

[Ramirez und Nahon 2020] Ramirez, J. C. H. ; Nahon, M.: Trajectory Tracking Control of Highly Maneuverable Fixed-Wing Unmanned Aerial Vehicles. In: *AIAA Scitech Guidance, Navigation, and Control Conference*. Orlando, FL, USA, January 2020

[Ritz und D'Andrea 2017] Ritz, Robin ; D'Andrea, R.: A global controller for flying wing tailsitter vehicles. In: *International Conference on Robotics and Automation (ICRA)*. Singapore, May 2017, S. 2731–2738

[Rodriguez-Fortun u. a. 2013] Rodriguez-Fortun, J. M. ; Rotella, F. ; Alfonso, J. ; Carrillo, F. J. ; Orús, J.: Model-free control of a 3-DOF piezoelectric nanopositioning platform. In: *Conference on Decision and Control (CDC)*. Florence, Italy, December 2013, S. 342–347

[Rohr u. a. 2019] Rohr, D. ; Stastny, T. ; Verling, S. ; Siegwart, R.: Attitude and Cruise Control of a VTOL Tiltwing UAV. In: *IEEE Robotics and Automation Letters* 4 (2019), July, Nr. 3, S. 2683–2690

[Rothhaar u. a. 2014] Rothhaar, P. M. ; Murphy, P. C. ; Bacon, B. J. ; Gregory, I. M. ; Grauer, J. A. ; Busan, R. C. ; Croom, M. A.: NASA Langley Distributed Propulsion VTOL Tilt-Wing Aircraft Testing, Modeling, Simulation, Control, and Flight Test Development. In: *AIAA Aviation Technology, Integration, and Operations Conference*. Atlanta, GA, June 2014, S. 1–14

[Saeed u. a. 2018] Saeed, A. S. ; Younes, A. B. ; Cai, C. ; Cai, G.: A survey of hybrid Unmanned Aerial Vehicles. In: *Progress in Aerospace Sciences* 98 (2018), April, S. 91–105

[Sanchez u. a. 2008] Sanchez, A. ; Escareno, J. ; Garcia, O. ; Lozano, R.: Autonomous Hovering of a Noncyclic Tiltrotor UAV: Modeling, Control and Implementation. In: *17th IFAC World Congress*. Seoul, Korea, July 2008, S. 803–808

[Shekhar und Sharma 2018] Shekhar, A. ; Sharma, A.: Review of Model Reference Adaptive Control. In: *International Conference on Information, Communication, Engineering and Technology (ICICET)*, August 2018, S. 1–5

[Silva u. a. 2018] Silva, N. B. F. ; Fontes, J. V. C. ; Inoue, R. S. ; Branco, K. R. L. J. C.: Dynamic Inversion and Gain-Scheduling Control for an Autonomous Aerial Vehicle with Multiple Flight Stages. In: *Journal of Control, Automation and Electrical Systems* 29 (2018), June, Nr. 3, S. 328–339

[Sman u. a. 2017] Sman, Elisabeth S. V. D. ; Smeur, E. J. J. ; Remes, Bart ; Wagter, C. D. ; Chu, Q. P.: Incremental Nonlinear Dynamic Inversion and Multihole Pressure Probes for Disturbance Rejection Control of Fixed-wing Micro Air Vehicles. In: *International Micro Air Vehicle Competition and Conference (IMAV)*. Toulouse, France, September 2017, S. 111–120

[Smeur u. a. 2019] Smeur, Ewoud J. J. ; Bronz, Murat ; Croon, Guido C. H. E. de: Incremental Control and Guidance of Hybrid Aircraft Applied to a Tailsitter Unmanned Air Vehicle. In: *Journal of Guidance, Control, and Dynamics* (2019), September

[Smeur u. a. 2016a] Smeur, Ewoud J. J. ; Chu, Qiping ; Croon., Guido C. H. E. de: Adaptive Incremental Nonlinear Dynamic Inversion for Attitude Control of Micro Air Vehicles. In: *Journal of Guidance, Control, and Dynamics* 39 (2016), March, Nr. 3, S. 450–461

[Smeur u. a. 2018] Smeur, Ewoud J. J. ; Croon, Guido C. H. E. de ; Chu, Qiping: Cascaded Incremental Nonlinear Dynamic Inversion Control for MAV Disturbance Rejection. In: *Control Engineering Practice* 73 (2018), January, S. 79–90

[Smeur u. a. 2016b] Smeur, Ewoud J. J. ; Croon, Guido C. de ; Chu, Qiping: Gust Disturbance Alleviation with Incremental Nonlinear Dynamic Inversion. In: *International Conference on Intelligent Robots and Systems (IROS)*. Daejeon, Korea, October 2016, S. 5626–5631

[Smith 1998] Smith, P. R.: A Simplified Approach to Nonlinear Dynamic Inversion Based Flight Control. In: *AIAA Atmospheric Flight Mechanics Conference and Exhibit*. Boston, MA, USA, 1998, S. 1998–4461

[Stevens u. a. 2015] Stevens, B. L. ; Lewis, F. L. ; Johnson, E. N.: *Aircraft Control and Simulation: Dynamics, Controls Design, and Autonomous Systems, 3rd Edition*. Wiley-Blackwell, 2015

[Stone u. a. 2008] Stone, R. H. ; Anderson, P. ; Hutchison, C. ; Tsai, A. ; Gibbens, P. ; Wong, K. C.: Flight Testing of the T-Wing Tail-Sitter Unmanned Air Vehicle. In: *Journal of Aircraft* 45 (2008), April, Nr. 2, S. 673–685

[Stone 2004] Stone, R. H.: Control architecture for a tail-sitter unmanned air vehicle. In: *Asian Control Conference*. Melbourne, Victoria, Australia, July 2004, S. 736–744

[Tran u. a. 2017] Tran, A. T. ; Sakamoto, N. ; Sato, M. ; Muraoka, K.: Control Augmentation System Design for Quad-Tilt-Wing Unmanned Aerial Vehicle via Robust Output Regulation Method. In: *IEEE Transactions on Aerospace and Electronic Systems* 53 (2017), February, Nr. 1, S. 357–369

[VanderMey 2011] VanderMey, Josiah T.: *A Tilt Rotor UAV for Long Endurance Operations in Remote Environments*, Massachusetts Institute of Technology, Master dissertation, 2011

[Verling u. a. 2016] Verling, S. ; Weibel, B. ; Boosfeld, M. ; Alexis, K. ; Burri, M. ; Siegwart, R.: Full Attitude Control of a VTOL Tailsitter UAV. In: *International Conference on Robotics and Automation (ICRA)*. Stockholm, Sweden, May 2016, S. 3006–3012

[Wang 2017] Wang, Alwin R.: Conceptual Design of a QuadPlane Hybrid Unmanned Aerial Vehicle. In: *AIAA Student Region VII Conference*. Melbourne, Australia, November 2017, S. 1–11

[Wang u. a. 2009] Wang, Q.-G. ; Zhang, Z. ; Astrom, K. J. ; Chek, L. S.: Guaranteed dominant pole placement with PID controllers. In: *Journal of Process Control* 19 (2009), February, Nr. 2, S. 349–352

[Wang u. a. 2018] Wang, W. ; Zhu, J. ; Kuang, M. ; Zhu, X.: Adaptive Attitude Control for a Tail-sitter UAV with Single Thrust-vectored Propeller. In: *International Conference on Robotics and Automation (ICRA)*. Brisbane, Australia, May 2018, S. 6581–6586

[Wang u. a. 2017] Wang, Y. ; Yu, J. ; Li, Q. ; Ren, Z.: Control strategy for the transition flight of a tail-sitter UAV. In: *Chinese Control Conference (CCC)*. Dalian, China, July 2017, S. 3504–3509

[Yildiz u. a. 2017] Yildiz, Y. ; Unel, M. ; Demirel, A. E.: Nonlinear hierarchical control of a quad tilt-wing UAV: An adaptive control approach. In: *International Journal of Adaptive Control and Signal Processing* 31 (2017), February, Nr. 9, S. 1245–1264

[Zeng und Guo 2018] Zeng, Y. ; Guo, H.: An euler angle calculation method for tailsitter UAV. In: *Chinese Automation Congress (CAC)*. Jinan, China, January 2018, S. 814–819

[Zhang u. a. 2018] Zhang, D. ; Chen, Z. ; Xi, L. ; Hu, Y.: Transitional Flight of Tail-Sitter Unmanned Aerial Vehicle Based on Multiple-Model Adaptive Control. In: *Journal of Aircraft, Engineering Notes* 55 (2018), January, Nr. 1, S. 389–394

[Zhong u. a. 2019] Zhong, J. ; Y. Li, B. S. nd ; Xuan, J.: L_1 Adaptive Control of a Dual-Rotor Tail-Sitter Unmanned Aerial Vehicle With Input Constraints During Hover Flight. In: *IEEE Access* 7 (2019), April, S. 51312–51328

[Zhong u. a. 2017] Zhong, L. ; Yuqing, H. ; Liying, Y. ; Jianda, H.: Control techniques of tilt rotor unmanned aerialvehicle systems: A review. In: *Chinese Journal of Aeronautics* 30 (2017), February, Nr. 1, S. 135–148

[Zhou u. a. 2019] Zhou, W. ; Boyang, L. ; Jingxuan, S. ; Chih-Yung, W. ; Chih-Keng, C.: Position control of a tail-sitter UAV using successive linearization based model predictive control. In: *Control Engineering Practice* 91 (2019), August, Nr. 1, S. 1–13

Chapter 7

Résumé en français

"*Vive la République! Vive la France!*."
— Charles de Gaulle

Ce chapitre présente un résumé de la thèse en français. Tout d'abord, les principaux éléments abordés dans l'introduction seront évoqués. Les différents travaux de la littérature qui ont traité à la fois les défis de la modélisation et du contrôle des micro drones hybrides seront cités. Ensuite, l'approche développée dans cette thèse pour stabiliser le micro drone hybride sur toute son enveloppe de vol, basée sur des algorithmes de commande sans modèle, sera détaillée. Cette approche a été évaluée par des simulations de vol, puis validée par des essais de vol en intérieur et en extérieur. Enfin, la conclusion est exposée en introduisant des indices pour les travaux futurs.

Contents

7.1 Introduction

7.1.1 Systèmes de vol autonomes

Au cours de la dernière décennie, le domaine des drones a explosé. D'énormes progrès ont été réalisés dans la conception de systèmes de vol autonomes, capables d'exécuter des missions répétitives, complexes ou dangereuses de manière plus sûre et plus efficace que les avions télécommandés. Alors qu'ils étaient auparavant conçus à des fins de surveillance et de destruction dans le secteur militaire, les drones font maintenant leurs preuves dans plusieurs domaines d'applications civiles. La possibilité d'utiliser des systèmes de vol autonomes dans ces domaines a commencé avec l'accessibilité croissante proposée par l'industrie commerciale par le biais de solutions à bas prix pour les applications d'imagerie aérienne. Ce qui a motivé le développement de plusieurs projets, notamment dans les domaines de l'aide humanitaire, des secours en cas de catastrophe, de la recherche et du sauvetage, des opérations de sécurité, de la surveillance, de l'agriculture de précision et de l'inspection des infrastructures civiles.

En outre, cette technologie porteuse offre la possibilité de créer encore plus d'applications dans l'espace aérien civil, notamment avec les services de livraison pour les magasins et des taxis aériens pour les déplacements urbains. Par conséquent, les drones devraient être de plus en plus intégrés dans le domaine de l'aviation civile. Face à cette réalité et afin d'assurer leur trafic à travers les zones urbaines, la commission européenne a adopté certaines règles relatives à leurs activités en élaborant un cadre institutionnel, réglementaire et architectural pour la prestation de services dans l'espace aérien, qui vise à gérer ces opérations complexes avec un degré élevé d'automatisation et de connectivité. La principale contribution est la définition de concepts, de services et d'applications potentielles pour faciliter leur insertion dans l'espace aérien civil et organiser le domaine des transports aériens. Enfin, un bilan systématique des règles aériennes existantes est en cours afin d'identifier les changements nécessaires pour préparer l'insertion sûre et sécurisée des services qui impliquent les drones dans l'espace aérien. Ce cadre de référence, à savoir l'US (de l'anglais U-Space), combine un ensemble de nouveaux services et de procédures spécifiques qui reposent sur un niveau élevé d'automatisation et de connectivité (voir figure 7.1). Ces services peuvent être introduits progressivement dans tout

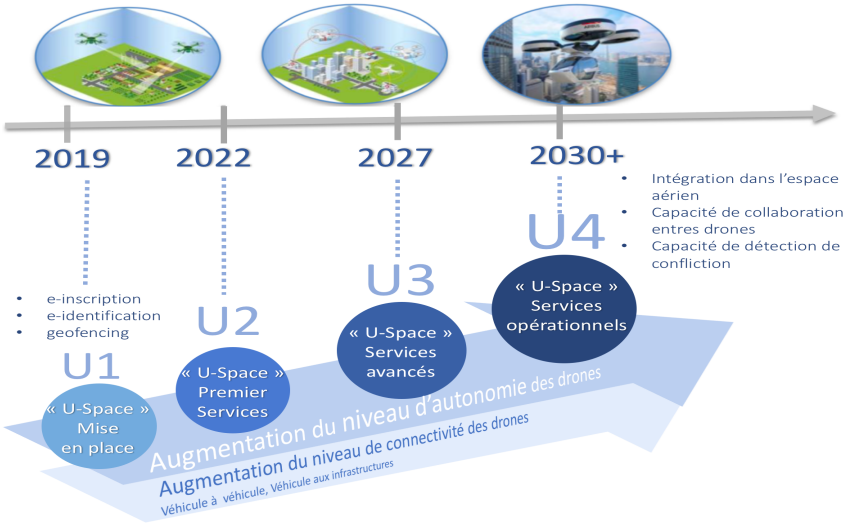

Figure 7.1: Cadre de reference "U-Space".

Figure 7.2: Prototype Airbus A^3 Vahana.

type de mission de routine en respectant quatre phases en fonction des objectifs souhaités et des technologies disponibles. Le premier US (U1) a été conçu pour des services de base qui assurent des fonctions simples, telles que l'enregistrement et l'identification des drones dans un système de base de données ou des outils de géofencing pour localiser le drone dans une zone géographique. Le deuxième US (U2) offre des services pour soutenir la gestion des opérations des drones et peut inclure la planification des vols, l'approbation des vols, le suivi, les informations dynamiques de l'espace aérien et les interfaces procédurales avec le contrôle du trafic aérien. Le troisième US (U3) offre des services plus avancés, avec des opérations plus complexes dans des zones particulièrement denses. Par exemple, l'assistance à la détection de conflits avec des fonctionnalités intelligentes DAA et des moyens de communication plus fiables entraînerait une augmentation significative des opérations dans différents environnements. Le dernier US (U4) contient des services complets. En particulier, des services qui offrent des interfaces intégrées

Figure 7.3: Drone hybride de la compagnie DHL à des fins de livraison.

avec l'aviation habitée reposant sur un niveau élevé d'automatisation et de connectivité tant pour le drone que pour l'ensemble du système US. Ce dispositif vise à assurer la flexibilité et le libre accès à l'espace aérien tout en garantissant la sécurité des opérations au sol ou en vol. En assurant le contrôle de l'espace aérien par l'enregistrement et l'identification des drones, les autorités de régulation seront en mesure de protéger la vie privée et de minimiser les incidences sur l'environnement. Les avantages attendus d'un espace aérien plus sûr pourraient encourager le développement de nouveaux modèles commerciaux, stimuler de nouveaux emplois et une mobilité aérienne urbaine plus autonome. Ces services futurs visent à relever les grands défis urbains prévus pour les dix prochaines années en apportant des solutions concrètes à la gestion du trafic aérien grâce à des recherches plus techniques et approfondies en matière de contrôle. En outre, le dénominateur commun des US indique la nécessité indispensable de développer des systèmes de contrôle intelligents afin de stabiliser la dynamique des aéronefs et d'aider les systèmes de guidage qui permettent d'accomplir les missions. Cela a été constaté non seulement dans le développement de prototypes de taxi aérien urbain (voir figure 7.2), mais aussi dans le cas de livraison par drones (voir figure 7.3). L'exécution de missions de vols de livraison dans des zones urbaines nécessite un haut niveau d'autonomie en termes d'énergie, afin d'effectuer des vols de longue durée, combinés à des capacités de décollage et atterrissage verticaux, qui ne sont pas naturellement compatibles.

Pour les missions de vol de longue endurance, l'utilisation de configurations à voilure fixe est plus appropriée en raison de leurs surfaces aérodynamiques optimisées qui, au contact d'une masse d'air en mouvement, génèrent une force de portance qui permet de diminuer la consommation d'énergie du système de propulsion. En fonction de leur taille et de leur charge utile, les drones à voilure fixe peuvent rester en vol plus d'une heure. La contrainte de cette technologie est liée aux phases de vol de décollage et d'atterrissage qui nécessitent une longueur de piste non négligeable. En termes de manœuvrabilité, les configurations à voilures tournantes sont plus adaptées en raison de leur polyvalence pour effectuer des décollages et des atterrissages verticaux, ainsi que des vols stationnaires. Cependant, cette configuration présente un inconvénient lié à sa consommation énergétique élevée, qui se traduit par une réduction du temps de vol, généralement compris entre 15 et 30 minutes. Par conséquent, les inconvénients des drones à voilures tournantes (par exemple, les hélicoptères, les quadrirotors et les multirotors) en termes d'endurance et d'autonomie, avec le manque de capacité de décollage et d'atterrissage à partir de petites zones des drones à voilure fixe, ont également encouragé le développement d'une nouvelle configuration, à savoir les micro drones hybrides HMAVs (voir figure 7.4). Les configurations des

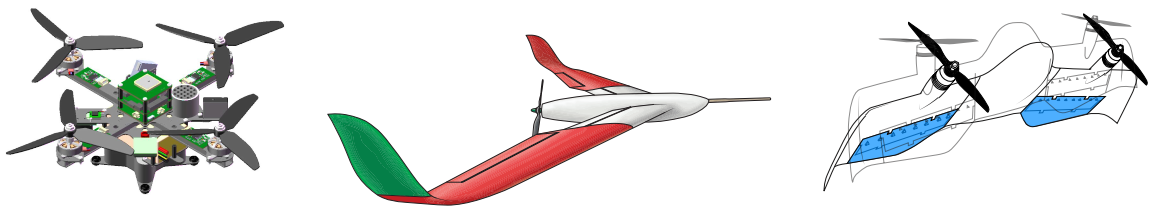

Figure 7.4: Principales configurations des drones : voilures tournantes, voilures fixe and hybrides.

HMAVs sont capables d'effectuer des missions de vol complexes avec des capacités de décollages et atterrissages verticaux combinées à des vols en croisière rapides et durables pour atteindre des zones éloignées. Les HMAVs seront l'un des acteurs clés des opérations de transport aérien urbain. Bien que la combinaison de deux configurations de drones différentes en une seule offre un champ d'application plus large, le système de contrôle doit prendre en compte les particularités de chacune d'entre elles afin de mener à bien la mission de vol prévue. La figure 7.5 illustre cette large enveloppe de vol avec le décollage vertical, le vol de transition, le vol en croisière, le vol stationnaire et l'atterrissage vertical. En raison de leur large domaine de vol, les HMAV peuvent être appliqués dans une grande variété de scénarios et de missions. D'autre part, ce système complexe présente des défis qui restent à résoudre, notamment dans le processus de conception des systèmes de pilotage automatique.

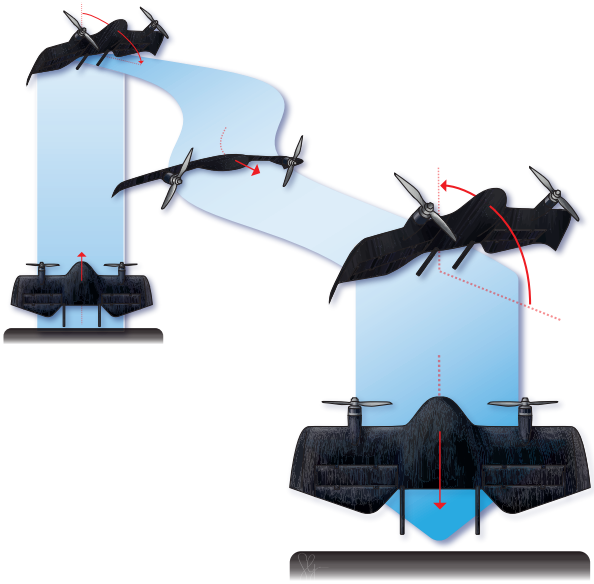

Figure 7.5: Phases de vol typiques des HMAVs.

En effet, le niveau de complexité croissant de ces différentes phases de vol nécessite le développement de nouvelles solutions technologiques. La conception de techniques de contrôle efficaces afin de stabiliser l'attitude des HMAVs semble être une préoccupation majeure en raison de la complexité du traitement de leur dynamique non linéaire, en particulier pendant les vols de transition. Ce domaine de vol particulier présente des effets aérodynamiques instables qui sont difficiles à gérer. C'est pourquoi l'utilisation d'algorithmes de contrôle précis est essentielle pour améliorer à la fois la sécurité des opérations et la stabilité des HMAVs, même dans des conditions de vol venteuses. D'un point de vue aérodynamique et structurel, différents concepts de HMAV ont été conçus. De plus, de nouvelles solutions mécaniques ont été développées afin de faciliter le processus de conception des commandes pour les vols de transition. Dans ce qui suit, un aperçu des principales configurations HMAV est présenté afin de montrer la particularité de chacune d'entre elles et ses mécanismes de transition.

(a) QuadPlane

(b) Tilt-Wing

(c) Tilt-Rotor

(d) Tail-Sitter

Figure 7.6: Exemples de configurations de drones hybrides.

► QuadPlanes

Les QuadPlanes sont conçus avec deux systèmes de propulsion, ce qui simplifie la stratégie de contrôle pour stabiliser l'ensemble de son domaine de vol (voir figure 7.6a). Le premier système de propulsion, composé de quatre rotors et de quatre hélices, est disposé vers le haut et contrôle pendant la majeure partie du vol les mouvements verticaux de l'avion. Ces actionneurs sont principalement demandés lors des décollages, des atterrissages et des vols stationnaires. Le second système de propulsion est composé d'un rotor-hélice supplémentaire afin d'atteindre des vitesses de vol en croisière.

Les mécanismes de transition ne sont pas nécessaires pour les configurations QuadPlane, ce qui assure un degré de fiabilité accru pour le système. Ainsi, cette configuration est relativement simple, avec un risque réduit de défaillance mécanique (Wang, 2017). En revanche, lors de vols en croisière à des vitesses relativement élevées, le premier système de propulsion est désactivé et la dynamique vertical est désormais contrôlée par la force de portance aérodynamique générée par les ailes. Le montage fixe des hélices du premier système de propulsion dans une orientation perpendiculaire par rapport à la direction du vol en croisière entraîne une charge supplémentaire pour le deuxième système de propulsion, et donc une consommation d'énergie supplémentaire. Pour la plupart, les configurations QuadPlanes sont stabilisées par des méthodes de contrôle de commutation (Gu u. a., 2017)(Flores u. a., 2017)(Hadi u. a., 2016). Le critère de commutation est basé sur la vitesse de vol actuelle du MAV.À faible vitesse de vol, le pilote automatique active les

algorithmes de stabilisation pour le domaine de vol stationnaire, ce qui implique essentiellement la stabilisation d'un drone à voilures tournantes. Ensuite, à des vitesses de vol relativement élevées, les algorithmes de stabilisation sont commutés pour le contrôle d'une configuration d'aile fixe. Le passage d'un mode de vol à l'autre est souvent considéré comme un point critique dans un point de vue du contrôle des QuadPlanes (Hadi u. a., 2016).

▶ Tilt-Wings

La particularité de la configuration des tilt-wings est liée aux vols de transition, où les ailes doivent être basculées en même temps que les rotors (voir figure 7.6b). Ainsi, un actionneur supplémentaire et puissant est nécessaire pour surmonter le couple de l'aile afin de la positionner dans l'orientation souhaitée. L'entrée pour contrôler cet actionneur supplémentaire doit être prise en compte lors de la conception du système de pilotage automatique. Pendant le décollage, l'atterrissage et les vols stationnaires, les ailes doivent être positionnées vers le haut afin de produire une force de poussée opposée au vecteur poids du HMAV, qui assure le contrôle du niveau de vol (voir figure 7.7). Dans ces domaines de vol, avec les ailes orientées vers le haut, l'avion sera plus vulnérable aux vents latéraux et le système de pilotage automatique doit fournir des efforts supplémentaires pour faire face à ces perturbations.

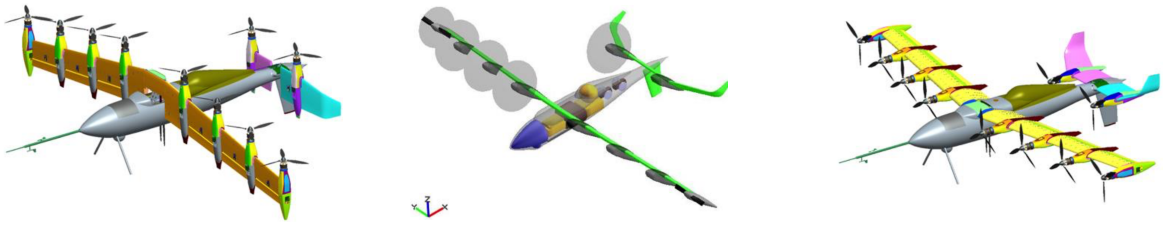

Figure 7.7: Modèles CAO de tilt-wing GL-10 montrant les différentes phases de vol: vol stationnaire, transition et vol en croisière (Rothhaar u. a., 2014).

Un nouveau concept tilt-wing MAV a été proposé par (Phung, 2015). Inspirés par les quadrotors classiques, les auteurs ont inclus deux ailes dans la structure, qui peuvent être tournées séparément du système de propulsion. L'approche de modélisation développée pour une telle configuration HMAV ainsi que l'évaluation de sa consommation énergétique se trouvent dans (Phung und Morin, 2014a). En outre, une méthodologie de contrôle pour cette configuration particulière de tilt-wing a été proposée par la (Phung und Morin, 2014b) qui évalue les performances des commandes de vol sans mesure de la vitesse air. Dans la littérature, il existe plusieurs configurations de tilt-wings et différentes approches de contrôle conçues pour stabiliser leur dynamique de vol (Rohr u. a., 2019)(Binz u. a., 2019)(Yildiz u. a., 2017)(Tran u. a., 2017).

▶ Tilt-Rotor

Comme pour les configurations tilt-wings, les tilt-rotors nécessitent la mise en œuvre d'un actionneur supplémentaire pour effectuer les vols de transition. Les rotors sont montés sur des dispositifs basculants, et la transition entre le vol stationnaire et le vol en croisière s'effectue progressivement en fonction de l'inclinaison du rotor (voir figure 7.6c et figure 7.8). D'un point de vue mécanique, cette configuration présente un avantage par rapport aux tilt-wings. Dans le cas des tilt-rotors, l'angle entre l'aile et le souffle de l'hélice peut être ajusté en contrôlant le système d'un dispositif basculant. Cet angle joue un rôle important dans le contrôle des

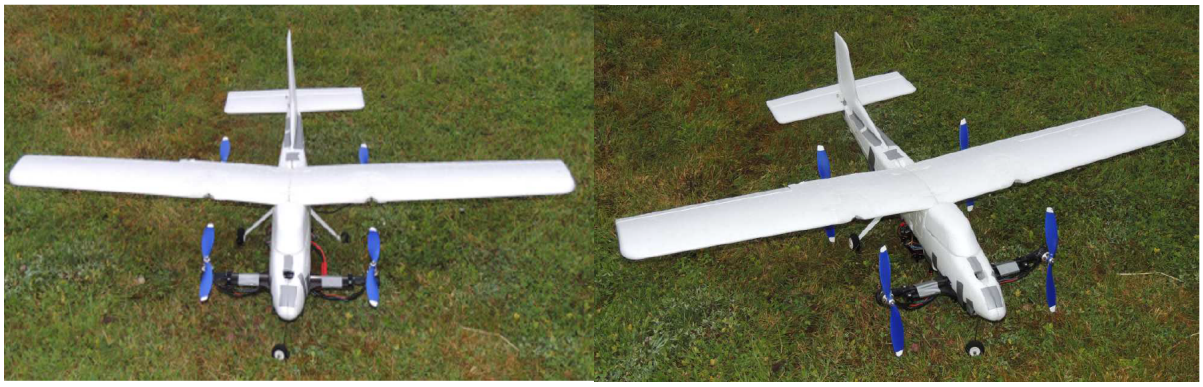

Figure 7.8: Configuration tilt-rotor indiquant les positions du rotor pendant les phases de vol stationnaire et de croisière (Flores u. a., 2014).

forces et des moments aérodynamiques: le contrôler permet de mieux gérer non seulement les performances aérodynamiques lors des vols de transition, mais aussi la stabilité du système pour l'ensemble du domaine de vol. La revue de la littérature sur le contrôle des tilt-rotors (Zhong u. a., 2017) présente un point critique : "Un modèle raisonnable de dynamique de vol est la base des méthodes de contrôle. Il est donc nécessaire de se concentrer sur la modélisation précise des drones tilt-rotors, la simplification du modèle et le compromis entre la précision et la complexité du modèle. Simultanément, l'identification du système combinée à la technique de modélisation active permettrait d'obtenir un modèle dynamique plus précis, et la combinaison de la technique de controle des erreurs du modèle avec la conception classique du contrôle améliorerait l'adaptabilité du contrôleur dans le mode de transition". Cependant, la modélisation de la dynamique reste un processus difficile, long et coûteux, non seulement pour les tilt-rotors, mais aussi pour toutes les configurations HMAV (Bronz u. a., 2017) (Verling u. a., 2016). Par conséquent, la mise en œuvre de contrôleurs basés sur un modèle et donc leurs performances seront directement affectées par la qualité du modèle dynamique.

▶ Tail-Sitter

Contrairement aux précédentes configurations des HMAVs, le tail-sitter MAV décolle et atterrit verticalement sur sa propre queue. Pendant la transition du vol stationnaire au vol en croisière, toute la structure est inclinée de la position verticale à la position horizontale. Selon la configuration des tail-sitters, les vols de transition peuvent être effectués soit par la génération du

Figure 7.9: Exemples de cellules de Tail-Sitter MAV.

moment aérodynamique créé par les volets, soit par le couple créé par le système de propulsion. La figure 7.9 montre trois configurations de tail-sitters. Les deux premières effectuent la transition en créant un moment aérodynamique par la déflexion des volets, et la troisième par le couple créé par le système de propulsion. Pendant le vol en croisière, en position horizontale, le tail-sitter vole comme un avion conventionnel. En utilisant des techniques aérodynamiques classiques, les concepteurs peuvent optimiser le profil de l'aile du tail-sitter MAV pour le rendre plus durable afin de réduire la consommation d'énergie. Grâce à ce processus d'optimisation aérodynamique, les tail-sitter MAVs peuvent effectuer des missions de vol de plus d'une heure.

L'inconvénient lié à cette configuration HMAV concerne le domaine de vol stationnaire. Dans cette phase de vol, les tail-sitter MAVs sont plus vulnérables aux vents latéraux en raison de la position verticale des ailes. Cependant, les perturbations causées par le vent peuvent être maîtrisées en utilisant un système de pilotage automatique efficace. En outre, les missions de vol classiques impliquant des tail-sitters sont caractérisées par 90% du vol en croisière et seulement le reste pour le décollage, l'atterrissage et les vols stationnaires. La communauté des automaticiens fait d'autant plus attention à la stabilisation de l'attitude des tail-sitter HMAVs sur toute son enveloppe de vol. En effet, la dynamique des tail-sitter MAVs est fortement non linéaire avec des effets aérodynamiques instables qui sont difficiles à modéliser et à contrôler. En outre, leur domaine de vol présente des problèmes de singularité avec la représentation de l'attitude en termes d'angles d'Euler (Zeng und Guo, 2018). Pour résoudre ce problème, l'attitude du tail-sitter est généralement représentée en utilisant les quaternions (Liu u. a., 2018).

D'un point de vue mécanique, les tail-sitter MAVs sont caractérisés comme des systèmes sous-actionnés avec une dynamique fortement couplée. Ces caractéristiques mécaniques génèrent un défit supplémentaire au processus de modélisation et d'identification. Cela peut s'expliquer par le fait que, pour ce type de système, une entrée de commande donnée agit simultanément sur des dynamiques différentes. Ainsi, l'identification de l'influence d'une commande donné sur une dynamique particulière reste un processus difficile qui nécessite une attention particulière. La figure 7.10 illustre les effets des actionneurs sur la dynamique de l'attitude du tail-sitter MAV. L'angle de roulis (ϕ) peut être contrôlé par des déflexions asymétriques des volets, l'angle de tangage (θ) par des déflexions symétriques des volets et la rotation autour de l'axe de lacet (ψ) est contrôlée à partir d'une configuration de poussée différentielle, qui crée un couple temporaire non nul autour de son axe. Le réglage de la poussée différentielle crée une différence entre les rotations des hélices gauche et droite, et modifie ainsi le comportement aérodynamique autour

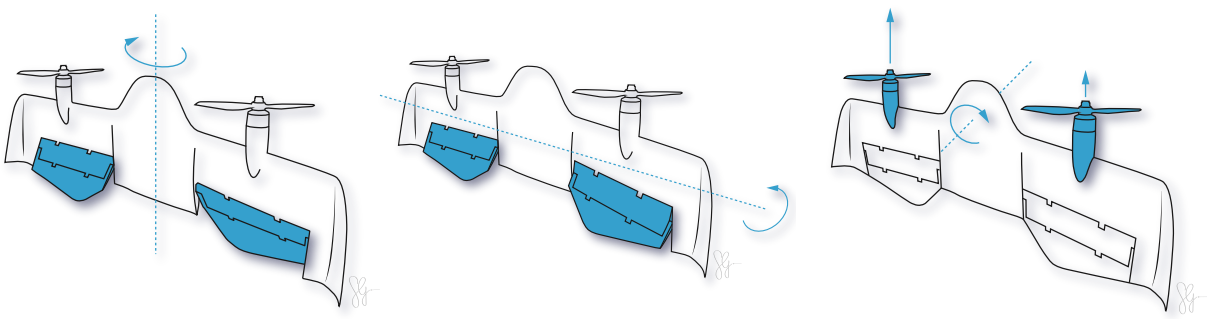

Figure 7.10: Effets des actionneurs du tail-sitter sur son attitude. De gauche à droite : angle de roulis (ϕ), angle de tangage (θ) et angle de lacet (ψ).

des volets. Cela peut s'expliquer par l'effet de sillage causé par le mouvement de l'hélice. Cet effet aérodynamique est situé dans une région derrière l'hélice où se trouvent les volets. Lorsque le comportement du flux d'air est laminaire, la pression derrière l'hélice est plus élevée que l'air environnant, ce qui augmente l'efficacité des volets en fonction de la rotation de l'hélice. Lorsque la poussée différentielle est activée, le souffle d'un côté de l'aile est différent du souffle de l'autre côté, ce qui implique une efficacité de contrôle différente avec un impact sur la dynamique de tangage et de roulis contrôlée par ces volets. Par conséquent, l'interaction entre l'hélice et l'aile crée un couplage aérodynamique mais également un couplage mécanique sur la dynamique de tangage et de roulis, car ils sont contrôlés par les mêmes surfaces de contrôle aérodynamique.

Les interactions aérodynamiques entre l'hélice et la surface de l'aile sont connues pour être réciproques. La vitesse induite en aval dans le sillage de l'hélice entraîne une variation de l'angle d'attaque local et des variations de pression dynamique au niveau des sections d'ailes immergées, d'où une répartition différente de la portance (voir figure 7.11). La vitesse de retour induite par l'aile modifie la condition du flux d'entrée de l'hélice, et donc une force et un moment supplémentaires sont créés dans le disque du rotor. L'analyse de la dynamique du vol et la conception des lois de pilotage des tail-sitter MAVs doivent tenir compte de ces effets pour garantir les caractéristiques de vol souhaitées au cours de leurs missions.

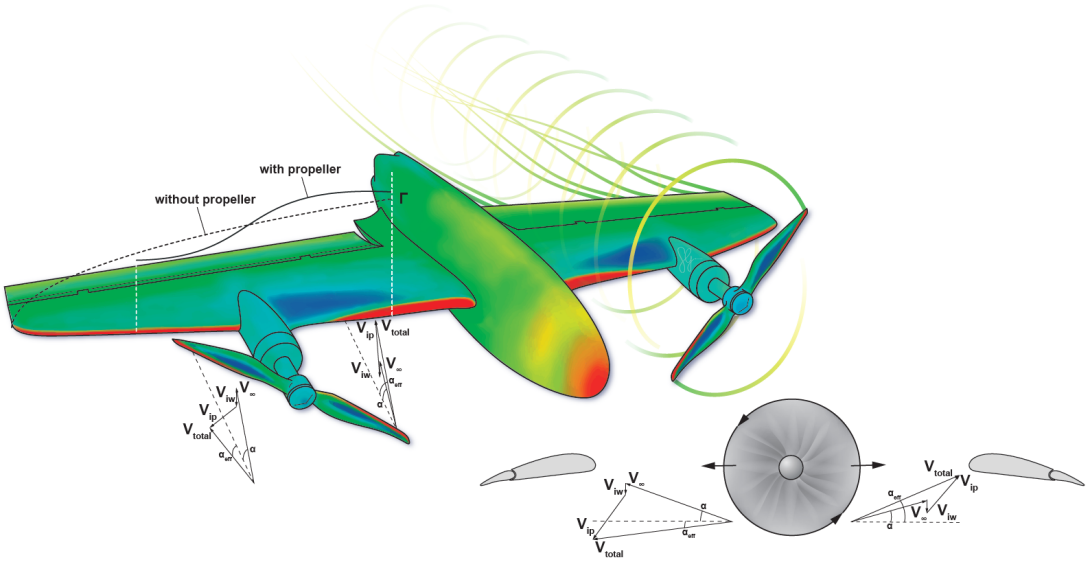

Figure 7.11: Interaction entre l'hélice et la surface de l'aile.

Ainsi, différents travaux de recherche peuvent être trouvés dans la littérature sur l'interaction entre l'hélice et l'aile (Leng u. a., 2019a) (Leng u. a., 2019b). L'identification de ces effets aérodynamiques nécessite, pour chaque point de fonctionnement du vol, les informations de l'air ambiant, les valeurs des entrées de commande plus les mesures des forces et moments aérodynamiques agissant sur le système. La manière la plus précise et la plus fiable d'identifier ces phénomènes aérodynamiques est probablement par le biais de campagnes en soufflerie, qui sont coûteuses et longues.

7.1.2 Contexte de la thèse

Dans le domaine des systèmes de vol autonomes, plusieurs missions de vol nécessitent l'utilisation de MAV qui peuvent voler pendant de longues périodes. Simultanément, ces missions imposent des trajectoires de vol contraignantes qui requièrent des configurations MAV agiles. Le moyen naturel d'obtenir l'efficacité de la puissance et la manœuvrabilité d'une plate-forme d'avion est de combiner les caractéristiques des voilures tournantes avec celles des avions à voilure fixe. C'est la raison pour laquelle de nouvelles méthodes de conception, qui associent la dynamique structurelle HMAV et la conception des systèmes de pilotage automatique, ont vu le jour. La figure 7.12 illustre un exemple de mission de vol impliquant des tail-sitter MAVs à partir d'un décollage vertical suivi de la transition du vol stationnaire au vol en croisière; puis, le vol en croisière suivi de la transition de retour au vol stationnaire et de l'atterrissage vertical. Par conséquent, l'ensemble du domaine de vol des tail-sitter MAVs peut se résumer aux phases de vol suivantes :

1. Décollage vertical
2. Transition entre le vol stationnaire et le vol en croisière
3. Vol en croisière
4. Transition entre le vol en croisière et le vol stationnaire
5. Atterrissage vertical

La dynamique des drones à voilures tournantes peut être observée dans les domaines de vol liés au décollage vertical et à l'atterrissage vertical, qui sont illustrés, respectivement, par ① et ⑤. Il est évident que le comportement dynamique des aéronefs à voilure fixe peut être observé pendant le vol en croisière, ce qui est illustré par é3. Par conséquent, les domaines de vol représentés par é2 et é4 mettent en évidence les interactions entre la dynamique des drones à voilures tournantes et des aéronefs à voilure fixe pendant les vols de transition. La dynamique des voilures tournantes et des aéronefs à voilure fixe est connue et bien modélisée dans leurs domaines de vol respectifs. Cependant, les vols de transition introduisent une dynamique particulière avec des comportements non linéaires rapides qui sont difficiles à modéliser et à contrôler

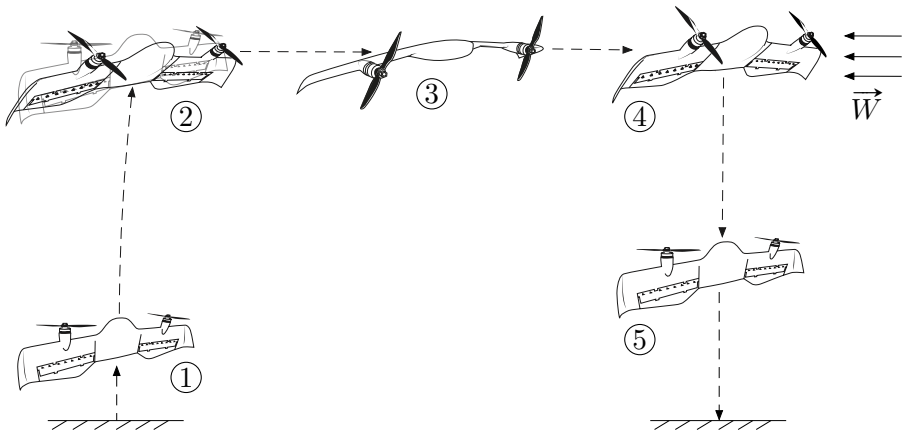

Figure 7.12: Domaines de vol typiques des tail-sitter MAVs. Le vecteur $\vec{W}$ représente les perturbations dues au vent.

avec précision. La conception de systèmes de pilotage automatique pour les HMAVs reste un processus délicat. Les contrôleurs basés sur des modèles demandent une meilleure compréhension de leur dynamique complexe. Cependant, les effets aérodynamiques non linéaires instables présents dans les vols de transition sont encore difficiles à caractériser en termes d'équations mathématiques pour la conception des commandes. Au vu de ces observations, nous pensons qu'il serait avantageux de développer des techniques de contrôle pour les HMAVs avec une estimation dynamique en temps réel. La présente thèse propose une stratégie de contrôle unifiée capable de stabiliser toute l'enveloppe de vol des HMAVs sans connaissance préalable de son modèle dynamique, ce qui répondrait à la problématique décrite précédemment.

7.1.3 Vue d'ensemble de la thèse

L'objectif de ce projet de recherche est de fournir un système de pilotage automatique pour les tail-sitter MAVs dans lequel la conception de la loi de commande nécessite peu de connaissances préalables de la dynamique du système. L'approche de la thèse permet donc de réduire à la fois les coûts des campagnes en soufflerie lors de l'identification des phénomènes aérodynamiques, et le temps d'obtention des modèles dynamiques. Plus précisément, l'architecture de contrôle sans modèle sera conçue et évaluée pour stabiliser toutes les phases de vol des tail-sitter MAVs. Cette étude implique non seulement des vols de simulation mais aussi des essais en vol pour démontrer les avantages pratiques d'une telle approche de contrôle.

Section 7.2 fournit une analyse documentaire des sujets de recherche actuels sur la modélisation et le contrôle des tail-sitter MAVs. Leur dynamique de vol, les phénomènes aérodynamiques et les systèmes de propulsion sont présentés en détail. En outre, un modèle simplifié de tail-sitter MAV est fourni. Nous concluons ce chapitre en mettant en relation les questions de modélisation pour la conception de contrôleurs basés sur un modèle et l'intérêt des approches de contrôle sans modèle.

Section 7.3 présente les algorithmes de contrôle sans modèle ainsi que certains travaux antérieurs sur l'estimation dynamique en ligne à des fins de contrôle. Ainsi, nous présentons trois expériences illustratives afin de montrer à la fois les principes et les propriétés potentielles d'un tel contrôleur.

Section 7.4 présente l'architecture MFC proposée pour les tail-sitter MAVs. Les résultats des vols de simulation sont évalués ainsi que les propriétés de chaque bloc de contrôle dans l'architecture MFC. Une analyse comparative est effectuée en simulation afin de mettre en évidence les avantages et les inconvénients des approches de contrôle basées sur un modèle ou sans modèle. Pour cette étude comparative, le LQR a été conçu selon le modèle dynamique du tail-sitter MAV décrit au chapitre 2.

Section 7.5 valide les algorithmes MFC dans des conditions de vol réelles. La stabilisation de l'attitude fournie par les algorithmes MFC est présentée dans des conditions de vol intérieures et extérieures. Enfin, la **Section 7.6** conclut ce mémoire de thèse et introduit des orientations pour les travaux futurs.

7.2 État de l'art

Cette section résume l'état de l'art concernant les approches méthodologiques sur la modélisation et le contrôle des différentes phases de vol des HMAVs. La grande majorité des études portant sur la modélisation de la dynamique des HMAVs est présentée. En outre, le développement d'architectures de contrôle et la conception de lois de commande sont abordés, pour l'ensemble du domaine de vol des HMAVs. Nous présentons également l'apport théorique et pratique des méthodes de contrôle sur les performances de vol des HMAVs, avec un accent particulier sur les tail-sitter MAVs.

7.2.1 Revue de la littérature sur la modélisation

Les équations du mouvement relatives à la dynamique des tail-sitter MAVs sont présentées dans le Chapite 2. Cette section met en évidence le fait que la précision de ces équations et leur fiabilité pour représenter la dynamique réelle des tail-sitter MAVs dépendent de l'identification de leurs coefficients. Le point critique, qui a été souligné par divers travaux dans la littérature, concerne l'approche difficile et longue lors de l'identification des coefficients aérodynamiques pour l'ensemble de l'enveloppe de vol.

En effet, le large domaine de vol des tail-sitter MAVs, et leurs conditions de vol inhabituelles à des angles d'attaque élevés, ont introduit quelques défis pour la communauté aérodynamique. Les questions les plus sensibles sont liées aux défis de l'écoulement à faible nombre de Reynolds, aux interactions entre l'hélice et l'aile, et à la variation rapide des forces et moments aérodynamiques pendant les phases de vol de transition. Les écoulements à faible nombre de Reynolds associés aux MAV ont tendance à être moins efficaces que ceux des grands aéronefs. De plus, dans le régime critique où volent les MAV, il est difficile de prévoir si la couche limite sera laminaire ou turbulente (Moschetta, 2014), ce qui augmente le niveau de complexité dans l'identification des coefficients aérodynamiques.

Une méthode d'identification des coefficients aérodynamiques est liée à l'analyse numérique, telle que le CFD. Cependant, la revue de la littérature dans le domaine des tail-sitter MAVs présente peu de travaux existants basés sur cette approche (Ang u. a., 2014) (Carrión u. a., 2017). En vue d'analyser les différents régimes de vol, la CFD a ses avantages et ses inconvénients, comme le fait remarquer (Frink u. a., 2017) : ès huit ans de collaboration entre un ensemble international de spécialistes de l'aérodynamique expérimentale et de la simulation de vol, la conclusion était que, bien que la méthodologie CFD actuelle puisse facilement prédire le comportement S&C (stabilité et contrôle) des avions volant dans des régions linéaires d'une enveloppe de vol, il est encore extrêmement difficile de saisir de manière adéquate les caractéristiques S&C statiques et dynamiques associées à des écoulements hautement non linéaires.

Les campagnes en soufflerie sont probablement le moyen le plus précis et le plus fiable pour identifier les coefficients aérodynamiques. Cependant, cette approche expérimentale nécessite, pour chaque domaine de vol, les informations de l'air ambiant, les valeurs des entrées de commande et les mesures des forces et moments aérodynamiques ($\boldsymbol{F_b}$, $\boldsymbol{M_b}$) agissant dans le système (voir figure 7.13). Dans une telle configuration, différents composants sont nécessaires, parmi lesquels on peut citer :

1. L'utilisateur afin de gérer l'expérience, les différents calibrages et les données acquises;

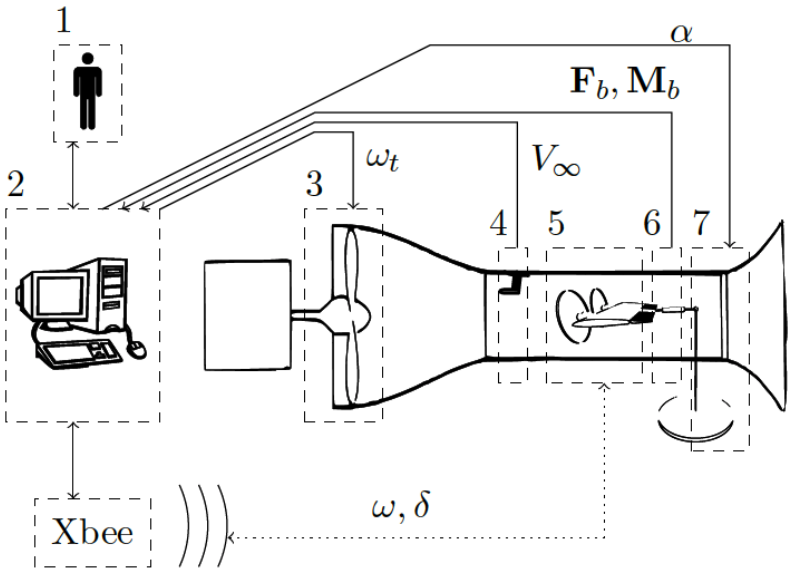

Figure 7.13: Campagne de soufflerie basse vitesse proposée par (Lustosa, 2017, p. 45).

2. Un système informatique pour synchroniser les différentes mesures, enregistrer les données et envoyer des commandes à la soufflerie ou au MAV. Par exemple, envoyer des modifications à la rotation de l'hélice de la soufflerie (ω_t) ou envoyer de nouvelles valeurs aux actionneurs du MAV (ω, δ);

3. Soufflerie à basse vitesse afin de faire correspondre les vitesses de vol MAV, avec des flux d'air suffisamment stables. Par basse vitesse, on entend le flux d'air inférieur à 100 m/s, pour lequel la condition d'incompressibilité du flux est respectée;

4. Capteur Pitot tube afin de mesurer la vitesse d'écoulement (V_∞) dans la section d'essai de la soufflerie;

5. MAV modèle adapté à la campagne de soufflerie avec une alimentation électrique externe ou propre;

6. Balance à six composantes afin de mesurer, avec précision et fiabilité, les trois forces (portance, force latérale et traînée) et les trois moments (roulis, tangage et lacet) du MAV;

7. Un bras mécanique pour fixer le MAV et l'orienter dans différentes positions. Ce bras mécanique définit les angles du nez du MAV par rapport au flux d'air (α, β);

Une analyse complète de la dynamique d'un quadrirotor tail-sitter MAV a été présentée par (Lyu u. a., 2018b) par le biais d'une campagne en soufflerie. Afin de comprendre le comportement des forces et des moments aérodynamiques dans l'ensemble du domaine de vol, les auteurs ont proposé d'étudier différents points de fonctionnement, pour lesquels divers angles d'attaque et vitesses de vent ont été définis. La figure 7.14 montre la campagne en soufflerie avec les capteurs et le mécanisme de rotation utilisés pour placer le tail-sitter MAV dans différentes orientations. Les coefficients aérodynamiques indiqués dans la figure 7.15 ont été identifiés pour différentes valeurs de vitesse du vent variant de 2,9 m/s à 18,9 m/s. La gamme complète des angles d'attaque a été évaluée.

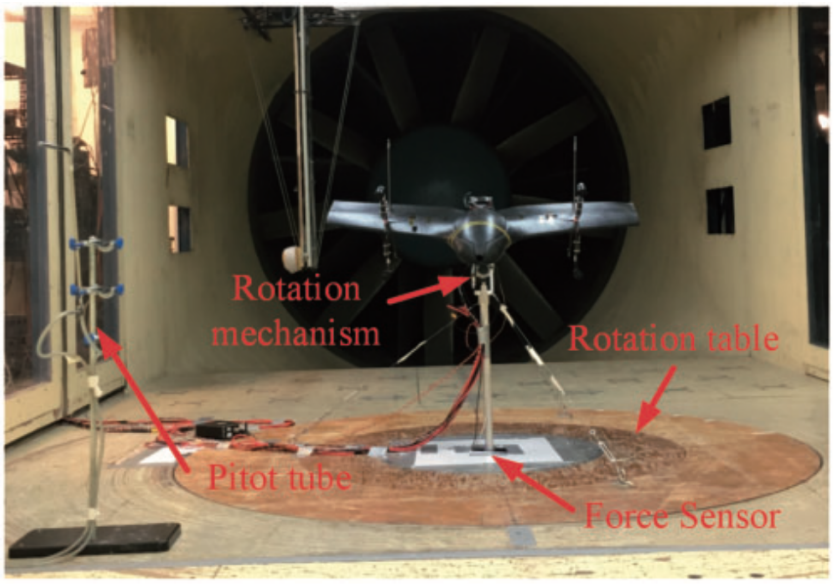

Figure 7.14: Essai en soufflerie d'un quadrirotor tail-sitter MAV sans hélices (Lyu u. a., 2018b, p. 310).

Les auteurs ont interpolés les variations des coefficients de portance et de traînée en fonction de l'angle d'attaque sans la contribution du système de propulsion. Par conséquent, l'effet de l'interaction entre l'hélice et l'aile a été négligé. Une approche similaire est employée dans (VanderMey, 2011) (Lustosa u. a., 2014), en négligeant les forces et les moments aérodynamiques créés par l'interaction entre le souffle de l'hélice et l'aile. En effet, du point de vue de la modélisation HMAV pour la synthèse des lois de contrôle, l'interaction entre l'hélice et l'aile est souvent négligée ou simplifiée. Cependant, les auteurs dans (Stone, 2004) ont modélisé un tail-sitter MAV en utilisant un modèle non linéaire de 6-DoF en tenant compte de cette interaction aérodynamique. Les auteurs ont mentionné une complexité particulière pour la modélisation des non-linéarités aérodynamiques due au changement des forces générées par l'hélice par rapport à celles dues à la pression dynamique du flux d'air. Ce changement se produit lorsque le MAV passe du vol stationnaire à basse vitesse (les forces de souffle de l'hélice et de l'hélice dominent) au vol en croisière à haute vitesse (la pression dynamique du flux d'air domine).

Les effets aérodynamiques sur le tail-sitter MAV sont directement associés à l'écoulement de l'air environnant, qui est affecté par l'écoulement induit par les hélices ainsi que par la perturbation de cet écoulement due à la fois au mouvement du tail-sitter MAV et aux perturbations dues au vent. Afin de déterminer la vitesse de sillage de l'hélice et ses effets dans l'aile, (Escareno u. a., 2007) a proposé un modèle basé sur la théorie de Froude (Chattot, 2014), avec quelques hypothèses. La force normale de l'hélice a été négligée, l'angle d'attaque du sillage est supposé être faible, les surfaces aérodynamiques du tail-sitter MAV sont entièrement immergées dans le sillage de l'hélice, la force de traînée est supposée faible par rapport aux forces de poussée et de portance en vol stationnaire. En outre, la force de traînée devrait être faible par rapport à la force de portance en vol en croisière. Pendant les phases de vol de transition, l'angle d'attaque du sillage et la force de traînée doivent être modélisés plus précisément afin de prévoir leur effet réaliste sur la dynamique du tail-sitter MAV. Comme l'ont fait valoir les auteurs, il est important de bien considérer ces forces car elles sont fondamentalement affectées par le mouvement du véhicule et modifient donc sa propre dynamique. L'auteur dans (Pucci, 2013) utilise une ap-

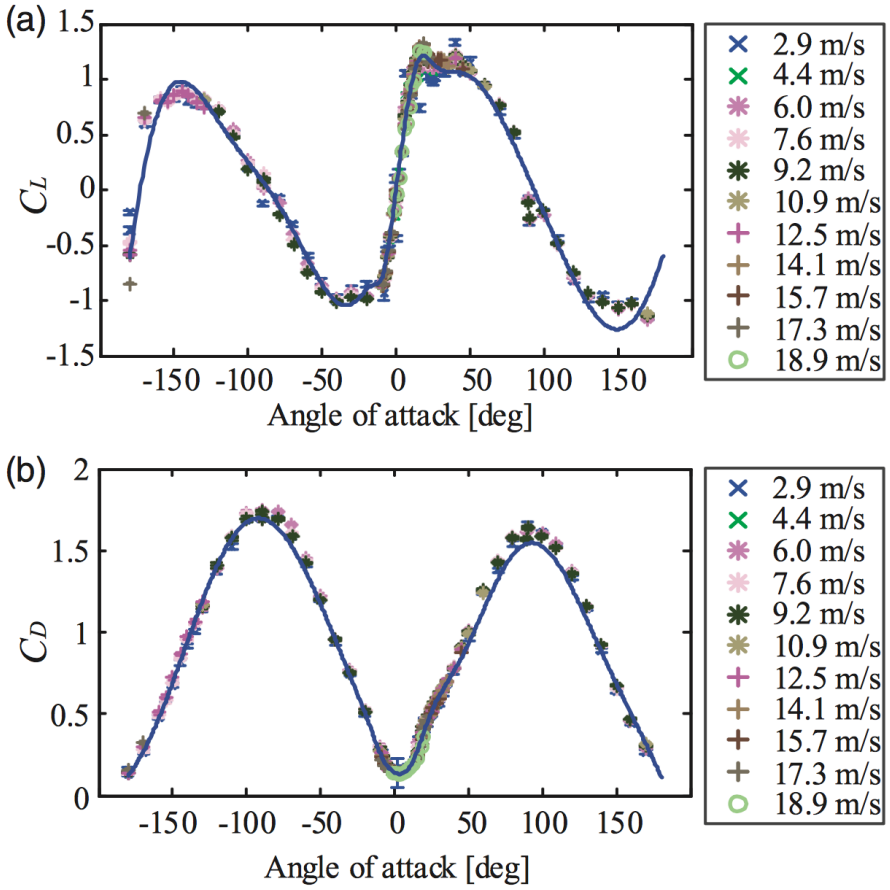

Figure 7.15: Coefficients de portance et de traînée identifiés en soufflerie (Lyu u. a., 2018b, p. 311).

proche différente avec un ensemble de fonctions algébriques pour déterminer approximativement les caractéristiques aérodynamiques expérimentales dans des équations analytiques. Les données expérimentales utilisées par l'auteur sont disponibles dans (Davis u. a., 2004) et correspondent à une aile plate de l'avion NACA 0021 avec des nombres de Mach et Reynolds égaux à ($M \approx 0.3$, $Re \approx 160.10^3$). La figure 7.16 montre les équations analytiques obtenues en fonction de l'angle d'attaque. Ces équations ont été utilisées pour développer un simulateur de vol générique afin de représenter la dynamique d'un véhicule aérien capable d'effectuer des vols de transition.

Dans le domaine des mesures PIV (Vélocimétrie par Images de Particules), (Kubo und Suzuki, 2012) a proposé l'analyse du flux d'air autour des volets d'un prototype de tail-sitter MAV à des angles d'attaque élevés. Dans cette analyse, le problème de l'efficacité du contrôle a été illustré à 60° d'angle d'attaque, ce qui montre les limites d'un tel système. A 60° d'angle d'attaque, les volets ne produisaient pas un moment de tangage suffisant pour assurer un vol de transition stable. Les auteurs ont invoqué deux options pour améliorer ce moment aérodynamique, telles que l'utilisation d'une hélice à pas variable ou d'un mécanisme supplémentaire de contrôle du pas cyclique, ce qui compliquerait probablement l'identification et le contrôle d'un tel nouveau système. Pour conclure cette revue de la littérature sur la modélisation et l'identification des tail-sitter MAVs, nous présentons un travail plus complet sur la modélisation des effets aérodynamiques en tenant compte de l'interaction hélice et aile (Lustosa, 2017).

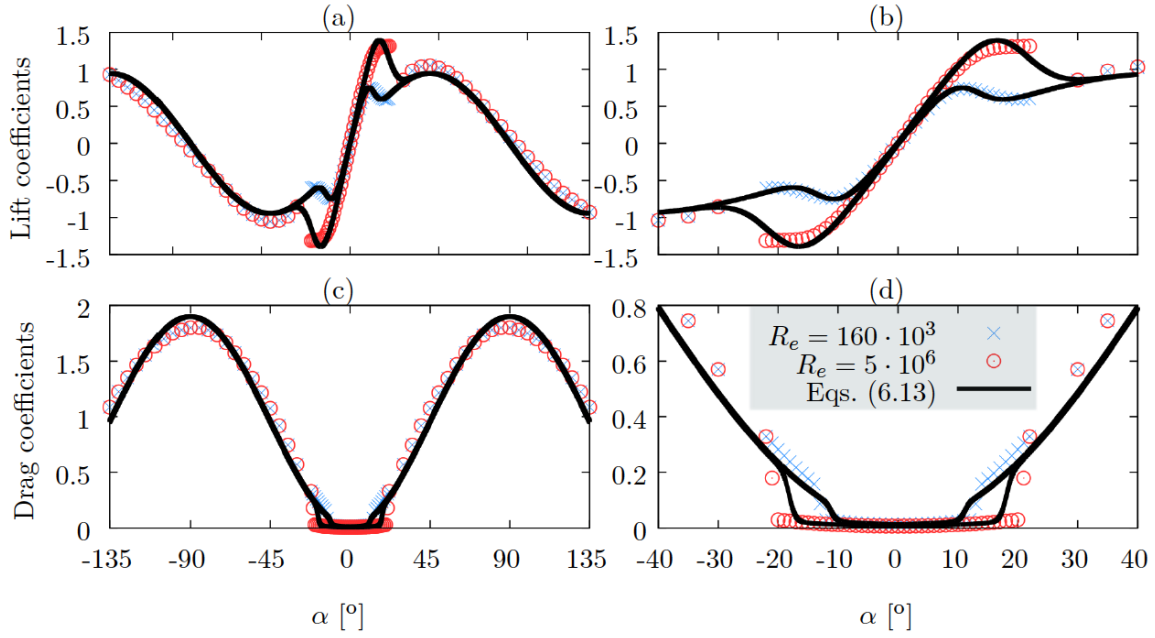

Figure 7.16: Coefficients aérodynamiques obtenus par (Pucci, 2013, p. 62).

A partir d'une campagne en soufflerie, l'auteur a analysé les différentes forces et moments du système, pour différentes valeurs d'angles d'attaque, d'angles de glissement latéral, de vitesses du vent, de rotations rotor-hélice et de déflexions des volets. En outre, un modèle analytique a été développé, décrivant, aussi précisément que possible, la dynamique du tail-sitter MAV en fonction des données de la soufflerie. Ce modèle sera détaillé dans la section suivante, avec des modifications mineures, et sera utilisé dans ce travail à des fins de simulation de vol.

7.2.2 Revue de la littérature sur la commande

La conception de lois de pilotage pour les HMAV a été et continue d'être un domaine de recherche très actif en raison de leur large domaine de vol, qui permet l'exécution de missions de vol complexes. D'une part, la combinaison de l'efficacité énergétique et des capacités de vol manœuvrables dans une seule configuration MAV nous a permis de franchir les limites de vol des drones à voilures tournantes et à voilure fixe. D'autre part, la conception d'algorithmes de contrôle pour stabiliser les différents domaines de vol des HMAVs, pose des défis intéressants pour la communauté des automaticiens. En fait, les problèmes ouverts concernant la modélisation des HMAV ont introduit certains obstacles à la conception et aux performances des contrôleurs classiques basés sur des modèles.

Comme nous l'avons vu dans la section précédente, la dynamique des HMAV et leurs nonlinéarités sont difficiles à modéliser, en particulier en ce qui concerne les phénomènes aérodynamiques. Ces défis ont motivé le développement de nouvelles stratégies de contrôle et de nouvelles architectures de contrôle, qui seront présentées dans cette revue de la littérature. Plusieurs domaines de méthodologies de contrôle appliquées aux HMAVs, les avantages et les inconvénients de chacune d'entre elles seront ainsi examinés en donnant d'avantage d'importance aux techniques de contrôle conçues pour les configurations des tail-sitter MAVs.

▶ Architecture de commande de vol

Du point de vue du contrôle, afin de pouvoir effectuer des missions de manière plus ou moins autonome avec les tail-sitter MAVs, trois points principaux doivent être abordés, à savoir, la stabilisation de son attitude en ce qui concerne le contrôle de son orientation, le contrôle de ses vitesses et le suivi des trajectoires ou le contrôle des positions. À travers le schéma fonctionnel présenté dans la figure 7.17, nous illustrons l'architecture de contrôle hiérarchique généralement utilisée dans le domaine aérospatial et également appliquée aux tail-sitter MAVs. Cette approche en cascade est une méthode de contrôle qui combine différentes boucles de rétroaction, où la sortie d'un bloc de contrôle ajuste le point de consigne du bloc suivant.

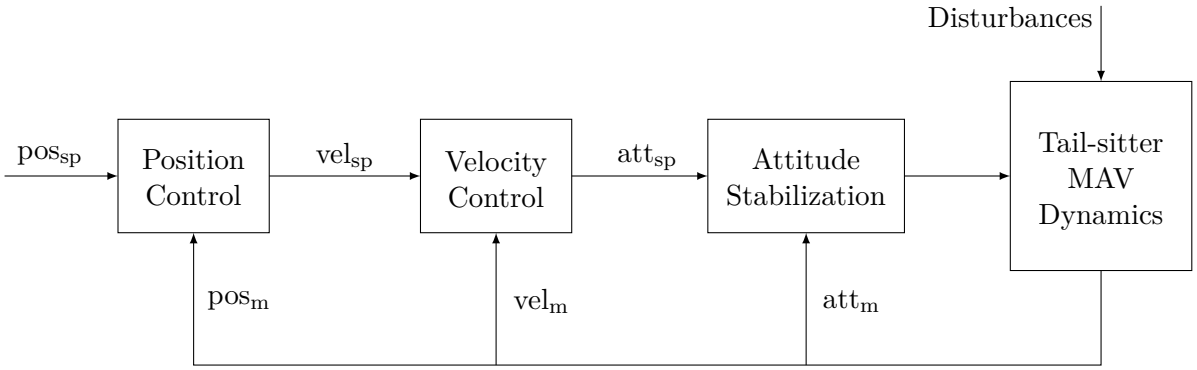

Figure 7.17: Architecture de contrôle hiérarchique pour les tail-sitter MAVs.

Le bloc de contrôle de position envoie les vitesses souhaitées (vel_{sp}) au bloc de contrôle de vitesse qui calcule la valeur de poussée nécessaire ainsi que les points de consigne (att_{sp}) pour la boucle de stabilisation d'attitude. Différents travaux dans la littérature ont adopté cette architecture de contrôle afin de concevoir des pilotes automatiques. Ainsi, diverses lois de contrôle ont été conçues pour répondre à la problématique de chaque bloc de contrôle. Par exemple, les défis du contrôle de la position et de la vitesse sont liés à leur robustesse contre les perturbations externes telles que les rafales de vent. Les exigences communes pour le contrôle de l'attitude des tail-sitter MAVs sont la capacité de stabiliser leur dynamique non linéaire au cours de leurs différentes phases de vol. En outre, l'algorithme de contrôle doit être capable d'adapter ses commandes aux variations de la dynamique du système, qui sont connues pour être différentes selon le domaine de vol du tail-sitter MAV.

▶ Approches de contrôle pour les tail-sitter MAVs

Les approches de contrôle listées dans la figure 7.18 ont été appliquées sur les tail-sitter MAVs. Ces méthodes de contrôle peuvent être classés en fonction de leurs aspects linéaires ou non linéaires, basés sur des capacités adaptatives ou prédictives et en ce qui concerne leur méthodologie de conception, qui peut être séparée en méthodologies de contrôle basées sur un modèle ou sans modèle. La performance des algorithmes de contrôle basés sur des modèles est liée à la précision des modèles dynamiques. Dans la section 2.1, les différents défis et problèmes concernant la modélisation des tail-sitter MAVs ont été présentés. Par conséquent, la première question qui apparaît est : si la performance d'un contrôleur basé sur un modèle dépend de la précision d'un tel modèle, et que la modélisation des tail-sitter MAVs reste un défi long et complexe dans laquelle des hypothèses aérodynamiques sont utilisées pour décrire une représentation approximative de la dynamique du système qui est à peine cohérente avec sa dynamique de vol réelle,

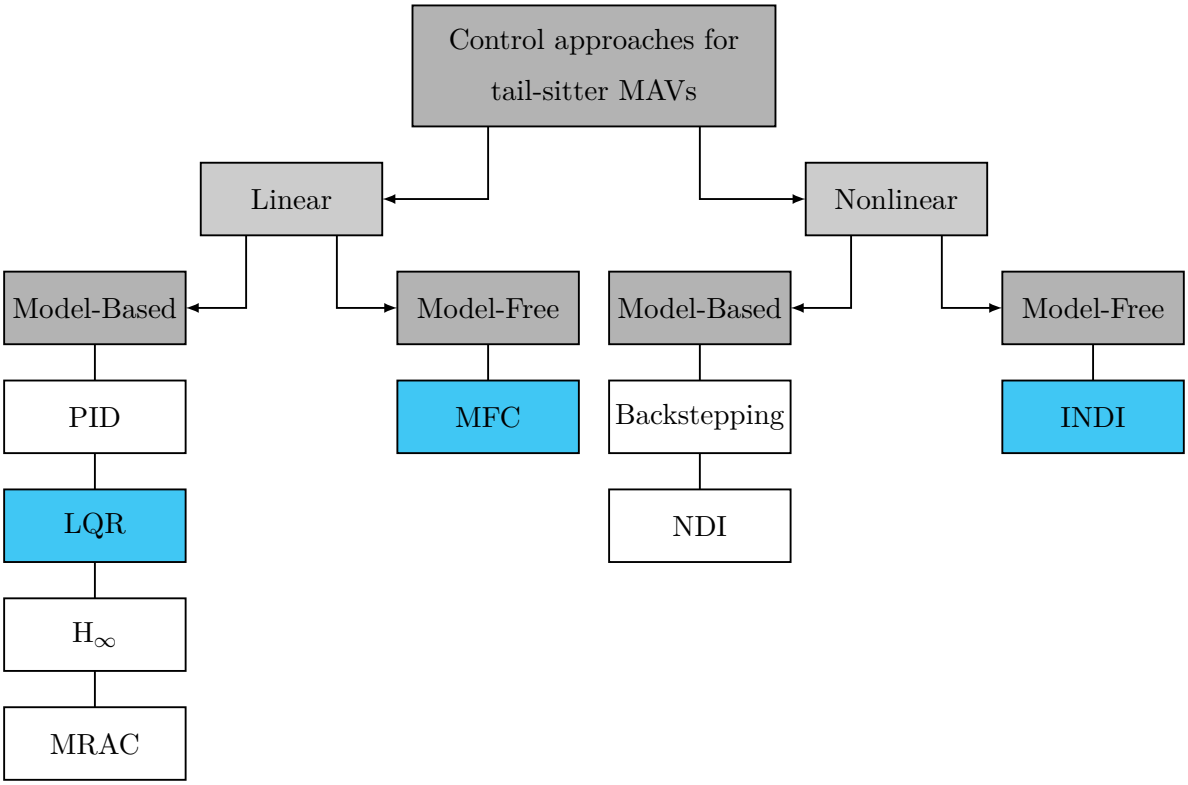

Figure 7.18: Les méthodes de contrôle conçues pour tail-sitter MAVs.

pourquoi concevoir des contrôleurs basés sur un modèle pour cette configuration de HMAV? La première réponse peut être liée au fait que les contrôleurs basés sur des modèles ont été étudiés et discutés par un grand nombre d'auteurs dans la littérature. Une diversité de méthodologies de conception de contrôle basées sur des modèles a été proposée, appliquée et validée sur différents systèmes avec des performances de contrôle efficaces pour des systèmes bien modélisés. En outre, la stabilité en boucle fermée des contrôleurs basés sur des modèles peut être facilement analysée, d'autant plus dans le cas des contrôleurs linéaires qui se sont appropriés des outils pour évaluer les pôles du système. Ces outils d'analyse ont certainement motivé l'utilisation d'une telle approche de contrôle. Cependant, la conception des contrôleurs linéaires nécessite le choix de points de fonctionnement sur lesquels la dynamique non linéaire sera linéarisée.

Cette linéarisation est généralement représentée par un état d'équilibre, comme un vol stable en palier, un vol stable en virage, un vol en montée stable et un roulis stable. Tous ces effets d'équilibre sont caractérisés par des accélérations linéaires et angulaires nulles. Cette simplification facilite le processus de conception des contrôleurs basés sur des modèles linéaires, mais néglige la dynamique non linéaire lors de la conception du contrôleur. Par exemple, dans le cas des tail-sitter MAVs l'itération de l'aile avec l'hélice et d'autres dynamiques non linéaires couplées seraient négligées car elles ne peuvent pas être correctement représentées par des équations linéarisées. Des contrôleurs non linéaires ont également été conçus et appliqués sur les tail-sitter MAVs. Ces contrôleurs ont de multiples points d'équilibre isolés et couvrent la dynamique d'un domaine de vol plus large par rapport aux lois de contrôle linéaires. La dernière catégorie de contrôleurs présentée dans cette revue de littérature concerne les approches de contrôle sans modèle. Leur particularité s'explique par le fait qu'ils peuvent être conçus avec peu de connaissances préalables du système. À cette fin, des algorithmes d'estimation ou des techniques de

mesure sont utilisés dans la boucle de contrôle pour obtenir des informations sur la dynamique contrôlée.

Contrôleurs PID: Les algorithmes classiques de contrôle linéaire ont été conçus pour les MAV en utilisant les gains PID (Bilodeau und Wong, 2010) (Hochstenbach u. a., 2015) (Verling u. a., 2016) (Fuhrer u. a., 2019) (Liu u. a., 2019) (Ramirez und Nahon, 2020). Bien que simple à régler sans la connaissance du système contrôlé (Oosedo u. a., 2013), les gains PID peuvent être conçus selon une technique appelée Root Locus, dans laquelle les pôles et les zéros du système en boucle fermée sont analysés en fonction des gains du contrôleur. La technique Root Locus consiste à tracer les trajectoires des pôles en boucle fermée dans le plan complexe en fonction des variations de gain du contrôleur. Par conséquent, le gain du contrôleur peut être défini afin de répondre aux exigences de performance, telles que le temps de réponse, le dépassement, etc. Comme les pôles en boucle fermée dépendent du modèle du système, si le modèle est mal défini, le gain du contrôleur le sera aussi. par conséquent, les contrôleurs PID sont connus pour leur manque de robustesse contre les perturbations dues au vent et la variation des paramètres internes.

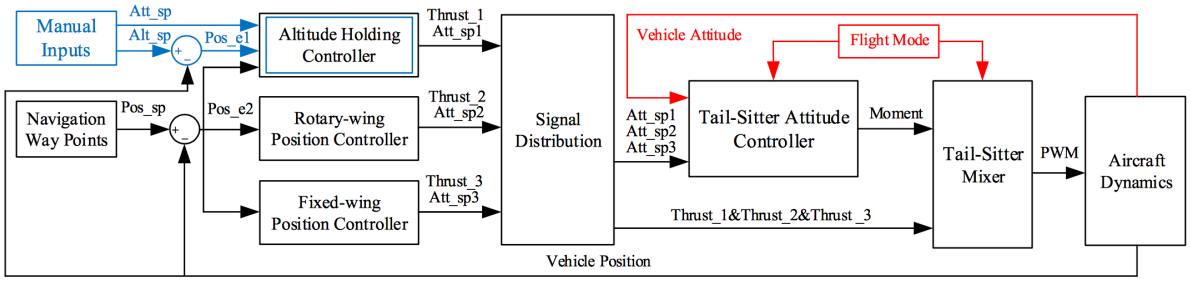

Figure 7.19: Architecture de contrôle hiérarchique proposée par (Lyu u. a., 2017b).

Une approche de contrôle hiérarchique a été mise au point par (Lyu u. a., 2017b) pour contrôler la position et l'attitude d'un tail-sitter MAV. La figure 7.19 présente le schéma fonctionnel d'une telle architecture de contrôle. Son bloc de contrôle de maintien d'altitude est conçu avec des gains PID combiné avec un terme de feedforward. Le contrôle de l'attitude est subdivisé en deux boucles de rétroaction: la boucle interne qui contrôle les taux angulaires également avec un contrôleur PID et la boucle extérieure, avec un simple gain proportionnel, pour assurer la stabilisation des angles. Cette architecture de contrôle hiérarchique a été validée lors de vols expérimentaux en utilisant une stratégie de commutation pour permuter les gains PID en fonction de la phase de vol en cours. La stratégie de permutation est représentée par le bloc rouge dans la figure. De plus, une stratégie de contrôle de position a été utilisée pendant les vols stationnaires et une autre pendant les vols en croisière. Les valeurs des points de consigne peuvent être envoyées manuellement au tail-sitter (bloc bleu) via un émetteur RC ou de manière autonome via le bloc Navigation Way Points.

L'approche LQR: Une deuxième raison d'appliquer des contrôleurs basés sur des modèles sur les tail-sitter MAVs peut être justifiée au moyen de la théorie du contrôle optimal. Par exemple, le LQR qui peut être optimisés selon le modèle de système contrôlé (Stone u. a., 2008) (Forshaw und Lappas, 2011) (Lustosa u. a., 2015). Les auteurs dans (Lustosa u. a., 2015) ont conçu et ont appliqué les gains LQR sur un tail-sitter MAV préalablement modélisé via la $\Phi-$theory. Cependant, les performances des contrôleurs basés sur un modèle diffèrent principalement par la fidélité avec laquelle le système est modélisé et la précision des paramètres du modèle identifiés. Par conséquent, les techniques de contrôle basées sur un modèle ne semblent pas être optimales

pour les tail-sitter MAVs ni facilement transposables pour une nouvelle configuration HMAV, car cela nécessiterait une nouvelle identification coûteuse et longue. Le LQR est une approche de contrôle linéaire qui, pour des applications sur des systèmes non linéaires, fait appel à des techniques de linéarisation. Par conséquent, l'ensemble de la dynamique de vol non-linéaire des tail-sitter MAVs doit être représenté par un ensemble de modèles linéaires et pour chaque modèle linéaire une matrix de gains LQR peut être conçu. Une approche commune pour gérer ces different gains LQRs dans l'ensemble du domaine de vol du tail-sitter MAVs est la programmation des gains. Les auteurs dans (Lustosa, 2017) ont proposé la technique de programmation des gains définie dans le schéma fonctionnel de la figure 7.20.

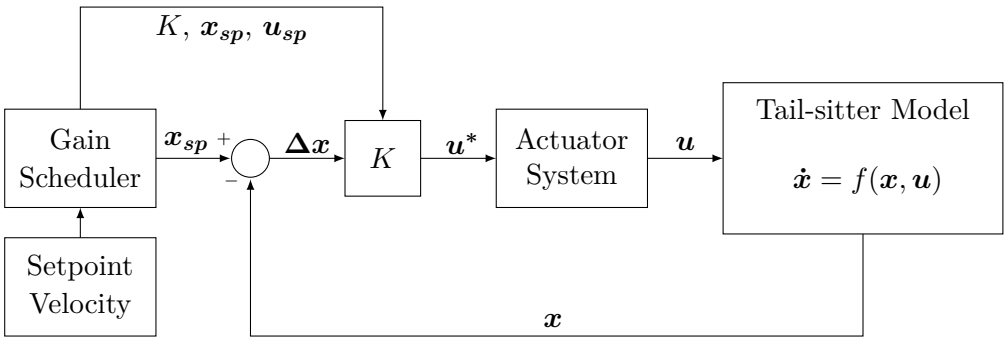

Figure 7.20: Schéma de programmation des gains LQRs proposé par (Lustosa, 2017, p. 80).

Cette approche de contrôle LQR permet l'optimisation du gain en boucle fermée K afin de répondre à la fois aux exigences de vitesse et de contrôle d'attitude définies par l'utilisateur. Par des simulations de vol et des vols expérimentaux, l'auteur souligne et prouve qu'une seule matrice de gains LQR n'est pas suffisante pour stabiliser le tail-sitter MAV dans toute son enveloppe de vol, ce qui justifie l'utilisation de méthodes de programmation des gains. La figure 2.14 montre les résultats des essais en vol obtenus avec un tel contrôleur. La région critique illustrée par l'auteur dans la zone ombrée correspond au domaine de vol en transition ($\theta \approx 45°$). Dans cette région critique, les gains LQR assurent la stabilité du système, mais il est difficile de conclure sur les performances LQR car les points de consigne ne sont pas présentés.

Synthèse de commande H_∞: Les propriétés de robustesse du contrôleur H_∞ ont été largement évaluées dans une diversité de systèmes avec des incertitudes paramétriques. Le principe de ce contrôleur est de garantir l'existence d'un gain en boucle fermée qui rend la norme H_∞ plus petite qu'une valeur prescrite, pour cela le modèle du système doit être à la fois contrôlable et observable (Kalman, 2010). En se basant sur la synthèse de contrôle H_∞ combinée à une approche de programmation des gains, les auteurs dans (Mix u. a., 2004) (Dickeson u. a., 2005) (Dickeson u. a., 2006) (Dickeson u. a., 2007) ont proposé la stabilisation d'un HMAV sur toute son enveloppe de vol.

Le contrôleur a été conçu autour de deux points d'équilibre distincts, c'est-à-dire un autour du domaine de vol en vol stationnaire et un autre autour du domaine de vol en croisière. La stabilisation pendant le vol de transition est assurée par la technique de programmation des gains, qui utilise le gain approprié en fonction de la phase de vol en cours. La performance de ce contrôleur a été analysée dans le domaine fréquentiel et temporel en simulation. Les paramètres du contrôleur ont été définis selon des modèles linéaires et simplifiés. Ainsi, malgré ses propriétés robustes, la performance de contrôle peut être différente lors des essais en vol. Les auteurs dans (Lyu u. a., 2018a) ont analysé les propriétés de rejet des perturbations du contrôleur

H_∞ pendant le suivi des trajectoires dans la phase de vol stationnaire (voir figure 7.21). À notre connaissance, cette approche de contrôle doit encore être évaluée sur des vols expérimentaux de transition avec des tail-sitter MAVs.

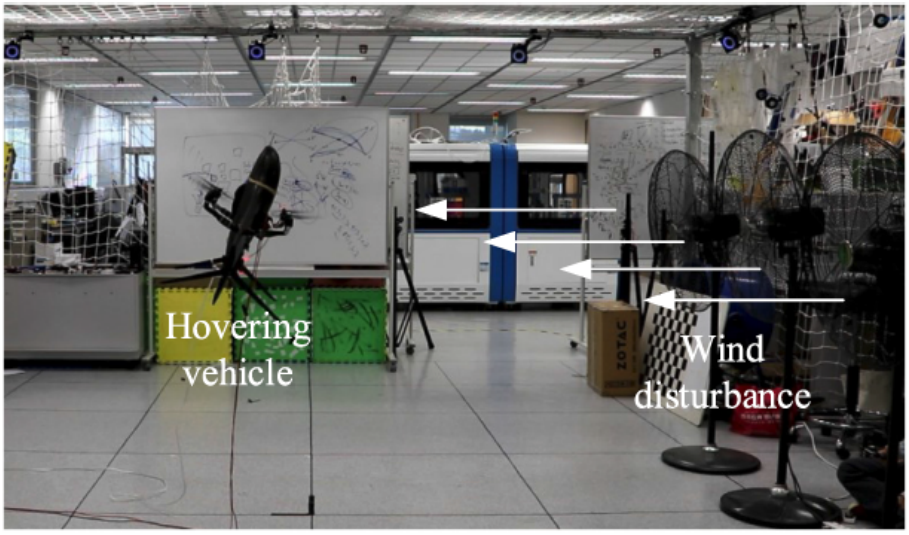

Figure 7.21: L'expérience de vol à l'intérieur proposée par (Lyu u. a., 2018a).

Contrôleurs non linéaires: Les recherches théoriques sur les contrôleurs à rétroaction non linéaire ont permis de développer un système en boucle fermée pour les MAVs (Pucci u. a., 2013) proposant une solution de contrôle étendue à un ensemble plus large de modèles aérodynamiques génériques avec leurs non-linéarités (Pucci u. a., 2015). En outre, diverses techniques de contrôle non linéaire basées sur les concepts de stabilité de Lyapunov ont été conçues pour les HMAVs (Flores u. a., 2018a) (Wang u. a., 2018). Dans (Flores u. a., 2018b), les auteurs ont proposé une approche de contrôle afin de stabiliser le tail-sitter MAV et sa dynamique non linéaire pendant les vols de transition.

Le contrôleur a été conçu sur la base de fonctions de saturation qui ont été réglées selon les fonctions de Lyapunov en assurant la stabilité asymptotique du système en boucle fermée. Dans (Kuang u. a., 2017), la dynamique d'un tail-sitter MAV a été stabilisée pendant les phases de vol stationnaire et en croisière. La différence entre la dynamique du vol stationnaire et celle du vol en croisière a été mise en évidence en ce qui concerne le changement aérodynamique en fonction de la vitesse et de l'angle d'attaque. Afin de contrôler ces phases de vol distinctes et leurs dynamiques respectives, les auteurs ont proposé une stratégie de commande de commutation avec une méthodologie d'hystérésis adaptée pour ce cas précis afin d'empêcher les oscillations au point de commutation.

Malgré la démonstration d'une dynamique non linéaire stabilisée lors des essais en vol, le contrôleur non linéaire proposé pourrait être sensible aux conditions de vol venteuses. En particulier, lors du suivi des trajectoires lorsque le tail-sitter MAV doit maintenir sa position en présence de vents. Dans un tel cas, le tail-sitter peut avoir besoin de maintenir son vol entre le vol stationnaire et le vol en croisière à proximité du point de commutation, ce qui peut entraîner une dynamique d'oscillation ou même des vols instables en raison des discontinuités et des vols de transition non fluides générés par la stratégie de commutation. Des techniques de recul qui sont des approches de contrôle non linéaires basées sur la fonction candidate de Lyapunov aug-

mentée ont également été appliquées sur le tail-sitter MAVs (Argyle, 2016). Cette stratégie de contrôle a une structure récursive dans laquelle le système contrôlé est construit à partir de sous-systèmes. Le concepteur de la commande peut commencer le processus de conception à un sous-système stable connu et reculer les nouveaux contrôleurs qui stabilisent progressivement les autres sous-systèmes jusqu'à l'ensemble du système. Pour cette raison, ce processus de contrôle est connu sous le nom de "backstepping". On peut citer, entre autres, les contrôleurs non linéaires suivants appliqués sur le tail-sitter MAVs (Miyazaki und Tsubakino, 2017) (Wang u. a., 2017).

Méthodologies de programmation des gains: Les méthodes d'ordonnancement des gains peuvent être conçues pour stabiliser les tail-sitter MAVs en utilisant différents algorithmes de contrôle, tels que les approches de contrôle linéaire (Kita u. a., 2012) et non linéaire (Silva u. a., 2018). Par conséquent, les techniques de programmation des gains permettent une compréhension facile et une mise en œuvre simple des gains de contrôle afin de couvrir l'ensemble du domaine de vol des HMAV. Toutefois, le principal inconvénient de cette méthode de contrôle, que l'on trouve dans la littérature (Saeed u. a., 2018), est le coût de calcul élevé pour les opérations en temps réel. Un contrôleur de vol unifié capable de voler dans différentes conditions de vol a été proposé par (Hartmann u. a., 2017). D'après des campagnes en soufflerie statique, des contrôleurs à gain programmé basés sur des modèles ont été conçus et mis en œuvre pour un ensemble étendu de points de compensation couvrant la totalité du domaine de vol HMAV.

Le vol de transition est effectué en changeant les états de compensation par une approche de table de gains prédéfinis. Comme pour les travaux précédents, un contrôleur d'attitude basé sur des algorithmes de contrôle optimal a été proposé par (Ritz und D'Andrea, 2017). Différentes solutions de contrôle optimal pour un ensemble d'erreurs d'attitude ont été précalculées et stockées dans une table de gains prédéfinis. En fonction des conditions de vol actuelles et pour chaque mise à jour du système de pilotage automatique, les paramètres de contrôle souhaités sont obtenus en lisant les valeurs prédéfinies dans le tableau. Des vols expérimentaux ont démontré la capacité d'un tel contrôleur à récupérer et à stabiliser les HMAV à partir d'une large gamme d'erreurs d'attitude. Les auteurs du (Ritz und D'Andrea, 2017) ont proposé un contrôleur global pour le suivi des trajectoires nominales avec un tail-sitter MAV.

L'approche de contrôle est basée sur une architecture en cascade dans laquelle la boucle de contrôle extérieure – en charge du contrôle de la position et de la vitesse – calcule l'attitude souhaitée pour la boucle de contrôle intérieure. Elle utilise un algorithme embarqué pour estimer les coefficients aérodynamiques inconnus en vol selon des équations aérodynamiques simplifiées. Malgré la démonstration de vols stables, des erreurs d'attitude importantes peuvent être observées, ce qui pourrait également dégrader la précision du suivi de la trajectoire. Ces erreurs sont justifiées par l'utilisation de modèles imprécis dans la boucle de contrôle, en particulier les équations aérodynamiques simplifiées comme le soulignent les auteurs.

Contrôleurs prédictifs: Il existe un nombre relativement restreint d'ouvrages qui s'intéressent à la conception de contrôleurs prédictifs pour les anticouple MAVs. Malgré cela, nous pouvons mentionner les travaux suivants (Boyang u. a., 2018a) (Boyang u. a., 2018b) (Zhou u. a., 2019). Les auteurs de (Boyang u. a., 2018a) (Boyang u. a., 2018b) ont proposé une approche basée sur les algorithmes MPC pour traiter à la fois le suivi des positions et la stabilisation de l'attitude d'un tail-sitter MAV dans son domaine de vol en stationnaire. Toujours en phase de vol stationnaire, (Zhou u. a., 2019) a développé un SLMPC mettant l'accent sur sa capacité à rejeter les perturbations dues au vent pendant les vols expérimentaux. La raison de cette absence de

conception des MPC sur les tail-sitter MAVs peut s'expliquer par le fait que, les MPC sont basés sur des algorithmes d'optimisation qui nécessitent un modèle dynamique précis et des coûts de calcul élevés. En outre, les incertitudes du modèle dynamique rendent le problème très difficile à résoudre.

Approches de contrôle adaptatives: D'autres techniques de contrôle avec des termes adaptatifs ont été créées pour résoudre le problème de stabilisation des systèmes qui varient dans le temps. Les régulateurs adaptatifs peuvent être classés en trois catégories : méthodes adaptatives directes, indirectes et hybrides, qui dépendent de la manière dont les paramètres du régulateur sont réglés. Les méthodes directes comparent la sortie du système contrôlé à celle d'un modèle de référence, créant ainsi un signal d'erreur. En fonction de l'évolution de l'erreur, les paramètres pertinents du contrôleur sont adaptés afin de ramener cette erreur à zéro. La boucle de contrôle est mise à jour et modifiée en fonction des paramètres estimés du système qui sont utilisés pour déterminer le gain requis du contrôleur. Les méthodes hybrides reposent à la fois sur l'estimation des paramètres et sur les ajustements directs du gain du contrôleur.

Dans le domaine de la théorie du contrôle adaptatif, MRAC est l'algorithme le plus classique et le plus utilisé (Shekhar und Sharma, 2018). Le MRAC est composé de trois éléments : le modèle de référence, le contrôleur et un mécanisme de réglage pour adapter les paramètres du contrôleur, afin de faire correspondre la sortie du système contrôlé y_m avec la sortie du modèle de référence y_{sp} (voir figure 7.22). Le mécanisme d'ajustement peut être développé à partir de la règle du MIT (Jain und Nigam, 2013), de la théorie de Lyapunov (Ge u. a., 1999) (Chakrabarty und Bhattachary, 2016) et d'autres approches mathématiques, telles que les fonctions d'ajustement de covariance, etc. La technique du mécanisme d'ajustement proposée par (Chakrabarty und Bhattachary, 2016), basée sur les fonctions de Lyapunov, vise à suivre la sortie du système et ses états avec le modèle de référence. À cette fin, tous les états sont supposés être disponibles pour la mesure, ce qui n'est pas toujours le cas dans les applications pratiques de contrôle.

Selon la règle du MIT (Shekhar und Sharma, 2018), le mécanisme d'ajustement vise à minimiser l'erreur entre la sortie du système contrôlé et la sortie du modèle de référence via une fonction de coût qui actualise le gain du contrôleur (K). Ces paramètres sont modifiés dans le sens du gradient négatif de la fonction de coût. Nous notons que le modèle de référence joue un rôle important dans les performances de contrôle fournies par ce contrôleur adaptatif parce que la règle du MIT essaie de faire correspondre la sortie des systèmes contrôlés avec la sortie du

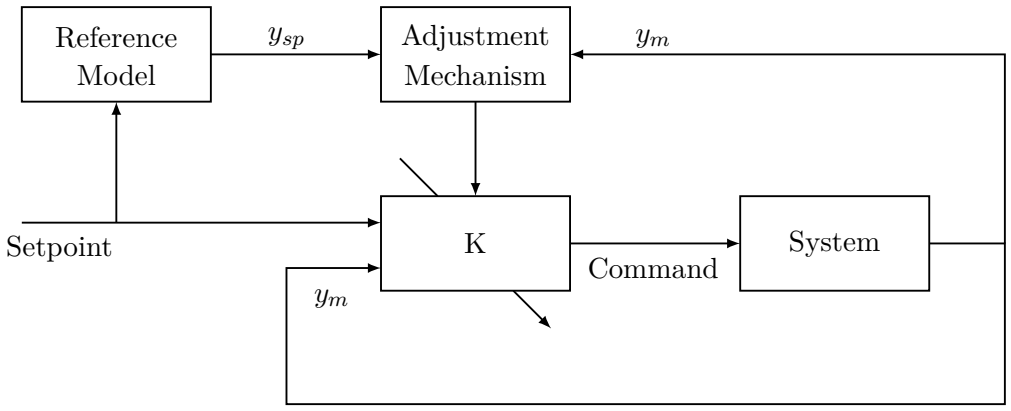

Figure 7.22: Schéma fonctionnel de la commande adaptative directe.

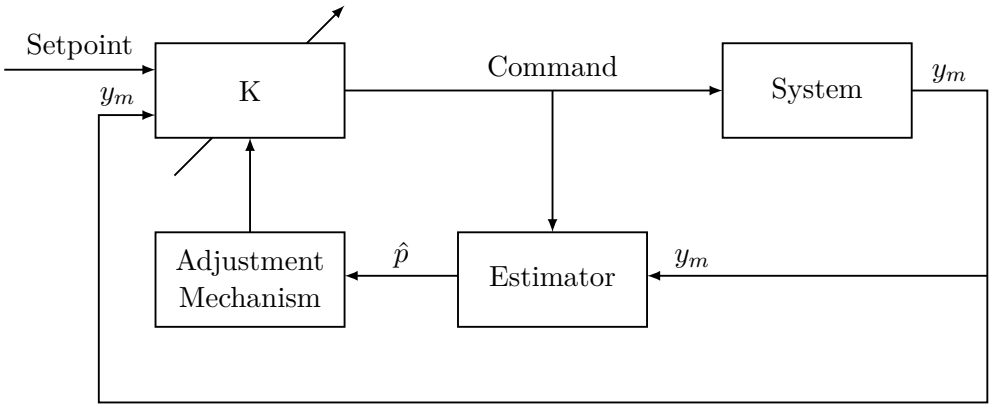

Figure 7.23: Schéma fonctionnel de la commande adaptative indirecte.

modèle de référence. Si ce modèle est mal modélisé, les performances de contrôle seront donc directement médiocres. En outre, la règle MIT est très sensible aux changements d'amplitude de l'entrée de référence. Le contrôleur adaptatif indirect divise le processus d'adaptation du gain du contrôleur en deux étapes. À la différence du contrôleur adaptatif direct qui met à jour continuellement le gain du contrôleur, la forme indirecte estime les paramètres du système afin de synthétiser le gain d'un contrôleur adapté à la situation actuelle. La performance en boucle fermée dépend directement de la fréquence d'adaptation qui doit suivre l'évolution de la dynamique du système. De la même manière, la fréquence de contrôle doit être compatible et synchronisée avec la mise à jour des paramètres estimés.

Pour l'estimation des paramètres en temps réel, les méthodes les plus couramment utilisées sont des dérivés de LMS, tels que NLMS, RLMS, et EKF. Ces méthodes permettent d'identifier des modèles linéaires qui sont représentés par un vecteur de paramètres, qui est défini par $\hat{p}$ dans la figure 7.23. L'EKF permet l'identification des paramètres des systèmes non linéaires en utilisant une linéarisation successive autour du point de fonctionnement dans lequel le paramètre sera identifié. Concernant les algorithmes d'adaptation qui mettent à jour le gain du contrôleur en fonction du vecteur estimé des paramètres $\hat{p}$, on pourrait envisager des méthodes plus complexes si ces méthodes sont suffisamment rapides pour des applications en temps réel. Les techniques de contrôle adaptatif qui tiennent compte des paramètres HMAV

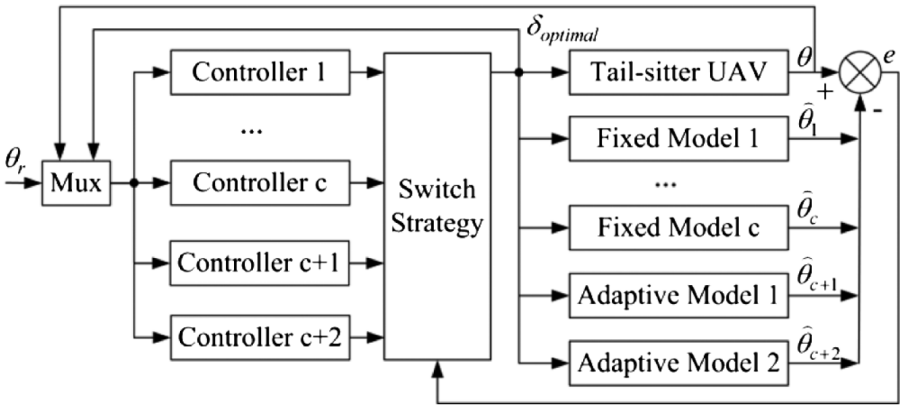

Figure 7.24: Architecture du contrôleur de vol MMAC proposée par (Zhang u. a., 2018).

variables dans le temps ont été développées par (Knoebel und McLain, 2008) (Jung und Shim, 2011). En outre, l'algorithme de contrôle peut s'adapter en permanence à l'évolution de la dynamique MAV lorsque le vol de transition est effectué. Les auteurs de (Zhang u. a., 2018) ont proposé un MMAC composé d'un ensemble de modèles multiples avec des sous-contrôleurs et un index de commutation. Le principe présenté dans la figure 7.24 est basé sur de multiples sous-modèles linéaires pour représenter la dynamique du tail-sitter MAV dans toute son enveloppe de vol. Les modèles linéaires cachent la dynamique non linéaire d'un tel système. Différentes architectures de contrôle adaptatif pour les tail-sitter MAVs peuvent être trouvées dans (Jung und Shim, 2011) (Jin u. a., 2015) (Zhong u. a., 2019). Toutefois, les performances de contrôle avec les méthodes de contrôle adaptatives peuvent encore être insuffisantes en ce qui concerne les modèles imprécis ou la dynamique non modélisée en raison des équations simplifiées utilisées dans le critère d'adaptation du gain du contrôleur.

INDI et MFC: pour conclure la revue de la littérature, nous présentons deux techniques de contrôle qui seront examinées plus en détail dans cette thèse et comparées entre elles par des essais en vol, à savoir les INDI et les MFC. Le contrôleur INDI, qui est une approche basée sur des capteurs, est moins dépendant du modèle et a été testé expérimentalement par des essais en vol avec des tail-sitter MAVs offrant d'excellentes performances contre les perturbations dues au vent. Cependant, ce contrôleur nécessite l'identification du système d'actionnement afin de concevoir ses paramètres de contrôle, tels que l'efficacité du contrôle de l'actionneur. Étant donné que l'efficacité des gouvernes aérodynamiques n'est pas constante pendant toute la durée du domaine de vol du tail-sitter MAV, par exemple en vol stationnaire ou en vol en croisière, une méthode de programmation des gains a été mise en œuvre pour adapter ces valeurs d'efficacité au domaine de vol respectif (Smeur u. a., 2019).

Par ailleurs, la méthodologie MFC proposée par (Fliess und Join, 2013) n'exige que peu de connaissances préalables du système contrôlé et aucune information sur ses paramètres n'est nécessaire pour concevoir le contrôleur. Le schéma fonctionnel présenté dans la figure 7.25 illustre le principe d'un tel contrôleur. Nous soulignons que le bloc estimateur ne modifie pas les gains de contrôle de rétroaction, contrairement aux méthodes de contrôle adaptatives directes et indirectes présentées ci-dessus. Le processus adaptatif MFC est réalisé par le bloc estimateur dans lequel l'estimation calculée $\hat{F}_y$ est directement affectée dans la commande en boucle fermée u. Sur la base d'un tel estimateur, il est possible de mettre en œuvre un contrôleur robuste et adaptatif qui assure la stabilité des systèmes à variation temporelle en estimant en temps réel leur dynamique à partir de mesures périodiques de y_m et u.

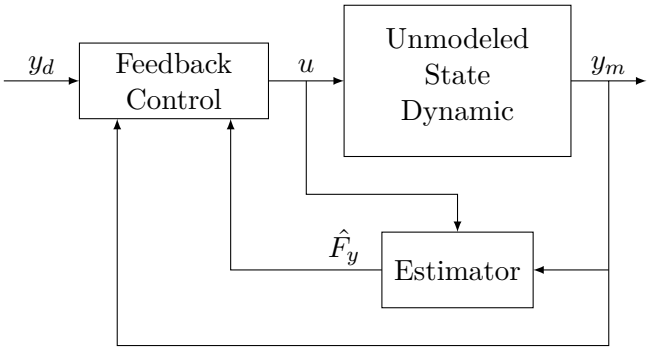

Figure 7.25: Schéma global de la commande sans modèle.

Un certain nombre de travaux dans la littérature ont abordé leurs défis avec l'approche MFC (Join u. a., 2017) (Rodriguez-Fortun u. a., 2013) (Bara u. a., 2018). De toute évidence, le dénominateur commun entre ces travaux est lié à la complexité de la modélisation de la dynamique du système. Les travaux proposés par (Menhour u. a., 2018) se sont concentrés sur le contrôle du mouvement longitudinal et latéral du véhicule, dont la définition de modèles mathématiques pour décrire son mouvement reste une tâche complexe en raison des incertitudes et des perturbations, telles que le frottement et les interactions non linéaires pneu-route. Bien qu'ils ne soient pas appliqués dans le domaine aérospatial, les résultats encourageants obtenus par les auteurs ont démontré les avantages de MFC dans la pratique. Une présentation plus approfondie de la technique MFC sera donnée dans le prochain chapitre. Les premiers résultats de l'approche MFC dans le domaine des tail-sitter MAVs et les principales contributions de cette thèse se trouvent dans (Barth u. a., 2020b) (Barth u. a., 2020a) (Barth u. a., 2019) (Barth u. a., 2018b) et (Barth u. a., 2018a). Ces articles se trouvent également respectivement dans les pages 198, 221, 244, 253 et 260 de ce manuscrit.

7.3 La commande sans modèle

L'estimation des signaux dérivés est impliquée dans l'approche algorithmique de contrôle MFC. À partir de cette technique d'estimation, une dynamique inconnue peut être déterminée de manière quantifiée et cette information peut être utilisée pour calculer la commande en boucle fermée. Par conséquent, le contrôleur proposé est capable de stabiliser une dynamique inconnue en utilisant des gains de contrôle conventionnels. Cette approche de contrôle sera détaillée dans les lignes qui suivent. Pour des raisons de simplicité, considérons un système inconnu de dimension finie avec une seule entrée de contrôle (u) et une seule sortie (y) décrit par la relation entrée/sortie suivante dans une formulation d'équation différentielle :

$$\mathbb{E}(y, \dot{y}, \ldots, y^{(a)}, u, \dot{u}, \ldots, u^{(b)}) = 0 \tag{7.1}$$

où $\mathbb{E}$ est une fonction polynomiale à coefficients réels inconnus. On peut également décrire

$$y^v = \mathbb{E}(t, y, \dot{y}, \ldots, y^{(v-1)}, y^{(v+1)}, \ldots, y^{(a)}, u, \dot{u}, \ldots, u^{(b)}) \tag{7.2}$$

avec $0 < v \leq a$ et $\frac{\delta \mathbb{E}}{\delta y^v} \neq 0$. L'idée derrière Fliess und Join (2013), est d'approcher cette dynamique inconnue (7.2) par une équation purement numérique, à savoir le *Modèle ultra local* :

$$y^{(v)}(t) = F(t) + \lambda \cdot u(t) \tag{7.3}$$

Dans (7.3), v est d'ordre de la dérivée de $y(t)$, $\lambda \in \mathbb{R}$ est un paramètre constant non physique utilisé pour obtenir le même ordre de grandeur entre les trois termes dans (7.3). De plus, l'exploitation de ce modèle numérique nécessite la connaissance de $F(t)$. Cette quantité représente la dynamique réelle du système ainsi que les différentes perturbations qui pourraient endommager les performances de contrôle. Ainsi, une estimation précise de $F(t)$, définie comme $\hat{F}(t)$, est cruciale et joue un rôle important dans la performance en boucle fermée du MFC.

Sur la base d'un tel estimateur, il est possible de concevoir un contrôleur robuste qui estime la dynamique du système en ligne via une fonction constante par morceaux $\hat{F}(t)$, périodiquement mise à jour à partir des mesures de $y(t)$ et pour les dernières valeurs de $u(t)$. La forme détaillée du schéma MFC présenté dans la figure 7.26 définit la commande en boucle fermée telle que :

$$u(t) = \underbrace{-\frac{\hat{F}(t)}{\lambda}}_{\text{Estimation}} + \underbrace{\frac{\ddot{y}_{sp}(t) + u_{\mathcal{K}}(t)}{\lambda}}_{\text{Closed-loop tracking}} \tag{7.4}$$

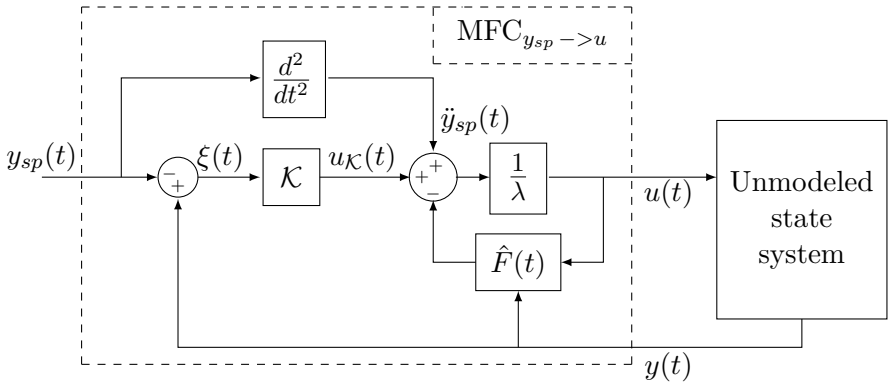

Figure 7.26: Schéma de contrôle sans modèle pour un système du second ordre.

où la quantité $\xi(t) = y(t) - y_{sp}(t)$ est l'erreur de suivi et $u_{\mathcal{K}}(t)$ est la commande en boucle fermée d'un contrôleur de retour $\mathcal{K}(\xi(t))$, généralement défini comme un gain P, PD ou même PID. Dans ce travail, nous définissons le contrôleur de rétroaction en boucle fermée comme un gain proportionnel K_p et dérivé K_d. Nous reconnaissons dans (7.4) l'expression mathématique typique d'un contrôle nominal dans la base de la planéité dans laquelle les termes non linéaires $\hat{F}(t)$ sont ajoutés avec un suivi en boucle fermée de la trajectoire du point de consigne $y_{sp}(t)$. La dynamique des erreurs peut être déduite de la combinaison de (3.13) avec (3.14), pour $v = 2$:

$$\ddot{\xi}(t) = \ddot{y}(t) - \ddot{y}_{sp}(t) = \overbrace{F(t) - \hat{F}(t)}^{\xi_F \approx 0} + K_p\,\xi(t) + K_d\,\dot{\xi}(t) \tag{7.5}$$

$$\ddot{\xi}(t) - K_d\,\dot{\xi}(t) - K_p\,\xi(t) = 0 \tag{7.6}$$

Prenons en considération que, si l'erreur entre l'estimateur et la dynamique réelle (ξ_F) est approximativement égale à zéro, un simple contrôleur PD suffira à assurer la convergence de l'erreur vers zéro, car les termes d'intégration sont implicitement impliqués dans l'algorithme MFC. En outre, on remarque à partir de (7.4) que le suivi en boucle fermée est découplé de l'algorithme d'estimation. De cette façon, nous pouvons concevoir séparément les performances de régulation et de poursuite.

7.3.1 Algorithme d'estimation

Afin d'obtenir des informations sur une dynamique inconnue, nous décrivons les équations d'estimation utilisées dans l'estimateur MFC $\hat{F}(t)$ sur la base de l'approche présentée dans la section 3.1 pour l'estimation des signaux dérivés. À cette fin, nous présentons les équations mathématiques permettant d'estimer la dynamique du premier et du second ordre. Enfin, nous proposons un algorithme pour obtenir l'estimateur MFC pour la dynamique d'ordre arbitraire (v).

- Selon (7.3), pour une dynamique du premier ordre ($v = 1$), on obtient :

$$\dot{y}(t) = F(t) + \lambda \cdot u(t) \tag{7.7}$$

  La première étape consiste à appliquer la *Transformée de Laplace* en (7.7), en considérant $F(t)$ comme une fonction constante par morceaux, ce qui donne :

$$sY(s) - y(0) = \frac{F}{s} + \lambda\,U(s) \tag{7.8}$$

Où $Y(s)$ et $U(s)$ correspondent respectivement aux *Transformées de Laplace* de $y(t)$ et $u(t)$. En différenciant l'équation précédente par rapport à la variable de Laplace s, nous sommes en mesure de supprimer la condition initiale :

$$Y(s) + s\frac{dY(s)}{ds} = -\frac{F}{s^2} + \lambda \frac{dU(s)}{ds} \tag{7.9}$$

Cependant, s est l'opération correspondant à la différenciation dans le domaine temporel et elle est sensible au bruit, ce qui pourrait amplifier le bruit de $y(t)$ dans la sortie de l'estimateur $\hat{F}(t)$. Par conséquent, afin de réduire à la fois le bruit et les erreurs de calcul numérique sur l'estimation, nous ajoutons deux intégrateurs ($\frac{1}{s^2}$) qui ont des propriétés robustes en ce qui concerne le bruit. Ainsi, en multipliant les deux côtés de (7.14) par s^{-2}, on obtient :

$$\frac{Y(s)}{s^2} + \frac{dY(s)}{s\,ds} = -\frac{F}{s^4} + \frac{\lambda}{s^2}\frac{dU(s)}{ds} \tag{7.10}$$

Enfin, l'expression de $\hat{F}(t)$ pour la dynamique du premier ordre peut être déterminée dans le domaine temporel en utilisant *Transformée de Laplace Inverse* avec le *Théorème de Cauchy* pour réduire les intégrales multiples en une simple :

$$\hat{F}(t) = \frac{-6}{T^3}\int_{t-T}^{t} \Big[(T-2\sigma)y_(\sigma) - \lambda\sigma(T-\sigma)u(\sigma)\Big]d\sigma \tag{7.11}$$

L'équation (7.11) estime la dynamique d'un système du premier ordre à partir des mesures d'un signal bruité $y(t)$. Le résultat est un paramètre constant $\hat{F}(t)$ qui est valable pendant l'intervalle $[t-T, t]$. Différents travaux pratiques dans la littérature ont prouvé que l'utilisation d'un *Modèle ultra local* de premier ordre ($v = 1$) est suffisant pour stabiliser une dynamique inconnue. Cependant, si la dynamique inconnue présente un comportement du second ordre avec de faibles coefficients de friction, l'utilisation d'un *Modèle ultra local* du premier ordre serait insuffisante pour stabiliser cette dynamique mal amortie (Fliess und Join, 2013). Dans ce contexte, nous proposons de développer des algorithmes MFC basés sur un *Modèle ultra local* du second ordre ($v = 2$).

- Ensuite, pour la dynamique du second ordre, nous avons :

$$\ddot{y}(t) = F(t) + \lambda \cdot u(t) \tag{7.12}$$

La méthodologie pour obtenir l'estimateur MFC reste la même que pour une dynamique du premier ordre. Pour cela, la première étape consiste à appliquer la *Transformée de Laplace* en (7.12) :

$$s^2Y(s) - sy(0) - \dot{y}(0) = \frac{F}{s} + \lambda U(s) \tag{7.13}$$

Où $Y(s)$ et $U(s)$ correspondent aux *Transformées de Laplace* de $y(t)$ et $u(t)$ respectivement. En différenciant deux fois l'équation précédente par rapport à s, nous pouvons supprimer les conditions initiales $y(0)$ et $\dot{y}(0)$:

$$2Y(s) + 4s\frac{dY(s)}{ds} + s^2\frac{d^2Y(s)}{ds^2} = \frac{2F}{s^3} + \lambda\frac{d^2U(s)}{ds^2} \tag{7.14}$$

Dans ce cas, afin de réduire à la fois le bruit et les erreurs de calcul numérique causées par le terme s^2 dans le numérateur de l'équation précédente, nous devons multiplier les deux

côtés de (7.14) par s^{-3}. Cette opération mathématique ajoute au moins un intégrateur ($\frac{1}{s}$) à l'équation, ce qui garantit des propriétés robustes par rapport au bruit :

$$\frac{2Y(s)}{s^3} + \frac{4}{s^2}\frac{dY(s)}{ds} + \frac{1}{s}\frac{d^2Y(s)}{ds^2} = \frac{2F}{s^6} + \frac{\lambda}{s^3}\frac{d^2U(s)}{ds^2} \tag{7.15}$$

Enfin, les estimations de la dynamique du second ordre peuvent être obtenues en appliquant la *Transformée de Laplace Inverse* avec le *Théorème de Cauchy* en (7.15) afin de réduire les intégrales multiples en une simple :

$$\hat{F}(t) = \frac{5!}{2T^5}\int_{t-T}^{t}\left[\Big[(T-\sigma)^2 - 4\sigma(T-\sigma) + \sigma^2\Big]y(\sigma) - \Big[\frac{\lambda}{2}\sigma^2(T-\sigma)^2u(\sigma)\Big]\right]d\sigma \tag{7.16}$$

À partir des mesures du signal bruité $y(t)$ et de l'entrée de contrôle $u(t)$ obtenues à partir des dernières secondes T, la dynamique inconnue de $y(t)$ et les perturbations agissant dans le système sont estimées par $\hat{F}(t)$, qui est mis à jour pour chaque intervalle d'intégration $[t-T, t]$. Cet intervalle correspond à la largeur de la fenêtre d'une stratégie à horizon dégressif qui donne lieu à un compromis. L'idée est de choisir une largeur de fenêtre suffisamment petite pour calculer l'estimation dans un délai de temps acceptable, mais suffisamment grande pour préserver les propriétés de filtre passe-bas de l'intégrateur afin d'atténuer le bruit dans les mesures de $y(t)$.

- En général, une dynamique inconnue avec un ordre arbitraire peut être estimée en utilisant la méthodologie décrite dans l'algorithme (4).

Algorithm 4 Détermination de l'estimateur $\hat{F}$

1: **procedure**
2: $v \leftarrow$ Définir l'ordre de la dynamique à estimer
3: **étape 1:** Écrire le *Modèle ultra local*
4: **étape 2:** Calculer la *Transformée de Laplace* de l'étape 1
5: **étape 3:** Dériver l'étape 2, v fois par rapport à s
6: **étape 4:** Multiplier l'étape 3 par $s^{-(v+1)}$
7: **étape 5:** Calculer la *Transformée de Laplace Inverse* de l'étape 4
8: **étape 5:** Appliquer le *Théorème de Cauchy* dans l'étape 5
9: **fin de la procédure**;

7.3.2 Méthodologie de synthèse du contrôleur

La boucle fermée MFC permet de concevoir à la fois des performances de poursuite et d'asservissement avec des paramètres distincts qui peuvent être réglés avec peu de connaissances préalables du système. Les points suivants décrivent la méthodologie de conception utilisée dans ce travail pour régler les paramètres MFC :

1. Les gains proportionnels-dérivés (K_p et K_d) ont été facilement ajustés selon la méthode classique du lieu de racine. En pratique, l'algorithme MFC fournit une estimation précise du système ($\xi_F \approx 0$). Ainsi, la dynamique des erreurs du système en boucle fermée

peut être approchée par un double intégrateur (7.6), qui peut être réglé par l'approche du placement des pôles. De ce point de vue, nous définissons les doubles pôles réels en boucle fermée à $-s_d$, ce qui donne le polynôme caractéristique suivant :

$$(s + s_d)^2 = s^2 + 2\, s_d\, s + {s_d}^2 \tag{7.17}$$

Le contrôleur avec ces gains proportionnels-dérivés peut être identifié en négligeant les conditions initiales dans la transformée de Laplace de (7.6) :

$$\frac{U_{\mathcal{K}}(s)}{\xi_y(s)} = s^2 - K_d\, s - K_p \tag{7.18}$$

Par conséquent, nous obtenons de (7.17) et (7.18) :

$$K_p = -{s_d}^2 \quad \text{with} \quad s_d > 0 \tag{7.19}$$

$$K_d = -2 s_d \quad \text{with} \quad s_d > 0 \tag{7.20}$$

2. La fenêtre d'intégration (T) pourrait être définie avec des informations préalables sur le bruit présent dans le signal mesuré $y(t)$. Le choix de la fenêtre d'intégration implique une certaine expertise avec un compromis entre des estimations rapides et des atténuations de bruit efficaces. Par exemple, grâce à l'intégrateur in (7.16) avec des caractéristiques de filtre passe-bas, une grande fenêtre d'intégration fournit une atténuation efficace du bruit, mais des estimations lentes avec un impact direct sur la réactivité de la boucle fermée.

   En revanche, une petite fenêtre d'intégration permet des estimations rapides avec la contrainte d'estimer les bruits. Dans ce contexte, des oscillations pourraient apparaître dans le système en boucle fermée avec des commandes à haute fréquence, connues sous le nom de *chattering*. Dans ce travail, nous utilisons un observateur invariant (Martin und Salaun, 2010) qui lisse les signaux mesurés, permettant le réglage des petites fenêtres d'intégration afin d'estimer la dynamique rapide du système tout en supprimant les oscillations générées par les bruits à haute fréquence.

3. Enfin, le coefficient constant λ est utilisé pour mettre à l'échelle l'amplitude entre la commande $u(t)$ et la dynamique de $\ddot{y}(t)$. Ce paramètre peut être représenté comme l'efficacité de commande du système nominal. Néanmoins, si ce paramètre est mal défini ou si l'efficacité de commande réelle du système change dans un domaine limité, l'estimateur $\hat{F}(t)$ est capable de compenser cet écart limité en assurant la stabilité en boucle fermée. Un réglage nominal de λ peut être obtenu en calculant le rapport entre la saturation de la commande et la valeur maximale autorisée de $\ddot{y}(t)$.

D'un point de vue pratique, la conception MFC proposée permet de gagner du temps pour stabiliser des systèmes dynamiques complexes. Entre autre, le fait que le système en boucle fermée puisse être approché par la dynamique d'un double intégrateur simplifie le processus de conception des paramètres du contrôleur.

7.4 Étude de la commande sans modèle en simulations de vol

Cette section présente l'architecture de contrôle MFC et fournit un ensemble complet de simulations de vol couvrant l'ensemble du domaine de vol des tail-sitter MAVs. Nous présentons une vue d'ensemble de chaque phase de vol avec ses défis et ses contraintes en ce qui concerne le contrôle et la dynamique du vol. Les performances en boucle fermée sont également évaluées afin de définir la stabilité dans le pire des cas en ce qui concerne la dynamique non modélisée et la variation paramétrique, mais aussi contre les perturbations externes. En outre, une analyse préliminaire comparant les performances du MFC avec celles du LQR est également présentée, en mettant l'accent sur le domaine de vol en transition. Cette analyse comparative met en évidence les avantages et les inconvénients de chaque contrôleur, tant en ce qui concerne les performances de contrôle que le processus de mise en œuvre des systèmes de pilotage automatique pour les tail-sitter MAVs.

7.4.1 Simulateur de vol Tail-Sitter

Un ensemble complet de simulations de vol, discrétisées à 500 Hz, a été réalisé à partir de MATLAB/Simulink à l'aide du modèle tail-sitter MAV décrit dans le chapitre 2. Notre simulateur de vol (voir figure 7.27) décrit la dynamique d'un tail-sitter MAV nommé DarkO, ses paramètres sont présentés dans le tableau 7.1. Les sorties du DarkO sont corrompues par un bruit gaussien, dont les écarts-types se trouvent dans (Chahl u. a., 2007). Un observateur invariant (Martin und Salaun, 2010) est utilisé pour fournir une mesure plus lisse du signal des états du DarkO, cependant, cette opération ajoute des retards dans la boucle fermée et ont été pris en compte lors de la conception du contrôleur.

Table 7.1: Paramètres du DarkO tail-sitter MAV.

Parameters	Values	SI Units
Mass (m)	0.492	[Kg]
Mean Chord (c)	0.135	[m]
Wingspan (b)	0.55	[m]
Wing Area (S)	0.0743	[m^2]
J_{xx}	0.00493	[Kg m^2]
J_{yy}	0.00532	[Kg m^2]
J_{zz}	0.00862	[Kg m^2]
J_p	5.1116e-06	[Kg m^2]
k_f	5.13e-6	[Kg m]
k_m	2.64e-7	[Kg m^2]
C_{d0}	0.133	No units
C_{y0}	0.145	No units
C_l	[0.47; 0.00; 0.00]	No units
C_m	[0.00; 0.54; 0.00]	No units
C_n	[0.00; 0.00; 0.52]	No units

Afin d'évaluer notre algorithme de contrôle, nous avons introduit des perturbations externes, telles qu'un vent de travers, pendant ces vols. Les résultats fournissent un moyen simple de valider les principes méthodologiques présentés dans ce travail, ainsi que de certifier les paramètres MFC conçus, et d'établir une conclusion concernant l'approche MFC dans des contextes théoriques et pratiques.

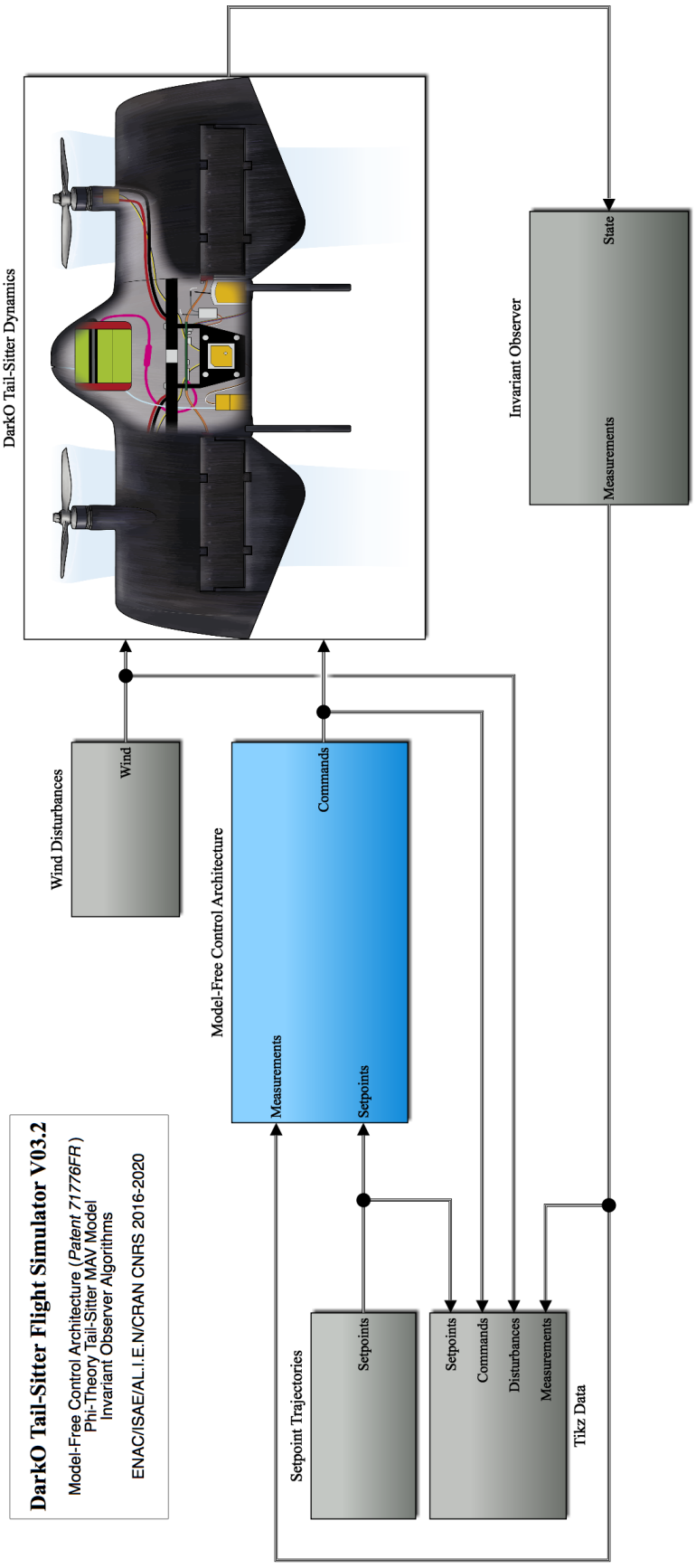

Figure 7.27: Simulateur de vol Matlab/Simulink - DarkO Tail-Sitter MAV.

7.4.2 Architecture de contrôle MFC pour les Tail-Sitter MAVs

Le bloc "Model-Free Control Architecture" dans la figure 7.27 sera détaillé dans cette section. Les algorithmes MFC peuvent être mis en œuvre sur les systèmes MIMO en supposant un découplage approximatif entre les dynamiques du système. Cette hypothèse majeure a été vérifiée par différentes expériences pratiques (Lafont u. a., 2015), mais jamais pour les tail-sitter MAVs. Malgré cette hypothèse de découplage, les algorithmes MFC peuvent compenser l'effet d'un état arbitraire du système sur celui qui est contrôlé en mesurant sa sortie avec l'estimateur MFC. Afin de développer les interactions correctes entre les blocs dans l'architecture de contrôle proposée, nous utilisons une connaissance préalable de la convention de signe entre les commandes et les états du tail-sitter MAV basée sur les équations de la mécanique du vol.

La figure 7.28 montre les principales idées de notre architecture de contrôle. Le bloc *générateur de trajectoire* est composé d'un algorithme de flux d'états qui définit constamment les positions souhaitées (x_{sp}, y_{sp}, z_{sp}) dans le système de coordonnées inertielles. Ces références sont prises en compte par le bloc *Contrôle de position* et sont comparées avec les mesures respectives (x_m, y_m, z_m) créant ainsi trois erreurs qui sont minimisées par les algorithmes MFC dans le bloc *Contrôle de position*. Ces trois algorithmes MFC en charge du suivi de position calculent également la vitesse souhaitée dans leurs axes respectifs. Ces valeurs de référence définies dans le cadre de coordonnées inertielles sont transformées en cadre de coordonnées du corps ainsi que les mesures de vitesse.

Par conséquent, le contrôle de vitesse $\text{MFC}_{v_{xb}}$ calcule la poussée nécessaire T_d pour atteindre la vitesse souhaitée le long de $\overrightarrow{\boldsymbol{x_b}}$, le bloc $\text{MFC}_{v_{zb}}$ assure le contrôle de vitesse le long de $\overrightarrow{\boldsymbol{z_b}}$ et détermine l'angle de tangage nécessaire θ_{sp} pour atteindre cette vitesse souhaitée $v_{zb_{sp}}$. Les deux blocs contrôlent leurs vitesses respectives et indiquent la poussée et l'angle de tangage souhaité pour l'ensemble du domaine de vol, c'est-à-dire le vol stationnaire, la transition et le vol vers en croisière. Cependant, le contrôle de la vitesse le long de $\overrightarrow{\boldsymbol{y_b}}$ est conçu en fonction de la phase de vol actuelle du tail-sitter MAV.

Ainsi, en vol stationnaire, le bloc $\text{MFC}_{v_{yb}}$ fixe l'angle de lacet souhaité ψ_{sp} et le bloc MFC_{ψ} s'active dans le système par une commande de poussée différentielle créant un moment autour de $\overrightarrow{\boldsymbol{z_b}}$ afin d'atteindre la vitesse souhaitée le long de $\overrightarrow{\boldsymbol{y_b}}$. En vol en croisière, cette vitesse latérale est atteinte par des rotations de roulis autour de $\overrightarrow{\boldsymbol{x_b}}$. Ces rotations orientent la force de portance et le HMAV peut effectuer des virages gauche-droite avec des angles de roulis ϕ négatifs et positifs. Les vitesses de rotation de l'hélice (ω_l, ω_r) sont définies par la somme de la rotation nominale de celle-ci ω_n avec une vitesse différentielle Δ_ω qui est chargée de la commande de lacet. Le signe négatif de ω_n pour l'hélice gauche ω_l est dû au sens de la contre-rotation. Les déflexions des volets (δ_l, δ_r), qui sont par convention négatives pour le cabrage, sont composées de la somme des déflexions symétriques δ_n avec les déflexions anti-symétriques des volets δ_δ qui sont les commandes de l'angle de tangage θ et de l'angle de roulis ϕ.

7.4.3 Simulations de vol

Les résultats des simulations de vol sont présentés dans une série d'études de cas afin d'analyser séparément chaque domaine de vol et les capacités du tail-sitter MAV en vol stationnaire, en transition et en vol en croisière. En premier lieu, nous présentons des missions de vol dans le domaine de vol stationnaire. Ensuite, nous analysons la capacité du contrôle de la vitesse et de l'attitude pour récupérer le tail-sitter MAV dans différentes conditions initiales instables dans le domaine de vol de transition. Dans la phase de vol en croisière, nous présentons deux missions

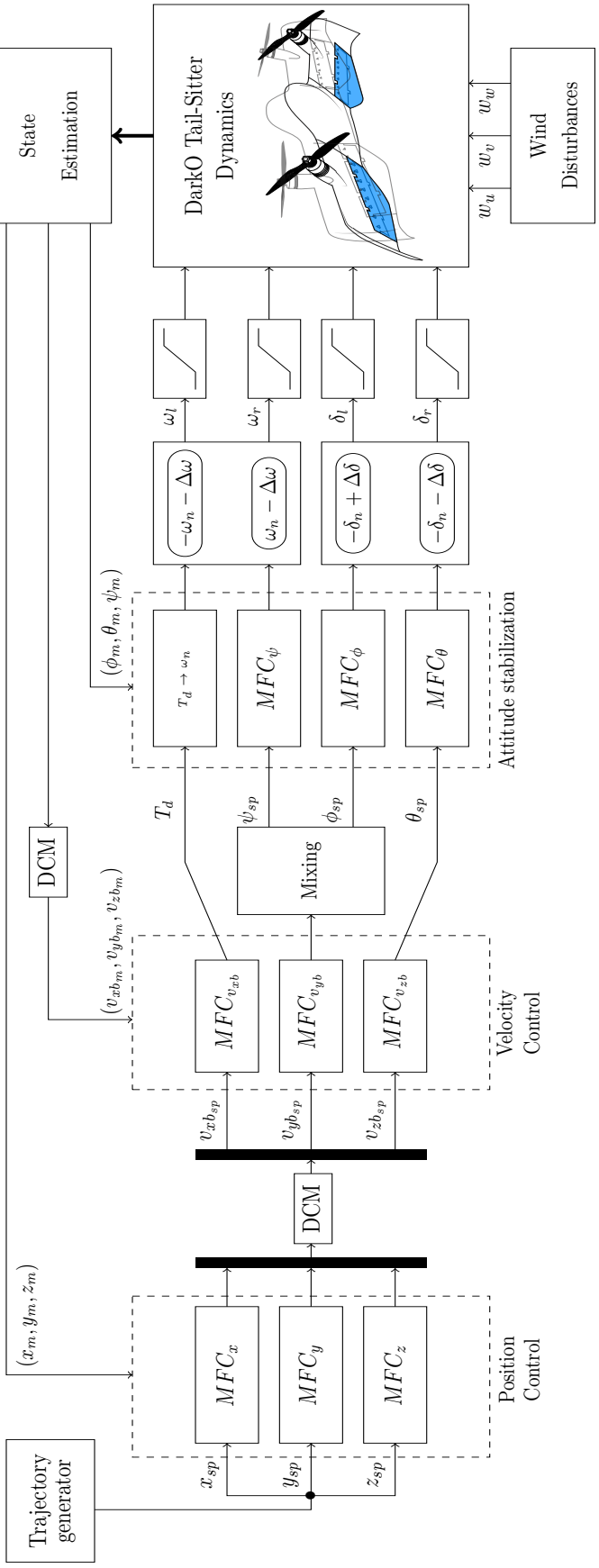

Figure 7.28: Architecture en cascade MFC conçue pour les tail-sitter MAVs. Les blocs de contrôle de position envoient les vitesses de référence pour les blocs de contrôle de vitesse qui calculent la valeur de poussée nécessaire ainsi que les références pour la boucle de stabilisation de l'attitude.

de suivi de position et nous vérifions l'interaction entre les blocs de contrôle de position, de vitesse et d'attitude.

► **Vol stationnaire**

L'objectif principal de la première simulation de vol en vol stationnaire, présentée sur la figure 7.29 est l'étude de l'influence du vent dans le suivi de position, pour les positions souhaitées suivantes :

$$x_{sp} = 0, \forall\, t$$

$$y_{sp} = 0, \forall\, t$$

$$z_{sp} = \begin{cases} 10, & t \in]0; 155]s \\ \\ 0, & t > 155s \end{cases}$$

Pendant ce mode de vol, le tail-sitter MAV est plus sensible aux perturbations dues au vent. On peut expliquer cela par le fait qu'en position verticale, la rafale de vent le long de l'axe x_i (respectivement, le long de l'axe z_b), est en contact avec la surface totale de l'aile de référence, générant une force de traînée considérable. En outre, le tail-sitter MAV n'est pas en mesure de compenser cette force en position verticale. C'est pourquoi la transition est effectuée et la force de traînée créée par le vent peut être compensée par la poussée afin d'assurer le suivi de la position. La poussée utilisée pour rejeter cette perturbation est présentée sur la figure 7.29d. Le vent de magnitude de 5 m/s (voir figure 7.29f) produit également une force latérale dans l'axe y_b. Cette force est compensée en orientant la force de portance avec une rotation symétrique autour de l'axe x_b correspondant à l'angle de roulis négatif indiqué sur la figure 7.29c.

Dans la deuxième simulation de vol, nous imposons une trajectoire circulaire de consigne afin de valider l'interaction entre tous les blocs de contrôle dans l'architecture de contrôle proposée. Les équations suivantes définissent les trajectoires souhaitées (x_{sp}, y_{sp}, z_{sp}),

$$x_{sp} = \begin{cases} 0, & t < 30s \\ x_c + r\, cos\Big(\frac{2\pi}{40} t\Big), & t \in [30; 130]s \\ 1, & t > 130s \end{cases}$$

$$y_{sp} = \begin{cases} 0, & t < 30s \\ y_c + r\, sin\Big(\frac{2\pi}{40} t\Big), & t \in [30; 130]s \\ 5, & t > 130s \end{cases}$$

$$z_{sp} = \begin{cases} 10, & t \in [0; 155]s \\ 0, & t > 155s \end{cases}$$

où x_c et y_c correspondent au centre du cercle et r son rayon. Cette manoeuvre nécessite que le tail-sitter MAV vole le long d'une trajectoire circulaire tout en pointant constamment son nez vers un point fixe précis. Un contrôle précis de la position, de la vitesse et surtout le contrôle de l'angle de lacet sont nécessaires pour suivre le plan de vol souhaité. La figure 7.30 montre les résultats de la simulation, qui a validé l'interaction entre tous les blocs de contrôle dans la phase de vol stationnaire.

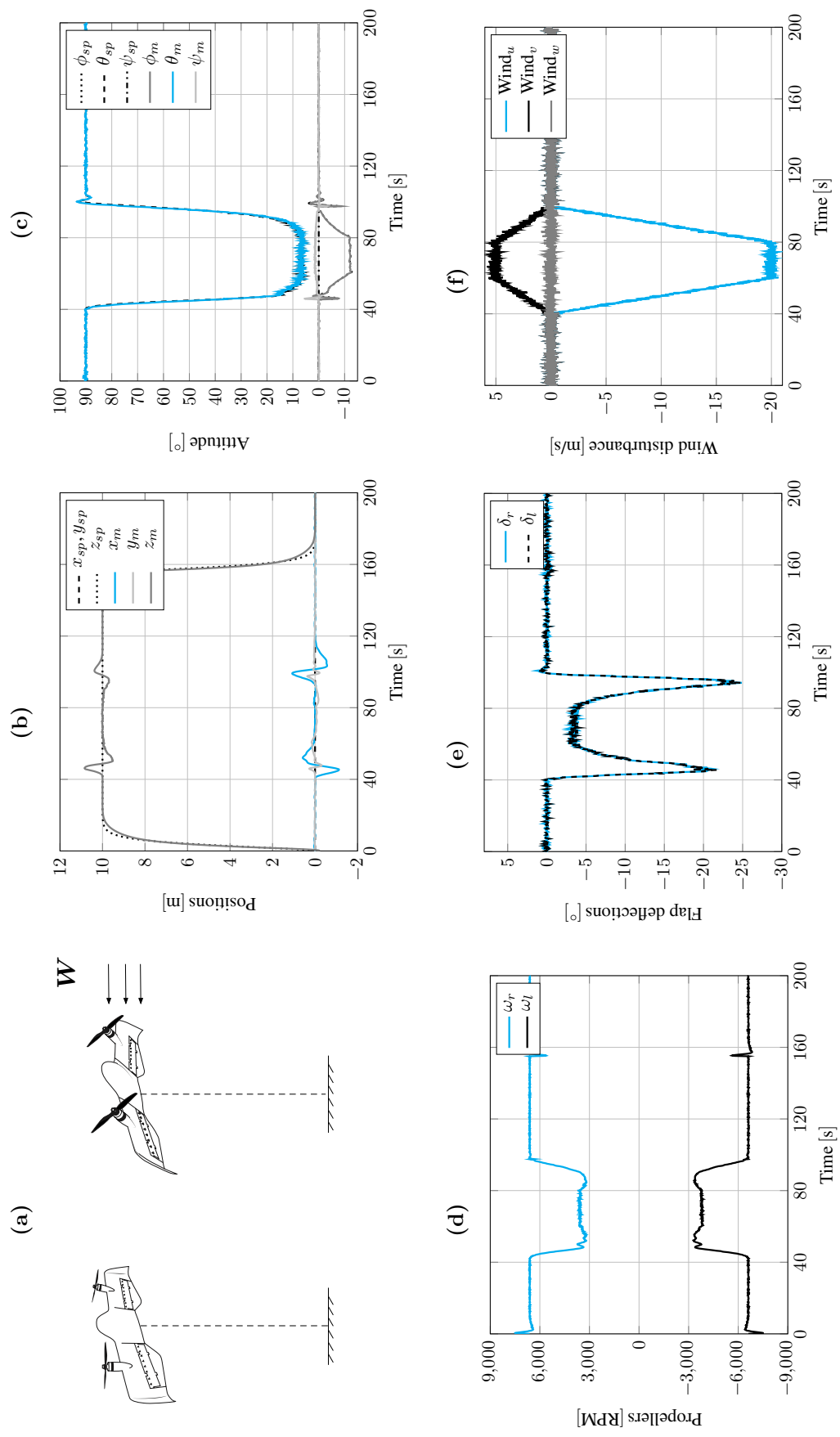

Figure 7.29: Décollage vertical et vol de transition pour assurer le suivi de la position dans un environnement venteux. En haut, de gauche à droite : illustration de la simulation de vol, positions dans le cadre des coordonnées inertielles et l'attitude d utail-sitter MAV. En bas : les rotations des hélices ($\omega_l < 0$ et $\omega_r > 0$) dues au sens de la contre-rotation, déflexions des volets (δ_l et δ_r) convention négative pour cabrer et les perturbations du vent.

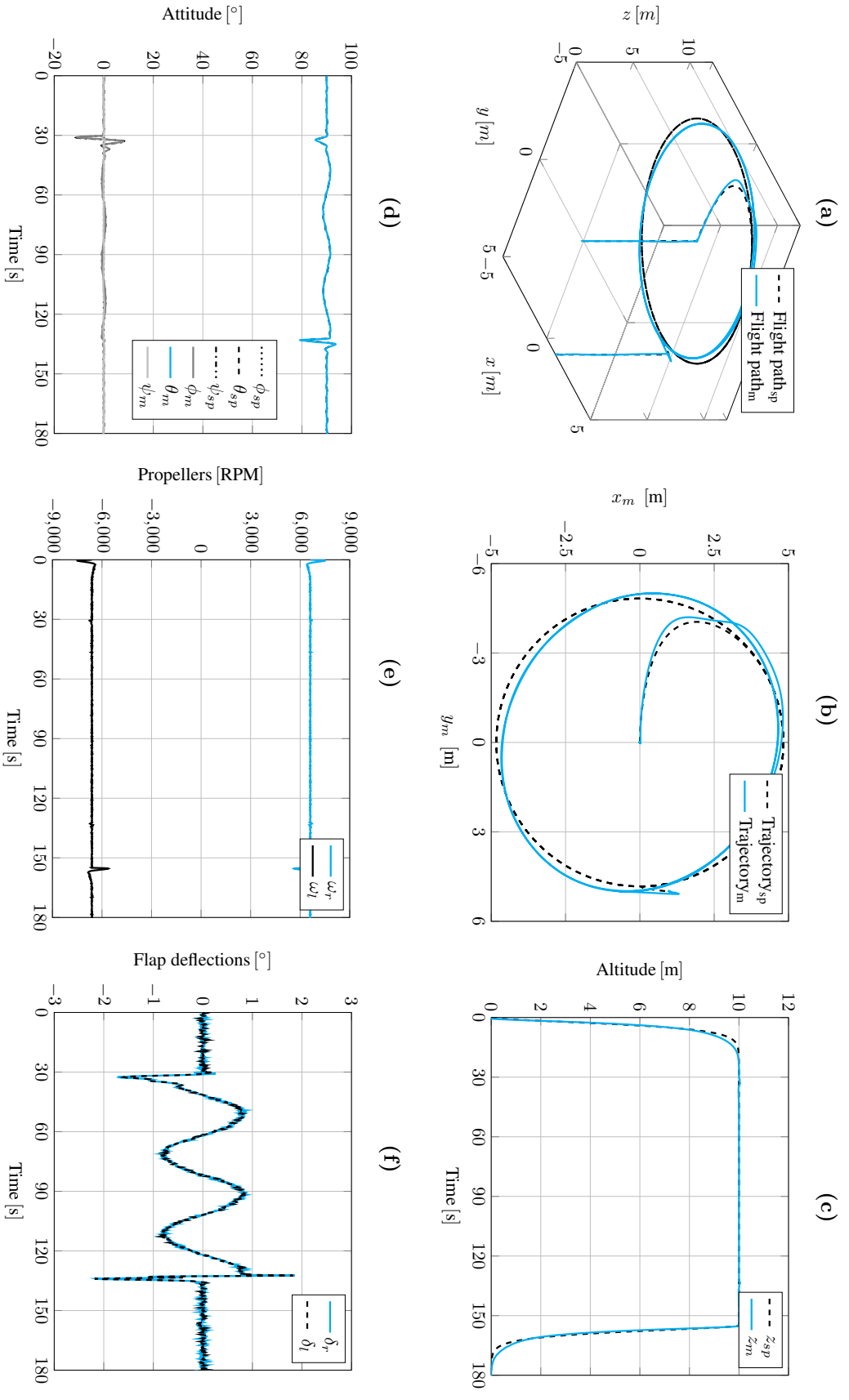

Figure 7.30: Suivi d'une trajectoire circulaire en mode de vol stationnaire. En haut, de gauche à droite : la trajectoire de vol en 3D, les positions et l'altitude du tail-sitter MAV. En bas : l'attitude, les vitesses de rotation des hélices et les déflexions des volets.

▶ Vol de transition

En vol de transition, nous analysons les blocks de contrôle en vitesse et de la stabilisation de l'attitude. Dans cette étude de cas, nous définissons un point de consigne de vitesse fixe (v_{xi}) qui est égal à 5 m/s et l'architecture en cascade MFC calcule un point de consigne d'angle de tangage d'environ 45°. Le point de consigne de vitesse souhaité a été choisi afin de valider, par des simulations de vol, que l'architecture de contrôle proposée est capable de stabiliser le tail-sitter MAV dans un domaine de vol critique, correspondant à la région de décrochage où le tail-sitter MAV vole à faible vitesse et à un angle d'attaque élevé. Les conditions initiales pendant l'analyse du vol de transition (θ_{ic} et $V_{x_{ic}}$), sont définies à partir d'une loi de distribution normale donnée par les équations suivantes (7.21) et (7.22).

$$\theta_{ic} \sim \mathcal{N}\left(\frac{\pi}{4},\, 30^2\right). \tag{7.21}$$

$$V_{x_{ic}} \sim \mathcal{N}\left(5,\, 2^2\right). \tag{7.22}$$

La limite de stabilité présentée dans la figure 7.31 a été définie empiriquement en évaluant toutes les trajectoires depuis les conditions initiales jusqu'au point de consigne souhaité. Pour ces analyses de conditions initiales, le tail-sitter MAV n'a pas été contrôlé en position permettant un degré de liberté supplémentaire pour récupérer le point de consigne d'attitude stable. Pendant le régime transitoire, qui correspond à la trajectoire des conditions initiales aux points de consigne, le tail-sitter MAV perd de l'altitude pour deux raisons. Premièrement, la condition initiale de l'angle de tangage et de la vitesse empêche la génération de la force de portance afin de maintenir le tail-sitter MAV à son niveau de vol. Deuxièmement, l'orientation de sa poussée n'est pas adéquate pour compenser son poids. Une stabilisation rapide de l'attitude est donc cruciale pour orienter le vecteur de poussée et ramener le tail-sitter MAV dans des conditions de vol convenables.

▶ Vol en croisière

Une mission de vol complète est présentée dans la figure 7.32. Ici, nous évaluons toutes les capacités de vol du tail-sitter MAV par un décollage vertical de zéro à 10 mètres d'altitude, suivi d'une transition du vol stationnaire au vol en croisière avec un suivi de position dans le plan xy et un changement d'altitude de 10 à 15 mètres. Ensuite, la transition du vol en croisière au vol stationnaire est effectuée avec un suivi de position dans la phase de vol stationnaire. La simulation de vol se termine par un atterrissage vertical. La trajectoire de vol 3D complète est présentée dans la figure 7.32a.

Le contrôleur assure le suivi de la position pendant toute la mission. Comme on peut le voir sur la figure 7.32b, l'altitude présente de petites oscillations à 45 et 165 secondes de simulation, ce qui est acceptable pour la classe des tail-sitter MAVs. Ces oscillations sont dues aux variations rapides des forces et moments aérodynamiques qui se produisent pendant les phases de vol de transition où l'angle de tangage change, entraînant des variations importantes de l'angle d'attaque (voir figure 7.32d). Sur la même figure, entre 45 et 90 secondes de simulation, on peut voir le comportement de l'angle de roulis en charge d'atteindre la position latérale en vol en croisière. De même, entre 180 et 215 secondes de simulation, le comportement en lacet pour suivre la position latérale en vol stationnaire. La figure 7.32c présente les vitesses dans le système de coordonnées du tail-sitter MAV et la dynamique de ses actionneurs, qui sont, les rotations

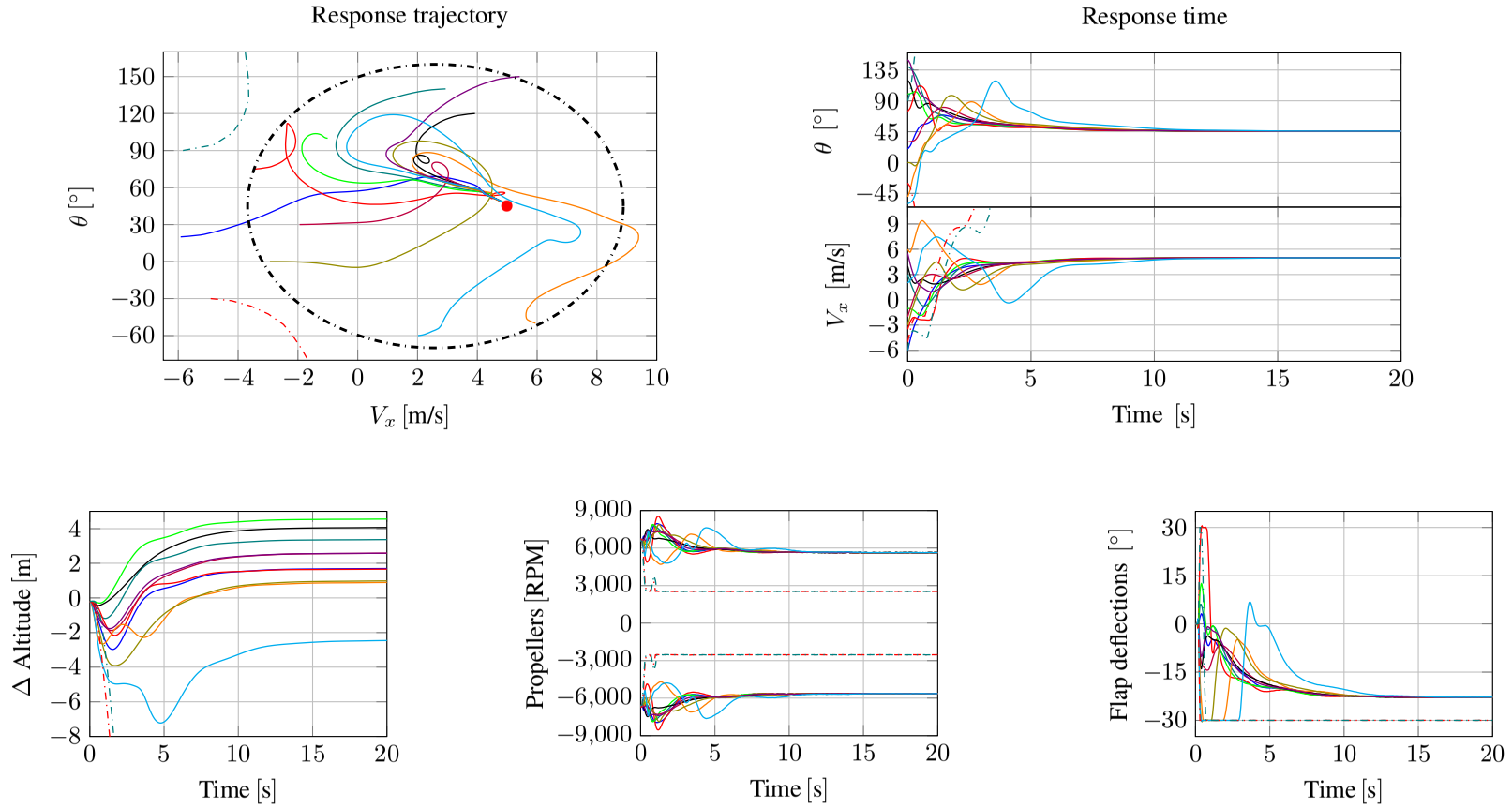

Figure 7.31: Analyse des conditions initiales d'angle de tangage et de vitesse (v_{xi}) pendant la phase de vol de transition sans perturbations du vent. Le point de consigne de la vitesse est égal à 5 , m/s, l'architecture de contrôle MFC calcule la consigne pour l'angle de tangage approximativement égal à 45 ,°.

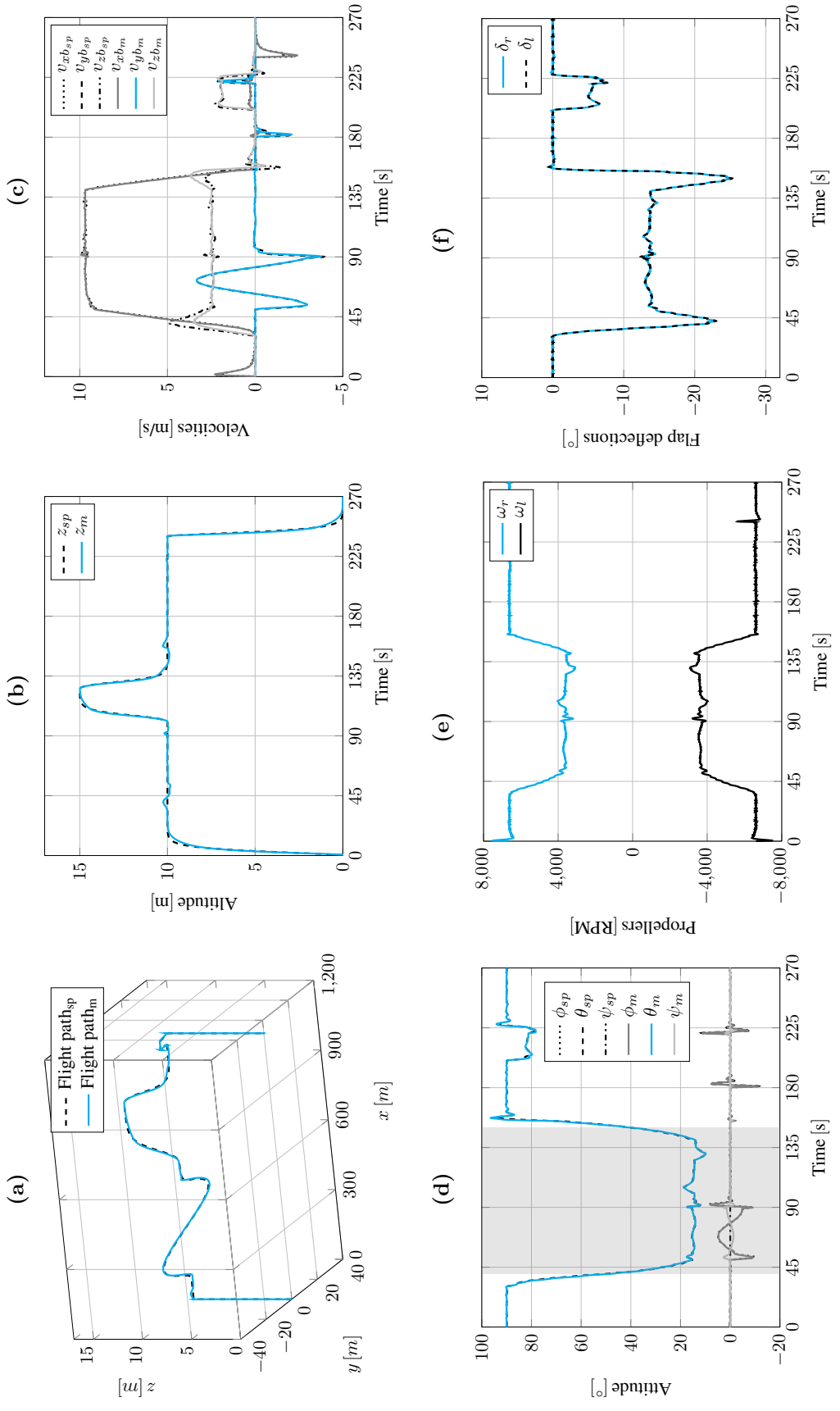

Figure 7.32: Simulation de vol complète avec toutes les phases de vol d'un tail-sitter MAV. En haut, de gauche à droite : la trajectoire de vol 3D, l'altitude et les vitesses dans le système de coordonnées du tail-sitter MAV. En bas : l'attitude, les vitesses des hélices et les déflexions des volets.

de l'hélice et les déflexions des volets, comme le montrent respectivement la figure 7.32e et la figure 7.32f.

► **Analyse des variations paramétriques par la méthode de Monte Carlo**

À travers les paramètres MFC conçus pour un modèle de tail-sitter MAV, cette section traite de l'utilité, de la fiabilité et des propriétés d'adaptation de l'architecture de contrôle proposée. Alors que les vols de simulation précédents analysaient les caractéristiques d'adaptabilité de MFC par rapport aux perturbations externes, cette section démontre les propriétés de MFC par rapport à la variation des paramètres internes. En outre, cette analyse vise à quantifier les variations maximales admissibles des paramètres du DarkO, pour lesquelles l'architecture MFC proposée, avec les mêmes paramètres MFC, assure la stabilité du vol.

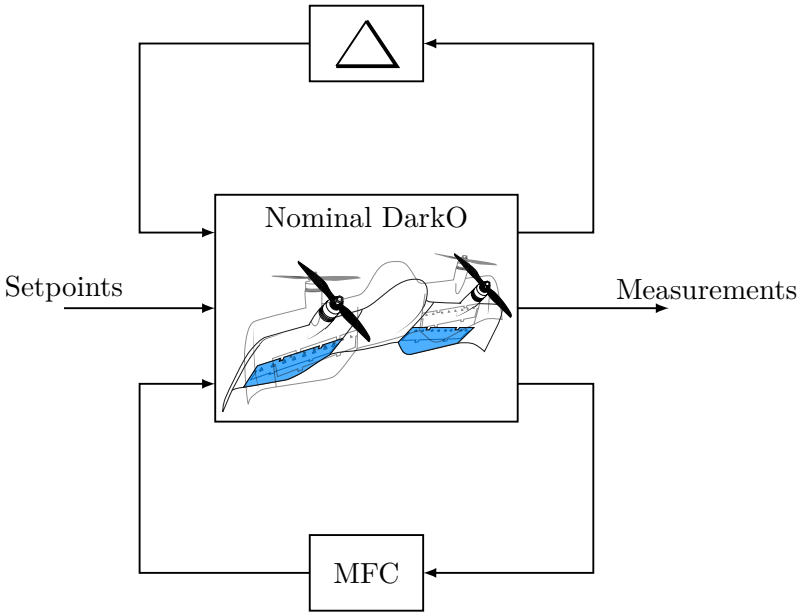

Figure 7.33: Analyse des variations paramétriques avec les algorithmes MFC.

Afin de réduire l'effort de calcul qui augmente de manière exponentielle avec le nombre de termes variables et en raison de la difficulté à comprendre les résultats lorsqu'on fait varier plus de trois ou quatre paramètres en combinaison, nous avons choisi de mettre en œuvre une méthode de Monte Carlo dans laquelle la masse, l'inertie et les coefficients géométriques sont correctement modifiés. Selon la formulation aérodynamique décrite dans le chapitre 2, les coefficients aérodynamiques dépendent de paramètres géométriques, tels que l'envergure et la longueur de la corde.

Ainsi, les variations des coefficients aérodynamiques et leur influence sur la stabilité du système en boucle fermée ont également été prises en compte. La quantification de l'ensemble des paramètres pour lesquels le DarkO reste stable détermine une classe de tail-sitter MAV qui peut être stabilisée par l'architecture proposée avec les mêmes paramètres MFC. Dans la figure 7.33, nous introduisons le schéma d'analyse d'un système à paramètres variants avec le

bloc d'incertitude (Δ) dans le système en boucle fermée. Ce bloc représente tous les paramètres du DarkO qui seront évalués, dans lequel leurs variations sont représentées en pourcentage des paramètres nominaux du DarkO :

$$\Delta = \begin{cases} \text{masse} & \in [-50\%; +100\%] \\ \text{inertie} & \in [-50\%; +100\%] \\ \text{envergure} & \in [-50\%; +100\%] \\ \text{corde} & \in [-50\%; +100\%] \end{cases}$$

Afin d'évaluer l'effet des variations paramétriques sur la dynamique du système, plusieurs simulations de vol ont été réalisées. La figure 7.34 montre la trajectoire de vol proposée dans laquelle la dynamique longitudinale du DarkO a été analysée. Au début de chaque simulation de vol, les paramètres du DarkO ont été modifiés et des trajectoires de consigne identiques ont été imposées au système.

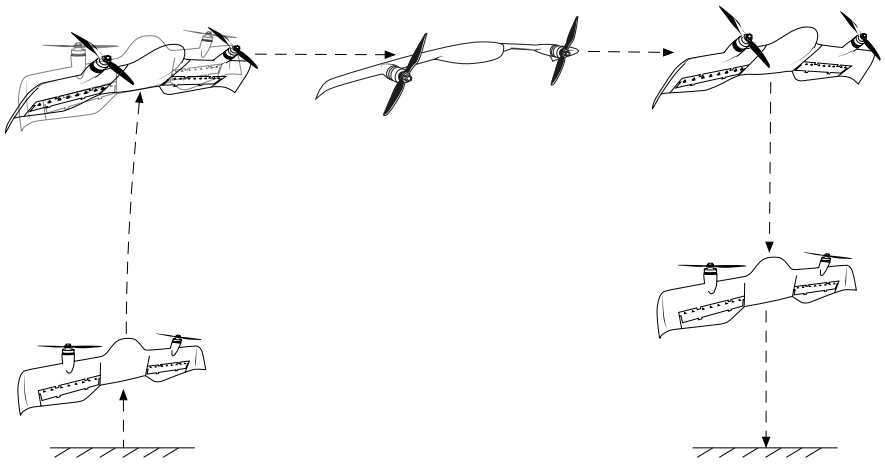

Figure 7.34: Trajectoire de vol évaluée lors de l'analyse des variations paramétriques.

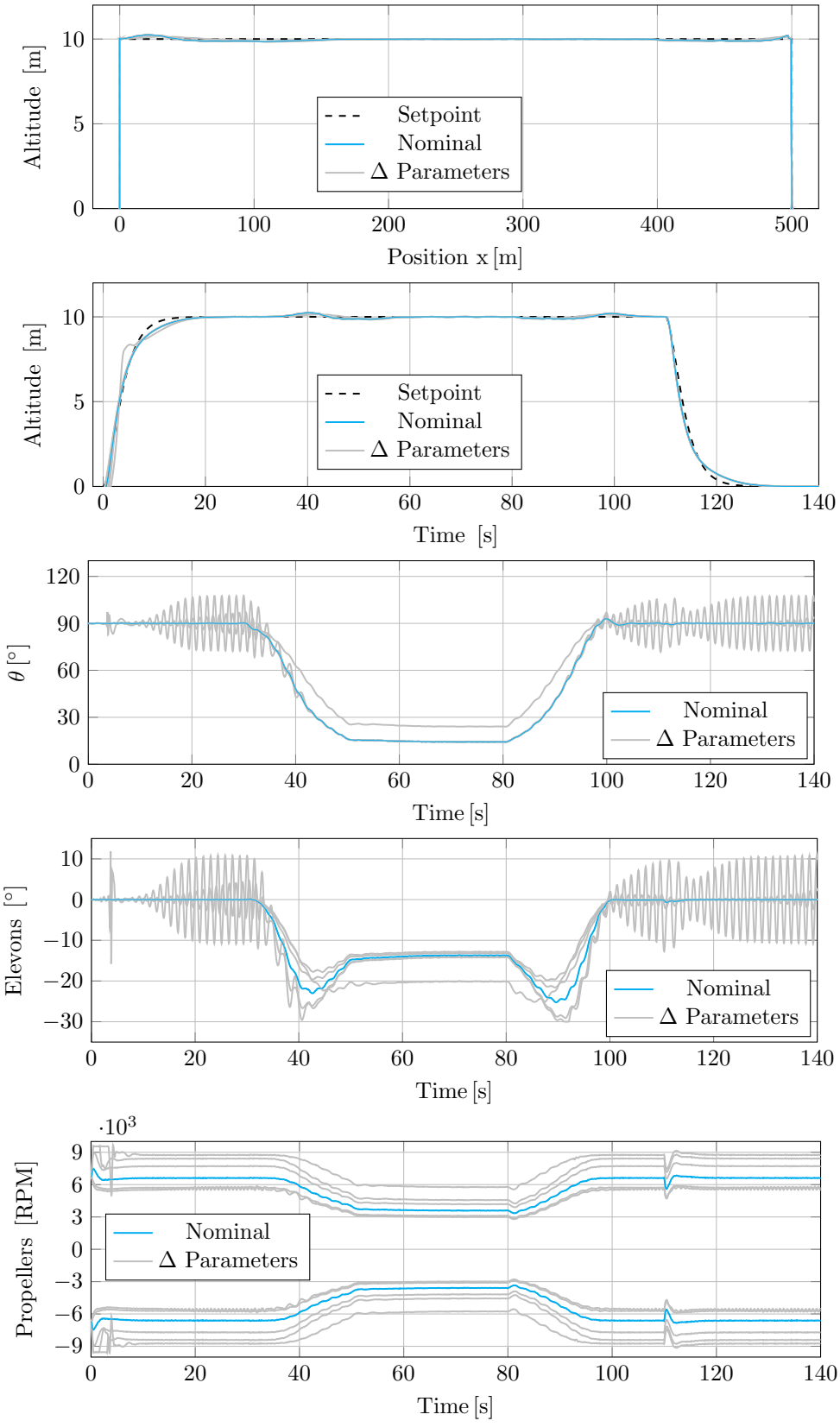

Figure 7.35: Analyse des variations paramétriques.

Pour des raisons de visibilité, la figure 7.35 présente les simulations de vol les plus significatives. La variation des paramètres internes attire l'attention sur les points suivants :

- (i) Les variations négatives des paramètres, inférieures à 25, % des paramètres nominaux, entraînent une dynamique de tangage instable dans le système en boucle fermée. Cela peut s'expliquer par la réduction des valeurs d'inertie dans cet axe qui introduit une dynamique oscillatoire caractérisée par de faibles coefficients d'amortissement. Dans ce cas, les paramètres MFC conçus ne peuvent pas contrôler précisément cette dynamique d'oscillation élevée.
- (ii) Les variations positives des paramètres, comme l'augmentation de la masse, ont conduit à la saturation des rotations de l'hélice au début des simulations. Les propriétés d'adaptabilité du MFC sont efficaces lorsque les actionneurs du système ne sont pas saturés. Par conséquent, une dynamique instable résulte des contraintes physiques du système qui empêchent le contrôleur de pouvoir ajuster correctement ses commandes.
- (iii) Le comportement en altitude a été peu affecté par les variations des paramètres internes du système.

On peut conclure de cette analyse que les algorithmes MFC et leurs caractéristiques d'adaptabilité ont pu stabiliser la dynamique du DarkO pour des variations entre $-25\,\%$ et $+75\,\%$ des paramètres nominaux du DarkO.

▶ Simulation de vol comparative entre MFC et LQR

La simulation de vol suivante illustre les performances de contrôle fournies par le LQR et par le MFC pendant le vol de transition. Les deux stratégies de contrôle ont été conçues pour stabiliser le MAVion, dont les paramètres sont présentés dans le tableau 7.2. La dynamique du MAVion a été discrétisée à 500 Hz, et la simulation comprend des bruits ajoutés aux capteurs, des erreurs d'estimation d'état et des perturbations du vent de 4 m/s (w_u, w_w), comme on peut le voir sur la figure 7.36e. Les perturbations du vent sont imposées le long des axes x et z afin de perturber la dynamique de tangage, en particulier pendant la phase de vol de transition. Les actionneurs du MAVion étaient saturés : vitesse de l'hélice à 9600 RPM et déflexion des volets à 30°. Ces saturations n'ont pas été atteintes, comme on peut le voir dans les figures 7.36c et 7.36d. La figure 7.36 montre la simulation du vol de transition du vol stationnaire au vol en croisière. La transition a été déclenchée au moyen d'une consigne de vitesse avant, qui est égale à zéro en mode de vol stationnaire.

Le tail-sitter MAV effectue naturellement la transition en fonction des incréments de la consigne de vitesse avant (voir figure 7.36a). Les deux contrôleurs fonctionnent selon ce principe, mais avec de petites différences. Le LQR programmé utilise un algorithme de table de conversion avec des gains prédéfinis. Grâce à cette approche de programmation des gains, les points de consigne de l'angle de tangage sont sélectionnés afin de respecter les conditions du point de compensation qui ont été définies à partir des campagnes en soufflerie. D'autre part, les points de consigne de l'angle de tangage sont calculés dans l'architecture MFC à partir de son bloc de contrôle de la vitesse, comme le montre la figure 7.28. La consigne d'attitude MFC est mise à jour en fonction de l'état actuel du système. Afin de stabiliser la MAV, cette stratégie de contrôle définit en permanence la consigne d'attitude, en tenant compte à la fois des perturbations externes et des changements dans la dynamique du système. Cette structure de contrôle en cascade fournit des propriétés robustes au système contre les perturbations dues au vent de travers.

Dans le domaine de vol stationnaire, l'attitude du MAVion est plus sensible aux perturbations dues au vent de travers (w_u), ce qui explique le comportement de tangage oscillant dans la figure 4.20b. Malgré ces oscillations, les deux contrôleurs ont assuré la stabilité du système pour la variation de l'angle de tangage du vol stationnaire ($\theta = 90°$) au vol en croisière ($\theta \approx 10°$).

Table 7.2: Paramètres du MAVion tail-sitter MAV.

Parameters	Values			SI Units
Mass (m)	0.45			[Kg]
Mean Chord (c)	0.21			[m]
Wingspan (b)	0.42			[m]
Wing Area (S)	0.0882			[m^2]
J_{xx}	0.0036			[Kg m^2]
J_{yy}	0.0036			[Kg m^2]
J_{zz}	0.0072			[Kg m^2]
J_p	3.46e-06			[Kg m^2]
k_f	4.48e-6			[Kg m]
k_m	2.4e-7			[Kg m^2]
C_{d0}	0.1			No units
C_{y0}	0.1			No units
C_l	[0.50;	0.00;	0.00]	No units
C_m	[0.00;	0.50;	0.00]	No units
C_n	[0.00;	0.00;	0.50]	No units

Afin de stabiliser l'ensemble du domaine de vol du MAVion et sa dynamique non linéaire avec des variations paramétriques, la stratégie de contrôle basée sur la synthèse LQR a employé 12 matrices de gain couvrant différents points de fonctionnement dans le vol de transition. D'autre part, les algorithmes MFC n'ont été conçus qu'une seule fois et leurs caractéristiques d'adaptabilité s'attaquent à toute l'enveloppe de vol et aux différentes non-linéarités présentes dans la dynamique du système. Dans le mode du vol en croisière, l'angle de tangage contrôlé par l'approche LQR présente une erreur statique qui pourrait être résolue en concevant une nouvelle synthèse LQR avec des termes d'action intégrales. Cependant, les termes d'action intégrale donneront lieu à un système en boucle fermée LQR plus complexe avec de nouveaux termes à concevoir.

En outre, la stratégie de programmation des gains devra tenir compte de ces nouveaux gains dans la boucle de contrôle de rétroaction. Cette simulation de vol comparative attire l'attention sur le fait que les approches de contrôle basées sur des modèles nécessitent l'utilisation de méthodes de programmation des gains. La variation des coefficients aérodynamiques sur leurs différents domaines de vol et leur dynamique non linéaire sont des raisons pour la mise en œuvre d'une telle méthodologie. Dans ce cas, les gains LQR ont été conçus pour chaque point de fonctionnement linéarisé et l'approche de programmation des gains est utilisée pour les gérer en fonction du domaine de vol correct du tail-sitter MAV. D'autre part, le MFC illustre la simplicité de ses algorithmes de contrôle avec des performances de stabilité et des propriétés efficaces de rejet des perturbations. En outre, les paramètres du MFC peuvent être conçus avec peu de connaissances préalables du système. La section suivante traite de l'analyse de l'approche MFC dans des conditions de vol réelles.

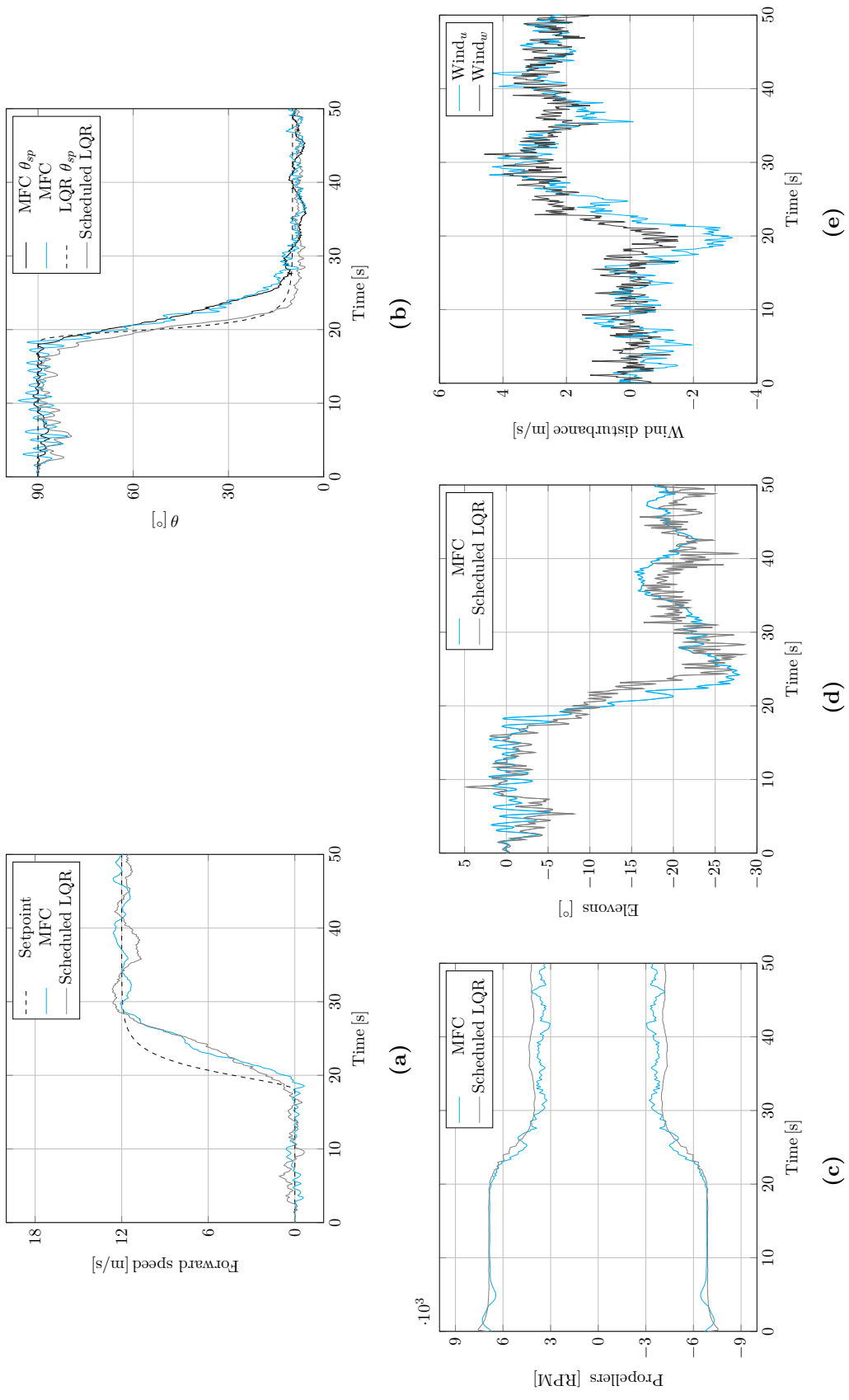

Figure 7.36: Simulation de vol de transition. En haut, de gauche à droite : Trajectoire de vol, vitesse et angle de tangage. En bas : vitesses de rotation des hélices ($\omega_l < 0$ et $\omega_r > 0$) dues au sens de la contre-rotation, déflexions de l'élevon (δ_l et δ_r) convention négative pour cabrer et perturbation du vent le long des axes x et z.

7.5 Validation de la commande sans modèle en essais de vol

Des essais en vol ont été effectués pour évaluer les performances de MFC dans des conditions de vol réelles. Les résultats suivants ont été obtenus lors de vols en intérieur et en extérieur en évaluant les paramètres MFC conçus pour la stabilisation de l'attitude. Les algorithmes MFC qui ont été introduits dans les sections précédentes ont été directement mis en œuvre sur le système de pilotage automatique et les paramètres MFC sont les mêmes que ceux utilisés dans la simulation.

Tout d'abord, des essais de vol en intérieur dans des conditions de vol calme sont réalisés afin de vérifier à la fois le bon fonctionnement des algorithmes MFC et la stabilité de vol du DarkO avec les paramètres MFC utilisés dans les simulations de vol. Ensuite, les résultats de rejet des perturbations MFC sont évalués à partir d'un vol de transition, avec des vents importants qui ont été générés par une soufflerie ouverte. Enfin, des essais de vol en extérieur sont réalisés pour montrer les propriétés de MFC pendant un vol de transition continuellement stabilisé.

7.5.1 Vols en intérieur

Figure 7.37: Dark0 au repos dans l'*ENAC flying arena* montrant deux des seize caméras *Optitrack* en haut et le générateur de vent *WindShape* en arrière-plan.

Les vols intérieurs ont été effectués dans l'*ENAC flying arena* qui présente un volume de vol de 10x10x10 mètres (voir figure 7.37). L'ensemble du domaine de vol est couvert par le système *Optitrack* qui informe l'orientation et la position du tail-sitter MAV. Dans les essais en vol, nous analysons la boucle de contrôle d'attitude en utilisant les caméras *Optitrack* pour les mesures uniquement le cap du tail-sitter MAV. Toute son attitude est calculée à bord à 500 Hz par un algorithme INS qui combine les signaux de l'accéléromètre et du gyroscope. Les points de consigne d'attitude sont définis en externe par le pilote de sécurité à partir d'un émetteur RC. Pour des raisons d'espace limité, l'attitude du DarkO a été principalement évaluée dans le domaine du vol stationnaire. En vol en croisière, le DarkO se déplace à des vitesses relativement rapides, ce qui rend difficile son utilisation dans des zones restreintes. Malgré ces contraintes d'espace, le pilote

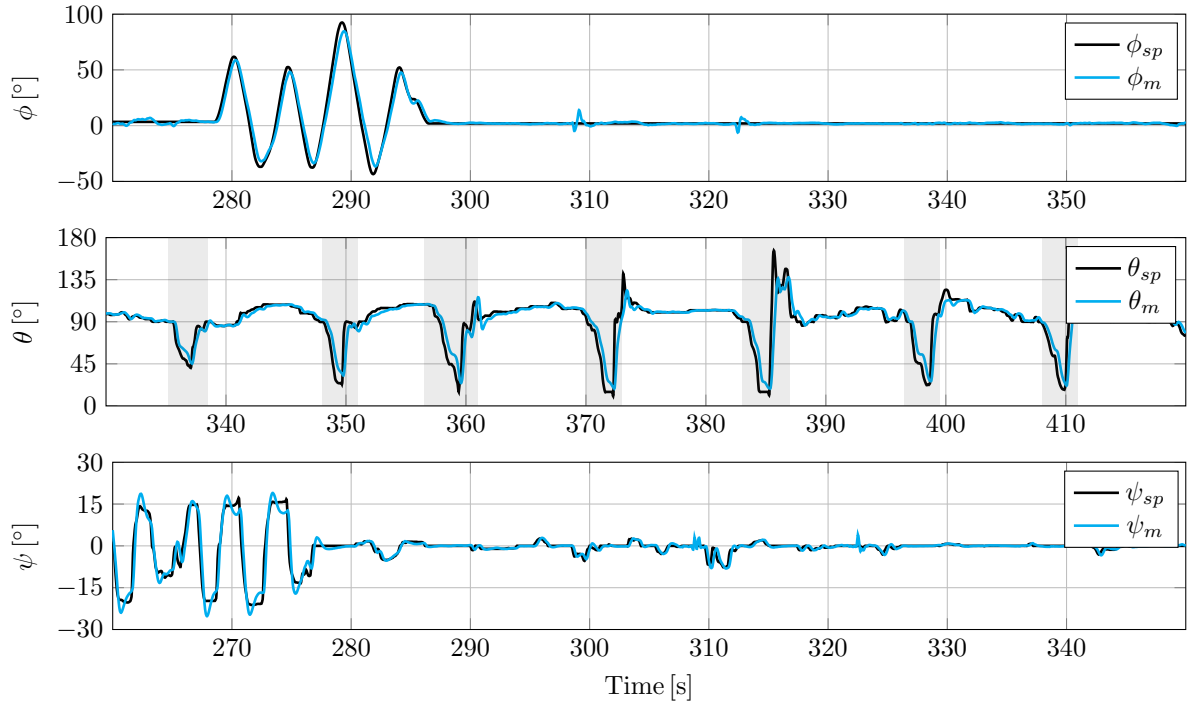

Figure 7.38: Stabilisation de l'attitude pendant les vols en intérieur.

de sécurité a imposé des vols de transition rapides afin d'évaluer les performances du contrôleur aux variations importantes de l'angle de tangage (voir figure 7.38). Le premier test conclut que l'approche MFC réalisée en simulation est capable de stabiliser le DarkO dans les domaines de vol stationnaire et de transition en intérieur. De plus, les vols de transition rapide induisent des variations significatives des forces et des moments aérodynamiques, qui sont correctement estimées et stabilisées par les propriétés adaptatives de l'approche MFC. C'est une caractéristique particulièrement puissante de cette approche de contrôle qui adapte sa commande pour suivre la dynamique souhaitée, même si le système contrôlé présente des variations de ses paramètres internes. Dans le cas des tail-sitter MAVs, les variations des coefficients aérodynamiques.

La figure 7.39 illustre le DarkO pendant un vol de transition particulier face à la soufflerie ouverte *WindShape*. Le comportement de l'attitude du DarkO pendant ce deuxième test de vol en intérieur est présenté dans la figure 7.40. Le DarkO démarre l'expérience en vol stationnaire face à la soufflerie, le point de consigne de l'angle de tangage a été imposé par le pilote de sécurité afin d'effectuer la transition du vol stationnaire vers le vol en croisière, suite à l'augmentation de la vitesse du vent de zéro à $9\,m/s$, le tail-sitter MAV effectue la transition. L'utilisation du *WindShape* permet l'analyse d'un vol de transition continu dans une zone de vol restreinte.

Les vitesses du vent générées par le *WindShape* créent des conditions de vol turbulantes autour du DarkO, ce qui affecte directement la dynamique de son attitude. La zone ombrée met en évidence la phase de vol où l'angle de tangage diminue à l'approche du vol en croisière, ainsi que le phase de vol où le vent a été augmenté. Malgré ces perturbations, le DarkO est resté stable. Par conséquent, la réactivité de la commande MFC s'est faite remarquer grâce à ses propriétés de rejet des perturbations. Des oscillations de roulis peuvent être observées à 100 secondes de vol avec une amplitude maximale de 8°. Ce comportement de roulis se produit dans le domaine du

Figure 7.39: DarkO face à la soufflerie ouverte *WindShape*.

vol où les pertubations sont intenses. Les performances du DarkO, en particulier sa dynamique de roulis, pourraient être optimisées en réduisant la fenêtre d'intégration de l'estimateur MFC qui fournira une plus grande réactivité au système. Toutefois, le compromis entre des estimations rapides avec une réactivité rapide en boucle fermée de l'MFC et une atténuation efficace du bruit semble approprié dans des conditions de vol calme sans vent, comme observé lors du précédent

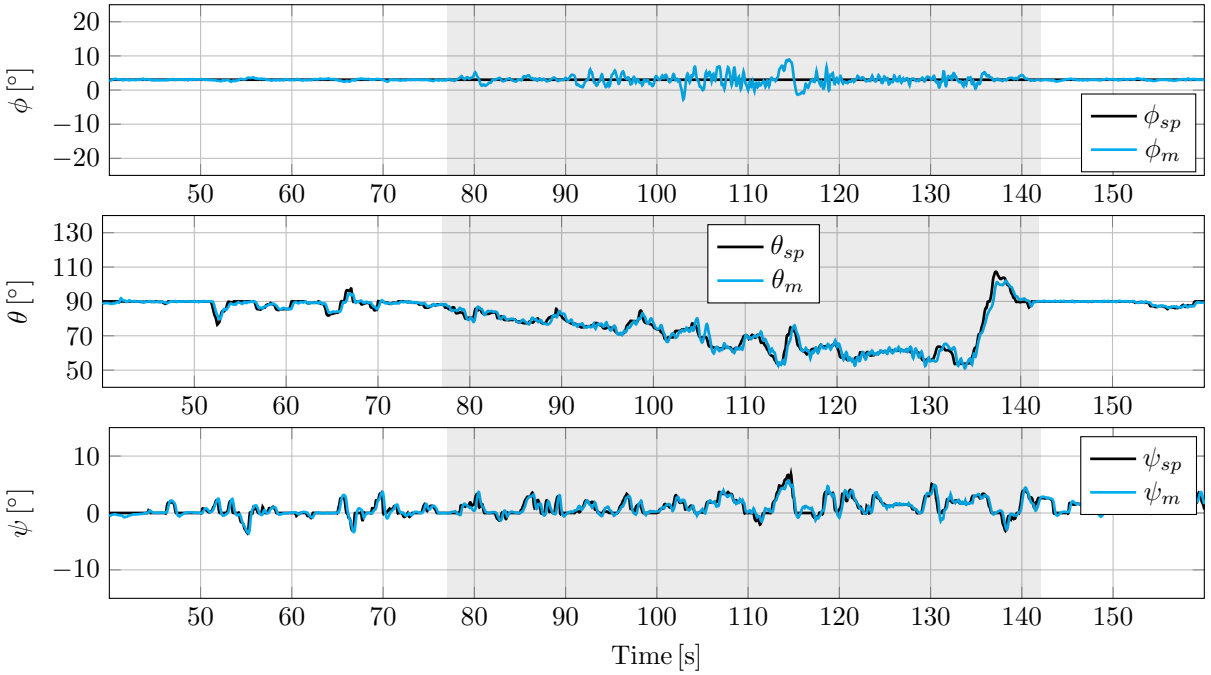

Figure 7.40: Essai en vol de transition à l'intérieur, face au *WindShape*.

essai en vol. C'est pourquoi les performances du système MFC et ses propriétés de rejet des perturbations seront évaluées dans des conditions de vol extérieures avec les mêmes paramètres MFC qui ont été utilisés dans les essais en vol à l'intérieur.

7.5.2 Vols en extérieur

Des essais de vol en extérieur ont été effectués dans l'installation d'essais en vol du Club Eole présentée dans la figure 7.41. L'installation d'essai en vol nous permet d'évaluer toutes les phases de vol du tail-sitter sans limite d'espace. Le DarkO a été équipé d'un magnétomètre pour mesurer son cap actuel par rapport aux pôles magnétiques de la terre. Comme pour les essais de vol à l'intérieur, toute l'attitude l'appareil est calculée à bord à 500 Hz par un algorithme qui combine les signaux de l'accéléromètre et du gyroscope. Enfin, les points de consigne d'attitude sont fixés à l'extérieur par le pilote de sécurité à partir d'un émetteur RC.

La figure 7.42 montre le comportement du DarkO pendant le test de vol en extérieur. L'objectif de ce test de vol était d'évaluer les performances de la boucle de contrôle d'attitude MFC dans des conditions de vol extérieures, en particulier la phase de vol de transition, et de comparer ses résultats avec ceux obtenus dans des conditions de vol intérieures venteuses. Pour ce test en vol extérieur, le tail-sitter MAV a couvert les domaines de vol stationnaire, de transition et en croisière. Le DarkO a commencé son premier test de vol en phase stationnaire et, en fonction des points de consigne de l'angle de tangage, différents vols de transition ont été effectués. La stabilisation détaillée de l'angle de tangage est illustrée sur la figure 7.43, à la fois pour les transitions du vol stationnaire vers le vol en croisière et du vol en croisière vers le vol stationnaire. Le MFC a assuré des vols de transition fluides, continus et stabilisés. Les oscillations de roulis mises en évidence lors de l'essai de vol en intérieur n'ont pas été observées lors de l'essai de vol en extérieur, bien que les mêmes paramètres MFC aient été utilisés. Toute l'enveloppe de vol du DarkO a été stabilisée avec un paramètre d'efficacité de contrôle linéaire constant λ dans l'architecture MFC. Ce paramètre n'est pas estimé pendant le vol. Cependant, l'estimateur $\hat{F}$ adapte la commande en boucle fermée MFC en fonction de l'efficacité de contrôle

Figure 7.41: Club Eole (GPS 43°27'45"N, 001°16'25"E) zone d'essai en vol extérieure.

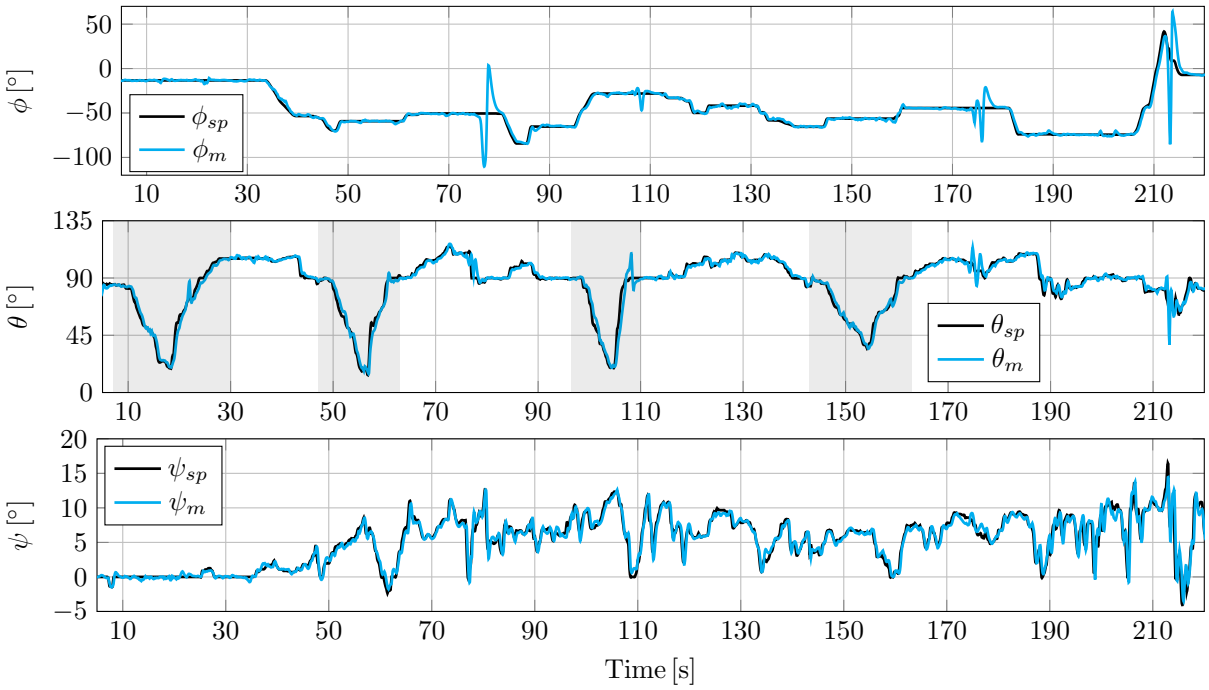

Figure 7.42: Stabilisation de l'attitude lors d'un test de vol en extérieur.

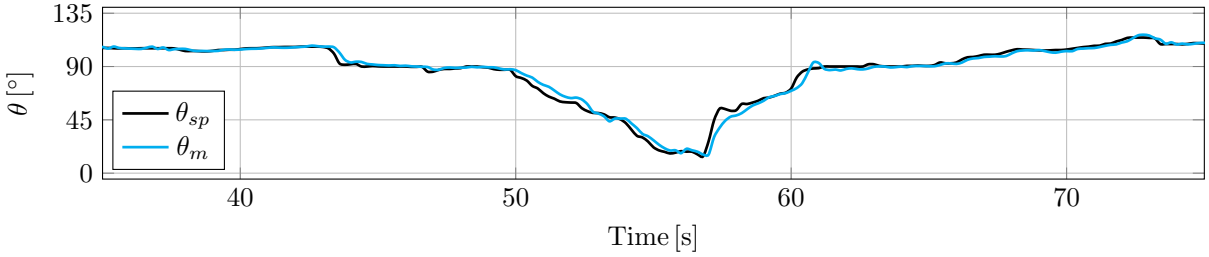

Figure 7.43: Angle de tangage pour $t \in [35; 75]$ secondes lors d'un test de vol en extérieur.

actuelle du système, dont on connait la différente en vol stationnaire et en vol en croisière. Par conséquent, l'ensemble du domaine de vol d'un tail-sitter MAV peut être stabilisé avec un seul ensemble de paramètres MFC.

7.6 Conclusion et travaux futurs

Cette section est un aperçu général des principales contributions de cette thèse, bien que tout au long de ce manuscrit la majorité des résultats aient été discutés et évalués. Au-delà des contributions de cette thèse, qui portait sur la conception d'algorithmes de contrôle pour les tail-sitter MAVs, nous présentons les limites scientifiques et techniques d'une telle approche de contrôle qui n'ont pu être résolues au cours de cette étude. Enfin, nous présentons des orientations pour les travaux futurs sur la conception de systèmes de pilotage automatique pour les missions de vol autonome avec tail-sitter MAVs.

▶ Contributions de cette thèse

Dans cette thèse, la dynamique hautement non linéaire et instable des tail-sitter MAVs a été étudiée numériquement et expérimentalement. Le premier objectif est d'estimer et de contrôler la variation rapide des forces et moments aérodynamiques liés aux phases de vol de transition des tail-sitter MAVs. Le second est de stabiliser les variations dynamiques présentes dans leur large enveloppe de vol. L'intention est de concevoir un système de pilotage automatique efficace qui nécessite peu de connaissances préalables de la dynamique contrôlée afin d'effectuer des missions de vol autonomes.

La première contribution de cette thèse est liée au chapitre 2, dans lequel nous abordons non seulement la revue de la littérature de modélisation des tail-sitter MAVs et les défis impliquant l'identification de leurs effets aérodynamiques, mais aussi le problème actuel de la conception des lois de contrôle sur ce système incertain et variable dans le temps. À l'aide de la revue de la littérature sur le contrôle, nous présentons les avantages et les inconvénients des contrôleurs basés sur un modèle. Par exemple, les propriétés des lois de contrôle optimales, qui peuvent être conçues à partir de modèles dynamiques, ont été mises en évidence. Bien que la théorie du contrôle optimal offre une marge de stabilité même si le modèle dynamique comporte des inexactitudes, les performances fournies par les contrôleurs lors des essais en vol avec les tail-sitter MAVs peuvent différer de celles définies dans le processus de conception du contrôle. Cela peut s'expliquer par le fait que les modèles dynamiques des tail-sitter MAVs sont difficiles à caractériser et que leurs coefficients aérodynamiques sont coûteux et longs à identifier. Ainsi, leurs modèles dynamiques sont souvent simplifiés à des fins de conception de contrôle et, dans la plupart des cas, la dynamique simplifiée ne décrit pas leur dynamique réelle.

En outre, la revue de la littérature sur le contrôle met en évidence que la mise en œuvre de contrôleurs qui ne sont pas basés sur des modèles dynamiques reste à explorer dans le domaine des tail-sitter MAVs (voir §2.2). Néanmoins, il est vrai que l'apport principal de cette thèse est la mise en place d'une loi de contrôle pour les tail-sitter MAVs, dont la conception du contrôle nécessite peu de connaissances préalables de la dynamique du système et aucune connaissance de ses paramètres. Les algorithmes MFC proposés par (Fliess und Join, 2013) ont été conçus afin de relever ce défi. Sur la base de ces algorithmes de contrôle, nous avons développé une architecture de contrôle complète pour le suivi des trajectoires, le contrôle de la vitesse et la stabilisation de l'attitude. L'architecture proposée MFC a été analysée par le biais de simulations de vol afin de valider les interactions entre ses blocs de contrôle pour différents domaines de vol couvrant l'ensemble du domaine de vol des tail-sitter MAVs (voir chapitre 4). Ensuite, grâce à des essais en vol, nous avons évalué les blocs de stabilisation d'attitude MFC lors de vols en intérieur et en extérieur (voir chapitre 5).

Les résultats des simulations en vol ont montré une performance efficace pour le suivi des trajectoires, le contrôle de la vitesse et la stabilisation de l'attitude sans méthodes de programmation des gains, ce qui est la technique de contrôle la plus utilisée dans ce contexte. Ainsi, les variations de la dynamique du tail-sitter MAV ont été estimées et contrôlées uniquement par les propriétés adaptatives des algorithmes MFC. Afin d'évaluer ces propriétés de manière plus détaillée, une analyse des variations des paramètres a été réalisée en utilisant l'approche de Monte Carlo (voir §4.3.4). Les algorithmes MFC ont démontré une capacité à stabiliser le système pour des variations importantes de ses paramètres internes. Ces variations se situent entre -25% et $+75\%$ des paramètres nominaux du système. Afin de comparer les techniques de contrôle basées sur un modèle et celles sans modèle, un LQR a été conçu et comparé à notre

approche de contrôle (voir §4.4). Pour des scénarios identiques, les deux contrôleurs ont assuré la stabilité du tail-sitter MAV dans la phase de vol de transition avec des perturbations de vent simulées. Les performances des contrôleurs étaient à peu près similaires, mais l'avantage de l'approche MFC a été mis en évidence lors de la conception du contrôle. En effet, les paramètres MFC ont été conçus une seule fois pour l'ensemble du domaine de vol du tail-sitter MAV, tandis que les gains LQR ont été synthétisés à plusieurs reprises pour couvrir onze sous-modèles linéarisés dans le domaine de vol en transition. Même s'ils sont théoriquement performants, les algorithmes de contrôle de vol n'ont d'utilité pratique que s'ils sont validés par des vols expérimentaux. Ce point a été analysé lors d'essais en vol, au cours desquels les algorithmes MFC ont été conçus pour stabiliser l'attitude du tail-sitter MAV dans des conditions de vol en intérieur et en extérieur. Les performances de stabilisation de l'attitude obtenues avec les algorithmes MFC lors des simulations en vol ont été validées cette fois-ci par des expériences en vol réel. Des essais supplémentaires de vol en intérieur ont été effectués afin de comparer les performances de MFC avec celles du contrôleur INDI (voir §5.3).

Pendant l'essai en vol, l'approche MFC a montré une meilleure performance de contrôle sur l'INDI. De plus, le contrôleur de l'INDI exige l'identification de l'efficacité des commandes de l'actionneur pour les phases de vol en stationnaire et en croisière. L'efficacité de contrôle des actionneurs est ensuite gérée par une technique de programmation des gains afin d'adapter leurs valeurs à l'ensemble du domaine de vol, ce qui implique la conception et la mise en œuvre d'algorithmes supplémentaires sur les microprocesseurs. D'autre part, l'approche MFC adapte leur boucle fermée grâce à son estimateur, qui est conçu pour l'ensemble du domaine de vol. Les algorithmes MFC peuvent être facilement mis en œuvre sans avoir recours à des méthodes d'ordonnancement des gains. Ainsi, on peut conclure que les algorithmes MFC ont été conçus pour la première fois pour les tail-sitter MAVs, offrant des performances de contrôle similaires par rapport à celles basée sur le modèle (LQR) et non linéaire, dépendant moins du modèle (INDI). Toutefois, la conception MFC réduit le temps et les coûts en contournant la nécessité d'identifier des modèles dynamiques, et ses équations récursives peuvent être facilement mises en œuvre sur des microprocesseurs.

Dans le domaine de la modélisation du tail-sitter MAV pour la conception de contrôle, les questions sur l'identification des paramètres peuvent perdre de leur importance si le besoin d'un modèle mathématique précis diminue. Ce point présente les nouveautés qui peuvent être améliorées afin de devenir des *routines du futur*. Par exemple, les efforts déployés pour étudier les questions de robustesse, en ce qui concerne la "mauvaise" modélisation et/ou les perturbations, peuvent être considérés comme obsolètes et donc moins importants (Fliess und Join, 2013).

▶ Limites de cette étude

Malgré le fait que l'architecture de contrôle proposée ait montré des performances efficaces tant lors des simulations de vol que des essais en vol, elle présente certaines limites. Plus précisément, la conception des paramètres MFC. Dans une autre perspective que celle utilisée pour la conception des contrôleurs classiques basés sur des modèles, la conception des MFC n'est pas établie sur la base de modèles dynamiques. Afin d'obtenir des informations sur la dynamique contrôlée, la boucle fermée MFC utilise un estimateur basé sur des algorithmes de différenciation numérique. L'entrée de l'estimateur est la commande du système et la mesure du signal contrôlé, qui est perturbée par le bruit. Cette perturbation peut affecter directement la performance du contrôleur, en particulier à haute fréquence. On peut remarquer qu'au-delà des

connaissances requises en matière de dynamique de vol et de la théorie du contrôle, la conception des algorithmes de l'estimateur MFC pour les anticouple MAV nécessite une certaine expertise technique en matière de traitement du signal afin de synthétiser les paramètres de l'estimateur MFC. Ainsi, il faut non seulement répondre aux besoins de contrôle, mais aussi aux besoins de filtrage et d'estimation.

▶ Travaux futurs

Étant donné que le développement de systèmes de vol autonomes concerne différents domaines de l'ingénierie, ce projet de recherche offre plusieurs possibilités d'amélioration dans le domaine du contrôle, de l'estimation et du traitement des signaux, entre autres. Cependant, nous concentrons la liste des priorités pour les travaux futurs impliquant le contrôle des tail-sitter MAVs en vue de réaliser des systèmes de vol autonomes comme ce qui suit :

Premièrement, les approches MFC et INDI devraient être comparées par des simulations de vol afin de consolider les avantages et palier aux inconvénients de chacune pour des scénarios égaux dans un environnement contrôlé. On remarque que l'utilisation de mesures d'accélération angulaire dans la boucle fermée de stabilisation de l'attitude améliore la réactivité de la commande. Il est vrai que la stabilisation d'attitude MFC basée sur des mesures d'angle a démontré une performance similaire par rapport à celle de INDI, qui est établie sur la base de mesures d'accélération angulaire. Pour ces raisons, la mise en œuvre des algorithmes MFC de stabilisation de l'attitude du tail-sitter MAV, basés sur des mesures d'accélérations angulaires, serait d'une grande pertinence pour les communautés du contrôle et de l'aérospatiale. En outre, les trajectoires de vol plus agressives nécessitent une représentation d'attitude avec des quaternions afin d'éviter les singularités, mais leur inconvénient est qu'elles n'ont pas de représentation intuitive.

Deuxièmement, il serait intéressant de procéder à une évaluation approfondie des propriétés d'adaptation de l'approche MFC par le biais d'un plus grand nombre d'essais en vol. Nous avons présenté une analyse numérique mettant en évidence ces propriétés potentielles de l'MFC par la méthode de Monte Carlo. Dans cette analyse, la stratégie de contrôle proposée a assuré la stabilité du tail-sitter MAV pour des variations comprises entre -25% et $+75\%$ de ses paramètres nominaux. En outre, la validation de ces résultats préliminaires par des essais en vol constituerait certainement une contribution importante pour la communauté des automaticiens. Par conséquent, un travail intéressant serait l'analyse de la stabilité d'une flotte de tail-sitter MAV de tailles, de géométries et de modèles aérodynamiques différents, en utilisant les mêmes paramètres MFC conçus. Par exemple, une première approche pourrait être réalisée avec les configurations de tail-sitter MAV modulaires présentées dans la figure 7.44, dans lesquelles leurs

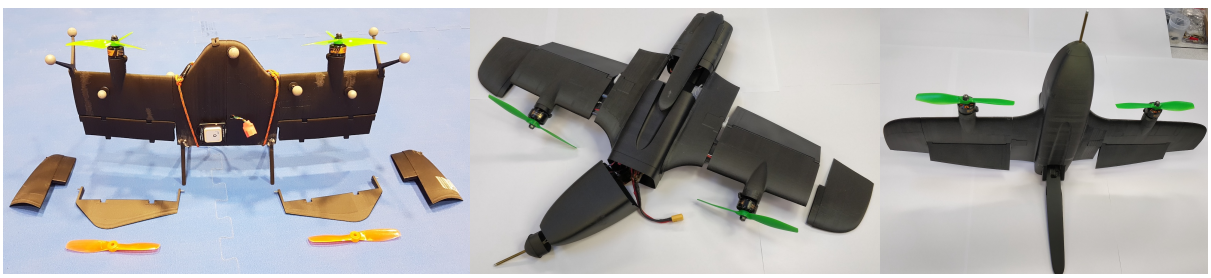

Figure 7.44: Tail-sitter MAVs modulaires conçus à l'ENAC UAV Lab (Bronz u. a., 2020).

structures peuvent être facilement modifiées. Des travaux futurs pourraient être menés en vue de la mise au point d'algorithmes de guidage pour les tail-sitter MAVs. Afin de gérer correctement leurs trajectoires de vol et de maximiser leurs contributions dans les missions de vol autonome, le contrôle des positions et des vitesses est essentiel. À ce sujet, ce travail a présenté des simulations de vol dans lesquelles les algorithmes MFC ont démontré de robustes propriétés de rejet des perturbations pour le suivi des positions. Cependant, il serait également intéressant de valider ces propriétés MFC dans des conditions de vol réelles. Malgré le principe connu de l'architecture de contrôle, les algorithmes MFC en cascade nécessitent des recherches plus approfondies. En effet, l'interaction entre les blocs de contrôle de position et de vitesse reste à analyser dans des environnements de vol réels.

Appendix A

Main Publications

"*Research teaches a man to admit he is wrong and to be proud of the fact that he does so, rather than try with all his energy to defend an unsound plan because he is afraid that admission of error is a confession of weakness when rather it is a sign of strength.*."
— H.E. Stocher

This appendix presents the main scientific contributions developed during this thesis, which have been published in international journals and conferences.

Contents

A.1 International Journal of Micro Air Vehicles

Barth, J. M. O., Condomines, J.-P., Bronz, M., Moschetta, J.-M., Join, C., and Fliess, M., "Model-free control algorithms for micro air vehicles with transitioning flight capabilities," *International Journal of Micro Air Vehicles (IJMAV)*, 12:1-22, April 2020. doi: https://doi.org/10.1177/1756829320914264

Review

International Journal of Micro Air Vehicles

International Journal of Micro Air Vehicles
Volume 12: 1–22

DOI: 10.1177/1756829320914264
journals.sagepub.com/home/mav
SAGE

Model-free control algorithms for micro air vehicles with transitioning flight capabilities

Jacson MO Barth[1], Jean-Philippe Condomines[1], Murat Bronz[1], Jean-Marc Moschetta[2], Cédric Join[3,4] and Michel Fliess[4,5]

Abstract

Micro air vehicles with transitioning flight capabilities, or simply hybrid micro air vehicles, combine the beneficial features of fixed-wing configurations, in terms of endurance, with vertical take-off and landing capabilities of rotorcrafts to perform five different flight phases during typical missions, such as vertical takeoff, transitioning flight, forward flight, hovering and vertical landing. This promising micro air vehicle class has a wider flight envelope than conventional micro air vehicles, which implies new challenges for both control community and aerodynamic designers. One of the major challenges of hybrid micro air vehicles is the fast variation of aerodynamic forces and moments during the transition flight phase which is difficult to model accurately. To overcome this problem, we propose a flight control architecture that estimates and counteracts in real-time these fast dynamics with an intelligent feedback controller. The proposed flight controller is designed to stabilize the hybrid micro air vehicle attitude as well as its velocity and position during all flight phases. By using model-free control algorithms, the proposed flight control architecture bypasses the need for a precise hybrid micro air vehicle model that is costly and time consuming to obtain. A comprehensive set of flight simulations covering the entire flight envelope of tailsitter micro air vehicles is presented. Finally, real-world flight tests were conducted to compare the model-free control performance to that of the Incremental Nonlinear Dynamic Inversion controller, which has been applied to a variety of aircraft providing effective flight performances.

Keywords

MAV with transitioning flight capabilities, hybrid MAVs, control system architecture, flight control, model-free control

Date received: 26 April 2019; Revised 6 December 2019; accepted: 13 February 2020

Introduction

Micro air vehicles (MAVs) with transitioning flight capabilities, or simply hybrid MAVs, operate over a wide flight envelope including different flight phases, such as vertical take-off, efficient forward flight, transitioning flights, hovering and vertical landing, see Figure 1. While this complete flight envelope enlarges the application range of MAVs, new aerodynamics optimization approaches must be developed to improve the MAV flight performance, considering the aerodynamics challenges of each flight domain. Furthermore, the autopilot system must ensure the stability and the tracking of trajectories for all these flight domains which results in a higher degree of challenge and complexity also for the guidance, navigation, and control community. Different hybrid MAV configurations such as tilt-rotors[1] or tilt-wings,[2] quadplanes,[3] and tilt-body or tailsitter[4] can be found in literature.

[1]ENAC, Université de Toulouse, Toulouse, France
[2]Department of Aerodynamics, Energetics and Propulsion, ISAE-Supaero, Toulouse, France
[3]CRAN, Université de Lorraine, Vandœuvre-lès-Nancy, France
[4]AL.I.E.N (ALgèbre pour Identification & Estimation Numérique), Vézelise, France
[5]LIX, École Polytechnique, Palaiseau, France

Corresponding author:
Jacson MO Barth, UAV Systems Group, ENAC, Université de Toulouse, France.
Email: jacson-miguel.olszanecki-barth@enac.fr

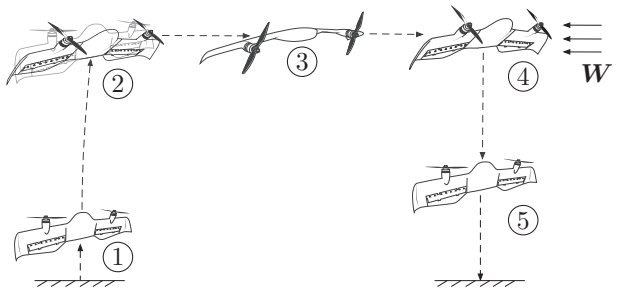

Figure 1. Typical flight phases of micro air vehicles with transitioning flight capabilities: 1 – Vertical take-off; 2 – Transition; 3 – Forward flight; 4 – Hover flight; 5 – Vertical landing. The vector ***W*** represents the wind disturbances.

These platforms have been designed in order to solve the aerodynamics and mechanical limitations of each of them, and the choice of the appropriated MAV configuration varies according to the imposed flight mission specifications, e.g., maximum payload, the desired endurance and range, etc. Generally, hybrid MAVs are designed and optimized to perform an efficient forward flight, since this flight phase represents most of its mission. Various studies have improved and assessed the aerodynamic properties of hybrid MAVs previously.[5,6] A critical point is the design of flap effectiveness which needs to be optimized in order to create sufficient pitch moment ensuring the control authority during transitioning flights. We focus this research project in the design and control of tailsitter MAVs, and we investigate the performance of this peculiar MAV class for three reasons: (1) Tailsitters have a better endurance in forward flight when compared to other configurations of hybrid MAVs; (2) The simple transition mechanism of tailsitters facilitates the control design for its entire flight envelope, unlike to tiltrotors that need additional actuators to orient the propeller in order to perform transitioning flights; (3) The design of controllers requiring little prior knowledge of the dynamics of tailsitter MAVs remains an attractive, motivating and challenging topic that needs to be answered by the control community. Typically, the entire flight envelope of tailsitter MAVs can be analyzed in three distinct flight modes, namely, hovering flight, forward flight and transitioning flight. The stabilization of hovering and forward flights can be achieved using linearized models around an equilibrium point facilitating the implementation of classical linear control algorithms. On the other hand, transitioning flights present some peculiarities that include fast changing of aerodynamic forces and moments with wing behaviors partially stalled. Based on such aerodynamic effects, the identification of a reliable model that accurately represents the nonlinear dynamics of a tailsitter MAV over its entire flight envelope remains an expensive, a time consuming and a difficult task. Because of these practical problems related to the characterization of a model for the design of model-based controllers, some research works considered the transition flight as an undesirable and transient flight phase. However, transitioning flights need to be continuously stabilized in order to ensure a smooth and safe flight, especially for flying missions in windy environments. Hybrid MAVs are often considered by the control community as a parameter varying system, e.g. the change of aerodynamic coefficients according to the hybrid MAV attitude orientation and the environmental wind conditions. Consequently, designing a control technique for autopilot systems that does not rely on prior knowledge of the hybrid MAV model becomes an intuitive, innovative and, from the point of view of the authors, an appropriate control methodology. Therefore, the development of such a controller that estimates the hybrid MAV dynamics and counteracts it, in real time, can be easily adaptable and implemented for different hybrid MAVs.

Literature review

Different control strategies have been designed for hybrid MAVs; we present some of them in the following with particular emphasis in the controllers developed for the tailsitter class. For practical reasons, classical linear controllers designed using PID techniques have been applied in the control of hybrid MAVs.[7–11] Although simple to tune without the knowledge of the controlled system, PID controllers have insufficient robustness properties against wind disturbances. Autopilot systems designed from optimal control theory, have been researched.[12,13] For instance, the linear quadratic regulator which was designed and applied for a tailsitter MAV previously modeled and identified from wind tunnel campaign.[14] However, the performance of model-based controllers may differ primarily in the fidelity with which the plant is modeled and the accuracy of the identified model parameters. Hence, classical model-based control techniques seem to be neither optimal for hybrid MAVs nor easily transposable for a new platform. Gain scheduling methods employing different control algorithms with both linear[15] and nonlinear approaches,[16] have been developed to stabilize hybrid MAVs at different pitch angle orientations within the transitioning flight. Gain scheduling techniques allow easy understanding and simple implementation of the control gains that cover the entire flight envelope of hybrid MAVs. However, the principal disadvantage of this control method, found in literature,[17] is the expensive computational

cost for operations in real time. In the same way, an attitude controller based on optimal control algorithms was proposed by Ritz and Andrea,[18] different control solutions for a set of attitude errors were precomputed and stored in a lookup table. According to the current flight conditions and for each autopilot system update, the desired control gains are obtained by reading their predefined values in the table. Further analysis is needed to determine if this proposed control strategy can be effective and easily adaptable for different hybrid MAVs. Adaptive control techniques which account for uncertainties present in the hybrid MAV model were developed by some authors.[19,20] However, instability problems with adaptive control methods can still exist with regard to unmodeled dynamics or inaccurate models used in the adaptation criterion of controller's gains. Different research topics applying nonlinear control techniques on hybrid MAVs, such as backstepping,[19,21,22] NDI[20,23,24] and INDI,[25] appears to be positively researched in literature. The INDI approach, which is a control that depends less on the model, was experimentally flight tested providing excellent performance against wind disturbances. This controller requires the identification of the system actuator behavior in order to estimate its control effectiveness. As the actuator's effectiveness varies according to the flight phase, e.g. hovering or forward flight, a gain scheduling method was implemented to fit the actuator effectiveness under the respective flight domain. Some theoretical research has analyzed the performance of nonlinear feedback control on axisymmetric aerial vehicles[26] proposing an extended control solution to a larger set of generic aerodynamic models[27] which could include hybrid MAVs. Additionally, a variety of nonlinear control strategies based on Lyapunov's stability concepts have been designed to hybrid MAVs.[4,28]

Links with the model-free control algorithm

The literature presents some particular control algorithms that do not rely on modeling. For instance, the model-free control (MFC) approach proposed by Fliess and Join[29] has been successfully illustrated in different concrete case-studies varying from wastewater denitrification,[30] nanopositioning of piezoelectric systems[31] up to inflammation resolution in biomedical applications,[32] see also its references for additional case-study examples and supplementary information. Some research works based on MFC techniques have led to patents, such as Join et al.[33] and Abouaïssa et al.[34] This control approach has been applied in the aerospace field[35,36] and, except for our previous work, it has never been applied on hybrid MAVs which is an additional motivation for the development of our research project. The advantage of the control methodology proposed in this paper is the capability to estimate the hybrid MAV dynamics, without a prior knowledge of its parameters, only from its output and input-control signal measurements. Thus, the disturbances that may affect flight performances are measured and the MFC algorithms are able to estimate as well as counteract the undesirable dynamics in order to continuously stabilize the hybrid MAV for arbitrary attitude orientations covering its entire flight envelope.

Present work

The main contribution of our current work is to develop a fully autonomous MAV with transitioning flight capabilities that performs a given mission accurately. Depending upon the mission complexity and its requirements, the MAV should fly at low and high air speeds, respectively corresponding to hovering and forward flight phase. Based on these mission requirements, and the modeling issue presented in the previous section involving this particular MAV class, we present a part of our previous work that deals with:

(i) comparison between a model-based controller and our MFC architecture during the transition flight in a disturbed environment;[37]
(ii) uncertain parameter analysis of fixed-wing MAVs in forward flight;[38]
(iii) full MFC architecture for position tracking, velocity control and attitude stabilization of a hybrid MAV during its entire flight envelope;[39]

Our intention is to analyze our control architecture through additional flight simulations and real-world flight tests in order to investigate its operational behavior, its limits and the interaction between each MFC control block. The new contributions of this paper, with respect to our previous works, are:

(i) initial condition analysis during hovering and transitioning flight phases in order to empirically determine a safe and stable boundary for distinguished initial conditions of attitudes and velocities;
(ii) control performance analysis in the frequency domain during hovering and forward flights;
(iii) study of MFC's adaptive properties for parametric variation illustrations during the forward-to-hover transition through flight simulations;
(iv) real-world flight tests to compare the MFC attitude stabilization performance to that of the INDI controller in indoor flight conditions;

The paper is organised as follows: in the next section, we present the manufacturing process and the particular aerodynamics of the hybrid MAV prototype named DarkO. Then, we describe the hybrid MAV behavior from a mathematical formulation based on equations of motion. This is followed by a section in which the control strategy is detailed as well as the proposed control architecture. Flight simulations are presented then and real-world flight tests follow. Finally, the reader can find the conclusion and the future work.

Hybrid MAV prototype

Throughout the whole study, we have used the DarkO vehicle which is a tailsitter configuration consisting of two motors, positioned in front of the wing, and two exceptionally large double-flapped control surfaces. Mission definition of DarkO has been mainly optimized for forward flight with the capability of taking off and landing vertically. Therefore, it has not been particularly designed for hovering for long duration.

Manufacturing

The DarkO's frame is completely manufactured by the 3D printing method using Onyx material. Figure 2 shows the printed pieces that are assembled in order to build the whole frame. The shell structure for the wing and the fuselage halves are manufactured as 0.7 mm thick skins, and the spar is manufactured with the addition of unidirectional concentric carbon fibers embedded into Onyx material. This method ensures to have a sufficiently rigid airframe that supports aerodynamic forces and yet also flexible enough to absorb harsh impacts during landing and test flights.

Control surface design

A particular feature that is required by the tailsitter configuration is to generate excessive amount of pitching moment in order to transition mainly from forward flight phase to hovering flight phase. Therefore, DarkO frame's control surfaces have been designed as double-flap which has a passive mechanical constant ratio. Traditionally, multi-section flaps have been designed for lift enhancement; however, in our case the design objective is to generate as much positive pitching moment as possible without having a massive flow separation on the bottom surface of the airfoil. The advantage of using double-flap (δ_{II}) control surface with respect to using a single-flap (δ_I) control surface has been shown in Figure 3. Variation of the sectional lift C_l, drag C_d, and moment coefficients C_m at different flap deflection angles have been compared for the two different flap configurations. The analysis has been

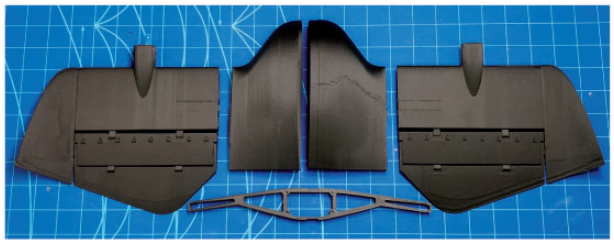

Figure 2. Printed parts of DarkO out of Onyx material.

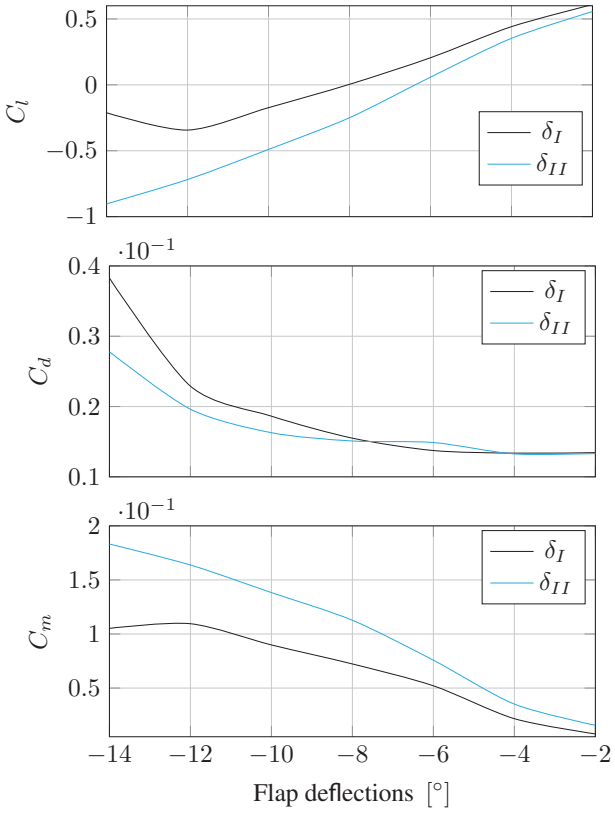

Figure 3. Variation of the sectional lift C_l, drag C_d, and moment coefficients C_m with respect to flap angles for different flap configurations: double-flap (δ_{II}) control surface and a single-flap (δ_I) control surface

done by using the open-source program XFOIL.[40] Reynolds number used during the analysis corresponds to the slipstream velocity seen by the blown portion of wing and is approximately 150k. The DarkO's motor mounts have an incidence angle of –6 degrees on DarkO's wings; therefore, the airfoil has been set to an angle of attack of + 6 degrees and then the flap angle has been varied between –2 and –14 degrees (negative flap angle being upward). Particular attention should be given to the pitching moment C_m in the figure. We notice that double-flap (δ_{II}) control surface

can generate almost two times the pitching moment generated by the single-flap (δ_I) control surface. As a side effect, the double-flap control surface also works efficiently for lift generation; however, as we are trying to increase the pitching moment (in positive direction), the lift generation happens in negative direction. The vehicle requires the excessive amount of pitching moment only during transition phase, and the duration of this maneuver is very short; therefore, lift reduction caused while increasing the pitching moment has not been taken as an issue.

Simplified tailsitter MAV model

This section is divided into two parts. First, we present the mathematical formulation of aerodynamic forces and moments, and the aerodynamic assumptions used in the hybrid MAV model. Then, the equations of motion, based on Newton's second law, are introduced to describe the hybrid MAV behavior. The obtained hybrid MAV dynamics are used to establish a flight simulator in order to analyze the proposed control approach before real-world flight tests.

Formulation of aerodynamic forces and moments

We present an analytic continuous singularity-free formulation of aerodynamic forces $\boldsymbol{F}_{a_b} \in \mathbb{R}^3$ and moments $\boldsymbol{M}_{a_b} \in \mathbb{R}^3$ acting in a wing over a complete 360° angle of attack, based on previous work proposed by Lustosa et al.[41] The wing with a surface S, is immersed in an incompressible and inviscid airflow with air density ρ. The free-stream velocity is composed by the linear element $\boldsymbol{v}_\infty \in \mathbb{R}^3$ and the angular component defined by $\boldsymbol{\omega}_\infty \in \mathbb{R}^3$ which, in the absence of wind, is equal to the hybrid MAV angular velocity $\boldsymbol{\omega_b} \in \mathbb{R}^3$. This formulation of aerodynamic forces and moments is given by

$$\begin{pmatrix} \boldsymbol{F}_{a_b} \\ \boldsymbol{M}_{a_b} \end{pmatrix} = -\frac{1}{2}\rho S \eta C \Phi(\boldsymbol{\eta_b}) C \boldsymbol{\eta_b} \tag{1}$$

where

$$\eta = \sqrt{v_\infty^2 + \mu c^2 \omega_\infty^2}, \quad \text{with} \quad \mu \in \mathbb{R} > 0 \tag{2}$$

and

$$\boldsymbol{\eta_b} = \begin{pmatrix} \boldsymbol{v}_\infty \\ \boldsymbol{\omega}_\infty \end{pmatrix} \tag{3}$$

The vector $\boldsymbol{\eta_b}$ describes the linear and angular free-stream velocities in the body coordinate frame. The matrix C denotes the reference wing parameters in an extended representation

$$C = \begin{pmatrix} I_{3\times3} & 0_{3\times3} \\ 0_{3\times3} & \begin{bmatrix} b & 0 & 0 \\ 0 & c & 0 \\ 0 & 0 & b \end{bmatrix} \end{pmatrix} \tag{4}$$

where b and c are, respectively, the wingspan and the mean chord. Finally, the matrix $\Phi \in \mathbb{R}^{6\times6}$, which is subdivided into four matrices $\Phi^{(\cdot)} \in \mathbb{R}^{3\times3}$, shows the interaction between aerodynamic forces and moments with linear and angular free-stream velocities

$$\Phi = \begin{pmatrix} \Phi^{(fv)} & \Phi^{(fw)} \\ \Phi^{(mv)} & \Phi^{(mw)} \end{pmatrix} \tag{5}$$

The Φ parameters are deduced from thin airfoil theory; we refer the interested reader to Lustosa[42] for further information. Nonetheless, we mention that

$$\Phi_0^{(fv)} = \begin{pmatrix} C_{d0} & 0 & 0 \\ 0 & C_{y0} & 0 \\ 0 & 0 & 2\pi + C_{d0} \end{pmatrix} \tag{6}$$

$$\Phi^{(f\omega)} = \begin{pmatrix} 0 & 0 & 0 \\ 0 & 0 & b^{-1}\Delta r C_{y0} \\ 0 & -c^{-1}\Delta r(2\pi + C_{d0}) & 0 \end{pmatrix} \tag{7}$$

$$\Phi_0^{(mv)} = \begin{pmatrix} 0 & 0 & 0 \\ 0 & 0 & -c^{-1}\Delta r(2\pi + C_{d0}) \\ 0 & b^{-1}\Delta r C_{y0} & 0 \end{pmatrix} \tag{8}$$

$$\Phi^{(m\omega)} = \frac{1}{2}\begin{pmatrix} C_{l_p} & C_{l_q} & C_{l_r} \\ C_{m_p} & C_{m_q} & C_{m_r} \\ C_{n_p} & C_{n_q} & C_{n_r} \end{pmatrix} \tag{9}$$

with C_{d0} the minimal drag coefficient and C_{y0} the minimal side force coefficient. The parameter Δr represents the distance between the center of gravity location and the aerodynamic center (neutral point). The negative values of Δr, according to the defined coordinate system, imply a positive static margin of the hybrid MAV. Finally, C_l, C_m and C_n are the aerodynamic moment coefficients which depend on the angular hybrid MAV velocities (p, q, r). The lift curve slope corresponding to 2π, in equations (6), (7) and (8), was deduced from the thin airfoil theory in 2D.

In this work, we evaluate the lift curve slope in 3D considering the wing aspect ratio (AR). According to Diederich's formula, we consider

$$\Phi_0^{(fv)}(:,3) = \begin{pmatrix} 0 \\ 0 \\ \dfrac{\pi AR}{1+\sqrt{1+(\frac{AR}{2})^2}} + C_{d0} \end{pmatrix} \tag{10}$$

$$\Phi^{(f\omega)}(:,2) = \begin{pmatrix} 0 \\ 0 \\ -c^{-1}\Delta r(\dfrac{\pi AR}{1+\sqrt{1+(\frac{AR}{2})^2}} + C_{d0}) \end{pmatrix} \tag{11}$$

$$\Phi_0^{(mv)}(:,3) = \begin{pmatrix} 0 \\ -c^{-1}\Delta r(\dfrac{\pi AR}{1+\sqrt{1+(\frac{AR}{2})^2}} + C_{d0}) \\ 0 \end{pmatrix} \tag{12}$$

where

$$AR = \frac{b^2}{S} \tag{13}$$

Finally, the flap deflections are modeled as varying cambered airfoils and the aerodynamic forces and moments created by these deflections are approximated by the following equations

$$\Phi^{(fv)}(\delta_i) = \Phi_0^{(fv)}(I - [\boldsymbol{\xi_f}]_\times \delta_i) \tag{14}$$

$$\Phi^{(mv)}(\delta_i) = \Phi_0^{(mv)}(I - [\boldsymbol{\xi_m}]_\times \delta_i) \tag{15}$$

the flap deflection effectiveness is represented by two skew-symmetric matrices, $[\boldsymbol{\xi_f}]_\times$ for the force effectiveness and $[\boldsymbol{\xi_m}]_\times$ for the moment effectiveness, given by

$$[\boldsymbol{\xi_f}]_\times = \begin{bmatrix} 0 & -\xi_f & \xi_f \\ \xi_f & 0 & -\xi_f \\ -\xi_f & \xi_f & 0 \end{bmatrix}$$

$$[\boldsymbol{\xi_m}]_\times = \begin{bmatrix} 0 & -\xi_m & \xi_m \\ \xi_m & 0 & -\xi_m \\ -\xi_m & \xi_m & 0 \end{bmatrix}$$

Equations of motion

The hybrid MAV model is divided into four rigid bodies (two propellers and two wings composing the fuselage) with constant mass (m), represented by 10 states $\boldsymbol{x} = (\boldsymbol{v_b}, \boldsymbol{\omega_b}, \boldsymbol{q})$, where $\boldsymbol{v_b} \in \mathbb{R}^3$ is the vehicle's linear velocity, $\boldsymbol{\omega_b} \in \mathbb{R}^3$ is the vehicle's angular velocity equals to $[p\,q\,r]^T$ both expressed in the body coordinate frame and $\boldsymbol{q} \in \mathbb{R}^4$ is the quaternion formulation. The system is controlled via four control-inputs, $\boldsymbol{u} = (\omega_l, \omega_r, \delta_l, \delta_r)$, respectively, the left and right propeller rotation speeds and the left and right flap deflections, which are represented in Figure 4.

In order to compute the forces and moments caused by the wing–propeller interaction, we define two segments. Each segment is composed of one wing j and one propeller k. Thus, the sum of aerodynamic forces acting on the wing j with the thrust $\boldsymbol{T}_k$ generated by the propeller rotation ω_k and the total moment described in the body coordinate frame, are given by

$$\boldsymbol{F_b} = \sum_{j,k=1}^{2} (\boldsymbol{F}_{a_{b_j}} + \boldsymbol{T}_k) \tag{16}$$

$$\boldsymbol{M_b} = \sum_{j,k=1}^{2} (\boldsymbol{M}_{a_{b_j}} + \boldsymbol{\tau}_{b_k} + \boldsymbol{p_p} \times \boldsymbol{T}_k + \boldsymbol{p_a} \times \boldsymbol{F}_{a_{b_j}}) \tag{17}$$

The vector $\boldsymbol{p_p} = [p_{p_x}\, p_{p_y}\, p_{p_z}]^T$ defines the distance between the propeller k with the hybrid MAV center of mass. Both propellers are positioned symmetrically with respect to the hybrid MAV center of mass. The distance between the aerodynamic center and the center of mass is represented by the vector $\boldsymbol{p_a} = [p_{a_x}\, p_{a_y}\, p_{a_z}]^T$. The internal torque of the propeller $\boldsymbol{\tau}_{b_k}$ that is a

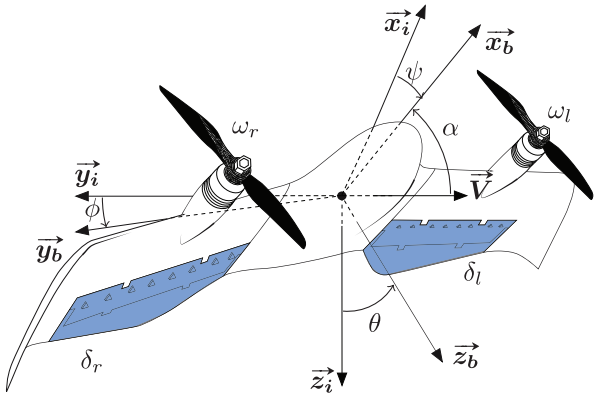

Figure 4. Illustration of the used coordinate frames, angles and actuators. The inertial coordinate frame is represented by $\mathcal{R}_i = \{\vec{x_i}, \vec{y_i}, \vec{z_i}\}$ and the body coordinate frame by $\mathcal{R}_b = \{\vec{x_b}, \vec{y_b}, \vec{z_b}\}$.

function of the vehicle's angular velocity ($p\,q\,r$), and the thrust force $\boldsymbol{T}_k$, are defined by

$$\boldsymbol{T}_k = k_f \omega_k^2 \vec{\boldsymbol{x}_b}, \quad k_f \in \mathbb{R} > 0 \tag{18}$$

$$\boldsymbol{\tau}_{b_k} = \boldsymbol{N}_{b_k} - J_p(p + \omega_j) \begin{pmatrix} 0 \\ r \\ -q \end{pmatrix} \tag{19}$$

where

$$\boldsymbol{N}_{b_k} = -\text{sign}(\omega_k) k_m \omega_k^2 \vec{\boldsymbol{x}_b}, \quad k_m \in \mathbb{R} > 0 \tag{20}$$

with k_f and k_m the propeller force and moment coefficients and $\boldsymbol{N}_{b_k}$ the propeller moment. Equation (19) describes the gyroscopic interaction between the propellers and the fuselage with J_p equals to the propeller inertia. The vehicle's equations of motion are given by equation (21).

$$\begin{cases} m\dot{\boldsymbol{v}} & = R^T \boldsymbol{F_b}(\boldsymbol{x}, \boldsymbol{u}, \boldsymbol{W}) + m\boldsymbol{g} \\ J\dot{\boldsymbol{\omega}}_{\boldsymbol{b}} & = \boldsymbol{M_b}(\boldsymbol{x}, \boldsymbol{u}, \boldsymbol{W}) - [\boldsymbol{\omega_b}]_\times J\boldsymbol{\omega_b} \\ \dot{\boldsymbol{q}} & = \frac{1}{2}\boldsymbol{q} \otimes \boldsymbol{\omega_b} \\ \dot{\boldsymbol{p}} & = \boldsymbol{v} \end{cases} \tag{21}$$

The gravitational acceleration vector is equals to $\boldsymbol{g} = g\vec{\boldsymbol{z_i}}$ and $\boldsymbol{W} \in \mathbb{R}^3$ is the wind disturbance vector. The rotation matrix R, namely the Direction Cosines Matrix (DCM, Note: The DCM can be defined with quaternion formulation.), represents the MAV rotation in three dimensions as a mathematical formulation. We assume that the hybrid MAV inertia matrix J is diagonal and it equals to $J = \text{diag}[J_{xx}\, J_{yy}\, J_{zz}]$. The position vector in the inertial coordinate frame is represented by $\boldsymbol{p} = [x\ y\ z]^T$. The highly maneuverable nature of the vehicle calls for a global numerically stable formulation of attitude and justifies the use of quaternions. The symbol $\otimes$ in the previous equation corresponds to the quaternion product. Supplementary Appendix A presents the tailsitter MAV parameters used in this work.

Control strategy

The proposed control strategy is based on MFC algorithms with no information about the tailsitter MAV parameters (e.g. mass, inertia, aerodynamics coefficients, etc.). This controller can be implemented on multiple-input multiple-output systems by assuming an approximate decoupling between the dynamics of the controlled system. This major assumption has been verified by different practical experiments.[43] Therefore, for simplicity reasons, we present the MFC algorithms for single-input single-output systems. We use a prior knowledge of sign-convention between control-input influence in the MAV states based on simple flight mechanics equations to develop the correct block interactions in the proposed control architecture. In terms of tuning model-based control approaches, the model given in the previous section is only used to simulate the tailsitter MAV dynamics and not for control design.

MFC principles

As introduced by Fliess and Join,[29] an unknown finite-dimensional system with a single control-input (u) and a single output (y) can be described by the following input/output relation in a differential equation formulation

$$\mathbb{E}\left(y, \dot{y}, \ldots, y^{(a)}, u, \dot{u}, \ldots, u^{(b)}\right) = 0 \tag{22}$$

where $\mathbb{E}$ is a polynomial function with real unknown coefficients. We can also describe

$$y^v = \mathbb{E}(t, y, \dot{y}, \ldots, y^{(v-1)}, y^{(v+1)}, \ldots, y^{(a)}, u, \dot{u}, \ldots, u^{(b)}) \tag{23}$$

with $0 < v \leq a$ and $\frac{\delta \mathbb{E}}{\delta y^v} \neq 0$. These unknown dynamics can be modeled by a purely numerical equation, so-called *Ultra-Local Model*

$$y_m^{(v)} = F_y + \lambda \cdot u \tag{24}$$

In equation (24), v is the order of the derivative of y_m, $\lambda \in \mathbb{R}$ is a non-physical constant parameter. Moreover, the exploitation of this numerical model requires the knowledge of F_y. This quantity represents the real dynamics of the model as well as the different disturbances which could damage the performance of the output-system. Thus, an accurate estimation of F_y, defined as $\hat{F}_y$, is crucial and plays an important role in the MFC control performance. Different works in literature proved that the use of a first-order *Ultra-Local Model* ($v = 1$) is enough to stabilize unknown dynamics. However, if the unknown dynamics present second-order behavior with small friction coefficients, the use of a first-order *Ultra-Local Model* would be insufficient to stabilize poorly damped dynamics.[29] In light of this, we propose to develop MFC algorithms with a second-order *Ultra-Local Model* ($v = 2$)

$$\ddot{y}_m = F_y + \lambda \cdot u \tag{25}$$

The first step to obtain an estimation of the system dynamics, is to apply the *Laplace Transform* in equation (25), considering F_y as a constant piece-wise function. According to elementary operational calculus we transform equations (25) to (26)

$$s^2 Y_m(s) - s y_m(0) - \dot{y}_m(0) = \frac{F_y}{s} + \lambda U(s) \tag{26}$$

where $Y_m(s)$ and $U(s)$ correspond to the *Laplace transforms* of y_m and u. By differentiating twice the previous equation, we can remove the initial conditions $y_m(0)$ and $\dot{y}_m(0)$

$$2Y_m(s) + 4s\frac{dY_m(s)}{ds} + s^2\frac{d^2Y_m(s)}{ds^2} = \frac{2F_y}{s^3} + \lambda\frac{d^2U(s)}{ds^2} \tag{27}$$

However, the variable s in the time domain corresponds to a derivative term with respect to time, which is sensitive to noise corruptions and could amplify the noise measurement in the output of $\hat{F}_y$. In order to reduce noise in the output estimation, we replace these derivative terms by integral functions ($\frac{1}{s}$) who have robust properties against noise. Thus, multiplying both sides of equation (27) by s^{-3}, we obtain

$$\frac{2Y_m(s)}{s^3} + \frac{4}{s^2}\frac{dY_m(s)}{ds} + \frac{1}{s}\frac{d^2Y_m(s)}{ds^2} = \frac{2F_y}{s^6} + \frac{\lambda}{s^3}\frac{d^2U(s)}{ds^2} \tag{28}$$

Equation (28) can be transferred back to the time domain employing elementary calculus and *Cauchy's formula* to reduce multiple integrals in a simple one

$$\hat{F}_y(t) = \frac{5!}{2T^5}\int_{t-T}^{t}[(T-\sigma)^2 - 4\sigma(T-\sigma) + \sigma^2]y_m(\sigma) - \left[\frac{\lambda}{2}\sigma^2(T-\sigma)^2 u(\sigma)\right]d\sigma \tag{29}$$

From measurements of $y_m(t)$ and $u(t)$ obtained in the last T seconds, the unmodeled dynamics of y and the disturbances are estimated by $\hat{F}_y(t)$ which is updated for each interval of integration $[t-T, t]$. This interval corresponds to the integration window of a receding horizon strategy which results in a trade-off. The idea is to choose small integration windows to calculate the estimation within an acceptable short delay but large enough in order to preserve the low-pass filter properties, whose noise attenuation of $y_m(t)$. Based on such estimator, it is possible to design a robust controller that estimates the system dynamics on-line by a piece-wise function $\hat{F}_y(t)$ periodically updated for each measure of $y_m(t)$ and $u(t)$. According to Figure 5, the MFC closed-loop command is given by

$$u(t) = \underbrace{-\frac{\hat{F}_y(t)}{\lambda}}_{\text{Nonlinear Cancellation}} + \underbrace{\frac{\ddot{y}_{sp}(t) + u_{\mathcal{K}}(t)}{\lambda}}_{\text{Closed-loop tracking}} \tag{30}$$

where $\xi_y(t) = y_m(t) - y_{sp}(t)$ represents the tracking error and $u(t)$ is the closed-loop command of a feedback controller $\mathcal{K}(\xi_y(t))$, usually defined as a proportional (P), proportional-derivative (PD) or even so as proportional-integral-derivative (PID) gains. In this paper, the feedback controller was composed of proportional K_p and derivative K_d gains. We recognize in equation (30) the typical mathematical expression of a nominal control in the flatness-based in which the nonlinear terms $\hat{F}_y(t)$ is added with a closed-loop tracking of a reference trajectory $t \rightarrow \ y_{sp}(t)$. The error dynamic can be deduced from the combination of equation (30) with equation (25)

$$\ddot{y}_m(t) - \ddot{y}_{sp}(t) = \overbrace{F_y(t) - \hat{F}_y(t)}^{\xi_{F_y}} + K_p\xi_y(t) + K_d\dot{\xi}_y(t) \tag{31}$$

$$\ddot{\xi}_y(t) = \xi_{F_y} + K_p\xi_y(t) + K_d\dot{\xi}_y(t) \tag{32}$$

$$\ddot{\xi}_y(t) - K_d\dot{\xi}_y(t) - K_p\xi_y(t) = \xi_{F_y} \tag{33}$$

Note that, if the error (ξ_{F_y}) between the estimator and the true dynamics is approximately zero during $[t-T, t]$, a simple proportional-derivative controller will be enough to ensure the error convergence to zero because an integration effect is implicitly involved in the MFC algorithm.

MFC design

The MFC closed-loop allows the design of both tracking and regulation performance with distinguished

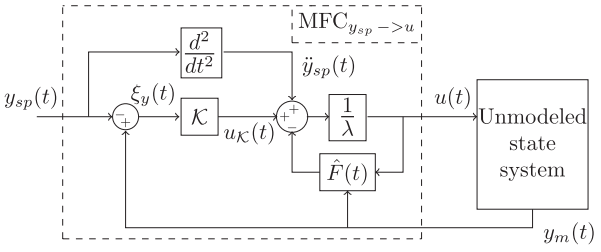

Figure 5. Overview of the model-free control schema.

Table 1. MFC parameters used in the simulations.

States	T_i	λ_i	Kp_i	Kd_i
x	5	25	−0.1225	−0.7
y	10	25	−0.04	−0.4
z	5	20	−0.25	−1
v_{xb}	2	10	−16	−8
v_{yb}	2	70	−7.84	−5.6
v_{zb}	5	2350	−4.6225	−4.3
ϕ	5	300	−4	−4
θ	5	450	−16	−8
ψ	3	1.15	−0.16	−0.8

parameters that can be tuned with little prior knowledge of the system. The following points describe the design methodology used in this work to obtain the MFC parameters presented in Table 1.

1. The proportional-derivative gains (K_p and K_d) have been easily tuned according to classical root locus method. In practice, the MFC estimator provides an accurate estimation of the system ($\xi_{F_y} \approx 0$). Thus, the error dynamics of the closed-loop system can be approximated by a double integrator (33), which can be tuned by pole location approach. In this perspective, we define double real closed-loop poles at $-s_d$, which results the following characteristic polynomial

$$(s + s_d)^2 = s^2 + 2s_d s + {s_d}^2 \tag{34}$$

The feedback controller with these proportional-derivative gains can be identified by neglecting the initial conditions in the Laplace transform of equation (33)

$$\frac{U_{\mathcal{K}}(s)}{\xi_y(s)} = s^2 - K_d s - K_p \tag{35}$$

Therefore, we obtain the following from equations (34) and (35)

$$K_p = -{s_d}^2 \quad \text{with} \quad s_d > 0 \tag{36}$$

$$K_d = -2s_d \quad \text{with} \quad s_d > 0 \tag{37}$$

2. The integration window (T) could be defined with prior information about the noise present in the measured signal (y_m). The choice of the integration window implies some expertise according to a trade-off between fast estimations and effective noise attenuation. For instance, due to the integrator in equation (29) with low-pass filter features, a large integration window provides an effective noise attenuation, but slow estimations with a direct impact on the control-loop responsiveness. On the other hand, small integration windows result in fast estimations with the constraint of estimating noises. In this context, oscillations could be observed in the closed-loop system with high frequency commands (u), which is known as 'chattering'. In this work, we use an invariant observer[44] that smooths the measured signals, allowing the set of small integration windows to estimate the fast dynamics of the DarkO tailsitter MAV while suppressing the oscillations generated by the noises in the closed-loop system.
3. Finally, the constant coefficient (λ) is used to scale the amplitude between the command (u) and the dynamics of ($\ddot{y}_m$). This parameter can be represented as the control effectiveness of the nominal system. Nonetheless, if this parameter is poorly defined or if the actual control effectiveness of the system changes on within a bounded domain, the estimator ($\hat{F}_y$) is able to compensate this bounded discrepancy ensuring the closed-loop stability. A nominal setting of λ can be achieved by calculating the ratio between the command saturation and the maximum allowable value of ($\ddot{y}_m$).

From a practical point of view, the proposed MFC design allows a time-saving approach to stabilize complex dynamic systems. The fact that, the closed-loop system can be approximated by the dynamics of a double integrator system simplifies the control design process of proportional-derivative gains.

Control architecture

Figure 6 shows the main ideas of our control architecture. The block *Trajectory generator* is composed of a state flow algorithm that defines constantly the desired positions (x_{sp}, y_{sp}, z_{sp}) in the inertial coordinate system. These references are taken into account by the *Position control* block and are compared with the respective measures (x_m, y_m, z_m) creating three errors that are minimized by the MFC algorithms in the *Position control* block. These three MFC algorithms in charge of the position tracking, also compute the desired velocity in their respective axes. These reference values which are defined in the inertial coordinate frame are transformed to the body coordinate frame as well as the velocities measurements. Thus, the velocity control $\text{MFC}_{v_{xb}}$ computes the required thrust T_d to reach this desired velocity along $\vec{x_b}$, the block $\text{MFC}_{v_{zb}}$ assures the velocity control along $\vec{z_b}$ and determine the necessary pitch angle θ_{sp} to reach this desired velocity $v_{zb_{sp}}$. Both blocks control their

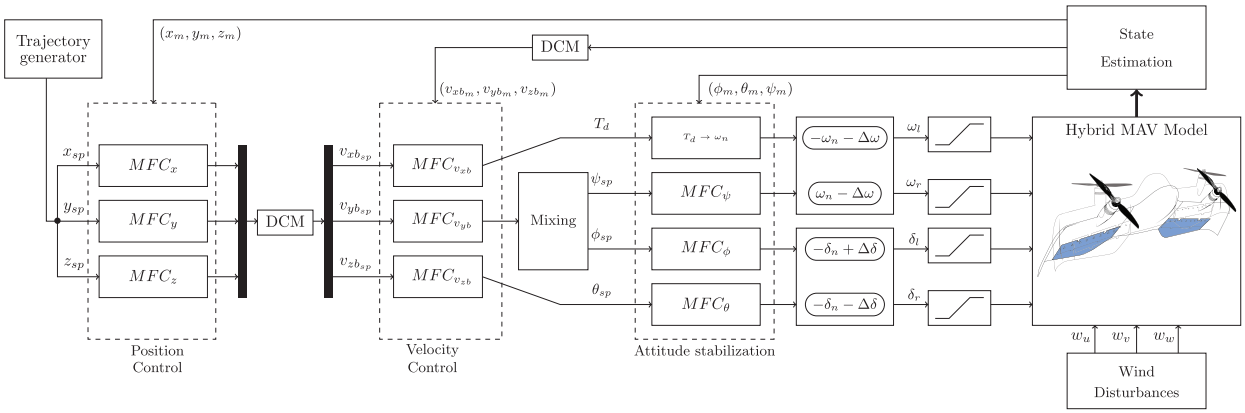

Figure 6. Cascaded MFC architecture designed for tailsitter MAVs. Position control blocks send desired velocities for the velocity control blocks that compute the necessary thrust value as well as the references for attitude stabilization control loop. Based on these desired values, propeller speeds (ω_l, ω_r) and flap deflections (δ_l, δ_r) are defined.
MAV: micro air vehicle; DCM: Direction Cosines Matrix.

respective velocities and define the desired thrust and pitch angle for the entire flight envelope, i.e. hover, transition and forward flight. However, the velocity control along $\vec{y_b}$ is designed depending on the current hybrid MAV flight phase. Therefore, in hover flight, the block $\text{MFC}_{v_{yb}}$ defines the desired yaw angle ψ_{sp} and the block MFC_ψ controls its dynamics through differential-thrust commands creating moments around $\vec{z_b}$ in order to reach the desired velocity along $\vec{y_b}$. In forward flight, this lateral velocity is reached from roll rotations around $\vec{x_b}$. These rotations orient the lift force and the hybrid MAV can perform left-right turns with, respectively, negative and positive roll angles ϕ. The propeller speeds (ω_l, ω_r) are defined by the sum of nominal propeller rotation ω_n with a differential propeller speed Δ_ω which is in charge of the yaw control. The negative sign of ω_n for the left-propeller ω_l is due to the counter-rotation sense. And the flap-deflections (δ_l, δ_r), which are in convention negative for pitch-up, are composed by the sum of symmetrical flap deflection δ_n with anti-symmetrical flap deflections Δ_δ that are respectively the control-input for the pitch angle θ and for the roll angle ϕ.

Flight simulation results

A comprehensive set of flight simulations, discretized at 500 Hz, were performed from MATLAB/Simulink using the tailsitter MAV model described in the 'Simplified tailsitter MAV model' section that is controlled by the proposed MFC architecture, see Figure 6. Our flight simulator is based on the DarkO tailsitter MAV dynamics with sensor measurements corrupted by Gaussian white noises, whose standard deviations can be found in literature.[45] The MFC parameters, i.e. λ_i, T_i, Kp_i and Kd_i, were tuned for the entire flight envelope of the DarkO with constant values for all flight simulations. In order to evaluate our control algorithm, we have introduced external perturbations such as wind disturbances during these flights. The results provide a straightforward way to validate the methodological principles presented in this article as well as to evaluate the designed MFC parameters, and to establish a conclusion regarding MFC benefits in both theoretical and practical contexts. The flight simulations are presented in a series of case studies in order to analyze separately each flight domain of the DarkO, such as hovering, transitioning and forward flights.

Hovering flight

In hovering flight, we analyze the velocity and attitude controller's ability to recover the MAV from different unstable initial condition points. Also, we present an average frequency content of yaw and pitch angle signals using the Fast Fourier Transform (FFT) algorithm over the entire time that the signals were acquired. In addition, we present two position tracking missions in hovering flight, and we verify the interaction between the position, velocity and attitude control blocks.

Initial condition analysis. The initial conditions for pitch angle and for forward speed during the hovering flight (θ_{ic} and $V_{x_{ic}}$), follow a normal distribution law according to equations (38) and (39).

$$\theta_{ic} \sim \mathcal{N}\left(\frac{\pi}{2}, \left(\frac{\pi}{6}\right)^2\right) \tag{38}$$

$$V_{x_{ic}} \sim \mathcal{N}\left(0, \left(\frac{5}{3}\right)^2\right) \tag{39}$$

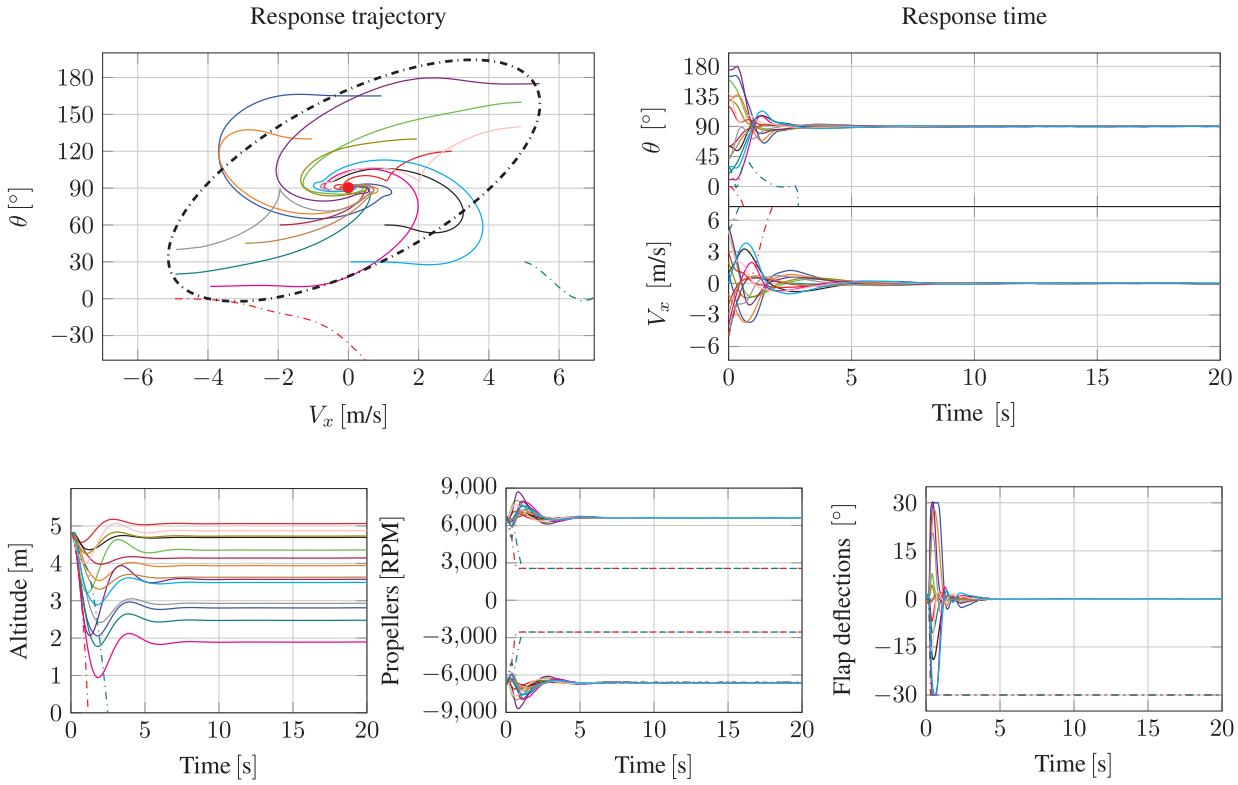

Figure 7. Initial pitch angle and forward speed condition analysis during hovering flight phase without wind disturbances. Forward speed setpoint equals to 0 m/s, the MFC architecture computes the pitch angle setpoint equals to 90° in order to reach the stationary flight.

The stability boundary presented in Figure 7, was empirically defined by evaluating all recovery trajectories from initial conditions to the desired setpoint. The desired setpoint corresponds to a stationary flight in the vertical position, respectively, 0 m/s for the forward speed and 90° for the pitch angle. Basically, three classes of trajectories were distinguished during these simulations. The first one combines trajectories with initial pitching angles larger than 90° with positive initial conditions for forward speeds. Likewise, trajectories with initial pitching angles smaller than 90° and negative initial conditions for forward speeds are also included in this class. The peculiarity of these trajectories is that, both converge directly to the desired equilibrium setpoint with small oscillations in the response time. This can be explained by the fact that, for initial pitching angles larger than 90°, the thrust vector is already well-oriented and it can be increased in order to decelerate the initial positive forward speeds. This thrust vector is increased from increments of the propeller rotations, which improves the flap effectiveness creating a powerful pitch moment that can easily align the attitude of the hybrid MAV in the right direction, towards the attitude setpoint. The same reasoning can be done for initial pitching angles smaller than 90° with negative forward speeds. In this initial flight condition and orientation, the controller generates the thrust vector in order to increase the forward speed resulting in an effective pitch moment which also steer the hybrid MAV towards the setpoint. The second class of trajectories is composed by all initial pitching angles smaller than 90° with positive initial forward speeds and by all initial pitching angles larger than 90° with negative initial forward speeds. These trajectories diverge at the beginning of the simulation. The thrust vector, in these flight orientations, is unable to generate an opposing force to decelerate the initial forward speed to zero. The only force opposing to the movement is the drag force. By increasing the pitch angle, in this case the angle of attack, the hybrid MAV generates more drag and can reach the forward speed setpoint. For extreme cases, within the stability boundary, we can observe flap saturation which justifies the shape of the concerned trajectories with overshoots and undershoots. By analyzing the altitude results, we can mention that the position control is not activated. However, we can observe that the altitude is stabilized at given values according to the velocity control block which cancels the vertical velocity component. The MFC can theoretically ensure a

stable flight for all initial points inside the boundary, with more or less oscillations, according to the initial conditions. Otherwise, the hybrid MAV performs an unstable flight, as shown by the two particular initial points outside the stability boundary corresponding to the third class of trajectories in this simulation.

FFT analysis. This analysis focuses on the MFC tuning problem. Usually, the flight controller parameters are adjusted according to a setpoint trajectory and with trim points in a respective flight condition. However, hybrid MAV covers different flight domains which would imply a variety of setpoint trajectories with different frequencies. Thus, we analyze the entire bandwidth of frequencies corresponding to the yaw and the pitch angle during the hovering flight. And, we compare its setpoint trajectory spectrum with its measured spectrum in order to evaluate the designed MFC parameters. We excite the attitude dynamics adequately in order to capture the important frequencies by varying the velocity setpoint along the $y_b - axis$ and the velocity setpoint along the $z_b - axis$. According to Figure 6, the block MFC_{v_y} generates, in hovering flight, the setpoint to the yaw angle ψ_{sp} and the block MFC_{v_z} the setpoint to the pitch angle θ_{sp}. Figure 8 shows the comparison between the desired yaw angle and its respective measured signal in both time and frequency domains. High precision tracking for frequencies up to 4 rad/s is observed which means that the controller is able to track, with high precision, yaw setpoint variations up to 285 degrees per second (°/s). Furthermore, the tuned yaw control parameters present a reasonable trade-off to track low and high frequencies that compose its bandwidth. The results of the pitch angle presented in Figure 9, shows an effective tracking over its entire frequency spectrum. In addition, for high frequencies, the controller filters the references providing a smooth pitch output, but with an offset between the signals creating a small error.

Hovering flight missions. The main objective of the first flight simulation in hovering mode, see Figure 10, is the study of wind influence in the position tracking, for the following desired positions

$$\begin{aligned} x_{sp} &= 0, \forall t \\ y_{sp} &= 0, \forall t \\ z_{sp} &= \begin{cases} 10, & t \in [0; 155]s \\ 0, & t > 155s \end{cases} \end{aligned}$$

During this flight mode (#**Flight 1**), the hybrid MAV is more susceptible to aerodynamics disturbances. We can explain this by the fact that, in the vertical position, the wind gust along the $x_i - axis$, respectively along the $z_b - axis$, is in contact with the total reference wing area generating a considerable drag force. Also, the hybrid MAV is not able to compensate this force in the vertical position. That is why, the transition is performed and the drag force created by the wind can be compensated by the thrust in order to ensure the position tracking. The thrust used to reject this

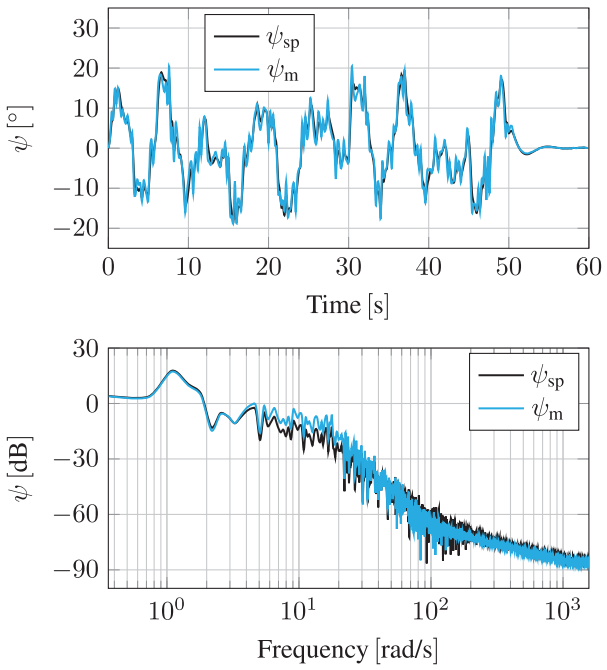

Figure 8. Frequency analysis of the yaw angle in hover flight.

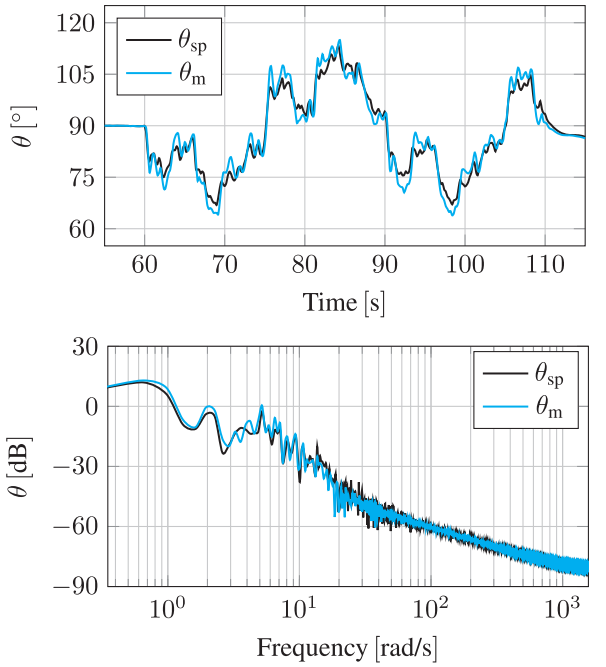

Figure 9. Frequency analysis of the pitch angle in hover flight.

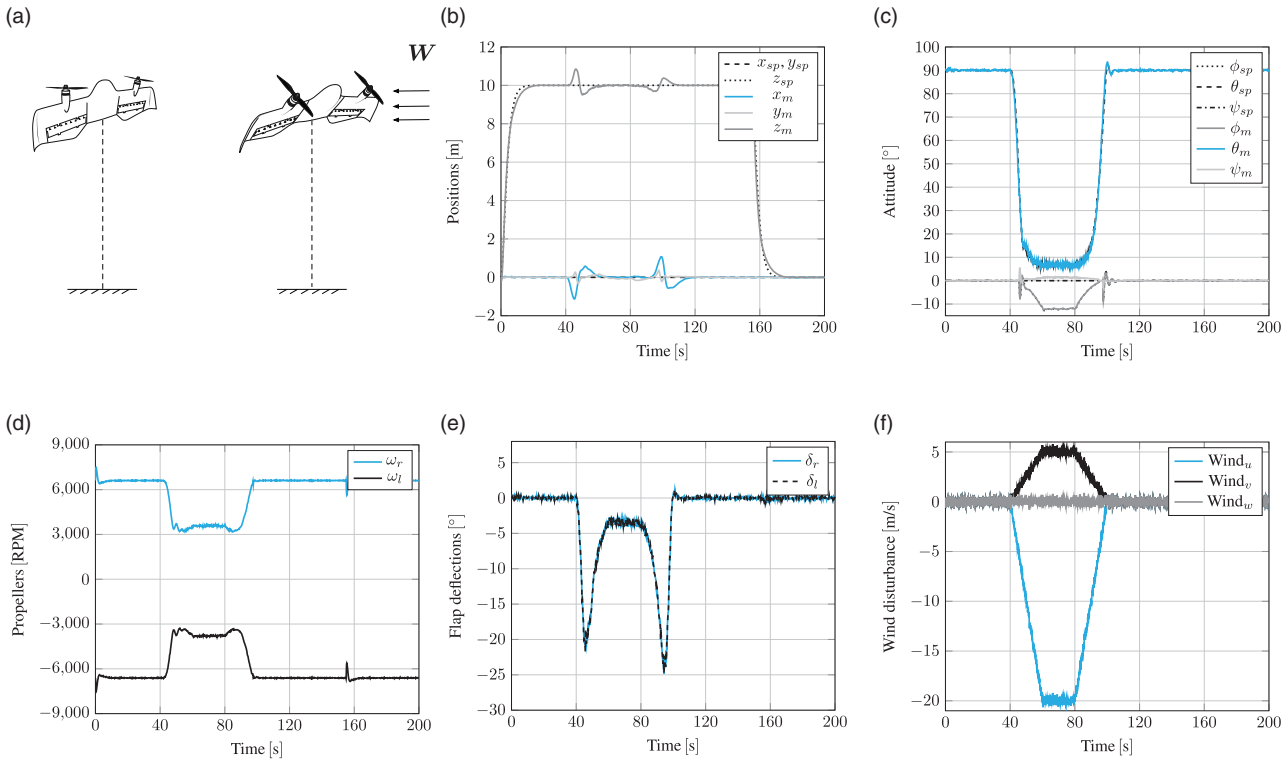

Figure 10. (**#Flight 1**) – Vertical take-off and transition flight to assure position tracking during high crosswind. On the top, from left to right: simulation illustration, positions in the inertial coordinate frame and attitude. On the bottom: propeller speeds ($\omega_l < 0$ and $\omega_r > 0$) due to counter-rotation sense, flap deflections (δ_l and δ_r) convention negative for pitch-up, and wind disturbance.

perturbation can be seen in Figure 10(d). And the wind from east with a magnitude of 5 m/s, see Figure 10(f), also produces a side force in the $y_b - axis$. This force is compensated by orienting the lift force with a symmetrical rotation around the $x_b - axis$, corresponding to the negative roll angle described in Figure 10(c).

In the second flight simulation, we impose a circular setpoint path (**#Flight 2**) in order to validate the interaction between all control blocks in the proposed control architecture. The following equations define the desired trajectories (x_{sp}, y_{sp}, z_{sp})

$$x_{sp} = \begin{cases} 0, & t < 30s \\ x_c + r\,cos\left(\frac{2\pi}{40}t\right), & t \in [30;130]s \\ 1, & t > 130s \end{cases}$$

$$y_{sp} = \begin{cases} 0, & t < 30s \\ y_c + r\,sin\left(\frac{2\pi}{40}t\right), & t \in [30;130]s \\ 5, & t > 130s \end{cases}$$

$$z_{sp} = \begin{cases} 10, & t \in [0;155]s \\ 0, & t > 155s \end{cases}$$

where x_c and y_c correspond to the center of the circle and r is its radius. This maneuver requires the hybrid MAV to fly along a circular trajectory while constantly pointing its nose towards the exact center of the circle. Accurate position, velocity and especially yaw angle control are needed to accurately follow the desired flight plan with the desired attitude. Figure 11 shows the simulation results.

Remark (Conclusion hovering flight phase). *In hovering flight simulations, the MFC architecture has shown the capability to recover the tailsitter MAV from a large range of initial conditions for both pitch angle and forward speed, thereby validating the interactions between attitude and velocity control blocks. The disturbances that deteriorate the controlled output signal, are estimated and annulled by the controller providing robust disturbance rejections in order to track a desired position. For strong wind disturbances, the tailsitter MAV performs a smooth transitioning flight ensuring position tracking. Indeed, the FFT analysis validated the designed MFC parameters for a wide attitude frequency spectrum.*

Transitioning flight

The transitioning flight simulations were examined in two parts. In the first one, similar to the hovering flight,

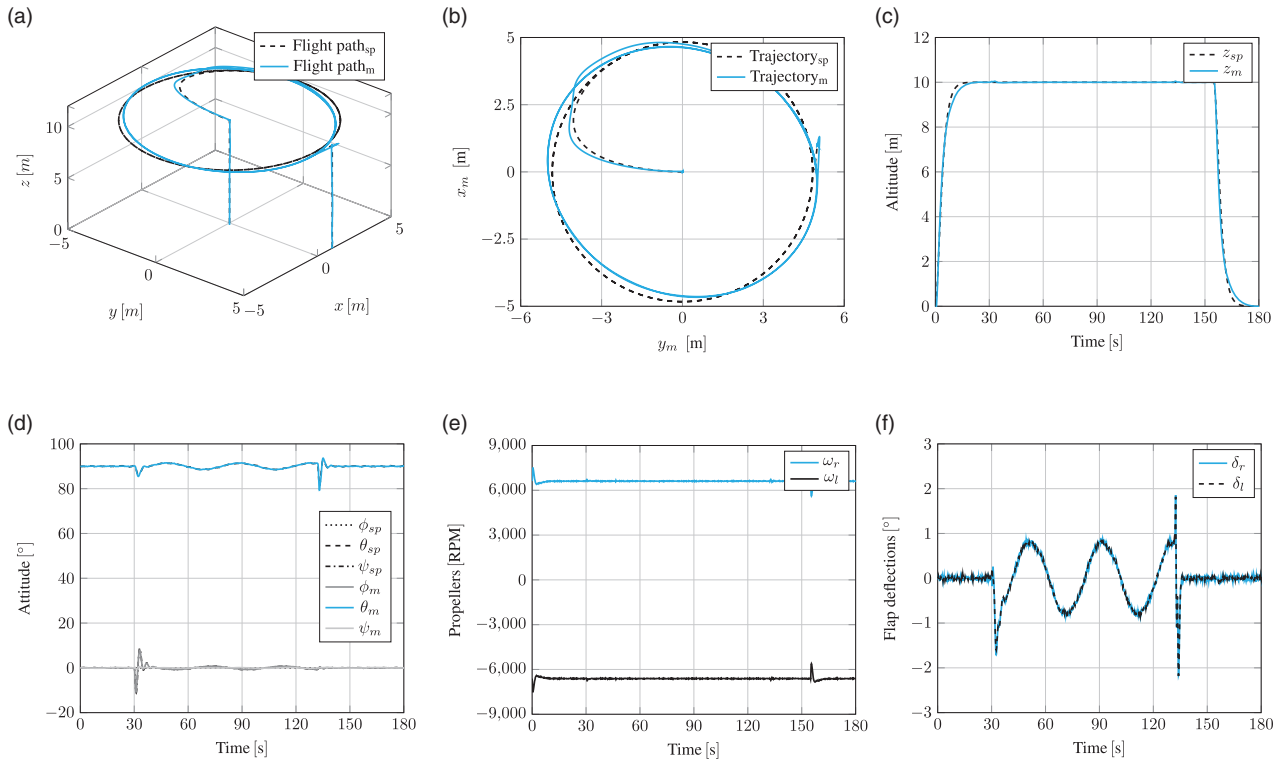

Figure 11. (**#Flight 2**) – Circular position tracking in hover flight mode. On the top, from left to right: the 3D flight path, North and East positions and altitude. On the bottom: attitude, propeller speeds and flap deflections.

we analyze the velocity and attitude controller's ability to recover the MAV from different unstable initial conditions to the desired stable setpoint. The second case study presents variations of nominal hybrid UAV parameters in flight at different pitch angles in order to evaluate the MFC adaptive properties during the forward-to-hover transition.

Initial condition analysis. In this case study, we define a forward speed setpoint of 5 m/s and the MFC architecture computes a pitch angle setpoint of around 45°. The desired forward speed setpoint was chosen to prove, by flight simulations without predefined gains or gain scheduling methods, that the proposed control architecture is able to stabilize the tailsitter MAV in a critical flight domain corresponding to stall region where the aircraft flies at low forward speed and high angle of attack. The initial conditions during the transitioning flight analysis (θ_{ic} and $V_{x_{ic}}$), are defined from a normal distribution law given by the following equations (40) and (41).

$$\theta_{ic} \sim \mathcal{N}\left(\frac{\pi}{4}, 30^2\right) \tag{40}$$

$$V_{x_{ic}} \sim \mathcal{N}(5, 2^2) \tag{41}$$

The empirically defined stability boundary, for initial conditions in transitioning flight, is presented in Figure 12. The three classes of trajectories discussed in the hovering flight analysis, can be also observed in this case study. These trajectories have a slower convergence time with respect to the trajectories in hovering flight domain. Flap saturation affects the response time, but the main reason for the slower convergence time, in the transitioning flight domain, is the difficulty to decelerate the tailsitter MAV which depends on only of the drag force. For these initial conditions, the tailsitter MAV was not controlled in position allowing a supplementary degree of freedom to recover the stable attitude setpoint. During the transitional regime, that corresponds to the trajectory from the initial conditions to the setpoints, the tailsitter MAV loses altitude because the initial condition for both pitch angle and forward speed precludes the production of lift force and the thrust orientation is not adequate to compensate the weight of the tailsitter MAV. Thus, fast attitude stabilization is crucial to steer the thrust and bring the tailsitter MAV back to safe flight conditions.

Parameter-varying analysis. In this analysis, we evaluate the altitude tracking and the attitude stabilization, more precisely, the pitch angle stabilization by imposing variations of mass and inertia at different points in

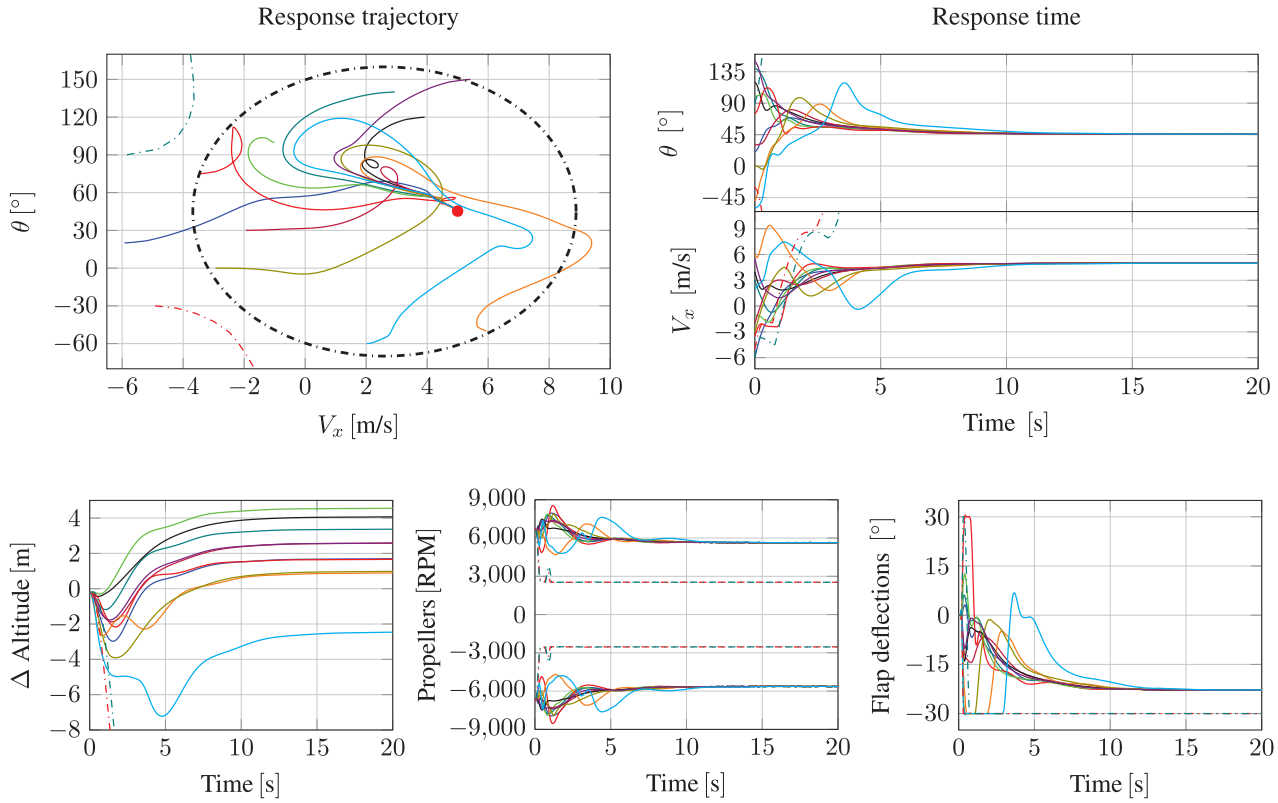

Figure 12. Initial pitch angle and forward speed condition analysis during the transitioning flight phase without wind disturbances. Forward speed setpoint equals to 5 m/s, the MFC architecture computes the pitch angle setpoint approximately equals to 45°.

the pitch angle trajectory during the forward-to-hover transition. For each point in which the variations occur, we compute the standard deviation between the altitude setpoint and its measurement. Figure 13 shows a typical pitch angle response time for the forward-to-hover transition with the nominal DarkO parameters. The altitude behavior and its standard deviation values computed for different mass and inertia values are also presented. We impose a maximum mass and inertia variation of around 45% of the nominal DarkO parameters. This study concludes that, the DarkO is less robust to variations of mass and inertia when it occurs between 20° and 40° of pitch angle. However, the impact of mass and inertia variations on altitude tracking remains very low with a maximum standard deviation of 0.3 m. The proposed control approach is able to stabilize the forward-to-hover flight transition with little prior knowledge of the tailsitter MAV. By using the estimator ($\hat{F}$) in the closed loop, any impact on the tailsitter MAV dynamics caused by parametric variations are estimated and immediately compensated in order to reach the altitude setpoint trajectory previously imposed.

Remark ((Conclusion transitioning flight phase)). *Fast changing of aerodynamic forces and moments present in this critical flight domain have been countered by the proposed control architecture. The tailsitter MAV is stabilized in a critical attitude setpoint from different initial conditions. Further, the parameter-varying analysis highlighted the promising adaptive properties of the proposed control technique.*

Forward flight

The last phase of flight studied corresponds to the forward flight. Given that, the MFC parameters are tuned for the entire flight envelope without any type of gain scheduled and the hybrid MAV dynamics change between the flight phases, we compute the FFT to the roll and the pitch angles in order to compare the frequency control performance with the previous results in hovering flight. In addition to this analysis, we present a full flight simulation exploring all hybrid MAV flight phases, with a major focus on forward flight, in which the hybrid MAV performs a position tracking.

FFT analysis. In forward flight, the roll setpoint ϕ_{sp} is generated from the velocity control block along the $y_b - axis$. This velocity is excited in order to create different setpoint values and frequencies to the roll angle. The roll tracking results in both time and frequency

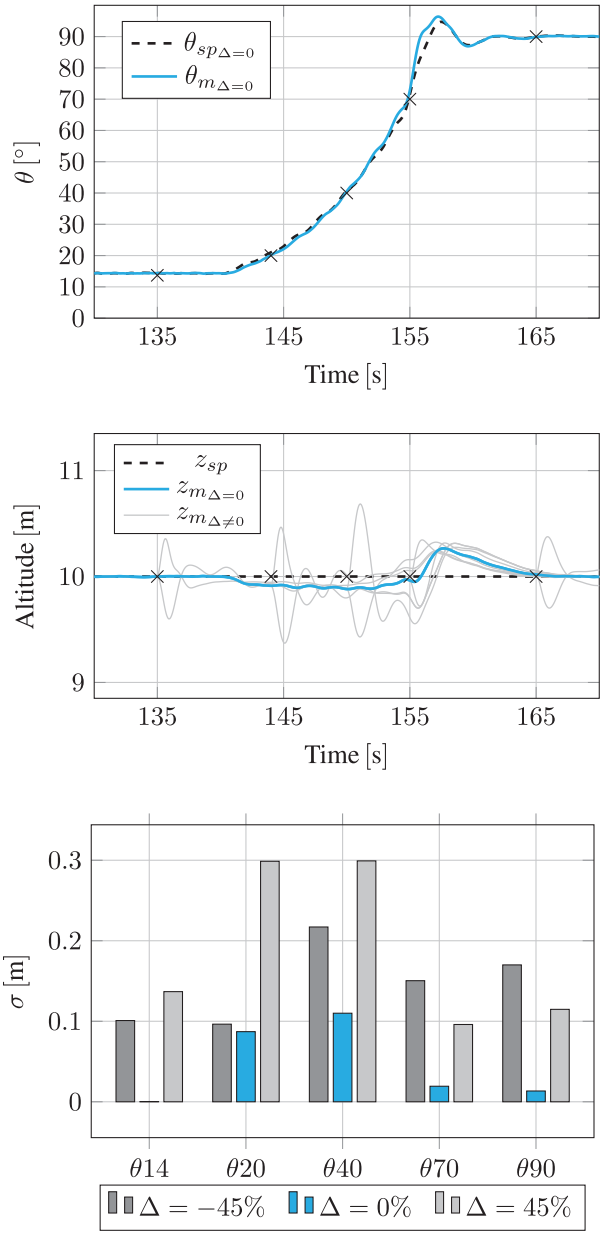

Figure 13. Parameter variation analysis for different points in the forward-to-hover transition. The black crosses in altitude and pitch angle trajectories indicate the points in which the parameters were changed. Δ represents the variation of nominal mass and inertia in percentage. The standard deviation between the altitude setpoint and its measurements is denoted by σ.

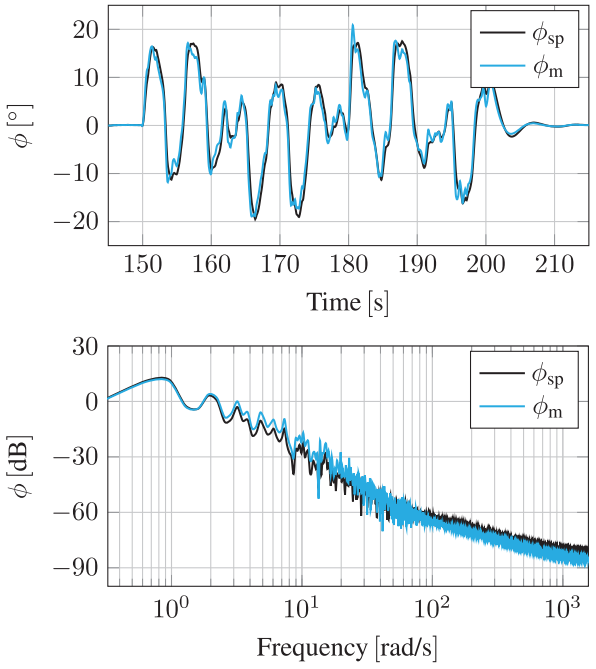

Figure 14. Frequency analysis of the roll angle in forward flight.

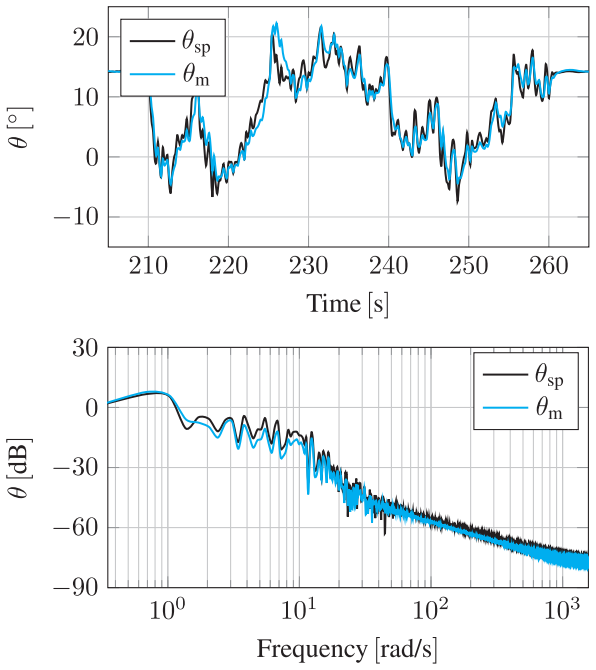

Figure 15. Frequency analysis of the pitch angle in forward flight.

domains are presented in Figure 14. The proposed controller provides a high quality tracking up to 3 rad/s which is equal to 170 (°/s). An offset between the roll setpoint trajectory and the roll measurement is observed at high frequencies. However, in this frequency range, the signals are almost negligible, given their respective attenuation in decibels.

Pitch angle results are presented in Figure 15. We quantify a maximum pitch tracking error of 1.58 (°) for pitch angle setpoints varying between 1 and 10 rad/s, which represent 57 and 573 (°/s). Overall, the FFT analysis revealed, in hovering and forward flight, the promising performance of MFC for attitude tracking. Further, this analysis shows that the MFC parameters were well-adjusted considering the trade-off between

the quality of attitude stabilization with delays and noises in the control loop.

Forward flight mission. A complete flight mission (#**Flight 3**) is presented in Figure 16 in which we evaluate all hybrid MAV flight capabilities through a vertical take-off from 0 to 10 m of altitude followed by the hover-to-forward transition with a position tracking in the xy – *plane* and an altitude change in forward flight. Then, the forward-to-hover transition is performed with a position tracking in hovering flight. The flight simulation ends with a vertical landing. The complete 3D flight path is presented in Figure 16(a). The controller assures the position tracking during the entire mission. As we can see in Figure 16(b), the altitude presents small oscillations at 45 and 165 s of simulation which is acceptable for this MAV class. These oscillations are due to the fast variations of aerodynamics forces and moments that occur during the transition flight phases where the pitch angle changes resulting in significant variations in the angle of attack, see Figure 16(d). In the same figure, between 45 and 90 s of simulation, we can see the roll dynamics to reach the desired east position in forward flight. Similarly, between 180 and 215 s of simulation, the yaw behavior to reach the east position in hovering flight. Figure 16(c) presents the velocities in the body coordinate system and the actuator dynamics, respectively, the propeller rotations and the flap deflections are shown in Figure 16(e) and (f).

Remark ((Conclusion forward flight)). *We confirm in this subsection that, the proposed MFC architecture also ensures the position tracking, velocity control and attitude stabilization in forward flight. With the FFT analysis, we show the attitude control performance for a large range of frequencies. Furthermore, we validate the interactions between each control block independently of the hybrid MAV attitude orientation that covers its entire flight envelope.*

Flight tests

In this section, we present real-world flight tests to compare the MFC attitude stabilization performance to that of the INDI controller in indoor flight conditions. For more details about the INDI, we refer the interested reader to literature.[25,46] Both controllers were tested using the Paparazzi Open Source Autopilot System.[47] The methodology used during the flight tests to define the DarkO's attitude setpoints are based on four steps. First, with an RC transmitter, the security pilot imposes slow yaw setpoints generating lateral motions in the system. Then, slow pitch

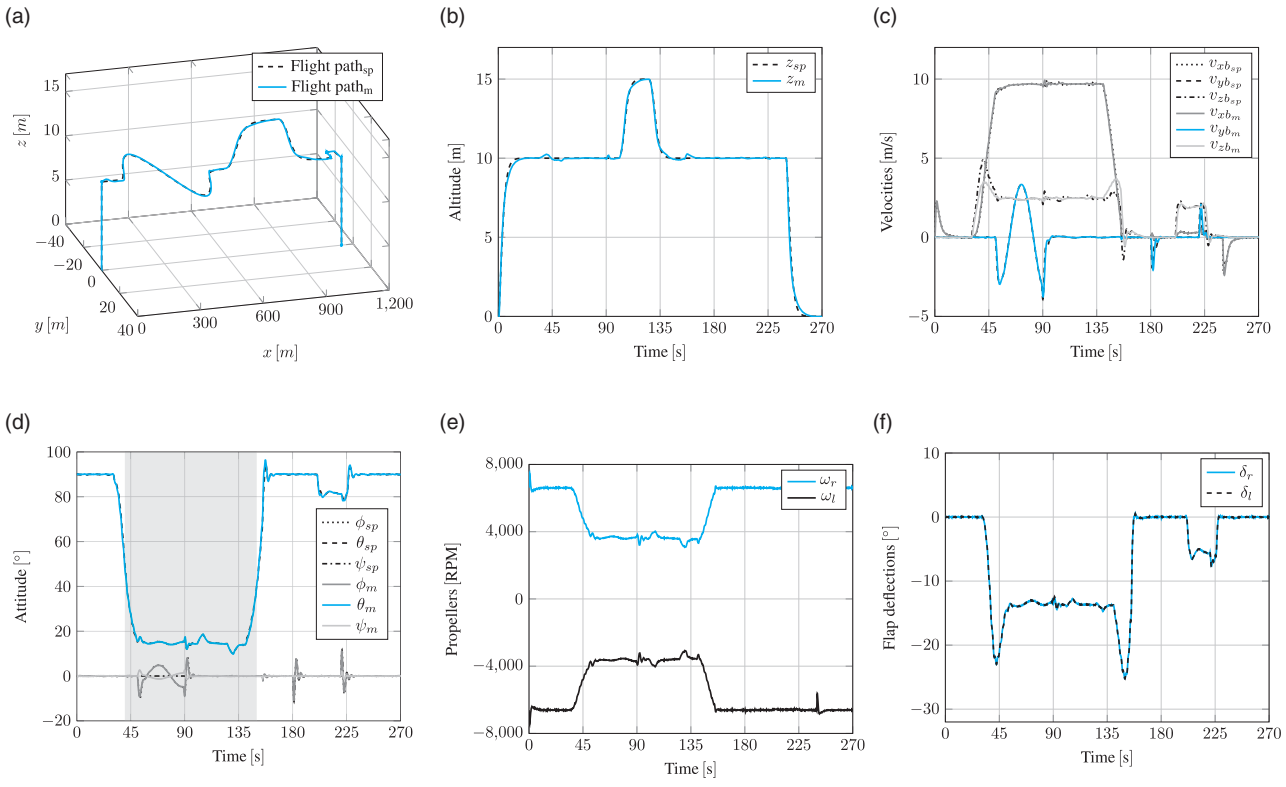

Figure 16. (**#Flight 3**) – Entire flight envelope simulation in relatively calm flight conditions. On the top, from left to right: the 3D flight path, altitude and velocities in the body coordinate system. On the bottom: attitude, propeller speeds and flap deflections.

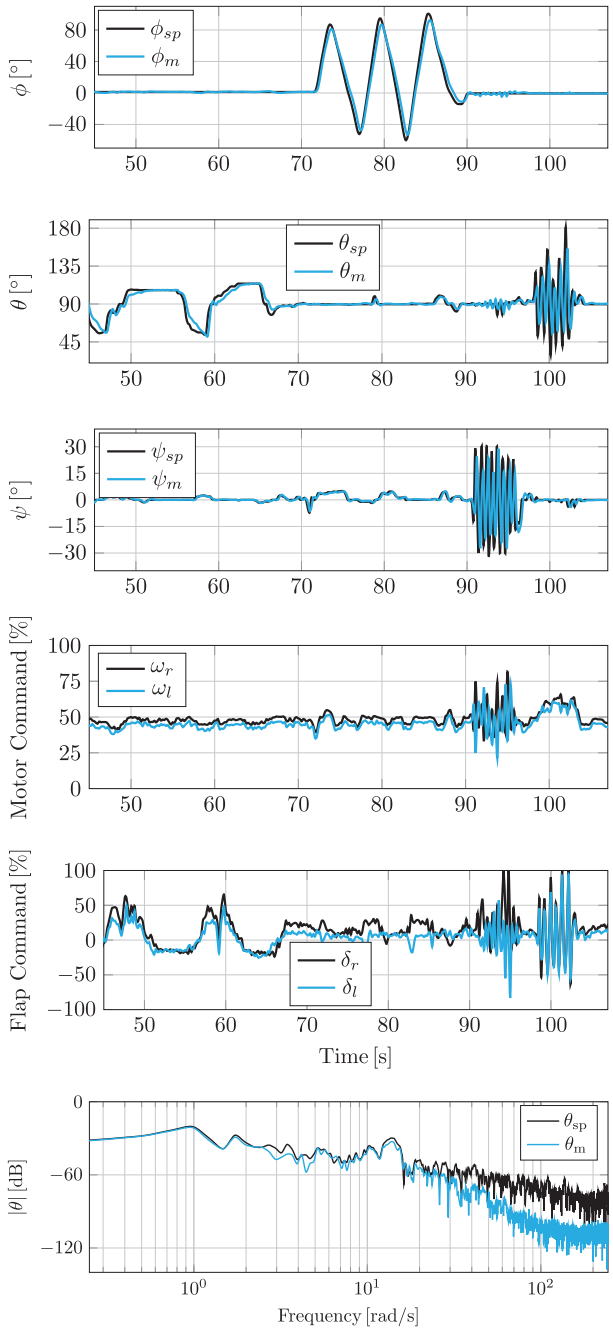

Figure 17. MFC attitude stabilization – nominal DarkO.

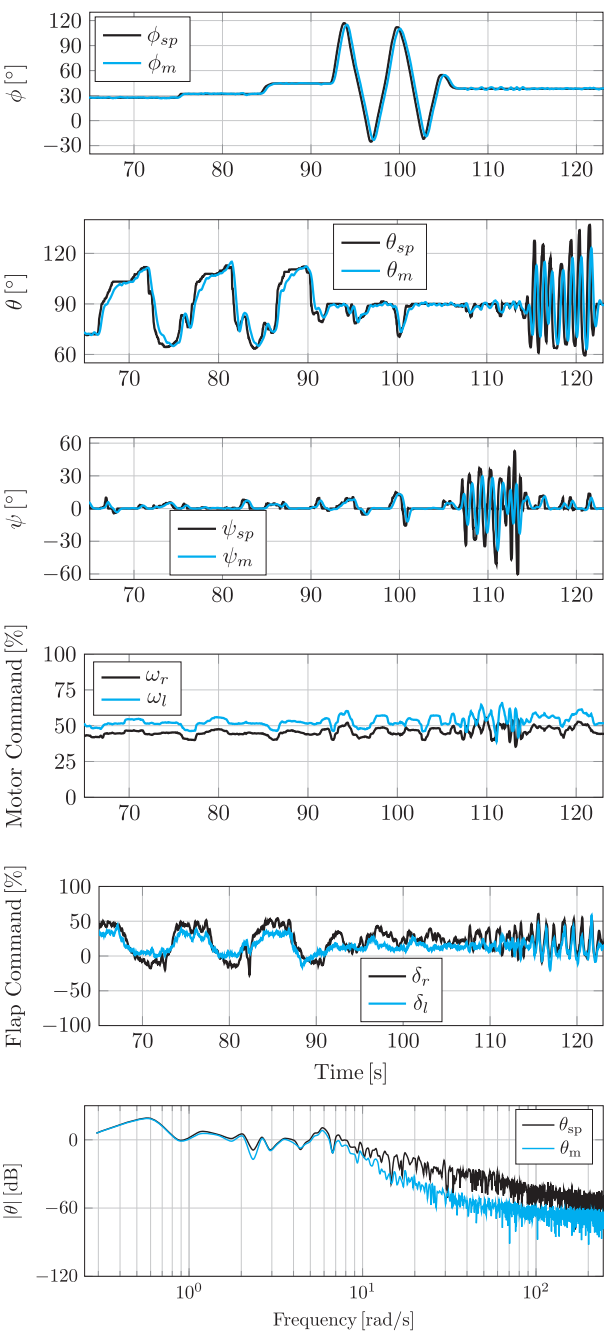

Figure 18. INDI attitude stabilization – nominal DarkO.

setpoints generate forward and backward movements according to positive and negative pitch setpoints, respectively. Then, slow roll setpoints which define the heading of the system. Finally, the pilot imposes fast yaw and pitch setpoints to evaluate the response of the system for high frequency attitude setpoints. Two flight test cases were conducted in indoor environment comparing MFC to INDI controllers. In the first case, both controllers stabilize the DarkO in its nominal configuration, i.e. wings and control surfaces are attached correctly. In the second case, the wingtips and half of the control surface are removed, and additionally the propulsion system has been modified by using a different set of propellers. The nominal components of the DarkO were changed to evaluate the adaptive properties of both controllers. The attitude stabilization results performed by MFC and INDI with the nominal DarkO, are presented in the Figures 17 and 18, respectively. Figures 19 and 20 show the MFC and INDI attitude stabilization performances

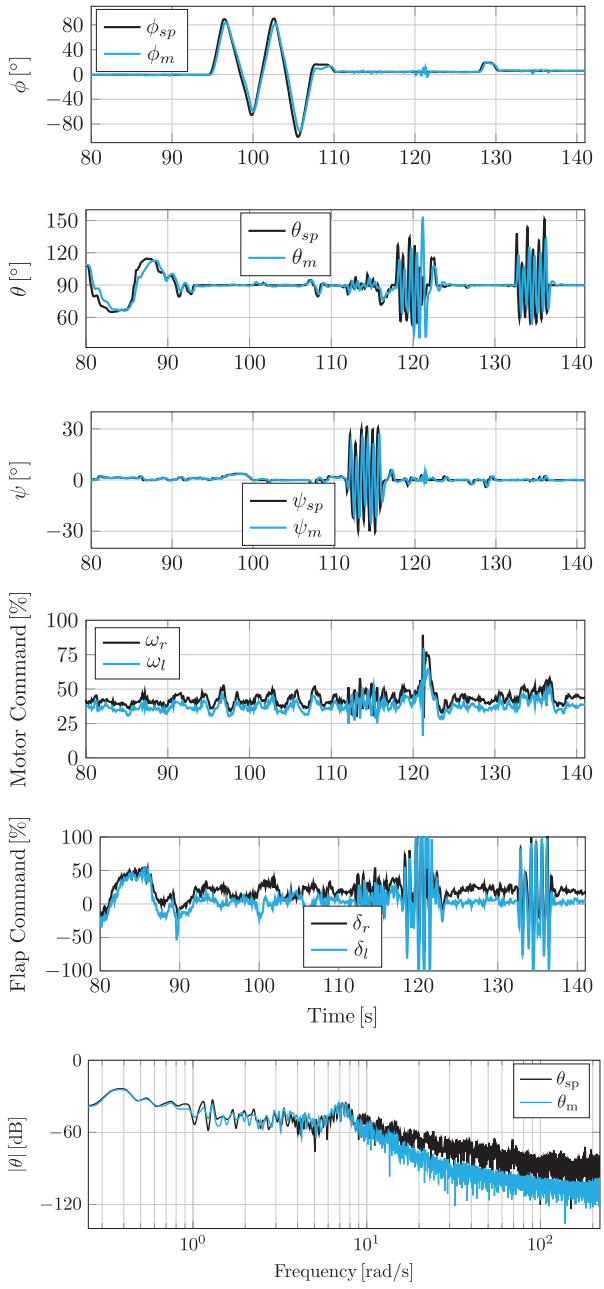

Figure 19. MFC attitude stabilization – modified DarkO.

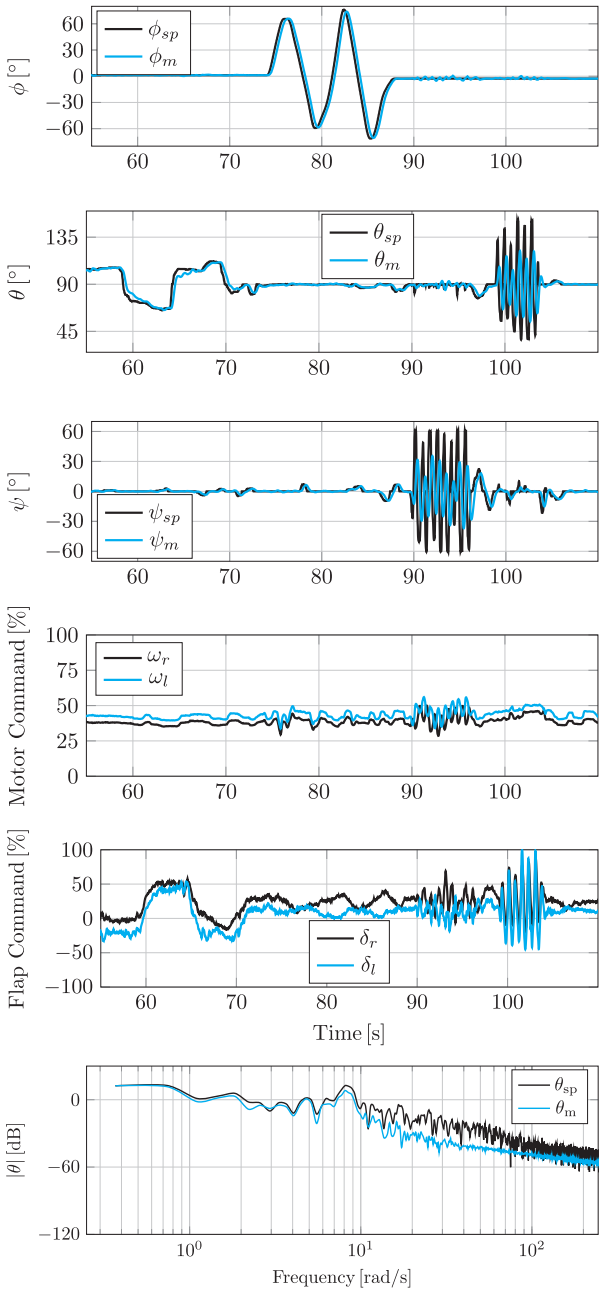

Figure 20. INDI attitude stabilization – modified DarkO.

for the modified DarkO configuration, see Figure 21. It is difficult to analyze graphically each controller in the time domain, because of their different setpoint trajectories. For this reason, we investigated their control performance in the frequency domain by calculating the FFT of the pitch angle, which is the dynamics most affected by a loss of control surface effectiveness. We observe a better tracking performance with a larger frequency spectrum for the MFC (20 rad/s) when compared to that of the INDI (7 rad/s) for the nominal flight test. Both controllers stabilized the modified DarkO, showing their adaptive control properties. The present study concludes that MFC and INDI provide satisfactory performance for hovering and transitioning flight domains in indoor flight conditions. These results suggested a more in-depth analysis to evaluate the performance of both controllers for the entire flight envelope of the DarkO, in particular during forward flights in outdoor environment.

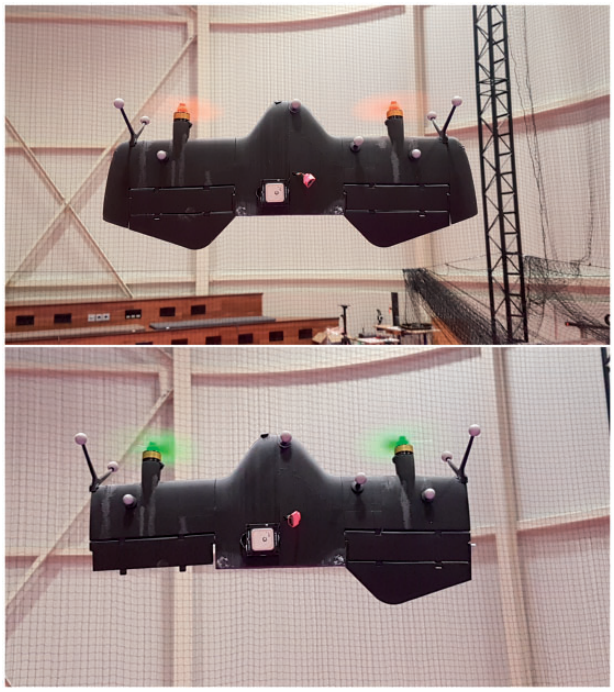

Figure 21. Tailsitter MAV configurations used during flight tests. At the top, DarkO with nominal wings, control surfaces and two-blade propellers. At the bottom, DarkO has been modified by removing its wingtips, half of its control surface and three-blade propellers were used.

Table 2. DarkO MAV parameters.

Parameters	Values	SI units
Mass (m)	0.492	(kg)
Mean chord (c)	0.13	(m)
Wingspan (b)	0.55	(m)
Wing area (S)	0.0743	(m^2)
J_{xx}	0.0070	(kg m^2)
J_{yy}	0.0028	(kg m^2)
J_{zz}	0.0061	(kg m^2)
J_p	5.1116e-06	(kg m^2)
k_f	5.13e-6	(kg m)
k_m	2.64e-7	(kg m^2)
C_{d0}	0.025	No units
C_{y0}	0.1	No units
C_{l_p}	0.2792	No units
C_{l_q}	0.0	No units
C_{l_r}	0.1145	No units
C_{m_p}	0.0	No units
C_{m_q}	1.2715	No units
C_{m_r}	0.0	No units
C_{n_p}	0.081	No units
C_{n_q}	0.0	No units
C_{n_r}	0.0039	No units
p_{p_x}	0.065	m
p_{p_y}	0.155	m
p_{p_z}	0.0	m
p_{a_x}	0.0	m
p_{a_y}	0.155	m
p_{a_z}	0.0	m
ξ_f	0.85	No units
ξ_m	0.55	No units

Discussion and conclusion

The main objective of this study is to show the easy implementation of the MFC algorithm to different hybrid MAV platforms. We have presented the development of a full control architecture based on MFC techniques, applied to MAV with transitioning flight capabilities. Numerical flight simulations were performed in order to validate the interactions between each control block for different flight domains covering the entire tailsitter MAV flight envelope. Attitude control loop performance was examined in frequency domain during the hovering and the forward flight. The FFT results demonstrated high tracking performance for most of the attitude bandwidth. As a critical point, during forward-to-hover transition, we have investigated the adaptive properties of the controller by varying the parameters of the tailsitter MAV during flight. MFC algorithms estimated and rejected the variations of 45% of the nominal parameters providing a stable transitioning flight. The velocity control performance has also been investigated simultaneously with the attitude control block in hovering and transitioning flights for different unstable initial conditions. Both control blocks are able to stabilize the tailsitter MAV from a variety of initial pitch angles and initial forward-speeds recovering the MAV to stable equilibrium points. The proposed control approach provides high performance position tracking, velocity control and attitude stabilization without gain scheduling method and by using only little prior knowledge of the tailsitter MAV. Furthermore, the MFC attitude stabilization performance, its real time estimation and its adaptive properties have been validated in real-world flight conditions. In addition, comparative indoor flight tests between MFC and INDI have been conducted. However, it has been realized that in order to come to a conclusion between the performance of the two controllers, additional flight experiments have to be performed. In particular, during the forward flight phase at outdoor environment so that the disturbance rejection properties of each control approach can be compared and evaluated properly.

Future work will include additional flight tests with different MAV configurations with a wide variety of design parameters. We would also like to investigate if a proof of stability can be established, analyzing the adaptation properties of the MFC estimator in the closed-loop system.

DarkO MAV parameters

The DarkO hybrid MAV's parameters used in this paper for all flight simulations, are presented in Table 2.

Declaration of conflicting interests

The author(s) declared no potential conflicts of interest with respect to the research, authorship, and/or publication of this article.

Funding

The author(s) received no financial support for the research, authorship, and/or publication of this article.

ORCID iD

Jacson MO Barth https://orcid.org/0000-0001-7132-2929

References

1. Santos MA, Cardoso DN, Rego BS, et al. A discrete robust adaptive control of a tilt-rotor UAV for an enlarged flight envelope. In: *IEEE 56th annual conference on decision and control (CDC)*, Melbourne, Australia, 12–15 December 2017. pp.5208–5214.
2. Hartmann P, Meyer C and Moormann D. Unified velocity control and flight state transition of unmanned tilt-wing aircraft. *J Guid Control Dyn* 2017; 40: 1348–1359.
3. Gu H, Lyu X, Li Z, et al. Development and experimental verification of a hybrid vertical take-off and landing (VTOL) unmanned aerial vehicle (UAV). In: *International conference on unmanned aircraft systems (ICUAS)*, Miami, FL, USA, 13–16 June 2017, pp. 160–169.
4. Flores A, Montes de Oca A and Flores G. A simple controller for the transition maneuver of a tail-sitter drone. In: *IEEE conference on decision and control (CDC)*, Miami Beach, FL, USA, 17–19 December 2018, pp. 4277–4281.
5. Chinwicharnam K, Gomez Ariza D, Moschetta J-M, et al. Aerodynamic characteristics of a low aspect ratio wing and propeller interaction for a tilt-body MAV. *Int J Micro Air Veh* 2013; 5: 245–260.
6. Bronz M, Smeur EJJ, de Marina HG, et al. Development of a fixed-wing mini UAV with transitioning flight capability. In: *35th AIAA applied aerodynamics conference, AIAA AVIATION forum*, Denver, CO, USA, 6 July 2017.
7. Argyle ME, Beard RW and Morris S. The vertical bat tailsitter: dynamic model and control architecture. In: *American control conference* (*ACC*), Washington, DC, USA, 7 June 2013, pp.806–811.
8. Forshaw JL, Lappas VJ and Briggs P. Transitional control architecture and methodology for a twin rotor tail-sitter. *J Guid Control Dyn* 2014; 37: 1289–1298.
9. Matsumoto T, Kita K, Suzuki R, et al. A hovering control strategy for a tail-sitter Vtol UAV that increases stability against large disturbance. In: *IEEE international conference on robotics and automation (ICRA)*, Anchorage, AK, USA, May 2010, pp. 54–59.
10. Bilodeau P-R and Wong F. Modeling and control of a hovering mini tail-sitter. *Int J Micro Air Veh* 2010; 2: 211–220.
11. Hochstenbach M, Notteboom C, Theys B, et al. Design and control of an unmanned aerial vehicle for autonomous parcel delivery with transition from vertical take-off to forward flight – VertiKUL, a quadcopter tailsitter. *Int J Micro Air Veh* 2015; 7: 395–405.
12. Casau P, Cabecinhas D and Silvestre C. Autonomous transition flight for a vertical take-off and landing aircraft. In: *IEEE conference on decision and control and European control conference (CDC-ECC)*, Orlando, FL, USA, December, 2011, pp. 3974–3979.
13. Park S, Bae J, Kim Y, et al. Fault tolerant flight control system for the tilt-rotor UAV. *J Franklin Instit* 2013; 350: 2535–2559.
14. Lustosa LR, Defay F and Moschetta J-M. Longitudinal study of a tilt-body vehicle: modeling, control and stability analysis. In: *International conference on unmanned aircraft systems (ICUAS)*, Denver, Colorado, USA, 9–12 June 2015, pp. 816–824.
15. Kita K, Konno A and Uchiyama M. Transition between level flight and hovering of a tail-sitter vertical takeoff and landing aerial robot. *Adv Rob* 2012; 24: 763–781.
16. Silva NBF, Fontes JVC, Inoue RS, et al. Dynamic inversion and gain-scheduling control for an autonomous aerial vehicle with multiple flight stages. *J Control Autom Elec Syst* 2018; 29: 328–339.
17. Saeed AS, Younes AB, Cai C, et al. A survey of hybrid unmanned aerial vehicles. *Progr Aerosp Sci* 2018; 98: 91–105.
18. Ritz R and D'Andrea R. A global controller for flying wing tailsitter vehicles. In: *IEEE international conference on robotics and automation (ICRA)*, Singapore, 29 May–3 June 2017 pp. 2731–2738.
19. Knoebel NB and McLain TW. Adaptive quaternion control of a miniature tailsitter UAV. In: *American control conference*, Seattle, WA, USA, June 2008 (ACC), pp.2340–2345.
20. Jung Y and Shim DH. Development and application of controller for transition flight of tail-sitter UAV. *J Intell Rob Syst* 2011; 65: 137–152.
21. Wang W, Zhu J and Kuang M. Design, modelling and hovering control of a tail-sitter with single thrust-vectored propeller. In: *International conference on intelligent robots and systems (IROS)*, Vancouver, BC, Canada, 24–28 September 2017, pp. 5971–5976.
22. Hajiloo A and Rodrigues L. Modeling and backstepping control of under-actuated spherical UAV. In: *IEEE conference on control technology and applications (CCTA),*

Kohala Coast, Hawai'i, USA, 27–30 August 2017, pp. 2069–2074.
23. Fang X, Lin Q, Wang Y, et al. Control strategy design for the transitional mode of tiltrotor UAV. In: *10th IEEE international conference on industrial informatics (INDIN)*, Beijing, China, July 2012, pp. 248–253.
24. Li Z, Zhou W, Liu H, et al. Nonlinear robust flight mode transition control for tail-sitter aircraft. *IEEE Access* 2018; 6: 65909–65921.
25. Smeur EJJ, Bronz M and de Croon GCHE. Incremental control and guidance of hybrid aircraft applied to a tail-sitter unmanned air vehicle. *J Guid Control Dyn* 2019; 43: 1–14.
26. Pucci D, Hamel T, Morin P, et al. Nonlinear feedback control of axisymmetric aerial vehicles. *Automatica* 2015; 53: 72–78.
27. Pucci D, Hamel T, Morin P, et al. Nonlinear control of aerial vehicles subjected to aerodynamic forces. In: *IEEE conference on decision and control (CDC)*, Florence, Italy, 10–13 December 2013, pp.4839–4846.
28. Wang W, Zhu J, Kuang M, et al. Adaptive attitude control for a tail-sitter UAV with single thrust-vectored propeller. In: *IEEE international conference on robotics and automation (ICRA)*, Brisbane, Australia, 21–25 May 2018, pp. 6581–6586.
29. Fliess M and Join C. Model-free control. *Int J Control* 2013; 86: 2228–2252.
30. Join C, Bernier J, Mottelet S, et al. A simple and efficient feedback control strategy for wastewater denitrification. In: *20th world IFAC congress*, Toulouse, France, 9–14 July 2017 (Vol. 50, No. 1) pp. 7657–7662.
31. Rodriguez-Fortun JM, Rotella F, Alfonso J, et al. Model-free control of a 3-DOF piezoelectric nanopositioning platform. In: *52nd IEEE conference on decision and control*, Florence, Italy, 10–13 December 2013, pp. 342–347.
32. Bara O, Fliess M, Join C, et al. Toward a model-free feedback control synthesis for treating acute inflammation. *J Theor Biol* 2018; 448: 26–37.
33. Join C, Robert G and Fliess M. Model-free based water level control for hydroelectric power plants. In: *IFAC conference on control methodologies and technologies for energy efficiency*, Vilamoura, Portugal, 29–31 March 2010 (Vol. 43, No. 1) pp. 134–139.
34. Abouaïssa H, Fliess M and Join C. Fast parametric estimation for macroscopic traffic flow model. In: *17th IFAC world congress*, Seoul, South Korea, 6–11 July 2008, pp. 13040–13045.
35. Chand AN, Kawanishi M and Narikiyo T. Non-linear model-free control of flapping wing flying robot using iPID. In: *IEEE international conference on robotics and automation (ICRA)*, Stockholm, Sweden, 16–20 May 2016, pp. 2930–2937.
36. Al Younes Y, Drak A, Noura H, et al. Robust model-free control applied to a quadrotor UAV. *J Intell Rob Syst* 2016; 84: 37–52.
37. Barth JMO, Condomines J-P, Bronz M, et al. Fixed-wing UAV with transitioning flight capabilities: model-based or model-free control approach? A preliminary study. In: *International conference on unmanned aircraft systems (ICUAS)*, Dallas, TX, USA, USA, 12–15 June 2018, pp. 1157–1164.
38. Barth JMO, Condomines J-P, Moschetta J-M, et al. Model-free control approach for fixed-wing UAVs with uncertain parameters analysis. In: *23rd international conference on methods and models in automation and robotics (MMAR)*, Miedzyzdroje, Poland, 27–30 August 2018, pp. 527–532.
39. Barth JMO, Condomines J-P, Moschetta J-M, et al. Full model-free control architecture for hybrid UAVs. In: *American control conference (ACC)*, Philadelphia, USA, 10–12 July 2019. Unpublished.
40. Drela M. XFOIL: an analysis and design system for low reynolds number airfoils. In: *Conference on low Reynolds number airfoil aerodynamics*, University of Notre Dame, 5–7 June 1989.
41. Lustosa LR, Defaý F and Moschetta J-M. Global singularity-free aerodynamic model for algorithmic flight control of tail sitters. *AIAA J Guid Control Dyn* 2019; 42: 303–316.
42. Lustosa LR. *The Phi-theory approach to flight control design of hybrid vehicles*. Ph.D. dissertation, Institut Supérieur de l'Aéronautique et de l'Espace, École Doctorale Aéronautique-Astronautique, Toulouse, France, ch. 2., 2017.
43. Lafont F, Balmat J-F, Pessel N, et al. A model-free control strategy for an experimental greenhouse with an application to fault accommodation. *Comput Electron Agric* 2015; 110: 139–149.
44. Martin P and Salaun E. Design and implementation of a low-cost observer-based attitude and heading reference system. *Control Eng Pract* 2010; 18: 712–722.
45. Chahl JS, Jain LC, Mizutani A, et al. *Innovations in intelligent machines-1*. Berlin Heidelberg: Springer-Verlag, 2007, pp.181.
46. Smeur EJJ, de Croon GCHE and Chu Q. Cascaded incremental nonlinear dynamic inversion control for MAV disturbance rejection. *Control Eng Pract* 2018; 73: 79–90.
47. Hattenberger G, Bronz M and Gorraz M. Using the paparazzi UAV system for scientific research. In: *International micro air vehicle conference and competition (IMAV)*, Delft, Netherlands, 12–15 August 2014, pp. 247–252.

A.2 AIAA SciTech Forum

Barth, J. M. O., Condomines, J.-P., Bronz, M., Hattenberger, G., Moschetta, J.-M., Join, C., and Fliess, M., "Towards a Unified Model-Free Control Architecture for Tail Sitter Micro Air Vehicles: Flight Simulation Analysis and Experimental Flights," *AIAA SciTech Forum: Guidance, Navigation, and Control Conference*, Orlando, Florida, USA, pp. 1-22, January 2020. doi: https://doi.org/10.2514/6.2020-2075.

Towards a Unified Model-Free Control Architecture for Tailsitter Micro Air Vehicles: Flight Simulation Analysis and Experimental Flights

Jacson Miguel Olszanecki Barth*, Jean-Philippe Condomines†, Murat Bronz‡, Gautier Hattenberger§
ENAC, Université de Toulouse, 31055, France

Jean-Marc Moschetta¶
Institut Supérieur de l'Aéronautique et de l'Espace, Toulouse, 31400, France

Cédric Join‖
Université de Lorraine, Vandœuvre-lès-Nancy, 54506, France

Michel Fliess**
École polytechnique, Palaiseau, 91128, France

Hybrid Micro Air Vehicles (MAVs) combine the beneficial features of rotorcraft with fixed-wing configurations providing a complete flight envelope that includes vertical take-off, hover, transitioning flights, forward flight and vertical landing. Tailsitter MAVs belong to a particular class of hybrid MAVs and its peculiar issue is related to the transitioning flight phase where, for high incidence angles, fast changing of aerodynamic forces and moments are observed which are difficult to model and control accurately. To overcome this issue, we proposed a control architecture with model-free control (MFC) algorithms that has been able to stabilize the hybrid MAV's attitude, velocity, and position without any modeling process. The proposed control architecture consisted basically two steps : 1) The attitude control, to ensure the hybrid MAV's attitude tracking and stability within the entire flight envelope; 2) The guidance system responsible to control both velocity and position. We validated the MFC architecture according to a comprehensive set of flight simulations and experimental flight tests. Experimental flight tests shown an effective and promising control strategy solving the principal issue of hybrid MAVs that was the formulation of accurate hybrid MAV's dynamic equations to design control laws. The obtained results have provided a straightforward way to validate the methodological principles presented in this article as well as to certify the designed MFC parameters, and to establish a conclusion regarding MFC benefits in both theoretical and practical contexts.

I. Introduction

Over the last decades, aerospace engineers have contributed to the design of different Micro Air Vehicle (MAV) configurations proposing innovative solutions for complex flight missions in outdoor or indoor environments. Recent advances in embedded systems which include sensors miniaturization and faster microprocessors allowing high frequency processes for on board computing operations brought together high flight performance demands which imply, for each flight mission, the assignment of an appropriated MAV configuration. For long endurance flight missions, the use of fixed-wing configurations is suitable due to their optimized aerodynamic surfaces that, in contact with mass of air in mouvement, generate lift force relieving the energy consumption. On the other hand, in terms of flight

*Ph.D. Candidate, ENAC, Université de Toulouse, e-mail:jacson-miguel.olszanecki-barth@enac.fr; AIAA Student Member
†Assistant Professor, ENAC, Université de Toulouse, e-mail:jean-philippe.condomines@enac.fr
‡Assistant Professor, ENAC, Université de Toulouse, Drones Research Group, e-mail:murat.bronz@enac.fr
§Assistant Professor, ENAC, Université de Toulouse, e-mail:gautier.hattenberger@enac.fr
¶Professor, ISAE-SUPAERO, Department of Aerodynamics, Energetics and Propulsion, e-mail:jean-marc.moschetta@isae-supaero.fr
‖Professor, Université de Lorraine, CRAN (CNRS, UMR 7039) & AL.I.E.N (ALgèbre pour Identification Estimation Numérique), 54330 Vézelise, France, e-mail:cedric.join@univ-lorraine.fr
**Research director emeritus at the CNRS, École polytechnique, LIX (CNRS, UMR 7161) & AL.I.E.N (ALgèbre pour Identification Estimation Numérique), 54330 Vézelise, France, e-mail:Michel.Fliess@polytechnique.edu

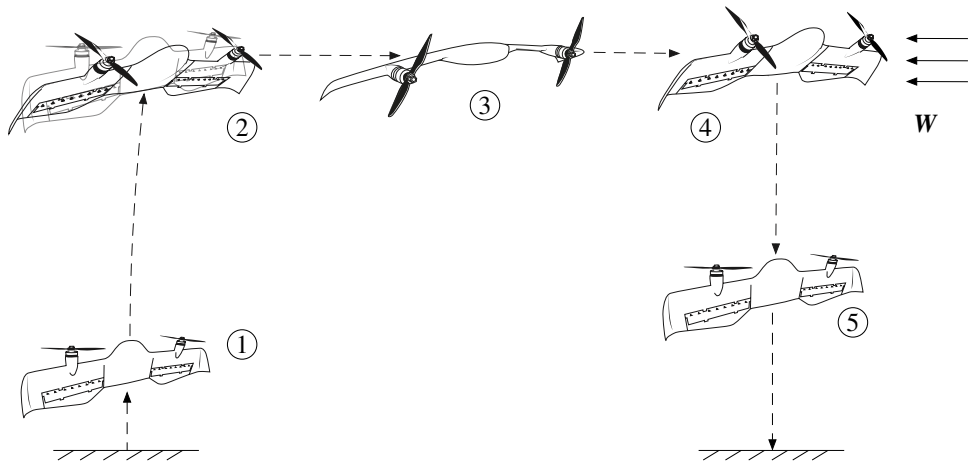

Fig. 1 Typical flight modes of Tailsitter Micro Air Vehicles: 1 - Vertical take-off; 2 - Transitioning flight; 3 - Forward flight; 4 - Hovering flight; 5 - Vertical landing. The vector *W* represents the wind disturbances.

maneuverability, rotorcraft are preferred due to their hovering flight capabilities that enable vertical take-off and landing, as well as stationary flights. However, their energetically expensive propulsion system is not viable for long endurance flights. For missions that demand the combination of endurance and maneuverability features, structural aerodynamic engineers developed the so-called hybrid MAVs that operate over a wide flight envelope including vertical take-off, efficient forward flight, transitioning flights, hovering, and vertical landing according to Fig. 1. While these different flight aptitudes enlarge its application range, aerodynamic optimization of the MAV cell must be led by aerodynamic designers considering the challenges of each flight domain. Furthermore, the autopilot system must ensure the stability and the tracking trajectories for the entire flight envelope considering the particularities of each flight domain and also the interactions between them which results a higher degree of challenge and complexity also for the guidance, navigation, and control community. Different hybrid MAV configurations can be found in the literature, such as tilt rotors [1] or tilt wings [2], quadplanes [3], and tilt body or tailsitter [4]. These platforms have been designed in order to solve the aerodynamic and mechanical limitations of each of them and the choice of the appropriated MAV configuration varies according to the imposed flight mission specifications. For instance, maximum payload, the desired endurance, the range and the inherent stability against the windy environment. Generally, tailsitter MAVs are designed and optimized to perform an efficient forward flight, since this flight phase represents most of its mission. Various studies have improved and assessed the aerodynamic properties of MAVs previously [5] [6]. However, the flap effectiveness needs to be optimized in order to create sufficient pitch moment ensuring the control authority during the transitioning flights. We focalize our research work in the design and control of tailsitter MAVs investigating the performance of this peculiar MAV class for three reasons : 1) Tailsitter are more enduring in forward flight when we compare to others; 2) The simple transition mechanisms, in relation to tilt rotors that need additional actuators to orientate the propeller in order to perform the transitioning flight; 3) The challenge of attitude stabilization during hovering and transitioning flights in windy conditions. Tailsitter are susceptible to wind disturbances during these flight phases, its stabilization remains an attractive, motivating and challenging control research topic. Typically, its entire flight envelope can be analysed in three distinct flight modes, namely, hovering flight, forward flight and transitioning flight. While hovering and forward flights were well researched and can be studied using a linearized system around an equilibrium point facilitating the impementation of classical linear control algorithms. The transition flight possesses some peculiarities that includes fast changing of aerodynamic forces and moments with wing behaviours partially stalled. Based on such aerodynamic effects, a reliable model that accurately represent the flight dynamics of a tailsitter MAVs over their entire flight envelope remains expensive, time consuming and a difficult task. Due to these practical modeling issues, some research works considered the transition flight as an undesirable and transient flight phase. However, we can not neglect the fact that, transitioning phase needs to be continuously stabilized in order to ensure a smooth and safe flight, especially against wind disturbances. Tailsitter MAV model is often considered by the control community as a parameter-varying system, e.g. the change of aerodynamic coefficients according to its attitude orientation and the environmental wind conditions. Consequently, design a control technique for autopilot systems that does not rely on prior knowledge of tailsitter MAV

model becomes an intuitive, inovative and, from the point of view of the authors, an appropriate control methodology. Therefore, the development of a such controller that estimates the tailsitter MAV dynamics and counteracts it, in real time, could be easily adaptable and implemented for different hybrid MAVs.

A. Control literature review

Different control strategies have been designed for hybrid MAVs, we present some of them in the following with particular emphasis in the controllers developed for the tailsitter class. For practical reasons, classical linear controllers designed using PID techniques have been used in some works [7] [8]. Although simple to tune without the knowledge of the controlled system dynamics, PID controllers are known by the lack of robustness against significant wind disturbances. Autopilot systems develop from optimal control theory, have been researched. For instance, the Linear Quadratic Regulator (LQR) which was designed and applied for a tailsitter MAV previously modelized and identified from wind tunnel campaign [9]. The performance of model-based controllers differs primarily in the fidelity with which the plant is modeled and the accuracy of the identified model parameters. Hence, classical model-based control techniques seem to be neither optimal for hybrid MAVs nor easily transposable for a new platform. Gain scheduling methods employing different control algorithms with both linear [10] and nonlinear approaches [11], have been developed to stabilize hybrid MAVs at different pitch angle orientations within the transitioning flight. Gain scheduling techniques allow easy understanding and simple implementation of the control gains that cover the entire flight envelope of hybrid MAVs. However, the principal disadvantage of this control method, found in the literature [12], is the expensive computational cost for operations in real time. In the same way, an attitude controller based on optimal control algorithms was proposed by [13], different control solutions for a set of attitude errors were precomputed and stored in a lookup table. According to the current flight conditions and for each autopilot system update, the desired control informations are obtained by reading the predefined values from the table. Experimental flights proven that this control approach enable the hybrid MAV to recover from a significant range of attitude errors. Further analysis is needed to determine if this proposed control strategy can be effective and easily adaptable for different hybrid MAVs. Adaptive control techniques which account for uncertainties present in the hybrid MAV model were developed by [14] [15]. However, instability problems with adaptive control methods can still exist with regard to unmodeled dynamics or inaccurate models used in the adaptation criterion of controller's gains. Different research topics applying nonlinear control techniques on hybrid MAVs, such as backstepping [16], NDI [17] and INDI [18], appears to be positively researched in the literature. The INDI approach, which is a control that depends less on the model, was experimentally flight tested providing excellent performance against wind disturbances. This controller requires the identification of the system actuator behaviour in order to estimate its control effectiveness. As the actuators effectiveness vary according to the flight phase, e.g hovering or forward flight, a gain scheduling method was implemented to fit the actuator effectiveness under the respective flight domain. Some theoretical research analyzed the performance of nonlinear feedback control on axisymmetric aerial vehicles [19] proposing an extended control solution to a larger set of generic aerodynamic models [20] which could include hybrid MAVs. Additionally, a variety of nonlinear control strategies based on Lyapunov's stability concepts have been designed to hybrid MAVs [4] [21].

B. Links with Model-Free Control algorithm

Although most of the controls described in the literature, are designed according to a modelling process, we can mention some particular techniques where the controller does not rely on modelling. For instance, the model-free control approach proposed by [22] that have been successfully used in different concrete case-studies varying from wastewater denitrification [23], nanopositioning of piezoelectric systems [24] up to inflammation resolution in biomedical applications [25], see also its references for additional case-study examples and supplementary information. Some research works based on model-free control techniques has been led to patents, such as [26] [27]. In the aerospace field, this control approach has been little applied [28] [29] and, except for our previous work, it has never been applied on hybrid MAVs which is an additional motivation for the development of our research project. The advantage of the control methodology proposed in this paper is the capability to estimate the hybrid MAV dynamics, without a prior knowledge of its parameters, only from its output and input-control signal measurements. Thus, any disturbance that may affect the flight performance are measured and the MFC algorithms are able to estimate and counteract the undesirable dynamics in order to continuously stabilize the hybrid MAV for arbitrary attitude orientations.

II. Related Work

Hybrid MAVs have now reached a level of maturity such that the problem of improving their autonomous flight capabilities is now becoming a major concern. While the different flight aptitudes of hybrid MAVs enlarge their application range, autopilot systems must ensure the stability and the tracking trajectories of all flight domains which results in a higher degree of challenge and complexity for the guidance, navigation, and control community. Often, the control community considers the hybrid MAV model as a parameter-varying system, e.g. the change of aerodynamic coefficients according to the hybrid MAV attitude and the environmental wind conditions. Consequently, design a control technique for autopilot systems that does not rely on prior knowledge of the hybrid MAV model becomes an intuitive, innovative and, from the point of view of the authors, an appropriate control methodology. Therefore, the development of a such controller that estimates the hybrid MAV dynamics and counteracts it, in real time, can be easily adaptable and implemented for different hybrid MAVs. The reviewed control approaches for hybrid MAVs draw attention to the following points :

- Control systems are usually designed from a linearized model of the hybrid MAV behaviour. Nonlinear dynamics that include aerodynamic effects, such as propeller-wing interaction and stall phenomena, are not correctly represented in the linearized model around equilibrium points of the hybrid MAV.
- The entire flight envelope of hybrid MAVs, in terms of control design, is usually addressed by considering two different flight phases: one for hovering and one for forward flight. After the control design of each flight phase tackling their respective dynamics, the transitioning phase stability is assured by gain scheduling techniques or by switching between these two control designs.
- Model-based control approaches require an identification of aerodynamic forces and moments acting in the system in order to properly design the controller. This identification, especially for high incidence angles, remains a difficult, expensive and time consuming process.

This work focuses on the development of a new control architecture for hybrid MAVs composed of model-free control algorithms. We propose a control strategy that ensures the stability of the system without switching or gain scheduling methods contributing to the development of a unified control architecture. The present work covers different steps of flight dynamics field including control design, simulation flight analysis, algorithm implementation up to experimental flight tests. In terms of flight simulation, a good understanding of aerodynamic forces and moments that act in the system is required in order to define a realistic hybrid MAV flight simulator. Unfortunately, accurate and realistic hybrid MAV model remains a very complex task without certain simplifications. Thus, in the following section, we present a simplified tailsitter MAV model with its aerodynamic assumptions. The obtained tailsitter MAV model is used to establish a flight simulator in order to test the proposed control approach before of its implementation in real flight experiments. However, we emphasize that the tailsitter MAV dynamics are unknown to the control and they are not used to design the controller.

III. Simplified Tailsitter MAV Model

We present an analytic continuous singularity-free formulation of aerodynamic forces $\boldsymbol{F_{a_b}} \in \mathbb{R}^3$ and moments $\boldsymbol{M_{a_b}} \in \mathbb{R}^3$ acting in a wing over a complete 360° angle of attack, based on previous work proposed by [30]. The wing with a surface S, is immersed in an incompressible and inviscid airflow with air density ρ. The free-stream velocity is composed by the linear element $\boldsymbol{v_\infty} \in \mathbb{R}^3$ and the angular component defined by $\boldsymbol{\omega_\infty} \in \mathbb{R}^3$ which, in the absence of wind, is equal to the hybrid MAV angular velocity $\boldsymbol{\omega_b} \in \mathbb{R}^3$. This formulation of aerodynamic forces and moments is given by :

$$\begin{pmatrix} \boldsymbol{F_{a_b}} \\ \boldsymbol{M_{a_b}} \end{pmatrix} = -\frac{1}{2}\rho S \eta C \Phi(\boldsymbol{\eta_b}) C \boldsymbol{\eta_b} \tag{1}$$

where

$$\eta = \sqrt{v_\infty^2 + \mu\, c^2 \omega_\infty^2}, \quad \text{with} \quad \mu \in \mathbb{R} > 0 \tag{2}$$

and

$$\boldsymbol{\eta_b} = \begin{pmatrix} \boldsymbol{v}_\infty \\ \boldsymbol{\omega}_\infty \end{pmatrix} \tag{3}$$

The vector $\boldsymbol{\eta_b}$ describes the linear and angular free-stream velocities in the body coordinate frame. The matrix C denotes the reference wing parameters in an extended representation,

$$C = \begin{pmatrix} I_{3\times3} & 0_{3\times3} \\ 0_{3\times3} & \begin{bmatrix} \mathrm{b} & 0 & 0 \\ 0 & \mathrm{c} & 0 \\ 0 & 0 & \mathrm{b} \end{bmatrix} \end{pmatrix} \tag{4}$$

where b and c are, respectively, the wingspan and the mean chord. Finally, the matrix $\Phi \in \mathbb{R}^{6\times6}$, which is subdivided into four matrices $\Phi^{(\cdot)} \in \mathbb{R}^{3\times3}$, shows the interaction between aerodynamic forces and moments with linear and angular free-stream velocities :

$$\Phi = \begin{pmatrix} \Phi^{(fv)} & \Phi^{(fw)} \\ \Phi^{(mv)} & \Phi^{(mw)} \end{pmatrix} \tag{5}$$

The Φ parameters are deduced from thin airfoil theory, we refer the interested reader to [30] for further information. Nonetheless, we mention that,

$$\Phi_0^{(fv)} = \begin{pmatrix} C_{d0} & 0 & 0 \\ 0 & C_{y0} & 0 \\ 0 & 0 & 2\pi + C_{d0} \end{pmatrix} \tag{6}$$

$$\Phi^{(f\omega)} = \begin{pmatrix} 0 & 0 & 0 \\ 0 & 0 & b^{-1}\Delta r C_{y0} \\ 0 & -c^{-1}\Delta r(2\pi + C_{d0}) & 0 \end{pmatrix} \tag{7}$$

$$\Phi_0^{(mv)} = \begin{pmatrix} 0 & 0 & 0 \\ 0 & 0 & -c^{-1}\Delta r(2\pi + C_{d0}) \\ 0 & b^{-1}\Delta r C_{y0} & 0 \end{pmatrix} \tag{8}$$

$$\Phi^{(m\omega)} = \frac{1}{2}\begin{pmatrix} C_{l_p} & C_{l_q} & C_{l_r} \\ C_{m_p} & C_{m_q} & C_{m_r} \\ C_{n_p} & C_{n_q} & C_{n_r} \end{pmatrix} \tag{9}$$

with C_{d0} the minimal drag coefficient and C_{y0} the minimal side force coefficient. The parameter Δr represents the distance between the center of gravity location and the aerodynamic center (neutral point). The negative values of Δr, according to the defined coordinate system, imply a positive static margin of the hybrid MAV. Finally, C_l, C_m and C_n are the aerodynamic moment coefficients which depend on the angular hybrid MAV velocities (p, q, r). The lift curve slope corresponding to 2π, in (6), (7) and (8), was deduced from the thin airfoil theory in 2D. In this work, we evaluate the lift curve slope in 3D considering the wing aspect ratio (AR). According to Diederich's formula, we consider :

$$\Phi_0^{(fv)}(:,3) = \begin{pmatrix} 0 \\ 0 \\ \frac{\pi AR}{1+\sqrt{1+(\frac{AR}{2})^2}} + C_{d0} \end{pmatrix} \tag{10}$$

$$\Phi^{(f\omega)}(:,2) = \begin{pmatrix} 0 \\ 0 \\ -c^{-1}\Delta r\Big(\frac{\pi AR}{1+\sqrt{1+(\frac{AR}{2})^2}} + C_{d0}\Big) \end{pmatrix} \tag{11}$$

$$\Phi_0^{(mv)}(:,3) = \begin{pmatrix} 0 \\ -c^{-1}\Delta r\Big(\frac{\pi AR}{1+\sqrt{1+(\frac{AR}{2})^2}} + C_{d0}\Big) \\ 0 \end{pmatrix} \tag{12}$$

where

$$AR = \frac{b^2}{S} \tag{13}$$

Finally, the flap deflections are modeled as varying cambered airfoils and the aerodynamic forces and moments created by these deflections are approximated by the following equations :

$$\Phi^{(fv)}(\delta_i) = \Phi_0^{(fv)}(I - [\boldsymbol{\xi_f}]_\times \delta_i) \tag{14}$$

$$\Phi^{(mv)}(\delta_i) = \Phi_0^{(mv)}(I - [\boldsymbol{\xi_m}]_\times \delta_i) \tag{15}$$

the flap deflection effectiveness is represented by two skew-symmetric matrices, $[\boldsymbol{\xi_f}]_\times$ for the force effectiveness and $[\boldsymbol{\xi_m}]_\times$ for the moment effectiveness, given by :

$$[\boldsymbol{\xi_f}]_\times = \begin{bmatrix} 0 & -\xi_f & \xi_f \\ \xi_f & 0 & -\xi_f \\ -\xi_f & \xi_f & 0 \end{bmatrix}$$

$$[\boldsymbol{\xi_m}]_\times = \begin{bmatrix} 0 & -\xi_m & \xi_m \\ \xi_m & 0 & -\xi_m \\ -\xi_m & \xi_m & 0 \end{bmatrix}$$

A. Equations of motion

The tailsitter MAV model is divided into four rigid bodies (two propellers and one fuselage composed by two wings) with constant mass (m), represented by ten states $\boldsymbol{x} = (\boldsymbol{v_b}, \boldsymbol{\omega_b}, \boldsymbol{q})$, where $\boldsymbol{v_b} \in \mathbb{R}^3$ is the vehicle's linear velocity, $\boldsymbol{\omega_b} \in \mathbb{R}^3$ is the vehicle's angular velocity equals to $[p\ q\ r]^T$ both expressed in the body coordinate frame and $\boldsymbol{q} \in \mathbb{R}^4$ is the quaternion formulation. The system is controlled via four control-inputs, $\boldsymbol{u} = (\omega_l, \omega_r, \delta_l, \delta_r)$, respectively, the left and right propeller rotation speeds and the left and right flap deflections, which are represented in the Fig. 2. In order to compute the forces and moments caused by the wing-propeller interaction, we define two segments. Each segment is composed by one wing j and by one propeller k. Thus, the sum of aerodynamic forces acting on the wing j with the thrust $\boldsymbol{T}_k$ generated by the propeller rotation ω_k and the total moment described in the body coordinate frame, are given by :

$$\boldsymbol{F_b} = \sum_{j,k=1}^{2} (\boldsymbol{F_{a_{b_j}}} + \boldsymbol{T}_k) \tag{16}$$

$$\boldsymbol{M_b} = \sum_{j,k=1}^{2} (\boldsymbol{M_{a_{b_j}}} + \boldsymbol{\tau_{b_k}} + \boldsymbol{p_p} \times \boldsymbol{T}_k + \boldsymbol{p_a} \times \boldsymbol{F_{a_{b_j}}}) \tag{17}$$

The vector $\boldsymbol{p_p} = [p_{p_x}\ p_{p_y}\ p_{p_z}]^T$ defines the distance between the propeller k with the hybrid MAV center of mass. Both propellers are positioned symmetrically with respect to the hybrid MAV center of mass. The distance between the

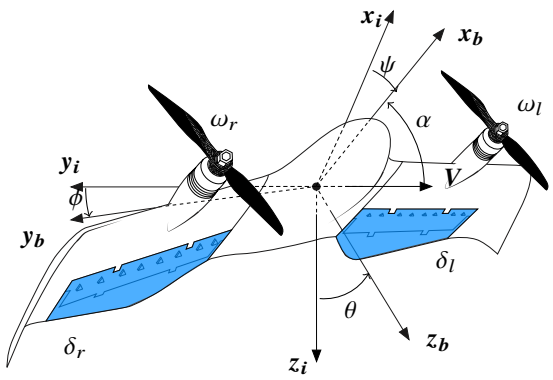

Fig. 2 Illustration of the used coordinate frames, angles and actuators. The inertial coordinate frame is represented by $\mathcal{R}_i = \{x_i, y_i, z_i\}$ and the body coordinate frame by $\mathcal{R}_b = \{x_b, y_b, z_b\}$.

aerodynamic center and the center of mass is represented by the vector $\boldsymbol{p_a} = [p_{a_x}\ p_{a_y}\ p_{a_z}]^T$. The internal torque of the propeller $\boldsymbol{\tau_{b_k}}$ that is a function of the vehicle's angular velocity $(p\ q\ r)$, and the thrust force $\boldsymbol{T}_k$, are defined by :

$$\boldsymbol{T}_k = k_f \omega_k^2 \boldsymbol{x_b}, \qquad k_f \in \mathbb{R} > 0 \tag{18}$$

$$\boldsymbol{\tau_{b_k}} = \boldsymbol{N_{b_k}} - J_p\,(p + \omega_j) \begin{pmatrix} 0 \\ r \\ -q \end{pmatrix} \tag{19}$$

where

$$\boldsymbol{N_{b_k}} = -\text{sign}(\omega_k) k_m \omega_k^2 \boldsymbol{x_b}, \qquad k_m \in \mathbb{R} > 0 \tag{20}$$

with k_f and k_m the propeller force and moment coefficients and $\boldsymbol{N_{b_k}}$ the propeller moment. Equation (19) describes the gyroscopic interaction between the propellers and the fuselage with J_p equals to the propeller inertia. The vehicle's equations of motion are given by (21).

$$\begin{cases} m\,\dot{\boldsymbol{v}} & = R^T \boldsymbol{F_b}(\boldsymbol{x}, \boldsymbol{u}, \boldsymbol{W}) + m\boldsymbol{g} \\ J\,\dot{\omega_b} & = \boldsymbol{M_b}(\boldsymbol{x}, \boldsymbol{u}, \boldsymbol{W}) - [\boldsymbol{\omega_b}]_\times J \boldsymbol{\omega_b} \\ \dot{\boldsymbol{q}} & = \frac{1}{2} \boldsymbol{q} * \boldsymbol{\omega_b} \\ \dot{\boldsymbol{p}} & = \boldsymbol{v} \end{cases} \tag{21}$$

The gravitational acceleration vector is equals to $\boldsymbol{g} = g\boldsymbol{z_i}$ and $\boldsymbol{W} \in \mathbb{R}^3$ is the wind disturbance vector. The rotation matrix R, namely the Direction Cosines Matrix (DCM), represents the MAV rotation in three dimensions as a mathematical formulation. We assume that the hybrid MAV inertia matrix J is diagonal and it equals to $J = \text{diag}\,[J_{xx}\ J_{yy}\ J_{zz}]$. The position vector in the inertial coordinate frame is represented by $\boldsymbol{p} = [x\ y\ z]^T$. The highly maneuverable nature of the vehicle calls for a global numerically stable formulation of attitude and justifies the use of quaternions. The symbol $*$ in the previous equation corresponds to the quaternion product.

IV. Model-Free Control

The following section outlines briefly the main features of model-free control approach and some previous research-works dealing with on-line dynamic state estimation. These research-works have been applied in different areas of the science including aerospace systems. However, we present for the first time the development of a such controller for hybrid MAVs, see Fig. 3.

A. Principles

As introduced by [22], an unknown finite-dimensional system with a single control-input (u) and a single output (y) can be described by the following input/output relation in a differential equation formulation :

$$\mathbb{E}(y, \dot{y}, \ldots, y^{(a)}, u, \dot{u}, \ldots, u^{(b)}) = 0 \tag{22}$$

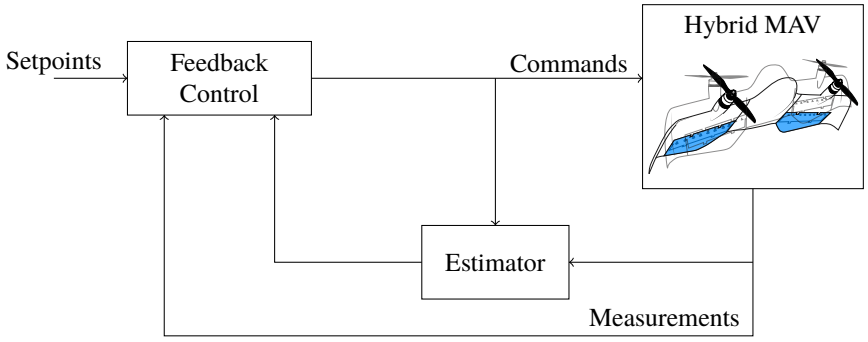

Fig. 3 Overall Model-Free Control schema for hybrid MAVs.

where $\mathbb{E}$ is a polynomial function with real unknown coefficients. We can also describe

$$y^v = \mathbb{E}(t, y, \dot{y}, \ldots, y^{(v-1)}, y^{(v+1)}, \ldots, y^{(a)}, u, \dot{u}, \ldots, u^{(b)}) \tag{23}$$

with $0 < v \leq a$ and $\frac{\delta \mathbb{E}}{\delta y^v} \neq 0$. This unknown dynamic can be approximated by a purely numerical equation, the so-called *Ultra-Local Model* :

$$y_m^{(v)} = F_y + \lambda \cdot u \tag{24}$$

In (24), v is the order derivative of y_m, $\lambda \in \mathbb{R}$ is a non-physical constant parameter. Moreover, the exploitation of this numerical model requires the knowledge of F_y. This quantity represents the real dynamics of the model as well as the different disturbances which could damage the performance of the output-system. Thus, an accurate estimation of F, defined as $\hat{F}$, is crucial and plays an import role in the control performance. Different practical experiments proved that a first order *Ultra-Local Model* ($v = 1$) is enough to stabilize with precision an unknown dynamic. In this work, we propose to develop a second-order *Ultra-Local Model* ($v = 2$) due to viscous friction and actuator dynamics that could add an extra order to the system. Assuming that we do not have any information about an arbitrary second order dynamic, its estimation can be computed directly by the following methodology, see algorithm (1).

Algorithm 1 Computing the estimator $\hat{F}$

1: **procedure**
2: $v \leftarrow$ Define estimator order
3: **step 1:** Write the *Ultra-Local Model*
4: **step 2:** Calculate the *Laplace transforms*
5: **step 3:** Derive step 2 v times with respect to s
6: **step 4:** Multiply the step 3 by $s^{-(v+1)}$
7: **step 5:** Calculate the *Inverse Laplace transforms*
8: **end procedure**;

In a mathematical formulation, we obtain :

$$\ddot{y}_m = F_y + \lambda \cdot u \tag{25}$$

The first step is to apply the *Lapace Transform* in (25). Referring to elementary operational calculus we transform (25) to (26) :

$$s^2 Y_m(s) - s y_m(0) - \dot{y}_m(0) = \frac{F_y}{s} + \lambda U(s) \tag{26}$$

Where $Y_m(s)$ and $U(s)$ correspond to the *Laplace transforms* of y_m and u. By differentiating twice the previous equation we are able to rid the initial conditions $y_m(0)$ and $\dot{y}_m(0)$:

$$2Y_m(s) + 4s\frac{dY_m(s)}{ds} + s^2\frac{d^2Y_m(s)}{ds^2} = \frac{2F_y}{s^3} + \lambda\frac{d^2U(s)}{ds^2} \tag{27}$$

However, the variable s in the time domain corresponds to the derivation with respect to time that is sensitive to noise corruptions and can amplify the noise measurement. Therefore, in order to reduce both noise and numerical computation errors on the output estimation, we replace the derivative terms by integrators ($\frac{1}{s}$) who have robust properties with respect to noise. Thus, multiplying both sides of (27) by s^{-3}, we obtain :

$$\frac{2Y_m(s)}{s^3} + \frac{4}{s^2}\frac{dY_m(s)}{ds} + \frac{1}{s}\frac{d^2Y_m(s)}{ds^2} = \frac{2F_y}{s^6} + \frac{\lambda}{s^3}\frac{d^2U(s)}{ds^2} \tag{28}$$

Equation (28) can be transferred back to the time domain employing elementary calculus and *Cauchy's formula* to reduce multiple integrals in a simple one :

$$\hat{F_y}(t) = \frac{5!}{2T^5}\int_{t-T}^{t}[(T-\sigma)^2 - 4\sigma(T-\sigma) + \sigma^2]y_m(\sigma) - [\frac{\lambda}{2}\sigma^2(T-\sigma)^2 u(\sigma)]d\sigma \tag{29}$$

From measurements of the corrupted signal $y_m(t)$ and $u(t)$ obtained in the last T seconds, the unmodeled dynamic of y and the disturbances are estimated by $\hat{F}_y(t)$ which is updated for each interval of integration $[t-T, t]$. This interval

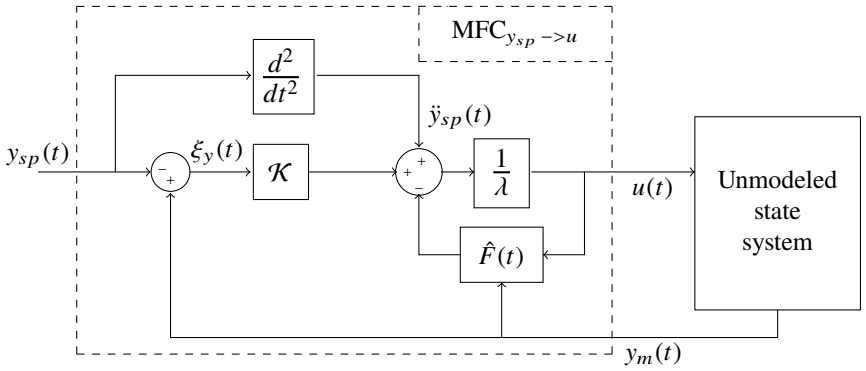

Fig. 4 Detailled model-free control schema.

corresponds to the window width of a receding horizon strategy which results in a trade-off. The idea is to choose the window width small so as to calculate the estimation within an acceptable short delay but large enough in order to preserve the low-pass filter properties for suppressing measurement noise on $y_m(t)$. Based on such estimator, it is possible to design a robust controller that estimates the system dynamic by a piecewise function $\hat{F}_y(t)$, periodically updated for each measure of $y_m(t)$ and $u(t)$. The detailed form of the MFC schema presented in Fig. 4 allows us to define the closed-loop control such as :

$$u(t) = \underbrace{-\frac{\hat{F}_y(t)}{\lambda}}_{\text{Nonlinear Cancellation}} + \underbrace{\frac{y_{sp}^{(2)}(t) + \mathcal{K}(\xi_y(t))}{\lambda}}_{\text{Closed loop tracking}} \tag{30}$$

The quantity $\xi_y(t) = y_m(t) - y_{sp}(t)$ represents the tracking error and $\mathcal{K}(\xi_y(t))$ is a closed-loop feedback controller, usually defined as a proportional, proportional-derivative or even so as proportional-integral-derivative gain. In this paper, we define the closed loop feedback controller as a proportional K_p and derivative gain K_d. We recognize in (30) the typical mathematical expression of a nominal control in the flatness-based in which the non-linear terms $\hat{F}_y(t)$ is added with a closed loop tracking of a reference trajectory $t \rightarrow y_{sp}(t)$. The error dynamic can be deduced from the combination of (30) with (25) :

$$\ddot{\xi}_y(t) = \ddot{y}_m(t) - \ddot{y}_{sp}(t) = \overbrace{F_y(t) - \hat{F}_y(t)}^{\xi_{F_y} \approx 0} + K_p\, \xi_y(t) + K_d\, \dot{\xi}_y(t) \tag{31}$$

$$\ddot{\xi}_y(t) - K_d\, \dot{\xi}_y(t) - K_p\, \xi_y(t) = 0 \tag{32}$$

Note that, if the error (ξ_{F_y}) between the estimator and the true dynamic, is approximately zero during $[t - T, t]$, a simple proportional-derivative controller will be enough to ensure the error convergence to zero if $K_p < 0$ and $K_d < 0$. Whereas, an integration effect is implicitly involved in the model-free control algorithm.

B. Discretized MFC equations

Expressing (25) in discrete-time domain, with k the index of the current sampling time T_s, we obtain

$$\frac{y_m(kT_s) - 2y_m(kT_s - T_s) + y_m(kT_s - 2T_s)}{T_s^2} = F(kT_s) + \lambda u(kT_s) \tag{33}$$

where the left-hand side (LHS) of (33), represents the discrete second order derivative of y_m. The discretized plant model $F(kT_s)$ represents not only the dynamic of $y_m[kT_s]$ but also the different disturbances which could damage the output-system. $u(kT_s)$ is the input-control signal, λ a constant parameter that allows us to set the same magnitude between the LHS of (33) and $\lambda u(kT_s)$. The dynamic of a SISO system is approximated by a linear model, called *Ultra-Local Model*, that is valid around a given operating point, i.e. $[kT_s, kT_s - T\,T_s]$. Different operating points may lead to several different linear models that are continuously estimated by $\hat{F}(kT_s)$. The discretized closed loop tracking is achieved by using a proportional and derivative gain, yielding the control-input $u(kT_s)$ in (34).

$$u(kT_s) = \underbrace{-\frac{\hat{F}(kT_s)}{\lambda}}_{\text{Nonlinear Cancellation}} + \underbrace{\frac{y_d^{(v)}(kT_s) + K_p\,\xi(kT_s) + K_d\,\dot{\xi}(kT_s)}{\lambda}}_{\text{Closed loop tracking}} \tag{34}$$

where $y_d^{(v)}(kT_s)$ denotes the v-th order derivative of y_d. The tracking error $\xi(kT_s)$ and the derivative of the tracking error $\dot{\xi}(kT_s)$, are defined respectively as

$$\xi(kT_s) = y_m(kT_s) - y_d(kT_s) \tag{35}$$

$$\dot{\xi}(kT_s) = \dot{y}_m(kT_s) - \dot{y}_d(kT_s) \tag{36}$$

Remark : The derivative of the tracking error can be measured directly in the system or computed with simple finite difference formulas such as backward finite difference. In this case, the derivative of the tracking error is :

$$\dot{\xi}(kT_s) = \frac{\xi(kT_s) - \xi(kT_s - T_s)}{T_s} \tag{37}$$

Substituting the control-input $u(kT_s)$ from (34) in (33), we obtain the following expression :

$$\begin{aligned}\underbrace{y_m(kT_s) - 2\,y_m(kT_s - T_s) + y_m(kT_s - 2T_s)}_{\text{Numerical second-order derivative of } y_m} &= \overbrace{F(kT_s) - \hat{F}(kT_s)}^{\xi_F \approx 0} \\ &+ \underbrace{y_d(kT_s) - 2\,y_d(kT_s - T_s) + y_d(kT_s - 2T_s)}_{\text{Numerical second-order derivative of } y_d} \\ &+ K_p\,\xi(kT_s) + K_d\,\dot{\xi}(kT_s)\end{aligned} \tag{38}$$

If $\xi_F \approx 0$, then the effect of disturbances is negligible on the error dynamic.

$$\begin{aligned}\ddot{\xi}(kT_s) = &\frac{y_m(kT_s) - 2y_m(kT_s - T_s) + y_m(kT_s - 2T_s)}{T_s^2} \\ &- \frac{y_d(kT_s) + 2y_d(kT_s - T_s) - y_d(kT_s - 2T_s)}{T_s^2}\end{aligned} \tag{39}$$

So, (40) shows that

$$\ddot{\xi}(kT_s) = K_p\xi(kT_s) + K_d\dot{\xi}(kT_s) \tag{40}$$

We can see that the system can be guaranteed to be stable if K_p and K_d are negatives and the control law (34) can be shown to be stable resulting in $\xi(kT_s) \to 0$ as $kT_S \to \infty$. The algorithm (2) describes the main steps of the MFC.

Algorithm 2 Model-free Control algorithm

1: **procedure** INITIALIZATION
2: Define sampling time $\to T_s$
3: Initial conditions $\to \boldsymbol{x_0}, \boldsymbol{u_0}$
4: Define MFC parameters $\to \lambda, T, K_p$ and K_d
5: **end procedure**;
6: **procedure** MFC COMMAND
7: *Control loop*:
8: Define the desired trajectory $\to y_d[kT_s]$
9: Read output measurement $\to y_m[kT_s]$
10: Read control value from the last sampling period $\to u[kT_s - T_s]$
11: Compute the discretized estimator from equation $\to \hat{F}[kT_s]$
12: Compute error $\to \xi[kT_s]$
13: Compute closed-looping tracking $\to \mathcal{K}(\xi)$
14: Compute new command from equation (34) $\to u[kT_s]$
15: **goto** *Control loop*
16: **end procedure**;

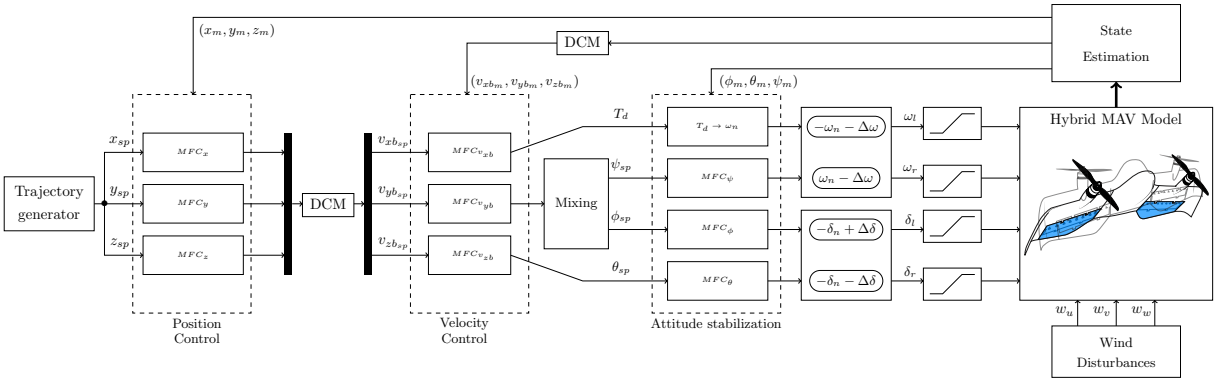

Fig. 5 Cascaded MFC architecture designed for hybrid MAVs. Velocity control block receives desired ground velocities and computes references for attitude stabilization control loop. Based on these desired values, propeller speeds (ω_l, ω_r) and flap deflections (δ_l, δ_r) are defined.

C. Proposed MFC architecture

Figure 5 shows the main ideas of our control architecture. The block *Trajectory generator* is composed of a state flow algorithm that defines constantly the desired positions (x_{sp}, y_{sp}, z_{sp}) in the inertial coordinate system. These references are taken into account by the *Position control* block and are compared with the respective measures (x_m, y_m, z_m) creating three errors that are minimized by the MFC algorithms in the *Position control* block. These three MFC algorithms in charge of the position tracking, also compute the desired velocity in their respective axes. These references values which are defined in the inertial coordinate frame are transformed to the body coordinate frame as well as the velocities measurements. Thus, the velocity control MFC$_{v_{xb}}$ computes the required thrust T_d to reach this desired velocity along $\boldsymbol{x_b}$, the block MFC$_{v_{zb}}$ assures the velocity control along $\boldsymbol{z_b}$ and determine the necessary pitch angle θ_{sp} to reach this desired velocity $v_{zb_{sp}}$. Both blocks control their respective velocities and inform the desired thrust and pitch angle for the entire flight envelope, i.e. hover, transition and forward flight. However, the velocity control along $\boldsymbol{y_b}$ is designed depending on the current hybrid MAV flight phase. Therefore, in hover flight, the block MFC$_{v_{yb}}$ set the desired yaw angle ψ_{sp} and the block MFC$_{\psi}$ actuates in the system by a differential-thrust command creating a moment around $\boldsymbol{z_b}$ in order to reach the desired velocity along $\boldsymbol{y_b}$. In forward flight, this lateral velocity is reached from roll rotations around $\boldsymbol{x_b}$. These rotations orient the lift force and the hybrid MAV can perform left-right turns with, respectively, negative and positive roll angles ϕ. The propeller speeds (ω_l, ω_r) are defined by the sum of nominal propeller rotation ω_n with a differential propeller speed Δ_ω which is in charge of the yaw control. The negative sign of ω_n for the left-propeller ω_l is due to the counter-rotation sense. And the flap-deflections (δ_l, δ_r), which are in convention negative for pitch-up, are composed by the sum of symmetrical flap deflection δ_n with anti-symmetrical flap deflections Δ_δ that are respectively the control-input for the pitch angle θ and for the roll angle ϕ. We compute the control-output of each block according to the algorithm described beforehand, algorithm (2).

V. DarkO Tailsitter MAV

Throughout the whole study, we have used the DarkO vehicle which is a tailsitter configuration consisting of two motors, positioned in front of the wing, and two exceptionally large double-flapped control surfaces, see Fig. 6. We briefly present its manufacturing process and the characteristics of motors, propellers, servos, and battery that were used during the experimental flight tests.

A. Setup and specifications

Mission definition of DarkO has been mainly oriented for forward flight with the capability of taking off and landing vertically. The frame completely manufactured by 3-D printing method using Onyx material. Figure 7 shows the printed pieces that is assembled in order to build the whole frame. The shell structure for the wing and the fuselage halves are manufactured as $0.7mm$ thick skins, and the spar is manufactured with the addition of unidirectional concentric carbon fibres embedded into Onyx material. This method ensures to have a sufficiently rigid airframe that supports

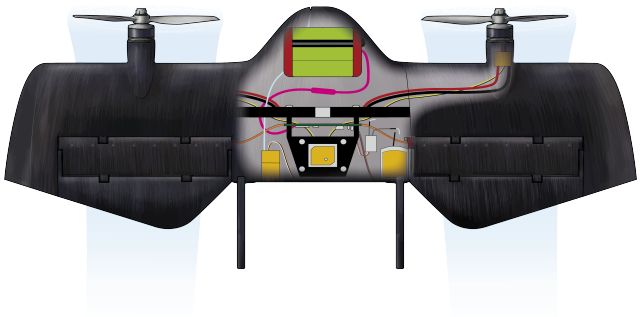

Mass	0.492 Kg
Wingspan	0.55 m
Mean Chord	0.13 m
Propellers	2-blades Bullnose 5x4.5
Motors	T-Motor Brushless F30 2800KV
Servos	MKS DS65K 0.2s/60°
Battery	3 cells 12V 3500 mAh

Fig. 6 General DarkO tailsitter MAV specifications.

aerodynamic forces and yet also flexible enough to absorb harsh impacts during landing and test flights. The different physical and geometric parameters of the DarkO MAV, are described in the Table 1. Inertia coefficients were estimated by using the classical pendulum method and the aerodynamic coefficients calculated from the open-source program XFOIL [31]. These different parameters were used in the simplified hybrid MAV model, described in the following section, in order to develop, analyze and validate the proposed control architecture, as realistic as possible, in simulation before the experimental flights.

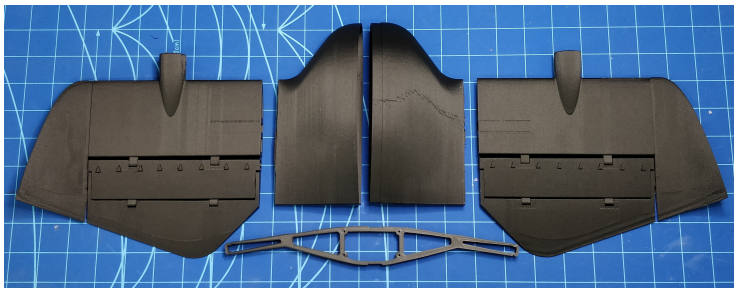

Fig. 7 Printed parts of DarkO out of Onyx material.

B. Actuators and attitude dynamics

The attitude dynamic is controlled according to the actuation principle described in the Fig. 8, 9, and 10. Hybrid MAVs are characterized as nonlinear systems with high coupled dynamics. In fact, pitch and roll angles are controlled respectively by symmetric and asymmetric flap deflections who are dependents of the propeller slipstream. The differential thrust in order to control the yaw angle modifies the propeller slipstream impacting the control-effectiveness

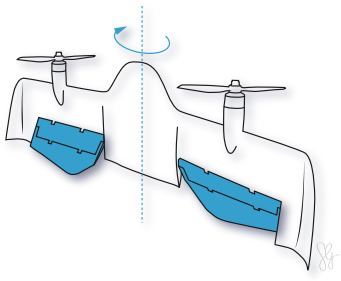

Fig. 8 Roll angle dynamic

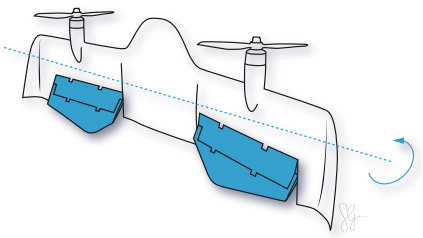

Fig. 9 Pitch angle dynamic

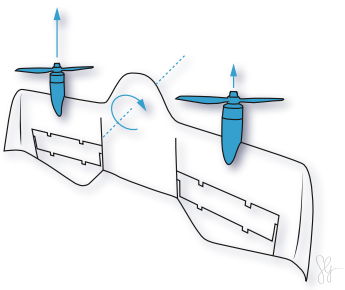

Fig. 10 Yaw angle dynamic

Table 1 DarkO MAV parameters used during flight simulations.

Parameters	Values	SI Units
Mass (m)	0.492	[Kg]
Mean Chord (c)	0.135	[m]
Wingspan (b)	0.55	[m]
Wing Area (S)	0.0743	[m^2]
J_{xx}	0.004 93	[Kg m^2]
J_{yy}	0.005 32	[Kg m^2]
J_{zz}	0.008 62	[Kg m^2]
J_p	5.1116×10^{-6}	[Kg m^2]
k_f	5.13×10^{-6}	[Kg m]
k_m	2.64×10^{-7}	[Kg m^2]
C_{d0}	0.133	No units
C_{y0}	0.145	No units
C_l	[0.47; 0.00; 0.00]	No units
C_m	[0.00; 0.54; 0.00]	No units
C_n	[0.00; 0.00; 0.52]	No units

of the flaps as well as the dynamic of both pitch and roll angles.

C. Control surface design

A particular feature that is required by the tailsitter configuration is to generate excessive amount of pitching moment in order to transition mainly from forward flight phase to hovering flight phase. Therefore, DarkO frame's control surfaces have been designed as double-flap which has a passive mechanical constant ratio. Traditionally, multisection flaps have been designed for lift enhancement, however in our case the design objective is to generate as much positive pitching moment as possible without having a massive flow separation on the bottom surface of the airfoil.

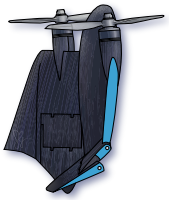

D. On-board avionics

The DarkO MAV is equipped with an *Apogee v1.00* board, presented in the Fig. 11, that contains a Cortex M4 168 MHZ processor to run the *Paparazzi* open-source autopilot system, which includes algorithms for state estimation, control laws, servo and motor drivers, software for communication, etc. In addition, the *Apogee v1.00* board is equipped with a SD logger which allows us to record the flight data for flight post-processing analysis.

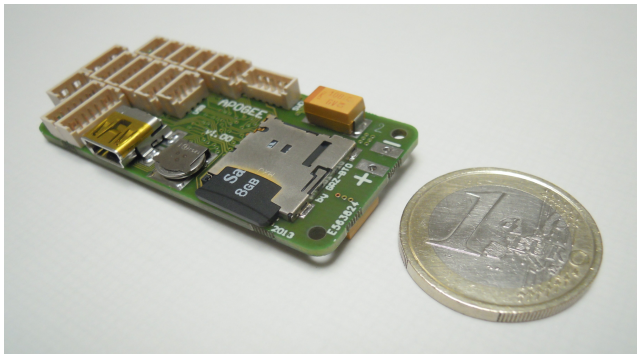

STM32F405RGT6 Cortex M4 168MHz processor
9(6) DOF integrated IMU MPU-9150(6050)
1 x Barometer/altimeter MPL3115A2
1 x MicroSD card slot
4 bit SDIO interface (high speed data logging)
6 x Servo PWM outputs
3 x UART, 2 x I2C bus, 1 x SPI bus
10.4 grams
53 mm x 25 mm

Fig. 11 Overview of *Apogee v1.00* autopilot from *Paparazzi Autopilot system*.

Inertial measurement units (IMUs) typically contain rate-gyroscopes and accelerometers on three axes, measuring angular velocities and linear accelerations respectively. By processing signals from these devices, with attitude and heading reference system (AHRS) and inertial navigation system (INS), it is possible to obtain the attitude orientations, velocities and positions of an air vehicle. The main features of each sensor device embedded in the *Apogee v1.00* board, is presented in the Table 2.

Table 2 *Apogee V1.00* embedded sensors

	Device	Noise	Bias
Accelerometer	MPU-9150	400 ($\mu g/\sqrt{Hz}$)	150 (mg)
Rate-Gyro	MPU-9150	0.005 ($^\circ/s/\sqrt{Hz}$)	20 ($^\circ/s$)
Magnetometer	MPU-9150	N/A	N/A
GNSS position	NEO-6M	σ = 2.5 (m)	0 (m)
GNSS velocity	NEO-6M	σ = 0.1 (m/s)	0 (m/s)

VI. Flight Simulations

A comprehensive set of flight simulations for hybrid MAV, discretized at 500 Hz, were performed from MATLAB/Simulink using the tailsitter MAV model described in the Section III that is controlled by the proposed MFC architecture, see Fig. 5. Our flight simulator is based on the DarkO hybrid MAV physical parameters including sensor measurements which were corrupted by gaussian white noises whose standard deviations can be found in [32]. An invariant observer [33] is used providing a smoother signal measurement of the MAV states, this operation adds delays in the closed loop and must be taken into account during the controller's synthesis. The MFC parameters, i.e. λ_i, T_i, Kp_i and Kd_i, were tuned for the entire flight envelope and are the same for all flight simulations. In particular, two different experiments were performed. First, we analyze the capabilities of the control architecture to recover the hybrid MAV from different initial conditions to a stable setpoint in hovering flight mode. In this flight simulation, only the velocity and the attitude stabilization blocks are activated. Then, we check the entire flight envelope of hybrid MAVs with the positioning tracking, velocity control and attitude stabilization as well.

A. Initial condition analysis in hovering flight

The initial conditions for pitch angle and for forward speed during the hovering flight (θ_{ic} and $V_{x_{ic}}$), follow a normal distribution law according to (29) and (30).

$$\theta_{ic} \sim \mathcal{N}\left(\frac{\pi}{2}, \left(\frac{\pi}{6}\right)^2\right). \tag{29}$$

$$V_{x_{ic}} \sim \mathcal{N}\left(0, \left(\frac{5}{3}\right)^2\right). \tag{30}$$

The stability boundary presented in the Fig. 12, was empirically defined by evaluating all recovery trajectories from initial conditions to the desired setpoint. The desired setpoint corresponds to a stationary flight in the vertical position, respectively, 0 m/s for the forward speed and 90° for the pitch angle. Basically, three classes of trajectories were distinguished during these simulations. The first one combines trajectories with initial pitching angles larger than 90° with positive initial conditions for forward speeds. Likewise, trajectories with initial pitching angles smaller than 90° and negative initial conditions for forward speeds are also included in this class. The peculiarity of these trajectories is that, both converge directly to the desired equilibrium setpoint with small oscillations in the response time. This can be explained by the fact that, for initial pitching angles larger than 90°, the thrust vector is already well-oriented and it can be increased in order to decelerate the initial positive forward speeds. This thrust vector is increased from increments of the propeller rotations, which improves the flap effectiveness creating a powerful pitch moment that can easily orientate the attitude of the hybrid MAV in the right direction, towards the attitude setpoint. The same reasoning can be done for initial pitching angles smaller than 90° with negative forward speeds. In this initial flight condition and orientation, the controller generates the thrust vector in order to increase the forward speed resulting in an effective pitch moment which also steer the hybrid MAV towards the setpoint. The second class of trajectories is composed by

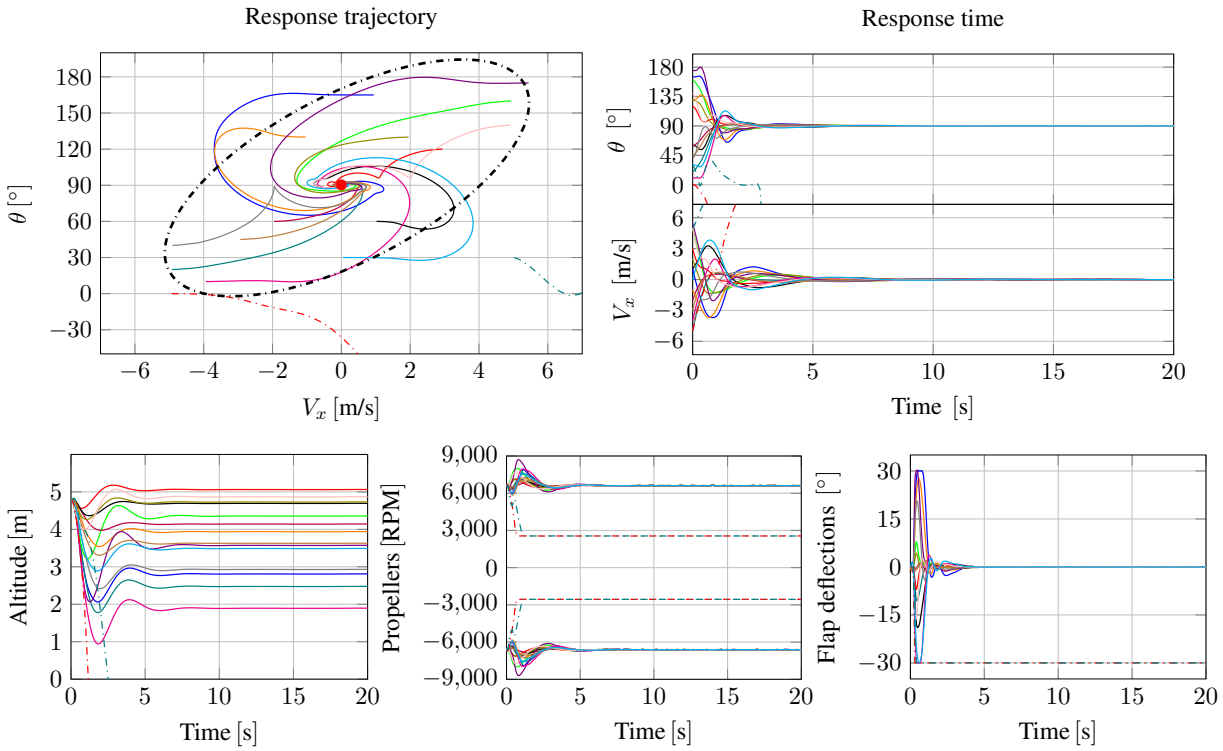

Fig. 12 Initial pitch angle and forward speed condition analysis during hovering flight phase without wind disturbances. Forward speed setpoint equals to 0 m/s, the MFC architecture computes the pitch angle setpoint equals to 90° in order to reach the stationary flight.

all initial pitching angles smaller than 90° with positive initial forward speeds and by all initial pitching angles larger than 90° with negative initial forward speeds. These trajectories diverge at the beginning of the simulation. The thrust vector, in these flight orientations, is unable to generate an opposing force to decelerate the initial forward speed to zero. The only force opposing to the movement is the drag force. By increasing the pitch angle, in this case the angle of attack, the hybrid MAV generates more drag and can reach the forward speed setpoint. For extreme cases, within the stability boundary, we can observe flap saturations which justify the shape of the concerned trajectories with overshoots or undershoots. By analyzing the altitude results, we can mention that the position control is not activated. However, we can observe that the altitude is stabilized at given values according to the velocity control block which cancels the vertical velocity component. The MFC can theoretically ensure a stable flight for all initial points inside the boundary, with more or less oscillations, according to the initial conditions. Otherwise, the hybrid MAV performs an unstable flight, as shown by the two particular initial points outside the stability boundary corresponding to the third class of trajectories in this simulation.

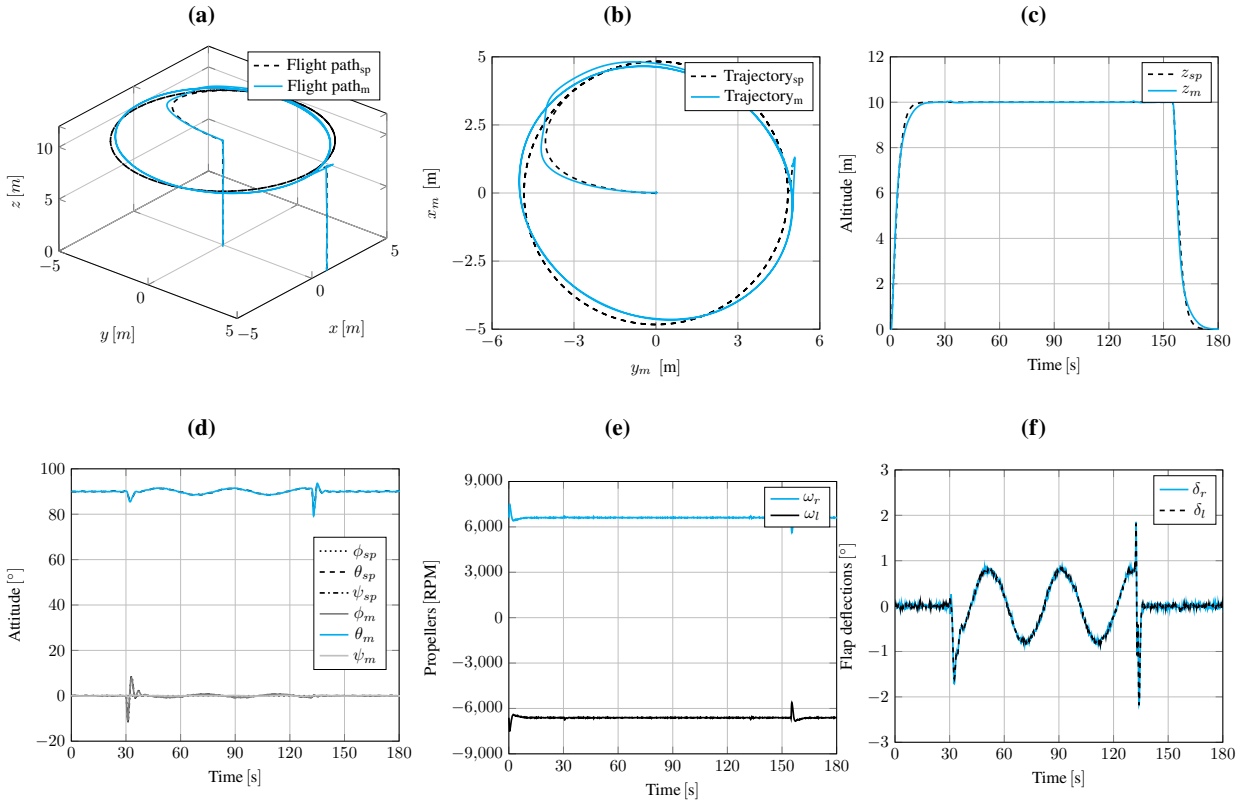

Fig. 13 Circular position tracking in hover flight mode. On the top, from left to right: the 3D flight path, North and East positions and altitude. On the bottom: attitude, propeller speeds and flap deflections.

B. Position tracking in hovering flight

In the second flight simulation, we impose a circular setpoint path in order to validate the interaction between all control blocks in the proposed control architecture. The following equations define the desired flight path,

$$x_{sp} = \begin{cases} 0, & t < 30s \\ x_c + r\,cos\left(\frac{2\pi}{40}t\right), & t \in [30;130]s \\ 1, & t > 130s \end{cases}$$

$$y_{sp} = \begin{cases} 0, & t < 30s \\ y_c + r\,sin\left(\frac{2\pi}{40}t\right), & t \in [30;130]s \\ 5, & t > 130s \end{cases}$$

$$z_{sp} = \begin{cases} 10, & t \in [0;155]s \\ 0, & t > 155s \end{cases}$$

where x_c and y_c correspond to the center of the circle and r is its radius. This maneuver requires the hybrid MAV to fly along a circular trajectory while constantly pointing its nose towards the exact center of the circle. Accurate position, velocity and especially yaw angle control are needed to accurately follow the desired flight plan with the desired attitude. Figure 13 shows the simulation results.

C. Entire flight envelope

The following flight simulation, see Fig. 14, shows a complete mission in which we evaluate all hybrid MAV flight capabilities through a vertical take-off from zero to ten meters of altitude followed by the hover-to-forward transition

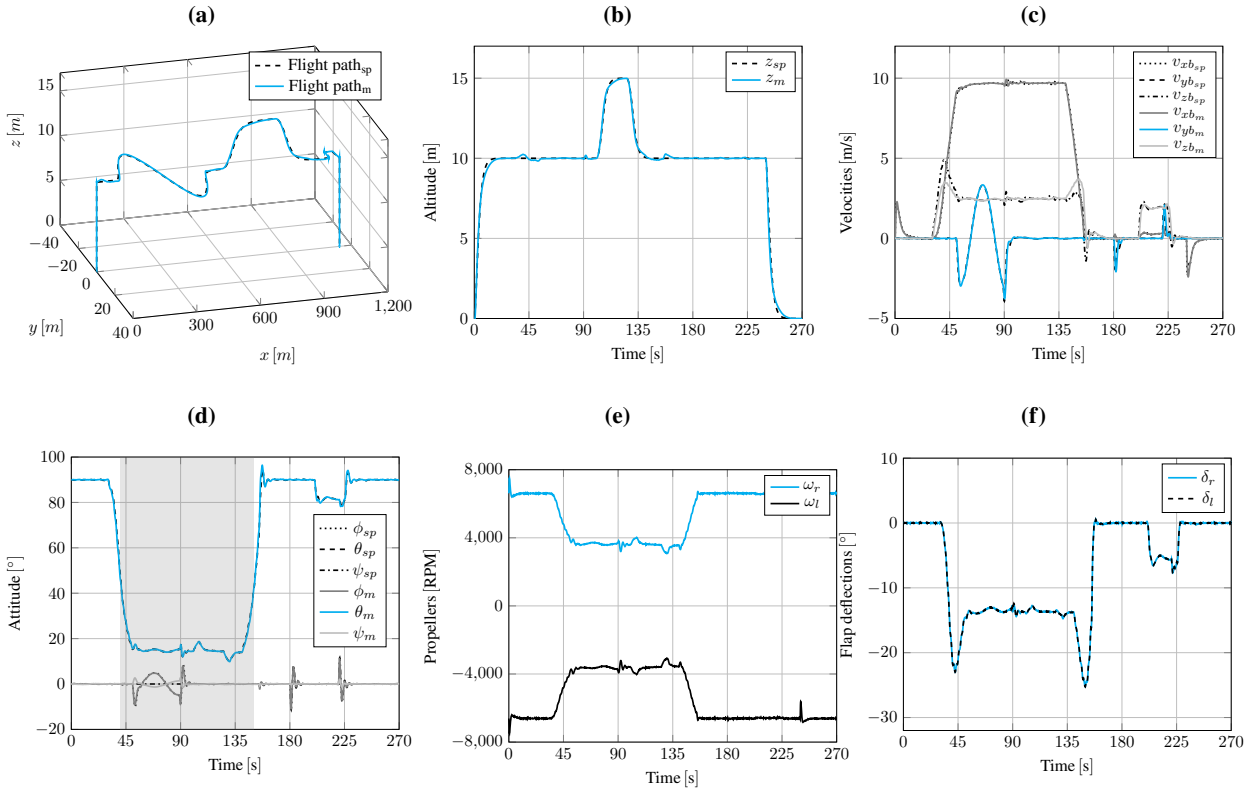

Fig. 14 Entire flight envelope simulation in relatively calm flight conditions. On the top, from left to right: the 3D flight path, altitude and velocities in the body coordinate system. On the bottom: attitude, propeller speeds and flap deflections.

with a position tracking in the $xy-plane$ and an altitude change in forward flight. Then, the forward-to-hover transition is performed with a position tracking in hovering flight. The flight simulation ends with a vertical landing. The complete 3D flight path is presented in the Fig. 14a. The controller assures the position tracking during the entire mission. As we can see in the Fig. 14b, the altitude presents small oscillations at 45 and 165 seconds of simulation which is acceptable for this MAV class. These oscillations are due to the fast variations of aerodynamic forces and moments that occur during the transition flight phases where the pitch angle changes resulting in significant variations in the angle of attack, see Fig. 14d. In the same figure, between 45 and 90 seconds of simulation, we can see the roll angle behaviour in charge of reach the desired east position in forward flight. Similarly, between 180 and 215 seconds of simulation, the yaw behaviour in charge of reach the east position in hovering flight. Figure 14c presents the velocities in the body coordinate system and the actuator dynamics, respectively, the propeller rotations and the flap deflections are shown in the Fig. 14e and Fig. 14f.

VII. Preliminary Flight Experiments

We present in this section first experimental flight results with MFC algorithms for tailsitter MAV in outdoor and indoor environments. Two indoor experiments were performed in the *ENAC's flying arena* which has a flight volume of about 10x10x10 meters, see Fig. 15. The entire flight domain is covered by *Optitrack* cameras that informs in real time the DarkO's attitude orientation and position. However, in these experiments, we analyse only the attitude control loop by using the *Optitrack* cameras for heading measurements. For the outdoor flight, a compass is used to obtain the heading orientation. The entire attitude is computed on-board at 500 Hz by a complementary filter algorithm that combines both accelerometer and gyroscope signals. The attitude setpoints are set externally by the pilot from a RC transmitter.

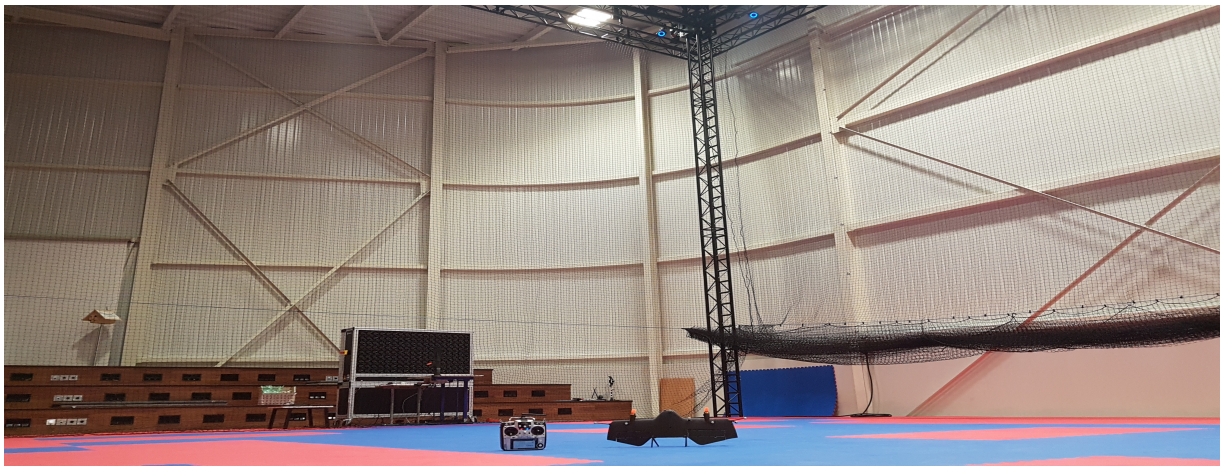

Fig. 15 Dark0 Tailsitter MAV at rest in the *ENAC's flying arena* showing two of sixteen *Optitrack* cameras in the top and the *WindShape* wind generator in the background.

A. Indoor transitioning flights

The first indoor experiment show the adaptation properties of the controller during flights with high incidence angle variations, see Fig. 16. The pitch angle trajectories do not remain on angles below 20 degrees, for a long time, in forward flight due to size limitation of the flight area. In order to avoid the collision with the protective nets, the pilot imposes a pitch angle setpoint of around 90° bringing the DarkO back to stationary flights in hovering flight phase. The nonlinear cancelation term (30) and (34), has fast adaptation properties that keeps the correct commands up-to-date for the entire flight envelope ensuring the DarkO attitude stabilization despite the fast variations of aerodynamic forces and moments. This is a particularly powerful feature of this control architecture in the sense that it can, in principle, adjust the control output in order to achieve desired dynamics for an unknown nonlinear system.

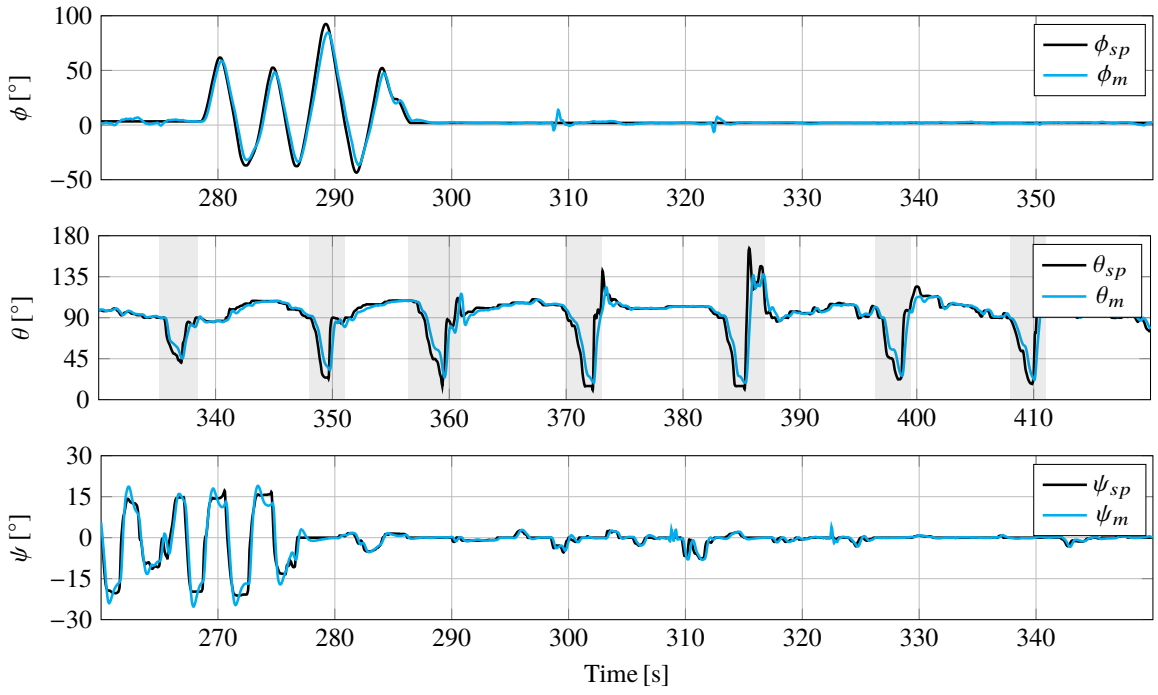

Fig. 16 Attitude stabilization during indoor flights with fast transitioning flights.

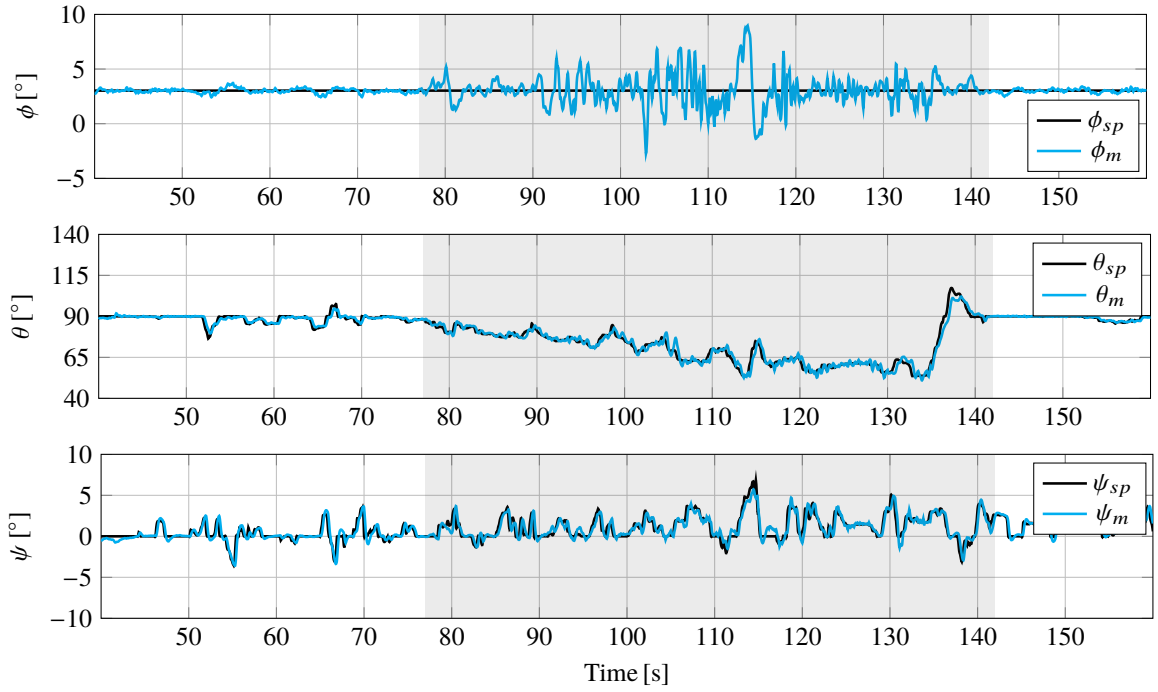

Fig. 17 Experimental transitioning flight faced to the *WindShape* small wind generator.

The second flight experiment analyzes the disturbance rejection properties of the model-free control algorithm for attitude stabilization during indoor transitioning flight. For this experiement, we reproduce the conditions that are met by MAV in outdoor environments using the *WindShape* open type wind tunnel*. DarkO starts the mission in hovering flight mode faced to the *WindShape* and, according to increase of the wind speed from zero to 9 m/s, the pilot continually updates the pitch angle to perform the transition with the objective of counteract and reduce major wind influences on the position of the DarkO, while maintaining its heading to stay upwind. The stabilized attitude angles are presented in the Fig. 17. The shaded area highlights the roll angle (ϕ) oscillations as well as the flight domain where the pitch angle (θ) decreases by approaching to the forward flight. The roll angle is controlled by asymmetric flap deflections, and the pitch angle by symmetric flap deflections. Thus, for high incidence angles, the roll oscillations of around 8° can be explained by the coupled dynamics between these axes. We can reduce the dynamic dependencies of one axis on the other by optimizing the MFC parameters in order to improve the DarkO performance, particularly during transitioning flights with wind disturbances.

B. Outdoor transitioning flights

The objective of this flight experiment is to validate the attitude control loop performance in outdoor flight conditions, in particular the disturbance rejection properties, and compare the results with the previous indoor flight experiment. Figure 18 shows the attitude behaviour for the outdoor flight experiment. We analyse the tailsitter MAV flight modes 2, 3, and 4 as described in the Fig. 1. The DarkO starts the experiment in the hovering flight phase and, according to pitch angle setpoints from RC transmitter, different transitioning flights are performed, from both hover-to-forward and forward-to-hover. The detailed pitch angle result is shown in the Fig. 19, we can observe a smooth and continuous stabilized flight transition. The roll oscillations highlighted in the indoor flight were not observed on this flight. Yet, we used exactly the same MFC parameters.

*www.windshape.ch

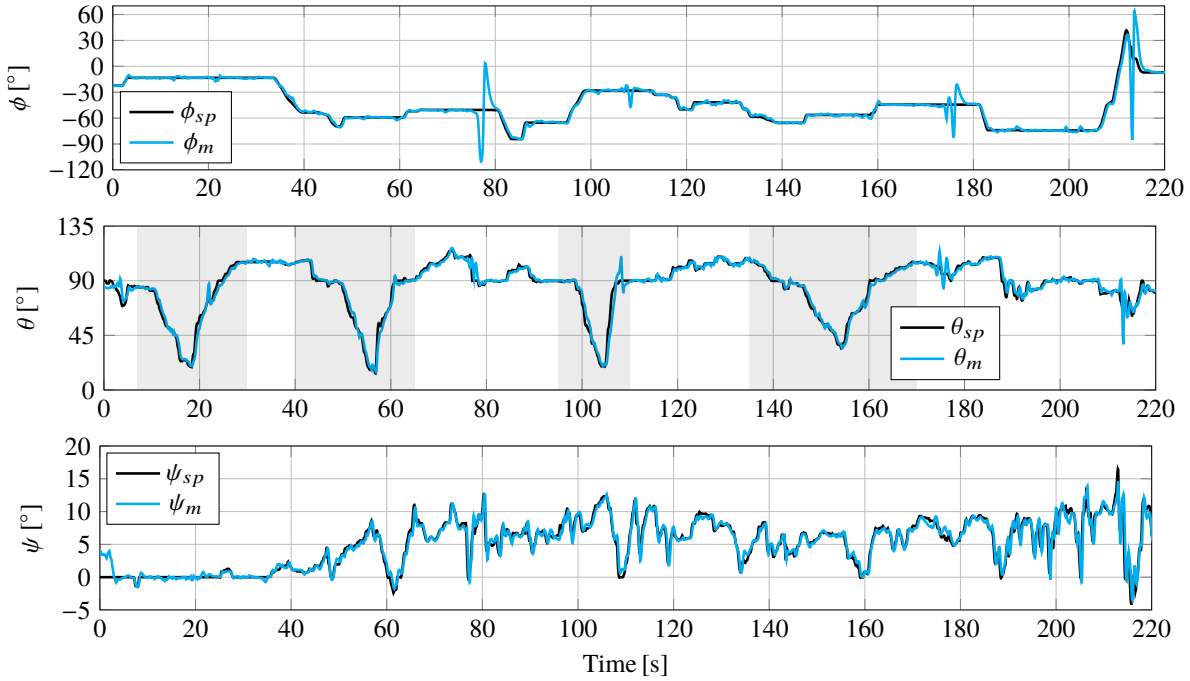

Fig. 18 Attitude stabilization during outdoor flight experiment.

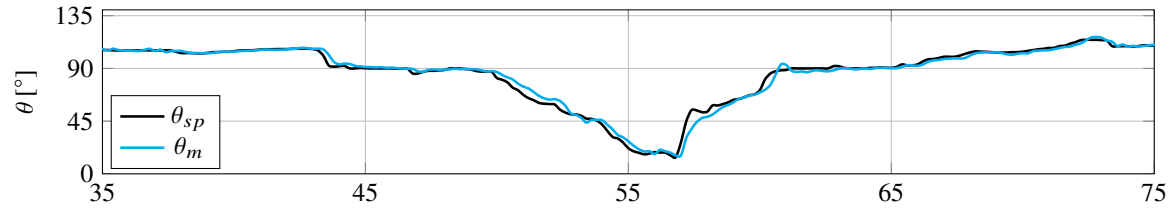

Fig. 19 Pitch angle result for $t \in [35; 75]$ seconds during outdoor flight experiment.

VIII. Conclusion

This work described a control architecture based on model-free control algorithms, tackling the entire flight envelope of tailsitter MAVs. Flight simulations were performed in order to validate the interactions between each control block covering the wide flight domain of tailsitter MAVs. The proposed control approach provides, according to flight simulation results, high performance for position tracking, velocity control, and attitude stabilization without neither gain scheduling methods nor any prior knowledge of tailsitter MAV parameters. Because unmodeled dynamics are measured at the controller input, no complex modeling processes are needed which facilitates its implementation in new MAVs. We also examined the attitude control loop performance during experimental flights in outdoor and indoor environments which highlighted the disturbance rejection properties of such a controller against the winds. Given the adaptive properties of MFC algorithms, the most obvious finding to emerge from this study is the easy application of the proposed control architecture to different hybrid MAV platforms. However, this finding must be verified by implementing the proposed control methodology on different MAVs with different physical characteristics. Additionally, we would like to investigate the guidance challenges involving tailsitter MAVs in real flight conditions.

Acknowledgments

Authors would like to thank Xavier Paris and Michel Gorraz for their support during flight experiments.

References

[1] Santos, M. A., Cardoso, D. N., Rego, B. S., Raffo, G. V., and Esteban, S., "A Discrete Robust Adaptive Control of a Tilt-rotor UAV for an Enlarged Flight Envelope," *IEEE 56th Annual Conference on Decision and Control (CDC)*, Melbourne, Australia, December 2017, pp. 5208–5214.

[2] P. Hartmann, C. M., and Moormann, D., "Unified Velocity Control and Flight State Transition of Unmanned Tilt-Wing Aircraft," *Journal of Guidance, Control, and Dynamics*, Vol. 40, No. 6, June 2017, p. 1348–1359.

[3] H. Gu, Z. L.-S. S., X. Lyu, and Zhang, F., "Development and Experimental Verification of a Hybrid Vertical Take-Off and Landing (VTOL) Unmanned Aerial Vehicle(UAV)," *International Conference on Unmanned Aircraft Systems (ICUAS)*, Miami, FL, USA, June 2017, pp. 160–169.

[4] Flores, A., de Oca, A. M., and Flores, G., "A simple controller for the transition maneuver of a tail-sitter drone," *IEEE Conference on Decision and Control (CDC)*, Miami Beach, FL, USA, December 2018, pp. 4277–4281.

[5] K. Chinwicharnam, J.-M. M., D. Gomez Ariza, and Chinnapat, T., "Aerodynamic Characteristics of a Low Aspect Ratio Wing and Propeller Interaction for a Tilt-Body MAV," *International Journal of Micro Air Vehicles*, Vol. 5, No. 4, 2013, pp. 245–260.

[6] Bronz, M., Smeur, E. J. J., de Marina, H. G., and Hattenberger, G., "Development of A Fixed-Wing mini UAV with Transitioning Flight Capability," *35th AIAA Applied Aerodynamics Conference, AIAA AVIATION Forum*, 2017, pp. 1–14.

[7] Bilodeau, P.-R., and Wong, F., "Modeling and control of a hovering mini tail-sitter," *International Journal of Micro Air Vehicles*, Vol. 2, 2010, pp. 211–220.

[8] Hochstenbach, M., Notteboom, C., Theys, B., and Schutter, J. D., "Design and Control of an Unmanned Aerial Vehicle for Autonomous Parcel Delivery with Transition from Vertical Take-off to Forward Flight - VertiKUL, a Quadcopter Tailsitter," *International Journal of Micro Air Vehicles*, Vol. 7, No. 4, 2015, pp. 395–405.

[9] Lustosa, L. R., Defaÿ, F., and Moschetta, J.-M., "Longitudinal study of a tilt-body vehicle: modeling, control and stability analysis," *International Conference on Unmanned Aircraft Systems (ICUAS)*, Denver, Colorado, USA, June 2015, pp. 816–824.

[10] Kita, K., Konno, A., and Uchiyama, M., "Transition between Level Flight and Hovering of a Tail-Sitter Vertical Takeoff and Landing Aerial Robot," *Advanced Robotics*, Vol. 24, No. 5-6, April 2012, pp. 763–781.

[11] Silva, N. B. F., Fontes, J. V. C., Inoue, R. S., and Branco, K. R. L. J. C., "Dynamic Inversion and Gain-Scheduling Control for an Autonomous Aerial Vehicle with Multiple Flight Stages," *Journal of Control, Automation and Electrical Systems*, Vol. 29, No. 3, June 2018, pp. 328–339.

[12] Saeed, A. S., Younes, A. B., Cai, C., and Cai, G., "A survey of hybrid Unmanned Aerial Vehicles," *Progress in Aerospace Sciences*, Vol. 98, April 2018, pp. 91–105.

[13] Ritz, R., and D'Andrea, R., "A global controller for flying wing tailsitter vehicles," *IEEE International Conference on Robotics and Automation (ICRA)*, Singapore, May 2017, pp. 2731–2738.

[14] Knoebel, N. B., and McLain, T. W., "Adaptive quaternion control of a miniature tailsitter uav," *American Control Conference (ACC)*, Seattle, Washington, USA, June 2008, pp. 2340 – 2345.

[15] Jung, Y., and Shim, D. H., "Development and application of controller for transition flight of tail-sitter uav," *Journal of Intelligent & Robotic Systems*, Vol. 65, No. 1-4, January 2012, pp. 137–152.

[16] Hajiloo, A., and Rodrigues, L., "Modeling and Backstepping Control of Under-Actuated Spherical UAV," *IEEE Conference on Control Technology and Applications (CCTA)*, Kohala Coast, Hawaii, August 2017, pp. 2069–2074.

[17] Li, Z., Zhou, W., Liu, H., Zhang, L., and Zuo, Z., "Nonlinear Robust Flight Mode Transition Control for Tail-Sitter Aircraft," *IEEE Access*, Vol. 6, October 2018, pp. 65909–65921.

[18] Smeur, E. J. J., Bronz, M., and de Croon, G. C. H. E., "Incremental control and guidance of hybrid aircraft applied to the Cyclone tailsitter UAV," 2018 (Unpublished).

[19] Pucci, D., Hamel, T., Morin, P., and Samson, C., "Nonlinear feedback control of axisymmetric aerial vehicles," *Automatica*, Vol. 53, March 2015, pp. 72–78.

[20] Pucci, D., Hamel, T., Morin, P., and Samson, C., "Nonlinear Control of Aerial Vehicles Subjected to Aerodynamic Forces," *IEEE Conference on Decision and Control (CDC)*, Florence, Italy, December 2013, pp. 4839–4846.

[21] Wang, W., Zhu, J., Kuang, M., and Zhu, X., "Adaptive Attitude Control for a Tail-sitter UAV with Single Thrust-vectored Propeller," *IEEE International Conference on Robotics and Automation (ICRA)*, Brisbane, Australia, May 2018, pp. 6581–6586.

[22] Fliess, M., and Join, C., "Model-free control," *International Journal of Control, Taylor & Francis*, Vol. 86, No. 12, July 2013, pp. 2228 – 2252.

[23] Join, C., Bernier, J., Mottelet, S., Fliess, M., Rechdaoui-Guérin, S., Azimi, S., and Rocher, V., "A simple and efficient feedback control strategy for wastewater denitrification," *20th World IFAC Congress*, 1, Vol. 50, Toulouse, France, July 2017, pp. 7657–7662.

[24] Rodriguez-Fortun, J. M., Rotella, F., Alfonso, J., Carrillo, F. J., and Orús, J., "Model-free control of a 3-DOF piezoelectric nanopositioning platform," *52nd IEEE Conference on Decision and Control (CDC)*, Florence, Italy, December 2013, pp. 342–347.

[25] Bara, O., Fliess, M., Join, C., Daye, J., and Djouadi, S. M., "Toward a model-free feedback control synthesis for treating acute inflammation," *Journal of Theoretical Biology, Elsevier*, Vol. 448, No. 7, July 2018, pp. 26–37.

[26] Join, C., Robert, G., and Fliess, M., "Model-Free Based Water Level Control for Hydroelectric Power Plants," *IFAC Conference on Control Methodologies and Technology for Energy Efficiency*, 1, Vol. 43, Vilamoura, Portugal, March 2010, pp. 134–139.

[27] Abouaïssa, H., Fliess, M., and Join, C., "Fast parametric estimation for macroscopic traffic flow model," *17th IFAC World Congress*, Seoul, South Korea, July 2008, pp. 13040–13045.

[28] Chand, A. N., Kawanishi, M., and Narikiyo, T., "Non-linear Model-free Control of Flapping Wing Flying Robot using iPID," *IEEE International Conference on Robotics and Automation (ICRA)*, Stockholm, Sweden, May 2016, pp. 2930–2937.

[29] Younes, Y. A., Drak, A., Noura, H., Rabhi, A., and Hajjaji, A. E., "Robust Model-Free Control Applied to a Quadrotor UAV," *Journal of Intelligent & Robotic Systems*, Vol. 84, No. 1-4, December 2016, pp. 37–52.

[30] Lustosa, L. R., Defaÿ, F., and Moschetta, J.-M., "Global Singularity-Free Aerodynamic Model for Algorithmic Flight Control of Tail Sitters," Vol. 42, No. 2, February 2019, pp. 303–316.

[31] Drela, M., "XFOIL: An Analysis and Design System for Low Reynolds Number Airfoils," *Conference on Low Reynolds Number Airfoil Aerodynamics*, University of Notre Dame, June 1989.

[32] Chahl, J. S., Jain, L. C., Mizutani, A., and Sato-Ilic, M., *Innovations in Intelligent Machines-1, pp. 181*, Springer-Verlag Berlin Heidelberg, July 2007.

[33] Martin, P., and Salaun, E., "Design and implementation of a low-cost observer-based attitude and heading reference system," *Control Engineering Practice*, Vol. 18, No. 7, July 2010, pp. 712–722.

A.3 American Control Conference

Barth, J. M. O., Condomines, J.-P., Moschetta, J.-M., Cabarbaye, A., Join, C., and Fliess, M., "Full Model-Free Control Architecture for Hybrid UAVs," *American Control Conference (ACC)*, Philadelphia, PA, USA, pp. 71-78, August 2019. doi: https://doi.org/10.23919/ACC.2019.8814993.

Full Model-Free Control Architecture for Hybrid UAVs

Jacson M. O. Barth[1], Jean-Philippe Condomines[1],
Jean-Marc Moschetta[2], Aurélien Cabarbaye[1], Cédric Join[3,5] and Michel Fliess[4,5]

***Abstract*— This paper discusses the development of a control architecture for hybrid Unmanned Aerial Vehicles (UAVs) based on model-free control (MFC) algorithms. Hybrid UAVs combine the beneficial features of fixed-wing UAVs with Vertical Take-Off and Landing (VTOL) capabilities to perform five different flight phases during typical missions, such as vertical take-off, transitioning flight, forward flight, hovering and vertical landing. Based on model-free control principles, a novel control architecture that handles the hybrid UAV dynamics at any flight phase is presented. This unified controller allows autonomous flights without discontinuities of switching for the entire flight envelope with position tracking, velocity control and attitude stabilization. Simulation results show that the proposed control architecture provides an effective control performance for the entire flight envelope and excellent disturbance rejections during the critical flight phases, such as transitioning and hovering flights in windy conditions.**

I. INTRODUCTION

Autonomous flight of Unmanned Aerial Vehicles (UAVs) remains an interesting and active research domain after decades of studies in the subject. The wide variety of missions involving UAVs, combined with advances in the fields of materials and computer science, have contributed to the design of new UAV configurations. Therefore, the drawbacks of rotatory-wing UAVs (e.g. helicopters, quad-rotors and multi-rotors) in terms of endurance and range, with the lack of capability to take-off and landing from small areas of fixed-wing UAVs have also encouraged the development of a new UAV class namely hybrid UAV. This hybrid UAV configuration is able to perform complex flight missions in windy environments through its large flight envelope, as described in Fig. 1, with vertical take-off and landing with fast and efficient forward flight to reach a distant position. Although the combination of two different UAV configurations in a single one provides a wider application field, the control system needs to consider the particularities of each one in order to properly carry out the position tracking, velocity control and attitude stabilization during the entire flight envelope for a given mission.

[1]Are with ENAC, Université de Toulouse, France. **[jacson-miguel.olszanecki-barth; jean-philippe.condomines]@enac.fr**

[2]Is with the Department of Aerodynamics, Energetics and Propulsion, Institut Supérieur de l'Aéronautique et de l'Espace, 31400 Toulouse, France. **jean-marc.moschetta@isae-supaero.fr**

[3]Is with the CRAN (CNRS, UMR 7039)), Université de Lorraine, BP 239, 54506 Vandœuvre-lès-Nancy, France. **cedric.join@univ-lorraine.fr**

[4]Is with the LIX (CNRS, UMR 7161), École polytechnique, 91128 Palaiseau, France. **Michel.Fliess@polytechnique.edu**

[5]Are with the AL.I.E.N (ALgèbre pour Identification & Estimation Numérique), 7 rue Maurice Barrès, 54330 Vézelise, France. **[michel.fliess; cedric.join]@alien-sas.com**

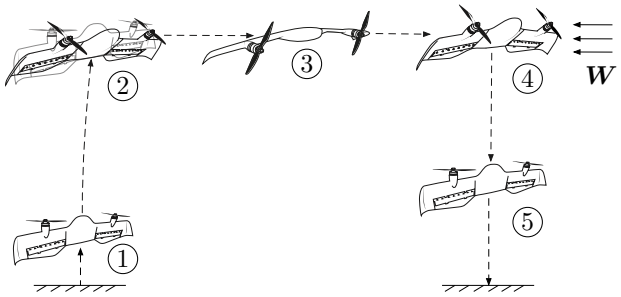

Fig. 1: Typical flight modes of Hybrid Unmanned Aerial Vehicles: 1 - Vertical take-off; 2 - Transition; 3 - Forward flight; 4 - Hover flight; 5 - Vertical landing. The vector $\boldsymbol{W}$ represents the wind disturbances.

While attitude stabilization for hovering and forward flights are commonly researched and quite known [1] [2], the attitude stabilization during the transition phase poses a major challenge due to the fast variations of aerodynamic forces and moments at high angles of attack. Sometimes considered as an undesirable and temporally transient between hover and forward flight [3], the transition phase needs to be continuously stabilized in order to ensure a smooth and safe flight. One of the control approach to handle the attitude stabilization relies on adaptive control laws, [4] proposes an adaptive quaternion algorithm in order to avoid singularities during the control of the entire flight envelope. On the other hand, instability problems with adaptive control methods can still exist with regard to unmodeled dynamics or inaccurate models in the adaptation law of the controller's parameters. Conventional model-based controls are also designed, for instance, nonlinear feedback techniques [5] [6], based on Lyapunov designs [7], linear optimal controls [8], linear optimal control with gain scheduling techniques [9] which require sophisticated wind-tunnel characterizations to get an understanding of forces and moments acting on the system. The performance of model-based controllers differs primarily in the fidelity with which the plant is modeled. Accurate modeling of aerodynamic forces and moments of a partially stalled wing is a difficult and time consuming task. Additionally, these models usually require several flight measurements that are hard to obtain such as angle of attack during hovering flights, and low airspeed due to small dynamic pressures. In terms of flight validation, [10] proposes a simple control strategy based on Proportional Integral and Derivative (PID) gains in order to control the

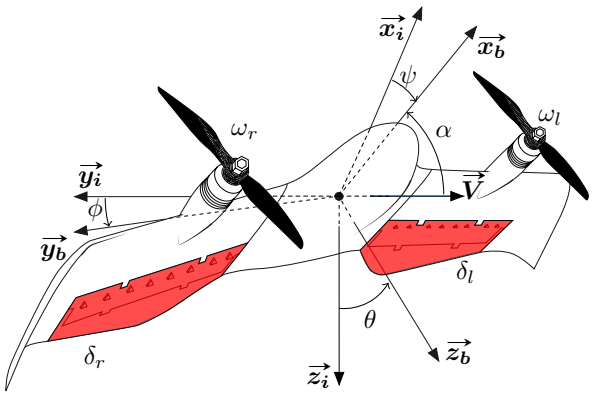

Fig. 2: Illustration of the used coordinate frames, angles and actuators. The *Darko* hybrid UAV was designed by Murat Bronz at ENAC.

position and the attitude of a hybrid UAV. Although simple to tune without the knowledge of the model, PID controllers are limited in terms of disturbance rejection. Another flight experiment, employing a cascaded control architecture composed by Incremental Nonlinear Dynamic Inversion (INDI) algorithms, was developed and flight-tested to demonstrate the performance of a such controller for position tracking, velocity control and attitude stabilization [11]. This sensor-based control approach needs a prior identification of the actuator effectiveness which are computed from real flight data implying a prior adjustment of the controller's gains. As an alternative, some control approaches can handle the system dynamics without requiring any model, such as the Model-Free Control (MFC) approach. Apart from aerospace applications [12] [13], including our previous work [14] [15], MFC was also applied on a wide list of different industrial cases sometimes providing patents, see [16] and its references for additional information. However to the best of our knowledge, this control methodology was never designed for hybrid UAVs. Thus, the new contributions presented in this paper, with respect to our previous work, are :

- guidance formulation (position and velocity control) for the entire flight envelope in a disturbed environment.
- numerical results of different flight cases to numerically validate the performance and the interaction between each component of the control architecture.
- disturbance rejection analysis in a critical flight phase under strong wind gusts.

The remainder of this paper is organized as follows. Section II contains the mathematical hybrid UAV model and explains the main features of this UAV class. In Section III, we present the new control architecture based on model-free control algorithms. Subsequently, in section IV, the control performance is analyzed for different flight cases, i.e. hover, transition and forward flight. Finally, section V concludes the paper and introduces the main challenges ahead to improve our control system.

II. HYBRID UAV MODEL

This section is subdivided into two parts. First, we present the mathematical formulation of aerodynamic forces and moments, and the aerodynamic assumptions used in the hybrid UAV model. Then, the equations of motion, based in the Newton's second law, are introduced to describe the hybrid UAV behavior.

A. Formulation of aerodynamic forces and moments

We present an analytic continuous singularity-free formulation of aerodynamic forces $\boldsymbol{F_{a_b}} \in \mathbb{R}^3$ and moments $\boldsymbol{M_{a_b}} \in \mathbb{R}^3$ acting in a wing over a complete 360° angle of attack, based on previous work proposed by [17]. The wing with a surface S, is immersed in an incompressible and inviscid airflow with air density ρ. The free-stream velocity is composed by the linear element $\boldsymbol{v_\infty} \in \mathbb{R}^3$ and the angular component defined by $\boldsymbol{\omega_\infty} \in \mathbb{R}^3$ which, in the absence of wind, is equal to the hybrid UAV angular velocity $\boldsymbol{\omega_b} \in \mathbb{R}^3$. This formulation of aerodynamic forces and moments is given by :

$$\begin{pmatrix} \boldsymbol{F_{a_b}} \\ \boldsymbol{M_{a_b}} \end{pmatrix} = -\frac{1}{2}\rho S \eta C \Phi(\boldsymbol{\eta_b}) C \boldsymbol{\eta_b} \tag{1}$$

where

$$\eta = \sqrt{v_\infty^2 + \mu\, c^2 \omega_\infty^2}, \quad \text{with } \mu \in \mathbb{R} > 0 \tag{2}$$

and

$$\boldsymbol{\eta_b} = \begin{pmatrix} \boldsymbol{v_\infty} \\ \boldsymbol{\omega_\infty} \end{pmatrix} \tag{3}$$

The vector $\boldsymbol{\eta_b}$ describes the linear and angular free-stream velocities in the body coordinate frame. The matrix C denotes the reference wing parameters in an extended representation,

$$C = \begin{pmatrix} I_{3\times3} & 0_{3\times3} \\ 0_{3\times3} & \begin{bmatrix} \mathrm{b} & 0 & 0 \\ 0 & \mathrm{c} & 0 \\ 0 & 0 & \mathrm{b} \end{bmatrix} \end{pmatrix} \tag{4}$$

where b and c are, respectively, the wingspan and the mean chord. Finally, the matrix $\Phi \in \mathbb{R}^{6\times6}$, which is subdivided into four matrices $\Phi^{(\cdot)} \in \mathbb{R}^{3\times3}$, shows the interaction between aerodynamic forces and moments with linear and angular free-stream velocities :

$$\Phi = \begin{pmatrix} \Phi^{(fv)} & \Phi^{(fw)} \\ \Phi^{(mv)} & \Phi^{(mw)} \end{pmatrix} \tag{5}$$

The parameters of Φ are deduced from thin airfoil theory, we refer the interested reader to [17] for further information.

Nonetheless, we mention that,

$$\Phi_0^{(fv)} = \begin{pmatrix} C_{d0} & 0 & 0 \\ 0 & C_{y0} & 0 \\ 0 & 0 & 2\pi + C_{d0} \end{pmatrix} \tag{6}$$

$$\Phi^{(f\omega)} = \begin{pmatrix} 0 & 0 & 0 \\ 0 & 0 & b^{-1}\Delta r C_{y0} \\ 0 & -c^{-1}\Delta r(2\pi + C_{d0}) & 0 \end{pmatrix} \tag{7}$$

$$\Phi_0^{(mv)} = \begin{pmatrix} 0 & 0 & 0 \\ 0 & 0 & -c^{-1}\Delta r(2\pi + C_{d0}) \\ 0 & b^{-1}\Delta r C_{y0} & 0 \end{pmatrix} \tag{8}$$

$$\Phi^{(m\omega)} = \frac{1}{2}\begin{pmatrix} C_{l_p} & C_{l_q} & C_{l_r} \\ C_{m_p} & C_{m_q} & C_{m_r} \\ C_{n_p} & C_{n_q} & C_{n_r} \end{pmatrix} \tag{9}$$

with C_{d0} the minimal drag coefficient, C_{y0} the minimal side force coefficient, Δr represents the distance between the aerodynamic center and the UAV center of gravity, and C_l, C_m and C_n are the aerodynamic moment coefficients which depend on the angular hybrid UAV velocities (p, q, r). Finally, the flap deflection dynamics are modeled as varying cambered airfoils and the aerodynamic forces and moments created by these deflections δ_j are approximated by the following equations :

$$\Phi^{(fv)}(\delta_j) = \Phi_0^{(fv)}(I - [\boldsymbol{\xi_f}]_\times \delta_j) \tag{10}$$

$$\Phi^{(mv)}(\delta_j) = \Phi_0^{(mv)}(I - [\boldsymbol{\xi_m}]_\times \delta_j) \tag{11}$$

the flap deflection effectiveness is represented by two skew-symmetric matrices, $[\boldsymbol{\xi_f}]_\times$ for the force effectiveness and $[\boldsymbol{\xi_m}]_\times$ for the moment effectiveness, given by :

$$[\boldsymbol{\xi_f}]_\times = \begin{bmatrix} 0 & -\xi_f & \xi_f \\ \xi_f & 0 & -\xi_f \\ -\xi_f & \xi_f & 0 \end{bmatrix}$$

$$[\boldsymbol{\xi_m}]_\times = \begin{bmatrix} 0 & -\xi_m & \xi_m \\ \xi_m & 0 & -\xi_m \\ -\xi_m & \xi_m & 0 \end{bmatrix}$$

B. Equations of motion

The hybrid UAV model is divided into four rigid bodies (two propellers and one fuselage composed by two wings) with constant mass (m), represented by ten states $\boldsymbol{x} = (\boldsymbol{v_b}, \boldsymbol{\omega_b}, \boldsymbol{q})$, where $\boldsymbol{v_b} \in \mathbb{R}^3$ is the vehicle's linear velocity, $\boldsymbol{\omega_b} \in \mathbb{R}^3$ is the vehicle's angular velocity equals to $[p\ q\ r]^T$ both expressed in the body coordinate frame and $\boldsymbol{q} \in \mathbb{R}^4$ is the quaternion formulation. The system is controlled via four control-inputs, $\boldsymbol{u} = (\omega_l, \omega_r, \delta_l, \delta_r)$, respectively, the left and right propeller rotation speeds and the left and right flap deflections, which are represented in the Fig. 2. In order to compute the forces and moments caused by the wing-propeller interaction, we define two segments. Each segment is composed by one wing j and by one propeller k. Thus, the sum of aerodynamic forces acting on the wing j with the thrust $\boldsymbol{T}_k$ generated by the propeller rotation ω_k and the total moment described in the body coordinate frame, are given by :

TABLE I: *Dark0* UAV parameters.

Parameters	Values	SI Units
Mass (m)	0.492	[Kg]
Mean Chord (c)	0.13	[m]
Wingspan (b)	0.55	[m]
Wing Area (S)	0.0743	[m^2]
J_{xx}	0.0070	[Kg m^2]
J_{yy}	0.0028	[Kg m^2]
J_{zz}	0.0061	[Kg m^2]
J_p	5.1116×10^{-6}	[Kg m^2]
k_f	5.13×10^{-6}	[Kg m]
k_m	2.64×10^{-7}	[Kg m^2]
C_{d0}	0.025	No units
C_{y0}	0.1	No units
C_{l_p}	0.2792	No units
C_{l_q}	0.0	No units
C_{l_r}	0.1145	No units
C_{m_p}	0.0	No units
C_{m_q}	1.2715	No units
C_{m_r}	0.0	No units
C_{n_p}	0.081	No units
C_{n_q}	0.0	No units
C_{n_r}	0.0039	No units
p_{p_x}	0.065	m
p_{p_y}	0.155	m
p_{p_z}	0.0	m
p_{a_x}	0.0	m
p_{a_y}	0.155	m
p_{a_z}	0.0	m
ξ_f	0.85	No units
ξ_m	0.55	No units

$$\boldsymbol{F_b} = \sum_{j,k=1}^{2} (\boldsymbol{F_{a_{b_j}}} + \boldsymbol{T}_k) \tag{12}$$

$$\boldsymbol{M_b} = \sum_{j,k=1}^{2} (\boldsymbol{M_{a_{b_j}}} + \boldsymbol{\tau_{b_k}} + \boldsymbol{p_p} \times \boldsymbol{T}_k + \boldsymbol{p_a} \times \boldsymbol{F_{a_{b_j}}}) \tag{13}$$

The vector $\boldsymbol{p_p} = [p_{p_x}\ p_{p_y}\ p_{p_z}]^T$ defines the distance between the propeller k with the hybrid UAV center of mass. Both propellers are positioned symmetrically with respect to the hybrid UAV center of mass. The distance between the aerodynamic center and the center of mass is represented by the vector $\boldsymbol{p_a} = [p_{a_x}\ p_{a_y}\ p_{a_z}]^T$. The internal torque of the propeller $\boldsymbol{\tau_{b_k}}$ and its thrust force $\boldsymbol{T}_k$, are defined by :

$$\boldsymbol{T}_k = k_f \omega_k^2 \overrightarrow{\boldsymbol{x_b}}, \qquad k_f \in \mathbb{R} > 0 \tag{14}$$

$$\boldsymbol{\tau_{b_k}} = \boldsymbol{N_{b_k}} - J_p\,(p + \omega_j) \begin{pmatrix} 0 \\ r \\ -q \end{pmatrix} \tag{15}$$

where

$$\boldsymbol{N_{b_k}} = -\text{sign}(\omega_k) k_m \omega_k^2 \overrightarrow{\boldsymbol{x_b}}, \qquad k_m \in \mathbb{R} > 0 \tag{16}$$

with k_f and k_m the propeller force and moment coefficients and $\boldsymbol{N_{b_k}}$ is the propeller moment. Equation (15) describes

the gyroscopic interaction between the propellers and the fuselage with J_p equals to the propeller inertia. The vehicle's equations of motion are given by (17) described in the inertial coordinate frame.

$$\begin{cases} m\,\dot{\boldsymbol{v}} & = R^T \boldsymbol{F_b}(\boldsymbol{x}, \boldsymbol{u}, \boldsymbol{W}) + m\boldsymbol{g} \\ J\,\dot{\boldsymbol{\omega_b}} & = \boldsymbol{M_b}(\boldsymbol{x}, \boldsymbol{u}, \boldsymbol{W}) - [\boldsymbol{\omega_b}]_\times J\boldsymbol{\omega_b} \\ \dot{\boldsymbol{q}} & = \frac{1}{2}\boldsymbol{q} * \boldsymbol{\omega_b} \\ \dot{\boldsymbol{p}} & = \boldsymbol{v} \end{cases} \tag{17}$$

The gravitational acceleration vector is equals to $\boldsymbol{g} = g\overrightarrow{\boldsymbol{z_i}}$ and $\boldsymbol{W} \in \mathbb{R}^3$ is the wind disturbance vector. The rotation matrix R, namely the Direction Cosines Matrix (DCM), represents the UAV rotation in three dimensions as a mathematical formulation. We assume that the hybrid UAV inertia matrix J is diagonal and it equals to $J = \text{diag}\,[J_{xx}\, J_{yy}\, J_{zz}]$. The position vector in the inertial coordinate frame is represented by $\boldsymbol{p} = [x\ y\ z]^T$. The highly maneuverable nature of the vehicle calls for a global numerically stable formulation of attitude and justifies the use of quaternions. The symbol $*$ in the previous equation corresponds to the quaternion product. All hybrid UAV parameters used in this paper correspond to the *Darko* UAV shown in Fig. 2, and they are described in the Table I.

III. CONTROL STRATEGY

The proposed control algorithm has no information about the Hybrid UAV parameters (e.g. mass, inertia, aerodynamic coefficients, etc.). Though, we use a prior knowledge of sign-convention between control-input influence in the UAV states based on flight mechanics equations to develop the correct interaction of blocks in the control architecture. Therefore, the model given in the previous section is used only to simulate the hybrid UAV system and not for control design.

A. Model-Free Control Principles

As introduced by [18], an unknown finite-dimensional system with a single control-input (u) and a single output (y) can be described by the following input/output relation in a differential equation formulation :

$$\mathbb{E}(y, \dot{y}, \ldots, y^{(a)}, u, \dot{u}, \ldots, u^{(b)}) = 0 \tag{18}$$

where $\mathbb{E}$ is a polynomial function with real unknown coefficients. We can also describe

$$y^v = \mathbb{E}(t, y, \dot{y}, \ldots, y^{(v-1)}, y^{(v+1)}, \ldots, y^{(a)}, u, \dot{u}, \ldots, u^{(b)}) \tag{19}$$

with $0 < v \leq a$ and $\frac{\delta \mathbb{E}}{\delta y^v} \neq 0$. This unknown dynamic can be modeled by a purely numerical equation, so-called *Ultra-Local Model* :

$$y_m^{(v)} = F_y + \lambda \cdot u \tag{20}$$

In (20), v is the order derivative of y_m, $\lambda \in \mathbb{R}$ is a non-physical constant parameter. Moreover, the exploitation of this numerical model requires the knowledge of F_y. This quantity represents the real dynamics of the model as well as the different disturbances which could damage the performance of the output-system. Thus, an accurate

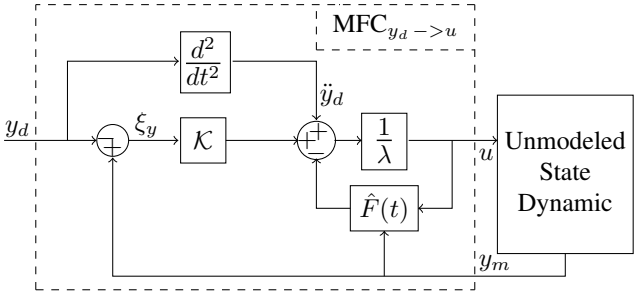

Fig. 3: Overview of Model-Free Control schema.

estimation of F, defined as $\hat{F}$, is crucial and plays an import role in the control performance. Assuming that we do not have any information about the plant, its estimation can be computed directly by the following methodology in which we use a second-order *Ultra-Local Model* :

$$\ddot{y}_m = F_y + \lambda \cdot u \tag{21}$$

The first step is to apply the *Lapace Transform* in (21). Referring to elementary operational calculus we transform (21) to (22) :

$$s^2 Y_m(s) - s y_m(0) - \dot{y}_m(0) = \frac{F_y}{s} + \lambda U(s) \tag{22}$$

Where $Y_m(s)$ and $U(s)$ correspond to the *Laplace transforms* of y_m and u. By differentiating twice the previous equation we are able to rid the initial conditions $y_m(0)$ and $\dot{y}_m(0)$:

$$2Y_m(s) + 4s\frac{dY_m(s)}{ds} + s^2\frac{d^2Y(s)}{ds^2} = \frac{2F_y}{s^3} + \lambda\frac{d^2U(s)}{ds^2} \tag{23}$$

However, the variable s in the time domain corresponds to the derivation with respect to time that is sensitive to noise corruptions and can amplify the noise measurement. Therefore, in order to reduce both noise and numerical computation errors on the output estimation, we replace the derivative terms by integrators ($\frac{1}{s}$) who have robust properties with respect to noise. Thus, multiplying both sides of (23) by s^{-3}, we obtain :

$$\frac{2Y_m(s)}{s^3} + \frac{4}{s^2}\frac{dY_m(s)}{ds} + \frac{1}{s}\frac{d^2Y(s)}{ds^2} = \frac{2F_y}{s^6} + \frac{\lambda}{s^3}\frac{d^2U(s)}{ds^2} \tag{24}$$

Equation (24) can be transferred back to the time domain employing elementary calculus and *Cauchy's formula* to reduce multiple integrals in a simple one :

$$\hat{F_y} = \frac{5!}{2T^5}\int_{t-T}^{t} [(T-\sigma)^2 - 4\sigma(T-\sigma) + \sigma^2] y_m(\sigma) - [\frac{\lambda}{2}\sigma^2(T-\sigma)^2 u(\sigma)] d\sigma$$

From measurements of y_m and u obtained in the last T seconds, the unmodeled dynamic of y and the disturbances are estimated by $\hat{F_y}$ which is updated for each interval of integration $[t-T, t]$. This interval corresponds to the window width of a receding horizon strategy which results in a trade-off. The idea is to choose the window width small so as to calculate the estimation within an acceptable short delay

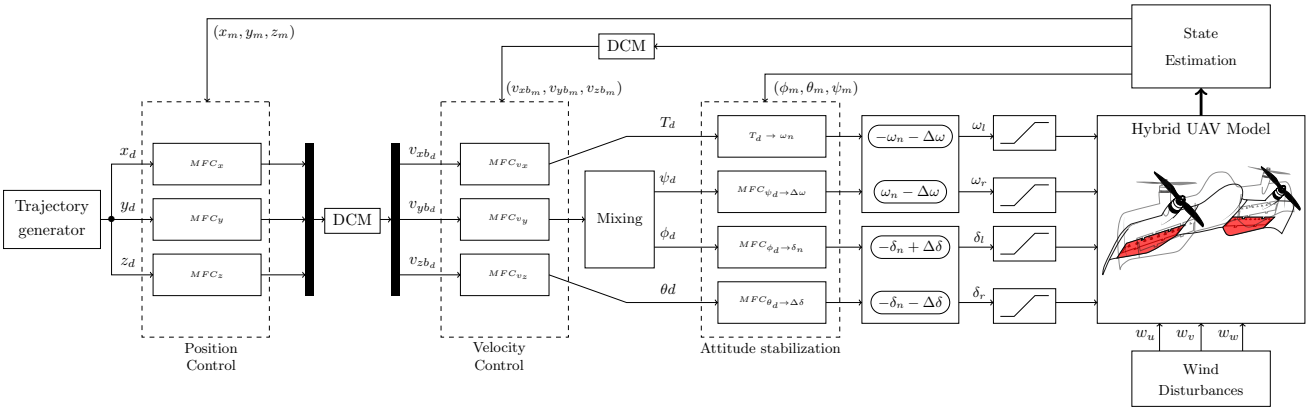

Fig. 4: Cascaded MFC architecture designed for hybrid Unmanned Aerial Vehicles. Position control blocks send desired velocities for the velocity control blocks that compute the necessary thrust value as well as the references for attitude stabilization control loop. Based on these desired values, propeller speeds (ω_l, ω_r) and flap deflections (δ_l, δ_r) are defined.

but large enough in order to preserve the low-pass filter properties whose noise attenuations of y_m. Based on such estimator, it is possible to design a robust controller that estimates the system dynamic on-line by a piecewise constant function $\hat{F}_y$ periodically updated for each measure of y_m and u. The general form of the control-input can be defined as in the Fig. 3 and is given by,

$$u = \underbrace{-\frac{\hat{F}_y}{\lambda}}_{\text{Nonlinear Cancellation}} + \underbrace{\frac{y_d^{(2)} + \mathcal{K}(\xi)}{\lambda}}_{\text{Closed loop tracking}} \tag{25}$$

where the quantity $\xi = y_m - y_d$ is the tracking error and $\mathcal{K}(\xi)$ is a closed loop feedback controller, usually defined as a proportional, proportional-derivative or even so as proportional-integral-derivative gain. In this paper, we define the closed loop feedback controller as a proportional K_p and derivative gain K_d. We recognize in (25) the typical mathematical expression of a nominal control in the flatness-based in which the non-linear terms $\hat{F}_y$ is added with a closed loop tracking of a reference trajectory $t \rightarrow\ y_d(t)$. The error dynamic can be deduced from the combination of (25) with (21) :

$$\ddot{\xi}_y = \ddot{y}_m - \ddot{y}_d = \overbrace{F_y - \hat{F}_y}^{\xi_F \approx 0} + K_p\,\xi_\theta + K_d\,\dot{\xi}_\theta \tag{26}$$

Note that, if the error (ξ_{F_y}) between the estimator and the true dynamic, is approximately zero during $[t-T, t]$, a simple proportional-derivative controller will be enough to ensure the error convergence to zero. Whereas, an integration effect is implicitly involved in the model-free control algorithm.

B. Control architecture

Figure 4 shows the main ideas of our control architecture. The block *Trajectory generator* is composed of a state flow algorithm that defines constantly the desired positions (x_d, y_d and z_d) in the inertial coordinate system. These references are taken into account by the *Position control* block and are compared with the respective measures (x_m, y_m, z_m) creating three errors that are minimized by the MFC algorithms in the *Position control* block. These three MFC algorithms in charge of the position tracking, also compute the desired velocity in their respective axes. These references values which are defined in the inertial coordinate frame are transformed to the body coordinate frame as well as the velocities measurements. Thus, the velocity control MFC$_{v_x}$ computes the required thrust T_d to reach this desired velocity along $\overrightarrow{\boldsymbol{x_b}}$, the block MFC$_{v_z}$ assures the velocity control along $\overrightarrow{\boldsymbol{z_b}}$ and determine the necessary pitch angle θ_d to reach this desired velocity $v_{b_{z_d}}$. Both blocks control their respective velocities and inform the desired thrust and pitch angle for the entire flight envelope, i.e. hover, transition and forward flight. However, the velocity control along $\overrightarrow{\boldsymbol{y_b}}$ is designed depending on the current hybrid UAV flight phase. Therefore, in hover flight, the block MFC$_{v_y}$ set the desired yaw angle ψ_d and the block MFC$_{\psi_d}$ actuates in the system by a differential-thrust command creating a moment around $\overrightarrow{\boldsymbol{z_b}}$ in order to reach the desired velocity along $\overrightarrow{\boldsymbol{y_b}}$. In forward flight, this lateral velocity is reached from roll rotations around $\overrightarrow{\boldsymbol{x_b}}$. These rotations orient the lift force and the hybrid UAV can perform left-right turns with, respectively, negative and positive roll angles ϕ. The propeller speeds (ω_l, ω_r) are defined by the sum of nominal propeller rotation ω_n with a differential propeller speed Δ_ω which is in charge of the yaw control. The negative sign of ω_n for the left-propeller ω_l is due to the counter-rotation sense. And the flap-deflections (δ_l, δ_r), which are in convention negative for pitch-up, are composed by the sum of symmetrical flap deflection δ_n with anti-symmetrical flap deflections Δ_δ that are respectively the control-input for the pitch angle θ and for the roll angle ϕ.

IV. SIMULATION RESULTS

In order to investigate the performance of the model-free control architecture, we design a set of numerical flight simulations with distinct target scenarios that include vertical take-off and landing, hover-to-forward transition, forward-to-hover transition and forward flights. All simulations are

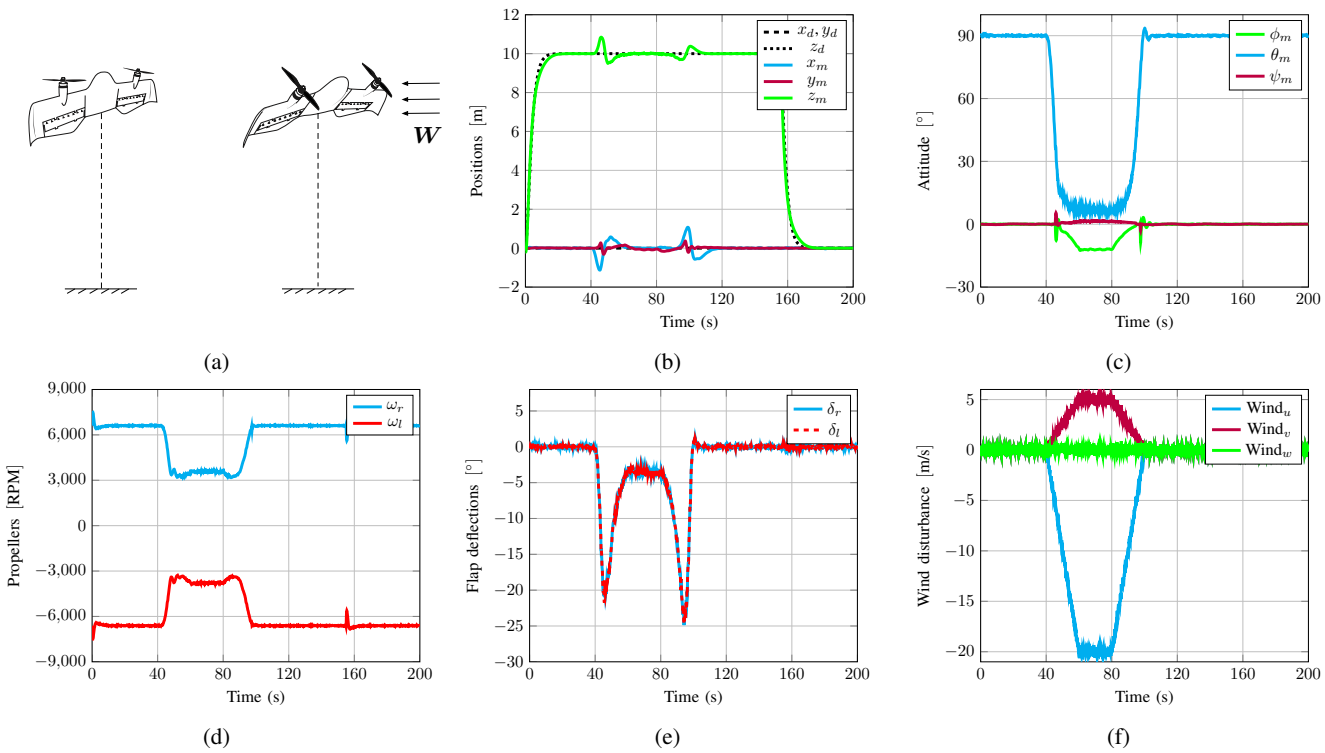

Fig. 5: (**#Flight 1**) - Vertical take-off and transition flight to assure position tracking during high wind disturbances. On the top, from left to right: simulation illustration, positions in the inertial coordinate frame and attitude. On the bottom: propeller speeds ($\omega_l < 0$ and $\omega_r > 0$) due to counter-rotation sense, flap deflections (δ_l and δ_r) convention negative for pitch-up, and wind disturbance.

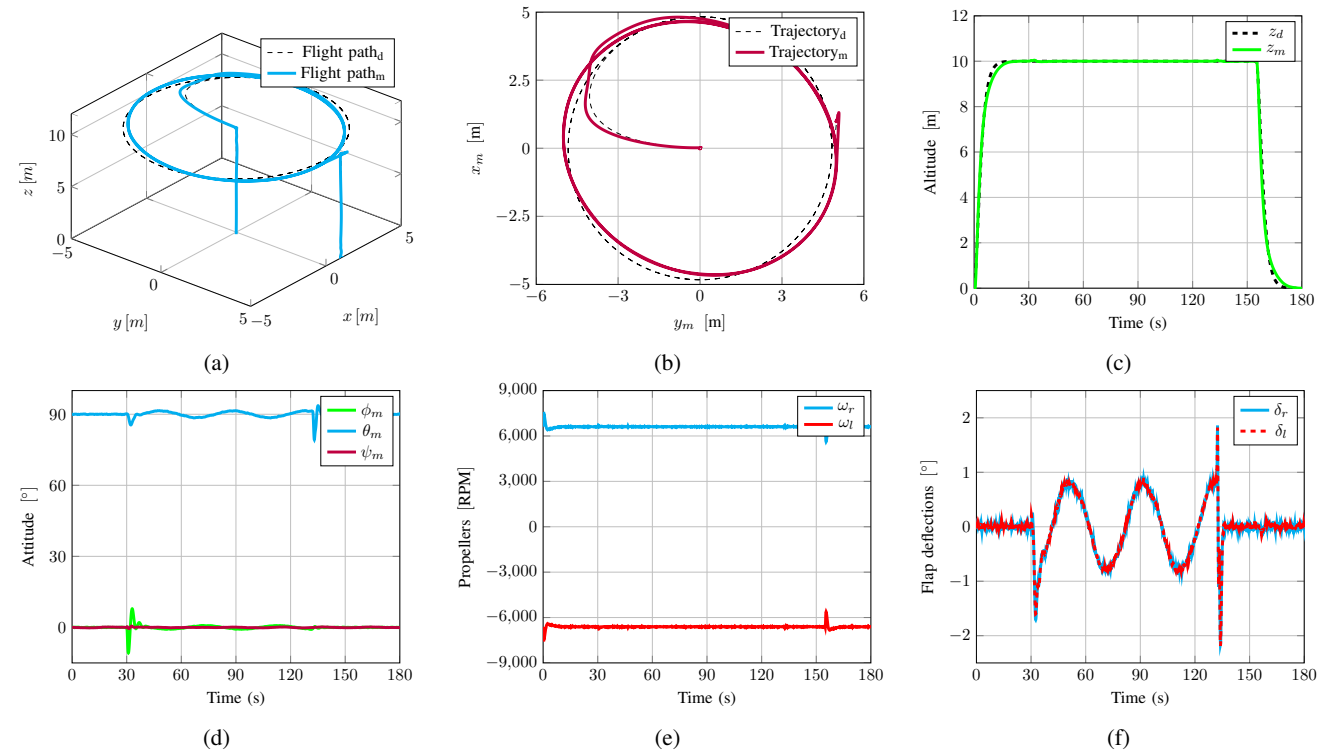

Fig. 6: (**#Flight 2**) - Circular position tracking in hover flight mode. On the top, from left to right: the 3D flight path, North and East positions and altitude. On the bottom: attitude, propeller speeds and flap deflections.

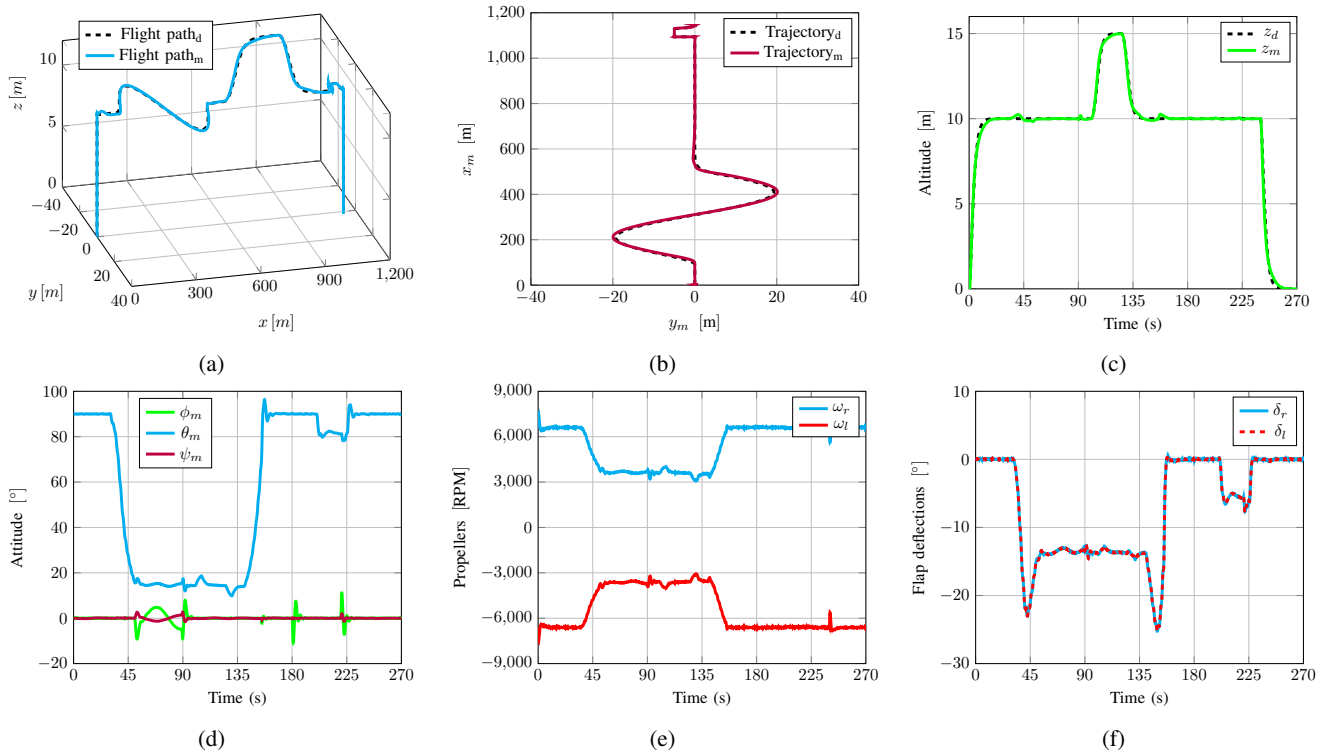

Fig. 7: (**#Flight 3**) - Entire flight envelope simulation in relatively calm flight conditions. On the top, from left to right: the 3D flight path, North and East positions and altitude. On the bottom: attitude, propeller speeds and flap deflections.

discretized at 500 Hz and include noise measurements and wind disturbances. An invariant observer [19] is used to estimate the UAV states providing a smoother signal, this operation adds delays in the closed loop and must be taken into account during the controller's synthesis. The MFC parameters were tuned for the entire flight envelope and are the same for all simulations.

A. *Flight simulations*

In hover flight mode, we analyzed two flight tests. The main objective of the first flight simulation shown in the Fig. 5, is the study of wind influence in the position tracking (**#Flight 1**), for the following desired positions :

$$x_d = 0, \forall\, t$$
$$y_d = 0, \forall\, t$$
$$z_d = \begin{cases} 10, & t \in [0; 155]s \\ 0, & t > 155s \end{cases}$$

Indeed, during this flight mode the hybrid UAV is more susceptible to aerodynamic disturbances. We can explain this by the fact that, in the vertical position, the wind gust along the $z_b - axis$ is in contact with the total reference wing area generating a considerable drag force. Also, the hybrid UAV is not able to compensate this force in the vertical position. Which is why, the transition is performed and the drag force created by the wind is now along the $x_b - axis$. This makes the vehicle add thrust in order to compensated this undesirable aerodynamic force in order to assure the position tracking. The thrust used to reject this perturbation can be seen in the Fig. 5d. And the wind from east with a magnitude of 5 m/s, see Fig. 5f, also produces a drag force in the $y_b - axis$. This force is compensated by orienting the lift force with a symmetrical rotation around the $x_b - axis$, the roll angle shown in the Fig. 5c. In the second flight simulation, we impose a circular desired path (**#Flight 2**) in order to validate the interaction between all control blocks in the proposed control architecture. The following equations define the desired trajectories (x_d, y_d, z_d),

$$x_d = \begin{cases} 0, & t < 30s \\ x_c + r\,cos(\frac{2\pi}{40}t), & t \in [30; 130]s \\ 1, & t > 130s \end{cases}$$
$$y_d = \begin{cases} 0, & t < 30s \\ y_c + r\,sin(\frac{2\pi}{40}t), & t \in [30; 130]s \\ 5, & t > 130s \end{cases}$$
$$z_d = \begin{cases} 10, & t \in [0; 155]s \\ 0, & t > 155s \end{cases}$$

where x_c and y_c correspond to the center of the circle and r is its radius. This maneuver requires that the hybrid UAV follow a circular trajectory while stabilizing its attitude. Accurate position, velocity and attitude control are needed to accurately follow the desired flight plan with the desired attitude orientation. Figure 6 shows the simulation results.

Finally, a complete flight mission (**#Flight 3**) is presented in the Fig. 7 in which we evaluate all hybrid UAV flight capabilities through a vertical take-off from zero to ten meters of altitude followed by the transition to forward flight with a position tracking in the $xy - plane$ and an altitude change in forward flight. Then, the forward-to-hover transition is performed and the simulation ends with a vertical landing. The complete 3D flight path is presented in the Fig. 7a. The controller assures the position tracking during the entire mission, as we can see in the Fig. 7b. The altitude presents small oscillations at 40 and 140 seconds of simulation which is quite acceptable for this UAV class. These oscillations are due to the fast variations of aerodynamic forces and moments that occur during the transition flight phase where the pitch angle decreases causing an important variation in the angle of attack, see Fig. 7d.

B. Results analysis

The controller's performance was evaluated through a quantitative analysis for all previous flight simulations. So, in this analysis, we compute the root mean square error for the vertical take-off and transition flight under high wind disturbances (**#Flight 1**), circular position tracking in hover (**#Flight 2**) and for the entire flight envelope (**#Flight 3**). The results are presented in the Table II, with a RMSE less than 0.8 meter, 0.6 meter per second and 0.8 degrees, respectively, for the position tracking, velocity control and for the attitude stabilization.

TABLE II: Root Mean Square Errors - RMSE

States	**#Flight 1**	**#Flight 2**	**#Flight 3**	SI Units
x	0.2335	0.2348	0.7140	[m]
y	0.0636	0.1258	0.3681	[m]
z	0.1913	0.1384	0.1335	[m]
v_{xb}	0.1505	0.0897	0.1052	[m/s]
v_{yb}	0.0849	0.0899	0.0612	[m/s]
v_{zb}	0.5523	0.1135	0.3684	[m/s]
ϕ	0.1968	0.0183	0.1464	[°]
θ	0.7720	0.1800	0.6094	[°]
ψ	0.1434	0.1553	0.0416	[°]

V. CONCLUSIONS

In this paper, we focused on the development of a model-free control architecture of hybrid UAVs. The proposed controller was designed to stabilize the entire flight envelope of hybrid UAVs including vertical take-off and landing, transition and forward flight with no information about its parameters. Simulation results shown an effective control performance for the entire flight envelope and excellent disturbance rejections during the critical flight phases. Furthermore, the control strategy overcomes the tightly nonlinear, coupled and under-actuated nature of the hybrid UAV. Also, takes into account the many degrees of freedom of the system and ensures attitude stability, velocity control and position tracking for all flight phases.

REFERENCES

[1] K. Alexis, A. Tzes, and G. Nikolakopoulos, "Model predictive quadrotor control: attitude, altitude and position experimental studies," IET Control Theory & Applications, Vol. 6, No. 12, pp. 1812-1827, March 2012.

[2] T. Espinoza-Fraire, A. Dzul, F. Cortés-Martínez, and W. Giernack, "Real-time Implementation and Flight Tests using Linear and Nonlinear Controllers for a Fixed-wing Miniature Aerial Vehicle (MAV)," International Journal of Control, Automation and Systems, Vol. 16, No. 1, pp. 392-396, February 2018.

[3] R. Hugh Stone, P. Anderson, C. Hutchison, A. Tsai, P. Gibbens, and K. C. Wong, "Flight Testing of the T-Wing Tail-Sitter Unmanned Air Vehicle," Journal of Aircraft, Vol. 45, No. 2, pp. 673-685, April 2008.

[4] N. B. Knoebel, and T. W. McLain, "Adaptive Quaternion Control of a Miniature Tailsitter UAV," American Control Conference, Seattle, Washington, USA, pp. 2340-2345, June 2008.

[5] J. Hauser, S. Sastry, and G. Meyer, "Nonlinear control design for slightly non-minimum phase systems: application to v/stol aircraft," Automatica, Vol. 28, pp. 665-679, January 1992.

[6] D. Pucci, T. Hamel, P. Morin, and C. Samson, "Nonlinear Control of Aerial Vehicles Subjected to Aerodynamic Forces," IEEE Conference on Decision and Control (CDC), Florence, Italy, pp. 4839-4846, December 2013.

[7] G. R. Flores-Colunga, and R. Lozano-Leal, "A Nonlinear Control Law for Hover to Level Flight for the Quad Tilt-rotor UAV," Proceedings of the 19th World Congress The International Federation of Automatic Control, South Africa, pp. 11055-11059, August 2014.

[8] A. Frank, J.S. McGrew, M. Valenti, D. Levine, and J.P. How, "Hover, transition, and level flight control design for a single-propeller indoor airplane." In Proc. AIAA Guidance, Navigation Control Conference, Hilton Head, South Carolina, pp. 1-43, August 2007.

[9] L. R. Lustosa, F. Defay, and J.-M. Moschetta, "Longitudinal study of a tilt-body vehicle: modeling, control and stability analysis," International Conference on Unmanned Aircraft Systems (ICUAS), Denver, Colorado, USA, pp. 816-824, June 2015.

[10] J. Zhou, L. Ximin, Z. Li, S. Shen, and F. Zhang, "A Unified Control Method for Quadrotor Tail-sitter UAVs in All Flight Modes: Hover, Transition, and Level Flight," International Conference on Intelligent Robots and Systems (IROS), pp. 4835-4841, September 2017.

[11] E.J.J. Smeur, M. Bronz, and G.C.H.E. de Croon, "Incremental control and guidance of hybrid aircraft applied to the Cyclone tailsitter UAV," to be published.

[12] Haoping Wang, Xuefei Ye, Yang Tian, Gang Zheng, and Nicolai Christov, "Model-Free Based Terminal SMC of Quadrotor Attitude and Position," IEEE Transactions on Aerospace and Electronic Systems, Vol. 52, No, 5, pp. 2519-2528, October 2016.

[13] Y. Al Younes, A. Drak, H. Noura, A. Rabhi, and A. El Hajjaji, "Robust Model-Free Control Applied to a Quadrotor UAV," Journal of Intelligent & Robotic Systems, Vol. 84, No. 1-4, pp. 37-52, December 2016.

[14] J. M. O. Barth, J.-P. Condomines, M. Bronz, L. R. Lustosa, J.-M. Moschetta, C. Join, and M. Fliess, "Fixed-wing UAV with transitioning flight capabilities : Model-Based or Model-Free Control approach? A preliminary study," International Conference on Unmanned Aircraft Systems (ICUAS), Dallas, TX, USA, USA, pp. 1157-1164, June 2018.

[15] J. M. O. Barth, J.-P. Condomines, J.-M. Moschetta, C. Join, and M. Fliess, "Model-Free Control Approach for Fixed-Wing UAVs with Uncertain Parameters Analysis," 23rd International Conference on Methods and Models in Automation and Robotics (MMAR), Miedzyzdroje, Poland, pp. 527-532, August 2018.

[16] O. Bara, M. Fliess, C. Join, J. Daye, and S. M. Djouadi, "Toward a model-free feedback control synthesis for treating acute inflammation," Journal of Theoretical Biology, Elsevier, Vol. 448, No. 7, pp. 26-37, July 2018.

[17] L. R. Lustosa, F. Defay, and J.-M. Moschetta, "Global Singularity-Free Aerodynamic Model for Algorithmic Flight Control of Tail Sitters," AIAA Journal of Guidance, Control, and Dynamics, Vol. 42, No. 2, pp. 303-316, February 2019.

[18] M. Fliess, and C. Join, "Model-free control," International Journal of Control, Taylor & Francis, Vol. 86, No. 12, pp. 2228-2252, July 2013.

[19] P. Martin, and E. Salaun, "Design and implementation of a low-cost observer-based attitude and heading reference system," Control Engineering Practice, Vol. 18, No. 7, pp. 712-722, July 2010.

A.4 International Conference on Methods and Models in Automation and Robotics

Barth, J. M. O., Condomines, J.-P., Moschetta, J.-M., Join, C., and Fliess, M., "Model-Free Control Approach for Fixed-Wing UAVs with Uncertain Parameters Analysis," *23rd International Conference on Methods and Models in Automation and Robotics (MMAR)*, Miedzyzdroje, Poland, pp. 527-532, August 2018. doi: https://doi.org/10.1109/MMAR.2018.8486083.

Model-Free Control Approach for Fixed-Wing UAVs with Uncertain Parameters Analysis

Jacson M. O. Barth[1], Jean-Philippe Condomines[1],
Jean-Marc Moschetta[2], Cédric Join[3,5] and Michel Fliess[4,5]

***Abstract*— This paper presents first results of an innovative Model-Free Control (MFC) architecture applied to fixed-wing UAVs. MFC is an algorithm dedicated to systems with poor modeling knowledge. Indeed, the costs to derive a reliable and representative aerodynamic model for UAVs motivated the use of such a controller. By exploiting a purely numerical model, this algorithm provides an intuitive method to tune the control loop without any information about the controlled system. We propose to extend the MFC architecture to the case of fixed-wing UAVs and study the MFC properties in terms of uncertain parameters. As a first result, our designed MFC architecture provides a continuous controller able to stabilize the entire flight envelope of two different fixed-wing UAVs. These results show promising adaptive perspectives and demonstrate that MFC presents robust properties for both uncertain parameters and disturbance rejection.**

I. INTRODUCTION

The number and diversity of applications involving Micro Air Vehicles (MAVs) are extensive and have received a considerable attention in recent years. Among possible applications, different missions such as aerial imaging [1], atmospheric research [2], or even agricultural tasks [3] require effective performance in terms of endurance, range and high-speed flights which are obtained more efficiently in fixed-wing configurations. These characteristics can be improved for a specific mission profile by using aerodynamic optimization approaches which led to many innovative MAVs [4] [5] [6]. Motivated by the practical problems to find an effective control strategy which is both, simple to transpose for a new MAV and robust in terms of disturbance-rejection remains an interesting challenge for the control community. Therefore, the development of reliable and effective model-based controllers has been an important research topic (e.g., backstepping sliding mode [7], H_∞ controller [8] [9], adaptive control [10] [11], optimal linear controllers [12]). However, these approaches require the development of an accurate model describing the aircraft dynamics that is costly and time consuming. More recently, research works on incremental non-linear dynamic inversion (INDI) [13] have been led and provide a less model-dependent controller that is robust for disturbance rejection. Unfortunately, INDI requires a model of actuators and test flight data to tune the control parameters. For this purpose, Model-Free Control algorithms have been developed providing a potential strategy for designing autopilots without considering any model [14] [15] [16] [17] [18]. Among them, nonlinear MFC strategy [16], has been applied in a nonlinear and strongly coupled system providing good performances in real flights with low computational costs which encourages its use in embedded systems. Whereas MFC approach can be viewed as a potential and efficient method for dealing with identification problems [19] [20]. A recent preliminary study proposed by [21] compared the MFC architecture with a model-based control for Fixed-Wing UAV with transitioning flight capabilities. This comparative study showed a better control performance obtained by the MFC approach during transition flight simulations. While recalling basic motion equations of Fixed-Wing MAVs in §II, the main contributions of this paper are therefore :

- expliciting in §III the theoretical equations that describe MFC architecture in the benchmarking case of the Fixed-Wing MAVs;
- studying the MAV stability in §IV, for desired trajectories in forward-flight mode;
- providing new preliminary results focusing on robust properties for both uncertain parameters and disturbance rejection.

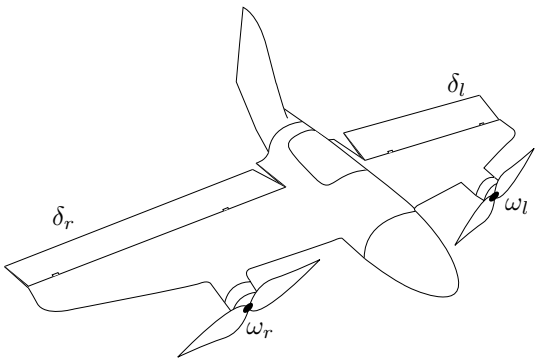

Fig. 1: A typical representation of fixed-wing MAV actuators: Propeller speeds (ω_l, ω_r) and flap deflections (δ_l, δ_r).

[1]Are with the UAV Systems Group, French Civil Aviation School, 31400 Toulouse, France. **[jacson-miguel.olszanecki-barth; jean-philippe.condomines]@enac.fr**

[2]Is with the Department of Aerodynamics, Energetics and Propulsion, Institut Supérieur de l'Aéronautique et de l'Espace, 31400 Toulouse, France. **jean-marc.moschetta@isae-supaero.fr**

[3]Is with the CRAN (CNRS, UMR 7039), Université de Lorraine, BP 239, 54506 Vandœuvre-lès-Nancy, France. **cedric.join@univ-lorraine.fr**

[4]Is with the LIX (CNRS, UMR 7161), École polytechnique, 91128 Palaiseau, France. **Michel.Fliess@polytechnique.edu**

[5]Are with AL.I.E.N (Algèbre pour Identification & Estimation Numérique), 7 rue Maurice Barrès, 54330 Vézelise, France. **[michel.fliess; cedric.join]@alien-sas.com**

II. FIXED-WING MAV MODEL

In order to tackle a wide range of innovative mini-UAVs, various flight dynamics models, in terms of assumptions and numerical techniques, therefore exist. Fixed-wing MAVs are commonly represented by non-linear equations of motion with six-Degrees-of-Freedom (DoF) : 3 DoF correspond to the translation motion (u, v, w) and the 3 remaining DoF to the rotation motion (ϕ, θ, ψ). Based on *Newton's second law* with all forces and moments expressed in the body frame, we can describe the MAV dynamics whose angular rates are denoted by $\mathbf{\Omega} = [p\, q\, r]^T$ and their resulting derived equations are given by equation (1) [22].

$$\begin{aligned}
\dot{p} &= \frac{I_{xz}}{I_{xx}} r - qr\frac{(I_{zz} - I_{yy})}{I_{zz}} + qp\frac{I_{xz}}{I_{xx}} + \frac{L^A}{I_{xx}} \\
\dot{q} &= pr\frac{I_{xz}}{I_{xx}} - (p^2 - r^2)\frac{I_{xz}}{I_{yy}} + \frac{M^A}{I_{yy}} \\
\dot{r} &= \frac{I_{xz}}{I_{zz}} \dot{p} - pq\frac{(I_{yy} - I_{zz})}{I_{zz}} - qr\frac{I_{xz}}{I_{zz}} + \frac{N^A}{I_{zz}}
\end{aligned} \tag{1}$$

Conveniently, the coordinate system was chosen so that the MAV is symmetric with respect to the $x_b z_b - plane$, thus $I_{xy} = I_{yx} = I_{zy} = I_{yz} = 0$. And the inertia matrix becomes :

$$\mathbf{I} = \begin{bmatrix} I_{xx} & 0 & -I_{xz} \\ 0 & I_{yy} & 0 \\ -I_{xz} & 0 & I_{zz} \end{bmatrix} \tag{2}$$

The resulting translational equations (3) [22], correspond to the linear accelerations.

$$\begin{aligned}
\dot{u} &= (rv - qw) + \frac{X^A}{m} - g\sin\theta + \frac{T_h}{m} \\
\dot{v} &= (pw - ru) + \frac{Y^A}{m} + g\cos\theta\sin\phi \\
\dot{w} &= (qu - pv) + \frac{Z^A}{m} + g\cos\theta\cos\phi
\end{aligned} \tag{3}$$

Where (u, v, w) are the linear velocities expressed in the body frame, g the gravitational constant and ϕ, θ, ψ the MAV attitude, respectively, roll, pitch and yaw angles. The thrust of the propellers (T_h) which is a squared function of propeller speeds also depends of the air density (ρ) and propeller characteristic, such as the diameter, etc. Aerodynamic forces $(X^A,\ Y^A,\ Z^A)$ and aerodynamic moments $(L^A,\ M^A,\ N^A)$ are subject to aerodynamic coefficients :

$$\begin{bmatrix} X^A \\ Y^A \\ Z^A \end{bmatrix} = \frac{1}{2}\rho S V^2 \begin{bmatrix} C_X \\ C_Y \\ C_Z \end{bmatrix} \tag{4}$$

$$\begin{bmatrix} L^A \\ M^A \\ N^A \end{bmatrix} = \frac{1}{2}\rho S V^2 \begin{bmatrix} b\,C_l \\ c\,C_m \\ b\,C_n \end{bmatrix} \tag{5}$$

where S, b, c are respectively, the wing area, the wingspan and the mean chord.

Remark : Aerodynamic forces can also be modelled using the Φ-Theory proposed by [23].

The kinematic attitude equations (6) are used to relate the angular rates to Euler angles [22].

$$\begin{aligned}
\dot{\phi} &= p + \tan\theta(q\sin\phi + r\cos\phi) \\
\dot{\theta} &= q\cos\phi - r\sin\phi \\
\dot{\psi} &= \sec\theta(q\sin\phi + r\cos\phi)
\end{aligned} \tag{6}$$

The nonlinear state space representation corresponding to the Fixed-Wing MAV can be described in a compact form such as: $\dot{\boldsymbol{x}} = f(\boldsymbol{x}, \mathbf{u})$ and $\boldsymbol{y} = h(\boldsymbol{x}, \boldsymbol{u})$, where $\boldsymbol{x} = (\boldsymbol{v}_l\, \boldsymbol{\omega}_b\, q)^T$ and $\boldsymbol{v}_l$, $\boldsymbol{\omega}_b \in \mathbb{R}^3$, $q \in \mathbb{R}^4$, denote respectively, vehicle velocity (u, v, w) in body frame, angular velocity in body frame, and vehicle attitude represented in quaternion formulation. Control inputs $\boldsymbol{u} = (\omega_l\, \omega_r\, \delta_l\, \delta_r)^T$ are defined according to Fig. 1.

III. MODEL-FREE CONTROL

Model-Free Control term appears many times in the literature, but in distinct meanings from this paper. Actually, the growing importance of artificial intelligence and machine learning techniques, particularly through neural networks, has naturally been implanted into the model-free terms: see, for example [24] [25]. However, in this paper, we assume model-free control terms according to [20].

A. MFC Theory

We present briefly the main theoretical principles of some research works dealing with model-free control approach. Let's consider the following non linear state-space representation defined by :

$$\begin{cases} \dot{\mathbf{x}} = f(\mathbf{x}, \mathbf{u}) \\ \mathbf{y} = h(\mathbf{x}, \mathbf{u}) \end{cases} \tag{7}$$

where $\mathbf{x}$, $\mathbf{u}$, $\mathbf{y}$ are the state, input and output vectors respectively. The output $\mathbf{y}$ is not directly available but rather it is observed through a noise corruption. A model for the output can be described by the following equation :

$$y_m(t) = y(t) + \omega_n(t) \tag{8}$$

where $\omega_n(t)$ is the observation noise. The exploitation of the MFC principles required the definition of a particular SISO model, named *Ultra-Local Model*, which corresponds to replace the unknown dynamic by a purely numerical model :

$$y_m^{(v)} = F_y + \alpha \cdot u \tag{9}$$

In equation (9), v is the order derivative of y_m, α is a non-physical constant parameter and is an element of $\mathbb{R}$. Moreover, the exploitation of this numerical model requires the knowledge of F_y. This quantity represents the real dynamics of the model as well as the different disturbances which could damage the output-system performances. Thus, an accurate estimation of F, defined as $\hat{F}$, is crucial and plays an import role in the MFC performance. Assuming that we do not have any information about the plant, its estimation can be

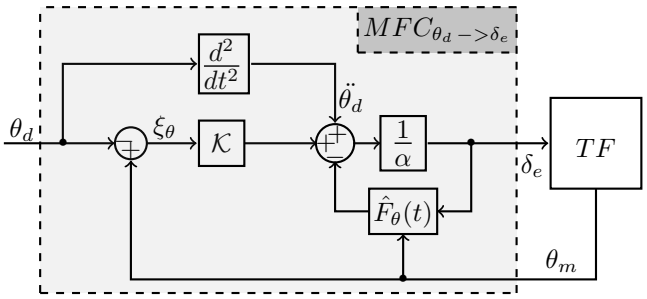

Fig. 2: Detailed Model-Free Control schema applied on equation (16). Proportional-Derivative control $\mathcal{K}$. $\hat{F}_\theta(t)$ estimator of pitch dynamic and disturbances with α a non-physical constant parameter.

computed directly by considering the following methodology in which we use a second-order[1] *Ultra-Local Model* :

$$\ddot{y}_m = F_y + \alpha \cdot u \tag{10}$$

The first step is to apply the *Lapace Transform* in the equation (10). Referring to elementary operational calculus we transform the equation (10) to equation (11) :

$$s^2 Y_m(s) - s y_m(0) - \dot{y}_m(0) = \frac{F_y}{s} + \alpha U(s) \tag{11}$$

Where $Y_m(s)$ and $U(s)$ correspond to the *Laplace transforms* of y_m and u. By differentiating twice the previous equation we are able to rid the initial condition :

$$2Y_m(s) + 4s\frac{dY_m(s)}{ds} + s^2\frac{d^2Y(s)}{ds^2} = \frac{2F_y}{s^3} + \alpha\frac{d^2U(s)}{ds^2} \tag{12}$$

However, s in the time domain corresponds to the derivation with respect to time and it is sensitive to noise corruptions. Therefore, in order to reduce both noise and numerical computation errors on the output estimation, we replace the derivative terms by integrators ($\frac{1}{s}$) who have robust properties with respect to noise. Thus, multiplying both sides of equation (12) by s^{-3}, we obtain :

$$\frac{2Y_m(s)}{s^3} + \frac{4}{s^2}\frac{dY_m(s)}{ds} + \frac{1}{s}\frac{d^2Y(s)}{ds^2} = \frac{2F_y}{s^6} + \frac{\alpha}{s^3}\frac{d^2U(s)}{ds^2} \tag{13}$$

Equation (13) can be transferred back to the time domain employing elementary calculus and *Cauchy's formula* to reduce multiple integrals in a simple one :

$$\hat{F}_y = \frac{5!}{2T^5}\int_{t-T}^{t}[(T-\sigma)^2 - 4\sigma(T-\sigma) + \sigma^2]y_m(\sigma) - [\frac{\alpha}{2}\sigma^2(T-\sigma)^2 u(\sigma)]d\sigma \tag{14}$$

From measurements of y_m and u the unmodeled dynamic of y and the disturbances ω_n are estimated by $\hat{F}_y$ which is updated for each interval of integration $[t-T, t]$. This interval corresponds to the window width of a receding horizon strategy which results in a trade-off. The idea is to choose the window width small so as to calculate the estimation within an acceptable short delay but large enough in order to preserve the low-pass filter properties whose noise attenuation of y_m. Based on such estimator it is possible to design a robust controller that estimates on-line the system dynamic from periodic measurements of y_m and u. The general form of the close-loop control can be defined such as :

$$u = \underbrace{-\frac{\hat{F}_y}{\alpha}}_{\text{NL Cancellation}} + \underbrace{\frac{y_d^{(v)} + \mathcal{K}(\xi)}{\alpha}}_{\text{Closed loop tracking}} \tag{15}$$

where the quantity $\xi = y_m - y_d$ is the tracking error and $\mathcal{K}(\xi)$ is a closed loop feedback controller. We recognize in equation (15) the typical mathematical expression of a "nominal control" in the "flatness-based" control (see [26] [27] for details) in which the non-linear terms $\hat{F}_y$ is summed with a closed loop tracking of a reference trajectory $t \rightarrow\ y_d(t)$.

B. Illustrative example

We consider now a simple pitch angle dynamic of a given aircraft, the transfer function between the output (θ) and the elevator control input (δ_e) is described as follows :

$$TF(s) = \frac{\theta(s)}{\delta_e(s)} = \frac{1.151s + 0.1774}{s^3 + 0.739s^2 + 0.921s} \tag{16}$$

A second order *Ultra-Local Model* (v=2) was chosen to estimate the pitch dynamic (θ) :

$$\ddot{\theta}_m = F_\theta + \alpha \cdot \delta_e \tag{17}$$

Fig. 3: Dark-Knight MAV.

Fig. 4: Cyclone MAV.

[1]The same methodology can be applied to find the mathematical expression of $\hat{F}_y$ for a first-order *Ultra-Local Model*.

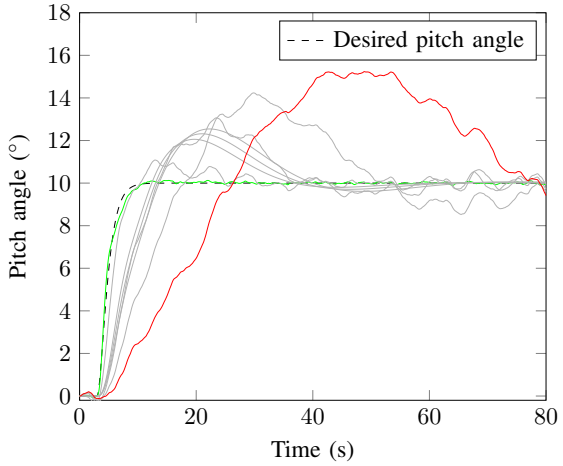

Fig. 5: Pitch angle responses with noise for different combinations of α and T with $K_p = -1.5$ and $K_d = -2.5$.

Figure 2 shows the MFC schema which the closed-loop control can be computed by :

$$\delta_e = \frac{-\hat{F}_\theta + \ddot{\theta}_d + \mathcal{K}(\xi_\theta)}{\alpha} \tag{18}$$

Replacing (18) in (17) with $\mathcal{K}$ equal to Proportional-Derivative gains, we have :

$$\ddot{\theta}_m = F_\theta - \hat{F}_\theta + \ddot{\theta}_d + K_p\,\xi_\theta + K_d\,\dot{\xi}_\theta \tag{19}$$

It follows that theoretically, if the error between the pitch angle estimator and the real pitch angle, is approximately zero during $[t-T, t]$:

$$F_\theta - \hat{F}_\theta \approx 0 \tag{20}$$

The pitch angle and the dynamic error (ξ_θ) can be easily tuned by proportional and derivative gains, respectively K_p and K_d such that :

$$\ddot{\xi}_\theta = \ddot{\theta}_m - \ddot{\theta}_d \tag{21}$$

$$\ddot{\xi}_\theta - K_p\,\xi_\theta - K_d\,\dot{\xi}_\theta = 0 \tag{22}$$

The MFC performance varies according to the following parameters: the length of the integration window T; The coefficient α that is chosen to set the same magnitude between θ_m and the control input δ_e. Kp and Kd which are used to set the error dynamic, see Fig. 5.

Remark : It is important to emphasize that MFC algorithms have been developed to Single-Input Single-Output (SISO) systems and Fixed-Wing MAVs are Multiple-Input Multiple-Output (MIMO) systems. In our study-case, a second order *Ultra-Local Model* (υ=2) was chosen to represent each state dynamic of the MAV (attitude and velocities). Wherefore, a control architecture composed by multiple SISO MFCs, is proposed, and developed in the *MFC architecture* block, see Fig. 6.

IV. FLIGHT SIMULATIONS

We now apply the control approach described in the previous section for two fixed-wing MAVs (Fig. 3 and Fig. 4) whose specifications are described in Table I. The idea is to study the MFC properties in terms of uncertain parameters. The simulation is discretized at 500 Hz and includes addi-

TABLE I: Fixed-Wing specifications

Parameters	Cyclone	Dark-Knight	SI Units	Δ %
Mass	0.852	0.586	[Kg]	45.39
I_{xx}	0.008 21	0.005 41	[Kg m^2]	52.30
I_{yy}	0.007 98	0.005 23	[Kg m^2]	52.47
I_{zz}	0.016 41	0.010 82	[Kg m^2]	51.20
Propeller radius	0.2032	0.1524	[m]	33.33
Mean Chord	0.17	0.175	[m]	2.94
Wingspan	0.88	1	[m]	13.64
Wing area	0.1496	0.175	[m^2]	16.98

tional sensor noises and state estimation errors. Also, inspired by the Dryden Wind Turbulence Model, we add wind gusts of around 4 (m/s) along x and y axes to perturb the lateral and longitudinal motions. An overview of the simulation is shown in Fig. 7. The flight path describes a take-off with a constant rate of climbing fixed at 2.5 (m/s), see Fig. 7d. Reaching a desired altitude, the rate of climbing is ordered to zero to maintain the flight level. During this part of the flight, we can analyze especially the longitudinal dynamics, such as forward speed, rate of climbing and pitch angle. At constant altitude, left-right trajectories were imposed to validate the roll and yaw control loops. Positive east-velocity defines a positive-desired roll angle and the MAV turns right, see Fig. 7c and Fig. 7e. By analogy, a rate of climb greater than zero calls for positive pitch angles (Fig. 7d and Fig. 7f) and a higher flight level will be reached. The reverse is also true, the MAV can turn left and reaches a smaller flight level with negative-desired velocities. The thrust computed by MFC can be analyzed into two parts : the nominal thrust and the differential thrust. In the first one, both propellers turn at the same speed to ensures a forward velocity around fifteen meters per second, Fig. 7b. In the second one, propellers turn at different speeds creating a moment around the z axis. This

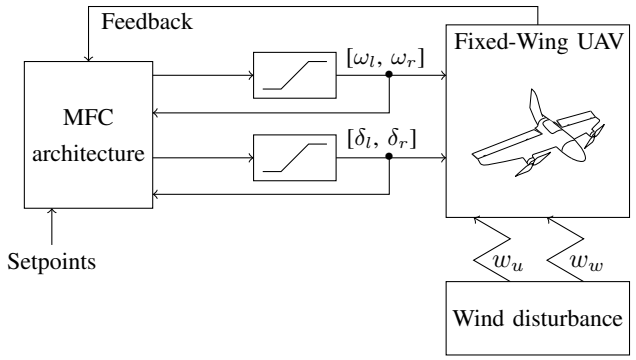

Fig. 6: MFC architecture designed for HMAVs with saturated control inputs. Propeller speeds (ω_l, ω_r) and flap deflections (δ_l, δ_r) are computed by means of *MFC architecture* block.

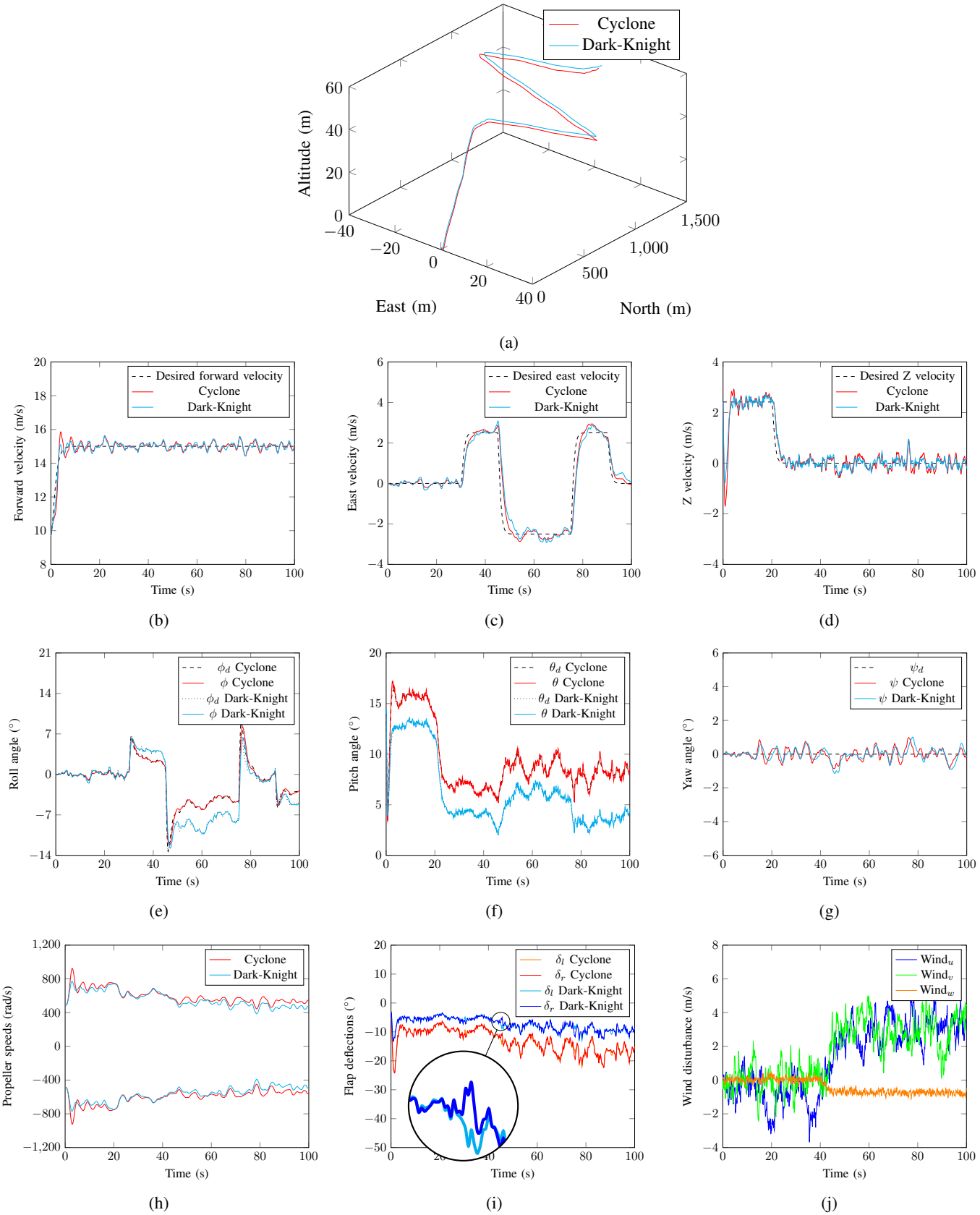

Fig. 7: Forward flight simulations. On the top : the flight path. From left to right : forward-speed, east velocity and velocity along z axis. Attitude in the third ligne and on the bottom : propeller speeds ($\omega_l < 0$ and $\omega_r > 0$) due to counter-rotation sense, elevon deflections, convention negative for pitch-up (δ_l and δ_r) and wind disturbances.

moment controls the yaw angle that is set to zero throughout the simulation, as shown in the Fig. 7g. The performance of the actuators are presented in the Fig. 7h and Fig. 7i. Cyclone flaps present greater deflection angle than for Dark-Knight. This difference may be attributed to the fact that the Cyclone has a smaller wingspan. Thus, for an equivalent airspeed, the Cyclone needs a higher pitch angle to generate lift and to reach the desired rate of climbing. The zoom in the Fig. 7i (around 45 seconds), allows us to see the command which generates a negative roll moment that corresponds to a left turn. Despite windy conditions Fig. 7j, MFC ensures effective attitude stabilization and tracking velocities for both MAVs during lateral and longitudinal trajectories.

V. CONCLUSION

We have presented velocity and attitude control using MFC architecture for fixed-wing MAVs. The proposed approach is able to stabilize the entire flight envelope without any knowledge about the controlled MAV. First results demonstrated an effective disturbance rejection and control of unmodeled dynamics with MFC by the means of its adaptive properties.

This control architecture and MFC algorithms are being implemented in *Paparazzi* open-source autopilot system (cf. Paparazzi project at: `https://wiki.paparazziuav.org/`) and experimental flights will be presented soon.

REFERENCES

[1] Donate A. Flores, Carlos Saito and Juan A. Paredes, "Multispectral imaging of crops in the Peruvian Highlands through a fixed-wing UAV system," *IEEE International Conference on Mechatronics (ICM)*, Churchill, VIC, Australia, pp. 399-403, February 2017.

[2] Benjamin D. Reineman, Luc Lenain and W. Kendall Melville, "The Use of Ship-Launched Fixed-Wing UAVs for Measuring the Marine Atmospheric Boundary Layer and Ocean Surface Processes," *Journal of Atmospheric and Oceanic Technology*, 2016.

[3] James V. Henrickson, Cameron Rogers and Han-Hsun Lu, "Infrastructure assessment with small unmanned aircraft systems," *International Conference on Unmanned Aircraft Systems (ICUAS)*, Arlington, VA USA, pp. 933-942, June 2016.

[4] Bronz, M., Hattenberger, G. and Moschetta, J.-M, "Development of a Long Endurance Mini-UAV: ETERNITY," *International Journal of Micro Air Vehicles*, Volume 5 (4), pp. 261-272, 2013.

[5] Bronz, M., Condomines, J.-P and Hattenberger, G., "Development of an 18cm Micro Air Vehicle : QUARK," *International Micro Air Vehicle Conference and Flight Competition (IMAV)*, Toulouse, France, September 2013.

[6] Bronz, M., Smeur, E. J. J., de Marina, H. G., Hattenberger, G., "Development of A Fixed-Wing mini UAV with Transitioning Flight Capability," *35th AIAA Applied Aerodynamics Conference, AIAA Aviation Forum*, Denver, Colorado, pp. 1-14, June 2017.

[7] Espinoza, T., Dzul, A., Lozano, R. and Parada, P., "Backstepping-Sliding mode controllers applied to a fixed-wing UAV," *In IEEE International Conference on Unmanned Aircraft Systems (ICUAS)*, Atlanta, GA, USA, pp. 95-104, May 2013.

[8] Yang, C. D. and Kung, C. C., "Nonlinear H_∞ Flight Control of General Six-Degree-of-Freedom Motions," *Journal of Guidance, Control and Dynamics*, 23(2), pp. 278-288, April 2000.

[9] Ferreira, H. C., Baptista, R. S., Ishihara, J. Y. and Borges, G. A., "Disturbance rejection in a fixed wing UAV using nonlinear H_∞ state feedback," *In IEEE International Conference on Control and Automation*, Santiago, Chile, pp. 386-391, December 2011.

[10] Narendra, K. S. and Balakrishnan, J., "Adaptive control using multiple models," *IEEE transactions on automatic control*, 42(2), pp. 171-187, February 1997.

[11] A. T. Espinoza Fraire, YangQuan Chen and A. Dzul, "Fixed-wing MAV adaptive PD control based on a modified MIT rule with sliding-mode control," *International Conference on Unmanned Aircraft Systems (ICUAS)*, Miami, FL, USA, June 2017.

[12] Teng D. Chollom1, Nkemdilim Ofodile1 and Dr. Osichinaka Ubadike, "Application Techniques of Multi-objective particle swarm optimization: Aircraft flight control," *11th International Conference on Control (UKACC)*, Belfast, UK, September 2016.

[13] Elisabeth S. V. D. Sman, E. J. J. Smeur, Bart Remes, C. De Wagter and Q. P. Chu, "Nonlinear Dynamic Inversion and Multihole Pressure Probes for Disturbance Rejection Control of Fixed-wing Micro Air Vehicles," *International Micro Air Vehicle Competition and Conference (IMAV)*, Toulouse, France, pp. 111-120, 2017.

[14] Younes AI Younes, Ahmad Drak, Hassan Noura, Abdelhamid Rabhi and Ahmed EI Hajjaji, "Model-Free Control of a Quadrotor Vehicle," *International Conference on Unmanned Aircraft Systems (ICUAS)*, Orlando, FL, USA, pp. 1126-1131, May 2014.

[15] Pérez-Arancibia, N. O., Duhamel, P.-E. J., Ma, K. Y., Wood, R. J., "Model-Free Control of a Hovering Flapping-Wing Microrobot," *Journal of Intelligent & Robotic Systems*, pp. 95-111, January 2015.

[16] Aneesh N. Chand, Michihiro Kawanishi, Tatsuo Narikiyo, "Nonlinear model-free control of flapping wing flying robot using iPID," *IEEE International Conference on Robotics and Automation (ICRA)*, Stockholm, Sweden, pp. 2930-2937, May 2016.

[17] Younes Al Younes, Ahmad Drak, Hassan Noura, Abdelhamid Rabhi and Ahmed El Hajjaji, "Robust Model-Free Control Applied to a Quadrotor UAV," *Journal of Intelligent & Robotic Systems*, pp. 37-52, December 2016.

[18] Haoping Wang, Xuefei Ye, Yang Tian, Gang Zheng, and Nicolai Christov, "Model-FreeBased Terminal SMC of Quadrotor Attitude and Position," *IEEE Transactions on Aerospace and Electronic Systems*, Vol. 52, pp. 2519-2528, October 2016.

[19] Fliess M. and Join C., "Model-free control and intelligent PID controllers: towards a possible trivialization of nonlinear control?," *15th IFAC Symposium on System Identification (SYSID)*, 2009.

[20] Fliess M. and Join C., "Model-free control," *International Journal of Control, Taylor & Francis*, vol. 28(12), pp. 2228-2252, 2013.

[21] J. M. O. Barth, J.-P. Condomines, M. Bronz, L. R. Lustosa, J.-M. Moschetta, C. Join and M. Fliess, "Fixed-wing UAV with transitioning flight capabilities : Model-Based or Model-Free Control approach? A preliminary study," *International Conference on Unmanned Aircraft Systems (ICUAS)*, Dallas, TX, USA, June 2018.

[22] Warren F. Phillips, "Mechanics of Flight," Second Edition, Wiley, 2009.

[23] L. R. Lustosa, F. Defay, and J.-M. Moschetta, "A global singularityless polynomial-like aerodynamics model for algorithmic flight control of tail-sitters," *AIAA Journal of Guidance, Control, and Dynamics* (to appear).

[24] Lillicrap, T. P., Hunt, J. J., Pritzel, A., Heess, N., Erez, T., Tassa, Y., Silver, D., and Wierstra, D., "Continuous control with deep reinforcement learning," *6th International Conference on Learning Representations*, Vancouver, 2016.

[25] Radac M.-B., Precup R.E., Roman R.C., "Model-Free control performance improvement using virtual reference feedback tuning and reinforcement Q-learning," *International Journal of Systems Science*, September 2016.

[26] M. Mboup, C. Join and M. Fliess, "A revised look at numerical differentiation with an application to nonlinear feedback control," *In 15th Mediterranean conference on Control and automation (MED'07)*. Athenes, Greece, July 2007.

[27] J. Zehetner, J. Reger and M. Horn, "A Derivative Estimation Toolbox based on Algebraic Methods - Theory and Practice," *2007 IEEE International Conference on Control Applications*, Singapore, pp. 331-336, 2007.

A.5 International Conference on Unmanned Aircraft Systems

Barth, J. M. O., Condomines, J.-P., Bronz, M., Lustosa, L. R., Moschetta, J.-M., Join, C., and Fliess, M., "Fixed-wing UAV with transitioning flight capabilities : Model-Based or Model-Free Control approach? A preliminary study," *International Conference on Unmanned Aircraft Systems (ICUAS)*, Dallas, TX, USA, pp. 1157-1164, June 2018. doi: https://doi.org/10.1109/ICUAS.2018.8453404.

Fixed-wing UAV with transitioning flight capabilities : Model-Based or Model-Free Control approach? A preliminary study.

Jacson M. O. Barth[1], Jean-Philippe Condomines[1], Murat Bronz[1], Leandro R. Lustosa[2]
Jean-Marc Moschetta[3], Cédric Join[4,6] and Michel Fliess[5,6]

***Abstract*— Transitioning vehicles experience three different flight phases during typical missions. The hovering and forward flight phases have been researched widely, however the transition phase in between is more challenging and has been the subject of less research. One of the control approaches to handle the transition phase relies on model-based methods which require sophisticated wind-tunnel characterization. Accurate modeling of force and moments of a partially stalled wing and control surfaces is highly challenging and time consuming. In addition, these models usually require several flight measurements (such as angle of attack and low airspeed) that are difficult to obtain. As an alternative, some control approaches manage the transition phase without the need for sophisticated models. One example of such an approach is the Model Free Control (MFC). This paper compares the results obtained from both MFC and Linear Quadratic Regulator (LQR) applied to fixed-wing UAV with transitioning flight capability during hovering, transition and forward flight modes. Both of the controllers are designed for a transitioning vehicle called *MAVion*. The simulation results demonstrated that MFC increases the stability of the aircraft, especially in disturbed flight conditions.**

I. INTRODUCTION

The number and diversity of applications involving Micro Air Vehicles (MAVs) are extensive and have received a considerable attention in recent years. Among possible applications, different missions require the possibility of a take-off and landing from a small area. Rotary-wing configurations are more suitable for their vertical or short take-off and landing capabilities, however, fixed-wing configurations offer a better performance in terms of range, endurance and high-speed flight. On the other hand, Hybrid MAVs (HMAVs) are capable of performing efficient forward flight with the versatility of a rotary-wing vehicle for hovering applications, see Figure 1.

[1]Are with the UAV Systems Group, French Civil Aviation School, 31400 Toulouse, France. **[jacson-miguel.olszanecki-barth; jean-philippe.condomines; murat.bronz]@enac.fr**

[2]Is with the MIST Lab, École Polytechnique de Montréal, QC H3T 1J4, Canada. **leandro.lustosa@polymtl.ca**

[3]Is with the Department of Aerodynamics, Energetics and Propulsion, Institut Supérieur de l'Aéronautique et de l'Espace, 31400 Toulouse, France. **jean-marc.moschetta@isae-supaero.fr**

[4]Is with the CRAN (CNRS, UMR 7039)), Université de Lorraine, BP 239, 54506 Vandœuvre-lès-Nancy, France. **cedric.join@univ-lorraine.fr**

[5]Is with the LIX (CNRS, UMR 7161), École polytechnique, 91128 Palaiseau, France. **Michel.Fliess@polytechnique.edu**

[6]Are with the AL.I.E.N (Algèbre pour Identification & Estimation Numérique), 7 rue Maurice Barrès, 54330 Vézelise, France. **[michel.fliess; cedric.join]@alien-sas.com**

During transition phase maintaining constant altitude, HMAVs encounter very large angles of attack, often a partially stalled wing, and rapidly changing pitching moments [1]. Finding an effective control strategy is important in order to improve the flight performance and it remains an interesting challenge for the control community. In hover or forward flights, autopilots are able to stabilize MAV attitude by using linear controllers [2] and simple Proportional Integral Derivative (PID) control [3]. Although being simple to tune without the knowledge of the model, PID controllers are limited in terms of disturbance rejection [2][4]. Among the current techniques that are used to stabilize the Hybrid MAVs, nonlinear controls [5][6][7], and control laws based on "switching" [8][9] can be mentioned. However these are case-specific, and their adaptation to different models is a difficult task. HMAVs are usually classified as under-actuated and highly non-linear systems. Therefore, defining an appropriate model structure that is both reliable in terms of aerodynamic interaction between propeller and wing, and that can also model post-stall intricacies effects, remains a complex work. Nevertheless, there are recent efforts validating a tail-sitter MAV model by wind tunnel campaign and experimental flight tests for the entire flight envelope [10][11][12]. These specific aerodynamic characteristics were computed to design a series of gain matrices which are then used in a scheduled Linear Quadratic Regulator [11]. However, modeling of the forces and moments at different airspeeds and different angles of attack is costly and time consuming, and not accessible easily by everyone.

Alternatively, a sensor-based approach called incremental

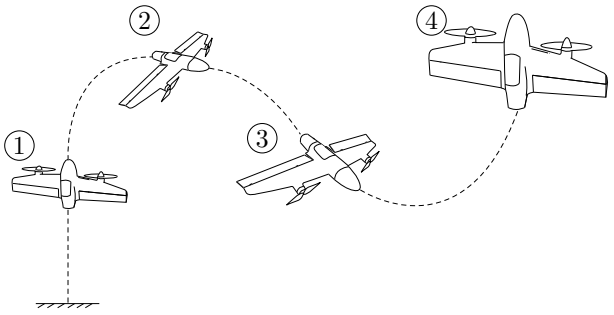

Fig. 1: Typical flight modes of Hybrid Micro Aerial Vehicles: 1 - Take-Off; 2 - Transition; 3 - Forward; 4 - Hover.

nonlinear dynamic inversion (INDI) which is less model-dependent and robust at disturbance rejection, was proposed [4][13]. This controller requires a sensor measurement to estimate a large part of the UAV model, except the actuator dynamics that must be characterized beforehand. By filtering and differentiating the gyroscope measurements, the angular acceleration is estimated, and an increment of the control input is calculated based on a desired increment in angular acceleration. Thus, disturbances as well as unmodeled dynamics are measured, computed and compensated. As a main drawback, INDI uses test flight data to tune off-line the control coefficients. *Of course, to do this, the MAV needs to be flying* [13], with predefined parameters.

The Model-Free Control term appears many times in the literature, but in distinct meanings from this paper. In fact, the growing importance of artificial intelligence and machine learning techniques, particularly through neural networks, has naturally been implanted into the model-free terms [14][15]. In this paper, we assume model-free control terms according to the simple algorithms proposed by [16][17] which have adaptive properties. MFC algorithms have been developed, and applied on MAVs providing a potential strategy for designing autopilots without considering any model [18][19][20][21][22]. Among them, nonlinear MFC strategy [20], has been applied in a nonlinear and strongly coupled system providing good performances in real flights with low computational costs which encourages its use in embedded systems. MFC guarantees a straightforward form of the tuning of the control loop which needs no modeling of the vehicle dynamics and is efficient at disturbance rejection. Whereas MFC approach can be viewed as a potential efficient method for dealing with post-stall phenomena, this model free based control has never been studied on HMAVs in pre-stall region and never compared with traditional approaches for transitioning fixed-wings. The main contributions of this paper are therefore :

- to make explicit (in §III-A and §III-B) the theoretical equations that describe both MFC and LQR controllers in the benchmarking case of the transitioning flight;
- to propose a novel preliminary comparative study (in §IV), focusing on transitioning flight, between traditional control methods and model free approach;

II. AERODYNAMIC PRELIMINARIES

Characterized by increased mission complexity, many innovative HMAVs are constantly emerging. These platforms may be divided into different groups: tilt-rotors [23], quadplanes [24] and tail-sitters or tilt-bodies [10][25][26]. Also, combination of the previous cited designs can be found, such as quad-tilt-rotors [27][28]. Quadplanes have independent propulsion systems for hovering and forward flight. Thus, the control laws can be optimized for each flight mode separately. By contrast, these configurations present more drag in cruise flight mode due to the additional quad-mechanical structure which does not always have optimized aerodynamic characteristics. In terms of endurance, tail-sitters are more promising. However, transition phase of tail-sitters include high angles of attack, and often a partially stalled wing and fast variations of pitching moment which increase the difficulty in modeling and control aspects [1].

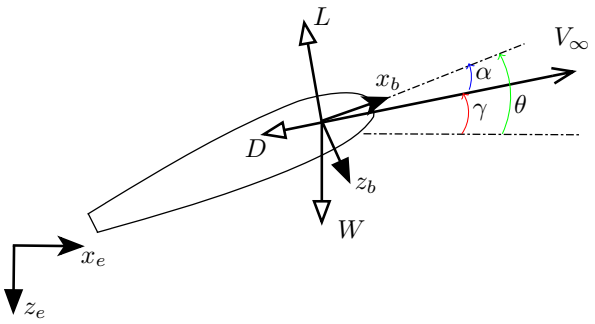

Fig. 2: Coordinate systems with vector forces and angles.

A. Coordinate system

In this paper we assume the same coordinate systems as a conventional fixed-wing aircraft. In Figure 2, the body frame denoted by (x_b, y_b, z_b) represents the front, right and down directions of the HMAV. Similarly, the inertial frame denoted by (x_e, y_e, z_e) describes the north, east and down directions. The HMAV orientations are defined by the attitude angles ϕ, θ, ψ, respectively, roll, pitch and yaw. Aerodynamic forces that act in the HMAV are described by lift (L) and the drag (D). The weight force is represented by the vector (W). In addition, the angle of attack (α) and the flight path angle (γ) which describes whether the aircraft is climbing or descending, can be seen in Figure 2.

B. Tail-sitter model

In this work, tail-sitter vehicle dynamics simulation is based on ϕ-theory [29] assumptions. The ϕ-theory framework for modeling aerodynamics allows us to write the differential equations of motion of the vehicle which specifications are presented in Table I, in the form

$$\dot{\boldsymbol{x}} = \gamma(\boldsymbol{x}, \boldsymbol{u}, \boldsymbol{w}) \tag{1}$$

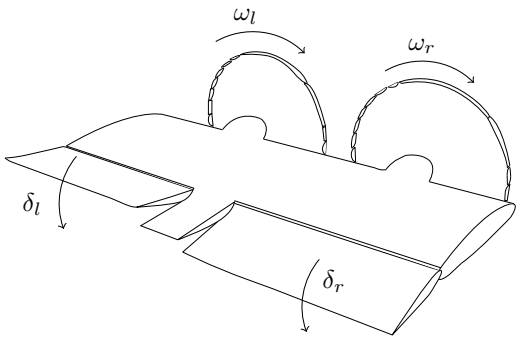

Fig. 3: A typical representation of the *MAVion* with our definitions of control inputs.

TABLE I: *MAVion* specifications.

Parameters	Values	SI Units
Mass	0.438	[Kg]
Mean Chord	0.21	[m]
Wingspan	0.42	[m]
Max Forward Speed	30	[m/s]
Wing Area	0.0882	$[m^2]$
I_{xx}	0.0036	[Kg m^2]
I_{yy}	0.0036	[Kg m^2]
I_{zz}	0.0072	[Kg m^2]

where $\boldsymbol{x} \in \mathbb{R}^{10}$, $\boldsymbol{u} \in \mathbb{R}^4$, $\boldsymbol{w} \in \mathbb{R}^3$ are, respectively, vehicle state, actuation inputs and wind disturbances, given by

$$\boldsymbol{x} = \begin{pmatrix} \boldsymbol{v}_l & \boldsymbol{\omega}_b & q \end{pmatrix}^T \tag{2}$$

and

$$\boldsymbol{u} = \begin{pmatrix} \omega_l & \omega_r & \delta_l & \delta_r \end{pmatrix}^T \tag{3}$$

In equation (2), $\boldsymbol{v}_l \in \mathbb{R}^3$, $\boldsymbol{\omega}_b \in \mathbb{R}^3$, $q \in \mathbb{R}^4$, denote respectively, vehicle velocity in local NED frame, angular velocity in body frame, and vehicle attitude. Each of the control inputs in $\boldsymbol{u}$ are defined according to Figure 3. The mathematical description of $\gamma(\cdot)$ is relatively intricate and, therefore, we refer the interested reader to [29] for further information. Nonetheless, we mention that $\gamma(\cdot)$ is an analytic continuous singularity-free formulation over a complete 360^o angle-of-attack and sideslip flight envelope, and therefore, control-engineering-friendly, in sharp contrast with other switched models or look-up-table-based methods present in the literature. Additionally, the model incorporates fundamental nonlinear aerodynamics effects – e.g., post-stall and propeller-induced prop-wash. Incidentally, the tilt-body nature of the vehicle calls for a global numerically stable formulation of attitude and justifies the use of quaternions.

III. THEORETICAL CONTROL BACKGROUND

Considering all the above mentioned, control laws used to stabilize the transition from hover to forward flight mode of HMAVs are, in most cases, based on the principle of "switching" between different control approaches. Here we propose, two global control methods: a scheduled LQR algorithm which is model-based and has the advantage of being simple to tune in MIMO systems; and a continuous adaptive controller, where no knowledge about the controlled system is required, called MFC. In our transition flight application, the choice to use such approach is due to the difficulty to derive a reliable and representative aerodynamic model for HMAVs.

A. Scheduled Linear Quadratic Regulator

For comparison purposes, we pursue a traditional full-state feedback scheduled-LQR control design, as previously done in [10]. LQR cost function gains are carefully chosen to accommodate for non-modeled effects of $\gamma(\cdot)$ in equation (1), e.g., discretization (bandwidth) of actuation inputs, wind disturbances and state estimation errors. For a given trim point the scheduled LQR computes a new matrix of gains K. As a result, it requires several gains to control the entire flight envelope (in the order of 10 matrix of gains, each one composed by 4 rows and 9 columns). An additional interesting point – although often overlooked or not commented in detail – is that quaternion-based nonlinear models linearization yields non-controllable linear models that preclude LQR control design. To overcome this issue we employ the virtual input strategy detailed in [30].

B. Model-free control approach

We present briefly the main theoretical principles of some research works dealing with on-line estimation and model-free control approach. Let's consider the following non linear state-space representation defined by :

$$\begin{cases} \dfrac{dx}{dt} = f(x,u) \\ y = h(x,u) \end{cases} \tag{4}$$

where $x(t)$, $u(t)$, $y(t)$ are the state, input and output vectors respectively. The output $y(t)$ is not directly available but rather it is observed through a noise corruption. A model for the output can be described by the following equation :

$$y_m(t) = y(t) + \omega(t) \tag{5}$$

where $\omega(t)$ is the observation noise. The exploitation of MFC principles requires the definition of a particular SISO model, named *Ultra-Local Model*, which corresponds to replace the unknown dynamic by a purely numerical model :

$$y_m^{(v)} = F + \alpha \cdot u \tag{6}$$

In equation (6), α is an element of $\mathbb{R}$ and is a non-physical constant parameter which allows us to define the same magnitude between $y_m^{(v)}$ and u. Moreover, the exploitation of this numerical model requires the knowledge of F. This quantity represents the real dynamics of the model as well as the different disturbances which could damage the output-system performances. Thus, an accurate estimation of F, defined as $\hat{F}$, is crucial and plays an import role in the MFC performance. Assuming that we do not know any model of the plant, its estimation can be calculated directly from measurements of y_m and u, with y_m corrupted by various noise sources provided from measurements devices.

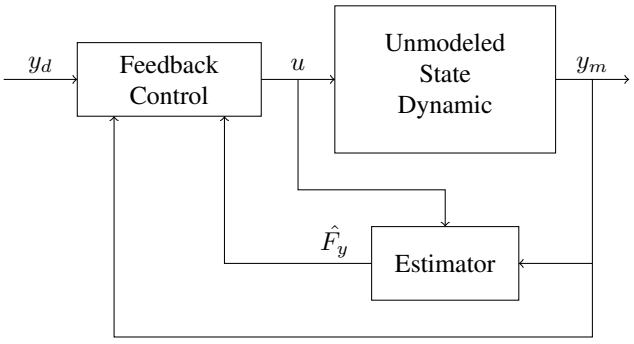

Fig. 4: Overall Model-Free Control schema.

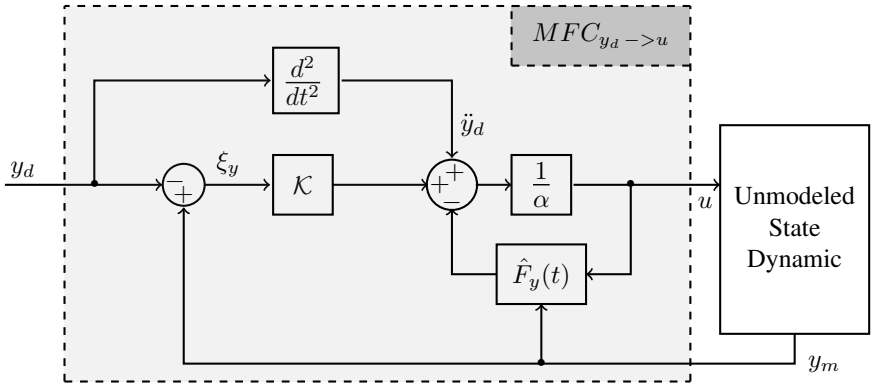

Fig. 5: Detailed Model-Free Control schema for a specific output dynamic y. Proportional-Derivative control $\mathcal{K}$. $\hat{F}_y(t)$ estimator of dynamic and disturbances and α a non-physical constant parameter.

Although significant work has been done on the development of derivative estimators such as [31] which uses recent algebraic identification techniques to estimate the derivative of noised measurements. We propose a simpler method that facilitates its implementation in real-time applications. Therefore, a suitable approximation of F in equation (6) is explained for the particular case of v = 1 and v = 2 using the classic *Laplace transform*. The following describe our proposed algorithm for a first-order dynamic estimation :

- For ($v = 1$), the *Ultra-Local Model* becomes :

$$\dot{y}_m = F + \alpha \cdot u \tag{7}$$

Referring to elementary operational calculus we transform the equation (7) to equation (8) :

$$sY_m(s) - y_m(0) = \frac{F}{s} + \alpha U(s) \tag{8}$$

Where $Y_m(s)$ and $U(s)$ corresponds to the *Laplace transforms* of y_m and u. By differentiating one the previous equations we are able to rid the initial condition $y_m(0)$:

$$s\frac{dY_m(s)}{ds} + Y_m(s) = -\frac{F}{s^2} + \alpha\frac{dU(s)}{ds} \tag{9}$$

However, s in the time domain corresponds to the derivation with respect to time and it is sensitive to noise corruptions. Therefore, in order to reduce both noise and numerical computation errors on the output estimation, we replace the derivative terms by integrators ($\frac{1}{s}$) who have robust properties with respect to noise. Thus, multiplying both sides of equation (9) by s^{-2}, we obtain :

$$\frac{dY_m(s)}{s\,ds} + \frac{Y_m(s)}{s^2} = -\frac{F}{s^4} + \frac{\alpha}{s^2}\frac{dU(s)}{ds} \tag{10}$$

Using inverse Laplace operator, equation (10) can be transferred back to the time domain employing convolution formula and classic *Inverse Laplace transforms* or *Cauchy's formula* to reduce multiple integrals in a simple one :

$$\hat{F} = \frac{-6}{T^3}\int_{t-T}^{t}[(T-2\sigma)y_m(\sigma) - \alpha\sigma(T-\sigma)u(\sigma)]d\sigma \tag{11}$$

Equation (11) estimates the dynamic of a first-order system from measurements of a corrupted signal (y_m). The result is a constant parameter $\hat{F}$ which is valid during the interval $[t-T, t]$. $\hat{F}$ is updated for each new sampling time and integral properties assure the attenuation of the noise.

- For ($v = 2$), the *Ultra-Local Model* becomes :

$$\ddot{y}_m = F + \alpha \cdot u \tag{12}$$

We apply exactly the same steps from equation (8) to equation (11). This time, for a second-order dynamic described in equation (12).

$$s^2Y_m(s) - sy_m(0) - \dot{y}_m(0) = \frac{F}{s} + \alpha U(s) \tag{13}$$

The initial condition is rid by differentiating twice the previous equation which leads to equation (14) :

$$2Y_m(s) + 4s\frac{dY_m(s)}{ds} + s^2\frac{d^2Y_m(s)}{ds^2} = \frac{2F}{s^3} + \alpha\frac{d^2U(s)}{ds^2} \tag{14}$$

The sensitivity to the noise generated by both differentiators s and s^2, is eliminated by adding integrators. Therefore, multiplying both sides of equation (14) by s^{-3} leads to equation (15).

$$\frac{2Y_m(s)}{s^3} + \frac{4}{s^2}\frac{dY_m(s)}{ds} + \frac{1}{s}\frac{d^2Y_m(s)}{ds^2} = \frac{2F}{s^6} + \frac{\alpha}{s^3}\frac{d^2U(s)}{ds^2} \tag{15}$$

Applying *Inverse Laplace transform*, we obtain the estimator ($\hat{F}$) for a second-order system represented in the time domain :

$$\hat{F} = \frac{5!}{2T^5}\int_{t-T}^{t}[(T-\sigma)^2 - 4\sigma(T-\sigma) + \sigma^2]y_m(\sigma)d\sigma - [\frac{\alpha}{2}\sigma^2(T-\sigma)^2u(\sigma)]d\sigma \tag{16}$$

Algorithm 1 $\hat{F}$ Estimator

1: **procedure**
2: $v \leftarrow$ Define estimator order
3: **step 1:** Write the *Ultra-Local Model*
4: **step 2:** Calculate the *Laplace transforms*
5: **step 3:** Derive step 2 v times with respect to s
6: **step 4:** Multiply the step 3 by $s^{-(v+1)}$
7: **step 5:** Calculate the *Inverse Laplace transforms*
8: **end procedure**;

The interval integration, with length T, corresponds to the window width of a receding horizon strategy. The choice of this quantity results in a trade-off. The idea is to choose the window width small so as to calculate the derivative estimate within an acceptable short delay but large enough in order to sustain the low pass filtering property for suppressing measurement noise on $y_m(t)$. Based on such estimator it is possible to design a model-free control estimating on-line the dynamic of $y(t)$ from a purely numerical model of the system.

The general form of the MFC architecture presented in Figure 4 and detailed in Figure 5 allows us to define the close-loop control such as :

$$u = \underbrace{-\frac{\hat{F}}{\alpha}}_{\text{NL Cancellation}} + \underbrace{\frac{y_d^{(v)} + \mathcal{K}(\xi)}{\alpha}}_{\text{Closed loop tracking}} \tag{17}$$

where the quantity $\xi = y_m - y_d$ is the tracking error and $\mathcal{K}(\xi)$ is a closed loop feedback controller. Usually, in order to control a first-order system we use $\mathcal{K}$ as a proportional gain and for a second-order stabilization $\mathcal{K}$ represent a proportional-derivative gain. We recognize in equation (17) the typical mathematical expression of a "nominal control" in the "flatness-based" control (see [32] for details) in which the non-linear terms $\hat{F}$ is summed with a closed loop tracking of a reference trajectory $t \rightarrow y_d(t)$.

Remark : In our study-case, a second order *Ultra-Local Model* (v=2) was chosen to represent each attitude dynamic of the MAV. It is important to emphasize that MFC algorithms have been developed to Single-Input Single-Output (SISO) systems and *MAVion* has been modeled by four inputs and ten outputs. Wherefore, a control architecture composed by multiple SISO MFCs, is proposed. Let's consider a single state dynamic, for example the pitch angle θ, that is controlled by symmetric flap deflections (δ_l,δ_r), see Figure 3. Thus, by analogy with equation (12) and from Figure 6, the *Ultra-Local Model* can be represented by the following equation :

$$\ddot{\theta} = F_\theta + \alpha_\theta \cdot \delta_e \tag{18}$$

From the general form of equation (17), the closed-loop can be computed by :

$$\delta_e = \frac{-\hat{F}_\theta + \ddot{\theta}_d + \mathcal{K}(\xi_\theta)}{\alpha_\theta} \tag{19}$$

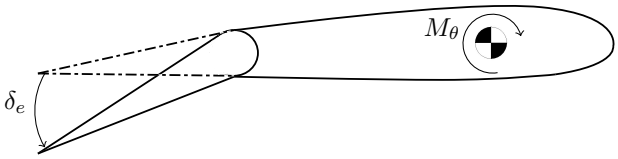

Fig. 6: Moment generated around *y-axis* by symmetrical flap deflections.

Substituting equation (19) in equation (18) with $\mathcal{K}$ equals to proportional-derivative gains, leads to :

$$\ddot{\theta} = F_\theta - \hat{F}_\theta + \ddot{\theta}_d + K_p\,\xi_\theta + K_d\,\dot{\xi}_\theta \tag{20}$$

It follows that theoretically, if the error (ξ_{F_θ}) between the pitch angle estimator ($\hat{F}_\theta$) and the real pitch angle dynamic (F_θ), is approximately zero during $[t-T, t]$:

$$\xi_{F_\theta} = F_\theta - \hat{F}_\theta \approx 0$$

The previous assumption allows us to simplify the equation (20) to equation (22).

$$\ddot{\xi}_\theta = \ddot{\theta} - \ddot{\theta}_d \tag{21}$$

$$\ddot{\xi}_\theta - K_p\,\xi_\theta - K_d\,\dot{\xi}_\theta = 0 \tag{22}$$

Combining all these results, the pitch angle and its dynamic error (ξ_θ) can be easily tuned by proportional and derivative gains, respectively K_p and K_d. The *NL Cancellation* term in equation (17), compensates the disturbances that could perturb the output state. Such an approach is easy and systematic for more complex dynamical systems than the ones represented in §II. Note that, a simple proportional-derivative controller is enough to ensure convergence of the error to zero. Such integration effect is implicitly involved in the model-free control.

The same steps from equation (18) to equation (22) have been done to control the forward speed in order to assure the flight stability during the transitioning flight. The MFC parameters that were used in this preliminary study are shown in the Table II.

TABLE II: MFC parameters

Gains	Pitch angle (θ)	Forward speed
T	6	5
α	850	4000
Kp	5	2
Kd	5	2

IV. SIMULATION FLIGHT AND ANALYSIS

We now illustrate the control performance reached by the scheduled-LQR and MFC during a transitioning flight, both strategies were used to stabilize the tail-sitter model described in §II-B. The simulation is discretized at 500 Hz and includes additional sensor noises, state estimation errors and wind disturbances around 4 m/s (w_u, w_w), as we can see in Figure 8f. Wind disturbances are imposed along x and z axes in order to disturb the pitch angle, especially during the transition phase. Propeller speed saturation is set at 1000 (rad/s) and flap deflections are saturated at 30 degrees, however they are not reached as can be seen in Figure 8d and 8e, respectively. In Figure 8a, the flight path describes a vertical take-off, followed by transitioning flight and the simulation ends when the aircraft is stabilized in forward flight mode. Transition from hovering to forward flight is triggered and controlled by means of desired forward speed, which is zero in hovering mode. Transitioning flight is performed naturally by increasing desired forward speed. Both controllers work according to this strategy, but with small differences. Scheduled LQR uses a look-up-table with predefined trim points and knows the desired pitch angle which was predefined by means of wind-tunnel campaigns. MFC does not have any informations about the system or about trim points. In order to compute the pitch angle reference for transitioning phase, MFC uses a different control architecture in Figure 7, where the desired attitude, such as desired pitch angle, is computed by an outer-loop. This strategy allows us to define a singular and continuous controller with constant gains that is able to stabilize the entire flight envelope.

The vertical takeoff is realized at the beginning of the simulation (t ∈ [0;5]) where the propeller rotations, shown in Figure 8d, increase to reach a higher altitude. During hovering flight (t ∈ [5;18]), the aircraft is more susceptible to perturbations caused by horizontal wind (w_u). However, because of low forward speed, aerodynamic effects are predominantly caused by prop wash. In this phase of the flight, the prop wash is high and important due to high propeller rotations that generate thrust to equalize the weight force, in order to maintain a desired altitude. Despite pitch oscillations in Figure 8c due to winds, both controllers are able to stabilize the MAV and the control authority of both controllers is also sufficient to handle disturbances. However, LQR can not manage these disturbances as good as MFC. That implies oscillations in forward speed, as can be seen in Figure 8b, and position errors may result.

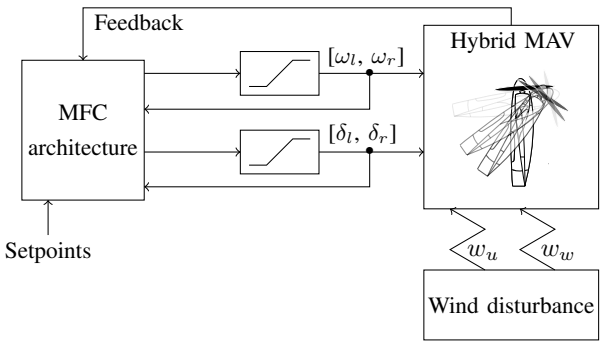

Fig. 7: MFC architecture designed for HMAVs with saturated control inputs. Propeller speeds (ω_l, ω_r) and flap deflections (δ_l, δ_r) are computed by means of *MFC architecture* block.

Figure 8c also clearly shows the pitch angle during the transitioning flight. The desired pitch angle trajectory computed by the LQR takes 5 seconds to perform the transition and MFC perform the transition in about 10 seconds. In this part of the flight (t ∈ [18;28]), both controllers ensured stability for pitch angle variation from hovering ($\theta = 90°$) to forward flight ($\theta \approx 10°$). In forward flight, a static error in the trajectory controlled by LQR is highlighted. This is visible especially at 30th seconds of simulation when wind disturbances are increased.

For comparison purposes, we evaluate the performance of both controllers, LQR and MFC, according to the following criterion :

$$RMSE_y = \sqrt{\frac{\sum_1^n (y - y_d)^2}{n}} \tag{23}$$

where n is the sample quantity. *Root Mean Square Error (RMSE)* is frequently employed in estimation to measure the differences between values predicted by an estimator and the values actually observed. Similarly, we propose to use this criterion to quantifies the error between the desired output reference and the measured value. The smaller the RMSE, the higher the controller performance. As the RMSE is sample-dependent, both control algorithms run at the same sampling frequency.

Table III shows the RMSE results for hovering flight mode (t ∈ [0;18]). We compute this criterion for pitch angle and for forward speed in disturbed flight conditions. MFC presents better robustness properties than LQR.

TABLE III: LQR vs MFC : RMSE - Hovering flight

y	Scheduled LQR	MFC	SI Units
Pitch angle (With wind)	4.8131	3.2893	[°]
Forward speed (With wind)	0.3170	0.2293	[m/s]

In Table IV, the performance of both controllers is demonstrated for the entire flight envelope : hovering, transition and forward flight (t ∈ [0;50]). Firstly, RMSE was computed for pitch angle and for forward speed in calm conditions (No wind). Secondly, the RMSE was computed in disturbed flight conditions (With wind).

TABLE IV: LQR vs MFC : RMSE - Entire flight envelope

y	Scheduled LQR	MFC	SI Units
Pitch angle (No wind)	3.0646	1.5131	[°]
Forward speed (No wind)	0.8699	1.4613	[m/s]
Pitch angle (With wind)	4.5357	2.7858	[°]
Forward speed (With wind)	1.8349	1.4700	[m/s]

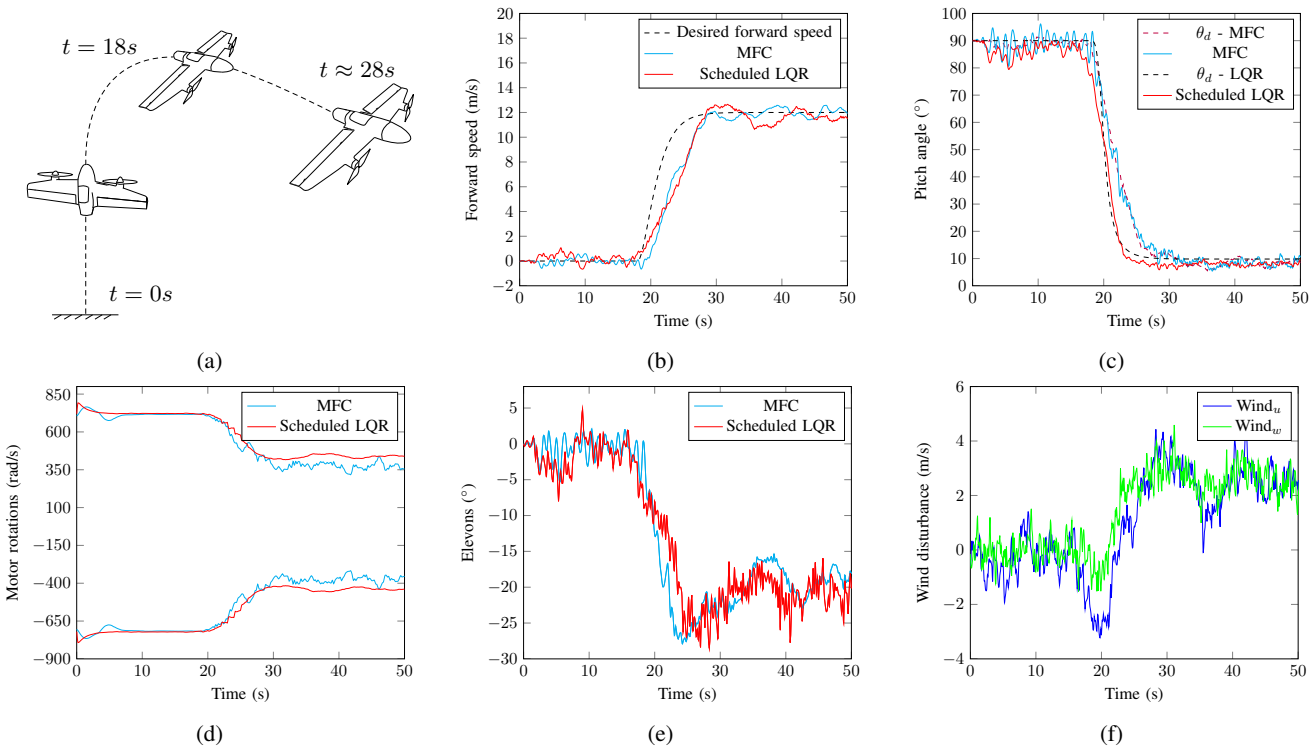

Fig. 8: Transition flight tests. On the top, from left to right: Flight path, forward-speed and pitch angle. On the bottom: propeller speeds ($\omega_l < 0$ and $\omega_r > 0$) due to counter-rotation sense, elevon deflections (δ_l and δ_r) convention negative for pitch-up, and wind disturbance along x and z axes.

Fig. 9: Cyclone MAV.

It can be concluded that LQR approach performed a better velocity tracking than MFC for simulations without wind. On the other hand, MFC exhibited strong disturbance-rejection properties in windy conditions for hovering and forward flight, and for the transitioning between both. Thus, the new control strategy employed herein which is based on the properties of MFC ensures a stable flight during the hovering-to-forward trajectory. Furthermore, MFC is able to control an unmodeled and under-actuated system despite all aerodynamic-coefficients alterations due to variations in angle of attack and control effectiveness.

The performance of the proposed control architecture based on MFC algorithms is shown through numerical simulation during hovering, transitioning and forward flight for a generic HMAV. The next steps consist to implement this control architecture in a new HMAV whose aerodynamic characteristics were improved, such as the *Cyclone* shown in Figure 9. Therefore, we will be able to study more precisely the MFC's adaptability.

V. CONCLUSION

This preliminary study proposed a potential method for designing controllers without any knowledge of the MAV. Initial results of attitude and velocity control using MFC for a Fixed-Wing MAV with transitioning flight capabilities, are presented. Simulation results showed a better attitude control obtained by MFC, both with wind or without wind. The flight velocity is controlled more accurately with scheduled LQR when there is no wind, however MFC showed a better performance when there is uncertainty in the environment, such as wind. This demonstrates the disturbance rejection and control of unmodeled dynamics with MFC by the means of its adaptive properties. Overall, MFC demonstrates a promising performance over LQR, and can be used for unconventional configurations such as tail-sitters, as well as during the unmodeled flight phases such as post-stall.

VI. FUTURE WORK

Further research is required to analyze the MFC properties in detail, such as exhaustive comparative studies between MFC, nonlinear control approaches and adaptive control

technique. MFC algorithms are being implemented in *Paparazzi* open-source autopilot system (cf. Paparazzi project at: `https://wiki.paparazziuav.org/`) and experimental flights will be presented soon.

REFERENCES

[1] M. Bronz, E. J. J. Smeur, H. G. de Marina, and G. Hattenberger, "Development of A Fixed-Wing mini UAV with Transitioning Flight Capability," *35th AIAA Applied Aerodynamics Conference, AIAA Aviation Forum*, (AIAA 2017-3739), June 2017.

[2] Adnan S. Saeed, Ahmad Bani Younes, Shafiqul Islam, Jorge Dias, Lakmal Seneviratne, Guowei Cai, "A Review on the Platform Design, Dynamic Modeling and Control of Hybrid UAVs," *International Conference on Unmanned Aircraft Systems (ICUAS)*, Denver, Colorado, USA, pp. 806-815, June 2015.

[3] Jason M. Beach, Matthew E. Argyle, Timothy W. McLain, Randal W. Beard and Stephen Morris, "Tailsitter Attitude Control Using Resolved Tilt-Twist," *International Conference on Unmanned Aircraft Systems (ICUAS)*, Orlando, FL, USA, May 27-30, 2014.

[4] E. J. J. Smeur, G. C. H. E. de Croon, and Q. Chu, "Cascaded Incremental Nonlinear Dynamic Inversion Control for MAV Disturbance Rejection," *Control Engineering Practice*, pp. 79-90, January 2018.

[5] J. Escareño, R. H. Stone, A. Sanchez and R. Lozano, "Modeling and Control Strategy for the Transition of a Convertible Tail-sitter UAV," *Proceedings of the European Control Conference*, Kos, Greece, July 2007.

[6] D. Pucci, T. Hamel, P. Morin and C. Samson, "Nonlinear Control of Aerial Vehicles Subjected to Aerodynamic Forces," *52nd IEEE Conference on Decision and Control*, December 10-13 2013.

[7] V. Martinez, O. Garcia, A. Sanchez, V. Parra, and A. Escobar, "Adaptive backstepping control for a convertible UAV," *Workshop on Research, Education and Development of Unmanned Aerial Systems (RED-UAS)*, November 23-25, 2015.

[8] P. Casau, D. Cabecinhas, and C. Silvestre, "Hybrid Control Strategy for the Autonomous Transition Flight of a Fixed-Wing Aircraft," *50th IEEE Conference on Decision and Control and European Control Conference (CDC-ECC)*, November 2013.

[9] P. Casau, D. Cabecinhas, and C. Silvestre, "Autonomous Transition Flight for a Vertical Take-Off and Landing Aircraft," *IEEE transactions on control systems technology*, Orlando, FL, USA, December 12-15, 2011.

[10] L. R. Lustosa, F. Defay, and J.-M. Moschetta, "Longitudinal study of a tilt-body vehicle: modeling, control and stability analysis," *International Conference on Unmanned Aircraft Systems (ICUAS)*, Denver, Colorado, USA, pp. 816-824, June 2015.

[11] L. R. Lustosa, J. M. O. Barth, J.-P. Condomines, F. Defay, and J.-M. Moschetta, "Team MAVion entry in the IMAV17 outdoor challenge A tail-sitting trajectory-tracking μUAV," *International Micro Air Vehicle Conference and Competition*, Toulouse, France, September 2017.

[12] D. Chu, J. Sprinkle, R. Randall, and S. Shkaraye, "Simulator development for transition flight dynamics of a vtol mav," *International Journal of Micro Air Vehicles*, 2(2):6989, 2010.

[13] E. J. J. Smeur, Q. Chu, and G. C. H. E. de Croon, "Adaptive Incremental Nonlinear Dynamic Inversion for Attitude Control of Micro Air Vehicles," *Journal of guidance, control and dynamics*, Vol. 39, No. 3, pp. 450-461, March 2016.

[14] T. P. Lillicrap, J. J. Hunt, A. Pritzel, N. Heess, T. Erez, Y. Tassa, D. Silver, and D. Wierstra, "Continuous control with deep reinforcement learning," *6th International Conference on Learning Representations*, Vancouver, 2016.

[15] M.-B. Radac, R. E. Precup, R. C. Roman, "Model-Free control performance improvement using virtual reference feedback tuning and reinforcement Q-learning," *International Journal of Systems Science*, 2017.

[16] M. Fliess, and C. Join, "Model-free control," *International Journal of Control, Taylor & Francis*, pp. 2228-2252, 2013.

[17] Ouassim Bara, M. Fliess, C. Join, Judy Daye, and Seddik M. Djouadi, "Toward a model-free feedback control synthesis for treating acute inflammation," *Journal of Theoretical Biology*, pp. 26-37, 2018.

[18] Younes AI Younes, Ahmad Drak, Hassan Noura, Abdelhamid Rabhi and Ahmed EI Hajjaji, "Model-Free Control of a Quadrotor Vehicle," *International Conference on Unmanned Aircraft Systems (ICUAS)*, Orlando, FL, USA, pp. 1126-1131, May 2014.

[19] N. O. Pérez-Arancibia, P.-E. J. Duhamel, K. Y. Ma, R. J. Wood, "Model-Free Control of a Hovering Flapping-Wing Microrobot," *Journal of Intelligent & Robotic Systems*, pp. 95-111, January 2015.

[20] Aneesh N. Chand, Michihiro Kawanishi, Tatsuo Narikiyo, "Non-linear model-free control of flapping wing flying robot using iPID," *IEEE International Conference on Robotics and Automation (ICRA)*, May 2016.

[21] Younes Al Younes, Ahmad Drak, Hassan Noura, Abdelhamid Rabhi and Ahmed El Hajjaji, "Robust Model-Free Control Applied to a Quadrotor UAV," *Journal of Intelligent & Robotic Systems*, pp. 37-52, December 2016.

[22] Haoping Wang, Xuefei Ye, Yang Tian, Gang Zheng, and Nicolai Christov, "Model-FreeBased Terminal SMC of Quadrotor Attitude and Position," *IEEE Transactions on Aerospace and Electronic Systems*, Vol. 52, pp. 2519 - 2528, October 2016.

[23] Gabriele Di Francesco and Massimiliano Mattei, "Modeling and Incremental Nonlinear Dynamic Inversion Control of a Novel Unmanned Tiltrotor," *Journal of Aircraft*, 2015.

[24] Haowei Gu, Ximin Lyu, Zexiang Li, Shaojie Shen, and Fu Zhang, "Development and Experimental Verification of a Hybrid Vertical Take-Off and Landing (VTOL) Unmanned Aerial Vehicle (UAV)," *International Conference on Unmanned Aircraft Systems (ICUAS)*, Miami, FL, USA, June 13-16, 2017.

[25] J. L. Forshaw, V. J. Lappas, and P. Briggs, "Transitional Control Architecture and Methodology for a Twin Rotor Tailsitter," *Journal of Guidance, Control and Dynamics*, Vol. 37, No. 4, JulyAugust 2014.

[26] J. L. Forshaw, and V. J. Lappas, "High-Fidelity Modeling and Control of a Twin Helicopter Rotor Tailsitter," *AIAA Guidance, Navigation, and Control Conference*, August 2011, Portland, Oregon, 2011.

[27] Gerardo Flores and R. Lozano, "Transition Flight Control of the Quad-Tilting Rotor Convertible MAV," *International Conference on Unmanned Aircraft Systems (ICUAS)*, pp.789-794, 2013.

[28] Christos Papachristos, Kostas Alexis and Anthony Tzes, "Hybrid Model Predictive Flight Mode Conversion Control of Unmanned Quad-TiltRotors," *European Control Conference (ECC)*, pp.1793-1798, July 17-19, Zürich, Switzerland, 2013.

[29] L. R. Lustosa, F. Defay, and J.-M. Moschetta, "A global singularityless polynomial-like aerodynamics model for algorithmic flight control of tail-sitters," *AIAA Journal of Guidance, Control, and Dynamics* (to appear).

[30] L. R. Lustosa, F. L. Cardoso-Ribeiro, F. Defay, and J.-M. Moschetta, "A new look at the uncontrollable linearized quaternion dynamics with implications to LQR design in underactuated systems," *European Control Conference*, 2018.

[31] J. Zehetner, J. Reger, and M. Horn, "A Derivative Estimation Toolbox based on Algebraic Methods - Theory and Practice," *2007 IEEE International Conference on Control Applications*, pp. 331-336, Singapore, 2007.

[32] M. Mboup, C. Join, and M. Fliess, "A revised look at numerical differentiation with an application to nonlinear feedback control," *In 15th Mediterranean conference on Control and automation (MED'07)*, Athenes, Greece, 2007.